Transition-metal-mediated electrocatalytic CO_2 reduction: from nanoparticles to single-atom catalysts

by

Song Lu

Thesis submitted in fulfilment of

the requirements for the degree of

PHILOSOPHIAE DOCTOR

(PhD)

Faculty of Science and Technology

Department of Energy and Petroleum Engineering

2023

University of Stavanger
NO-4036 Stavanger
NORWAY
www.uis.no

ISBN: 978-82-8439-176-2
ISSN: 1890-1387
PhD thesis UiS No. 709

Acknowledgement

First and foremost, I would like to express my sincere gratitude to my supervisor Prof. Zhixin Yu for his invaluable guidance and unwavering support throughout my research journey. His expertise and insightful feedback have been instrumental in shaping my ideas and strengthening my arguments. Moreover, his constant encouragement and motivation have been a source of inspiration and have helped me overcome the challenges I encountered during this process. I am truly grateful for the opportunity to work with such a dedicated and knowledgeable supervisor, and I will always cherish the lessons and skills I have gained under his mentorship. I also would like to extend my heartfelt appreciation to my co-supervisor, Dr. Fengliu Lou from Beyonder AS, for his exceptional mentorship, and continuous motivation that have contributed significantly to the success of my thesis.

Special thanks to previous PhD and master students from catalysis group, Huong Lan Huynh, Kristian Stangeland, Yang Zhang, Obinna Egwu Eleri, Vladislav Volkov who gave me much help in the beginning of my project. Their friendship has made this journey more enjoyable and rewarding.

To all staff and engineers at IEP, I am extremely grateful to get substantial help in the past three years. Special thanks to Kim Vorland, Dagfinn Sleveland, Inger Johanne Olsen, Jorunn Vrålstad who give me crucial help. Without your help in laboratory, my experiments cannot be performed smoothly.

Last but not the least, great thanks and appreciation to my wife, for your love, support and understanding. To my parents and all close friends, I really appreciate your support.

Song Lu

June 2023, Stavanger

Abstract

With the rapid development of the global economy, energy crisis and environment issues have become increasingly prominent. Carbon dioxide (CO_2) is a primary greenhouse gas (CHG), while it could also be a valuable carbon source. In recent years, electrochemical CO_2 reduction reaction (ECR) has received considerable attention among various CO_2 conversion technologies. Nevertheless, physicochemical properties of the CO_2 molecule make electrochemical conversion of CO_2 challenging. Despite that great progress has been made to exploit electrocatalysts for ECR, the process is still impeded by the sluggish kinetics, poor product selectivity, catalyst deactivation, and high overpotential. Therefore, it is highly desirable to develop electrocatalysts with high activity and selectivity for ECR.

Loading metal nanoparticles (NPs) on two-dimensional (2D) materials as electrocatalysts for ECR has been reported extensively in literature. Herein, we studied silver loaded boron-doped g-C_3N_4 nanocomposite (Ag-B-g-C_3N_4) for efficient ECR to CO by combined experimental work and first-principles study. Theoretical simulation demonstrated that introduction of Ag NPs and the B atom could greatly decrease the adsorption free energy for the *COOH intermediate generation. B-g-C_3N_4 could not exhibit the obvious enhancement of ECR performance, while the Ag-B-g-C_3N_4 catalyst exhibited a total current density of 2.08 mA cm^{-2} and a CO Faradaic efficiency of 93.2% under the potential of −0.8 V vs the reversible hydrogen electrode (RHE).

It has been well established that the catalytic activity can be further improved by reducing the size of catalysts. Specifically, single atoms catalysts (SACs) with single atom as active center have aroused huge interest due to maximum atom utilization and excellent performance in various catalytic reactions. Therefore, we investigated the single transition metal atoms (V, Cr, Mn, Fe, Co, Ni) embedded O group terminated Nb_2N monolayer (Nb_2NO_2) as ECR catalysts by first-principles calculation. It is found that TM@Nb_2NO_2 show excellent CO_2 adsorption capacity, which benefits CO_2 activation. V, Cr and Ni@ Nb_2NO_2 are identified as efficient electrocatalysts for ECR

to CH_4.

Subsequently, 2D metal material antimonene from VA group have been studied as support for single transition metal atoms (TM = Sc, Ti, V, Cr, Mn, Fe, Co, Ni, Cu, Zn, Mo, Ru, Rh, Pd, Ag, Cd, Ir, Pt and Au) atoms in ECR by first-principles calculation. Interestingly, non-precious TM atoms supported on Sb monolayer show higher ECR selectivity than hydrogen evolution reaction (HER). Moreover, the primary ECR product of these non-precious metal-based SACs is CH_4, except for Zn which produces HCOOH. The interaction between TM atom and Sb monolayer greatly affects the intrinsic activity of SACs.

The intrinsic activity of SACs for ECR could be further enhanced by coordination environment. Therefore, we prepared N, S-codoped carbon black incorporating Ni single atoms as SAC for ECR. The Ni-NS-C catalyst exhibited a very high conversion efficiency of 99.7 % to CO with a high total current density of 20.5 mA cm^{-2} under −0.8 V (vs. RHE), outperforming S-free Ni−N−C electrocatalyst. It also displayed excellent stability without activity decay after electrocatalysis for 19 h. A combination of experimental investigations and first-principles calculation demonstrates that the high activity and selectivity of ECR to CO is due to a synergistic effect of the S and Ni−N_X moieties.

Furthermore, it is worth noting that most studies could only reveal inadequate structural details of metal centers and NM ligands in M−N−C due to the limitations of experimental techniques. Meanwhile, structures with subtle differences are treated similarly, resulting in ambiguous reaction mechanisms on active centers. Therefore, a series of NM heteroatom dopants modified TM@N_4 configurations embedded on graphene sheet are proposed. We performed a computational screening of the ECR to CO activity and stability of the NM decorated TM@N_4. We found that NM atoms could effectively improve the ECR activity to CO on Ni and Cu@N_4 but deteriorate the ECR activity on Co@N_4. However, NM dopants could not break linear relationship between key intermediates for the catalysts.

Except for NM atom modifying SACs properties, constructing heteronuclear dimer sites to form dual-atom catalysts (DACs) is another efficient way to tune the coordination environment and the electronic properties of the SAC active centers. Therefore, Mn and Ni SACs, Mn and Ni homonuclear DACs, and Mn−Ni heteronuclear DAC were synthesized. Mn−Ni DAC displayed the highest CO Faradaic efficiency of 98.7% at −0.7 V versus reversible hydrogen electrode (vs. RHE) with CO partial current density of 16.8 mA cm^{-2} and excellent stability. First-principles calculation disclosed that high valence state of Mn atom and low valence state of Ni atom could deteriorate *CO desorption and enhance *COOH binding strength. Moreover, the active sites of Mn−Ni−NC could facilitate CO_2 protonation by enhanced *COOH adsorption because C and O atom of *COOH prefer to bind Ni and Mn atoms, respectively. During the *CO desorption process, only Ni atom bonds with C atom of *CO, promoting *CO desorption. Therefore, the scaling relationship between binding strength of intermediates was broken, resulting in superior performance for the Mn−Ni−NC catalyst in ECR to CO.

List of Publications

I. Recent Progress in Two Dimensional Materials for Electrocatalytic CO_2 Reduction

S. Lu, F. Lou and Z. Yu

Catalysts, 2022, 12, 228

DOI: 10.3390/catal12020228

II. Efficient Electrochemical Reduction of CO_2 to CO by Ag-Decorated B-Doped g-C_3N_4: A Combined Theoretical and Experimental Study

S. Lu, Y. Zhang, M. F. Mady, W. M. Tucho, F. Lou and Z. Yu

Industrial & Engineering Chemistry Research, 2022, 61, 10400–10408.

DOI: 10.1021/acs.iecr.2c00152

III. Theoretical study of single transition metal atom catalysts supported on two-dimensional Nb_2NO_2 for efficient electrochemical CO_2 reduction to CH_4

S. Lu, Y. Zhang, F. Lou and Z. Yu

Journal of CO_2 Utilization, 2022, 62, 102069

DOI: 10.1016/j.jcou.2022.102069

IV. Electrochemical reduction of CO_2 to CH_4 over transition metal atom embedded antimonene: First-principles study

S. Lu, H. L. Huynh, F. Lou, M. Guo and Z. Yu

Journal of CO_2 Utilization, 2021, 51, 101645

DOI: 10.1016/j.jcou.2021.101645

V. Sulfur-Decorated Ni−N−C Catalyst for Electrocatalytic CO_2 Reduction with Near 100 % CO Selectivity

S. Lu, Y. Zhang, M. F. Mady, O. E. Eleri, W. M. Tucho, M. Mazur, A. Li, F. Lou, M. Gu and Z. Yu

ChemSusChem, 2022, 15, e202200870

DOI: 10.1002/cssc.202200870

VI. Regulating the Coordination Environment of Single-Atom Catalysts for Electrocatalytic CO_2 Reduction

S. Lu, F. Lou, Y. Zhao and Z. Yu

Journal of Colloid and Interface Science, 2023, 646, 301-310

DOI: 10.1016/j.jcis.2023.05.064

VII. Breaking scaling relations for highly efficient electroreduction of CO_2 to CO on atomically dispersed heteronuclear dual-atom catalyst

S. Lu, M. Mazur, K. Guo, D. C. Stoian, M. Gu, W. M. Wakshum and Z. Yu

(Submitted)

This thesis is based on above seven papers.

Additional Publications

I. Single transition metal atom embedded antimonene monolayers as efficient trifunctional electrocatalysts for the HER, OER and ORR: a density functional theory study

S. Lu, H.L. Huynh, F. Lou, K. Guo and Z. Yu

Nanoscale, 2021, 13, 12885

DOI: 10.1039/D1NR02235K

II. Non-precious metal activated $MoSi_2N_4$ monolayers for high-performance OER and ORR electrocatalysts: A first-principles study

S. Lu, Y. Zhang, F. Lou, K. Guo and Z. Yu

Applied Surface Science, 2022, 579, 152234

DOI: 10.1016/j.apsusc.2021.152234

III. Transition metal single-atom supported on PC_3 monolayer for highly efficient hydrogen evolution reaction by combined density functional theory and machine learning study

S. Lu, J. Cao, Y. Zhang, F. Lou and Z. Yu

Applied Surface Science, 2022, 606, 154945

DOI: 10.1016/j.apsusc.2022.154945

IV. Unexpected Bi-functional Co-g-GaN monolayer for detecting and scavenging toxic gases

Y. Zhao, Y. Wu and **S. Lu**

Materials today communications, 2023, 35, 105781

DOI: 10.1016/j.mtcomm.2023.105781 (corresponding author)

V. High-performance precious metal-free direct ammonia fuel cells endowed by Co-doped Ni_4Cu_1 anode catalysts

Z. Hu, **S. Lu**, F. Tang, D. Yang, C. Zhang, Q. Xiao and P. Ming

Applied Catalysis B: Environmental, 2023, 334, 122856

DOI: 10.1016/j.apcatb.2023.122856 (co-first author)

VI. A fullerene seeded strategy for facile construction of nitrogen-doped carbon nano-onions as robust electrocatalysts

K. Guo, Z. He, **S. Lu**, P. Zhang, N. Li, L. Bao, Z. Yu, L. Song, X. Lu

Advanced Functional Materials, 2023, 202302100

DOI: 10.1002/adfm.202302100 (co-first author)

Conference Presentations

I. **S. Lu**, H. L. Huynh, F. Lou, K. Guo and Z. Yu. Pt@Sb monolayer can be a trifunctional electrocatalyst for HER, OER and ORR. Poster presentation at the 19th Nordic Symposium on Catalysis. Espoo, Finland, 6-8 June 2022.

II. **S. Lu**, Y. Zhang, M. F. Mady, O. E. Eleri, F. Lou and Z. Yu. Sulfur-Decorated Ni−N−C Catalyst for Electrocatalytic CO_2 Reduction with Near 100% CO Selectivity. Oral presentation at the 19th International Symposium on Relations between Homogeneous and Heterogeneous Catalysis (online). Oslo, Norway, 27-30 June 2022.

III. **S. Lu**, F. Lou, Z. Yu. Sulfur-Decorated Ni−N−C Catalyst for Electrocatalytic CO_2 Reduction with Near 100% CO Selectivity. Oral presentation at the Norwegian catalysis symposium 2022. Stavanger, Norway, 1-2, December 2022.

Table of Contents

List of Figures

List of Tables

1. Introduction

1.1. CO_2 conversion

CO_2 is the main component of greenhouse gases which leads to environment concerns, and its concentration increased from approximately 280 ppm in early 1800s to 410 ppm today [1-3]. Without proper strategies to combat this problem, the steadily growing CO_2 emission will arouse the increase of the global-average temperature, loss of glaciers, rise of sea level and other climate issues [4]. To reverse these negative courses, technologies such as carbon capture and storage (CCS) have been pursued [5-7]. Despite tremendous efforts on CCS, including separating CO_2 from air or flue gas, storing the captured CO_2 is still a daunting challenge due to the risk of leakage, massive energy consumption, high cost and social acceptance [8-12]. An alternative approach is to utilize CO_2 as a raw material and convert them into value-added products, which has received extensive attention in the past decades [13-15]. Therefore, the conversion of CO_2 has been regarded as a promising route for closing the carbon cycle and producing value-added chemicals and fuels.

The conversion of CO_2 can be realized by a variety of technologies such as thermochemical, electrochemical, photochemical, radiochemical and biochemical reactions [16-24]. Among which, the reduction of CO_2 by electrochemical strategy is attractive and exhibits many advantages [25, 26]. For instance, the energy required for electrochemical reduction reactions can be provided by renewable energy such as solar, geothermal or wind energy. Besides, the reaction can be performed under ambient pressure and temperature. Moreover, the external voltages as well as electrolytes solutions can be adjusted to produce specific products. However, the physicochemical properties of CO_2 molecule make the electrochemical conversion processes challenging. To convert CO_2 into other products, the dissociation of C=O bond is essential and must overcome high energy barriers of about 750 kJ/mol. Besides, electrolyte solutions are generally water-based, which makes the reaction inefficient due to the poor CO_2 dissolution in water. In the past decades, both theoretical and experimental work have disclosed that the electrocatalysts play a vital role in catalytic processes [27-32]. For example, it had been proven that traditional metal electrocatalysts such as copper, platinum and gold can activate CO_2 and reduce it into valuable chemical products [33-35]. However, these catalysts suffer drawbacks such as high overpotential, poor stability, low selectivity, complex separation and low efficiency for specific products. In addition, the prices of the precious metals hamper the large-scale application of Pt catalysts. Therefore, developing efficient, cost-effective and durable alternatives to the traditional metal catalysts for electrocatalytic CO_2 reduction (ECR)

reaction is urgent.

1.2. Fundamentals of electrochemical CO_2 reduction

1.2.1. CO_2 properties and the reduction products

CO_2 is one of the most stable molecules with a strong O=C=O double bond, and its bond energy is higher than that of C−H and C−C bonds. During electrocatalytic processes, the breaking of the O=C=O bond requires a high activation energy. In addition, since ECR consists of multiple elementary steps, these electrocatalytic processes are more demanding than for example water splitting reaction. As ECR reaction is normally carried out in aqueous solution, another critical issue is the low solubility of CO_2 in water which impedes the diffusion-controlled reactions. There are certain ways to improve CO_2 dissolution, including using nonaqueous electrolytes and increasing CO_2 partial pressure. For instance, some metal catalysts with low activity for ECR under atmospheric pressure, however, can reduce CO_2 to CO and HCOOH efficiently at high pressures [36].

Electrocatalysts can effectively reduce the activation energy, accelerate reactions or increase desired product selectivity in ECR. It should also dissociate water in solution to promote proton-electron transfer, because the proton assisted multiple-electron transfer can be beneficial for CO_2 activation. Depending on the different pathways and the number of protons and electrons transferred, a range of products can be formed, including C_1 products such as carbon monoxide (CO), methanol (CH_3OH), formic acid (HCOOH), methane (CH_4), or C_2 products such as ethylene (C_2H_4), ethanol (C_2H_5OH) and others [37]. C_2 products with higher energy density are more valuable, but the synthesis of C_2 products is more difficult than C_1 products because of larger number of required protons during conversion. Meanwhile, high formation energy of the C−C bonds can decrease the efficiency of the reaction. To achieve specific product selectivity, the design and synthesis of high performance ECR electrocatalysts is essential.

1.2.2. Single electron vs. proton-coupled electron reaction

The research on ECR has been conducted ever since the early 19th century. ECR contains two half reactions occurring in anode and cathode, where different number of protons-coupled electrons transfer occurs. The standard electrode potentials of different reactions with reference to standard hydrogen electron (SHE) for different products in aqueous solution are summarized in Table1.1 For a typical single electron ECR, CO_2 is reduced to the CO_2 anion radical (CO_2^-) at the cathode, and water is oxidized to oxygen at the anode. Since the kinetics of the reactions are quite sluggish, the first step for converting CO_2 into reduced carbon species is difficult. The

thermodynamic potential for driving one electron CO_2 reduction to CO_2^- is about −1.90 V vs. SHE at a PH of 7, indicating that this reaction is highly energetic and unfavorable [38-40]. Besides, this first step is also the rate-limiting step, and the generation of the CO_2^- intermediate plays a significant role in forming $2e^-$ reduction products. Interestingly, a more favorable route that bypasses the formation of CO_2^- by protons-coupled electrons transfer processes has been identified. The transfer of protons-coupled electrons benefits ECR within the potential range of −0.20 to −0.60 V vs. SHE, and the final products are determined by the choice of electrocatalysts and electrolyte as well as the number of electrons and proton transferred [41, 42]. For instance, two protons-coupled electrons transfer in CO_2 hydrogenation reaction mainly produces HCOOH and CO.

Table 1.1. Standard electrochemical potentials for reducing CO_2 into different products.

CO_2 reduction reactions	Standard electrode potentials *vs.* SHE (V)
$CO_2 + e^- \rightarrow CO_2^-$	−1.900
$CO_2 + 2H^+ + 2e^- \rightarrow HCOOH$	−0.610
$CO_2 + 2H^+ + 2e^- \rightarrow CO + H_2O$	−0.530
$2CO_2 + 2H^+ + 2e^- \rightarrow H_2C_2O_4$	−0.913
$CO_2 + 4H^+ + 4e^- \rightarrow HCHO + H_2O$	−0.480
$CO_2 + 6H^+ + 6e^- \rightarrow CH_3OH + H_2O$	−0.380
$CO_2 + 8H^+ + 8e^- \rightarrow CH_4 + 2H_2O$	−0.240
$2CO_2 + 12H^+ + 12e^- \rightarrow C_2H_4 + 4H_2O$	−0.349
$2CO_2 + 12H^+ + 12e^- \rightarrow C_2H_5OH + 3H_2O$	−0.329
$2CO_2 + 14H^+ + 14e^- \rightarrow C_2H_6 + 4H_2O$	−0.270
$3CO_2 + 18H^+ + 18e^- \rightarrow C_3H_7OH + 5H_2O$	−0.310

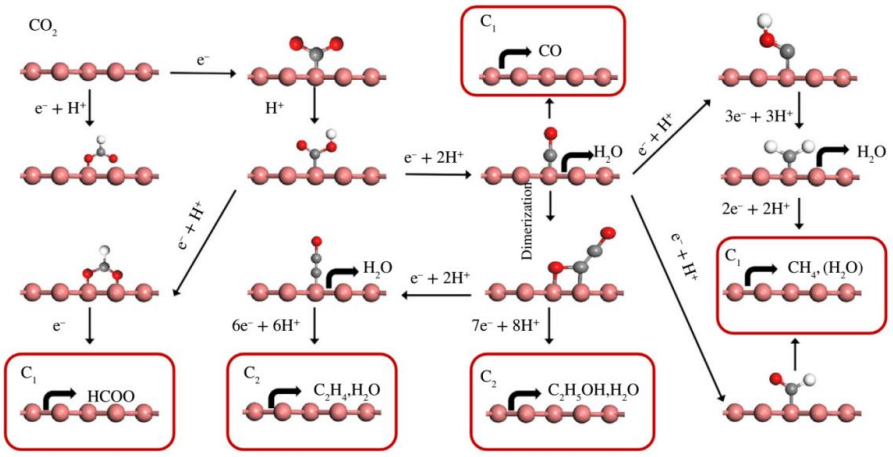

Figure 1.1. Potential electrochemical CO_2 reduction pathways to form the C1 products of CO, HCOOH, CH_4, and the C2 products of C_2H_4 and C_2H_5OH. Reprinted from [43], Copyright (2019), with permission from Wiley.

As shown in Figure 1.1, ECR starts by transferring first proton-electron pair to form carboxyl (*COOH) or formate (*OCHO) intermediate species [43]. These two intermediates can be further reduced by accepting different number of proton-electron pairs. Note that there is much

competition between intermediate species. For example, the OHCO* species can be converted to HCOOH, and the biformate (H_2COO*) can also be reduced to HCOOH. Meanwhile, the different products also show similar reduction potentials. Thus, further reactions of these intermediate species are important for the reaction rate and formation of the final products. Moreover, as the equilibrium potential of hydrogen evolution reaction (HER) (0 V vs. reversible hydrogen electrode (RHE)) is more positive than that of CO_2 reduction to HCOOH (−0.17 V vs. RHE), H_2 will be the by-product, which seriously limits the ECR efficiency [44].

1.2.3. Factors determining product selectivity

Factors such as the type of electrocatalysts (morphology, composition, chemical state, and crystallographic structure), electrolytes (composition, concentration, and pH), temperature, pressure, and applied potential all influence ECR. For instance, solid and aqueous electrolytes have been used in ECR, exhibiting remarkable difference in efficiency [45, 46]. To date, $NaHCO_3$ and $KHCO_3$ solutions are frequently chosen as electrolytes because they can maintain the pH at the electrode surface. Meanwhile, the pH of the solution can affect the generation of by-products such as H_2.

ECR with a more positive potential vs. SHE is thermodynamically more favourable. In this regard, the conversion of CO_2 to alcohol or hydrocarbon products should be thermodynamically more favorable than other products including CO, HCOOH and HCHO (Table 1.1). Nevertheless, ECR not only needs to overcome the thermodynamic barrier, but also the kinetic challenge determined by the concentration of available protons in reaction. Namely, the electrocatalysts prefer to transfer electrons from their catalytic sites to adjacent sites which can provide protons. Thus, the formation of hydrogenated C_1 intermediates such as HCOOH can be kinetically more favorable than the formation of C−C bonds, which hinders the selectivity to C_2 and higher hydrocarbon products. To date, only the Faraday efficiency (FE) of C_1 products CO and HCOOH can reach 100%, while the maximum FE of C_2 product C_2H_4 is 80% and the maximum FE of C_3 products C_3H_7OH is 30% [47, 48].

Many theoretical studies proposed that for multi-electron transfer reduction of CO_2, the adsorption energies of intermediates follow linear scaling relationship, and breaking such linear scaling relationship can improve catalytic performance. Some strategies have been proposed, including reducing coordination numbers, doping with p-block elements, engineering oxyphilic sites, and coating the catalyst surface with active ligands. Up to now, the majority of the ECR electrocatalysts are metal and carbon-based materials. It has been demonstrated that some

heterogeneous electrocatalysts follow the two-electron-transfer mechanisms in CO_2 reduction to HCOOH or CO. For example, Hori et al. investigated a series of metals for ECR reaction, and indicated that metallic electrocatalysts such as Cd, Sn, Hg and Pb prefer HCOOH formation [49]. However, noble metals including Pt, Ag and Au can convert CO_2 into CO. Especially, copper-based electrocatalysts is the only electrocatalysts that has been reported for converting CO_2 into alcohols and hydrocarbons with good activity and selectivity. However, as mentioned above, the interaction between intermediates and electrocatalysts plays a crucial role in forming final products, demonstrating the importance of electrocatalysts.

1.2.4. ECR efficiency evaluation

In experimental ECR study, there are several key parameters for evaluating the electrocatalysts performance, including overpotential, current density, Tafel slope, FE, turnover frequency (TOF) and stability of electrocatalysts. The overpotential can be regarded as the energy needed to drive the reaction. In other words, the higher the overpotential, the higher the energy required for the reaction, and the more difficult the reaction to be realized. Current density reflects the rate of electrochemical reaction, and the larger the current density, the faster the electrocatalytic reaction. The Tafel slope can be obtained by fitting the linear region of the Tafel curve. With the increase of overpotential, if the current density increases dramatically, the slope will be small. FE is regarded as the fraction between charges transferred to specific product and the total charges in the electrocatalytic process, accounting for the selectivity and efficiency of the reaction. Larger FE suggests less energy loss, and smaller FE indicates more energy loss. TOF is the catalytic activity of each site under a certain overpotential, indicting the intrinsic activity of catalysts. The stability of electrocatalysts can be evaluated by long-term use under a specific voltage.

In summary, the electrocatalytic reaction is a complicated multistep reaction occurred at the multiphase interface. Small overpotential and high current density can boost ECR, but it is difficult to satisfy them simultaneously. Developing excellent electrocatalyst to overcome these problems is the key.

1.3. Efficient ECR electrocatalysts

1.3.1. Metallic materials

Bulk metal catalysts in ECR have been investigated for decades [50-52]. Metal electrocatalysts can be divided into two groups: noble metal (Au, Ag, Pt, etc.) and other earth-abundant transition metals (Co, Ni, Cu, etc.). Theoretical work has well disclosed that noble metals are

better electrocatalysts compared with earth-abundant metals. Nevertheless, some intermediates such as CO could poison the active sites, which affects their stability. Large-scale application of precious metals is also not possible due to their high price and scarcity.

It has been revealed that precious metals with 2D nanosheet structures can enhance their electrocatalytic performance effectively and improve the utilization of noble metals [53]. Huang et al. prepared hexagonal Pd structure with 2.5 times higher electrocatalytic activity for the oxidation of formic acid compared to commercial Pd black [54]. The high performance could be attributed to nanosheet structure with more active sites, better electronic structure and larger surface area as well as high atom utilization. Zhu et al. synthesized ultrathin Pd nanosheet for ECR which exhibited a FE of 94% for CO production at a potential of −0.50 V vs. RHE [55]. Meanwhile, experimental and theoretical work revealed that ultrathin Pd nanosheets with high edge exposure ratio is beneficial for CO_2 adsorption and CO desorption as well as suppressing HER. Nanostructured Au also showed great activity in ECR. Mistry et al. studied the electrocatalytic activity of Au nanoparticles (NPs) in the range of 1-8 nm for CO_2 reduction to CO [56]. The results suggested that the current density increased with the decrease of particle sizes.

Moreover, multi-metal composite nanosheets also exhibit excellent performance in electrocatalytic reaction because of the synergistic effect of different metals compared to single metal electrocatalysts [57-59]. Wang et al. showed that 2D Pd-Au bimetallic catalyst had lower activation energy than monometallic Au in ECR via density functional theory (DFT) calculation [60]. Very recently, Au-Cu bimetallic thin films with various ratio were synthesized for ECR [61]. The activity of Au-Cu alloy was found to be correlated with the variation of electronic structures determined by alloy composition. As shown in Figure 1.2a, the surface valence bands of the Au-Cu catalysts present different patterns with different alloy composition. The *d*-band center gradually moves away from the Fermi level with the increase of Au concentration (Figure 1.2b), which could influence the occupancy of antibonding states. Meanwhile, the interaction strength between substrate and intermediates decreased. The *d*-band center did not shift after ECR, implying great stability. Therefore, the catalytic performance for CO formation was enhanced as Au concentration increased, with the highest current density and FE at −0.80 V vs. RHE (Figure 1.2c and d).

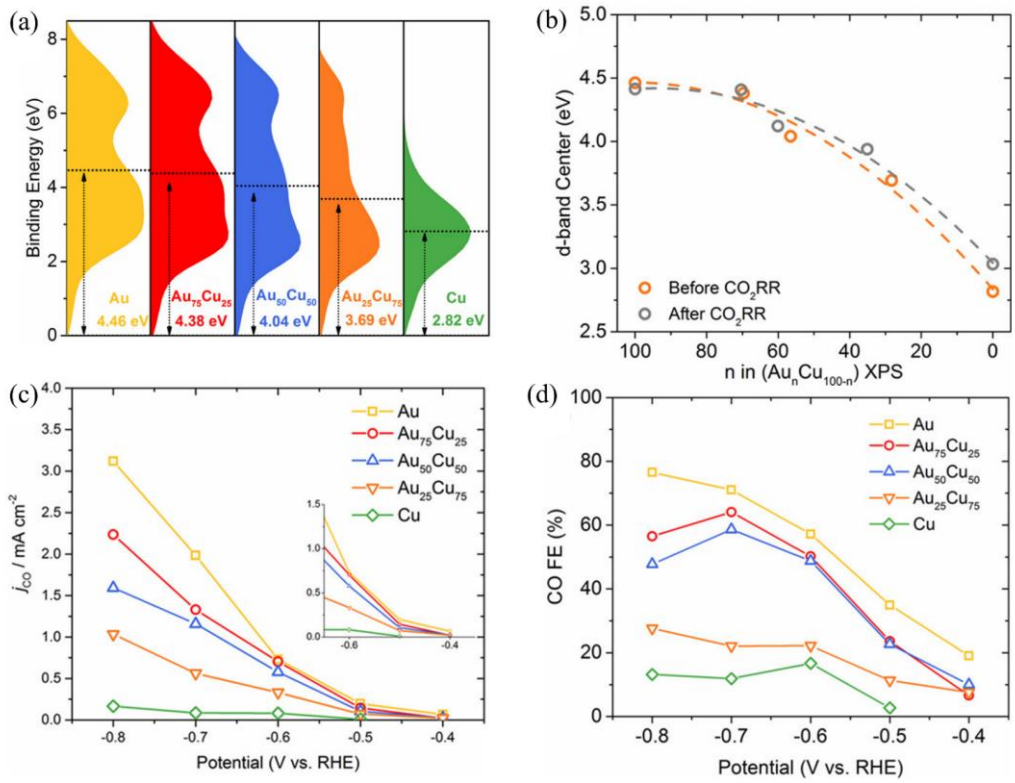

Figure 1.2. (a) Surface valence band x-ray photoemission spectra of the as-prepared Au, Cu, and Au-Cu alloys. (b) d-band center of different samples before and after ECR at −0.7 V vs. RHE for 1 h. The gravity center of the valance band center is shown by the dotted lines compared to 0 eV. The binding energy is the value of $|E - E_{Fermi}|$. (c) Faradaic efficiency of and (d) Partial current densities of CO. Reprinted from [61], Copyright (2018), with permission from American Chemical Society.

Non-precious metals include Fe, Co, Ni, etc. have also attracted much attention in electrocatalysis due to the low prices, abundant resources and promising electrochemical properties as well as tunable electronic structures [62, 63]. Studies have shown that Fe, Ni and Ti produce H_2 as the major product in ECR due to their low HER overpotential and strong CO adsorption capability. Sn, Pb and In have poor binding energy with CO_2^- intermediates and the final products are usually formate or formic acid. Moreover, Cu is the only metal catalyst that can produce C_3 hydrocarbons by C-C coupling mechanism [64]. Generally, modulating the electronic and surface structures of these metals could effectively enhance their electrocatalytic activity. Kuang et al. synthesized ultrathin Ni nanosheet arrays by in-situ topology reduction technique. The electrocatalyst showed excellent HER activity compared with Pt/C, because ultrathin nanosheet structure could expose more active sites which boost electrocatalytic reaction [65]. Besides, 2D structured bismuth (Bi) exhibited more active sites and promising selectivity to formate compared to bulk Bi. Zhang et al. prepared ultrathin Bi by liquid phase stripping technique, which displayed excellent electrocatalytic performance for formate generation with an FE of 86% and a current density of 16.5 mA/cm^2 at −1.1 V vs. RHE, which is obviously higher than bulk Bi and acetylene black decorated carbon paper (AB/CP) (Figure

1.3a and b). As presented in Figure 1.3c and d, CO_2 conversion to HCOOH underwent lower Gibbs free energy change on edge (003) and (012) [66]. Special surface structure could also improve the catalytic efficiency and selectivity. It has been reported that ultrathin porous Cu nanosheets synthesized by a simple replacement method could achieve a FE of 74.1% and current density of 23.0 mA/cm^2 at −1.0 V vs. RHE for CO_2 conversion to CO, remarkably better than traditional bulk Cu [67]. DFT calculations clarified that the porous Cu nanosheet structure could accelerate the formation of CO intermediate, thus promoting ECR efficiency. Similarly, Wang et al. synthesized Cu nano-cubes which demonstrated better electrocatalytic activity and selectivity in comparison with Cu nanospheres with same size. The nano-cubes could reach a FE of 60% and a partial current density of 144 mA/cm^2 towards C_2H_4 production [68]. Zhang et al. prepared the pipet-like bismuth (Bi) nanorods semifilled in nitrogen-doped carbon nanotubes (BiNRs@NCNTs) for ECR [69]. The catalyst acts as nanoscale conveyors which can facilitate mass transport and reactant adsorption on active sites. As a result, The FE for formate generation reached 90.9% at a moderate applied potential of −0.9 V (vs. RHE).

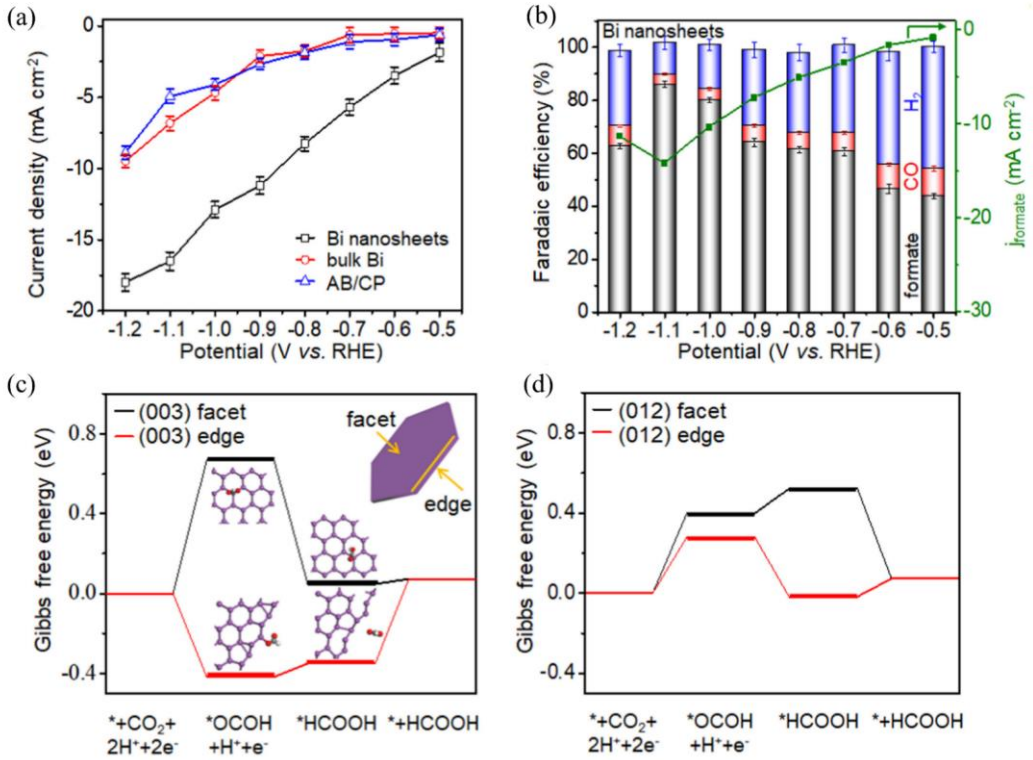

Figure 1.3. (a) Current densities of Bi nanosheets, bulk Bi and acetylene black decorated carbon paper (AB/CP) within a potential window of −0.5 to −1.2 V vs. RHE in CO_2-saturated 0.1 M $KHCO_3$ aqueous solution. (b) Faradaic efficiencies (left Y axes) and partial current densities of formate product (right Y axes) of Bi nanosheets. DFT calculated ΔG in the reaction pathways of CO_2 conversion to formate from the facet sites and edge sites of (003) plane (c) and of (012) plane (d) on Bi. Reprinted from [66], Copyright (2018), with permission from Elsevier.

Therefore, metal catalysts are effective for electrocatalysis due to their intrinsic activity and good conductivity. When the metal catalysts are synthesized with 2D nanosheets or other

special nanostructures, the atom utilization, activity and selectivity could be improved, thus increasing the electrocatalytic efficiency. Precious metal such as Pd or Au or multi-metals with different ratios show excellent selectivity for CO generation. Non-precious metals such as Fe, Co and Ni show poor ECR performance, while Sn, Pb and In could have good activity for the production of formate or formic acid. Particularly, Cu-based catalysts with different morphologies could exbibits different activity and selectivity for different products. Accordingly, the choice of metal, small nanosheet size and different morphology will have positive effect on the ECR activity and selectivity.

1.3.2. Graphene and graphene-based materials

Generally, graphene is a single layer of graphite with zero-band gap. It is a promising electrocatalysts for CO_2 reduction due to its high electron mobility, conductivity, unique electronic structure and large surface area. Besides, the high thermal conductivity can improve heat diffusion during the exothermic process, benefiting electrocatalysis. However, pristine graphene exhibits some drawbacks in ECR. For instance, the delocalized π bonding network of graphene negatively affects the adsorption of intermediates such as *COOH or *OCHO, therefore graphene cannot effectively activate CO_2 molecule and presents high energy barriers for intermediates formation, leading to low ECR activity [70]. Some studies have clarified that the undoped zigzag edge of graphene shows a metastable adsorbed CO_2 state, and the energy barrier is quite high at about 1.3 eV [71]. As the modification of electronic structures can efficiently tackle these problems, many researchers have focused on tailing its electronic structures. For example, incorporating heteroatoms such as B, N can effectively modify graphene structures and decrease CO_2 adsorption barrier. Studies have disclosed that N doped graphene can exhibit a low overpotential of around 0.19 V for converting CO_2 into CO [72]. Duan et al. reported that doping boron can stabilize the negatively polarized O atoms of CO_2 and improve CO_2 chemisorption on carbon surface [73]. Similarly, Sreekanth et al. reported B doped graphene as metal-free electrocatalyst for CO_2 reduction in 0.1 M $KHCO_3$ solutions. They concluded that the presence of boron dopants could introduce spin density distribution, and these atoms can be active sites for intermediates adsorption [74]. Some doped systems have been investigated in more detail by DFT calculations. Wu and co-workers systematically studied the effect of N doped graphene for ECR. Three different N atom sites, including graphitic N, pyrrolic N and pyridinic N, were investigated as active sites for ECR. They suggested that the three different N sites can significantly decrease the free energy barrier for intermediate adsorption. The triple-pyridinic N can most effectively reduce the barrier for

COOH adsorption, indicating that pyridinic N is highly active sites for converting CO_2 to CO [72]. However, there are different views on the mechanism of N doped graphene for ECR. Chai et al. reported that the graphitic N-doped edges of graphene sites have low CO_2 activation barrier and are the most active sites for ECR among graphene-based materials [71]. Liu et al. demonstrated that pyrrolic N site performs the best for CO_2 reduction to HCOOH with a low overpotential [75]. It has also been reported that N doped graphene quantum dots with predominant pyridinic N at edges can electrochemically convert CO_2 to C_2 compounds with low overpotentials [37].

Compared with nonmetal dopants, introducing single or multiple metal dopants to construct special graphene nanostructures could also exploit materials with excellent catalytic performance. Au nanoparticles embedded in graphene nanoribbon exhibited low overpotential, high FE for CO generation and excellent stability compared to amorphous carbon supported Au nanoparticles, attributed to the change of electronic properties and the increase of active sites [76]. Liu et al. synthesized Pd and Cu mono- and bi-metallic nanoparticles embedded graphene and suggested that 1 wt.% Pd-2 wt.% Cu/graphene had the highest ECR efficiency [77]. Su et al. prepared nickel-nitrogen co-modified graphene (Ni−N−Gr) with more active centers by short-duration heat treatment and found that the Ni−N site was the active center for CO_2 reduction [78]. As shown Figure 1.4a and c, the Ni−N−Gr and Ni foil exhibit obvious enhancement of current density in the presence of CO_2. However, there is a remarkable difference in FE of CO. The Ni−N−Gr showed a FE of 90% at −0.7 to −0.9 V vs. RHE for CO production, where Ni foil produced mostly H_2 (Figure 1.4b and d), demonstrating that the synergistic effect of Ni and N is critical to improve CO selectivity.

Graphene-based composite materials also possess excellent conductivity and larger surface areas compared to pristine graphene. Huang et al. synthesized N-doped graphene monolayer coated Sn foil, showing excellent flexibility with a high FE of 92% for formate at −1.0 V vs. RHE [79]. Lei et al. prepared Sn quantum sheets confined in graphene, offering more active sites for CO_2 adsorption [80]. Li et al. successfully prepared SnS_2 nanosheets supported on reduced graphene oxide for CO_2 conversion to formate, displaying a low overpotential of 0.23 V and a maximum faradaic efficiency of 84.5%. The spectroscopic and electrochemical characterizations suggested that the improvement of electrocatalytic performance can be attributed to the residual SnS_2 [81].

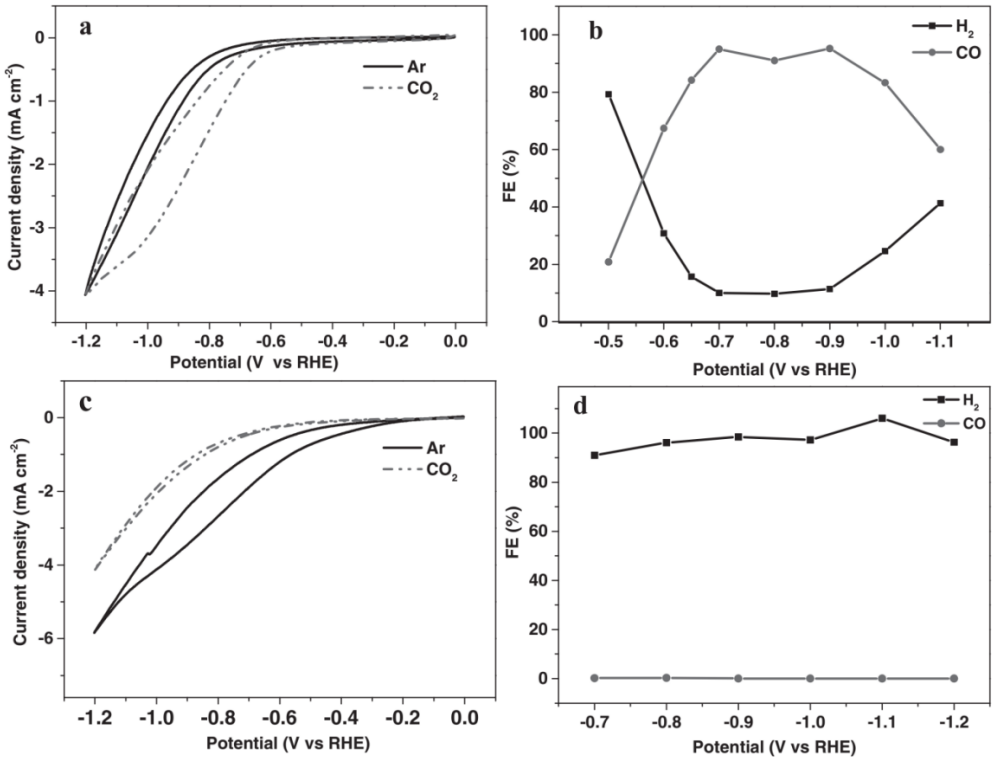

Figure 1.4. (a) Cyclic voltammograms of nickel-nitrogen co-modified graphene (Ni−N−Gr) catalyst and (c) Ni foil in CO2-saturated 0.1 M $KHCO_3$ and Ar-saturated 0.1 M KH_2PO_4/K_2HPO_4 (pH = 6.8) at 10 mV/s. FEs for the reduction products by Ni−N−Gr catalyst (b) and Ni foil (d). Reprinted from [78], Copyright (2016), with permission from Wiley.

For graphene-like materials, graphitic carbon nitride (g-C_3N_4) typically exhibits good chemical and thermal stability under ambient conditions. However, poor conductivity and less active sites limit its potential application in ECR. Strategies including doping metal and constructing composite have been developed to increase the activity of g-C_3N_4. Metal atoms could effectively modulate the electronic structure of g-C_3N_4 thus improve the catalytic activity. The g-C_3N_4 nanosheet and multiwalled carbon nanotubes composite have been show to exhibit excellent stability and good electrocatalytic performance for CO_2 reduction to CO [82]. The electrocatalytic activity of the composite arises from the C−N bonds, and the high conductivity allows numerous electrons to transfer rapidly to the C−N sites. Guo et al. synthesized Co_3O_4-CDots-g-C_3N_4 tri-component electrocatalysts for syngas production [83]. They suggested that different catalytic components have different functionality. For instance, g-C_3N_4 and Co_3O_4 provide active sites for ECR and HER respectively, whereas CDots are the sites for proton generation.

It can be concluded that the electronic structure of graphene-based materials could be tuned to effectively improve ECR selectivity. Doping non-metal or metal atoms is efficient way for the design and synthesis of high performance ECR catalysts. To date, nitrogen and metal atoms co-

doping has been widely reported and shown excellent activity for CO production. Constructing highly active interfaces in graphene-based nanocomposite is also a good strategy in ECR catalyst design.

1.3.3. Single-atom catalysts

Single-atom catalysts (SACs) have enormous advantages in electrocatalysis in terms of 100% atom utilization and intriguing electronic structures [84, 85]. The traditionally supported nanoparticles or clusters exhibit structural irregularities on the nanoparticle surface. The surface reactivity has close relationship with surface free energy, and the ratio between fully coordinated surface atoms and the number of vacancies distinguishes the reactivity of atoms with identical chemical composition but different positions [86-88]. Therefore, the conventional clusters with different surface reactivity can result in poor product selectivity. Single atom is different from clusters because the surface free energy is homogeneous and the number of vacancies in the nearest neighbors is the same. Thus, single atom could show good stability and special intrinsic activity [89]. Single atom exhibits uniform active sites as ideal catalysts, however, one major challenge for SACs is the synthesis because SACs are unstable and can agglomerate quickly due to the high surface energy. Furthermore, the supported structures in the neighboring environment increase the heterogeneity of SACs active sites, and thus uniform activity could not be easily achieved. However, 2D materials could be utilized as support to improve the uniformity and performance of SACs in electrocatalytic reactions [90, 91]. Studies have evidenced that 2D materials such as MoS_2, graphene, and MXene could stabilize the single atoms and maintain their single-atom state [92-98]. For instance, Back et al. investigated single transition metal atom anchored on graphene with single or double vacancies as ECR catalyst by DFT calculations [99]. They suggested that many SACs exhibited high selectivity for ECR over the competitive HER because of favorable adsorption of *COOH or *OCHO over *H on the catalysts (Figure 1.5). SACs such as Ni and Pt for CH_3OH production showed limiting potential of −0.41 V and −0.27 V, while Os and Ru systems have the same limiting potential (−0.52 V) for CH_4 production. The activity improvement of SACs can be partially attributed to the unique electronic structure of the SACs and orbital interaction.

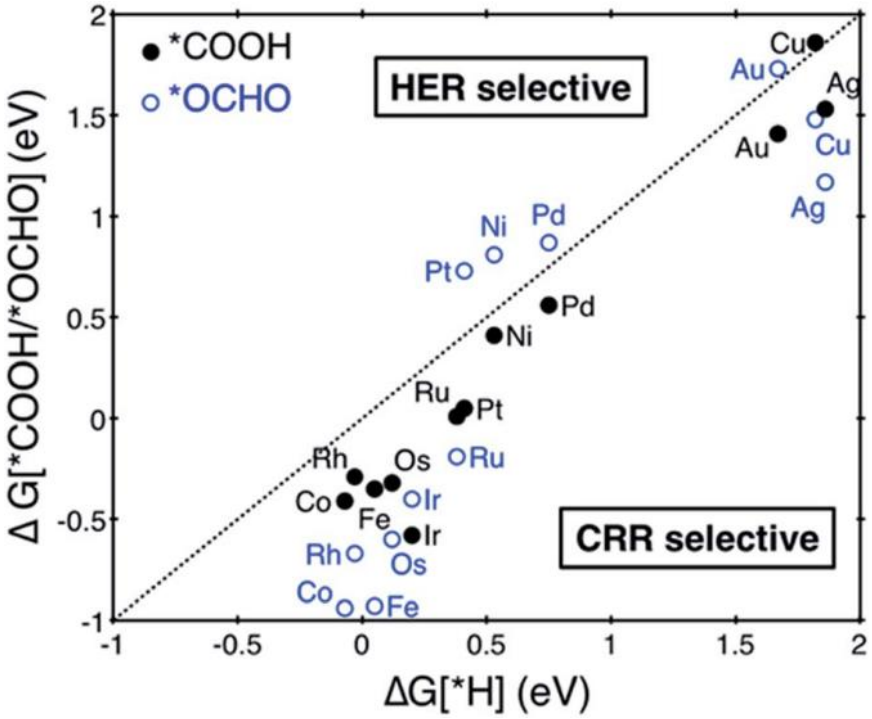

Figure 1.5. Free energy change of the first protonation step in the ECR and HER on different SACs. Catalysts below the dotted parity line are ECR selective. Reprinted from [99], Copyright (2017), with permission from Royal Society of Chemistry.

Constructing 3*d* transition Metal−Nitrogen atom ($M-N_x$) system based 2D materials for ECR is prevailing. Huan et al. investigated activity and selectivity of N doped Fe-N_4 and Fe nanoparticles moieties. They reported that samples with Fe-N_4 active sites performed a FE of 80% for CO generation, but Fe nanoparticles could mostly only produce H_2 [100]. Zhang et al. synthesized Fe single atoms anchored on N-doped graphene and revealed that Fe-N_4 with Fe^{2+} oxidation state was the active sites for ECR [101]. They also recognized that N dopants on the graphene substrate can be beneficial for ECR. However, there are some debates on the active sites and the corresponding ECR mechanisms on Fe SACs. For instance, Zhang et al. synthesized single Fe atom anchored on N-doped graphene by prolonged thermal pyrolysis [102]. The SAC exhibited high FE of about 97.0% for CO production under a low overpotential of 0.35 V. The excellent performance resulted from the presence of highly efficient dispersed Fe-N_5 active sites. Theoretical calculations disclosed that a fifth N atom coordinates to Fe^{3+} to form Fe-N_5 moieties, where the additional axial pyrrolic N ligand further depletes the electron density of Fe 3*d* orbitals and reduces the π back-donation of Fe-CO bonding, which resulted in rapid CO desorption and high selectivity for CO formation.

Zhang et al. reported single Fe atom confined in carbon foams forming Fe-N_4 active sites [103]. However, they also detected Fe^{3+} state in their samples because Fe^{2+} can be oxidized to Fe^{3+} when the samples are exposed to air, but the difference was not distinguishable in ECR. Gu et

al. investigated single Fe atom loaded on N doped carbon with an overpotential as low as 0.08 V for CO production [104]. They confirmed the persistent presence of Fe^{3+} in the whole ECR process by in situ X-ray absorption near edge structure (XANES) measurements. Further studies indicated that Fe^{3+}−N−C showed excellent performance for CO formation than that of Fe^{2+}−N−C because of weaker CO absorption on the Fe^{3+} sites. Yang et al. prepared N-anchored Zn single atom catalyst on carbon [105]. From HAADF-STEM characterization, it can be clearly seen that individual single Zn atom was supported on carbon (Figure 1.6a), and extended X-ray absorption fine-structure (EXAFS) spectra demonstrated the existence of Zn−N_4 moiety (Figure 1.6b). The catalyst could reduce CO_2 to CO with high selectivity and a high FE of about 95% under the potential of −0.43 V (Figure 1.6c). It also exhibited remarkable durability over 75 h without any FE_{CO} decay (Figure 1.6d). Further experimental work and DFT calculations suggested that the remarkable activity can be attributed to the existence of Zn−N_4, which was the main active sites for ECR and had low free energy barrier for the rate-limiting step of *COOH formation. Zhao et al. synthesized single Ni atom loaded on graphene oxide. The catalyst showed a FE for CO production of 96.5% at a potential of −0.63V, with a TOF of 325.9 h^{-1} [106].

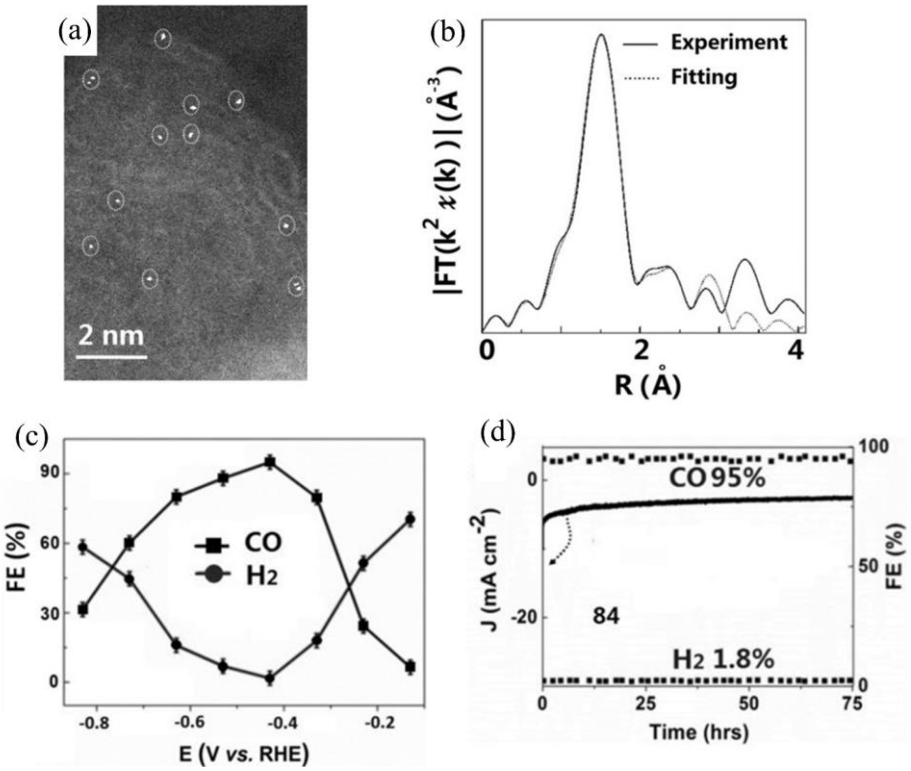

Figure 1.6. (a) Typical high-angle annular dark-field scanning transmission electron microscope (HAADF-STEM) image of the optimal ZnNx/C catalyst. The circles indicate the individual Zn atoms. (b) A typical fitting curve of the EXAFS signal in R-space for the adsorbed ZnN_x/C catalyst. (c) FEs of CO and H_2 at various applied potentials on ZnN_x/C catalyst. (d) Long-term stability of ZnN_x/C at a potential load of −0.43 V and the corresponding FEs of CO and H_2. Reprinted from [105] Copyright (2018), with permission from Wiley.

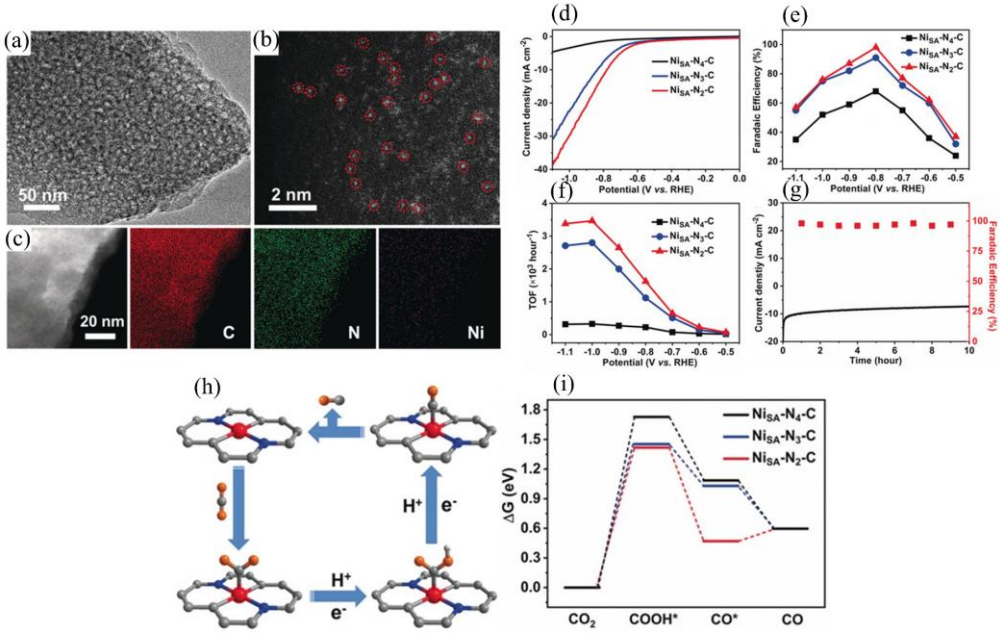

Figure 1.7. (a) Transmission electron microscope (TEM) and (b) HAADF-STEM images of NiSA−N_2−C. (c) EDS mapping of Ni, N and C elements in NiSA−N_2−C. (d) LSV curves in CO_2-saturated 0.5 M $KHCO_3$ electrolyte. (e) FEs of CO at different applied potentials. (f) The corresponding TOFs of CO production over NiSA−N_x−C. (g) Stability of NiSA−N_2−C at −0.8 V during 10 h. (h) Proposed reaction paths for ECR with NiSA−N_2−C as an example. (i) Free-energy diagram of CO_2 reduction to CO over NiSA−N_x−C catalysts. Reprinted from [109], Copyright (2020), with permission from Wiley.

Yang et al. prepared single Ni atom supported on N-doped graphene. The TOF reached 14800 h^{-1}, and the FE of CO was 97% at a potential of −0.61 V [107]. The catalyst also displayed great stability with very stable electrocatalytic activity for 100 h. Liu et al. constructed a model SAC with precise structure using two-steps by linking Ni−TAPc to CNTs and by C−C coupling [108]. This model Ni SAC exhibited excellent activity, selectivity and durability in CO_2 conversion to CO. Experimental study suggested that Ni^+ in Ni−TAPc is highly active for CO_2 activation and is the catalytically active site. Besides, $*CO_2^- + H^+ \rightarrow *COOH$ was the rate-determining step. Gong et al. prepared a series of single-atom Ni catalysts (Ni−SA−N_x−C) with different N coordination numbers by controlling the pyrolysis temperature [109]. Figure 1.7a and b clearly indicated the existence of isolated Ni atoms from TEM characterizations. The homogeneous distribution of Ni, N and C was demonstrated by energy dispersive spectroscopy (EDS) mapping (Figure 1.7c). It was found that sample with Ni-N_2 moiety showed a higher current density than Ni−N_3−C and Ni−N_4 in CO_2-saturated 0.5 M $KHCO_3$, indicating the best activity of NiSA−N_2−C among all three SACs (Figure 1.7d). In addition, it exhibited a maximum FE_{CO} of 98 % at −0.8 V, which is also the highest (Figure 1.7e). The TOF for CO production on NiSA−N_2−C reached 3467 h^{-1} at the potential of −1.0 V, which are much higher than those of NiSA−N_4−C and NiSA−N_3−C (Figure 1.7f), elucidating that the coordination environment plays a crucial role in ECR performance. The current density and FE for CO

generation were almost unchanged on NiSA−N_2−C catalyst after electrolyzation for 10 h at the potential of −0.8 V vs. RHE (Figure 1.7g), demonstrating excellent stability. DFT calculations suggested that the reaction path is proton-coupled electron transfer (Figure 1.7h). The low N coordinated single-atom Ni sites in NiSA−N_2−C is beneficial for the formation of *COOH intermediate, thereby enhancing the ECR activity (Figure 1.7i).

Han et al. designed a free-standing ultrathin 2D SAC by self-assembly of Co-porphyrin complex, which showed a CO production FE of 96% under an overpotential of 0.5 V [110]. They indicated that the improvement of activity was attributed to nitrogen coordination from the bottom layer, which increased the d_z energy level of the Co atoms. Jiang et al. investigated a series of SACs supported on graphene nanosheets with different defect structures [111]. Ni SAC exhibited a CO formation FE of 95% under an overpotential of 0.55 V and excellent stability. Experimental study and theoretical calculations suggested that Ni sites with slightly larger vacancies benefit CO_2 conversion to CO by decreasing CO desorption barrier. Recently, Zheng et al. investigated ECR performance of Cu SACs on N doped graphene matrix with highly exposed and coordinatively unsaturated Cu−N_2 center, as shown in Figure 1.8a [112]. Experimental work showed an onset potential of −0.33 V and FE for CO production of about 81% under a low potential of −0.50 V vs. RHE, obviously higher than the sample with Cu−N_4 moiety (Figure1.8b). DFT calculations manifested that Cu−N_2 centers can facilitate CO_2 activation and accelerate electron transfer from Cu−N_2 sites to *CO_2, which can greatly improve *COOH generation and the overall ECR activity. Jiao et al. investigated single Cu atom anchored on g-C_3N_4 as electrocatalysts for CO_2 conversion to various hydrocarbons [113]. A slightly negative shift of photon energy demonstrated that N accepts extra charges from Cu atom (Figure 1.8c). They reckoned that the *d*-orbital of Cu can be efficiently elevated by coordination with the g-C_3N_4 framework, enhancing the adsorption of carbonaceous intermediates. Therefore, Cu−g-C_3N_4 had better ECR activity with lower onset potential and exhibited higher C_2 products rate than conventional Cu supported on nitrogen-doped graphene (Figure 1.8d).

Single metal atom loaded 2D materials are a class of very promising catalysts for ECR due to their high atom utilization and catalytic activity. Their activity is determined by the type of metal atom and the electronic structures of the metal atom. Furthermore, the coordination number of metal atoms could be tuned by the 2D materials support, which could further optimize the activity and selectivity of the SACs.

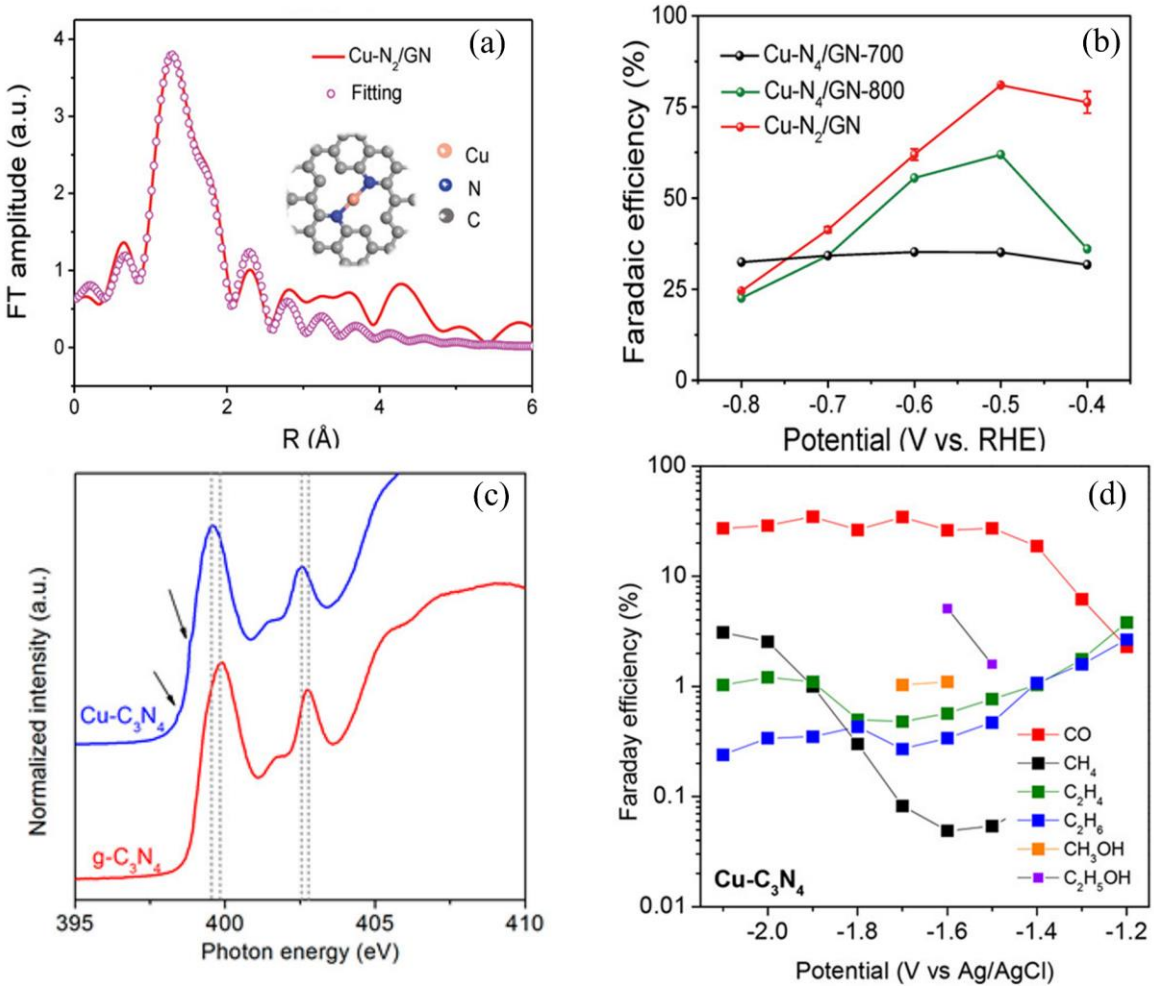

Figure 1.8. (a) Fourier transformed (FT)-EXAFS fitting results of Cu−N_2/GN. (b) CO FE of Cu−N_4/GN-700, Cu−N_4/GN-800 and Cu−N_2/GN. Reprinted from [112], Copyright 2020, with permission from Wiley. (c) Nitrogen K-edge NEXAFS of Cu−C_3N_4 and pure g-C_3N_4. Arrows show the weak shoulders in the N K-edge assigned to the Cu−N interaction. Dotted lines show the channels of photon energy in the two samples. (d) Measured Faradaic efficiencies of various products on Cu−C_3N_4. Reprinted from [113], Copyright (2017), with permission from American Chemical Society.

1.4. Objectives and scope of the study

This thesis aims at rational design and synthesis of catalysts from NPs to SACs for efficient ECR based on DFT calculations and experimental studies.

A brief review of ECR development, mechanisms and catalysts has been presented in the chapter 1 that is from part of **Paper I**. Downsizing the metal to single atom can improve the activity and selectivity of ECR remarkably. Thus, SACs applied ECR could show obvious advantages in comparison with traditional homogeneous and heterogeneous catalysts.

We start the experimental study from the preparation of Ag NPs supported on 2D B doped g-C_3N_4 (**Paper II**). Nobel metal such as Ag and Au has demonstrated good activity for ECR to CO, but finding appropriate support is still challenging. g-C_3N_4 possesses many merits such as high surface area, low cost, and easy preparation, which enables it to be an ideal molecular

scaffold for engineering metal NPs for excellent performance in multiple electrocatalytic applications. More importantly, doping NM atoms into support can change its electron structures, while the modified framework could serve as a better support for metal NP deposition and to activate metal NPs. DFT calculations was employed to reveal the effect of B dopant on g-C_3N_4 support. The ECR to CO reaction mechanism was also studied. ECR activity and stability were tested in H type cell.

Although noble metal NPs show high ECR selectivity for CO generation, the current density is quite low. Thus, decreasing the size of NPs to single atom is necessary. Therefore, in **Paper III and IV** we predicted some SACs which were supported on 2D materials based on DFT calculations. 2D MXene (Nb_2NO_2) and metal (antimonene) were employed as support for transition metal atoms. The stability of SACs, ECR selectivity against HER and ECR pathways for different products were compared. The origin of activity was also investigated. Some descriptors for ECR activity were discussed.

Numerous theoretical and experimental studies have demonstrated that 3d transition metal-based SACs embedded into N doped carbon (TM−N−C) shows good selectivity and density current for ECR to CO. However, it is necessary to further improve activity and selectivity of TM−N−C catalysts. NM can tune the coordination environment of TM−N−C, resulting in the change of electron structure of TM−N−C. Therefore, we prepared Ni−N−C and S modified Ni−N−C supported on N doped carbon for ECR application (**Paper V**). The ECR performance of S decorated Ni SAC was evaluated. The combination of experimental investigations and DFT calculations demonstrates that the high activity and selectivity of ECR to CO is due to a synergistic effect of the S and Ni−N_X moiety.

Based on above study, we believe that there are more possible coordination environments for NM modified TM−N−C. However, most studies could only reveal inadequate structural details of metal centers and NM ligands, due to the limitations of experimental techniques. Therefore, we proposed design principles for advanced NM doped TM−N_X−C SACs for CO generation and investigated their ECR performance and mechanism for different TM atoms in various coordination environments (**Paper VI**).

Another strategy to tune the structure of SACs is constructing dual-atom catalysts (DACs) by introducing second transition metal atom. The single active center of SACs makes it difficult to break the constraint of scaling relationship between the adsorption energies of intermediates due to the complicated multiple proton-coupled electron transfer in ECR. Therefore, in **Paper**

VII, Ni SAC (Ni−NC), Mn SAC (Mn−NC), Mn−Ni DAC (Mn−Ni−NC), Ni−Ni DAC (Ni−Ni−NC) and Mn−Mn DAC (Mn−Mn−NC) were synthesized. The coordination environments of SACs and DACs were studied by X-ray absorption spectroscopy (XAS). The performances for ECR to CO on these catalysts were compared. DFT calculations were employed to reveal the origin of the difference of activity.

Reference

[1] Caldeira, K.; E. Wickett, M. Anthropogenic carbon and ocean pH. *Nature* **2003**, *425*, 365.

[2] Fu, Y.; Sun, D.; Chen, Y.; Huang, R.; Ding, Z.; Fu, X.; Li, Z. An amine-functionalized titanium metal-organic framework photocatalyst with visible-light-induced activity for CO_2 reduction. *Angew. Chem. Int. Ed*. **2012**, *51*, 3364-3367.

[3] Li, J.R.; Ma, Y.; McCarthy, M.C.; Sculley, J.; Yu, J.; Jeong, H.K.; Balbuena, P.B.; Zhou, H.C. Carbon dioxide capture-related gas adsorption and separation in metal-organic frameworks. *Coord. Chem. Rev.* **2011**, *255*, 1791-1823.

[4] Li, X.; Yu, J.; Jaroniec, M.; Chen, X. Cocatalysts for selective photoreduction of CO_2 into solar fuels. *Chem. Rev*. **2019**, *119*, 3962-4179.

[5] Rubin, E.S.; Davison, J.E.; Herzog, H.J. The cost of CO_2 capture and storage. *Int. J. Greenh. Gas Control*. **2015**, *40*, 378-400.

[6] Keith, D.W.; Holmes, G.; St. Angelo, D.; Heidel, K. A process for capturing CO_2 from the atmosphere. *Joule* **2018**, *2*, 1573-1594.

[7] Drage, T.C.; Snape, C.E.; Stevens, L.A.; Wood, J.; Wang, J.; Cooper, A.I.; Dawson, R.; Guo, X.; Satterley, C.; Irons, R. Materials challenges for the development of solid sorbents for post-combustion carbon capture. *J. Mater. Chem*. **2012**, *22*, 2815-2823.

[8] Orr, J.F.M. CO_2 capture and storage: are we ready? *Energy Environ. Sci.* **2009**, *2*, 449-458.

[9] Maginn, E.J. What to do with CO_2. *J. Phys. Chem. Lett.* **2010**, *1*, 3478-3479.

[10] Ramdin, M.; de Loos, T.W.; Vlugt, T.J.H. State-of-the-art of CO_2 capture with ionic liquids. *Ind. Eng. Chem. Res*. **2012**, *51*, 8149-8177.

[11] Wang, J.Y.; Huang, L.; Yang, R.Y.; Wu, J.W.; Gao, Y.S.; Wang, Q.; O'Hare, D.; Zhong, Z.Y. Recent advances in solid sorbents for CO_2 capture and new development trends. *Energy Environ. Sci.* **2014**, *7*, 3478-3518.

[12] Yu, C.H.; Huang, C.H.; Tan, C.S. A review of CO_2 capture by absorption and adsorption. *Aerosol Air Qual. Res*. **2012**, *12*, 745-769.

[13] Inoue, T.; Fujishima, A.; Konishi, S.; Honda, K. Photoelectrocatalytic reduction of carbon dioxide in aqueous suspensions of semiconductor powders. *Nature* **1979**, *277*, 637-638.

[14] Halmann, M. Photoelectrochemical reduction of aqueous carbon dioxide on p-type gallium phosphide in liquid junction solar cells. *Nature* **1978**, 275,115-116.

[15] Li, W. Electrocatalytic Reduction of CO_2 to Small Organic Molecule Fuels on Metal Catalysts. In Advances in CO_2 Conversion and Utilization; *ACS Symposium Series*; **2010**, *5*, 55-76.

[16] Kortlever, R.; Peters, I.; Koper, S.; Koper, M.T.M. Electrochemical CO_2 reduction to

formic acid at low overpotential and with high faradaic efficiency on carbon-supported bimetallic Pd-Pt nanoparticles. *ACS Catal*. **2015**, *5*, 3916-3923.

[17] Zafar, Q.; Mattisson, T.; Gevert, B. Integrated hydrogen and power production with CO_2 capture using chemical-looping reformings redox reactivity of particles of CuO, Mn_2O_3, NiO, and Fe_2O_3 using SiO_2 as a support. *Ind. Eng. Chem. Res*. **2005**, *44,* 3485-3496.

[18] Chen, X.; Wang, J.; Huang, C.; Zhang, S.; Zhang, H.; Li, Z.; Zou, Z. Barium zirconate: a new photocatalyst for converting CO_2 into hydrocarbons under UV irradiation. *Catal. Sci. Technol*. **2015**, *5*, 1758-1763.

[19] Ding, J.; Bu, Y.; Ou, M.; Yu, Y.; Zhong, Q.; Fan, M. Facile decoration of carbon fibers with Ag nanoparticles for adsorption and photocatalytic reduction of CO_2. *Appl. Catal. B: Environ*. **2017**, *202*, 314-325.

[20] Wang, W.; Wang, S.; Ma, X.; Gong, J. Recent advances in catalytic hydrogenation of carbon dioxide. *Chem. Soc. Rev.* **2011**, *40*, 3703-3727.

[21] Shi, J.F.; Jiang, Y.J.; Jiang, Z.Y.; Wang, X.Y.; Wang, X.L.; Zhang, S.H.; Han, P.P.; yang, C. Enzymatic conversion of carbon dioxide. *Chem. Soc. Rev.* **2015**, *44*, 5981-6000.

[22] Gong, Q.; Ding, P.; Xu, M.; Zhu, X.; Wang, M.; Deng, J.; Ma, Q.; Han, N.; Zhu, Y.; Lu, J.; Feng, ZX.; Li, Y.F.; Zhong, W.; Li, Y.G. Structural defects on converted bismuth oxide nanotubes enable highly active electrocatalysis of carbon dioxide reduction. *Nat. Commun.* **2019**, *10*, 2807.

[23] Li, T.T.; Shan, B.; Xu, W.; Meyer, T.J. Electrocatalytic CO_2 reduction with a ruthenium catalyst in solution and on nanocrystalline TiO_2. *ChemSusChem* **2019**, *12*, 2402-2408.

[24] Grodkowski, J.; Neta. P. Copper-catalyzed radiolytic reduction of CO_2 to CO in aqueous solutions. *J*. Phys. Chem. B **2001**, *105*, 4967-4972.

[25] Agarwal, A.S.; Zhai, Y.; Hill, D.; Sridhar, N. The electrochemical reduction of carbon dioxide to formate/formic acid: engineering and economic feasibility. *ChemSusChem* **2011**, *4*, 1301-1310.

[26] Pritchard, J.; Filonenko, G.A.; Putten, R.; Hensen, E.J.; Pidko, E.A. Heterogeneous and homogeneous catalysis for the hydrogenation of carboxylic acid derivatives: history, advances and future directions. *Chem. Soc. Rev.* **2015**, *44*, 3808-3833.

[27] Zhu, Q.; Sun, X.; Yang, D.; Ma, J.; Kang, X.; Zheng, L.; Zhang, J.; Wu, Z.; Han, B. Carbon dioxide electroreduction to C_2 products over copper-cuprous oxide derived from electro synthesized copper complex. *Nat. Commun.* **2019**, *10*, 3851.

[28] Gao, S.; Lin, Y.; Jiao, X.; Sun, Y.; Luo, Q.; Zhang, W.; Li, D.; Yang, J.; Xie, Y. Partially oxidized atomic cobalt layers for carbon dioxide electroreduction to liquid fuel. *Nature* **2016**,

529, 68-71.

[29] Kaneco, S.; Katsumata, H.; Suzuki, T.; Ohta, K. Electrochemical reduction of carbon dioxide to ethylene at a copper electrode in methanol using potassium hydroxide and rubidium hydroxide supporting electrolytes. *Electrochim. Acta* **2006**, *51*, 3316-3321.

[30] Lu, Q.; Rosen, J.; Zhou, Y.; Hutchings, G.S.; Kimmel, Y.C.; Chen, J.G.; Jiao, F. A selective and efficient electrocatalyst for carbon dioxide reduction. *Nat. Commun.* **2014**, *5*, 3242.

[31] Durand, W.J.; Peterson, A.A.; Studt, F.; Abild-Pedersen, F.; Nørskov, J.K. Structure effects on the energetics of the electrochemical reduction of CO_2 by copper surfaces. *Surf. Sci.* **2011**, *605*, 1354-1359.

[32] Siahrostami, S.; Jiang, K.; Karamad, M.; Chan, K.; Wang, H.; Nørskov, J. Theoretical investigations into defected graphene for electrochemical reduction of CO_2. *ACS Sustain. Chem. Eng.* **2017**, *5*, 11080-11085.

[33] Chen, Y.; Li, C.W.; Kanan, M.W. Aqueous CO_2 reduction at very low overpotential on oxide-derived Au nanoparticles. *J. Am. Chem. Soc.* **2012**, *134*, 19969-19972.

[34] Sui, S.; Wang, X.; Zhou, X.; Su, Y.; Riffat, S.; Liu, C.j. A comprehensive review of Pt electrocatalysts for the oxygen reduction reaction: Nanostructure, activity, mechanism and carbon support in PEM fuel cells. *J. Mater. Chem. A* **2017**, *5*, 1808-1825.

[35] Gattrell, M.; Gupta, N.; Co, A. A review of the aqueous electrochemical reduction of CO_2 to hydrocarbons at copper. *J. Electroanal. Chem.* **2006**, *594*, 1-19.

[36] Sun, Z.; Ma, T.; Tao, H.; Fan, Q.; Han, B. Fundamentals and challenges of electrochemical CO_2 reduction using two-dimensional materials. *Chem* **2017**, *3*, 560-587.

[37] Zou, X.; Liu, M.; Wu, J.; Ajayan, P.M.; Li, J.; Liu, B.; Yakobson, B.I. How nitrogen-doped graphene quantum dots catalyze electroreduction of CO_2 to hydrocarbons and oxygenates. *ACS Catal.* **2017**, *7*, 6245-6250.

[38] García Rey, N.; Dlott, D.D. Structural transition in an ionic liquid controls CO_2 electrochemical reduction. *J. Phys. Chem. C* **2015**, *119*, 20892-20899.

[39] Ma, T.; Fan, Q.; Li, X.; Qiu, J.; Wu, T.; Sun, Z. Graphene-based materials for electrochemical CO_2 reduction. *J. CO_2 Util*. **2019**, *30*, 168-182.

[40] Benson, E.E.; Kubiak, C.P.; Sathrum, A.J.; Smieja, J.M. Electrocatalytic and homogeneous approaches to conversion of CO_2 to liquid fuels. *Chem. Soc. Rev.* **2009**, *38*, 89-99.

[41] Qiao, J.; Liu, Y.; Hong, F.; Zhang, J. A review of catalysts for the electroreduction of carbon dioxide to produce low-carbon fuels. *Chem. Soc. Rev*. **2014**, *43*, 631-675.

[42] Sun, Z.; Talreja, N.; Tao, H.; Texter, J.; Muhler, M.; Strunk, J.; Chen, J. Catalysis of carbon

dioxide photoreduction on nanosheets: fundamentals and challenges. *Angew. Chem. Int. Ed.* **2018**, *57*, 7610-7627

[43] Zhu, X.; Li, Y. Review of two-dimensional materials for electrochemical CO_2 reduction from a theoretical perspective. *Wiley Interdiscip. Rev. Comput. Mol. Sci.* **2019**, *9*, e1416.

[44] Zhang, L.; Zhao, Z.J.; Gong, J. Nanostructured materials for heterogeneous electrocatalytic CO_2 reduction and their related reaction mechanisms. *Angew. Chem. Int. Ed.* **2017**, *56*, 11326-11353.

[45] DeCiccio, D.; Ahn, S.T.; Sen, S.; Schunk, F.; Palmore, G.T.R.; Rose-Petruck, C. Electrochemical reduction of CO_2 with clathrate hydrate electrolytes and copper foam electrodes. *Electrochem. commun.* **2015**, *52*, 13-16.

[46] Appel, A.M.; Bercaw, J.E.; Bocarsly, A.B.; Dobbek, H.; DuBois, D.L.; Dupuis, M.; Ferry, J.G.; Fujita, E.; Hille, R.; Kenis, P.J.; et al. Frontiers, opportunities, and challenges in biochemical and chemical catalysis of CO_2 fixation. *Chem. Rev*. **2013**, *113*, 6621-6658.

[47] Zhong, M.; Tran, K.; Min, Y.; Wang, C.; Wang, Z.; Dinh, C.T.; De Luna, P.; Yu, Z.; Rasouli, A.S.; Brodersen, P. Accelerated discovery of CO_2 electrocatalysts using active machine learning. *Nature* **2020**, *581*, 178-183.

[48] Geioushy, R.A.; Khaled, M.M.; Alhooshani, K.; Hakeem, A.S.; Rinaldi, A. Graphene/ZnO/Cu_2O electrocatalyst for selective conversion of CO_2 into n-propanol. *Electrochim. Acta* **2017**, *245*, 456-462.

[49] Hori. Y. Electrochemical CO_2 reduction on metal electrodes. *Mod. Aspect. Electroc*. **2008**, *42*, 89-189.

[50] Murata, A.; Hori, Y. Product selectivity affected by cationic species in electrochemical reduction of CO_2 and CO at a Cu electrode. *Bull. Chem. Soc. Jpn.* **1991**, *64*, 123-127.

[51] Qin, B.; Li, Y.; Fu, H.; Wang, H.; Chen, S.; Liu, Z.; Peng, F. Electrochemical reduction of CO_2 into tunable syngas production by regulating the crystal facets of earth-abundant Zn catalyst. *ACS Appl. Mater. Interfaces* **2018**, *10*, 20530-20539.

[52] Jiang, K.; Huang, Y.; Zeng, G.; Toma, F.M.; Goddard, W.A.; Bell, A.T. Effects of surface roughness on the electrochemical reduction of CO_2 over Cu. *ACS Energy Lett.* **2020**, *5*, 1206-1214.

[53] Zhu, W.; Zhang, Y.J.; Zhang, H.; Lv, H.; Li, Q.; Michalsky, R.; Peterson, A.A.; Sun, S. Active and selective conversion of CO_2 to CO on ultrathin Au nanowires. *J. Am. Chem. Soc.* **2014**, *136*, 16132-16135.

[54] Huang, X.; Tang, S.; Mu, X.; Dai, Y.; Chen, G.; Zhou, Z.; Ruan, F.; Yang, Z.; Zheng, N. Freestanding palladium nanosheets with plasmonic and catalytic properties. *Nat. Nanotechnol.*

2011, *6*, 28-32.

[55] Zhu, W.; Zhang, L.; Yang, P.; Hu, C.; Luo, Z.; Chang, X.; Zhao, Z.J.; Gong, J. Low-coordinated edge sites on ultrathin palladium nanosheets boost carbon dioxide Electroreduction performance. *Angew. Chem. Int. Ed*. **2018**, *57*, 11544-11548.

[56] Mistry, H.; Reske, R.; Zeng, Z.; Zhao, Z.J.; Greeley, J.; Strasser, P.; Cuenya, B.R. Exceptional size-dependent activity enhancement in the electroreduction of CO_2 over Au nanoparticles. *J. Am. Chem. Soc.* **2014**, *136*, 16473-16476.

[57] Yang, Q.; Shi, L.; Yu, B.; Xu, J.; Wei, C.; Wang, Y.; Chen, H. Facile synthesis of ultrathin Pt–Pd nanosheets for enhanced formic acid oxidation and oxygen reduction reaction. *J. Mater. Chem. A* **2019**, *7*, 18846-18851.

[58] Gao, F.; Zhang, Y.; Ren, F.; Shiraishi, Y.; Du, Y. Universal surfactant-free strategy for self-standing 3D tremella-like Pd-M (M = Ag, Pb, and Au) nanosheets for superior alcohols electrocatalysis. *Adv. Funct. Mater.* **2020**, *30*, 2000255.

[59] Zhang, S.; Fan, Q.; Xia, R.; Meyer, T.J. CO_2 Reduction: from homogeneous to heterogeneous electrocatalysis. *Acc. Chem. Res.* **2020,** *53*, 255-264.

[60] Wang, Y.; Cao, L.; Libretto, N.J.; Li, X.; Li, C.; Wan, Y.; He, C.; Lee, J.; Gregg, J.; Zong, H.; Su, D.; Miller, J.T.; Mueller, T.; Wang, C. Ensemble effect in bimetallic electrocatalysts for CO_2 reduction. *J. Am. Chem. Soc.* **2019**, *141*, 16635-16642.

[61] Liu, K.; Ma, M.; Wu, L.; Valenti, M.; Cardenas-Morcoso, D.; Hofmann, J.P.; Bisquert, J.; Gimenez, S.; Smith, W.A. Electronic effects determine the selectivity of planar Au-Cu bimetallic thin films for electrochemical CO_2 reduction. *ACS Appl. Mater. Inter.* **2019**, *11*, 16546-16555.

[62] Wu, Z.P.; Lu, X.F.; Zang, S.Q.; Lou, X.W. Non-noble-metal-based electrocatalysts toward the oxygen evolution reaction. *Adv. Funct. Mater.* **2020**, *30*, 1910274.

[63] Zhu, Y.P.; Guo, C.; Zheng, Y.; Qiao, S.Z. Surface and interface engineering of noble-metal-free electrocatalysts for efficient energy conversion processes. *Acc. Chem. Res*. **2017**, *50*, 915-923.

[64] Kuhl, K.P.; Cave, E.R.; Abram, D.N.; Jaramillo, T.F. New insights into the electrochemical reduction of carbon dioxide on metallic copper surfaces. *Energy Environ. Sci.* **2012**, *5*, 7050-7059.

[65] Kuang, Y.; Feng, G.; Li, P.; Bi, Y.; Li, Y.; Sun, X. Single-crystalline ultrathin nickel nanosheets array from in situ topotactic reduction for active and stable electrocatalysis. *Angew. Chem. Int. Ed.* **2016**, *55*, 693-697.

[66] Zhang, W.; Hu, Y.; Ma, L.; Zhu, G.; Zhao, P.; Xue, X.; Chen, R.; Yang, S.; Ma, J.; Liu, J.;

Jin, Z. Liquid-phase exfoliated ultrathin Bi nanosheets: uncovering the origins of enhanced electrocatalytic CO_2 reduction on two-dimensional metal nanostructure. *Nano Energy* **2018**, *53*, 808-816.

[67] Pan, J.; Sun, Y.; Deng, P.; Yang, F.; Chen, S.; Zhou, Q.; Park, H.S.; Liu, H.; Yu Xia, B. Hierarchical and ultrathin copper nanosheets synthesized via galvanic replacement for selective electrocatalytic carbon dioxide conversion to carbon monoxide. *Appl. Catal. B: Environ*. **2019**, *255*, 117736.

[68] Wang, Y.; Shen, H.; Livi, K.J.T.; Raciti, D.; Zong, H.; Gregg, J.; Onadeko, M.; Wan, Y.; Watson, A.; Wang, C. Copper nanocubes for CO_2 reduction in gas diffusion electrodes. *Nano Lett*. **2019**, *19*, 8461-8468.

[69] Zhang, W.; Yang, S.; Jiang, M.; Hu, Y.; Hu, C.; Zhang, X.; Jin, Z. Nanocapillarity and nanoconfinement effects of pipet-like bismuth@carbon nanotubes for highly efficient electrocatalytic CO_2 reduction. *Nano Lett*. **2021**, *21*, 2650-2657.

[70] Tao, H.; Gao, Y.; Talreja, N.; Guo, F.; Texter, J.; Yan, C.; Sun, Z. Two-dimensional nanosheets for electrocatalysis in energy generation and conversion. *J. Mater. Chem. A* **2017**, *5*, 7257-7284.

[71] Chai, G.L.; Guo, Z.X. Highly effective sites and selectivity of nitrogen-doped graphene/CNT catalysts for CO_2 electrochemical reduction. *Chem. Sci.* **2016**, *7*, 1268-1275.

[72] Wu, J.; Liu, M.; Sharma, P.P.; Yadav, R.M.; Ma, L.; Yang, Y.; Zou, X.; Zhou, X.D.; Vajtai, R.; Yakobson, B.I.; Lou, J.; Ajayan, P.M. Incorporation of nitrogen defects for efficient reduction of CO_2 via two-electron pathway on three-dimensional graphene foam. *Nano Lett.* **2016**, *16*, 466-470.

[73] Duan, X.; Xu, J.; Wei, Z.; Ma, J.; Guo, S.; Wang, S.; Liu, H.; Dou, S. Metal-free carbon materials for CO_2 electrochemical reduction. *Adv. Mater.* **2017**, *29*. 1701784

[74] Sreekanth, N.; Nazrulla, M.A.; Vineesh, T.V.; Sailaja, K.; and Phani, K.L.; Chem. Commun. Metal-free boron-doped graphene for selective electroreduction of carbon dioxide to formic acid/formate. **2015**, *51*, 16061.

[75] Liu, Y.; Zhao, J.; Cai, Q. Pyrrolic-nitrogen doped graphene: a metal-free electrocatalyst with high efficiency and selectivity for the reduction of carbon dioxide to formic acid: a computational study. *Phys. Chem. Chem. Phys.* **2016**, *18*, 5491-5498.

[76] Rogers, C.; Perkins, W.S.; Veber, G.; Williams, T.E.; Cloke, R.R.; Fischer, F.R. Synergistic enhancement of electrocatalytic CO_2 reduction with gold nanoparticles embedded in Functional graphene nanoribbon composite electrodes. *J. Am. Chem. Soc*. **2017**, *139,* 4052-4061.

[77] Liu, X.; Zhu, L.; Wang, H.; He, G.; Bian, Z. Catalysis performance comparison for

electrochemical reduction of CO_2 on Pd-Cu/graphene catalyst. *RSC Adv*. **2016**, *6*, 38380-38387.

[78] Su, P.; Iwase, K.; Nakanishi, S.; Hashimoto, K.; Kamiya, K. Nickel-nitrogen-modified graphene: an efficient electrocatalyst for the reduction of carbon dioxide to carbon monoxide. *Small* **2016**, *12*, 6083-6089.

[79] Huang, J.; Guo, X.; Wei, Y.; Hu, Q.; Yu, X.; Wang, L. A renewable, flexible and robust single layer nitrogen-doped graphene coating Sn foil for boosting formate production from electrocatalytic CO_2 reduction. *J. CO_2 Util*. **2019**, *33*, 166-170.

[80] Lei, F.; Liu, W.; Sun, Y.; Xu, J.; Liu, K.; Liang, L.; Yao, T.; Pan, B.; Wei, S.; Xie, Y. Metallic tin quantum sheets confined in graphene toward high-efficiency carbon dioxide electroreduction. *Nat. Commun.* **2016**, *7*, 12697.

[81] Li, F.; Chen, L.; Xue, M.; Williams, T.; Zhang, Y.; MacFarlane, D.R.; Zhang, J. Towards a better Sn: efficient electrocatalytic reduction of CO_2 to formate by Sn/SnS_2 derived from SnS_2 nanosheets. *Nano Energy* **2017**, *31*, 270-277.

[82] Lu, X.; Tan, T.H.; Ng, Y.H.; Amal, R. Highly selective and stable reduction of CO_2 to CO by a graphitic carbon nitride/carbon nanotube composite electrocatalyst. *Eur. J. Chem*. **2016**, *22*, 11991-11996.

[83] Guo, S.; Zhao, S.; Wu, X.; Li, H.; Zhou, Y.; Zhu, C.; Yang, N.; Jiang, X.; Gao, J.; Bai, L.; Liu, Y.; Lifshitz, Y.; Lee, T.S.; Kang, Z.H. A Co_3O_4-CDots-C_3N_4 three component electrocatalyst design concept for efficient and tunable CO_2 reduction to syngas. *Nat. Commun*. **2017**, *8*, 1828.

[84] Yang, X.F.; Wang, A.Q.; Qiao, B.T.; Li, J.; Liu, J.Y.; Zhang, T. Single-atom catalysts: a new frontier in heterogeneous catalysis. *Acc. Chem. Res*. **2013**, *46*, 1740-1748.

[85] Wang, A.; Li, J.; Zhang, T. Heterogeneous single-atom catalysis. *Nat. Rev. Chem*. **2018**, *2*, 65-81.

[86]Chorkendorff, I.; Niemantsverdriet, J.W. Concepts of modern catalysis and kinetics. *Wiley: Weinheim*, **2003**.

[87] Jaramillo, T. F.; Jorgensen, K. P.; Bonde, J.; Nielsen, J. H.; Horch, S.; Chorkendorff, I. Identification of active edge sites for electrochemical H_2 evolution from MoS_2 nanocatalysts. *Science* **2007**, *317*, 100-102.

[88] Seh, Z.W.; Kibsgaard, J.; Dickens, C.F.; Chorkendorff, I.; Norskov, J.K.; Jaramillo, T.F. Combining theory and experiment in electrocatalysis: Insights into materials design. *Science* **2017**, *355*.

[89] Kyriakou, G.; Boucher, M. W.; Jewell, A. D.; Lewis, E. A.; Lawton, T. J.; Baber, A. E.; Tierney, H. L.; Flytzani-Stephanopoulos, M.; Sykes, E. C. Isolated metal atom geometries as a

strategy for selective heterogeneous hydrogenations. *Science* **2012**, *335*, 1209-1212.

[90] Zhang, N.; Zhou, T.; Chen, M.; Feng, H.; Yuan, R.; Zhong, C.a.; Yan, W.; Tian, Y.; Wu, X.; Chu, W.; Wu, C.Z.; Xie, Y. High-purity pyrrole-type FeN_4 sites as a superior oxygen reduction electrocatalyst. *Energy. Environ. Sci*. **2020**, *13*, 111-118.

[91] Yin, X.P.; Wang, H.J.; Tang, S.F.; Lu, X.L.; Shu, M.; Si, R.; Lu, T.B. Engineering the coordination environment of single-atom platinum anchored on graphdiyne for optimizing electrocatalytic hydrogen evolution. *Angew. Chem. Int. Ed.* **2018**, *57*, 9382-9386.

[92] Wang, Y.; Chen, Z.; Han, P.; Du, Y.; Gu, Z.; Xu, X.; Zheng, G. Single-atomic Cu with multiple oxygen vacancies on ceria for electrocatalytic CO_2 reduction to CH_4. *ACS Catal.* **2018**, *8*, 7113-7119.

[93] Xiao, M.; Gao, L.; Wang, Y.; Wang, X.; Zhu, J.; Jin, Z.; Liu, C.; Chen, H.; Li, G.; Ge, J.; He, Q.G.; Wu, Z.J.; Chen, Z.W.; Xing, W. Engineering energy level of metal center: Ru single-atom site for efficient and durable oxygen reduction catalysis. *J. Am. Chem. Soc.* **2019**, *141*, 19800-19806.

[94] Zhang, H.; Yu, L.; Chen, T.; Zhou, W.; Lou, X.W.D. Surface modulation of hierarchical MoS_2 nanosheets by Ni single atoms for enhanced electrocatalytic hydrogen evolution. *Adv. Funct. Mater*. **2018**, *28*, 1807086.

[95] Li, H.; Wang, L.; Dai, Y.; Pu, Z.; Lao, Z.; Chen, Y.; Wang, M.; Zheng, X.; Zhu, J.; Zhang, W.; Si, R.; Zeng, J. Synergetic interaction between neighboring platinum monomers in CO_2 hydrogenation. *Nat. Nanotechnol*. **2018**, *13*, 411-417.

[96] Ye, S.; Luo, F.; Zhang, Q.; Zhang, P.; Xu, T.; Wang, Q.; He, D.; Guo, L.; Zhang, Y.; He, C.; Ouyang, X.P.; Gu, M.; Liu, J.H.; Sun, X.L. Highly stable single Pt atomic sites anchored on aniline-stacked graphene for hydrogen evolution reaction. *Energy. Environ. Sci.* **2019**, *12*, 1000-1007.

[97] Yuan, J.; Zhang, W.; Li, X.; Yang, J. A high-performance catalyst for methane conversion to methanol: graphene supported single atom Co. *Chem. Commun*. **2018**, *54*, 2284-2287.

[98] Ramalingam, V.; Varadhan, P.; Fu, H.C.; Kim, H.; Zhang, D.; Chen, S.; Song, L.; Ma, D.; Wang, Y.; Alshareef, H.N.; He, J.H. Heteroatom-Mediated Interactions between ruthenium single atoms and an MXene Support for efficient hydrogen evolution. *Adv. Mater.* **2019**, *31*, e1903841.

[99] Back, S.; Lim, J.; Kim, N.Y.; Kim, Y.H.; Jung, Y. Single-atom catalysts for CO_2 electroreduction with significant activity and selectivity improvements. *Chem. Sci*. **2017**, *8*, 1090-1096.

[100] Huan, T.N.; Ranjbar, N.; Rousse, G.; Sougrati, M.; Zitolo, A.; Mougel, V.; Jaouen, F.;

Fontecave, M. Electrochemical reduction of CO_2 catalyzed by Fe-N-C materials: a structure–selectivity study. *ACS Catal.* **2017**, *7,* 1520-1525.

[101] Zhang, C.; Yang, S.; Wu, J.; Liu, M.; Yazdi, S.; Ren, M.; Sha, J.; Zhong, J.; Nie, K.; Jalilov, A.S.; Li, Z.Y.; Li, H.M.; Yakobson, B.I.; Wu, Q.; Ringe, E.; Xu, H. Electrochemical CO_2 reduction with atomic iron-dispersed on nitrogen-doped graphene. *Adv. Energy. Mater* **2018**, *8*, 1703487.

[102] Zhang, H.; Li, J.; Xi, S.; Du, Y.; Hai, X.; Wang, J.; Xu, H.; Wu, G.; Zhang, J.; Lu, J.; Wang, J.Z. A graphene-supported single-atom FeN_5 catalytic site for efficient electrochemical CO_2 reduction. *Angew. Chem. Int. Ed*. **2019**, *58*, 14871-14876.

[103] Zhang, Z.; Ma, C.; Tu, Y.; Si, R.; Wei, J.; Zhang, S.; Wang, Z.; Li, J.F.; Wang, Y.; Deng, D. Multiscale carbon foam confining single iron atoms for efficient electrocatalytic CO_2 reduction to CO. *Nano Research* **2019**, *12*, 2313-2317.

[104] Gu, J.; Hsu, C.S.; Bai, L.; Chen, H. M.; Hu, X. Atomically dispersed Fe^{3+} sites catalyze efficient CO_2 electroreduction to CO. *Science* **2019**, *364*, 1091–1094.

[105] Yang, F.; Song, P.; Liu, X.; Mei, B.; Xing, W.; Jiang, Z.; Gu, L.; Xu, W. Highly efficient CO_2 electroreduction on ZnN_4 -based single-atom catalyst. *Angew. Chem. Int. Ed*. **2018**, *57*, 12303-12307.

[106] Zhao, S.; Chen, G.; Zhou, G.; Yin, L.C.; Veder, J.P.; Johannessen, B.; Saunders, M.; Yang, S.Z.; De Marco, R.; Liu, C.; Jiang, S.P. A universal seeding strategy to synthesize single atom catalysts on 2D Materials for electrocatalytic applications. *Adv. Funct. Mater*. **2019**, *30*, 1906157.

[107] Yang, H.B.; Hung, S.F.; Liu, S.; Yuan, K.; Miao, S.; Zhang, L.; Huang, X.; Wang, H.Y.; Cai, W.; Chen, R.; Gao, J.J.; Yang, X.F.; Chen, W.; Huang, Y.Q.; Chen, H.M.; Li, C.M.; Zhng, T.; Liu, B. Atomically dispersed Ni(i) as the active site for electrochemical CO_2 reduction. *Nat. Energy* **2018**, *3*, 140-147.

[108] Liu, S.; Yang, H.B.; Hung, S.F.; Ding, J.; Cai, W.; Liu, L.; Gao, J.; Li, X.; Ren, X.; Kuang, Z.; Huang, Y.Q.; Zhang, T.; Liu, B. Elucidating the electrocatalytic CO_2 reduction reaction over a model single-atom nickel catalyst. *Angew. Chem. Int. Ed.* **2020**, *59*, 798-803.

[109] Gong, Y.N.; Jiao, L.; Qian, Y.; Pan, C.Y.; Zheng, L.; Cai, X.; Liu, B.; Yu, S.H.; Jiang, H.L. Regulating the coordination environment of MOF-templated single-atom nickel electrocatalysts for boosting CO_2 reduction. *Angew. Chem. Int. Ed.* **2020**, *59*, 2705-2709.

[110] Han, J.; An, P.; Liu, S.; Zhang, X.; Wang, D.; Yuan, Y.; Guo, J.; Qiu, X.; Hou, K.; Shi, L.; Zhang, Y.; Zhao, S.L.; Long, C.; Tang, Z.Y. Reordering d orbital energies of single-site catalysts for CO_2 electroreduction. *Angew. Chem. Int. Ed.* **2019**, *58*, 12711-12716.

[111] Jiang, K.; Siahrostami, S.; Zheng, T.T.; Hu, Y.F.; Hwang, S.Y.; Stavitski, E.; Peng, Y.D.; Dynes, J.; Gangisetty, M.; Su, D.; Attenkofer, K.; Wang, H.T. Isolated Ni single atoms in graphene nanosheets for high-performance CO_2 reduction. *Energy Environ. Sci.* **2018**, *11*, 893-903.

[112] Zheng, W.; Yang, J.; Chen, H.; Hou, Y.; Wang, Q.; Gu, M.; He, F.; Xia, Y.; Xia, Z.; Li, Z.; Yang, B.; Lei, L.; Yuan, C.; He, Q.; Qiu, M.; Feng, X.L. Atomically defined undercoordinated active sites for highly efficient CO_2 electroreduction. *Adv. Func. Mater.* **2019**, 30, 1907658.

[113] Jiao, Y.; Zheng, Y.; Chen, P.; Jaroniec, M.; Qiao, S.Z. Molecular scaffolding strategy with synergistic active centers to facilitate electrocatalytic CO_2 reduction to hydrocarbon/alcohol. *J. Am. Chem. Soc.* **2017**, *139,* 18093-18100.

2. Methodology

2.1. Materials and Chemicals

Table 2.1. Information of chemicals and materials

Chemical	Formula	Supplier and Purity
silver nitrate	$AgNO_3$	Sigma-Aldrich, ≥99.0%
nickel hexahydrate nitrate	$Ni(NO_3)_2{\cdot}6H_2O$	Sigma-Aldrich, 98%
boric acid	H_3BO_3	Sigma-Aldrich, ≥99.5%
sodium borohydride	$NaBH_4$	Sigma-Aldrich, ≥98%
nickel(II) chloride hexahydrate	$NiCl_2{\cdot}6H_2O$	Sigma-Aldrich, 98 %
manganese(II) chloride tetrahydrate	$MnCl_2{\cdot}4H_2O$	Sigma-Aldrich, 98 %
dicyandiamide	$C_2H_4N_4$	Sigma-Aldrich, 99%
ammonium hydroxide solution	$NH_3{\cdot}H_2O$	Sigma-Aldrich, 28% NH_3 in H_2O
manganese(II) phthalocyanine	$C_{32}H_{16}MnN_8$	Sigma-Aldrich
nickel(II) phthalocyanine	$C_{32}H_{16}NiN_8$	Sigma-Aldrich
Trisodium citrate	$C_6H_5Na_3O_7$	Alfa Aesar
potassium bicarbonate	$KHCO_3$	Alfa Aesar, 98 %
nafion D-521 dispersion	-	Alfa Aesar, 5 % w/w in water and 1-propanol
nafion-117 ionic exchange membrane	-	Alfa Aesar
urea	$CO(NH_2)_2$	VWR, 99 %
hydrogen peroxide	H_2O_2	VWR
sulfuric acid	H_2SO_4	VWR, 25%
nitric acid	HNO_3	VWR, 65 wt%
Thiourea	CH_4N_2S	VWR, 99 %
ketjenblack EC-600 JD	-	AkzoNobel
Carbon dioxide	CO_2	Nippon, > 99.999%
Argon	Ar	Nippon, > 99.999%
Carbon paper	-	Toray
absolute ethanol	C_2H_5OH	Arcus, ≥99.0%

2.3. Computational methods

All spin-polarized calculations based on DFT were carried out via the Vienna ab initio Simulation Package (VASP) code [1, 2]. The projector augmented wave (PAW) method was adopted to describe the interactions between ions and electrons, the generalized gradient approximation (GGA) in the form of Perdew-Burke-Ernzerh (PBE) function was chosen to describe the electron exchange-correlation interaction [3-5]. In order to accurately explain the long-range van der Waals (vdW) interactions, the empirical correction (DFT-D3) was included [6]. The kinetic energy cutoff was set as 500 eV for the plane-wave basis set. The convergence criterion of energy and force was set to 1.0×10^{-5} eV and 1.0×10^{-2} eV/Å, respectively. Moreover, to explore defective structure stability, the ab initio molecular dynamics (AIMD) simulation was performed in NVT ensemble [7, 8]. The TM atom diffusion barrier was calculated by the climbing image nudged elastic band method (CINEB) [9]. The Bader charge analysis was employed to calculate the charge transfer [10]. The free energy diagrams of ECR were calculated by the computational hydrogen electrode (CHE) method [11].

The Gibbs free energy of each step can be expressed as Equation 1:

$$\Delta G = \Delta E + \Delta E_{ZPE} - T\Delta S \quad (1)$$

where ΔE, ΔE_{ZPE} and ΔS are the total energy changes obtained from DFT calculations, zero-point energy, and entropy between the reactants and the products, respectively. T is the temperature which is set to 298.15 K in our calculations. The limiting potential (U_L) can be calculated by $U_L = -\Delta G_{max}/ne$, where ΔG_{max} is the free energy change of the rate-determining step in ECR reactions. Then the overpotential can be calculated by the equation $\eta = U_{equ} - U_L$, where U_{equ} is the equilibrium potentials.

2.3. Catalysts preparation

2.3.1. Ag-B-g-C_3N_4 (Paper II)

For the synthesis of g-C_3N_4, 20 g $CO(NH_2)_2$ was put into a covered crucible and heated to 600 °C with a ramp rate of 5 °C min^{-1} and kept for 2 h in muffle furnace. After cooling to room temperature, the g-C_3N_4 sample was obtained. The sample was further sonicated under deionized water for 2 h to obtain thin g-C_3N_4 nanosheet.

For the synthesis of B doped g-C_3N_4, the mixture of 20 g $CO(NH_2)_2$ and 0.3 g H_3BO_3 was grinded evenly and placed in a covered crucible. The crucible was heated to 600 °C with a ramp rate of 5 °C min^{-1} and hold at 600 ºC for 2 h in a muffle furnace. After cooling down, sample was washed with hot water in order to remove B_2O_3, then vacuum dried for 24 h at 60 °C. The as-prepared B-g-C_3N_4 sample was sonicated for 2 h to obtain thin nanosheet.

The loading of Ag NPs on B-g-C_3N_4 was performed according to a procedure from a previous study [12]. Typically, 1.176 g $Na_3C_6H_5O_7$ and 0.085 g $AgNO_3$ were dissolved in 300 mL deionized water under dark environment. Then, the mixture of 0.081 g B-g-C_3N_4 and above solution was sonicated for 1 h. Subsequently, 50 mL of 0.05 M $NaBH_4$ solution was added dropwise under vigorous stirring for 8 h. The sample was collected by centrifugation and washed with deionized water, finally vacuum dried at 60 °C overnight. The Ag loading was 13.9 wt.% based on inductively coupled plasma optical emission spectroscopy (ICP-OES).

2.3.2. Ni−NS−C catalyst (Paper V)

The CB was firstly activated by concentrated HNO_3 solution to increase surface defects and oxygen-containing groups. Typically, 4 g CB was dispersed in 100 ml of HNO_3 solution followed by refluxing at 100 °C for 8 h with vigorously stirring. Subsequently, the suspension was washed with DI water several times until neutral pH and separated by vacuum filtration. Activated CB was obtained after drying at 120 °C in a vacuum oven for 24 h.

In a typical synthesis of Ni^{2+} adsorbed on CB (Ni^{2+}-CB), 1 g activated CB was dispersed in 400

mL DI water under sonication for 2 h. The Ni^{2+} solution (3 mg/mL) was prepared by dissolving 240 mg Ni $(NO_3)_2{\cdot}6H_2O$ in 80 mL DI water. Thereafter, 40 mL Ni^{2+} solution was added dropwise into the CB solution and kept under vigorous stirring for 12 h. The products were collected by vacuum filtration. After drying at 120 °C in a vacuum oven for 24 h, Ni-CB was obtained.

The Ni-NS-C catalyst was synthesized according to a modified method by Zheng et al. [13] Typically, 0.5 g Ni-CB and with 6.0 g thiourea was mixed and grinded to obtain fine powders. The powder was then transferred into a covered crucible and heated to 800 °C at a heating rate of 3 °C/min under 10 mL/min Ar flow and kept at 800 °C for 1 h. For comparison, the Ni−N−C catalyst was synthesized by replacing thiourea with urea. Metal free N−C and NS−C catalysts were also prepared by replacing Ni−CB with CB.

2.3.3. Mn−Ni−NC catalysts (Paper VII)

The preparation method of Mn-Ni-NC catalyst was based on Hao et al. [14] 9.89 mg $MnCl_2{\cdot}4H_2O$, 11.88 mg $NiCl_2{\cdot}6H_2O$ and 64.4 mg $C_6H_8O_7{\cdot}H_2O$ were dissolved in 2 ml ethanol and the solution was sonicated for 30 minutes. Meanwhile, 100 mg activated carbon black was dissolved in 3 ml ethanol and the solution was sonicated for 30 minutes. The two solutions were then mixed and stirred continuously under room temperature for 12 hours. The obtained suspension became black solid after drying at 75 ℃ for 12 h. The black solid was mixed with 1 g dicyandiamide and grinded for 10 minutes. Finally, the black mixture was transfer to a covered crucible and calcinated under Argon atmosphere (100 sccm) at 800 °C for 2 hours. The collected samples were washed by 3 M HCl several times, then were marked it as Mn−Ni−NC catalyst.

The preparation of Mn−Mn−NC and Ni−Ni−NC catalysts follows same procedure, except for adding single metal resource and 32.2 mg $C_6H_8O_7{\cdot}H_2O$.

The preparation of Mn−NC and Ni−NC catalysts use similar procedure, except that 50 μL $NH_3{\cdot}H_2O$ solution was added in the first step.

2.4. Characterizations

2.4.1. X-ray diffraction (XRD)

X-ray diffraction (XRD) diffractograms were collected on Bruker-AXS Micro-diffractometer D8 ADVANCE equipped with a CuKα radiation source (λ=1.54 Å) with a scan rate of 3° min^{-1} in the range of 10-80°.

2.4.2. Raman spectroscopy

The crystallinity was further examined by Raman spectroscopy (Renishaw, with a 532 nm excitation laser). The samples were focused with a × 50LWD objective lens and exposed to emission line for 10 s.

2.4.3. Transition Electron Microscopy (TEM)

Transmission electron microscopy (TEM), high-resolution TEM (HR-TEM) and energy-dispersive X-ray spectroscopy (EDS) mapping were conducted on JEM-2100 Plus (JEOL) electron microscope at 200 kV.

2.4.4. Aberration-corrected high-angle annular dark-field scanning transmission electron microscopy (HAADF-STEM)

The aberration-corrected high-angle annular dark-field scanning transmission electron microscopy (HAADF-STEM) was conducted on JEOL NEOARM 200 F with 200 kV of accelerating voltage.

2.4.5. X-ray absorption fine structure (XAFS) spectra

X-ray absorption fine structure (XAFS) spectra at the Mn and Ni K-edge was collected at Station Bending Magnet 31 (BM31) in European Synchrotron Radiation Facility (ESRF), Grenoble, France. The Mn and Ni K-edge X-ray absorption near edge structure (XANES) data were recorded in a fluorescence mode. Mn foil, Ni-Pc, Mn foil, and Mn-Pc were used as references.

2.4.6. X-ray photoelectron spectroscopy (XPS)

The surface compositions and element states of the catalysts were tested by X-ray photoelectron spectroscopy (XPS, ESCALAB Xi^+) using Al Kα excitation at 1486.6 eV.

2.4.7. N_2 physisorption

Nitrogen adsorption-desorption isotherms were measured on Micromeritics Tristar II 3020 instrument at −196 °C. The specific surface area was estimated by the Brunauer-Emmett-Teller (BET) method, and the pore size distribution was obtained from the Barrett-Joyner-Halenda (BJH) desorption isotherm. The temperature-programmed CO_2 desorption (CO_2-TPD) profile was measured on Micromeritics Autochem II ASAP 2920.

2.5. Electrochemical measurements

The electrocatalytic CO_2 reduction was carried out in three-electrode sealed H-type cell consisting of a working electrode (carbon paper, CP), a reference electrode (saturated Ag/AgCl

(3 M KCl)), and a counter electrode (Pt (1 cm^2)). All potentials were controlled by AUTOLAB PGSTAT302N workstation and converted to RHE by E (vs. RHE) = E (vs. Ag/AgCl) + 0.197 V + 0.059 × pH. The electrocatalyst ink was dropped uniformly on a piece of CP as the working electrode, followed by drying under an infrared lamp for 30 minutes. Nafion-117 membrane was used to separate the anode and cathode chamber. The pH value of 0.5 M $KHCO_3$ electrolyte is 7.2. High purity CO_2 was bubbled into the cathode chamber at a flow rate of 20 mL min^{-1} for 1 h before and during the test. Meanwhile, the electrolyte in the cathode was stirred at 1200 rmp. The linear sweep voltammetry (LSV) was collected in 0.5 M $KHCO_3$ at a scan rate of 10 mV s^{-1}. Electrochemical impedance spectroscopy (EIS) was measured in 0.5 M $KHCO_3$ at −0.8 V (vs.RHE) with an amplitude of 5 mV from 10^{-2} to 10^{-5} Hz.

Gaseous products CO and H_2 were quantified by an online gas chromatograph (GC, Agilent 7890B) with two TCD detectors equipped with a HayeSep Q column and a 5A molecular sieve column. Liquid products were determined by nuclear magnetic resonance (NMR) spectroscopy with a 400 MHz Bruker NMR spectrometer. The FE of gaseous products under different potentials were calculated by the equation 2 below:

$$FE = (Z \times P \times F \times V \times v)/(R \times T \times I) \quad (2)$$

where Z is the number of transferred electrons for one CO_2 molecule reduction to gaseous product, which is 2 for CO and H_2; P is atmospheric pressure of 1.01×10^5 Pa; F is Faraday constant 96485 C mol^{-1}; V is gas flow rate; v is the volume concentration of gas product; T is temperature of 298.15 K; R is the idea gas constant 8.314 J mol^{-1} K^{-1}; and I is the steady-state current at each applied potential.

References

[1] Kresse, G.; Joubert, D. From ultrasoft pseudopotentials to the projector augmented-wave method. *Phys. Rev. B* **1999**, *59*, 1758.

[2] Kresse, G.; Furthmüller, J. Efficiency of ab-initio total energy calculations for metals and semiconductors using a plane-wave basis set. *Comput. Mater. Sci*. **1996**, *6*, 15-50.

[3] Blöchl, P.E. Projector augmented-wave method. *Phys. Rev. B: Condens. Matter Mater. Phys*. **1994**, *50*, 17953-17979.

[4] Perdew, J. P. Burke, K.; Ernzerhof, M. Generalized gradient approximation made simple. *Phys. Rev. Lett*. **1996**, *77*, 3865-3868.

[5] Perdew, J.P.; Ernzerhof, M.; Burke, K. Rationale for mixing exact exchange with density functional approximations. *J. Chem. Phys.* **1996**, *105*, 9982-9985.

[6] Grimme, S.; Antony, J.; Ehrlich, S.; Krieg, H. A consistent and accurate ab initio parametrization of density functional dispersion correction (DFT-D) for the 94 elements H-Pu. *J. Chem. Phys*. **2010**, *132*, 154104-154123.

[7] Kresse, G.; Hafner, J.; Ab initio molecular dynamics for liquid metals. *Phys. Rev. B* **1993**, *47*, 558.

[8] Su, C.; Jiang, H.; Feng, J. Two-dimensional carbon allotrope with strong electronic anisotropy. *Phys. Rev. B* 2013, *87*, 075453.

[9] Henkelman, G.; Arnaldsson, A.; Jonsson, H. A fast and robust algorithm for Bader decomposition of charge density. *Comput. Mater. Sci*. **2006**, *36*, 354-360.

[10] Bader, R. Atoms in molecules: a quantum theory. Oxford University Press: New York, **1990**.

[11] Nørskov, J.K.; Rossmeisl, J.; Logadottir, A.; Lindqvist, L.; Kitchin, J.R.; Bligaard, T.; Jonsson, H. Origin of the overpotential for oxygen reduction at a fuel-cell cathode. *J. Phys. Chem. B* **2004**, *108*, 17886-17892.

[12] Zhang, L.; Mao, F.; Zheng, L. R.; Wang, H. F.; Yang, X. H.; Yang, H. G. Tuning metal catalyst with metal-C_3N_4 interaction for efficient CoO_2 electroreduction. *ACS Catal*. **2018**, *8*, 11035-11041.

[13] Zheng, T.; Jiang, K.; Ta, N.; Hu, Y.; Zeng, J.; Liu, J.; Wang, H. Large-scale and highly selective CO_2 electrocatalytic reduction on nickel single-atom catalyst. *Joule* **2019**, *3*, 265-278.

[14] Hao, Q.; Zhong, H.-X.; Wang, J.Z.; Liu, K.H.; Yan, J.M.; Ren, Z.H.; Zhou, N.; Zhao, X.; Zhang, H.; Liu, D.X.; Liu, X.; Chen, L.W.; Luo, J.; Zhang, X.B. Nickel dual-atom sites for electrochemical carbon dioxide reduction. *Nat. Synth.* **2022**, *1*, 719-728.

3. Result and Discussion

3.1. Efficient electrochemical reduction of CO_2 to CO by Ag-decorated B-doped g-C_3N_4: A combined theoretical and experimental study (Paper II)

In this paper, we prepared g-C_3N_4, B-g-C_3N_4 and Ag NPs loaded B-g-C_3N_4 catalysts, and their ECR performances were investigated by DFT calculations and experimental work.

3.1.1 DFT simulations

There are three different N atoms (N1, N2 and N3 sites), and two different C atoms (C1 and C2 sites) in g-C_3N_4, as shown in Appendix B, Figure S1. Previous studies have demonstrated that N2 atom with low coordination number is preferable to be substituted by nonmetal atoms [1, 2]. Therefore, B doped monolayer g-C_3N_4 was built with one B atom substituting one N2 atom. After geometric optimization, B atom bonds with the nearest N2 atom and C1 atom, forming pentagonal and hexagonal ring. The E_{sub} of B doped g-C_3N_4 is −1.38 eV, indicating the easiness to introduce B atom into g-C_3N_4 skeleton. The E_{ads} of Ag cluster on B-g-C_3N_4 is −1.98 eV, demonstrating that Ag_4 cluster are loaded stably on the B-g-C_3N_4 support and the resulting composite catalyst could possess good stability.

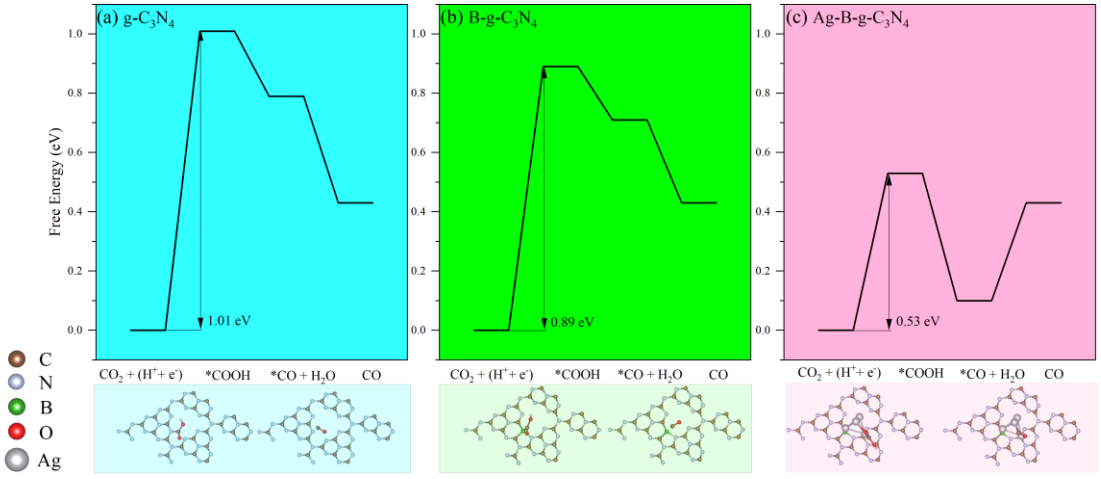

Figure 3.1. Calculated free energy profiles for ECR to CO on (a) g-C_3N_4, (b) B-g-C_3N_4 and (c) Ag-B-g-C_3N_4; The adsorption structures of key intermediates *COOH and *CO were depicted below.

The calculated Gibbs free energy change (ΔG) of the intermediates on g-C_3N_4, B-g-C_3N_4 and Ag-B-g-C_3N_4 were displayed in Figure 3.1a-c. The formation of intermediate *COOH is the potential determining step on the three electrocatalysts. The free energy barrier for CO production on pristine g-C_3N_4 is quite large at 1.01 eV, while the free energy barrier decreases by only 0.12 eV after introducing B atoms, indicating B atom alone cannot effectively improve the ECR performance. However, the combination of B and Ag atoms shows a large drop in free energy barrier of 0.53 eV, which suggested that B dopant and Ag NPs could be promising to enhance the ECR performance of g-C_3N_4. We further considered the possible active sites after

the doping of B and Ag, including S1(B atom), S2(N atom), S3 (C atom), S4(N atom), S5(N atom) and S6 (C atom) around the Ag cluster (Appendix B, Figure S2a). It turns outs that the intermediates could not be adsorbed on S1, S2, S3, S4 and S6. Only S5 can be a stable adsorption site for intermediates but with a free energy barrier of 1.16 eV (Appendix B, Figure S2b), larger than that of the Ag site. Thus, B, C and N atoms will not be the active sites for CO_2 activation, and Ag cluster is the only active center. The adsorption configurations of *COOH and *CO intermediates on the three electrocatalysts suggest that *COOH could bond with N, B and Ag atoms with different strength, leading to uphill in Gibbs free energy. In contrast, *CO could not bond well with the N and B atoms, exhibiting exothermic nature for CO desorption from pristine and B doped g-C_3N_4. However, it could interact strongly with Ag atoms, resulting in an endothermic reaction for CO desorption.

We further investigated the electronic structures of Ag-B-g-C_3N_4 by calculating total density of states, Bader charge and charge density difference. It is worth noting that there are more electron states between conduct band and valence band, and even near the Fermi level in B and Ag modified g-C_3N_4 (Figure 3.2a). In other words, the introduction of B atoms and Ag cluster could induce more impurity levels, which could improve the electrical conductivity and increase the ECR activity. Besides, the detailed charge transfer between B, Ag and g-C_3N_4 was shown in Figure 3.2b. B atom transferred 1.71e to C and N atoms, while the total charge transfer from Ag cluster to B-g-C_3N_4 scaffold is 0.74e, contributing to an electron-rich region at the interface of Ag and B-g-C_3N_4. It can be proposed that B dopant could improve electrical conductivity of the g-C_3N_4 support, while Ag NPs could sever as the ECR active center. Therefore, we synthesized the three catalysts (g-C_3N_4, B-g-C_3N_4 and Ag-B-g-C_3N_4) to verify the role of B and Ag NPs as proposed by DFT simulations.

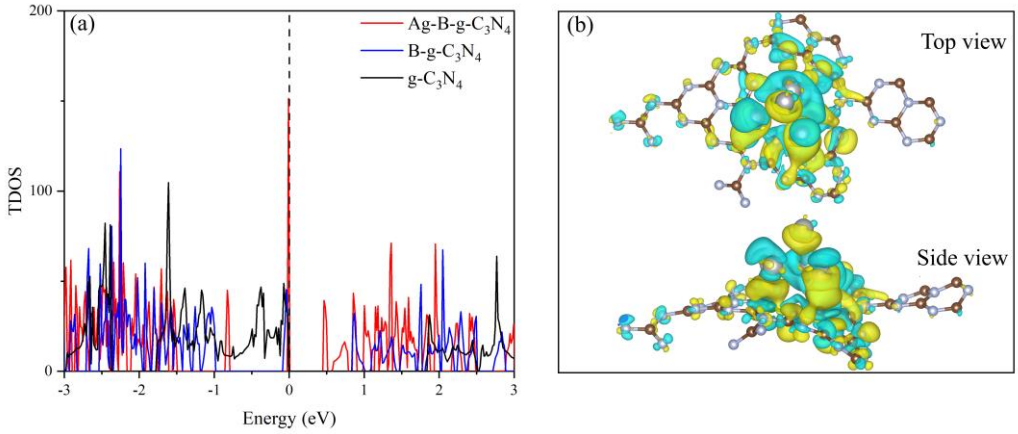

Figure 3.2. (a) Total density of states (TDOS) of g-C_3N, B- g-C_3N_4, and Ag-B-g-C_3N_4, where Fermi energy locates at 0 eV; (b) Charge density difference between Ag NPs and B-g-C_3N_4 for Ag-B-g-C_3N_4, where yellow and cyan denote electron accumulation and depletion, respectively; The isosurface value is set to be 0.001 e/Bohr^3.

3.1.2. Electrocatalysts characterization

To evidence the formation of nanocomposites, crystal structures were investigated by XRD characterization (Figure 3.3). Two characteristic peaks locating at 13.0° (100) and 27.6° (002) are assigned to the in-plane structure of tri-s-triazine motifs and the periodic stacking of layers of conjugated aromatic rings [3, 4]. The slight shift of the (002) peak towards high angle for B-g-C_3N_4 and Ag-B-g-C_3N_4 was probably related to structural variations such as the decreased interlayer distance after introducing B atoms [5]. The gradual decrease of the characteristic peak of g-C_3N_4 could be explained by the less ordered structure and reduced crystallinity after the doping of B and Ag. The XRD result could be supported by the structure deformation after introducing B and Ag NPs from DFT simulation study (Appendix B, Figure S1). Diffraction peaks located at 2θ = 38.1°, 44.3°, 64.4°, and 77.4° are the characteristic peaks of (111), (200), (220), and (311) crystal planes of Ag (Joint Committee for Powder Diffraction Standards (JCPDS) No. 65-2871). Meanwhile, the main characteristic peak of the B-g-C_3N_4 support was maintained. In addition, diffraction peaks of B_2O_3 or Ag_2O were not observed. Therefore, metallic Ag NPs loaded B-doped g-C_3N_4 (Ag-B-g-C_3N_4) was successfully prepared.

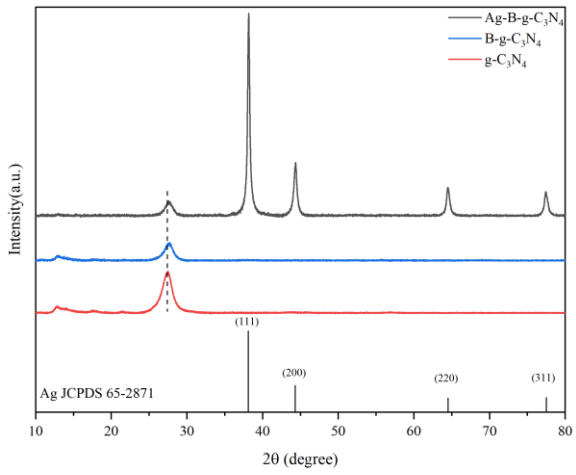

Figure 3.3. XRD patterns of g-C_3N_4, B-g-C_3N_4 and Ag-B-g-C_3N_4.

TEM was employed to study the morphology and size of Ag-B-g-C_3N_4. As exhibited in Figure 3.4a and b, spherical Ag NPs were evenly deposited on the B-g-C_3N_4. The average diameter of NPs is 4.95 nm, as further exemplified by TEM images in Appendix B, Figure S3, where the particle size distribution was also shown. It can be clearly seen that an interplanar spacing of 0.235 nm was obtained from the lattice fringes for Ag NPs (Figure 3.4c), attributing to the (111) plane of metallic Ag and close to the theoretical value of 0.236 nm. The selected area electron diffraction patten (SAED) of Ag-B-g-C_3N_4 was shown in Figure 3.4d. The diffraction circles corresponding to the (111), (200), (220) and (311) planes of Ag are apparent, consistent with the XRD results.

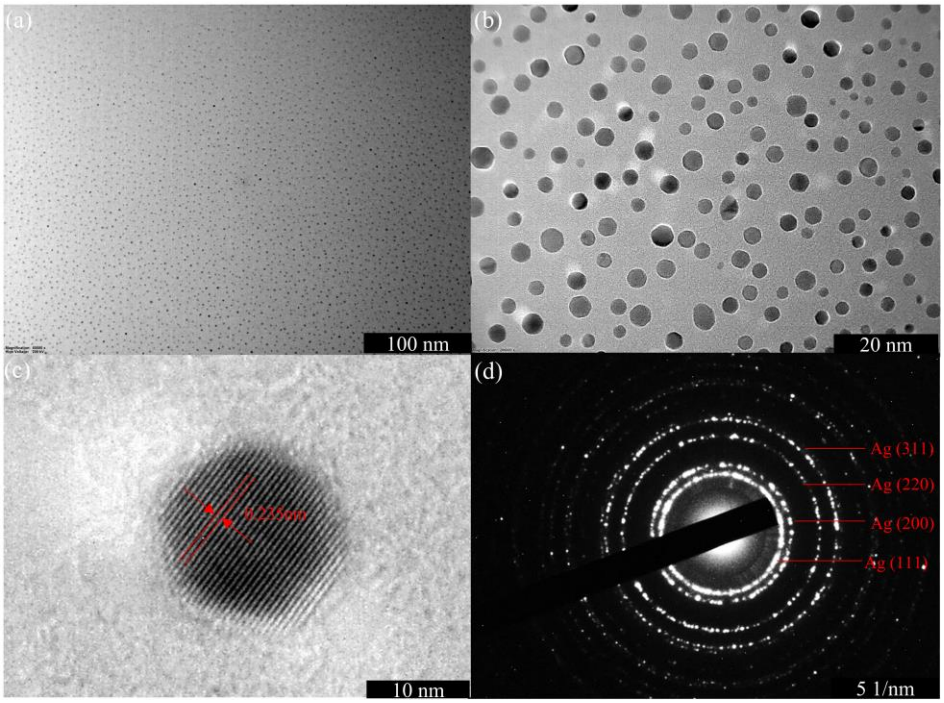

Figure 3.4. (a) and (b) TEM images of Ag-B-g-C_3N_4 with different magnifications; (c) HRTEM image of Ag-B-g-C_3N_4, which shows an interlayer distance of 0.235 nm for Ag; (d) SAED pattern of Ag NPs.

The high-resolution XPS spectra of C 1s, N 1s, B 1s and Ag 3d levels for Ag-B-g-C_3N_4 are shown in Figure 3.5. As the samples have been calcinated in air, O atoms would be inevitably introduced into the skeletons. Therefore, C−O and N−O spectra were detected. For C1s spectra (Figure 3.5a), three typical peaks at 288.3, 286.3 and 284.7 eV can be assigned to sp^2-bonded C−N−C of skeleton, C−O group and C−C of carbon contamination, respectively [6]. The N 1s spectrum could be deconvoluted into four peaks with binding energies at 404.3, 401.2, 399.4 and 398.7 eV (Figure 3.5b), which were attributed to the N−O, C−H−N, N− $(C)_3$ and C−N=C groups, respectively. A broad peak at 192.0 eV could be found in B 1s level (Figure 3.5c), which is ascribed to the C−NB group. This also evidences the successful doping of B atoms in g-C_3N_4. The spectra of Ag 3d exhibits two peaks with binding energies of 374.5 and 368.5 eV (Figure 3.5d), which are the standardized Ag $3d_{3/2}$ and Ag $3d_{5/2}$ levels of metallic Ag [7], demonstrating that Ag NPs was successfully loaded on B doped g-C_3N_4. The XPS spectra of g-C_3N_4 and B-g-C_3N_4 are shown in Appendix B, Figure S4 for comparison. The similar C 1s, N 1s and B ls spectra for the three catalysts indicate that the structure of the g-C_3N_4 support remains intact after doping with B and Ag (Appendix B, Figure S4).

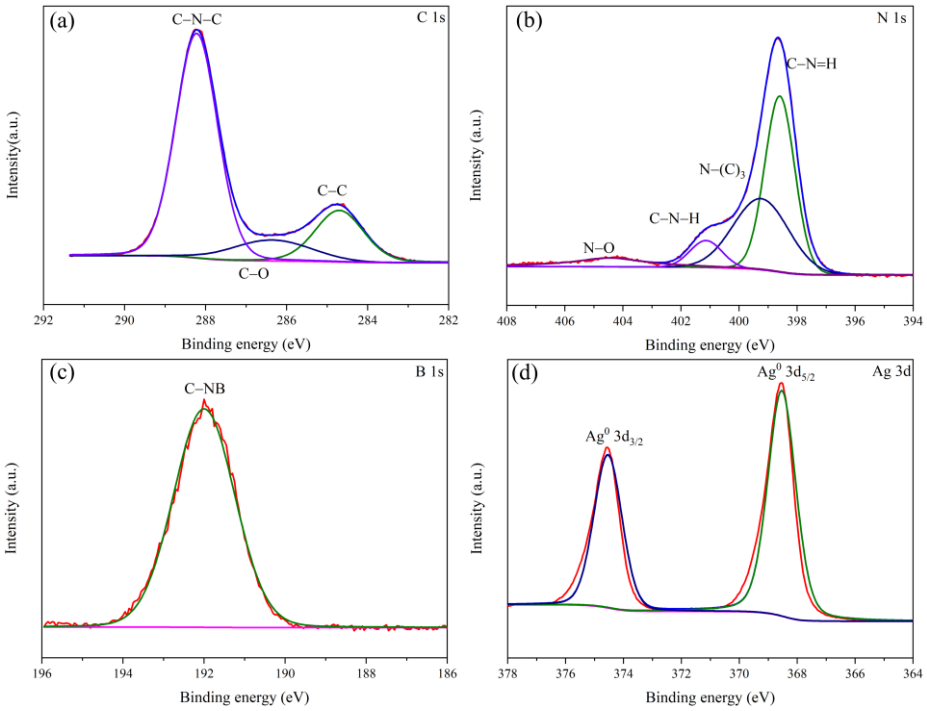

Figure 3.5. XPS spectra of Ag-B-g-C_3N_4 (a) C 1s, (b) N 1s, (c) B ls and (d) Ag 3d.

3.1.3. ECR activity test

The ECR catalytic performances were firstly evaluated by LSV, as exhibited in Figure 3.6a. In the presence of CO_2 feed gas, Ag-B-g-C_3N_4 catalyst showed apparently higher reduction current density in comparison with the other two samples, achieving a current density of −2.08 mA cm^{-2} at −0.8 V (vs. RHE). The bare carbon paper, and carbon black coated carbon paper were also tested as working electrodes but only exhibited a negligible weak current density (Appendix B, Figure S5). In N_2-saturated $KHCO_3$, the Faradic currents can be attributed to HER, whereas it displayed much higher current in CO_2-saturated $KHCO_3$ at the same potential (Figure 3.6b), indicting the catalytic activity of Ag-B-g-C_3N_4 for ECR. These results also suggested that Ag is the active center of the Ag-B-g-C_3N_4 electrocatalyst.

Constant potential electrolysis was performed by choosing the potential ranging from −0.5 V to −1.0 V (vs. RHE) to study the ECR selectivity over the Ag-B-g-C_3N_4 catalyst. The resultant gaseous products were analyzed by online GC, while liquid products were analyzed by 1H NMR spectroscopy. CO and H_2 were the only gaseous products with a total FE over 98% (Figure 3.6c). There is no liquid product found, as evidenced by ^{1}H NMR (Appendix B, Figure S6). The FE_{CO} of Ag-B-g-C_3N_4 increased firstly and then dropped with the increase of the applied potentials, achieving the maximum FE_{CO} of 93.2% at −0.8 V (vs. RHE). It was worth mentioning that both pristine g-C_3N_4 and B-g-C_3N_4 did not produce CO but only H_2 under potentials between −0.5 V to −1.0 V (vs. RHE). The bare carbon paper and carbon black coated

carbon paper also only generate H_2. These results are consistent with DFT calculations that Ag-B-g-C_3N_4 catalyst show the lowest Gibbs free energy for the *COOH generation, while B doping along could not obviously decrease its Gibbs free energy. Therefore, it can be concluded that Ag NPs is the only active center for ECR to CO.

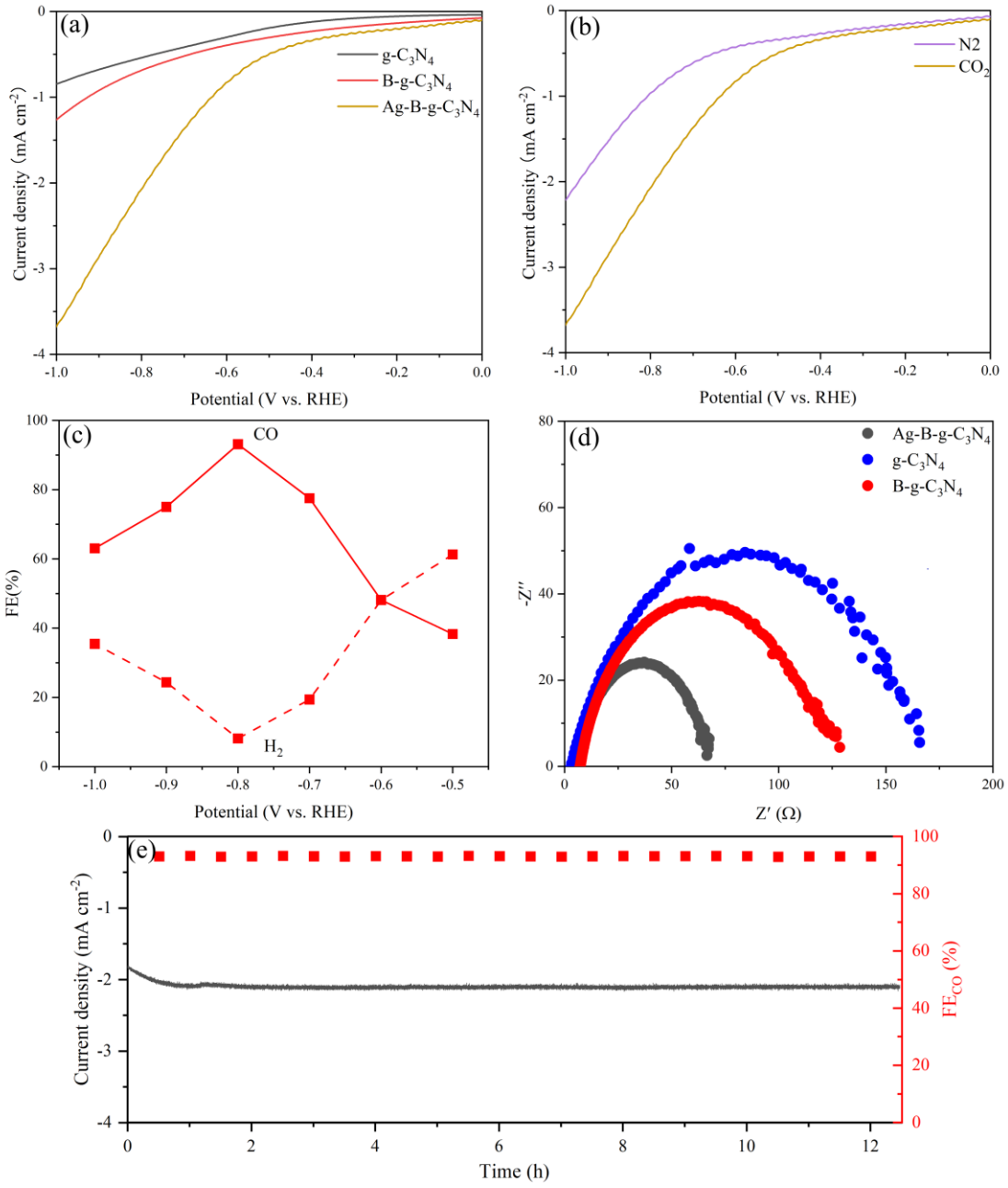

Figure 3.6. (a) LSV curves of g-C_3N_4, B-g-C_3N_4 and Ag-B-g-C_3N_4 catalysts in CO_2-saturated 0.5M $KHCO_3$ solution at a scan rate of 10 mV s^{-1}; (b) LSV curves of the Ag-B-g-C_3N_4 catalyst in N_2- and CO_2-saturated 0.5M $KHCO_3$ solution at a scan rate of 10 mV s^{-1}; (c) The Faradic efficiencies of CO generation and H_2 generation on the Ag-B-g-C_3N_4 catalyst; (d) EIS Nyquist plots for g-C_3N_4, B-g-C_3N_4 and Ag-B-g-C_3N_4 catalysts in 0.5 M $KHCO_3$ under potential of −0.8 V (vs. RHE); (e) Stability test of the Ag-B-g-C_3N_4 catalyst in 0.5 M $KHCO_3$ under −0.8 V (vs. RHE) for 12 h.

EIS was carried out at −0.8 V (vs. RHE) to disclose the origin of the excellent reactivity of the Ag-B-g-C_3N_4 nanocomposite. The Nyquist plots of g-C_3N_4, B-g-C_3N_4 and Ag-B-g-C_3N_4 were displayed in Figure 3.6d. Notably, B atoms could effectively improve g-C_3N_4 electron transport due to the generation of the impurity levels. After loading Ag NPs, a much lower charge transfer resistance (R_{CT}) was achieved on Ag-B-g-C_3N_4, validating that the decoration of Ag NPs could enhance electron transportation between the catalyst and CO_2 molecules thus the ECR capability. These results are in line with the DFT calculations that the electron accumulations at Ag/B-g-C_3N_4 interface could improve electrical conductivity and promote electron transport.

The long-term stability of Ag-B-g-C_3N_4 catalyst was examined by at −0.8 V (vs. RHE) (Figure 3.6e). Remarkably, the reduction current densities increased during the first hour and then remained stable at −2.08 mA cm^{-2} for 12 h. The corresponding FE_{CO} exhibited no obvious decay during the electrolysis process, indicting excellent stability of the catalyst for selective ECR to CO.

3.2. Theoretical study of single transition metal atom catalysts supported on two-dimensional Nb_2NO_2 for efficient electrochemical CO_2 reduction to CH_4 (Paper III)

In this work, we investigated the single transition metal atoms (V, Cr, Mn, Fe, Co, Ni) embedded O group terminated Nb_2N monolayer (Nb_2NO_2) as ECR catalysts by first-principles calculation.

3.2.1. Structure and stability of pristine Nb_2NO_2

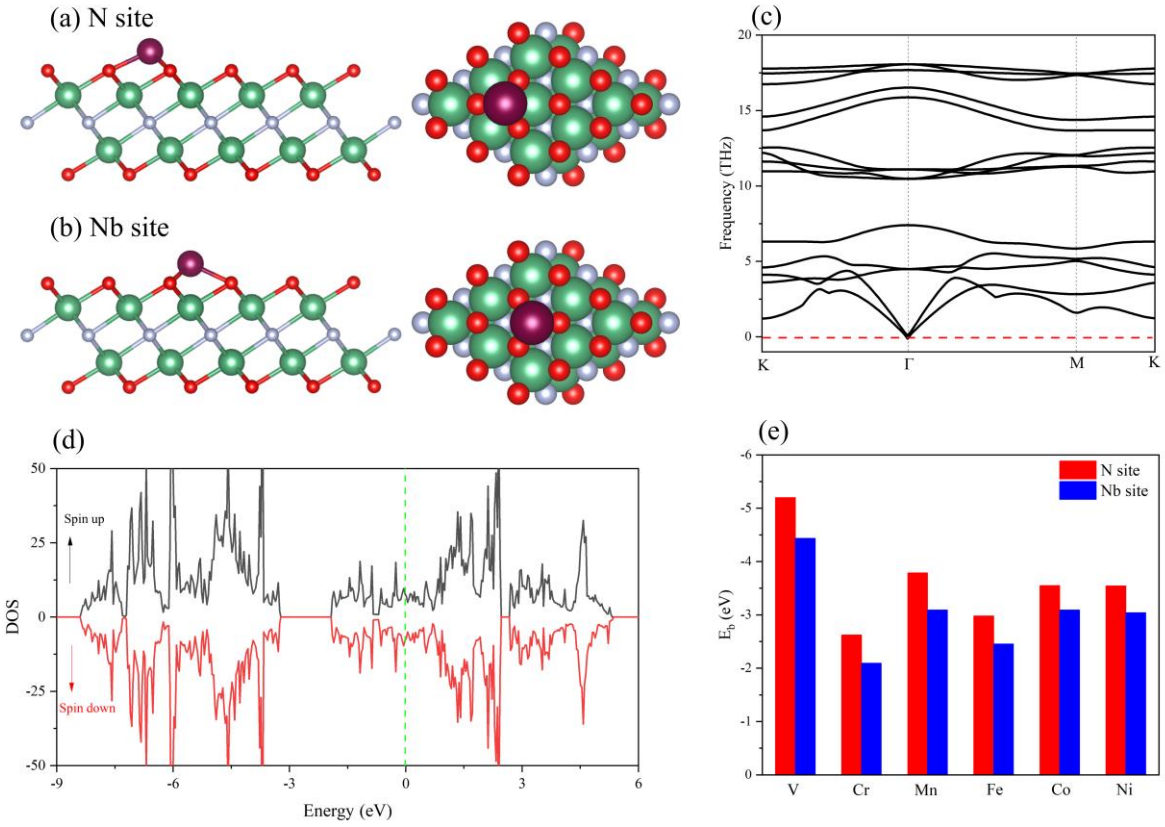

Figure 3.7. The two possible adsorption sites for TM atoms (a)N site and (b) Nb site, where the whitesmoke, red, turquoise and purple ball denote the N, O, Nb and TM atoms; (c) The phonon curves of Nb_2NO_2; (d) The total density of state of Nb_2NO_2, where the green dash line is Fermi energy level; (e) The binding energies of TM atoms on N site and Nb site.

After geometry optimization, the obtained lattice parameter *a* of clean Nb_2N monolayer is 3.11 Å, consistent with previous study [8]. Nb_2N monolayer shows a hexagonal symmetry with P63/mmc space group. O was then added on the centre of three Nb atoms, similar to the O functionalized Ti_2C MXene (Figure 3.7a and b) [9]. The binding energy (E_b) of O on Nb_2N monolayer was calculated by the equation: $E_b = (E(Nb_2NO_2) - E(O_2) - E(Nb_2N))/2$, where $E(Nb_2NO_2)$, $E(O_2)$, $E(Nb_2N)$ are the total energy of Nb_2NO_2, O_2 and Nb_2N [10]. A negative value of $E_b = -5.34$ eV demonstrates that Nb_2N monolayer can be easily covered by O atoms. It is possible for O group transforming to OH during ECR process. Therefore, we calculated the Gibbs free energy for H adsorption on O atoms, with ΔG^*H of −0.16 eV. A moderate ΔG^*H indicates that the proton can easily adsorb on and desorb from the surficial O atom, which may

promote protonation of the ECR intermediates. The phonon curves and AIMD simulation were performed to check its stability, as shown in Figure 3.7c and Appendix C, Figure S1. There are no imaginary bands in phonon spectra. The fluctuation of the total energy of Nb_2NO_2 is quite small and around the equilibrium. Meanwhile, the structure does not show any obvious changes, confirming that Nb_2NO_2 monolayer possesses excellent stability. On the other hand, the calculated density of state of Nb_2NO_2 exhibits metallic behavior, indicting good capability for electron transfer (Figure 3.7d). This endows Nb_2NO_2 monolayer excellent electrical conductivity, a prerequisite for an ideal substrate for SACs used in ECR.

3.2.2. Structure and stability of TM@Nb_2NO_2

As presented in Figure 3.7 a and b, there are two possible anchoring sites for single TM atoms: (1) the center site between three neighboring N atoms and the top of Nb atom (Nb site), (2) the center site between three neighboring Nb atoms and the top of N atom (N site). The thermodynamic stabilities of TM@Nb_2N were investigated by calculating E_b (Figure 3.7e and Appendix C, Table S1). Notably, a more negative value of E_b on N site indicates that TM atoms prefer to bind on N site. Moreover, the transition energy barriers (E_T) of single TM atoms from N to Nb site were calculated to evaluate its kinetic stability. The E_T were calculated by $E_T = E_{TS} - E_{IS}$, in which E_{TS} is the total energy of transition state (TS) from N to Nb site, while E_{IS} is the total energy of TM embedded in N site. As shown in Appendix C, Table S1, the E_T of TM atoms are quite large in the range of 0.87 to 2.58 eV, implying that it is difficult for TM atoms to diffuse and aggregate into clusters. These results suggest that single TM atom can be firmly anchored on N site.

3.2.3. CO_2 adsorption and activation on TM@Nb_2NO_2

The optimized CO_2 adsorption configurations on TM@Nb_2NO_2 were shown in Figure 3.8. Obviously, the carbon or oxygen atom of CO_2 molecule is absorbed on TM atoms. Meanwhile, it can be observed that CO_2 molecule is not absorbed on TM@Nb_2NO_2 in linear state, but with a certain degree of bending. The corresponding adsorption energies, bond lengths of C−TM and O−TM, bond angels of CO_2 molecule, and charge transfer between TM and CO_2 molecule are summarized in Table 3.1. The bond angle of CO_2 molecule on TM@Nb_2NO_2 increases with the atomic number, ranging from 138.39° to 154.34°. Specially, V@Nb_2NO_2 greatly deviated from the linear state, which indicates higher CO_2 adsorption capacity. The bond lengths of C−TM and O−TM are quite close to 2.00 Å, demonstrating strong adsorption between substrate and CO_2 molecule, consistent with previous studies [11, 12]. The negative adsorption energies indicate that CO_2 adsorption on the SACs is thermodynamically favorable. Bader charge

analysis confirm that there is a significant net charge transfer from V, Cr and Ni atoms to CO_2, with a value of −0.60e, −0.53e, −0.31e, respectively. Thus, CO_2 molecules can be effectively activated by V, Cr and Ni@Nb_2NO_2.

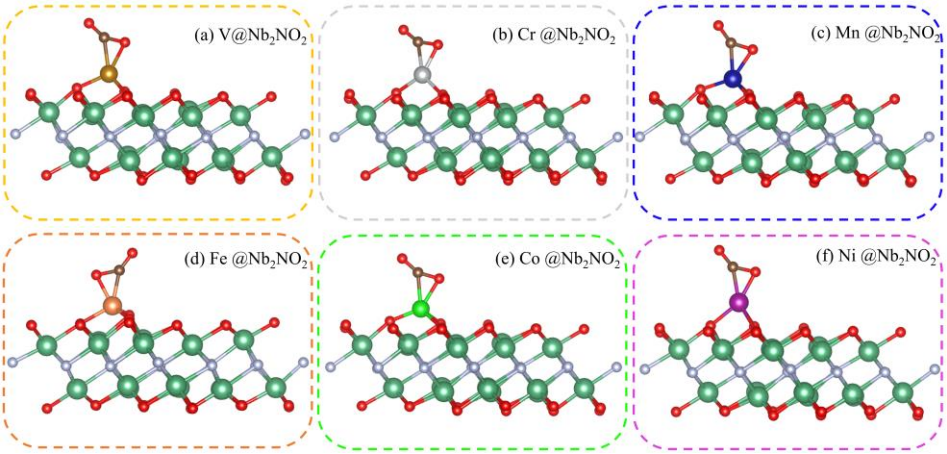

Figure 3.8. The most stable CO_2 adsorption configurations on (a) V@Nb_2NO_2, (b) Cr@Nb_2NO_2, (c) Mn@Nb_2NO_2, (d) Fe Ni@Nb_2NO_2, (e) Co@Nb_2NO_2 and (f) Ni@Nb_2NO_2.

Table 3.1. CO_2 adsorption on TM@Nb_2NO_2: adsorption energy (E_{ads}) with unit eV, the angel of O−C−O with unit °, the bond length of TM−O and TM−C with unit Å, net charge accepted by CO_2 molecule with unit e.

Catalysts	E_{ads} (CO_2)	O−C−O angle	d_{TM-C}	d_{TM-O}	Q
V@Nb_2NO_2	−0.77	138.39	2.00	1.93	−0.60
Cr@Nb_2NO_2	−0.51	142.59	2.00	1.97	−0.53
Mn@Nb_2NO_2	−0.34	141.62	2.00	1.93	−0.58
Fe@Nb_2NO_2	−0.46	150.77	2.04	2.00	−0.25
Co@Nb_2NO_2	−0.30	154.34	2.05	1.99	−0.26
Ni@Nb_2NO_2	−0.54	151.74	1.96	1.92	−0.31

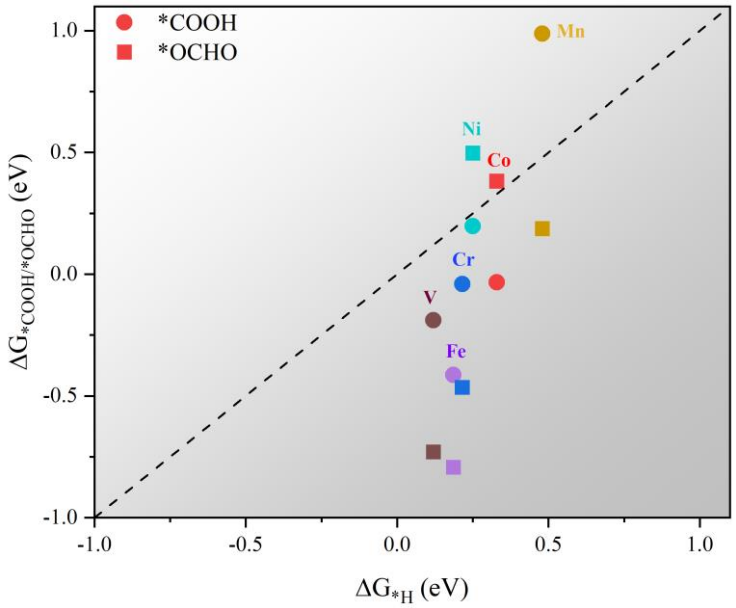

Figure 3.9. The Gibbs free energy changes (ΔG (eV)) for the first protonation step in ECR and HER on TM@Nb_2NO_2.

3.2.4. Competition between HER and ECR during first protonation

The ECR process starts with the hydrogenation of CO_2 molecule to form *COOH (* + CO_2 + (H^+ + e^-) → *COOH) or *OCHO (* + CO_2 + (H^+ + e^-) → *OCHO) on active centers by H atom binding O or C atom. However, the side-reaction HER (* + H^+ + e^- → *H) may occur due to the direct interaction between proton and TM atoms, resulting in low ECR selectivity. It has been widely accepted that the Gibbs free energy change (ΔG) for *COOH/*OCHO and *H formation can be used to evaluate the ECR selectivity versus HER selectivity [13]. Therefore, $\Delta G_{*COOH/*OCHO}$ were calculated and compared with ΔG_{*H}. As plotted in Figure 3.9, all TM@Nb_2NO_2 electrocatalysts prefer ECR (below the diagonal) to HER (above the diagonal). Notably, V, Cr and Fe@Nb_2NO_2 are ECR selective with two favorable initial protonation processes (*COOH and *OCHO), while Ni, Co and Mn@Nb_2NO_2 exhibit ECR selectivity only with one favorable initial protonation step (*COOH or *OCHO). Meanwhile, ΔG_{*OCHO} is smaller than ΔG_{*COOH} for V, Cr and Fe@Nb_2NO_2, demonstrating that the formation of *OCHO is more energetically favorable. Therefore, the *COOH reduction path and the corresponding CO product will not be considered on these three SACs in the further protonation process.

3.2.5. ECR to C_1 products on TM@Nb_2NO_2

The ECR products could involve C_1, C_2 and C_3 due to complex protonation and C−C coupling. However, the formation of high carbon products (C_{2+}) is impossible because C−C coupling will not occur on SACs. Therefore, only C_1 products by accepting 2e to 8e electrons, including CO, HCOOH, HCHO, CH_3OH, CH_4, were investigated in this work. These different products are formed by different number of protons binding C or O atoms. A possible pathway was plotted in Figure 3.10 by taking the optimized configuration of intermediates on Fe@Nb_2NO_2 as an example. It is obvious that only TM atom binds with the C or O atoms during the whole ECR process, demonstrating TM atom as active site.

After *COOH or *OCHO formation via accepting first proton-electron pair, further hydrogenation by obtaining a second proton-electron pair will produce *OCHOH or *CO intermediates. Therefore, the binding strength between these two intermediates and active center will decide HCOOH or CO generation. We calculated the E_{ads} of HCOOH and CO on TM@Nb_2NO_2 (Table 3.2). For HCOOH formation from *OCHO, V, Cr, Mn and Fe@Nb_2NO_2 show a large E_{ads} with −1.07, −1.25, −0.87 and −1.51 eV, respectively. For CO formation from *COOH, the E_{ads} of CO on Co and Ni@Nb_2NO_2 are −1.95 and −1.73 eV, respectively. It means that both HCOOH and CO could be further protonated on these SACs instead of desorbing from the SACs as final products. In addition, the generation of *OCHOH or *CO on Fe, Co, Cr, Ni

and V@Nb_2NO_2 are overall exothermic. The generation of *OCHOH is only slightly endothermic on Mn@Nb_2NO_2, benefiting the further reduction of intermediates.

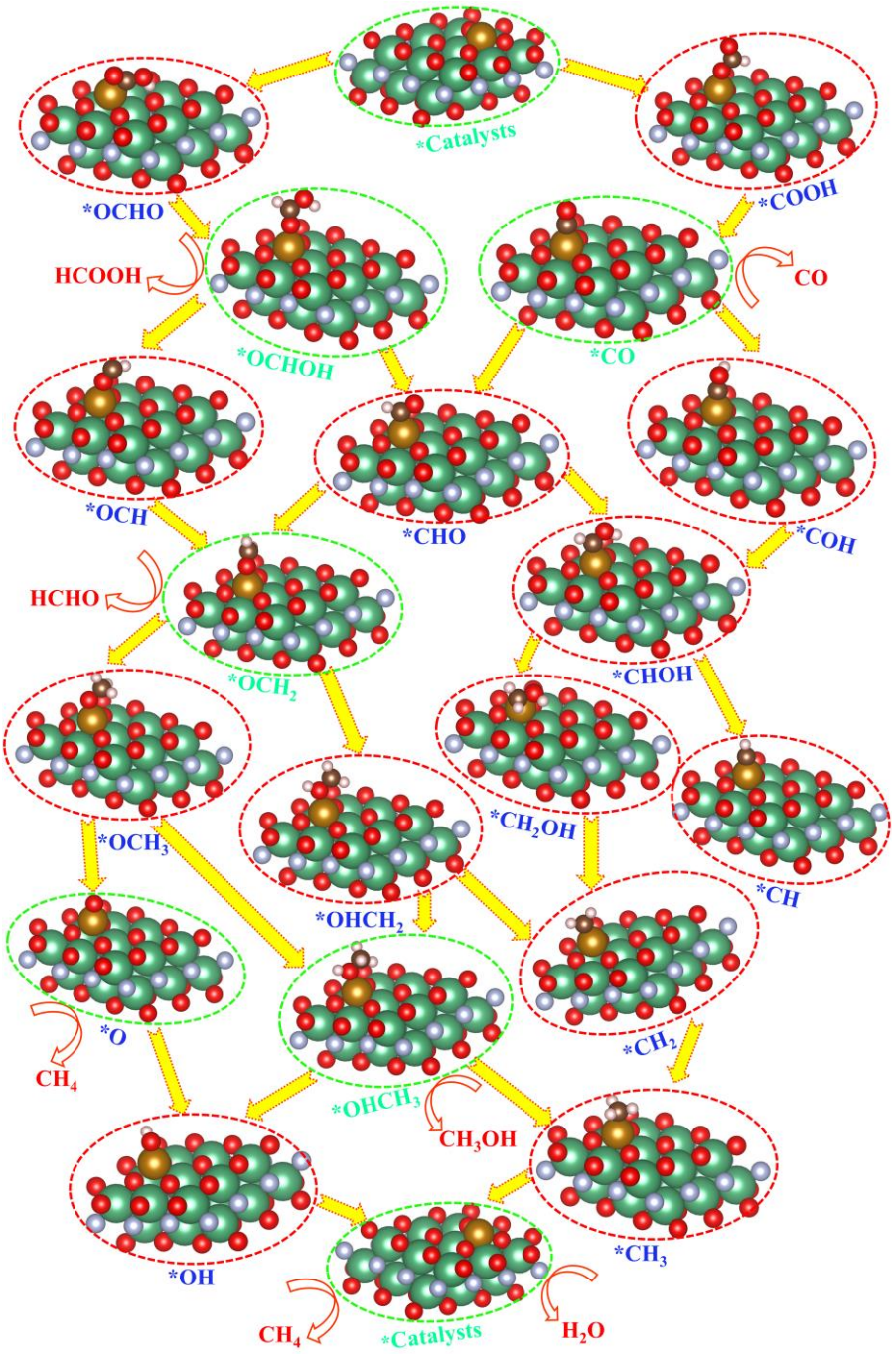

Figure 3.10. The optimized configuration of intermediates adsorbed on Fe@Nb_2NO_2 during the whole ECR process from one-electron to eight-electron products.

For further hydrogenation of *OCHOH or *CO, three possible intermediate including *CHO, *COH and *OCH could be generated. Notably, *COH from *CO (*CO + (H^+ + e^-) →*COH) on Co and Ni@Nb_2NO_2 underwent a larger energy uphill in comparison with the formation of *CHO (*CO + (H^+ + e^-) →*CHO). Similarly, For V, Cr, Mn and Fe@Nb_2NO_2, the formation

of *OCH from*OCHOH (*OCHOH + (H^+ + e^-) →*OCH + H_2O) are more energy consuming than the production of *CHO. Thus, it can be concluded that *CHO will be the key intermediates for the third hydrogenation process.

Table 3.2. The adsorption energy of different products CO, HCOOH, HCHO, CH_3OH and CH_4 with unit eV, and the limiting potential for generating final product CH_4 with unit eV.

Catalysts	E_{ads} (CO)	E_{ads} (HCOOH)	E_{ads} (HCHO)	E_{ads} (CH_3OH)	E_{ads} (CH_4)	$U_L(CH_4)$
V@Nb_2NO_2	–	−1.07	−1.59	−1.15	−0.35	-0.45
Cr@Nb_2NO_2	–	−1.25	−1.48	−1.17	−0.47	-0.47
Mn@Nb_2NO_2	–	−1.20	−0.96	−0.88	−0.23	-0.62
Fe@Nb_2NO_2	–	−1.51	−1.06	−0.75	−0.41	-0.89
Co@Nb_2NO_2	−1.95	–	−1.08	−1.07	−0.38	-0.57
Ni@Nb_2NO_2	−1.73	–	−1.20	−1.03	−0.36	-0.28

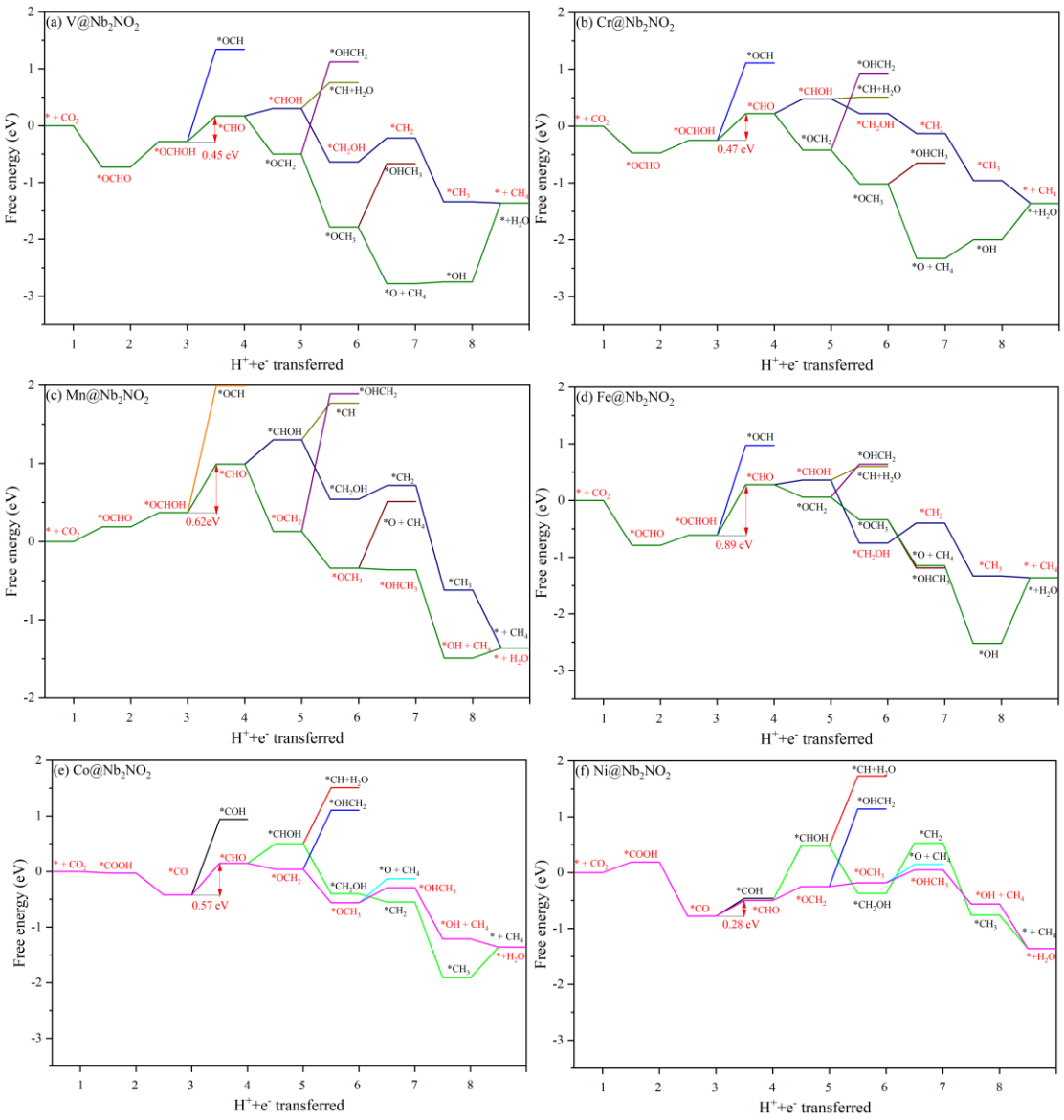

Figure 3.11. The Gibbs free energy diagram for ECR on TM@Nb_2NO_2 to produce the final product CH_4 under U = 0 V; the red pathway denotes the optimal pathway.

*OCH_2 and *CHOH intermediates can be produced after *CHO accepting the fourth proton-electron pair. It is evident from Figure 3.11 that the ΔG of *CHOH on these six SACs show energy uphill, while the ΔG for the formation of *OCH_2 on these SACs show energy downhill. Therefore, these TM atoms exhibit strong oxophilicity to form TM−O bonds. The four-electron product HCHO will be desorbed from the electrocatalyst if the interaction between *OCH_2 and TM atom is too weak. The calculated E_{ads} of HCHO on these SACs are in the range of −1.59 to −0.96 eV, suggesting that it is difficult for HCHO to desorb and thus can be further reduced.

*CHOH then accepted the fifth proton-electron pair to produce *CH and *CH_2OH intermediates, while the hydrogenation products of *OCH_2 are *OCH_3 and *$OHCH_2$. However, ΔG of *CH and *$OHCH_2$ are energetically unfavorable and will not form. In contrast, *CH_2OH and *OCH_3 will be the key intermediates and participate in later hydrogenation. CH_3OH is the six-electron product via *OCH_3 + (H^+ + e^-) →*$OHCH_3$ → * + CH_3OH. Nevertheless, the formation of *$OHCH_3$ only show energy downhill on Fe and Mn@Nb_2NO_2. The E_{ads} on V, Cr, Mn, Fe, Co, Ni@ Nb_2NO_2 is −1.15, −1.17, −0.88, −0.75, −1.07 and −1.03 eV, respectively. Thus, CH_3OH can still be stably bonded with SACs and further reduced. The eight-electron product CH_4 can be generated from diverse paths such as *CH_3 + (H^+ + e^-) → * + CH_4, *OCH_3 + (H^+ + e^-) → CH_4 + *O and *$OHCH_3$ + (H^+ + e^-) → CH_4 + *OH. Remarkably, the E_{ads} of CH_4 on TM@Nb_2NO_2 are significantly smaller than the other C_1 products, ranging from −0.47 to −0.23 eV, indicating that CH_4 can easily desorb from the SACs and become the final product. According to principle of minimum free energy increase at each step, the optimized paths for ECR to CH_4 on TM@Nb_2NO_2 were concluded as below (Figure 3.11):

(I) V, Cr and Fe@Nb_2NO_2: * + CO_2 → *OCHO → *OCHOH → *CHO → *CHOH → *CH_2OH → *CH_2 → *CH_3 → * + CH_4

(II) Mn@Nb_2NO_2: * + CO_2 → *OCHO → *OCHOH → *CHO → *OCH_2 → *OCH_3 → *$OHCH_3$ → *OH + CH_4 → * + H_2O

(III) Co and Ni @Nb_2NO_2: * + CO_2 → *COOH → *CO → *CHO → *OCH_2 → *OCH_3 → *$OHCH_3$ → *OH + CH_4 → * + H_2O

Thus, TM@Nb_2NO_2 can be promising candidates in electrochemically converting CO_2 to CH_4. To evaluate the ECR performance of TM@Nb_2NO_2, the PDSs and the corresponding U_L were summarized in Table 3.2. Generally, the lower the value of U_L, the higher the activity of SACs. In path I and II, *OCHOH → *CHO was identified as PDS for V, Cr, Mn and Fe@Nb_2NO_2. The U_L for CH_4 generation on these four SACs are −0.45, −0.47, −0.62 and −0.89 V. The PDS of Co and Ni@Nb_2NO_2 in path III is *CO → *CHO, and the corresponding U_L are −0.57 and

−0.28 V. Intriguingly, U_L for the ECR to CH_4 on V, Cr, Co and Ni@Nb_2NO_2 are lower than that the state-of-the-art catalyst Cu (211) (−0.74 V) [14], demonstrating potentially excellent performance of TM@Nb_2NO_2 for ECR to CH_4. Particularly, the U_L of Ni@Nb_2NO_2 is among the best reported in literature. Finally, we investigated the stability of Ni@Nb_2NO_2 by AIMD simulations with a time step of 3 fs at the temperature of 300 K for 18 ps (Appendix 3C, Figure S2). It can be found that Ni atom can still stay at the vacancy, which evidenced that diffusion will not occur.

3.2.6. Activity origin of ECR to CH_4 on TM@Nb_2NO_2

We further investigated the activity origin on TM@Nb_2NO_2 by using descriptors. The PDSs of TM@Nb_2NO_2 can be assigned to *OCHOH and *CO, therefore we distinguish them by two different areas (palegreen and slateblue in Figure 3.12). Since the *d*-band centre of TM atoms has often been used to correlate the catalytic properties, the locations of *d* band centres (ε) were calculated and plotted against U_L, as shown in Appendix, C Figure S3 and Figure 3.12a. With the increase of the TM-*d* electron number, ε shifts to a more negative energy level, resulting in the increase of U_L. When the key intermediate is *OCHOH, there is a good linear relationship between ε and U_L ($U_L = 0.35\varepsilon - 0.40$, $R^2 = 0.97$). For *CO as key intermediate, only Co and Ni@Nb_2NO_2 are distinguished. Generally, the more negative the value of ε, the weaker the adsorption between intermediates and catalysts. For example, it can be found that Mn@Nb_2NO_2 shows a lower ε, while the E_{ads} for *OCHOH is smaller, indicating weak adsorption and a large U_L. However, ε is not associated with E_{ads} for a specific TM atom in a small range because of the neglect of the *d*-band shape and the effect of the TM-*s* and *p* orbitals. Thus, the linear relationship is not apparent (Figure 3.12b). For *CO intermediate, the higher ε of Co atoms contributed a strong E_{ads} of *CO and high U_L.

The crystal orbital Hamilton populations (COHP) were employed to analyse the bonding and antibonding states of the TM and key intermediates *OCHOH and *CO. Meanwhile, the integrated COHP (ICOHP) was calculated to give a more quantitative explanation (Appendix C, Figure S4). For O atom bonding with V, Cr, Mn and Fe@Nb_2NO_2, it shows obvious antibonding states below Fermi level, demonstrating weak adsorption. The corresponding ICOHP values are −1.32, −1.44/−1.57, −1.47/−1.75, −1.28/−1.61 eV, respectively. V and Cr@Nb_2NO_2 have similar antibonding states in spin up state, resulting in similar U_L. For C atom bonding with Co and Ni@Nb_2NO_2, there is no antibonding state below Fermi level with value of −2.56/−2.66 and −2.40 eV, respectively, indicating strong adsorption. The more negative the ICOHP, the more stable of bonding, thus Fe@Nb_2NO_2 shows a large U_L. A good

linear relationship between ICOHP and U_L was obtained for V, Cr, Mn and Fe@Nb_2NO_2 (U_L = 1.58Φ + 1.70, R^2 = 0.86), disclosing the role of different metal centers in the bonding/antibonding orbital populations.

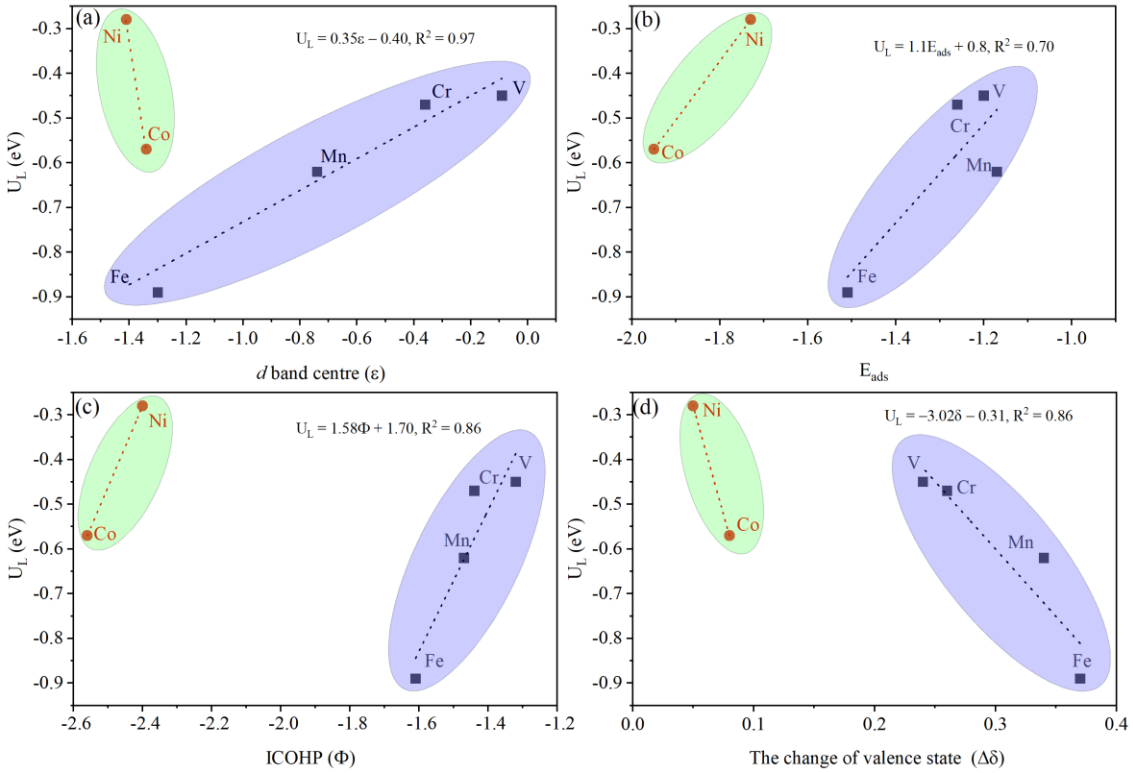

Figure 3.12. The limiting potential for the generation of CH_4 on TM@Nb_2NO_2 as a function of (a) d band centre (ε), (b) adsorption energy (E_{ads}), (c) ICOHP (Φ), and (d) the change of TM atom valence state (Δδ).

Recently, charge transfers of active atoms have been reported as descriptor to explain the performance of catalysts [15]. Herein, we calculated the valence state (δ) of TM atoms after adsorbing intermediates. The δ of different atoms for different binding atoms vary in a range from +0.55 to +1.32, indicating an increase of charge transfer from TM atoms after intermediates adsorption and different interaction strength between them. Fe atom had the largest Δδ increase of 0.37 after intermediates adsorption, implying a possible strong interaction between Fe and *OCHOH and a large U_L. Meanwhile, an approximate linear relationship (U_L = −3.02Δδ −0.31, R^2 = 0.86) was obtained, demonstrating that binding strength between catalysts and intermediates can be represented by Δδ. Therefore, ε, Φ and Δδ can be used as descriptors to describe the activity origin well. Meanwhile, the E_{ads} can be a nominal descriptor for the ECR activity to CH_4 due to the close connection between energy and electronic structure, while ε, Φ and Δδ can quantitively describe the intrinsic activity of ECR to CH_4 on TM@ Nb_2NO_2. Overall, the results show that Ni@Nb_2NO_2 is the best ECR catalyst for CH_4 generation, while Fe@Nb_2NO_2 is not an ideal catalyst.

3.3. Electrochemical Reduction of CO_2 to CH_4 over Transition Metal Atom Embedded Antimonene: First-Principles Study (Paper IV)

In this work, we built SACs by embedding TM atoms (Sc, Ti, V, Cr, Mn, Fe, Co, Ni, Cu, Zn, Mo, Ru, Rh, Pd, Ag, Cd, Ir, Pt and Au) into antimonene monolayer (TM@Sb) and investigated their ECR performance by first-principles study.

3.3.1. Structure and stability

After structure optimization, the lattice parameter *a* (4.11 Å) of pristine Sb monolayer and bond length d_{Sb-Sb} (2.89 Å) agree well with previous reports [16, 17]. The average d_{Sb-TM} (TM bonding three Sb atoms) ranges from 2.45 (Co) to 2.88 Å (Sc), resulting from the different atomic radius of TM and the relative positions of host and TM atoms. These results are similar to arsenene based SACs [18].

The vacancy formation energy E_f of Sb single vacancy was estimated to be 1.77 eV, which is smaller than previous studies on defective formation energies of other 2D materials [19-22]. Meanwhile, the total energy and structure exhibit slight change through AIMD simulation under 400 K. These results verify excellent stability of defective Sb monolayer (Figure 3.13a).

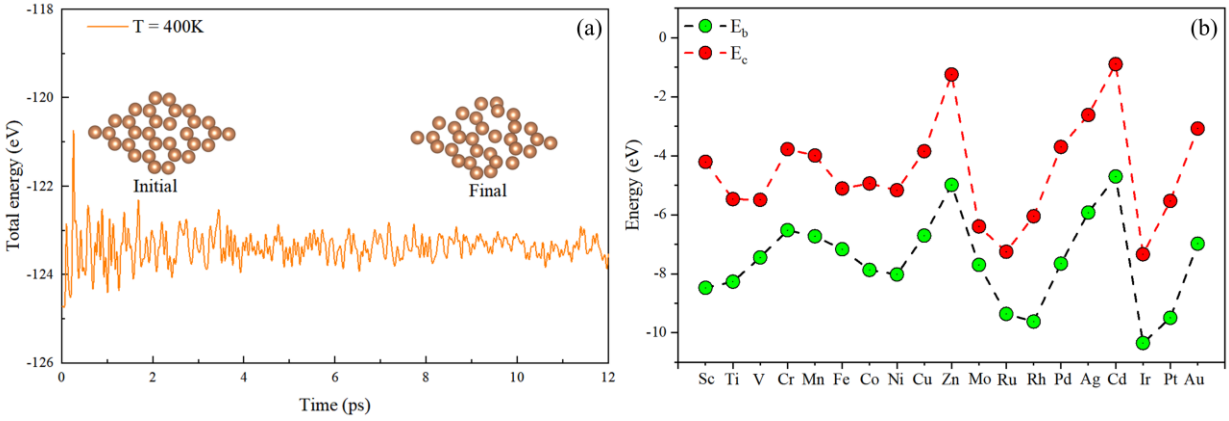

Figure 3.13. (a) The total energy variations of defective Sb monolayer under a target temperature of 400 K for AIMD simulation for 12 ps with a time step of 3 fs; (b) The binding energy E_b of TM embedded into Sb monolayers, the cohesive energy E_c of bulk metal.

To evaluate the stability of the SACs, the binding energies (E_b) of TM atoms in the Sb monolayer were calculated (Figure 3.13b). All TM@Sb monolayers show a negative E_b, demonstrating that Sb monolayer can stably anchor single TM atom. The cohesive energies of bulk metal (E_c) were also investigated. All Ec are larger than their corresponding E_b of TM@Sb monolayer. To better explore the ECR activity of different TM atoms, only TM atoms will be considered as the active site in this work.

3.3.2. Competition between ECR and HER for the first hydrogeneration step

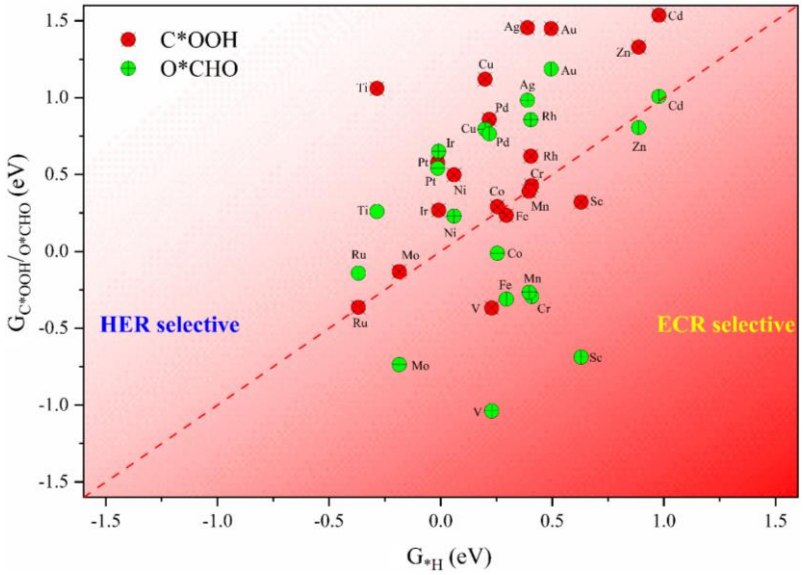

Figure 3.14. The Gibbs free energy changes for the first protonation steps in ECR and HER on TM @Sb monolayers.

In the first protonation process, eight SACs (Sc@, V@, Cr@, Mn@, Fe@, Co@, Zn@ and Mo@Sb monolayer) are demonstrated to be more ECR selective than HER, which are located below the dashed line (Figure 3.14). It is worth noting that Cr@, Co@, Zn@ and Mo@Sb monolayers can only catalyse the formation of O*CHO, because ΔG_{C*OOH} is larger than ΔG_{*H}. Therefore, for these four SACs, only O*CHO intermediate will be considered in the first hydrogenation step. Meanwhile, it can be highlighted that these SACs are nonprecious TM atoms exhibiting great ECR selectivity, which is obviously more valuable than noble TM based ECR catalysts reported previously.

TMs could bind C or O atom in the initial step of protonation, resulting in O*CHO and C*OOH for Sc@, V@, Mn@ and Fe@Sb monolayers, while only O*CHO for the other monolayers. The hydrogenation of O*CHO and C*OOH will produce O*CHOH and (C*O + H_2O), respectively. If the E_{ads} of CO or HCOOH is large enough, CO or HCOOH will participate in further ECR reactions as intermediates. In contrast, if their E_{ads} are too small, CO or HCOOH will detach from the active site and be released as the final products. As summarized in Table 3.3, only Zn@Sb monolayer shows physisorption property for HCOOH with E_{ads} of −0.32 eV, resulting in HCOOH desorption from the surface of catalysts. We also assumed that HCOOH could be reduced further, but a big uphill of ΔG for O*CH and C*HO will not favor its hydrogenation (Figure 3.15g). The optimal pathway for HCOOH generation is * + CO_2 → O*CHO → O*CHOH → * + HCOOH.

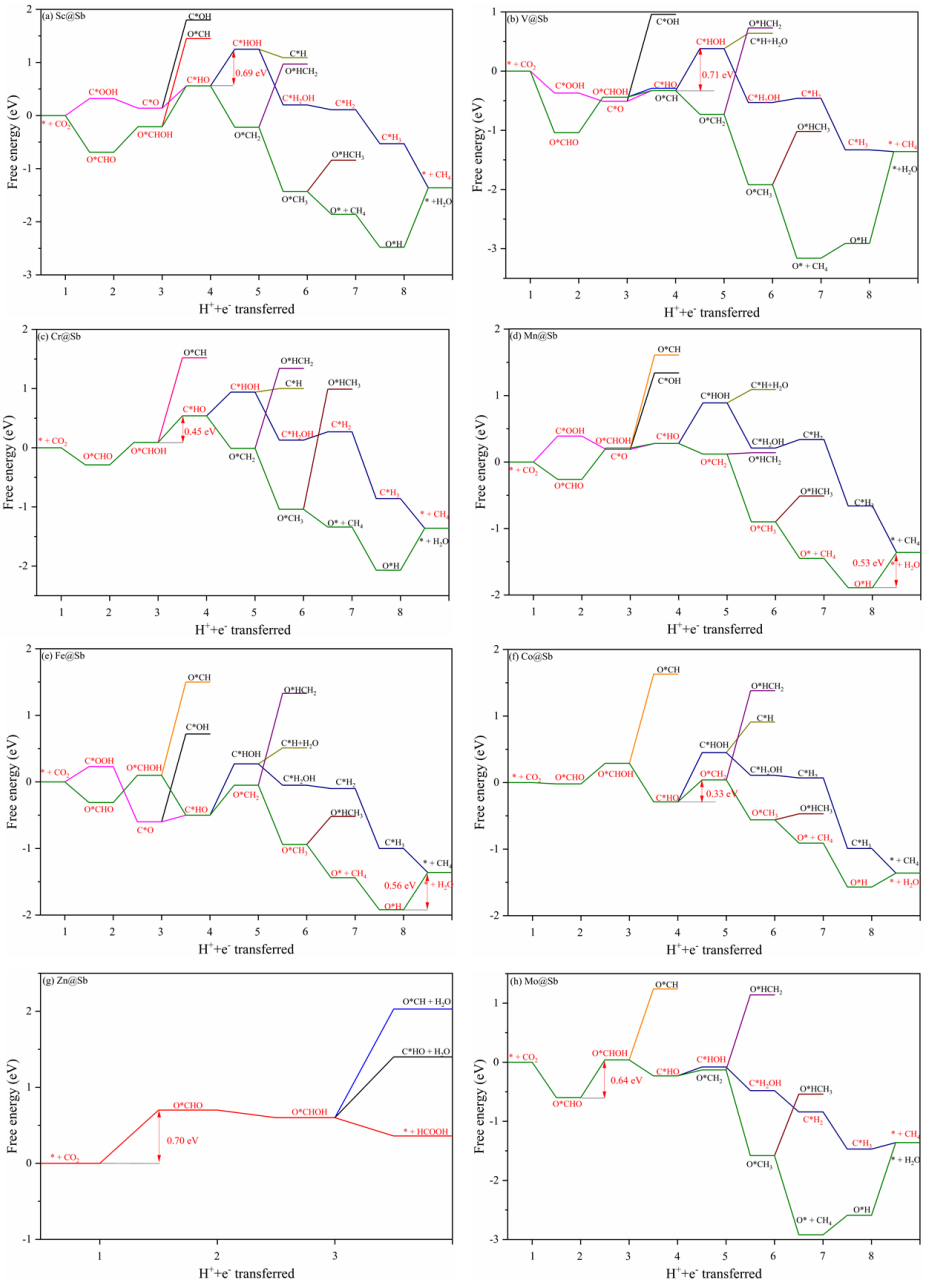

Figure 3.15. The Gibbs free energy diagram for ECR to the final C_1 product on TM@Sb monolayer under U = 0 V.

Table 3.3. Adsorption energy (E_{ads}) of different reduction products CO, HCOOH, HCHO, CH_3OH and CH_4 (unit eV); The potential determining steps (PDS) for CH_4 or HCOOH formation on TM@Sb monolayer; The limiting potential U_L, the equilibrium potential U_{eq} under pH= 0 of different products, and the overpotential η (all units in V).

System	E_{CO}	E_{HCOOH}	E_{HCHO}	E_{CH3OH}	E_{CH4}	PDS	U_L	U_{eq}	η
Sc	−0.99	−1.12	−1.33	−1.30	−0.42	C*HO→C*HOH	0.69	0.17(CH_4)	0.86
V	−1.64	−1.39	−1.82	−1.55	−0.48	C*HO→C*HOH	0.71	0.17(CH_4)	0.88
Cr	-	−0.81	−1.08	−1.04	−0.23	O*CHOH→C*HO	0.45	0.17(CH_4)	0.62
Mn	−0.99	−0.72	−0.86	−0.98	−0.25	O*H→* + H_2O	0.53	0.17(CH_4)	0.70
Fe	−1.77	−1.80	−1.17	−1.01	−0.26	O*H→* +H_2O	0.56	0.17(CH_4)	0.73
Co	-	−0.62	−1.04	−0.90	−0.23	C*HO→O*CH_2	0.33	0.17(CH_4)	0.50
Zn	-	−0.32	-	-	-	*+CO_2→O*CHO	0.70	−0.25(HCOOH)	0.45
Mo	-	−0.80	−1.39	−0.95	-0.19	O*CHO→O*CHOH	0.64	0.17(CH_4)	0.81

The E_{ads} of CO and HCOOH of the remaining seven SACs range from −0.99 to −1.77 eV and −0.62 to −1.80 eV, suggesting strong chemisorption of both on the SACs. This suggests that CO and HCOOH will be further reduced on these seven SACs. Among which, V@ and Fe@Sb monolayers exhibit stronger adsorption of CO and HCOOH, implying that these two catalysts possess the best capability in further ECR. Three different intermediates C*HO, C*OH and O*CH will be generated from CO and HCOOH hydrogenation. As shown in Figure 3.15, ΔG_{C*HO} is lower than ΔG_{C*OH} and ΔG_{O*CH}, demonstrating that C*HO is the crucial intermediate in the third hydrogenation process. These two processes can be expressed by C*O + (H^++e^-) →C*HO and O*CHOH + (H^++e^-) →C*HO + H_2O. C*HO could further accept the fourth proton-electron pair to produce O*CH_2 and C*HOH. It is evident from Fig. 3.15 that the formation of C*HOH on these seven SACs underwent an uphill in energy. On the contrary, the formation of O*CH_2 on Sc@, V@, Cr@ and Mn@Sb monolayer is energetically favorable, suggesting these TM atoms have strong oxophilicity to form TM−O configurations. This also indicates that the protonation of C*HO (C*HO + (H^++e^-) →C*HOH or O*CH_2) is most likely the PDS for further ECR products. The E_{ads} of 4e reduction product HCHO was estimated and summarized in Table 3.3. The E_{ads} of HCHO for these seven SACs is still quite negative from −0.86 to −1.39 eV, meaning that HCHO is difficult to desorb from the surface. Two intermediates O*CH_3 and O*HCH_2 could be generated in the next protonation step. However, ΔG_{O*HCH2} for all the seven SACs is big uphill. Then O*CH_3 will be the only intermediate for later reactions. When C*HOH intermediate accepting one proton-electron pair, the formation of *CH_2OH is thermodynamically favorable with a large energy downhill.

With the addition of one more proton-electron pair, 6e reduction product CH_3OH appears. The step can be expressed as: O*CH_3 + (H^++e^-) →O*HCH_3→ * + CH_3OH. Nevertheless, ΔG_{O*HCH3} also shows a large uphill, meaning that the step is thermodynamically unfavorable. Meanwhile, the E_{ads} of CH_3OH on these seven TM@Sb monolayers is large between −0.90 and −1.55 eV, showing strong adsorption capability. As a result, CH_3OH will continue in ECR reactions as an intermediate. Interestingly, the E_{ads} of 8e reduction product CH_4 are quite small, ranging from −0.19 to −0.48 eV. Thus, CH_4 can easily desorb from the surface of these SACs and become the final product in ECR. In Figure 3.15, the optimized pathways for CH_4 production from ECR are proposed for different TM@Sb electrocatalysts based on minimum free energy increase in each protonation step. Sc@, V@, Cr@ and Mo@Sb monolayer possibly follow path (I) for CH_4 formation:

$$C*HO \rightarrow C*HOH \rightarrow C*H_2OH \rightarrow C*H_2 + H_2O \rightarrow C*H_3 \rightarrow * + CH_4 \quad (I)$$

While Mn@, Fe@ and Co@Sb monolayers may follow pathway (II):

$$C^*HO \rightarrow O^*CH_2 \rightarrow O^*CH_3 \rightarrow O^* + CH_4 \rightarrow O^*H \rightarrow * + H_2O \quad (II)$$

As a result, we can conclude that antimonene based SACs can electrocatalytically convert CO_2 into CH_4.

To evaluate the performance of these SACs for CO_2 conversion to CH_4, it is essential to calculate the overpotential. In our work, we calculated the free energy change ΔG of each step, and the maximum change in free energy will be the potential determining steps (PDS) that determine U_L. η was then estimated according to the equation $\eta = U_{equ} - U_L$. The PDS, U_L and η for these SACs are summarized in Table 3.3. The PDS of these electrocatalysts are different, e.g., the PDS of V@Sb monolayer for CH_4 formation is $C^*HO \rightarrow C^*HOH$, whereas the PDS of Cr@Sb monolayer is $O^*CHOH \rightarrow C^*HO$. This demonstrates that different TM atoms exhibit different interactions with the intermediates. According to the Sabatier principle, too strong or too weak interaction between catalysts and the intermediates is not beneficial for catalytic activity [23]. For Sc@, V@, Cr@ and Mo@Sb monolayers, ΔG for the formation of H_2O show big uphill, indicating strong interaction between O*H and TM, which is not an optimal pathway and leads to high overpotential. Thus, path (I) is more favourable. In contrast, the proper interaction between Mn, Fe and Co atom and O*H brings about a small overpotential, making path (II) ideal for CO_2 converting into CH_4. Zn@Sb monolayer exbibit an overpotential of 0.45 V for the HCOOH product. For CH_4, the remaining seven SACs have overpotentials less than 0.90 V. Especially, Co@Sb monolayer shows an overpotential of only 0.50 V, which is comparable to or even smaller than the state-of-the-art catalysts Cu (211).

3.3.3. Electronic properties

Electrical conductivity is a crucial parameter to evaluate the electron transfer efficiency. The band structure of pristine and defective Sb monolayer was calculated and displayed in Appendix D, Figure S2a and b. The electron state of spin up and down are completely symmetric, demonstrating its nonmagnetic property. The pristine Sb monolayer shows an indirect bandgap of 1.28 eV, which is well consistent with previous studies [24, 25]. New energy levels crossing the Fermi level are beneficial for electron transfer. In the projected density of states (PDOS) of the TM@Sb monolayer (Appendix D, Figure S3), for instance, Sc@, Co@ and Zn@Sb monolayaer present nonmagnetic property, while others such as V@, Cr@, Mn@, Fe@ and Mo@Sb exhibit magnetic nature. Almost all samples exhibit the electron states crossing the Fermi level, and the main contribution is from TM atoms. Thus, the conductivity of these SACs is improved.

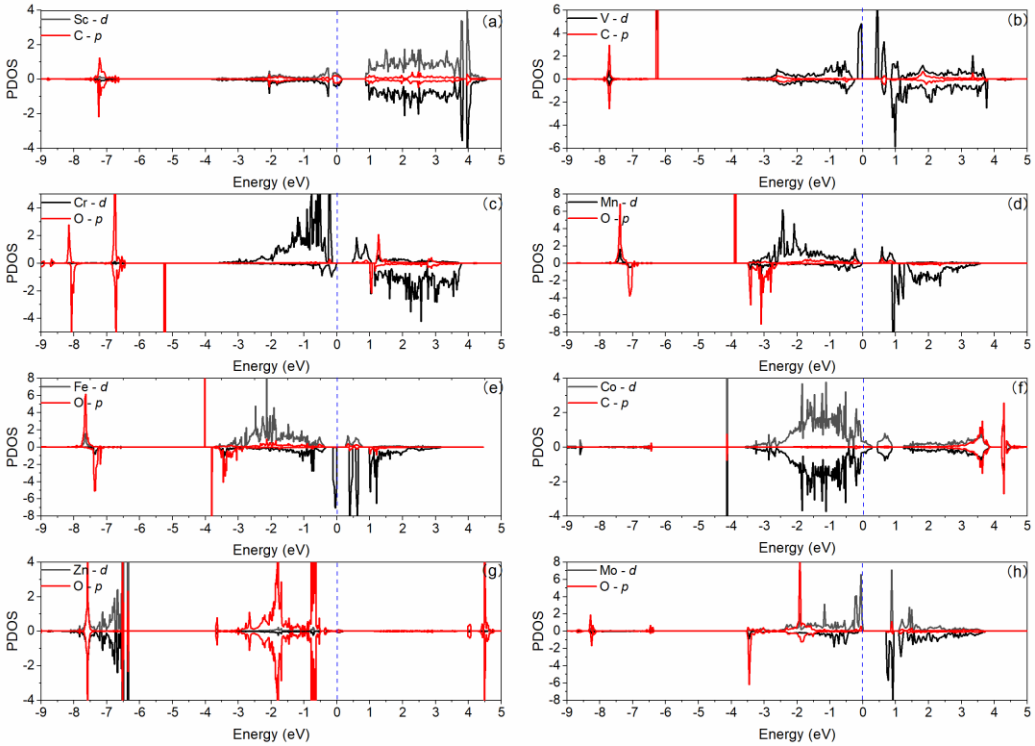

Figure 3. 16. The PDOS of C*HO adsorbed on (a) Sc, (b) V and (f) Co@Sb monolayer, O*CHOH adsorbed on (c) Cr@Sb monolayer, O*H adsorbed on (d) Mn and (e) Fe@Sb monolayer, and O*CHO adsorbed on (g) Zn and (h) Mo@Sb monolayer. The dashed line represents the Fermi level.

The interaction between TM atoms and Sb monolayer will greatly affect the ECR performance. It can be seen from Appendix D, Figure S3 that the *p* orbitals of the Sb atom have a different degree of overlap with *d* orbitals of TM atoms among the conduct band and valence band for these eight SACs. Particularly, the *d* orbitals of Co overlap better with *p* orbitals of the Sb atom from −4.0 to 4.0 eV, indicating that the interaction between Co atom and Sb monolayer is stronger than others. Table 3.3 shows that Co@Sb monolayer has the smallest overpotential for CH_4 generation. In contrast, Zn@Sb monolayer is preferred for HCOOH production with a smaller overpotential, but the value is still larger than those reported in other studies [26-29]. This is manifested by the PDOS of Zn@Sb monolayer exhibiting weak interaction, which suggests a low intrinsic activity for ECR. Therefore, the stronger the interaction between TM atoms and Sb monolayer, the higher the catalytic activity for CH_4 formation. The PDOS of intermediates in the PDS of TM@Sb monolayer for ECR is displayed in Figure 3.16. The Sc@, V@, Fe@ and Mo@Sb monolayer show stronger interaction between TM and C or O atoms both in the conduct band and valence band compared with the other samples, suggesting that these monolayers could interact strongly with the intermediates of PDS. Thus, these four SACs exhibit a relatively high overpotential for the final products in ECR. Meanwhile, the Bader charge analysis (Q_{TM-1}) in Table 3.4 shows that Sc and V atoms act as an electron donor on clean TM@Sb monolayer, while others are electron acceptor. Mn and Fe exhibit only 0.14e

transfer, demonstrating a weak interaction and poor intrinsic ECR activity. After the key intermediates adsorbed on the TM@Sb monolayer, the roles of TM atom were changed. The negative value of Q_{TM-2} indicate that all TM atoms act as electron donor except Co atom. The total charge transfer of C, H and O atom in respective intermediates suggests that OH in Mn@ and Fe@Sb monolayers is electron-accepting group, while CHO, OCHO, OCHOH in other TM@Sb monolayers work as electron-donating groups. Thus, Co as electron acceptor and CHO as electron-donating group will contribute to an appropriate interaction between them, resulting in a small overpotential. This is also verified by the optimal d_{Co-C} (1.88 Å), which is well consistent with the sum of atomic covalent radii of Co and C (1.86 Å) [30]. We also compared the charge transfer between TM atoms and intermediates before and after adsorption. The total charge transfer from C*HO to Co@Sb is 1.21e (Table 3.4) on C*HO adsorbed Co@Sb. Meanwhile, Co only accepts 0.14e, implying 1.07e is shared by three Sb atoms bonded with Co. Thus, it manifests a strong interaction between Co and Sb atom, which is consistent with the PDOS analysis.

Table 3.4. The charge transfer of TM (Q_{TM-1}) on clean TM@Sb monlayer, the charge transfer of TM (Q_{TM-2}) after adsorption of intermediates of PDS, and the charge transfer of C (Q_C), H (Q_C) and O(Q_O) after adsorption of intermediates of PDS on TM@Sb monlayer (all units in e); the positive or negative value denotes electron-acceptor and electron-donor, respectively; The bond length $d_{TM-C/O}$ between TM atoms and intermediates of PDS (unit Å).

System	Q_{TM-1}	Q_{TM-2}	Q_C	Q_H	Q_O	$d_{TM-C/O}$
Sc	−0.50	−0.86	−2.49	0.23	0.99	2.12
V	−0.26	−0.27	−2.83	0.27	0.96	1.92
Cr	0.04	−0.42	−3.27	−0.59, 0.22	1.02, 0.81	1.99
Mn	0.04	−0.16	-	−0.35	0.98	1.80
Fe	0.35	−0.14	-	−0.33	0.95	1.76
Co	0.49	0.14	−2.43	0.42	0.80	1.88
Zn	0.16	−0.13	−3.05	0.26	0.87, 0.82	1.93
Mo	0.33	−0.52	−3.11	0.17	0.93, 0.70	1.92

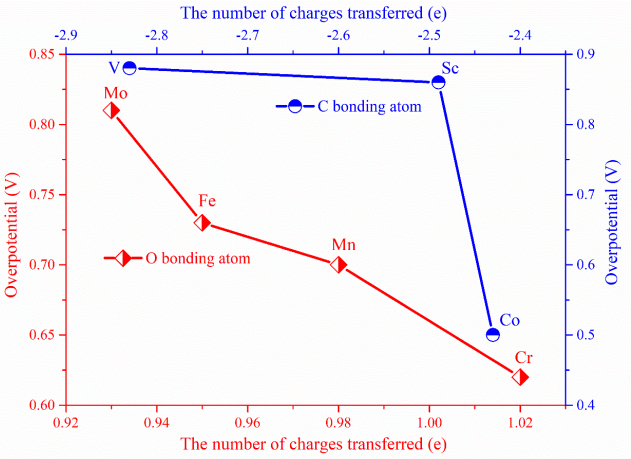

Figure 3.17. Relationship between overpotential and amount of charge transfer on bonding C or O atom from C*HO, O*H, O*CHO and O*CHOH.

Interestingly, we identified a strong relationship between the overpotential for CH_4 generation and the amount of charge transfer of TM bonding C or O atom of intermediates of PDS. As shown in Figure 3.17, for O*H, O*CHO and O*CHOH, the more charge the bonding O atom accept, the smaller the overpotential for CH_4 formation. Whereas the more charge the bonding C atom lose, the larger overpotential for CH_4 formation from C*HO.

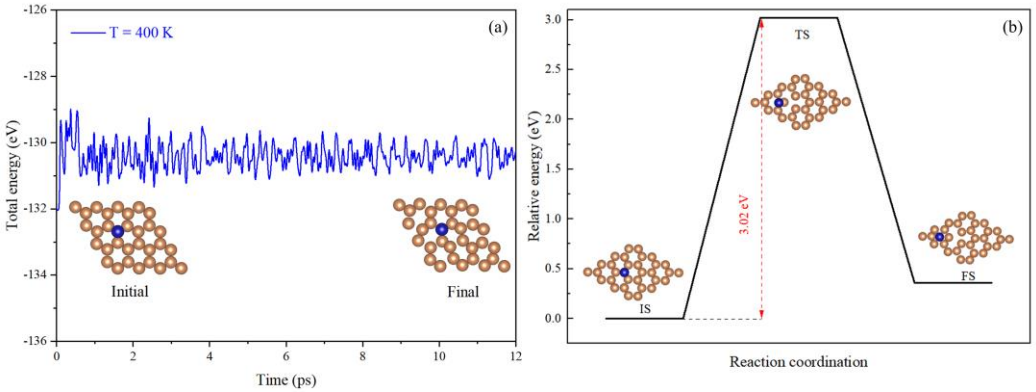

Figure 3.18. (a) The total energy variations of Co@Sb monolayer under a target temperature 400 of K for AIMD simulation for 12 ps with a time step of 3 fs; (b) The minimum energy pathway of adsorbed Co atom to diffuse from the vacancy site to neighboring site.

As Co@Sb monolayer shows excellent performance in ECR to CH_4, we further assess its stability by AIMD under a target temperature of 400 K (Figure 3.18a). The final structure of Co@Sb monolayer remains almost the same as the initial structure, while the total energy exbibits slight oscillation, demonstrating excellent stability of the Co@Sb monolayer. Besides, the diffusion barrier of Co atom is calculated, as displayed in Figure 3.18b. There is a large energy barrier of 3.02 eV to overcome for Co atom to diffuse from the anchored defective site to the neighboring hollow site, verifying that the embedded Co atom can hardly diffuse to form cluster. Thus, Co@Sb monolayer could be a highly efficient and stable SACs for CH_4 production from ECR.

3.4. Sulfur decorated Ni−N−C catalyst for electrocatalytic CO_2 reduction with near 100% CO selectivity (Paper V)

In this paper, we successfully synthesized N and S co-doped carbon black incorporating Ni atoms by facile ion-adsorption and subsequent pyrolysis treatment. The function of S atom was studied by theoretical and experimental work.

3.4.1. Electrocatalysts characterization

As shown in Figure 3.19a, the catalysts exhibit similar XRD patterns with two broad diffraction peaks at around 25.1° and 43.2°, corresponding to the (002) and (100) planes of carbon. It is worth noting that both peaks of NS−C and Ni−NS−C catalysts show low crystallinity and slight right-shift compared with the N−C and Ni−N−C catalysts, which can be explained by lattice contraction and the formation of C vacancy after the introduction of S atoms with larger radius [31, 32]. Furthermore, no peaks assignable to metallic Ni or its compounds were observable.

Raman spectra of the four catalysts exhibit two vibrational bands located around 1343 cm^{-1} (D band) and 1594 cm^{-1} (G band) (Figure 3.19b), which are ascribed to the defect and graphitic sp^2 carbon [33]. The intensity ratios of D and G band (I_D/I_G) of N−C, NS−C, Ni−N−C and Ni−NS−C catalysts were also calculated as marked in Figure 3.19b. It can be observed that the introduction of S atom into the N−C catalysts induces more defects, consistent with XRD study. However, incorporating Ni atoms decreases the I_D/I_G value, indicating that Ni atoms are embedded into C vacancies. Compared with the Ni−N−C catalyst, it can be found that the position of G band of Ni−NS−C catalysts shows a slight upshift due to the doping of non-metal S atom on carbon-based materials [34-36].

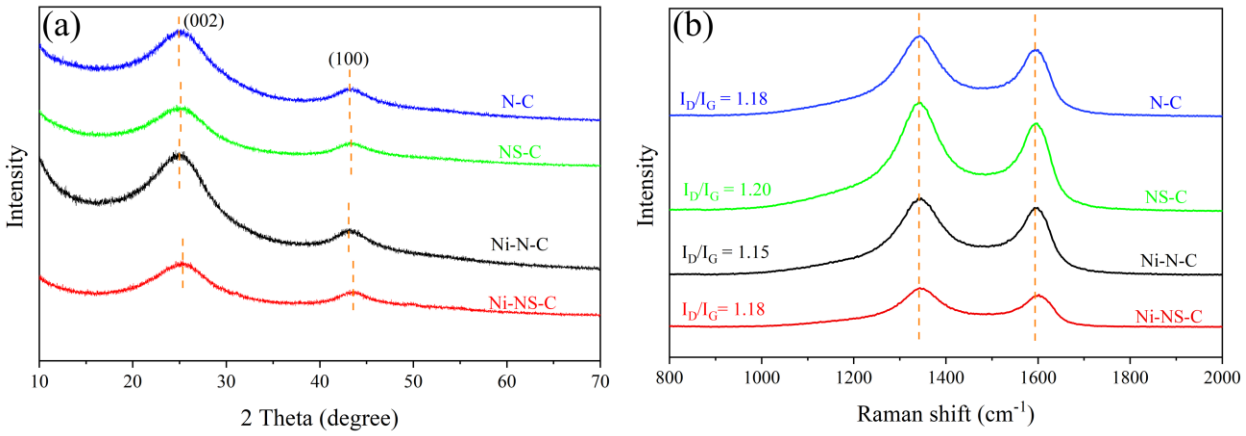

Figure 3.19. (a) XRD patterns and (b) Raman spectra of N−C, NS−C, Ni−N−C and Ni−NS−C catalysts

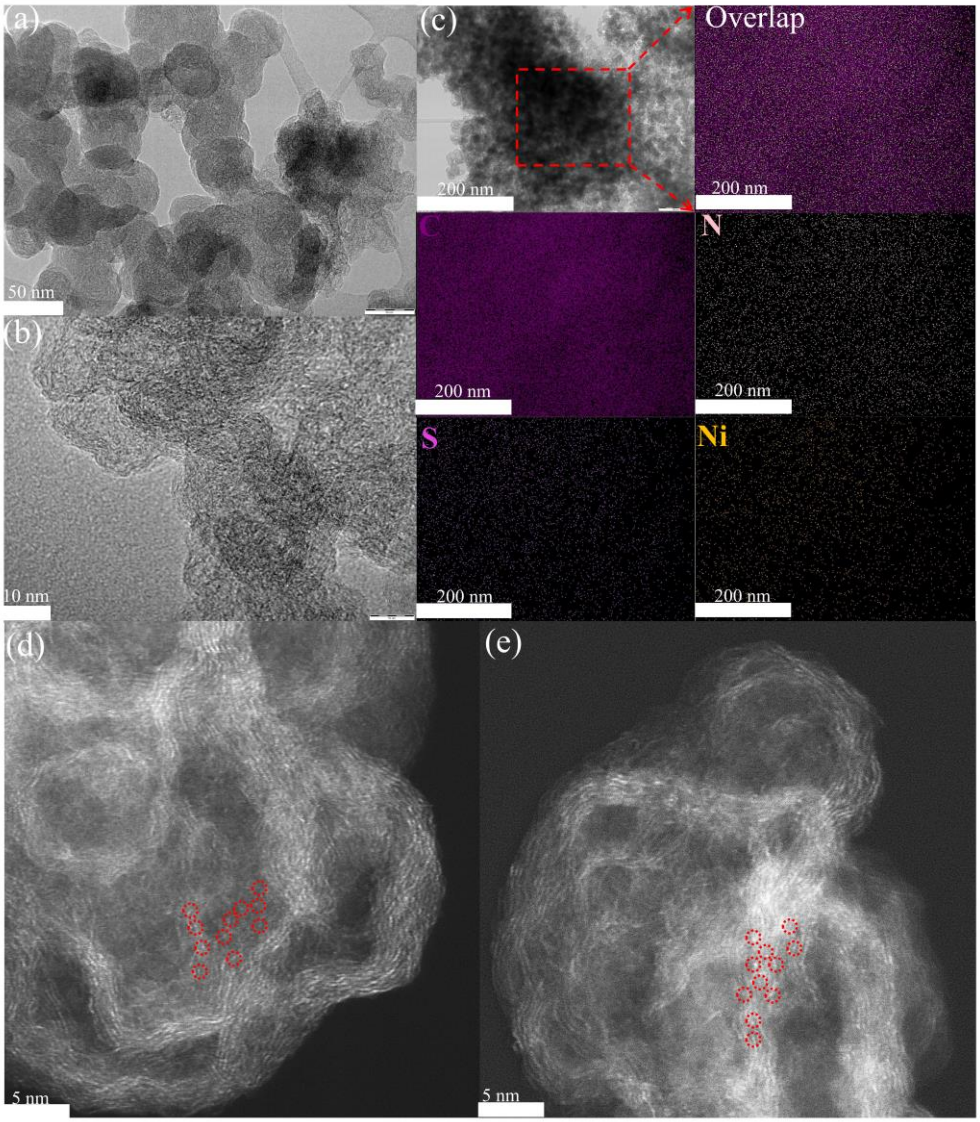

Figure 3. 20. (a) TEM, (b) HRTEM, (c) C, N, S and Ni EDX mapping images of Ni−NS−C catalyst; (d) and (e) HAADF-STEM images for Ni−N−C and Ni−NS−C catalysts, where the single Ni atoms are highlighted in red circles.

TEM was used to investigate the microscopic morphology of the Ni−NS−C catalyst. Carbon nanospheres with a diameter of 50 nm were observed (Figure 3.20a). The HRTEM images displays distorted short-range graphic stripes with winkle and interlaces (Figure 3.20b), indicating defective carbon structure. No distinct nanoparticles or clusters were observed, implying that the Ni atoms are likely to present in the form of single atoms. Besides, EDX elemental mapping images clearly demonstrate that Ni, N, S and C species distribute uniformly over the Ni−NS−C catalyst (Figure 3.20c). Furthermore, HAADF-STEM image shows the well-dispersed single Ni atoms in bright spots for the Ni−N−C and Ni−NS−C catalysts, while were highlighted by red circles (Figure 3.20d and e).

The surface area and pore structure of the catalysts were determined by N_2 adsorption-desorption measurements. As depicted in Figure 3.21a, the isotherms of the four electrocatalysts displayed sharp adsorption under relative pressures greater than 0.40 accompanied by an obvious hysteresis loop, which is indicative of dominant mesopores and is further corroborated by the pore size distributions (Figure 3.21b). The specific surface area and pore volume are summarized in Appendix E, Table S1. It can be found that the total pore volume increased from 1.26 to 1.39 m^3/g after doping S to the N−C structure, and increased further after introducing Ni atoms. The catalysts show quite close but very high surface areas in the range of 1073 to 1275 m^2/g, which also increase with the doping of S and Ni atoms. The high surface area and pore volume are beneficial for the dispersion of Ni atoms and the access of reactants to the active centers. As expected, the pore size distribution curve also shows more larger pores with the introduction of S and Ni atoms

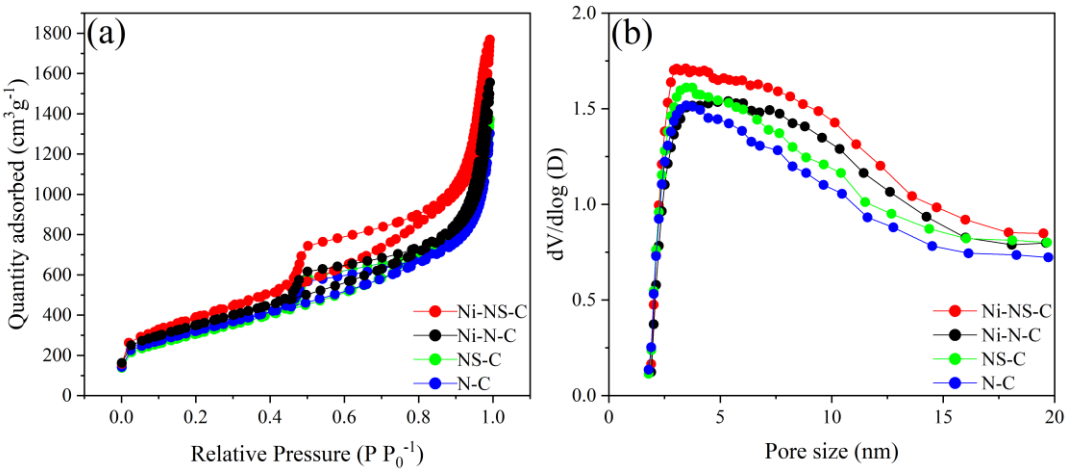

Figure 3. 21. (a) N_2 adsorption/desorption isotherms and (b) Pore size distributions of N−C, NS−C, Ni−N−C and Ni−NS−C catalysts.

X-ray photoelectron spectroscopy (XPS) was employed to characterize the chemical state and surface concentration of the elements. The high-resolution N 1s spectra of the Ni−NS−C catalyst can be fitted into four peaks cantered at 397.9, 399.7, 400.5 and 403.1 eV (Figure 3.22a), which can be assigned to pyridinic N (Pyri-N), pyrrolic (Pyrr-N), graphitic N (Grap-N) and oxidized N (Oxid-N), respectively [37-40]. The existence of these types of N could promote the electrocatalytic activity [41]. In addition, N atom concentrations are 4.43, 4.19, 4.11 and 4.18 at.% for N−C, NS−C, Ni−N−C and Ni−NS−C (Appendix E, Table S1). High-resolution S 2p spectra of Ni−NS−C catalyst (Figure 3.22b) at lower binding energy can be ascribed as C−S−C ($2p_{3/2}$ at 164.1 and $2p_{1/2}$ at 165.3 eV) and C−SO_x−C (167.6 and 168.8 eV) [31, 42]. The S content was estimated to be 0.37 and 0.42 at.% for the NS−C and Ni−NS−C catalyst, respectively. It was also observed that the percentages of N in these two catalysts remain almost unchanged,

implying that introducing S atoms had little effects on the bonding patterns of N atoms. In the high-resolution Ni 2p spectrum (Figure 3.22c), the Ni $2p_{3/2}$ binding energies for Ni−NS−C and Ni−N−C catalyst are 855.90 and 855.66 eV, higher than that of Ni^0 (852.5−853.0 eV) but lower than that of Ni^{2+} (856 eV) [43, 44], indicating that Ni species are likely to keep as ionic $Ni^{\delta+}$ ($0 < \delta < 2$). Therefore, these results further demonstrated the existence of single Ni atoms on the surface of Ni−NS−C and Ni−N−C catalysts [45]. Besides, it can be found that the peak of Ni $2p_{3/2}$ shifted slightly towards higher binging energy after incorporating S atoms, indicating that S could influence the electronic structure of Ni. The Ni contents in Ni−N−C and Ni−NS−C catalysts are 0.50 and 0.48 at.%, demonstrating that S atom doping has little effect on surface Ni atom distribution.

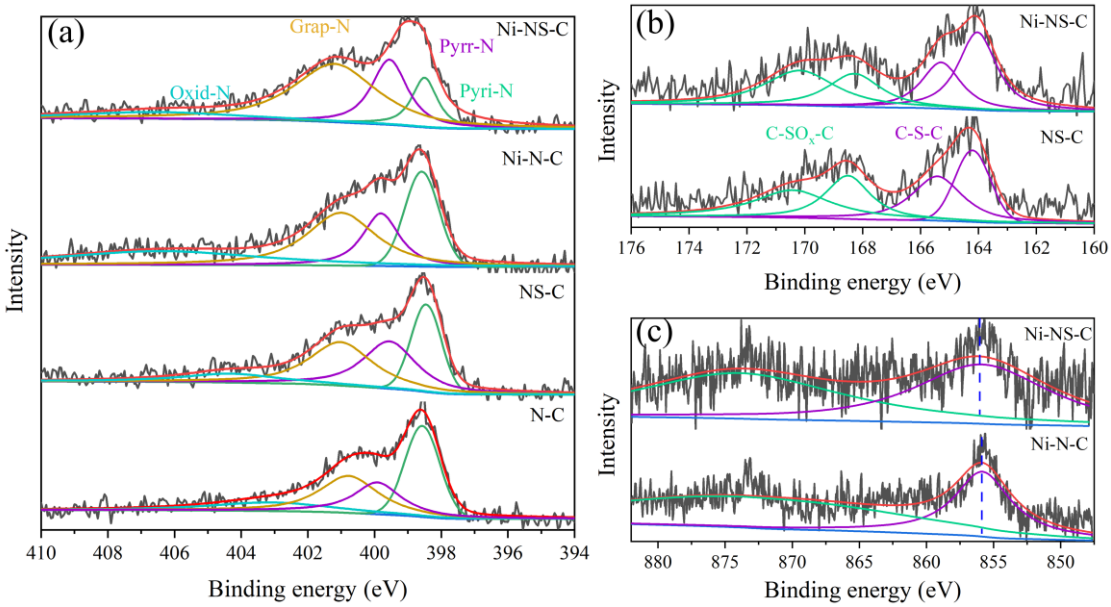

Figure 3.22. (a) High-resolution XPS spectra of N1s for N−C, NS−C, Ni−N−C and Ni−NS−C catalysts; (b) S 2p for NS−C and Ni−NS−C catalysts; (c) Ni 2p for Ni−N−C and Ni−NS−C catalysts.

3.4.2. Electrocatalysis activity test

The ECR performances of catalysts were evaluated in a membrane-separated two chambers H-type cell with a standard three-electrode system immersed in 0.5 M $KHCO_3$ electrolyte. Under CO_2-saturated electrolyte, the Linear sweep voltammetry (LSV) of N−C and NS−C catalysts show small current density (Figure 3.23a), exhibiting low electrocatalytic activity. Conversely, the Ni−NS−C and Ni−N−C catalyst display large current density thus high electrocatalytic activity. In addition, the doping of S atoms could boost the current density for both N−C and Ni−N−C, confirming the role of S atom in the activity enhancement. In the presence of CO_2, the current density of Ni−NS−C increases faster in comparison with the reaction under N_2 atmosphere (Figure 3.23b), suggesting the enhanced current density from ECR. The results

demonstrated that introducing Ni−N_X moiety into carbon-based materials could indeed improve its electrocatalytic performance. Meanwhile, the highest current density observed for the Ni−NS−C catalyst could be fairly attributed to the synergistic effect of Ni−N_X moiety and S doping.

To quantify the product selectivity, the ECR test was conducted in constant potentiostatic electrocatalysis under different potentials. H_2 and CO were detected as the only reduction products under the potential window of −0.20 V to −1.20 V (*vs*. RHE). No other gaseous products were detected by GC. Besides, no liquid products were produced, as evidenced by ^{1}H NMR analysis (Appendix E, Figure S1). As shown in Figure 3.23c, the FE(CO) over the four catalysts showed first increase then decrease with the decrease of applied potential. However, the FE(CO) of Ni−N−C and Ni−NS−C catalysts are always higher than the N−C and NS−C catalysts under the same applied potential, indicating that Ni−N_X are the true active centers. Meanwhile, the Ni−NS−C catalyst exhibits larger FE(CO) than Ni−N−C over the entire potential range, demonstrating that S atom could effectively enhance the ECR performance of the Ni−N_X moiety. The competing HER performance for the four catalysts were also compared, as displayed in Figure 3.23d. The FE(H_2) of Ni−NS−C catalyst is always lower than that of Ni−N−C catalyst, indicating that the HER performance of the Ni−N−C catalyst was suppressed after the doping of S atoms. In contrast, the FE(H_2) of N−C is lower than that of NS−C, suggesting that S atom could promote HER ability of N−C in the absence of Ni. Therefore, it can be deduced that more protons are involved in ECR compared to HER after the introduction of Ni and S atoms, and there is a synergistic effect between Ni and S. As a result, the Ni−NS−C catalyst exhibits high FE(CO) over 90% in a broad potential range of −0.60 to −1.10 V (*vs*. RHE), and the maximum FE(CO) is as high as 99.7% at a potential of −0.80 V (*vs*. RHE) with a total current density of 20.5 mA/cm^2.

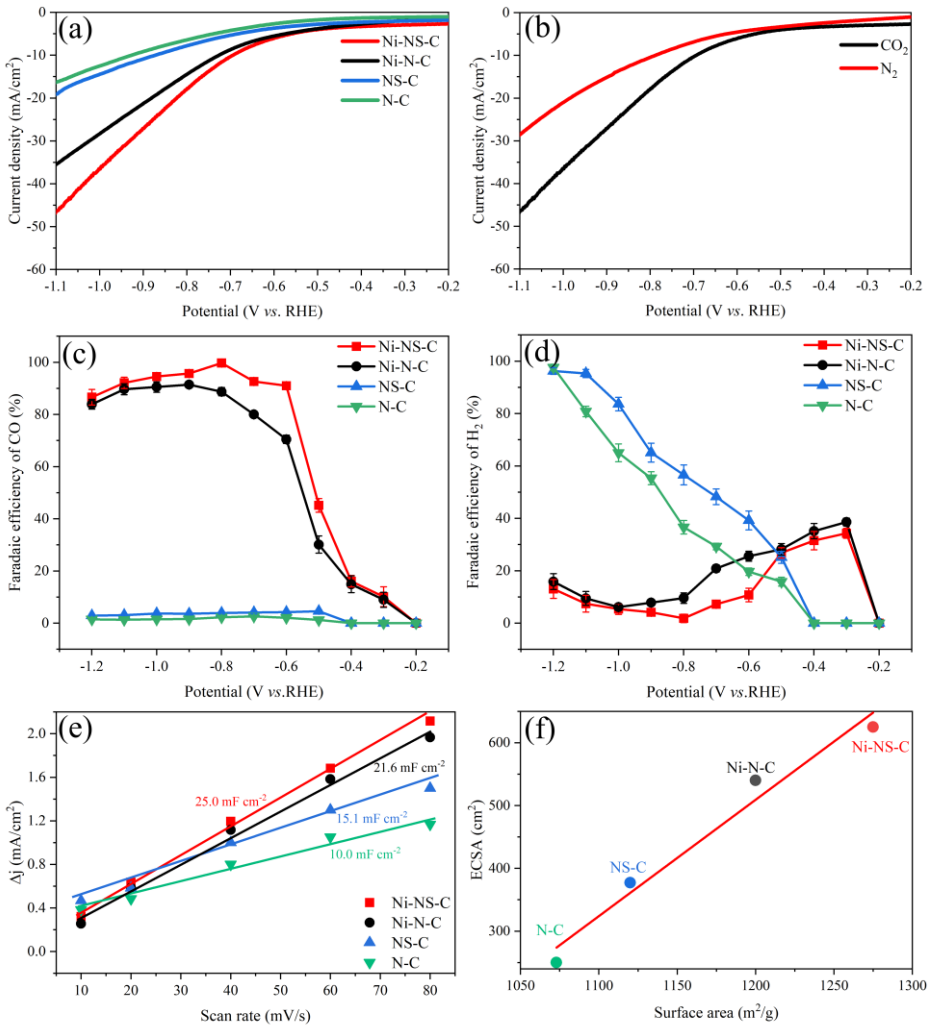

Figure 3.23. (a) LSV curves of N−C, NS−C, Ni−N−C and Ni-NS-C catalysts under CO_2-saturated 0.5M $KHCO_3$ solution at a scan rate of 10 mV/s; (b) LSV curves of Ni−NS−C catalyst under N_2- and CO_2-saturated 0.5M $KHCO_3$ solution at a scan rate of 10 mV/s; (c) The Faradic efficiencies of CO generation and (d) Faradic efficiencies of H_2 generation on N−C, NS−C, Ni−N−C and Ni−NS−C catalysts; (e) Charging current density differences against scan rates over N−C, NS−C, Ni−N−C and Ni−NS−C catalysts; (f) Relationship between double layer capacity and BET surface area of the N−C, NS−C, Ni−N−C and Ni−NS−C catalysts.

The increase of electrochemical active surface areas (ECSA) also contributes to the excellent activity towards ECR. ECSA can be directly estimated by measuring double layer (D−L) capacitance (Figure 3.23e and Appendix E, Figure S2). The Ni−NS−C and Ni−N−C catalysts exhibit 25.0 mF/cm^2 and 21.6 mF/cm^2, which are larger than that of the NS−C (15.1 mF/cm^2) and N−C catalysts (10.0 mF/cm^2). Consequently, the corresponding ECSA for Ni−NS−C, Ni−N−C, NS−C and N−C catalysts were 625, 540, 377 and 250 cm^2_{ECSA}, demonstrating that Ni and S atoms could effectively increase the ESCA (Appendix E, Table S1). It can also be found that there is a positive correlation between ECSA and BET surface area (Figure 3.23f), validating that larger surface area could expose more active sites.

CO_2 adsorption on catalyst surface plays an important role in ECR. Therefore, we conducted CO_2-TPD to investigate the effect of S dopant on their CO_2 adsorption ability. It turns out that Ni−NS−C shows slightly stronger CO_2 adsorption than that of Ni−N−C, which could boost the ECR performance (Appendix E, Figure S3). To further elucidate the effect of S atom on the reaction kinetics, the Tafel slope and electrochemical impedance spectroscopy (EIS) were conducted. As shown in Figure 3.24a, the Ni−NS−C catalyst exhibits a lower Tafel slope of 182 mV/dec than Ni−N−C of 193 mV/dec, suggesting that the introduction of S atom could improve the reaction kinetics. The Tafel slopes of these two samples are close to the theoretical value, revealing that CO_2-to-CO on these two catalysts proceed via the same mechanism that CO_2 accepting proton-electron pairs to form *COOH intermediate is the potential determining step (PDS) [46]. The EIS test was further conducted at −0.80 V (*vs*. RHE) and the corresponding complex-plane plot of Ni−N−C and Ni−NS−C catalysts were displayed in Figure 3.24b. The Ni−NS−C catalyst exhibited a smaller charge transfer resistance (R_{ct}), demonstrating that incorporating S atom could accelerate electron exchange between the catalysts and reactants. In addition, the electrochemical stability of Ni−NS−C was evaluated by chronoamperometric electrolysis under the potential of −0.80 V (*vs*. RHE) with the largest FE(CO). As shown in Figure 3.24c, there is a fast drop in current density during the initial 20 minutes, which can be attributed to unbalanced CO_2 adsorption on the catalyst. After that, the current density and FE (CO) is highly stable with negligible decay. The current density is still around 20.5 mA/cm^2 and the FE (CO) is about 98% after electrocatalysis reaction for >19 h. We also studied the structure and element information of the spent Ni−NS−C catalyst by TEM, EDX mapping and XPS, as shown in Appendix E, Figure S4, S5 and summarized in Appendix E, Table S1. It can be found that there is no obvious change in morphology and element content after ECR reaction, demonstrating excellent stability of the Ni−NS−C catalyst. The very recent studies on nonmetal decorated M−N−C catalysts from prominent literatures have been summarized in Appendix E, Table S2. Remarkably, the Ni−NS−C catalyst in this study outperformed most of the catalysts in terms of applied potential, FE(CO) and stability.

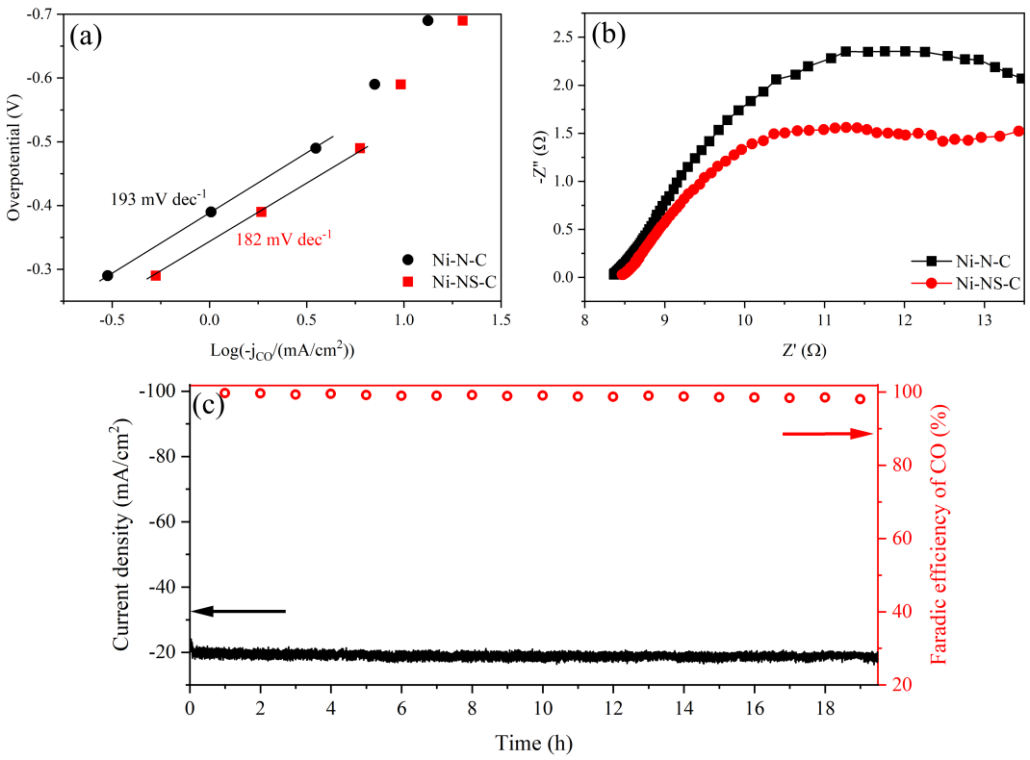

Figure 3.24. (a) Tafel plots for CO generation on Ni−N−C and Ni−NS−C catalysts; (b) EIS complex-plane plot for Ni−NS−C and Ni−N−C catalysts in 0.5 M $KHCO_3$ at potential of −0.8 V (vs. RHE); (c) Long-term electrocatalysis on Ni−NS−C catalyst in 0.5 M $KHCO_3$ at −0.8 V (vs. RHE).

3.4.3. DFT simulations

DFT calculations were performed to gain insight into the electrocatalytic reaction mechanisms of ECR and HER on Ni−N−C and Ni−NS−C catalysts based on the CHE model. As Ni atoms are more likely to form stable Ni−N_4 moiety in carbon-based materials, the Ni−N_4 structure was created in carbon matrix as active center in Ni−N_4−C catalyst [47-50]. It is worth noting that similar method for synthesizing Fe−N_4−C catalyst has been reported recently [51]. Meanwhile, previous study has shown that the good ECR ability of Ni decorated nitrogen doped carbon catalysts should be attributed to the single Ni atoms instead of Ni nanoparticles [45]. XRD indicated that the introduction of S atoms possibly induced the formation of C atom vacancies because the radius of S atom is larger than that of C atom. To exclude the possibility of S directly substituting C atom without breaking TM−N_4, we also built a configuration as shown in Appendix E, Figure S6, where S directly substituted C atom but TM−N_4 was maintained. Compared to the pristine S free structure, the CO desorption ability will be

quite weak in this structure because of high free energy change of 1.46 eV, while the HER ability was strengthened due to low free energy of −0.53 eV. These results are not consistent with the experimental data. Therefore, S atom embedded into C vacancy close to Ni site (Ni−NS−C) as model was proposed to investigate the effect of S atoms on the ECR performance of the Ni−N_4−C catalyst (Figure 3.25a). The adsorption energy of CO_2 on the Ni−N−C and Ni−NS−C catalysts were calculated to be −0.28 and −0.39 eV, further demonstrating that S dopant could promote CO_2 adsorption, consistent with the CO_2-TPD results. The adsorbed *COOH, *CO and *H intermediates were considered in ECR and HER. As shown in Figure 3.25b, the Gibbs free energy change (ΔG) diagram of CO_2-to-CO over these two catalysts suggests that the first proton-electron pair to generate *COOH is the PDS, consistent with the experimental results. The Ni−N−C catalyst shows ΔG_{*COOH} of 1.86 eV, which is higher than that of the Ni−NS−C catalyst at 1.66 eV, confirming that S atom could effectively decrease the CO_2 activation barrier. This is also consistent with the experimental result that introducing S atoms could enhance FE(CO) under all applied potentials. The calculated adsorption energy of CO over the Ni−N−C catalyst was reduced by 0.06 eV after the incorporation of S atom, demonstrating the increase of CO desorption ability. The HER activities over the two catalysts were compared by calculating the Gibbs free energy of *H (ΔG_{*H}) (Figure 3.25c). Notably, the ΔG_{*H} of Ni−NS−C catalyst increases from 1.53 to 1.82 eV, showing that S atom could effectively suppress HER when Ni is present, which again agrees with the experimental observation that FE(H_2) of the Ni−N−C catalyst decreased after doping S (Figure 3.25d).

It has been well established that the difference between the limiting potentials of ECR and HER (U_L (CO_2) − U_L (H_2)) could be a reasonable descriptor for ECR selectivity. A more positive U_L (CO_2) − U_L (H_2) indicates a higher selectivity towards ECR. As displayed in Figure 3.25d, the Ni−NS−C catalyst shows a positive value of U_L (CO_2) − U_L (H_2), which is negative for the Ni−N−C catalyst, demonstrating increased ECR selectivity after incorporating S atoms. Furthermore, the electronic structure of Ni-NS-C and Ni−N−C catalysts were compared. The d band center of Ni−N−C catalyst moved

towards the Fermi level after introducing the S atom, and the Ni-3d state of Ni−NS−C catalyst crossed the Fermi level (Figure 3.25e), thereby improving the intrinsic activity of 3d electrons. When the *COOH intermediate was adsorbed on the catalysts, Ni atom (Ni−NS−C) lost smaller charge (0.89e) (Figure 3.25f), accounting for moderate interaction. The results demonstrated that the synergistic effect of the Ni and S atom boosts the ECR performance where the Ni atoms sever as the active center and S atom plays a role in the modification of electronic properties.

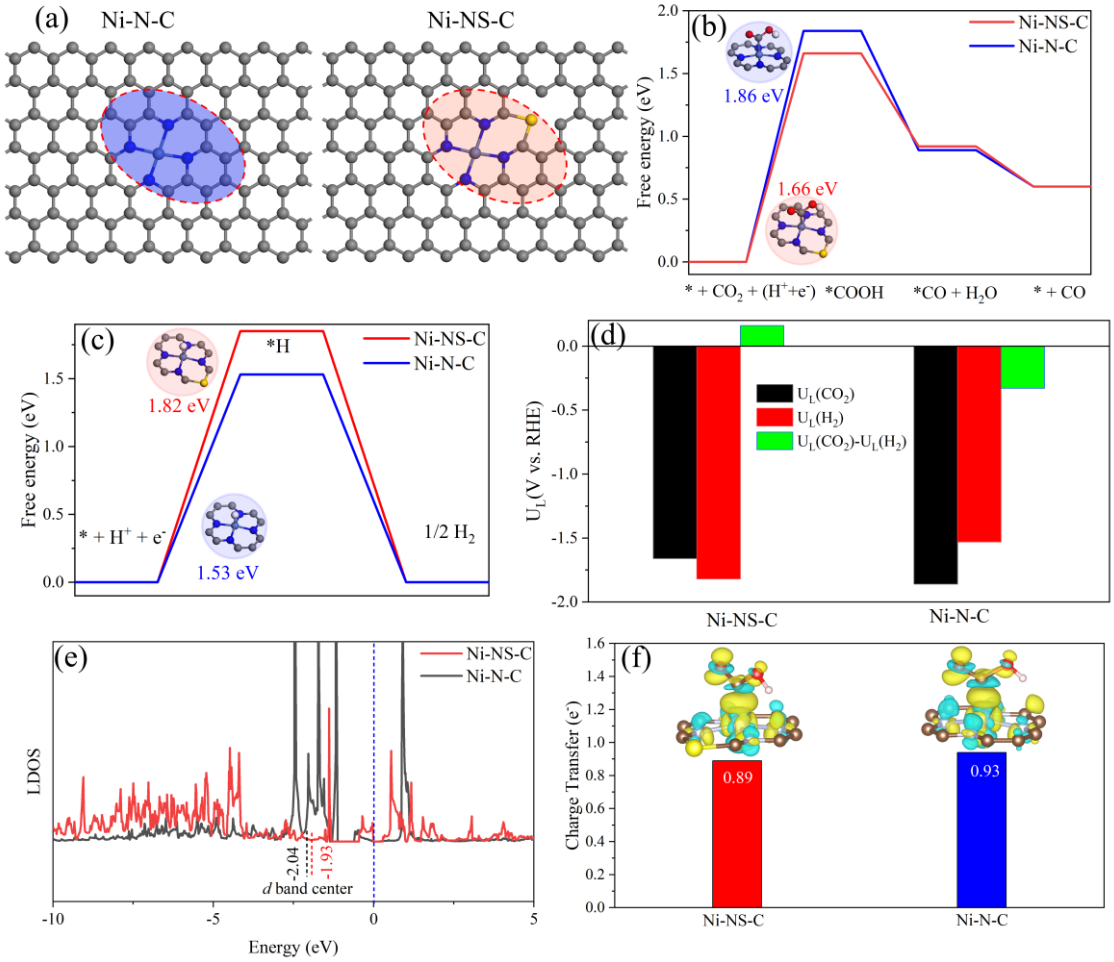

Figure 3.25. (a) The atomic structure of proposed Ni−N−C and Ni−NS−C catalysts; (b) Free energy diagrams for ECR to CO; (c) Free energy diagrams for HER; (d) The difference between the limiting potentials for ECR and HER; (e) The location of d band center; (f) The charge density difference after *COOH adsorption on Ni−N−C and Ni−NS−C catalysts, the isosurface value is set to be 0.003 e/Bohr^3.

3.5. Regulating the coordination environment of single-atom catalysts for electrocatalytic CO_2 reduction (Paper VI)

In this work, a series of NM (B, O, F, Si, P, S, Cl, As, Se and Br) heteroatom dopants modified TM (Fe, CO, Ni, Cu and Zn)@N_4 configurations embedded on graphene sheet are proposed. We performed a computational screening of the ECR to CO activity and stability of the NM decorated TM@N_4.

3.5.1. Structures and stabilities of nonmetal modified TM−N

Ten SACs configurations were built, as shown in Figure 3.26. After structure relaxation, the host N and TM atoms of the TM@N_4 configuration are on the same plane with all carbon atoms. To introduce axial ligands on TM sites, TM atoms of TM@N_4−NM_1(I) are above the graphene plane. Besides, the bond length of the newly formed bond such as F−Co, O−Fe and Cl−Fe are close to the sum of the respective atomic covalent radius, implying strong interaction between TM atom and axial ligand. For doping heteroatoms into the second and high shells, all atoms still stay in the graphene plane after structure relaxation. However, the compositions of resulting five- and six-membered rings are various, which can be attributed to the different atomic radius and electronegativity of the introduced heteroatoms. After first shell doping, almost no structures of TM@N_3−NM_1 had obvious changes. Nonetheless, with the increase of the number of dopant heteroatoms, e.g., Fe@N_2−Se_2(II), Co@N_1−F_3, Co@F_4, Co@N_1−As_3, Co@As_4, Co@Se_4, Co@N_2−Se_2(II), Ni@As_4, Ni@Se_4, Ni@N_2−Se_2(II), Cu@As_4, and Zn@N_2−Se_2(II) systems exhibited surface reconstruction, because the large difference in atomic radius in comparison with the host N or C atoms caused local strain and disruption of graphene plane. Therefore, these configurations are unstable and will be difficult to synthesize them experimentally. In Appendix F, Figure S1, a negative value of E_f indicates that heteroatoms doped TM@N_4 structure is thermodynamically stable. One heteroatom substituting N or C atom or binding axially on TM site exhibits great stability with negative E_f, such as Fe@N_3−B_1, Fe@N_3−P_1, Fe@N_4−Cl(I), which have been validated experimentally [52, 53]. Besides, it can be found that the value of E_f

becomes increasingly larger with the increase of coordination number, implying that introducing more heteroatoms could destabilize the host structure.

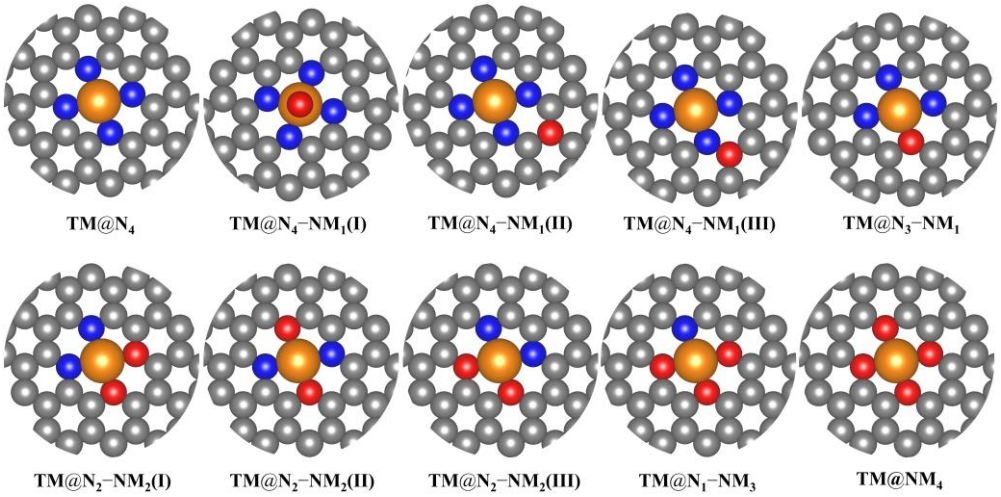

Figure 3.26. NM atoms doping sites on TM@N_4-graphene monolayer configurations. Gray, red, blue and orange balls represent C, NM dopants, N and TM atoms.

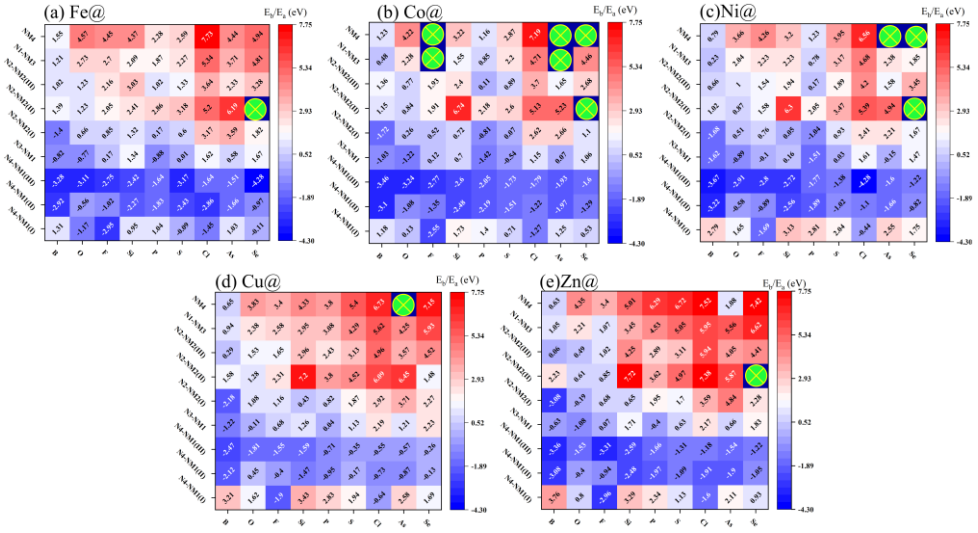

Figure 3.27. The binding energy (E_b) of TM atoms on NM doped (a)Fe@N_4, (b) Co@N_4, (c) Ni@N_4, (d) Cu@N_4 and (e) Zn@N_4 configurations, of which F and Cl atom are adsorbed on TM site with adsorption energy E_a. The green circle indicates surface reconstruction.

To further investigate the stability of anchored single TM atoms with different coordination environment based on formation energy, the binding energies (E_b) of TM atoms were calculated (Figure 3.27). In the pristine TM@N_4 systems, the E_b of single Fe, Co, Ni, Cu and Zn atoms are −2.47, −2.94, −2.81, −1.58, and −2.46 eV, respectively. The negative values of E_b indicate that the TM@N_4 configurations are very stable on graphene, in good agreement with experimentally synthesized TM@N_4 on carbon

skeletons. For NM heteroatoms decorated Fe@N_4 systems (Figure 3.27a), O, F, S, Cl and Se as axial ligands exhibit negative adsorption energy, indicating that these NM atoms could be anchored stably on Fe sites. When incorporated into carbon framework, Fe@N_4−NM(II) and Fe@N_4−NM(III) configurations are energetically favorable, whereas only Fe@N_3−B_1, Fe@N_3−O_1 and Fe@N_3−P_1 present negative E_b when one heteroatom substitutes one host N atom. When the dopant heteroatoms increase from two to four, the structures become unstable as confirmed by positive binding energies. For heteroatom doped Co@N_4, Ni@N_4, Cu@N_4 and Zn@N_4, the structures with more than more heteroatoms are more stable with negative E_b values, such as Co@N_2−P_2(I), Co@N_3−S_1, Ni@N_2−P_2(I), Ni@N_3−As_1 and Zn@N_2−O_2(I). Overall, for systems with single heteroatom, it can be concluded that halogen elements can be ideal axial ligand for TM@N_4 moiety. B, O and Si atoms prefer to form TM@N_4−NM_1(III) (second shell), while P, S, As and Se are more likely to form TM@N_4−NM_1(II) (high shell). For dopant heteroatoms substituting one or more host N atoms, B and P could be potential candidates. Therefore, heteroatom decorated TM@N_4 configurations with both negative values of E_f and E_b will be identified as stable structure. Consequently, there are 126 stable structures which are subsequently investigated for their ECR to CO performance.

3.5.2. ECR to CO performance

Fe, Co, Ni, Cu and Zn of TM−N_X−C SACs exhibit good potential in ECR to CO. Meanwhile, it has been demonstrated both theoretically and experimentally that introducing NM dopants can further improve their ECR activity. However, earlier studies of some configurations are oversimplified, which might have ignored other possible structures that affect the catalytic performance for CO generation. Therefore, we calculated Gibbs free energy changes during ECR to CO for NM decorated SACs. The ECR to CO process contains three elementary steps, of which ΔG_1 (the formation of *COOH), ΔG_2 (the formation of *CO) and ΔG_3 (the desorption of *CO) are important descriptors for ECR to CO activity. It can be found that the formation of *COOH on Fe, Co, Ni, Cu and Zn@N_4 structures are endothermic with large free

energy barriers, especially for Ni, Cu and Zn@N_4. The values of ΔG_2 are −1.04, −0.08, −0.78, −0.80 and −0.17 eV for Fe, Co, Ni, Cu and Zn@N_4, suggesting that it is easy to form *CO. CO selectivity is strongly dependent on the interaction strength between CO and TM sites, *i.e.*, the more negative the value of ΔG_3, the easier the CO desorption from TM sites. CO desorption on Fe and Co@N_4 moieties show energy uphill thus difficult desorption, while CO desorption on Ni, Cu and Zn@N_4 structures are spontaneous. The PDS of ECR to CO on Fe and Co are *CO desorption, while the formation of *COOH is the PDS for Ni, Cu and Zn@N_4 catalysts, consistent with experimental studies. Consequently, the corresponding overpotentials for ECR to CO are 1.00, 0.26, 1.62, 1.64 and 0.98 V for Fe, Co, Ni, Cu and Zn@N_4.

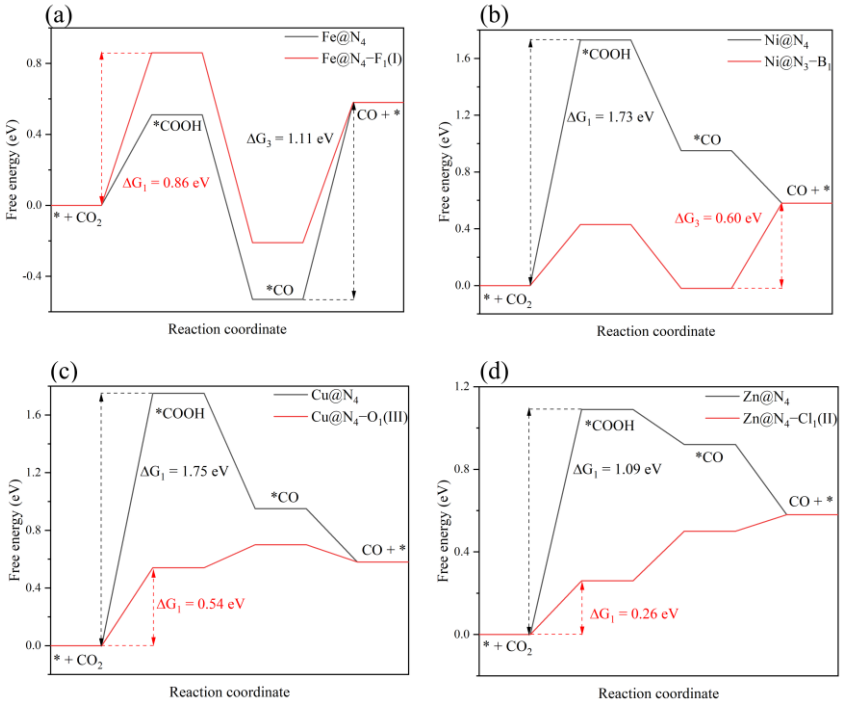

Figure 3.28. The Gibbs free energy change for ECR to CO on NM decorated (a)Fe@N_4, (b) Ni@N_4, (c) Cu@N_4 and (d) Zn@N_4 catalysts.

After incorporating heteroatoms into TM@N_4, the ΔG_1, ΔG_2 and ΔG_3 are varying (Appendix F, Table S1-S5), thus the PDS is changed. Interestingly, F and Cl could effectively adjust the PDS for ECR to CO on TM@N_4. Particularly, axial F and Cl atoms could enhance the ECR activity on Fe and Ni@N_4, but inhibit ECR to CO on Co, Cu and Zn@N_4. This is also consistent with previous report that Cl as axial ligands could effectively improve ECR to CO performance on Fe@N_4 catalyst [53]. In addition,

the formation of *CO on most NM doped TM@N_4 are energy downhill, revealing that NM dopants cannot affect *CO formation. Furthermore, it can be found that heteroatoms could effectively improve the ECR activity on Ni and Cu@N_4 but decrease the activity on Co@N_4. As shown in Figure 3.28, the PDS of Fe@N_4−F_1(I), Ni@N_3−B_1, Cu@N_4−O_1(III) and Zn@N_4−Cl_1(II) exhibit the lowest free energy barrier of 0.86, 0.60, 0.54 and 0.26 eV on NM decorated Fe, Ni, Cu and Zn@N_4, respectively.

It is also noteworthy that the decrease of free energy barrier for the formation of *COOH will increase the free energy barrier of *CO desorption and vice versa on these four catalysts with the lowest overpotentials. For example, for the Ni@N_3−B_1 catalyst, the free energy barrier for *COOH formation is greatly reduced, however, the desorption of *CO becomes PDS and changes from exothermic to endothermic reaction. These results indicate a negative relationship between ΔG_1 and ΔG_3. ΔG_1 and ΔG_3 were chosen as descriptors to identify their relationship. As illustrated in Figure 3.29, there is a linear relationship between ΔG_1 and ΔG_3, which are $\Delta G_3 = -0.93\Delta G_1+1.45$ (R^2 = 0.79), $\Delta G_3 = -0.94\Delta G_1+1.02$ (R^2 = 0.91), $\Delta G_3 = -1.01\Delta G_1+1.15$ (R^2 = 0.96), $\Delta G_3 = -0.86\Delta G_1+1.15$ (R^2 = 0.79), $\Delta G_3 = -0.80\Delta G_1+0.74$ (R^2 = 0.74) for NM doped Fe, Co, Ni, Cu and Zn@N_4 catalysts, respectively. Therefore, NM atoms doped TM@N_4 catalysts are still limited by linear relationship between key intermediates.

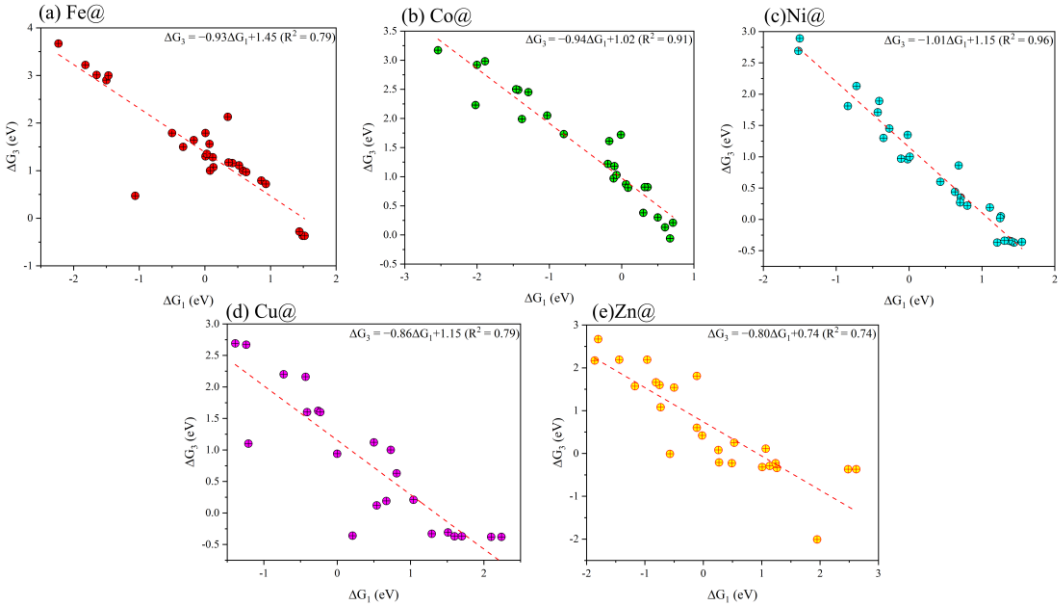

Figure 3.29. Scaling relationship between ΔG_1 and ΔG_3 on NM decorated (a)Fe@N_4, (b) Co@N_4, (c) Ni@N_4, (d) Cu@N_4 and (e) Zn@N_4 structures.

The overpotentials of heteroatoms doped TM@N_4 catalysts were further illustrated by two-dimensional contour maps (Figure 3.30). The ECR performance increases when it migrates from the blue to red area in this visualized cloud plot. Therefore, the lower overpotential can be found in the red area. Only NM dopants that have positive effect on overpotentials are marked by blue arrows. It can be found that the lowest overpotentials of ECR to CO on NM doped TM@N_4 are 0.75, 0.49, 0.43 and 0.15 V for Fe@N_4−F_1(I), Ni@N_3−B_1, Cu@N_4−O_1(III) and Zn@N_4−Cl_1(II), respectively, indicting remarkable decrease from their pristine TM@N_4 counterpart (Appendix F, Table S6). Remarkably, the overpotentials of Fe@N_4−F_1(I), Ni@N_3−B_1 and Cu@N_4−O_1(III) are lower than that of experimentally synthesized NM doped TM@N_4 catalysts such as axial Cl coordinated Fe with N_4 (0.93 V)[53], Ni@N_4 modified by S atom in C vacancy (1.55 V) [54], and Cu coordinated with three N and one O atoms (1.22 V) [55]. Furthermore, the stability of Fe@N_4−F_1(I), Ni@N_3−B_1, Cu@N_4−O_1(III) and Zn@N_4−Cl_1(II) is evaluated by the *ab initio* molecular dynamics (AIMD) simulation under T=300K. As shown in Appendix F, Figure S3a-d, the structures are maintained well, suggesting excellent thermodynamic stability.

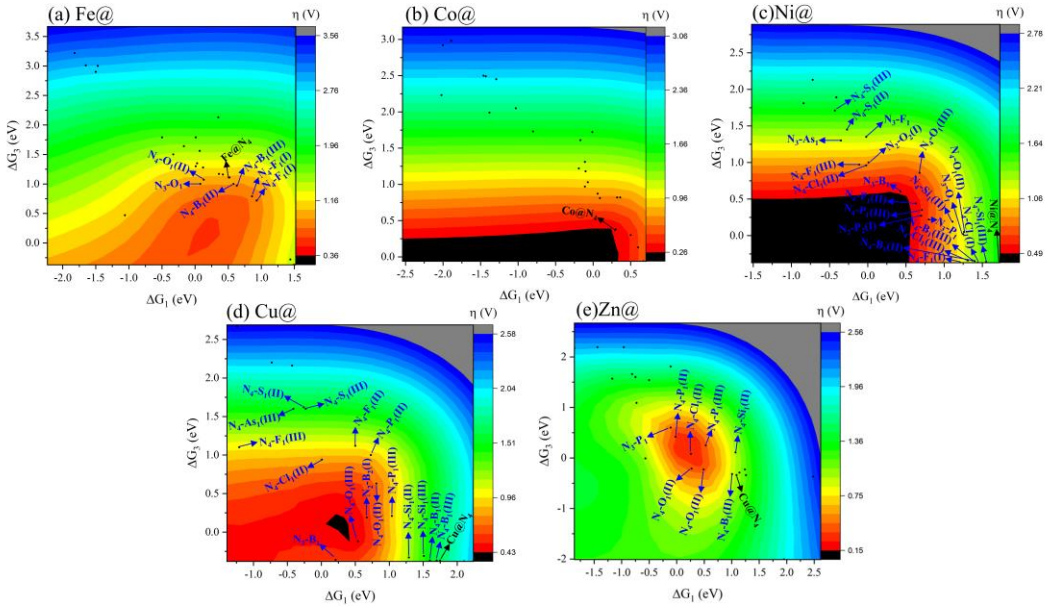

Figure 3.30. The contour maps of overpotential (η) for ECR to CO as a function of ΔG_1 and ΔG_3 on NM decorated (a)Fe@N_4, (b) Co@N_4, (c) Ni@N_4, (d) Cu@N_4 and (e) Zn@N_4 catalysts, in which blue arrows indicate that the overpotential is lower than pristine TM@N_4.

3.5.3. Activity origin

The optimized configurations of *COOH and CO* adsorption on Fe@N_4−F_1(I), Ni@N_3−B_1, Cu@N_4−O_1(III) and Zn@N_4−Cl_1(II) catalysts are shown in Appendix F, Figure S4a-d. CO_2 adsorption energy on Fe@N_4−F_1(I), Ni@N_3−B_1 and Zn@N_4−Cl_1(II) exhibits slight decrease in comparison with that of pristine Fe, Ni and Zn@N_4, indicting little reinforcement for CO_2 activation. Meanwhile, the substrates are also maintained well without bond breaking. For CO_2 adsorption on Cu@N_4−O_1(III), the adsorption energy is more negative with accompanying bond breakage. However, this configuration did not change after the adsorption of *COOH and CO. In contrast, Co@N_4−Cl_1(II) also exhibits lower adsorption energy for CO_2, but the coordination Cl ligand is altered after the adsorption of different intermediates (Appendix F, Figure S4e), which apparently changes the configuration of Co@N_4 center. Consequently, the performance of ECR to CO on Co@N_4−Cl_1(II) was reduced. Therefore, it can be deduced that after reactants adsorption on NM doped TM@N_4 SACs, the induced structural changes can promote the ECR to CO performance, which is related to the interaction between the active TM atom and substrate. d band center (ε_d) is an effective descriptor to reveal the binding strength between intermediates and active sites [56]. The ε_d of Fe, Ni, Cu and Zn@N_4 are −1.20, −2.24, −3.41 and −6.23 eV, respectively. As shown in Appendix F, Table S6, incorporating NM dopants could effectively tune ε_d. For Fe@N_4−F_1(I), a negative shift of ε_d contributed to weaker CO binding strength on Fe site, which changed the PDS from *CO desorption to *COOH formation. B dopants induced a positive shift of ε_d, enhancing the interaction strength between *CO and Ni site. As a result, the PDS changed from *COOH formation to *CO desorption. The ε_d of Cu@N_4−O_1(III) and Zn@N_4−Cl_1(II) shifted towards lower energy, which effectively promoted *COOH formation and accelerated the ECR process.

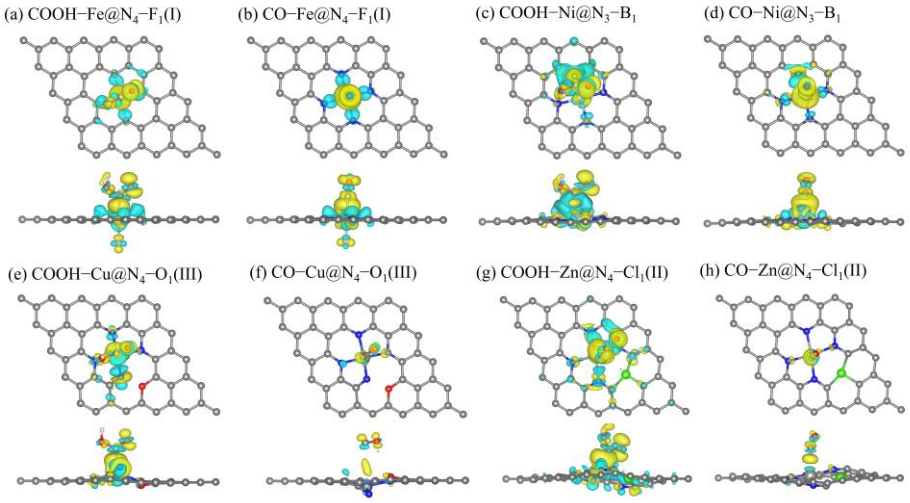

Figure 3.31. Charge density difference of *COOH and *CO adsorption on (a)-(b) Fe@N_4−F_1(I), (c)-(d) Ni@N_3−B_1, (e)-(f) Cu@N_4−O_1(III) and (g)-(h) Zn@N_4−Cl_1(II), where the isosurface value is set to be 0.001 e/$Bohr^3$.

As the changes of structure may influence electronic structures, the charge density difference and charge transfer between the intermediates and TM atoms were calculated and illustrated in Figure 3.31 and Appendix F, Figure S5. For *COOH−TM@N_4 moiety, Bader charge analysis reveals that the Fe, Ni, Cu and Zn atom donated 1.09e, 0.91e, 0.88e and 1.08e, respectively. For *CO−TM@N_4 system, the Fe, Ni, Cu and Zn atom lost 0.97e, 0.86e, 0.95e and 1.16e. After introducing NM atoms, for example, Fe atom in *COOH/*CO−Fe@N_4−F_1(I) donated more electrons (1.20e) because of larger electronegativity of F. However, this transfer did not affect the adsorbate, indicating that higher oxidized stated of Fe is not beneficial for *COOH activation as evidenced by the higher free energy for *COOH formation on Fe site. In addition, the yellow area between Fe atom and C atom of *CO was reduced, which weakened the binding strength between Fe and C and promoted CO desorption, in accordance with previous report that Fe with high valence could promote CO desorption [57]. For *COOH/*CO−Ni@N_4−B_1, one N atom was substituted by B atom with lower electronegativity, leading to lower oxidized state of Ni compared with Ni in Ni@N_4. Meanwhile, C atom of *CO lost less electrons (0.94e) than C atom of pristine *CO−Ni@N_4 (1.03e). However, a large yellow area between C and Ni atoms demonstrated a covalent bonding, indicating strong CO adsorption. As a result, CO desorption from Ni site is energy uphill. The valence states of Cu and Zn did not exhibit

much change with slight accumulation of electrons between metal and C atom, implying some enhancement of *COOH adsorption. For *CO adsorption on metal site, there is little electron transfer between them, indicating weak interaction of *CO with metal atom. These results are consistent with free energy change for *COOH formation and *CO desorption.

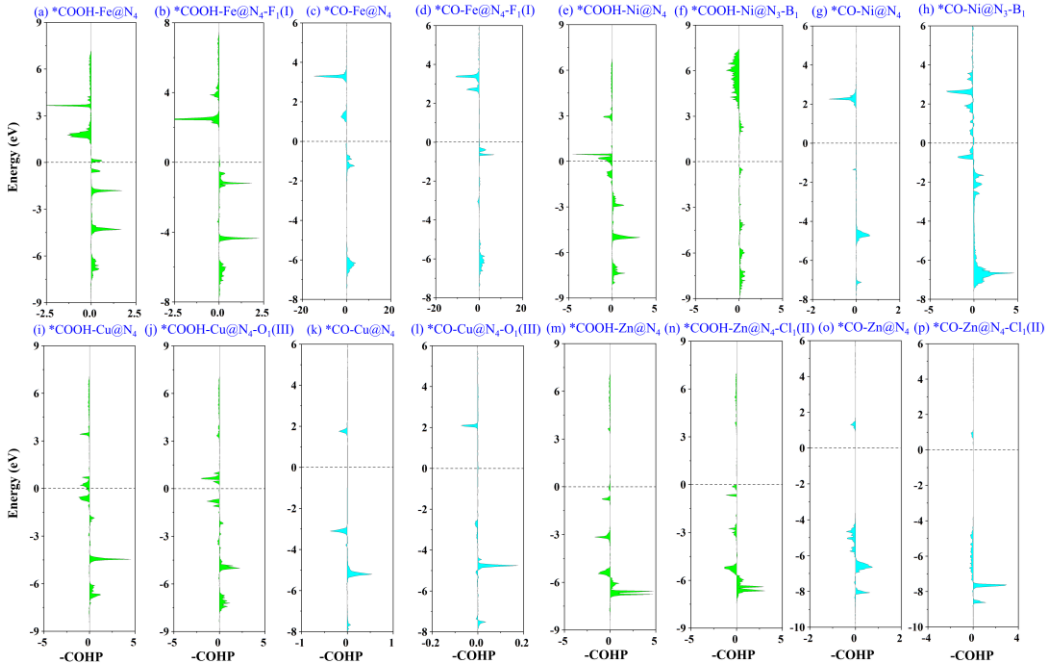

Figure 3.32. The COHP between C atom of *COOH and TM atom of catalysts (green), C atom of *CO and TM atom of catalysts (cyan). (a)-(d) Fe@N_4 and Fe@N_4−F_1(I), (e)-(h) Ni@N_4 and Ni@N_3−B_1, (i)-(l) Cu@N_4 and Cu@N_4−O_1(III), and (m)-(p) Zn@N_4 and Zn@N_4−Cl_1(II). The dashed line denotes Fermi level.

To reveal the relationship between binding strength and activity, projected crystal COHP was employed to analysis the interaction between C and metal atom. As shown in Figure 3.32, there are no antibonding states below fermi energy level for COOH−Fe@N_4, however, it appeared at around −3.5 eV after introducing F ligand. Therefore, the binding strength was weakened as evidenced by higher free energy barrier for *COOH formation. Meanwhile, there are antibonding orbital populations appearing between −2 and −4 eV on CO−Fe@N_4−F_1(I), indicating unstable adsorption of CO. Thus, the CO deposition energy barrier decreased.

To give a quantitative comparison of the interaction strength, the ICOHP was calculated (Appendix F, Table S6). The ICOHP for COOH−Fe@N_4−F_1(I) is −0.76 eV, which is

less negative than that of COOH−Fe@N_4 (−0.95 eV), demonstrating that F dopant could weaken *COOH binding strength. The ICOHP of CO−Fe@N_4 after introducing F atom increases from −3.32 to −3.00 eV, suggesting that CO binding strength decreases. B decorated Ni@N_4 also exhibits remarkable difference in bonding and antibonding states. As shown in Figure 6.8e-h, the antibonding orbital populations of *COOH adsorption on Ni@N_4 disappear after incorporating B atom, which contributes to the enhanced *COOH interaction with Ni. Meanwhile, there are antibonding states emerging between 0 and −1 eV for CO−Ni@N_3−B_1, indicating reduced CO adsorption strength on Ni. The calculated ICOHP for COOH−Ni@N_4 and COOH−Ni@N_3−B_1 are −1.14 and −0.19 eV or −3.52 eV (B site), while the ICOHP for *CO adsorption on Ni@N_4 and COOH−Ni@N_3−B_1 are −0.21 and −1.97 eV, respectively. Heteroatom doped Cu and Zn@N_4 did not show much difference in the distribution of antibonding and bonding states, however, the binding strength can be distinguished by ICOHP. Appendix F, Table S6 shows that O doped Cu@N_4 exhibits a decrease of ICOHP from −0.66 to −0.84 eV and a slight increase from −0.01 to −0.04 eV for *COOH and *CO adsorption, respectively. For Cl decorated Zn@N_4, the ICOHP for both *COOH and *CO absorption shows a decrease from −0.21 to −0.32 eV and −0.03 to −0.08 eV, respectively. Consequently, O and Cl dopants could improve the binding strengths of *COOH and *CO with TM atom.

3.5.4. Selectivity of ECR to CO vs. HER

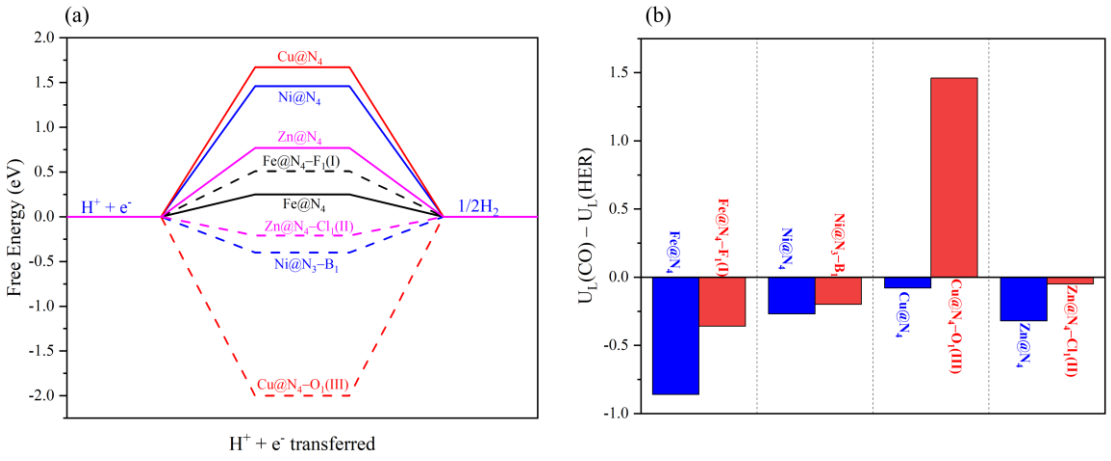

Figure 3.33. (a) The Gibbs free energy change for HER, and (b) The difference between the limiting potentials for ECR to CO and HER on pristine TM@N_4 and NM doped TM@N_4.

The hydrogen evolution reaction (HER) is a major competing reaction in ECR, which greatly decrease Faradic efficiency of CO product. Especially, under high potentials and low pH, the competitive HER is dominant. As exhibited in Figure 3.33a, free energy barriers for HER on Fe@N_4−F_1(I) and Cu@N_4−O_1(III) are 0.51 and 2.00 eV, which are larger than that of pristine Fe@N_4 and Cu@N_4. Therefore, HER is suppressed on Fe@N_4−F_1(I) and Cu@N_4−O_1(III) catalysts. It is worth mentioning that H atom prefers to adsorb on N site not Cu site after geometric relaxation, which caused a large free energy barrier for HER and promoted ECR intermediate adsorption on Cu site. However, the free energy barriers of Ni@N_3−B_1 and Zn@N_4−Cl_1(II) for HER decrease to 0.40 and 0.21 eV, implying increased HER activity. It has been widely accepted that the difference between limiting potentials of ECR and HER ($U_L(CO)$−$U_L(H_2)$) can be used to describe ECR selectivity [58]. As shown in Figure 3.33b, a more positive value of $U_L(CO)$−$U_L(H_2)$ indicates a higher selectivity towards CO. Remarkably, four catalysts exhibit increased CO selectivity compared with the pristine TM@N_4. Despite that heteroatom could deteriorate the ECR performance on Co@N_4, Co@N_4−Si_1(III) shows similar overpotential (0.27 V) as pristine Co@N_4 (0.26 V). Interestingly, The HER free energy barrier on Co@N_4−Si_1(III) is 0.18 eV, higher than that of Co@N_4 (0.09 eV). Thus, a larger value of ($U_L(CO)$−$U_L(H_2)$) for Co@N_4−Si_1(III) indicates that Si dopant could increase CO selectivity. It is worth noting that the free energy change for HER is not the single descriptor for HER activity, other parameters such as pH of electrolyte can effectively suppress the HER process. For example, the free energy barrier of HER can be tuned according to the relationship $\Delta G_{pH} = k_B T \times \ln 10 \times pH$ [59, 60]. Consequently, it will increase 0.42 eV when the pH increased from 0 to 7. Therefore, the Faradic efficiency of ECR to CO on these catalysts can be improved by changing reaction conditions.

3.6. Breaking scaling relations for highly efficient electroreduction of CO_2 to CO on atomically dispersed heteronuclear dual-atom catalyst (Paper VII)

In this work, Ni SAC, Mn SAC, Ni−Ni DAC and Mn−Mn DAC and Mn−Ni DAC were synthesized. The ECR activity mechanism on these catalysts was study by DFT calculations and experiment.

3.6.1. Electrocatalysts characterization

The crystal structures of the five catalysts were verified by powder XRD and Raman spectroscopy analyses. As shown in Appendix G, Figure S1a, the five catalysts all present the same diffraction patterns. Two characteristic peaks located around 24.9° and 43.3° can be assigned to the (002) and (001) planes of graphite with low crystallinity. Besides, no peaks attributable to metal or metallic compounds are identifiable, indicating that the metal atoms are possibly dispersed atomically in the carbon matrix.

Appendix G, Figure S1b presents the Raman spectroscopy of the five electrocatalysts, which exhibits two vibrational bands of graphite at around 1343 cm^{-1} (D band) and 1594 cm^{-1} (G band), corresponding to the defect and graphitic sp^2-hybridized carbon [54, 55]. The ratios between D and G bands of the catalysts range from 1.03 to 1.09, suggesting similar graphitization degree and the presence of defects such as vacancies, edge and non-hexagonal rings [61, 62].

The textural properties of the electrocatalysts were investigated by N_2 physisorption analyses. As illustrated in Appendix G, Figure S2, the isotherms of the five catalysts exhibited sharp adsorption under relative pressures higher than 0.40 accompanied with obvious hysteresis loop, which can be attributed to the dominant mesopores and is further confirmed by the pore size distributions. The Brunauer-Emmett-Teller (BET) surface area of Mn−NC, Ni−NC, Mn−Mn−NC, Ni−Ni−NC, and Mn−Ni−NC catalysts are 890, 987, 854, 964, and 935 $m^2\,g^{-1}$, respectively (Appendix G, Table S1). The average pore diameters are also very close at around 4.9 nm, while the pore volumes vary very narrowly from 1.02 to 1.11 cm^3g^{-1}. Therefore, all catalysts exhibit large BET surface area and abundant mesopores, which are beneficial for mass transfer and

accessible active sites. It is worth emphasizing that the differences on structure properties of the five catalysts are insignificant, implying that the performance of ECR to CO over the five electrocatalysts can be exclusively ascribed to the intrinsic activities of the catalysts.

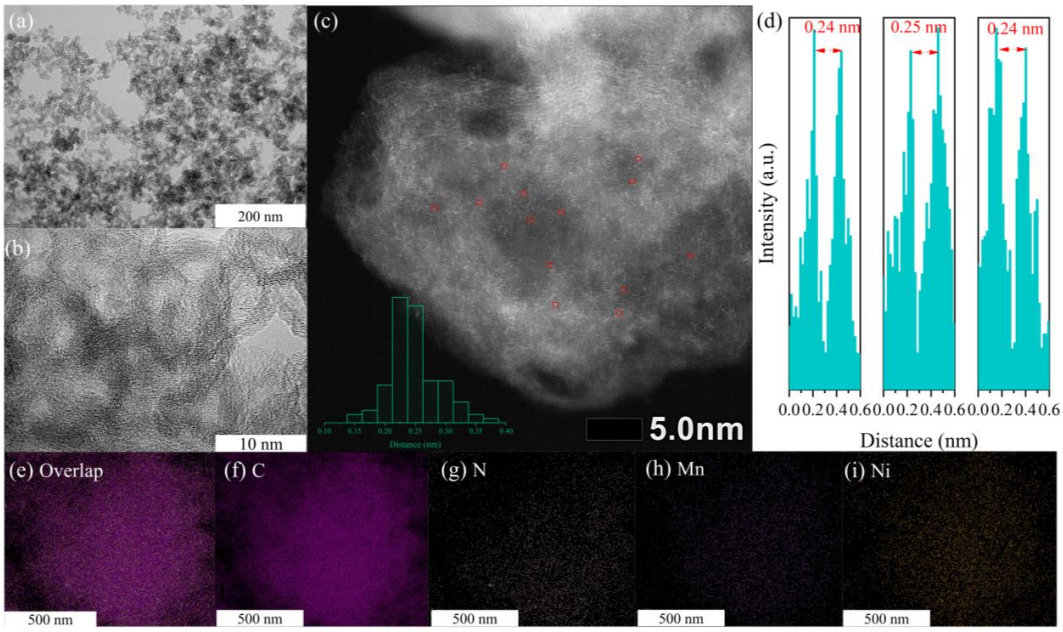

Figure 3.34. (a) TEM, (b) HRTEM, and (c) ADF-STEM of Mn−Ni−NC, where Mn-Ni atom pair are highlighted in red rectangles, and the histogram shows the proportion of different distances; (d) The intensity profile of distance between Mn and Ni atoms; (e)-(i) C, N, Mn, and Ni EDX mapping images of Mn−Ni−NC catalyst.

TEM characterization shows that the catalysts in general exhibit carbon pellets with a diameter of approximately 50 nm (Figure 3.34a). The high-resolution TEM reveals distorted short-range graphitic stripes with wrinkles and interlaces, suggesting the presence of structural defects in the carbon material (Figure 3.34b and Appendix G, S3a-S6a). Besides, no aggregates of metallic nanoparticles could be observed. We further employed ADF-STEM to verify the atomically dispersed metal atoms. As exhibited in Figure 3.34c and Appendix G, S3a, S4b-7b, evenly distributed bright spots could be observed on the carbon framework in the dark field for the Mn−Ni−NC catalyst. These dense bright dots with different brightness could be assigned to metallic Mn and Ni atoms because of the atomic number dependent contrast difference in the dark field [63]. Besides, the binding energy of Mn-Ni, Mn-Mn and Ni-Ni are -11.89, -9.21 and -11.40 eV, respectively. The formation energy of Mn-Ni, Mn-Mn and Ni-Ni

are -10.28, -9.38 and -10.02 eV, respectively. These results demonstrate that the formation of Mn-Ni pair is preferable. Moreover, numerous neighboring spots marked with red rectangle were observed, indicating that Mn and Ni atoms present in the form of atom-pairs. Statistical analysis was performed for the Mn−Mn−NC, Ni−Ni−NC and Mn−Ni−NC DAC catalysts. In each sample, 100 dots were fixed and the distance from its the closest bright dots were measured. For the Mn−Ni−NC catalyst, 58% dual-atom Mn−Ni pairs were counted, while 42% Mn and Ni atoms were counted as isolated atoms. The distances of the adjacent spots are estimated to be around 0.24±0.01nm (Figure 3.34d). Similarly, 39% Mn−Mn atom pairs were found in Mn−Mn−NC, and 46% Ni−Ni atom pairs were observed for the Ni−Ni−NC catalyst. The distances between the adjacent Mn−Mn and Ni−Ni atoms are both centered at around 0.23±0.01 nm (Appendix G, Figure S6c-S7c). Considering the great challenge to identify each atom by ADF-STEM, this statistic analysis can effectively figure out the distance of neighboring atoms [63]. In contrast, for the Mn−NC and Ni−NC SAC catalysts, isolated Mn and Ni atom can be easily observed, even though some Mn−Mn and Ni−Ni atom pairs are also present. Furthermore, EDX spectroscopy shows that in the Mn−Ni−NC catalyst, C, N, Mn and Ni elements are homogeneously distributed (Figure 3.34e-i), which is also apparent for all other electrocatalysts (Appendix G, Figure S4c-f, S5c-f, S6d-g and S7d-g). Therefore, it is fair to conclude that Mn−NC and Ni−NC are SACs, while Mn−Mn−NC, Ni−Ni−NC and Mn−Ni−NC are DACs.

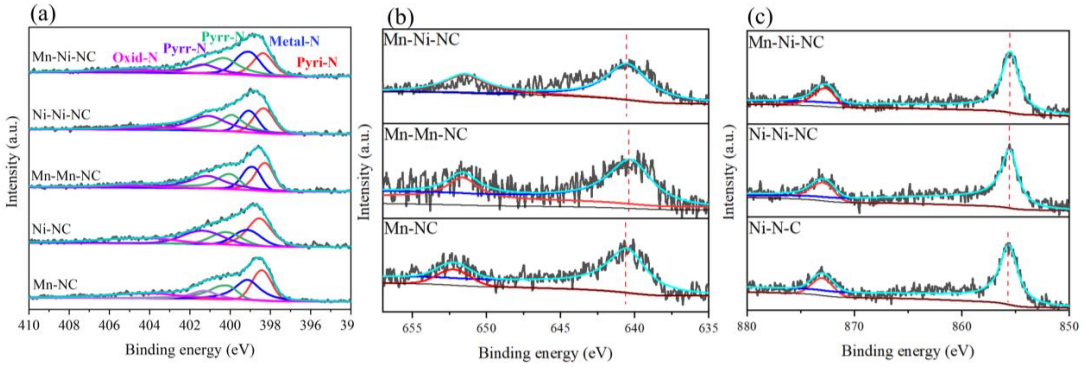

Figure 3.35. (a) High-resolution N 1s XPS spectra of Mn−NC, Ni−NC, Mn−Mn−NC, Ni−Ni−NC and Mn−Ni−NC catalysts; (b) High-resolution Mn 2p XPS spectra of Mn−Nc, Mn−Mn−NC and Mn−Ni−NC catalysts; (c) High-resolution Ni 2p XPS spectra of Ni−NC, Ni−Ni−NC and Mn−Ni−NC catalysts.

XPS was carried out to investigate the chemical species and element states of Mn, Ni, N and C in the electrocatalysts. As displayed in Figure 3.35a, the high-resolution N 1s spectra can be deconvoluted into five species: pyridinic (Pyri-N), metallic (Metal-N), pyrrolic (Pyrr-N), graphitic (Grap-N) and oxidized (Oxid-N), with corresponding binding energy of 398.3, 400.3, 401.4 and 404.5 eV, respectively [64-67]. Notably, the peak at 399.1 eV can be assigned to porphyrin-like metal-N coordination structure, which demonstrates that metal atoms are coordinated with N atoms in the carbon framework [68, 69]. In particular, the existence of Pyri-N in carbon substrates plays a significant role in anchoring and stabilizing single metal atoms as well as promoting the electrocatalytic activity [70]. The Pyri-N concentration is the lowest for the Mn−Ni−NC catalyst, while its metal-N concentration is the highest among the five electrocatalysts. On the other hand, the concentrations of Pyrr-N, Grap-N and Oxid-N did not show obvious differences (Appendix G, Table S2). The results indicate that most Mn and Ni atoms prefer to bond with Pyri-N. Moreover, the binding energy of Pyri-N in DACs shows slight downshift in comparison with that in SACs, while the binding energies of metal-N of DACs are similar. Therefore, the electronic structures of SACs and DACs are different. High resolution Mn-2p spectra in Figure 3.35b shows that the Mn-$2p_{3/2}$ peaks of Mn-NC (640.6 eV), Mn−Mn−NC (640.3 eV) and Mn−Ni−NC (640.5 eV) are located between Mn^0 (638.7 eV) and Mn^{2+} (641.4 eV) [71]. The Ni-$2p_{3/2}$ peaks of Ni-NC (855.7 eV), Ni−Ni−NC (855.6 eV) and Mn−Ni−NC (855.5 eV) are located between Ni0 (852.5 eV) and Ni^{2+} (856.0 eV) (Figure 3.35c) [72, 73]. Therefore, Mn and Ni species probably both have an oxidation state between 0 and +2. It is worth noting that the binding energies of Mn-$2p_{3/2}$ in Mn−Mn−NC and Mn−Ni−NC exhibit negative shift in comparison to the Mn−NC catalyst. Similarly, the binding energies of Ni-$2p_{3/2}$ in Ni−Ni−NC and Mn−Ni−NC also show a negative shift compared with Ni−NC. Consequently, the oxidation states of Mn and Ni atoms decreased when atom pairs are formed in DACs. Obviously, when the concentration of Metal-N decreases, less electron is donated from metal to coordinated N atoms. In particular, the binding energies of Mn-$2p_{3/2}$ and Ni-$2p_{3/2}$ in Mn−Ni−NC catalyst are more positive and

negative than that of Mn-$2p_{3/2}$ in Mn−Mn−NC, and Ni-$2p_{3/2}$ in Ni−Ni−NC, respectively. Consequently, there are apparent electron transfers between Mn and Ni in Mn−Ni−NC, in which Ni atom with higher electronegativity attracted electrons from the paired Mn atom. Therefore, XPS characterization evidenced that when atom pairs are formed, there are valence changes in the homonuclear DACs and electron transfer in the heteronuclear DAC.

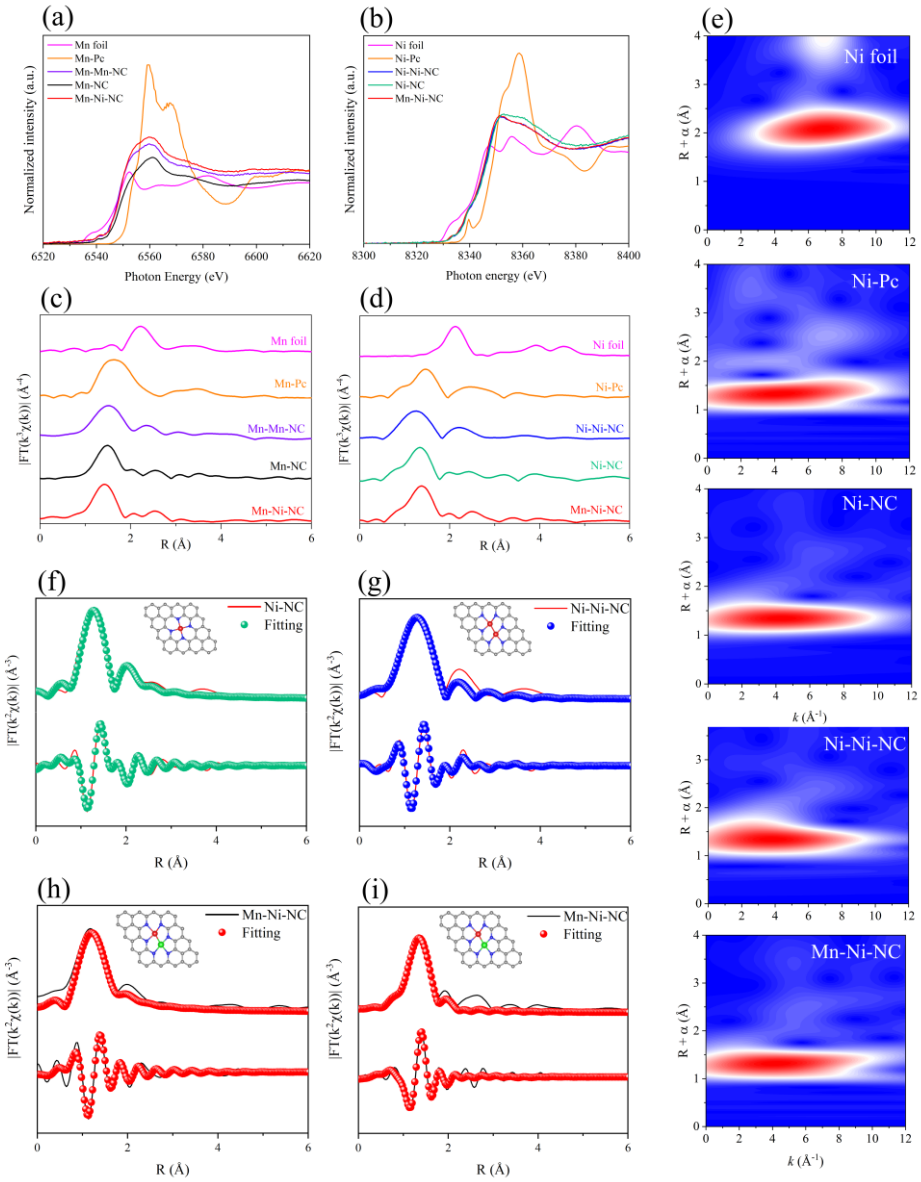

Figure 3.36. (a) Mn K-edge and (b) Ni K-edge XANES spectra of the catalysts; (c) Mn K-edge and (d) Ni K-edge Fourier transform (FT) k^3-weighted EXAFS (FT-EXAFS) spectra of the samples at R space; (e) Ni K-edge Wavelet transformed k^2-weighted EXAFS plots of Ni foil, Ni-Pc, Ni−NC, Ni−Ni−NC and Mn−Ni−NC; (f) Ni−N, (g) Ni−N, (h) Ni−N and (i) Mn−N fittings of the FT-EXAFS spectra for Ni−NC, Ni−Ni−NC, Mn−Ni−NC and Mn−Ni−NC catalysts. The gray, blue, red and green balls refer to C, N, Ni and Mn atoms, respectively.

XAS was conducted to reveal the detailed electronic structure and coordination environment of the metal active centers. Figure 3.36a and b depicted XANES of Mn and Ni atoms of different catalysts, reference Mn and Ni metal foils, and metal phthalocyanine (Mn-Pc and Ni-Pc). In the Mn K-edge XANES spectra, the near-edge absorption energies of Mn−NC, Mn−Mn−NC and Mn−Ni−NC are located between those of Mn foil and Mn-Pc, confirming that the oxidation states of Mn are between 0 and +2. Besides, the near-edge absorption energies of Mn atom in Mn−Ni−NC catalyst shows slightly positive shift compared with that of Mn−Mn−NC, indicating that the valence state of Mn atom increased. Similarly, Ni K-edge XANES spectra of Ni−NC, Ni−Ni−NC and Mn−Ni−NC are located between those of Ni foil and Ni-Pc, confirming that the valence states of Ni are also between 0 and +2. In comparison with Ni−Ni−NC, the near-edge absorption energies of Ni in Mn−Ni−NC catalyst show slight negative shift, demonstrating the decrease of the valence state of Ni. Consequently, Mn donated electrons to Ni in the heteronuclear Mn−Ni−NC DAC, in agreement with XPS analysis.

Figure 3.36c and d display the Fourier transform (FT) of k^3-weighted EXAFS of Mn and Ni K-edge in the R-space. The Mn K-edge spectra shows a major peak at around 1.5 Å, assigned to the Mn-N coordination in the Mn−NC, Mn−Mn−NC and Mn−Ni−NC catalysts. A dominant peak at around 1.3 Å for the Ni K-edge spectra of Ni−NC, Ni−Ni−NC and Mn−Ni−NC catalysts is associated with the Ni−N bonding. The Mn−Mn (2.3 Å) and Ni−Ni (2.1 Å) bonds are characteristic of Mn and Ni foils. However, the metal-metal bonds are absent in the Mn−NC and Ni−NC catalysts, which confirms atomically dispersed Ni and Mn atoms. Remarkably, peaks at 2.3 and 2.5 Å in the Mn K-edge spectra can be identified for the Mn−Mn−NC and Mn−Ni−NC catalysts, which can be assigned to Mn−Mn and Mn−Ni coordination, respectively. Similarly, peaks at 2.2 Å and 2.5 Å in the Ni K-edge spectra of Ni−Ni−NC and Mn−Ni−NC catalysts are attributed to Ni−Ni and Mn−Ni coordination. Therefore, the FT-EXAFS analysis demonstrated the formation of atom pairs for all three DACs.

Wavelet transform (WT) EXAFS (WT-EXAFS) oscillations was also conducted to discriminate the backscattering atoms and obtain high resolutions in both K and R

spaces. As displayed in Appendix G, Figure S8, the WT-EXAFS contour plot of Mn foil shows a strong signal with maximum intensity at around 5.1 $Å^{-1}$ of the Mn−Mn contributions. However, this signal is absent for the Mn−NC and Mn−Ni−NC catalysts but is slightly visible at around 7.5 $Å^{-1}$ for the Mn−Mn−NC catalyst. Similarly, WT-EXAFS of Ni foil shows a prominent feature centered around 7.0 $Å^{-1}$, which is not found for the Ni−NC and Mn−Ni−NC catalysts but visible at 6.8 $Å^{-1}$ for the Ni−Ni−NC catalyst. Similar to the WT-EXAFS contour plots of Mn-Pc, the spectra of Mn−NC, Mn−Mn−NC, Mn−Ni−NC also show strong features at 4.8 $Å^{-1}$, which can be attributed to the Mn−N coordination. Meanwhile, a weak signal at 6.0 $Å^{-1}$ can be observed for the Mn−Ni−NC catalyst, indicating the Mn−Ni coordination. For the Ni WT-EXAFS contour plots of Ni−NC, Ni−Ni−NC and Mn−Ni−NC electrocatalysts, a maximum intensity at 4.0 $Å^{-1}$ due to the Ni−N contribution can be observed (Figure 3.36e). A weak feature at 6.1 $Å^{-1}$ is also attributed to the Mn−Ni bonding. It is worth noting that the different models of atomic vibration could cause the difference of signal intensity [74]. The WT-EXAFS analysis demonstrated that Mn and Ni atoms dispersed atomically on the N doped carbon substrate, and the existence of Mn−Mn, Ni−Ni and Mn−Ni bonding for the DACs.

To elaborate the structures of the catalysts, theoretically optimized metal-N configurations based on DFT calculations and fitted-EXAFS curves were constructed. As show in Figure 3.36f-i and S8ab, the fitted results in R-space and K-space match well with the experimental spectra. The detailed fitting parameters, e.g., metal-N coordination numbers, metal-N path length are summarized in Appendix G, Table S3. The average metal-N coordination numbers are 4, 4, 3.5, 3.5 and 3.5 for Mn−NC, Ni−NC, Mn−Mn−NC and Ni−Ni−NC and Mn−Ni−NC catalysts, suggesting that Mn and Ni SACs have the usual metal-N_4 center, while the DACs exhibit metal-N_3 configurations. The fitting parameters for Ni−Ni, Mn−Mn and Mn−Ni interaction paths indicate that the average coordination number of metal-metal is one in the DAC catalysts (Appendix G, Figure S9c-e). More importantly, the average bond lengths of Mn−Mn, Ni−Ni and Mn−Ni are 2.40, 2.35 and 2.40 Å, consistent with HAADF-STEM

results. Therefore, non-bridged $(Mn-Mn)N_6$, $(Ni-Ni)N_6$ and $(Mn-Ni)N_6$ embedded carbon framework were successfully synthesized for DACs, as evidenced by the combination of EXAFS spectra, fitted curves and DFT calculations.

3.6.2. Electrocatalytic activity test

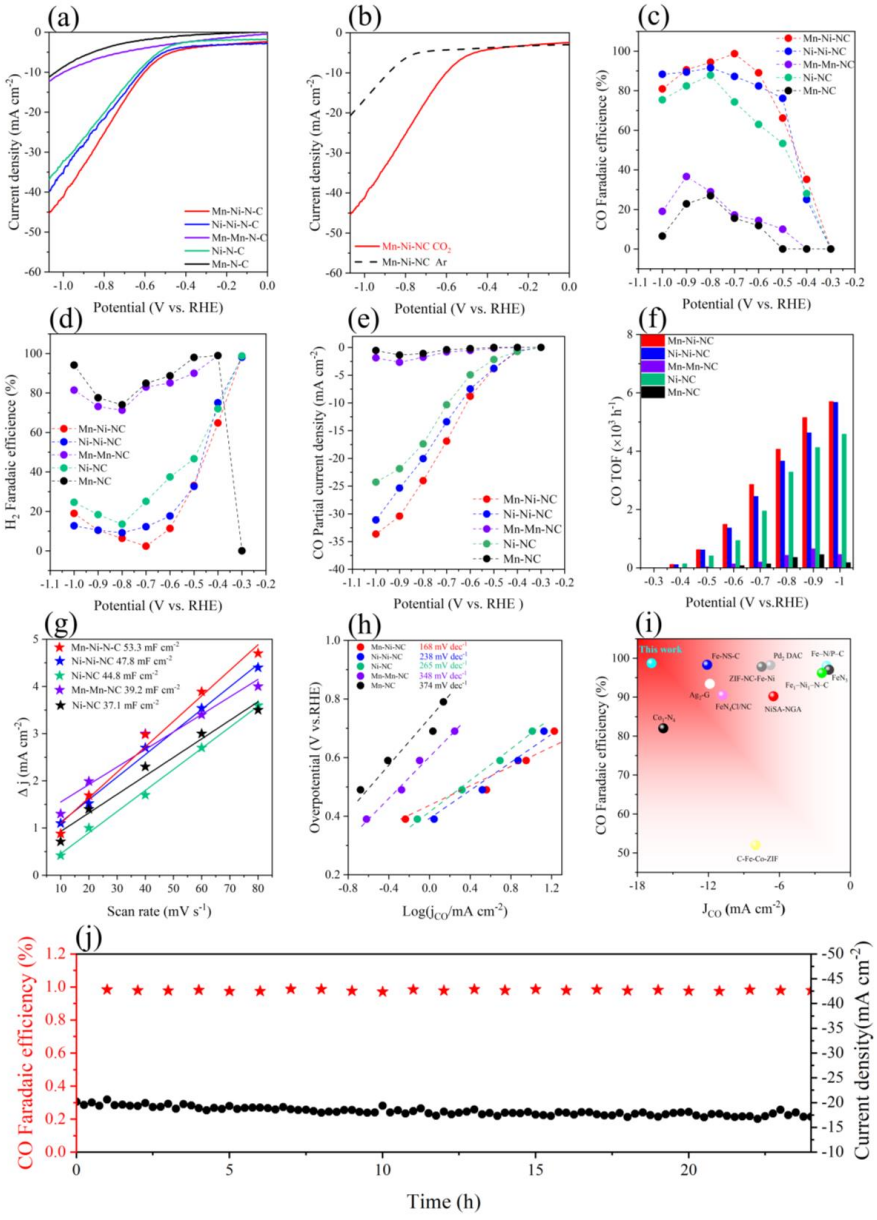

Figure 3.37**.** ECR to CO activity of different catalysts. (a) LSV curves of the catalysts obtained in CO_2-saturated 0.5 M $KHCO_3$ electrolyte at the scan rate of 10 mV s^{-1}; (b) LSV curves of the Mn−Ni−NC catalyst in Ar- and CO_2-saturated electrolyte; (c) Faradaic efficiency for CO; (d) Faradaic efficiency for H_2; (e) Partial current densities of CO and (f) TOF for different catalysts at different applied potentials; (g) Charge current density difference against scan rates of Mn−NC, Ni−NC, Mn−Mn−NC, Ni−Ni−NC and Mn−Ni−NC catalysts; (h) Tafel plots for the CO partial current density; (i) Comparison of Faradaic efficiency and current density on reported SACs and DACs in H-cell; (j) Stability test for Mn−Ni−NC at −0.7 V (vs. RHE) with 24 hours continuous electrocatalytic reaction.

As illustrated in Figure 3.37a, the Mn−Ni−NC electrocatalyst exhibits the largest current density at all applied potentials. It also exhibits an enhanced current response and a lower onset potential under CO_2 atmosphere than under Ar (Figure 3.37b), indicating the occurrence of ECR. The potentiostatic electrolysis was conducted under different potentials from −0.3 to −1.0 V versus reversible hydrogen electrode (vs. RHE). As displayed in Figure 3.37c, ECR to CO on Mn−Ni−NC, Ni−Ni−NC, Ni−NC catalysts occurred under −0.4 V (vs. RHE), showing the lower onset potential for ECR to CO. With the increase of the applied potential, the Mn−Ni−NC catalyst reaches the maximum FE_{CO} of 98.7% at the potential of −0.7 V (vs. RHE). Besides, FE_{CO} is higher than 90% between −0.5 and −0.9 V (vs. RHE), exhibiting wide potential windows. The Ni−Ni−NC and Ni−NC catalysts present the highest FE_{CO} of 91.6% and 87.8% at the potential of −0.8 V (vs. RHE).

The Ni−Ni−NC shows slower decay of FE_{CO} than the Ni−NC catalyst with the increase of potential, also implying a wide potential window for highly efficient ECR to CO. It has been reported that the formation of *COOH on Ni site is difficult due to a large energy barrier [75, 76]. Therefore, the enhanced ECR performance on Ni−Ni−NC could be attributed to the decrease of energy barrier for the formation of *COOH on Ni−Ni dual sites. The Mn−Mn−NC and Mn−NC catalysts exhibit low FE_{CO} at all applied potentials. Even though forming Mn−Mn atom pairs also improved the ECR performance of Mn−NC, the FE_{CO} of Mn−Mn−NC is still less than 40%. This can be explained by the strong adsorption of *CO on Mn site. The improvement of ECR performance on Mn−Mn−NC demonstrates that Mn−Mn site may moderate *CO adsorption to some certain extent. Nevertheless, the competing hydrogen evolution reaction on Mn and Mn−Mn−NC catalyst is dominating, as shown in Figure 3.37d. Remarkably, the ECR performance to CO on Mn−Ni DAC is greatly improved compared to the Mn and Ni SACs, implying that forming heteronuclear atom pairs could facilitate either *COOH formation or *CO desorption. This could be further ascribed to the moderate binding energies for intermediates due to the electron interaction between the heteronuclear atoms. For the Mn−Ni−NC catalysts, only CO

and H_2 products were identified as the products at all applied potentials, with a total FE_{CO} of around 100%. No liquid products were detected, as evidenced by ^1H NMR (Appendix G, Figure S10).

The CO partial current densities on the five catalysts were also calculated (Figure 3.37e). For the Mn−Ni−NC catalyst, it increased with the applied potential, reaching 16.8 mA cm^{-2} at −0.7 V (vs. RHE), which is 1.31, 1.62, 21.3 and 42.2 times higher than that of Ni−Ni−NC, Ni−NC, Mn−Mn−NC and Mn−NC catalysts. The turnover frequency (TOF) of the five catalysts was calculated to uncover the intrinsic activity of the active site [77]. As illustrated in Figure 3.37f, the TOF on the Mn−Ni−NC catalyst is the highest at 2859 h^{-1} at −0.7 V (vs. RHE), indicating its high intrinsic activity.

Electrochemical active surface areas (ECSA) play a significant role in ECR activity, which is calculated by measuring double layer (D-L) capacitance (Figure 3.37g and Appendix G, Figure S11). The Mn−Ni−NC catalyst has a capacitance of 53.3 mF cm^{-2}, slightly higher than the other catalysts. As a result, the ECSA for Mn−Ni−NC, Ni−Ni−NC, Ni−NC, Mn−Mn−NC and Mn−NC catalysts were 1332, 1195, 1120 and 980, 927 cm^2_{ECSA}, demonstrating that the Mn-Ni atoms pair could increase the ESCA. Furthermore, the Tafel slopes on the five samples were compared to disclose the kinetics for CO generation (Figure 3.37h). An improved Tafel slope of 168 mV dec^{-1} for CO generation on the Mn−Ni−NC catalyst is obtained, attributed to the synergistic effect of Mn−Ni pair. Additionally, the small Tafel slope also indicates that the rate-limiting step of ECR to CO on the Mn−Ni−NC catalyst is the first protonation of CO_2 [78, 79]. Overall, the DAC catalysts show lower Tafel slope than their SAC counterparts. Dual atom pairs especially with heteronuclear atoms, could effectively reduce the Tafel slope, which contributes to a more kinetically favorable ECR to CO. Electrochemical impedance spectroscopy (EIS) indicated that Mn−Ni−NC catalyst has the smallest charge-transfer resistance among the five catalysts (Appendix G, Figure S12), implying fastest charge transfer. Therefore, the heteroatomic pairs could act synergistically, which outperforms homoatomic pairs and SACs in ECR to CO. The Mn−Ni−NC catalyst in this study outperformed most of the recently reported SACs and

DACs applied for ECR to CO (Figure 3.37i and Appendix G, Table S4). Finally, continuous potentionstatic activity test for 24 h demonstrated that the Mn−Ni−NC catalyst exhibited stable current density and FE_{CO} with negligible decay under the potential of −0.7 V (vs. RHE) (Figure 3.37j).

3.6.3. DFT simulation

To uncover the activity origin, DFT calculations were employed based on the EXAFS fitting results. The distribution of electron density on N and coordinated metal atoms of catalysts are correlated with intrinsic activity and ECR selectivity [80]. After forming Mn−Mn, Ni−Ni and Mn−Ni atom pairs, the electron density around the N, Mn and Ni atom exhibit apparent changes (Appendix G, Figure S13). For instance, more electrons accumulated around the metal atoms of homonuclear atom pair. Charge transfer between Mn and Ni atoms can also be observed, indicating electron interactions after forming atom pairs. Moreover, Bader charge analysis demonstrated that the Mn and Ni atoms always act as electron-donor in the single atom center, homonuclear atom pair and heteronuclear atom pair. The amount of the lost electrons for Mn atom decreased first and then increased, while it always decreased for Ni atom (Figure 3.38a). This opposite trend for Mn and Ni atom in the change from homonuclear to heteronuclear pair discloses electron transfer from Mn to Ni atom, which vividly show the electron interaction between Mn and Ni atom. Therefore, the valence state of Mn and Ni atoms show increase and decrease, consistent with XPS and XANES analysis. Consequently, building dual-atom pair can regulate electron density of the active sites in different ways, which directly affects the binding strength of intermediates with active sites.

ECR to CO consists of three steps, i.e., the formation of *COOH, *CO generation, and the desorption of CO. The Gibbs free energy diagrams of each step at U = 0 V (vs. RHE) were calculated in Figure 3.38b. As expected, Mn and Ni SACs exhibits high energy barrier for *COOH production (1.83 eV) or *CO desorption (0.75 eV), resulting from the binding strength between intermediate and metal site. After forming homonuclear atom pair, the energy barrier for *COOH generation on the Ni−Ni−NC catalyst decreased greatly to 0.70 eV. For the Mn−Mn−NC DAC, although the free

energy barrier for the formation of *COOH decreased, the desorption of *CO deteriorated remarkably with an energy barrier of 1.88 eV. These changes can be explained by the coordination effect of the dual metal atoms. For the SACs, only one C−metal bond will form for *COOH generation. However, when the dual atom pairs are formed, the C atom of intermediates could bond with two metal atoms with two C−metal bonds. Consequently, the binding strength of intermediates to active sites increased. Notably, as the *COOH formation on Mn−Mn site is energy favorable, the rate-limiting step will become *CO desorption from Mn−Mn site, which is controlled by the thermodynamic process. Thus, Mn−Mn sites are potentially passivated by strongly adsorbed *CO, in agreement with other studies [77, 81]. An additional active site could be possible for CO_2 activation on CO-adsorbed Mn-Mn site (CO*Mn−Mn−NC). The free energy barrier of CO desorption on the site decreased remarkably (0.54 eV), which promotes *CO desorption from the Mn site. The results proved that the ECR performance is improved after incorporating the second homonuclear atom into SACs, in line with experimental observations. For the Mn−Ni−NC catalyst, the energy barrier for *COOH formation on Ni and Mn sites are 0.40 and 0.51 eV, lower than of Mn, Ni, CO*Mn−Mn, and Ni−Ni catalysts. However, the free energy barrier for *CO desorption from Ni site is only 0.39 eV, much lower than that of Mn site (0.85 eV). Although DACs may offer potential active sites for C-C coupling, it is not considered in this study because of difficult kinetics.

As depicted in Figure 3.38c, the free energy change for *COOH formation and *CO desorption was built to reveal the scaling relationship of intermediates. Unexpectedly, the scaling relationship of binding strength of intermediates on Mn−Ni DAC was broken. This can be explained by that C atom of *CO prefer to bond with Ni atom on Ni site, while the C atom of *CO will bond with both Mn and Ni atom on Mn site. In other word, during ECR to CO, the Mn atom can bind the intermediates selectively. For the CO_2 protonation, Mn and Ni atoms act together to accelerate the *COOH formation, which is not possible in Mn and Ni SACs. For the *CO desorption, Mn atom will not bond with *CO, which promotes the CO generation (Figure 3.38d). However, this

cannot be observed in Mn and Ni homonuclear DACs (Appendix G, Figure S14). Therefore, Mn−Ni−NC catalysts with the lowest energy barriers for both *COOH formation and *CO desorption, due to the synergistic effect of Mn and Ni atoms, which can selectively interact with intermediates. As a result, the restriction of scaling relationship on binding strength of intermediates was broken on the Mn−Ni−NC catalyst, resulting in the superior performance of ECR to CO.

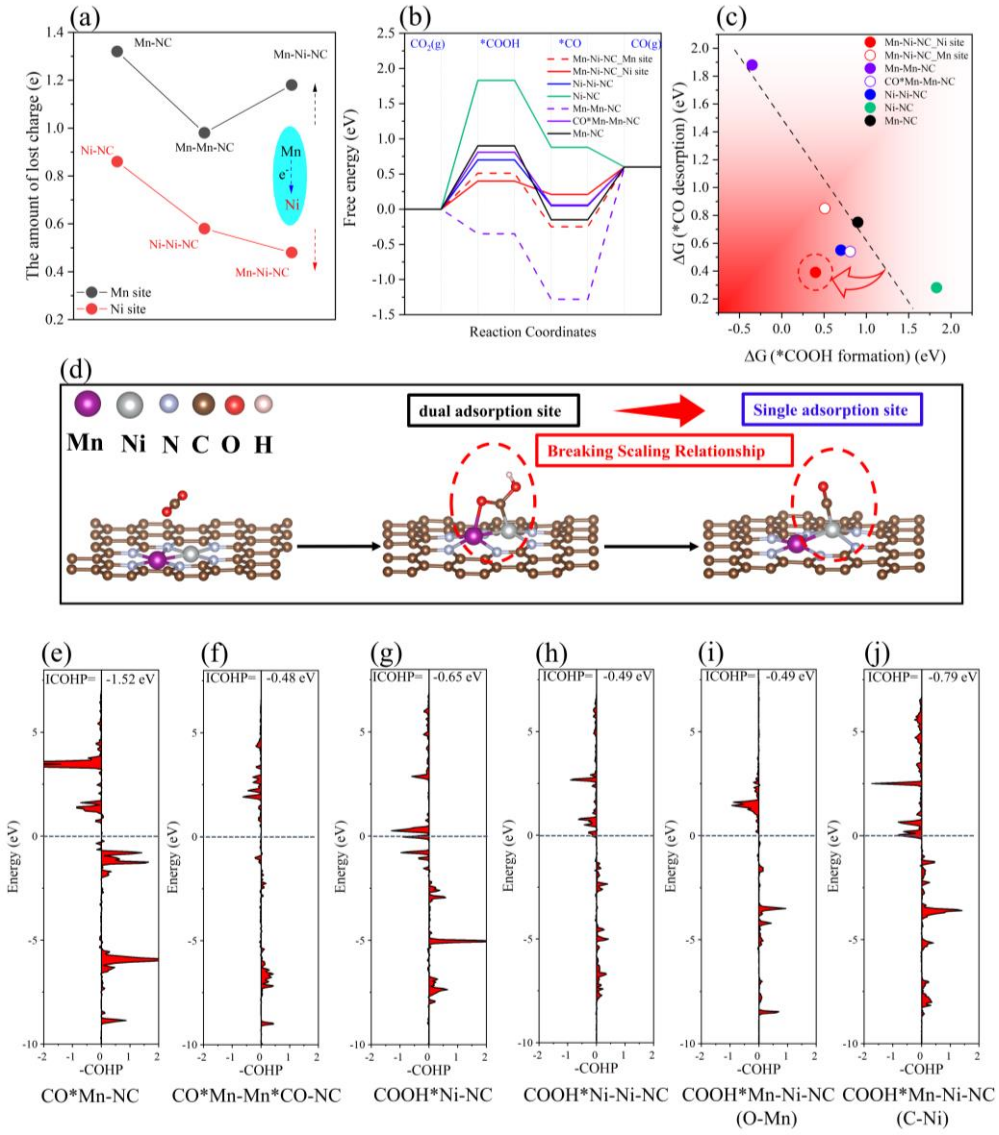

Figure 3.38. (a) Electron transfer between Mn and Ni atoms on different catalysts; (b) Gibbs free energy change diagram for ECR to CO on different catalysts; (c) Scaling relationship between *COOH and *CO; (d) The activity mechanism of ECR to CO on Mn−Ni−NC; The COHP distribution of (e) CO*Mn−NC, (f) the second CO adsorbed on CO passivated Mn−Mn−N, (g) COOH*Ni−NC, (h) COOH*Ni−Ni−NC, (i) COOH*Mn−Ni−NC (O bonded Mn); (j) COOH*Mn−Ni−NC (C bonded Ni), where Fermi level is set to zero.

As HER is the main competing reaction, the free energy changes of HER on the five catalysts were also calculated. As illustrated in Appendix G, Figure S15a, Ni−NC shows the largest energy barrier of 1.40 eV for *H generation, while both Ni−Ni−NC and Mn−Ni−NC shows an energy barrier of around 0.12 eV. Therefore, an excellent *H generation performance possibly boosts proton transfer, accelerating the ECR to CO process. The selectivity of ECR to CO against HER is evaluated by calculating the difference of limiting potentials between ECR and HER ($U_L(CO_2) - U_L(H_2)$), where a more positive value of $U_L(CO_2) - U_L(H_2)$ indicates higher ECR selectivity to CO. As depicted in Appendix G, Figure S15b, Mn−Mn−NC and Ni−Ni−NC show more positive values of $U_L(CO_2) - U_L(H_2)$ than their SACs counterparts, confirming that DACs have higher ECR selectivity. Heteronuclear Mn−Ni−NC presents the most positive $U_L(CO_2) - U_L(H_2)$ of −0.29 eV, demonstrating its superior ECR selectivity to CO by suppressing HER reaction.

To disclose the effects of electron structure on adsorption performance of intermediates, the crystal orbital Hamilton population (COHP) and integrated COHP (ICOHP) were employed to further study the interaction strength between active site and intermediates, in which a positive −COHP indicates bonding state, while a negative −COHP represents the anti-bonding state below Fermi energy. As shown in Figure 3.38e and f, more noticeable anti-bonding state appears in CO passivated Mn−Mn−NC catalyst (CO*Mn−Mn−NC) in comparison with Mn−NC, demonstrating weak CO adsorption on the CO*Mn−Mn−NC catalyst. This is also confirmed by the larger ICOHP (-0.48 eV) of CO passivated Mn-Mn-NC catalyst. *COOH cannot adsorb stably on single Ni sites due to the existence of anti-bonding states (Figure 3.38g). After introducing the second Ni atom, the anti-bonding states almost disappear, implying an improvement of binding strength between Ni and *COOH (Figure 3.38h). Despite that the ICOHP of C-Ni over Ni-NC is larger that of C-Ni over Ni-Ni-NC, C will bond with two Ni atoms, which increase the binding strength compared with single Ni atom. Finally, we compared the adsorption strength of C and O atoms of *COOH to Ni and Mn atom of the Mn−Ni−NC catalyst (Figure 3.38i and j). Remarkedly, both C and O atoms could

bind with Ni and Mn atom strongly, as demonstrated by the absence of anti-bonding states. Therefore, *COOH generation was enhanced greatly, which endows Mn−Ni−NC with excellent ECR activity. Overall, it can be concluded that Mn atom donated more electron in Mn−Ni than the Mn−Mn atom pairs, causing higher valence state of Mn and stronger *CO binding strength. However, the valence state of Ni atom decreased in Mn-Ni compared with the Ni−Ni center, resulting in superior *COOH binding strength. Consequently, electron interaction between Mn and Ni atom in Mn−Ni−NC catalyst result in moderate and low valence state for Mn and Ni atom respectively, which directly influenced the binding strength of intermediate. Meanwhile, the selective adsorption of intermediates on active center contribute to breaking the scaling relationship, which greatly improve the performance of ECR to CO.

4. Concluding remarks

This study focused on the rational design and preparation of high-performance catalysts for ECR based on theoretical calculations and experimental work. Catalysts including metal NPs, metal single-atom, dual-atom catalysts were synthesized and investigated the performance for CO_2 reduction.

Ag NPs loaded on B-decorated g-C_3N_4 was chosen as the nanocomposite electrocatalyst system for ECR study. DFT calculations showed that the Ag-B-g-C_3N_4 catalyst could remarkably decrease the adsorption free energy for *COOH generation. Besides, electron accumulation at the Ag-B-g-C_3N_4 interface could improve electrical conductivity and promote electron transport. The simulation results suggested that the introduction of B atoms and Ag NPs could improve the ECR performance of g-C_3N_4 effectively. Experimentally, the Ag-B-g-C_3N_4 catalyst with an average diameter of 4.95 nm exhibited CO Faradaic efficiency of 93.2% at the potential of −0.8 V (vs RHE) with a total current density of −2.08 mA cm^{-2}. Moreover, the FE_{CO} and current density were maintained without obvious decay for an electrocatalysis of 12 h, demonstrating excellent stability.

Single atoms catalysts (SACs) have attracted huge attention due to maximum atom utilization and excellent performance in various catalytic reactions. Especially, 2D MXenes have also been demonstrated to be promising substrates for anchoring single transition metal atoms in catalytic reactions. We investigated the single transition metal atoms (V, Cr, Mn, Fe, Co, Ni) embedded O group terminated Nb_2N monolayer (Nb_2NO_2) as ECR catalysts by first-principles calculation. It is found that Nb_2NO_2 can be an ideal support for anchoring sing TM atoms because of excellent stability and conductivity. TM@Nb_2NO_2 show excellent CO_2 adsorption capacity, which benefits CO_2 activation. V, Cr and Ni@ Nb_2NO_2 are identified as efficient electrocatalysts for ECR to CH_4.

2D antimonene from VA group have been studied as support for single transition metal atoms (TM = Sc, Ti, V, Cr, Mn, Fe, Co, Ni, Cu, Zn, Mo, Ru, Rh, Pd, Ag, Cd, Ir, Pt and Au) atoms in ECR by first-principles calculation. It is found that non-precious TM

atoms (Sc, V, Cr, Mn, Fe, Co, Zn) supported on Sb monolayer show higher ECR selectivity than HER. Moreover, the primary ECR product of these non-precious metal-based SACs is CH_4, except for Zn which produces HCOOH. The interaction between TM atom and Sb monolayer greatly affects the intrinsic activity of SACs. Meanwhile, the interaction between TM atoms and intermediates of the potential determining steps (PDS) will determine the overpotential and final products of ECR.

We developed a facile method for the synthesis of nonmetal atoms modified SAC. The prepared S doped Ni−N−C catalyst can selectively reduce CO_2 to CO with high a FE(CO) of over 90 % in a broad potential range of −0.60 to −1.10 V (vs. RHE). The maximum FE(CO) reaches 99.7 % at −0.80 V (vs. RHE) with a total current density of 20.5 mA cm^{-2}. ECR activity test demonstrated that Ni atoms served as active sites for ECR to CO, whereas S atoms could increase its activity further. Moreover, theoretical calculations disclosed that doping S atoms could decrease and increase the free energy barrier for the formation of *COOH and *H, respectively. Therefore, the excellent ECR performance of the Ni−NS−C catalyst can be attributed to the synergistic effect of the $Ni-N_X$ moiety and S dopant.

Tuning the coordination environment has been considered as a powerful strategy to improve the ECR performance for M−N−C based SACs. However, most studies could only reveal inadequate structural details of metal centers and NM ligands. Therefore, a series of NM (B, O, F, Si, P, S, Cl, As, Se and Br) heteroatom dopants modified TM (Fe, CO, Ni, Cu and Zn)@N_4 configurations embedded on graphene sheet are proposed. We performed a computational screening of the ECR to CO activity and stability of the NM decorated TM@N_4. We found that NM atoms could effectively improve the ECR activity to CO on Ni and Cu@N_4 but deteriorate the ECR activity on Co@N_4. However, NM dopants could not break linear relationship between key intermediates for the catalysts.

Constructing heteronuclear dimer sites to form dual-atom catalysts is another efficient way to modify the coordination environment and the electronic properties of the SAC

active centers. Therefore, we synthesized Mn and Ni SACs, Mn and Ni homonuclear DACs, and Mn−Ni heteronuclear DAC via a facile adsorption and pyrolysis treatment. XPS and XANES revealed that Mn donated electrons to Ni atom in Mn−Ni DAC. As a result, Mn−Ni DAC displayed the highest CO Faradaic efficiency of 98.7% at −0.7 V versus reversible hydrogen electrode (vs. RHE) with CO partial current density of 16.8 mA cm^{-2} and excellent stability. First-principles calculation disclosed that high valence state of Mn atom and low valence state of Ni atom could deteriorate *CO desorption and enhance *COOH binding strength. Moreover, the active sites of Mn−Ni−NC could facilitate CO_2 protonation by enhanced *COOH adsorption because C and O atom of *COOH prefer to bind Ni and Mn atoms, respectively. During the *CO desorption process, only Ni atom bonds with C atom of *CO, promoting *CO desorption. Therefore, the scaling relationship between binding strength of intermediates was broken, resulting in superior performance for the Mn−Ni−NC catalyst in ECR to CO.

References

[1] Lu, S.; Li, C.; Li, H. H.; Zhao, Y. F.; Gong, Y. Y.; Niu, L. Y.; Liu, X. J.; Wang, T. The effects of nonmetal dopants on the electronic, optical and chemical performances of monolayer g-C_3N_4 by first-principles study. *Appl. Surf. Sci*. **2017**, *392*, 966-974.

[2] Wei, B.; Wang, W.; Sun, J.; Mei, Q.; An, Z.; Cao, H.; Han, D.; Xie, J.; Zhan, J.; He, M. Insight into the effect of boron doping on electronic structure, photocatalytic and adsorption performance of g-C_3N_4 by first-principles study. *Appl. Surf. Sci*. **2020**, 511, 145549.

[3] Thaweesak, S.; Lyu, M.; Peerakiatkhajohn, P.; Butburee, T.; Luo, B.; Chen, H.; Wang, L. Two-dimensional g-C_3N_4/$Ca_2Nb_2TaO_{10}$ nanosheet composites for efficient visible light photocatalytic hydrogen evolution. *Appl. Catal. B: Environ*. **2017**, *202*, 184-190.

[4] Thorat, N.; Yadav, A.; Yadav, M.; Gupta, S.; Varma, R.; Pillai, S.; Fernandes, R.; Patel, M.; Patel, N. Ag loaded B-doped-g-C_3N_4 nanosheet with efficient properties for photocatalysis. *J. Environ. Manage* **2019**, *247*, 57-66.

[5] Hong, J.; Xia, X.; Wang, Y.; Xu, R. Mesoporous carbon nitride with in situ sulfur doping for enhanced photocatalytic hydrogen evolution from water under visible light. *J. Mater. Chem*. **2012**, *22*, 15006-15012.

[6] Caux, M.; Fina, F.; Irvine, J. T. S.; Idriss, H.; Howe, R. Impact of the annealing temperature on Pt/g-C_3N_4 structure, activity and selectivity between photodegradation and water splitting. *Catal. Today* **2017**, *287*, 182-188.

[7] Zhang, S.; Mo, Z.; Wang, J.; Liu, H.; Liu, P.; Hu, D.; Tan, T.; Wang, C. Ultra-stable oxygen species in Ag nanoparticles anchored on g-C_3N_4 for enhanced electrochemical reduction of CO_2. *Electrochim. Acta* **2021**, *390*, 138831.

[8] Wang, Y.; Tian, W.; Zhang, H.; Wang, Y. Nb_2N monolayer as a promising anode material for Li/Na/K/Ca-ion batteries: a DFT calculation. *Phys. Chem. Chem. Phys*. **2021**, *23*, 12288-12295.

[9] Zheng, S.S.; Zuo, C.J.; Liang, X.H.; Li, S.N.; Pan, F. Valence state of transition metal center as an activity descriptor for CO_2 reduction on single atom catalysts. *J.*

Energy Chem. **2021**, *56*, 444-448.

[10] Li, F.F.; Ai, H.Q.; Shi, C.M. Lo, K.H. Pan, H. Single transition metal atom catalysts on Ti_2CN_2 for efficient CO_2 reduction reaction. *Int. J. Hydrog. Energy* **2021**, *46*, 12886-12896.

[11] Ao, C.; Feng, B.; Qian, S.; Wang, L.; Zhao, W.; Zhai, Y.; Zhang, L. Theoretical study of transition metals supported on g-C_3N_4 as electrochemical catalysts for CO_2 reduction to CH_3OH and CH_4. *J. CO_2 Util.* **2020**, *36*, 116-123.

[12] Guo, C.; Zhang, T.; Deng, X.; Liang, X.; Guo, W.; Lu, X.; Wu, C.M.L. Electrochemical CO_2 Reduction to C1 Products on Single Nickel/Cobalt/Iron-Doped Graphitic Carbon Nitride: A DFT Study. *ChemSusChem* **2019**, *12*, 5126-5132.

[13] Lu, S.; Huynh, H.L.; Lou, F.L.; Guo, M.; Yu, Z.X. Electrochemical reduction of CO_2 to CH_4 over transition metal atom embedded antimonene: first-principles study. *J. CO_2 Util.* **2021**, *51*, 101645.

[14] Kour, G.; Mao, X.; Du, A.J. Computational screening of transition metal-phthalocyanines for the electrochemical reduction of carbon dioxide. *J. Phys. Chem. C* **2020**, *124*, 7708-7715.

[15] Li, L.; Wang, X.; Guo, H.; Yao, G.; Chen, L. Theoretical screening of single transition metal atoms embedded in MXene defects as superior electrocatalyst of nitrogen reduction reaction. *Small Methods* **2019**, *3*, 1900337.

[16] Aghdasi, P.; Ansari, R. Structural and mechanical properties of Sb and Sb_X (X = H, F, Cl and Br) monolayers. *Solid State Commun.* **2020**, *311*, 113849.

[17] Aghdsi, P.; Yousefi, S.; Ansari, R. Structural and mechanical properties of antimonene monolayers doped with transition metals: a DFT-based study. *J. Mol. Model.* **2021**, *15*, 27.

[18] Xu, Z.W.; Song, R.F.; Wang, M.Y.; Zhang, X.Z.; Liu, G.W.; Qiao, G.J. Single atom-doped arsenene as electrocatalyst for reducing nitrogen to ammonia: a DFT study. *Phys. Chem. Chem. Phys*. **2020**, *22*, 26223-26230.

[19] El-Barbary, A.A.; Telling, R.H.; Ewels, C.P.; Heggie, M.I.; Briddon, P.R. Structure and energetics of the vacancy in graphite. *Phys. Rev. B* **2003**, *68*, 144107.

[20] Oakes, L.; Carter, R.; Pint, C.L. Nanoscale defect engineering of lithium–sulfur battery composite cathodes for improved performance. *Nanoscale* **2016**, *8*, 19368-19375.

[21] Zhou, Q.X.; Ju, W.W.; Yong, Y.L.; Li. X.H. Electronic and magnetic properties of 3d transition-metal atom adsorbed vacancy-defected arsenene: A first-principles study. *J. Magn. Magn. Mater.* **2019**, *491*, 165613.

[22] Freysoldt, C.; Grabowski, B.; Hickel, T.; Neugebauer, J.; Kresse, G.; Janotti, A.; Walle, C.G.V.D. First-principles calculations for point defects in solids. *Rev. Mod. Phys.* **2014**, *86*, 253-305.

[23] Nørskov, J.K.; Bligaard, T.; Logadottir, A.; Kitchin, J.R.; Chen, J.G.; Pandelov, S.; Stimming, U. Trends in the exchange current for hydrogen evolution. *J. Electrochem. Soc.* **2005**, *152*, J23-J26.

[24] Singh, D.; Gupta, S.K.; Sonvane, Y.; Lukacevic, I. Antimonene: a monolayer material for ultraviolet optical nanodevices. *J. Mater. Chem. C* **2016**, *4*, 6386-6390.

[25] Üzengi Aktürk, O.; Ongun Özçelik, V.; Ciraci, S. Single-layer crystalline phases of antimony: antimonenes. *Phys. Rev. B: Condens. Matter Mater. Phys.* **2015**, *91*, 235446.

[26] Cui, X.D.; An, W.; Liu, X.Y.; Wang, H.; Men, Y.; Wang, J.G. C_2N-graphene supported single-atom catalysts for CO_2 electrochemical reduction reaction: mechanistic insight and catalyst screening. *Nanoscale* **2018**, 10, 15262-15272.

[27] Kim, S.K.; Zhang, Y.J.; Bergstrom, H.; Michalsky, R.; Pretrson, A. Understanding the low-overpotential production of CH_4 from CO_2 on Mo_2C catalysts. *ACS Catal.* **2016**, *6*, 2003-2013.

[28] Dong, H.L.; Li, Y.Y.; Jiang, D.E. First-principles insight into electrocatalytic reduction of CO_2 to CH_4 on a copper nanoparticle. *J. Phys. Chem. C* **2018**, *122*, 11392-11398.

[29] Liu, J.H.; Yang, L.M.; Ganz, E. Efficient electrocatalytic reduction of carbon dioxide by metal-doped β_{12}-borophene monolayers. *RSC Adv.* **2019**, *9*, 27710-27719.

[30] Pyykkö, P.; Atsumi, M. Molecular single-bond covalent radii for elements 1-118.

Chem. Eur. J. **2009**, *15,* 186-197.

[31] Ito, Y.; Cong, W.; Fujita, T.; Tang, Z.; Chen, M. High catalytic activity of nitrogen and sulfur co-doped nanoporous graphene in the hydrogen evolution reaction. *Angew. Chem. Int. Ed.* **2015**, *54*, 2131-2136.

[32] Zheng, Y.; Jiao, Y.; Li, L.H.; Xing, T.; Chen, Y.; Jaroniec, M.; Qiao, S.Z. Toward design of synergistically active carbon-based catalysts for electrocatalytic hydrogen evolution. *ACS Nano*, **2014**, *8*, 5290-5296.

[33] Ferrari, A.C.; Basko, D.M. Raman spectroscopy as a versatile tool for studying the properties of graphene. *Nat Nanotechnol* **2013**, *8*, 235-246.

[34] Endo, M.; Kim, C.; Karaki, T.; Tamaki, T.; Nishimura, Y.; Matthews, M.J.; Brown, S.D.M.; Dresselhaus, M.S. Structural analysis of the B-doped mesophase pitch-based graphite fibers by Raman spectroscopy. *Phys. Rev. B* 1**998**, *58*, 8991.

[35] Gao, H.; Liu, Z.; Song, L.; Guo, W.; Gao, W.; Ci, L.; Rao, A.; Quan, W.; Vajtai, R.; Ajayan, P.M. Synthesis of S-doped graphene by liquid precursor. *Nanotechnology* **2012**, *23*, 275605.

[36] Kim, Y.A.; Fujisawa, K.; Muramatsu, H.; Hayashi, T.; Endo, M.; Fujimori, T.; Kaneko, K.; Terrones, M.; Behrends, J.; Eckmann, A.; Casiraghi, C.; Novoselov, K.S.; Saito, R.; Dresselhaus, M.S. Raman spectroscopy of boron-doped single-layer graphene. *ACS Nano* **2012**, *6*, 6293-6300.

[37] Qu, K.; Zheng, Y.; Zhang, X.; Davey, K.; Dai, S.; Qiao, S.Z. Promotion of electrocatalytic hydrogen evolution reaction on nitrogen-doped carbon nanosheets with secondary heteroatoms. *ACS Nano* **2017**, *11*, 7293-7300,

[38] Pan, F.; Li, B.; Xiang, X.; Wang, G.; Li, Y. Efficient CO_2 electroreduction by highly dense and active pyridinic nitrogen on holey carbon layers with fluorine engineering. *ACS Catal.* **2019**, *9*, 2124-2133.

[39] Mamtani, K.; Jain, D.; Dogu, D.; Gustin, V.; Gunduz, S.; Co, A.C.; Ozkan, U.S. Insights into oxygen reduction reaction (ORR) and oxygen evolution reaction (OER) active sites for nitrogen-doped carbon nanostructures (CN_x) in acidic media. *Appl. Catal. B: Environ.* **2018**, *220*, 88-97.

[40] Pan, F.; Deng, W.; Justiniano, C.; Li, Y. Identification of champion transition metals centers in metal and nitrogen-codoped carbon catalysts for CO_2 reduction. *Appl. Catal. B: Environ.* **2018**, *226*, 463-472.

[41] Pan, F.; Li, B.; Deng, W.; Du, Z.; Gang, Y.; Wang, G.; Li, Y. Promoting electrocatalytic CO_2 reduction on nitrogen-doped carbon with sulfur addition. *Appl. Catal. B: Environ.* **2019**, *252*, 240-249.

[42] Yang, Z.; Yao, Z.; Li, G.; Fang, G.; Ni, H.; Liu, Z.; Zhou, X.; Chen, X.; Huang, S. Sulfur-doped graphene as an efficient metal-free cathode catalyst for oxygen reduction. *ACS Nano* **2012**, *6*, 205- 211,

[43] Yang, J.; Qiu, Z.; Zhao, C.; Wei, W.; Chen, W.; Li, Z.; Qu, Y.; Dong, J.; Luo, J.; Li, Z.; Wu, Y. In situ thermal atomization to convert supported nickel nanoparticles into surface-bound nickel single-atom catalysts. *Angew. Chem. Int. Ed.* **2018**, *57*,14095-14100.

[44] Lu, P.; Yang, Y.; Yao, J.; Wang, M.; Dipazir, S.; Yuan, M.; Zhang, J.; Wang, X.; Xie, Z.; Zhang, G. Facile synthesis of single-nickel-atomic dispersed N-doped carbon framework for efficient electrochemical CO_2 reduction. *Appl. Catal. B: Environ.* **2019**, *241*, 113-119.

[45] Liang, S.; Jiang, Q.; Wang, Q.; Liu, Y. Electrochemical reduction of CO_2 to CO over transition metal/N-doped carbon catalysts: the active sites and reaction mechanism. *Adv. Energy Mater.* **2021**, *11*, 2101477.

[46] Ma, M.; Trzesniewski, B.J.; Xie, J.; Smith, W.A. Selective and efficient reduction of carbon dioxide to carbon monoxide on oxide-derived nanostructured silver electrocatalysts. Angew Chem. Int. Ed. **2016**, *55*, 9748-9752.

[47] Xiong, W.; Li, H.; Wang, H.; Yi, J.; You, H.; Zhang, S.; Hou, Y.; Cao, M.; Zhang, T.; Cao, R. Hollow mesoporous carbon sphere loaded Ni-N_4 single-atom: support structure study for CO_2 electrocatalytic reduction catalyst. *Small* **2020**, *16*, e2003943.

[48] Chen, J.; Li, H.; Fan, C.; Meng, Q.; Tang, Y.; Qiu, X.; Fu, G.; Ma, T. Dual single-atomic Ni-N_4 and Fe-N_4 sites constructing Janus hollow graphene for selective oxygen electrocatalysis *Adv. Mater.* **2020**, *32*, e2003134.

[49] Li, P.; Zhao, G.; Cui, P.; Cheng, N.; Lao, M.; Xu, X.; Dou, S.X.; Sun, W. Nickel single atom-decorated carbon nanosheets as multifunctional electrocatalyst supports toward efficient alkaline hydrogen evolution. *Nano Energy* **2021**, *83*, 105850.

[50] Bi, W.; Li, X.; You, R.; Chen, M.; Yuan, R.; Huang, W.; Wu, X.; Chu, W.; Wu, C.; Xie, Y. Surface immobilization of transition metal ions on nitrogen-doped Graphene realizing high-efficient and selective CO_2 reduction. *Adv. Mater*. **2018**, *30*, e1706617.

[51] Li, K.; Zhang, S.B.; Zhang, X.L.; Liu, S.; Jiang, H.X.; Jiang, T L.; Shen, C.Y.; Yu, Y.; Chen, W. Atomic Tuning of Single-Atom Fe-N-C Catalysts with Phosphorus for Robust Electrochemical CO_2 Reduction. *Nano Lett*. **2022**, *22*, 1557-1565

[52] Liu, S.; Jin, M.; Sun, J.; Qin, Y.; Gao, S.; Chen, Y.; Zhang, S.; Luo, J.; Liu, X. Coordination environment engineering to boost electrocatalytic CO_2 reduction performance by introducing boron into single-Fe-atomic catalyst. *Chem. Eng. J*. **2022**, *437*, 135294.

[53] Li, Z.; Wu, R.; Xiao, S.; Yang, Y.; Lai, L.; Chen, J.S.; Chen, Y. Axial chlorine coordinated iron-nitrogen-carbon single-atom catalysts for efficient electrochemical CO_2 reduction. *Chem. Eng. J*. **2022**, *430*, 132882.

[54] Lu, S.; Zhang, Y.; Mady, M.F.; Egwu Eleri, O.; Mekonnen Tucho, W.; Mazur, M.; Li, A.; Lou, F.; Gu, M.; Yu, Z. Sulfur-decorated Ni-N-C catalyst for electrocatalytic CO_2 reduction with near 100 % CO selectivity. *ChemSusChem* **2022**, 15, e202200870.

[55] Leverett, J.; Tran-Phu, T.; Yuwono, J.A.; Kumar, P.; Kim, C.; Zhai, Q.; Han, C.; Qu, J.; Cairney, J.; Simonov, A.N. Tuning the coordination structure of Cu-N-C single atom catalysts for simultaneous electrochemical reduction of CO_2 and NO_3^- to Urea, *Adv. Energy Mater*. **2022**, *12*, 2201500.

[56] Lu, S.; Huynh, H.L.; Lou, F.; Guo, K.; Yu, Z. Single transition metal atom embedded antimonene monolayers as efficient trifunctional electrocatalysts for the HER, OER and ORR: a density functional theory study. *Nanoscale* **2021**, *13*, 12885-12895.

[57] Gu, J.; Hsu, C.S.; Bai, L.; Chen, H.M.; Hu, X. Atomically dispersed Fe^{3+} sites catalyze efficient CO_2 electroreduction to CO. *Science* **2019**, *364*, 1091-1094.

[58] Bi, W.; Li, X.; You, R.; Chen, M.; Yuan, R.; Huang, W.; Wu, X.; Chu, W.; Wu, C.; Xie, Y. Surface immobilization of transition metal ions on nitrogen-doped graphene realizing high-efficient and selective CO_2 reduction. *Adv. Mater*. **2018**, *30*, e1706617.

[59] Xing, G.; Cheng, L.; Li, K.; Gao, Y.; Tang, H.; Wang, Y.; Wu, Z. Efficient electroreduction of CO_2 by single-atom catalysts two-dimensional metal hexahydroxybenzene frameworks: A theoretical study. *Appl. Surf. Sci*. **2021**, 550, 149389.

[60] Ao, C.; Feng, B.; Qian, S.; Wang, L.; Zhao, W.; Zhai, Y.; Zhang, L. Theoretical study of transition metals supported on g-C_3N_4 as electrochemical catalysts for CO_2 reduction to CH_3OH and CH_4. *J. CO_2 Util.* **2020**, *36*, 116-123.

[61] Zheng, Y.; Jiao, Y.; Ge, L.; Jaroniec, M.; Qiao, S.Z. Two-step boron and nitrogen doping in graphene for enhanced synergistic catalysis. *Angew. Chem. Int. Ed.* **2013**, *52*, 3110-3116.

[62] Dong, W.; Zhang, N.; Li, S.; Min, S.; Peng, J.; Liu, W.; Zhan, D.; Bai, H. A Mn single atom catalyst with Mn-N_2O_2 sites integrated into carbon nanosheets for efficient electrocatalytic CO_2 reduction. *J. Mater. Chem. A* **2022**, *10*, 10892-10901.

[63] Yao, D.; Tang, C.; Zhi, X.; Johannessen, B.; Slattery, A.; Chern, S.; Qiao, S.Z. Inter-metal interaction with a threshold effect in NiCu dual-atom catalysts for CO_2 electroreduction. *Adv. Mater.* **2023**, *35*, e2209386.

[64] Lu, Z.; Wang, J.; Huang, S.; Hou, Y.; Li, Y.; Zhao, Y.; Mu, S.; Zhang, J.; Zhao, Y. N, B-co-doped defect-rich graphitic carbon nanocages as high performance multifunctional electrocatalysts. *Nano Energy* **2017**, *42*, 334-340.

[65] Li, X.; Huang, X.; Xi, S.; Miao, S.; Ding, J.; Cai, W.; Liu, S.; Yang, X.; Yang, H.; Gao, J.; Wang, J.; Huang, Y.; Zhang, T.; Liu, B. Single cobalt atoms anchored on porous N-doped graphene with dual reaction sites for efficient fenton-like catalysis. *J. Am. Chem. Soc.* **2018**, *140*, 12469-12475.

[66] Cheng, H.; Wu, X.; Li, X.; Zhang, Y.; Feng, M.; Fan, Z.; He, G. Zeolitic imidazole framework-derived FeN_5-doped carbon as superior CO_2 electrocatalysts. *J. Catal.* **2021**, *395*, 63-69.

[67] Chen, H.; Guo, X.; Kong, X.; Xing, Y.; Liu, Y.; Yu, B.; Li, Q.X.; Geng, Z.; Si, R.; Zeng, J. Tuning the coordination number of Fe single atoms for the efficient reduction of CO_2. *Green Chem.* **2020**, *22*, 7529-7536.

[68] Yang, H.; Zhang, P.; Yi, X.; Yan, C.; Pang, D.; Chen, L.; Wang, S.; Wang, C.; Liu, B.; Zhang, G.; Zhou, Z.; Li, X. Constructing highly utilizable Fe-N_4 single-atom sites by one-step gradient pyrolysis for electroreduction of O_2 and CO_2. *Chem. Eng. J.* **2022**, *440*, 135749.

[69] Li, Z.; Wu, R.; Xiao, S.; Yang, Y.; Lai, L.; Chen, J.S.; Chen, Y. Axial chlorine coordinated Iron-nitrogen-carbon single-atom catalysts for efficient electrochemical CO_2 Reduction. *Chem. Eng. J.* **2022**, *430*, 132882.

[70] Pan, F.; Li, B.; Deng, W.; Du, Z.; Gang, Y.; Wang, G.; Li, Y. Promoting electrocatalytic CO_2 reduction on nitrogen-doped carbon with sulfur addition. *Appl. Catal. B: Environ.* **2019**, *252*, 240-249.

[71] Feng, J.; Gao, H.; Zheng, L.; Chen, Z.; Zeng, S.; Jiang, C.; Dong, H.; Liu, L.; Zhang, S.; Zhang, X. A Mn-N_3 single-atom catalyst embedded in graphitic carbon nitride for efficient CO_2 electroreduction. *Nat. Commun.* **2020**, *11*, 4341.

[72] Yang, J.; Qiu, Z.; Zhao, C.; Wei, W.; Chen, W.; Li, Z.; Qu, Y.; Dong, J.; Luo, J.; Li, Z.; Wu, Y. In situ thermal atomization to convert supported nickel nanoparticles into surface-bound nickel single-atom catalysts. *Angew. Chem. Int. Ed.* **2018**, *57*, 14095-14100.

[73] Gong, Y.N.; Jiao, L.; Qian, Y.; Pan, C.Y.; Zheng, L.; Cai, X.; Liu, B.; Yu, S.H.; Jiang, H.L. Regulating the coordination environment of MOF-templated single-atom nickel electrocatalysts for boosting CO_2 reduction. *Angew. Chem. Int. Ed.* **2020**, *59*, 2705-2709.

[74] Li, Y.; Wei, B.; Zhu, M.; Chen, J.; Jiang, Q.; Yang, B.; Hou, Y.; Lei, L.; Li, Z.; Zhang, R.; Lu, Y. Synergistic effect of atomically dispersed Ni-Zn pair sites for enhanced CO_2 electroreduction. *Adv. Mater.* **2021**, *33*, e2102212.

[75] Yun, R.; Zhan, F.; Wang, X.; Zhang, B.; Sheng, T.; Xin, Z.; Mao, J.; Liu, S.; Zheng, B. Design of binary Cu-Fe sites coordinated with nitrogen dispersed in the porous carbon for synergistic CO_2 electroreduction. *Small* **2021**, *17*, e2006951.

[76] Yang, H.; Lin, Q.; Zhang, C.; Yu, X.; Cheng, Z.; Li, G.; Hu, Q.; Ren, X.; Zhang, Q.; Liu, J.; He, C. Carbon dioxide electroreduction on single-atom nickel decorated carbon membranes with industry compatible current densities. *Nat. Commun.* **2020**, *11*, 593.

[77] Li, Y.; Shan, W.; Zachman, M.J.; Wang, M.; Hwang, S.; Tabassum, H.; Yang, J.; Yang, X.; Karakalos, S.; Feng, Z.; Wang, G.; Wu, G. Atomically dispersed dual-metal site catalysts for enhanced CO_2 reduction: mechanistic insight into active site structures. *Angew. Chem. Int. Ed.* **2022**, *61*, e202205632.

[78] Ma, M.; Trzesniewski, B.J.; Xie, J.; Smith, W.A. Selective and efficient reduction of carbon dioxide to carbon monoxide on oxide-derived nanostructured silver electrocatalysts. *Angew. Chem. Int. Ed.* **2016**, *55*, 9748-9752.

[79] Zhang, N.; Zhang, X.; Tao, L.; Jiang, P.; Ye, C.; Lin, R.; Huang, Z.; Li, A.; Pang, D.; Yan, H.; Wang, Y.; Xu, P.; An, S.; Zhang, Q.; Liu, L.; Du, S.; Han, X.; Wang, D.; Li, Y. Silver single-atom catalyst for efficient electrochemical CO_2 reduction synthesized from thermal transformation and surface reconstruction. *Angew. Chem. Int. Ed.* **2021**, *60*, 6170-6176.

[80] Yi, J.D.; Gao, X.; Zhou, H.; Chen, W.; Wu, Y. Design of Co-Cu diatomic site catalysts for high-efficiency synergistic CO_2 electroreduction at industrial-level current density. *Angew. Chem. Int. Ed.* **2022**, *61*, e202212329.

[81] Ren, W.; Tan, X.; Yang, W.; Jia, C.; Xu, S.; Wang, K.; Smith, S.C.; Zhao, C. Isolated diatomic Ni-Fe metal-nitrogen sites for synergistic electroreduction of CO_2. *Angew. Chem. Int. Ed.* **2019**, *58*, 6972-6976.

Appendices

Appendix A – Paper I

Recent Progress in Two Dimensional Materials for Electrocatalytic CO_2 Reduction

S. Lu, F. Lou and Z. Yu

Catalysts, 2022, 12, 228

DOI: 10.3390/catal12020228

catalysts

MDPI

Review

Recent Progress in Two-Dimensional Materials for Electrocatalytic CO_2 Reduction

Song Lu [1], Fengliu Lou [2] and Zhixin Yu [1,*]

[1] Department of Energy and Petroleum Engineering, University of Stavanger, 4036 Stavanger, Norway; song.lu@uis.no
[2] Beyonder AS, Kanalsletta 2, 4033 Stavanger, Norway; fengliu@beyonder.no
* Correspondence: zhixin.yu@uis.no; Tel.: +47-51832238

Abstract: Electrocatalytic CO_2 reduction (ECR) is an attractive approach to convert atmospheric CO_2 to value-added chemicals and fuels. However, this process is still hindered by sluggish CO_2 reaction kinetics and the lack of efficient electrocatalysts. Therefore, new strategies for electrocatalyst design should be developed to solve these problems. Two-dimensional (2D) materials possess great potential in ECR because of their unique electronic and structural properties, excellent electrical conductivity, high atomic utilization and high specific surface area. In this review, we summarize the recent progress on 2D electrocatalysts applied in ECR. We first give a brief description of ECR fundamentals and then discuss in detail the development of different types of 2D electrocatalysts for ECR, including metal, graphene-based materials, transition metal dichalcogenides (TMDs), metal–organic frameworks (MOFs), metal oxide nanosheets and 2D materials incorporated with single atoms as single-atom catalysts (SACs). Metals, such as Ag, Cu, Au, Pt and Pd, graphene-based materials, metal-doped nitric carbide, TMDs and MOFs can mostly only produce CO with a Faradic efficiencies (FE) of 80~90%. Particularly, SACs can exhibit FEs of CO higher than 90%. Metal oxides and graphene-based materials can produce HCOOH, but the FEs are generally lower than that of CO. Only Cu-based materials can produce high carbon products such as C_2H_4 but they have low product selectivity. It was proposed that the design and synthesis of novel 2D materials for ECR should be based on thorough understanding of the reaction mechanism through combined theoretical prediction with experimental study, especially in situ characterization techniques. The gap between laboratory synthesis and large-scale production of 2D materials also needs to be closed for commercial applications.

Keywords: carbon dioxide; two-dimensional materials; electrocatalytic reduction; graphene; TMD; MOF; metal oxide nanosheet; SAC

check for updates

Citation: Lu, S.; Lou, F.; Yu, Z. Recent Progress in Two-Dimensional Materials for Electrocatalytic CO_2 Reduction. *Catalysts* **2022**, *12*, 228. https://doi.org/10.3390/catal12020228

Academic Editor: Bruno Fabre

Received: 17 January 2022
Accepted: 15 February 2022
Published: 17 February 2022

1. Introduction

CO_2 is the main component of greenhouse gases which lead to environmental concerns, and its concentration has increased from approximately 280 ppm in the early 1800s to 410 ppm today [1–3]. Without proper strategies to combat this problem, the steadily growing CO_2 emissions will arouse the increase in the global average temperature, loss of glaciers, rise of sea level and other climate issues [4]. To reverse these negative courses, technologies such as carbon capture and storage (CCS) have been pursued [5–7]. Despite tremendous efforts on CCS, including separating CO_2 from air or flue gas, storing the captured CO_2 is still a daunting challenge due to the risk of leakage, massive energy consumption, high cost and social acceptance [8–12]. An alternative approach is to utilize CO_2 as raw material and convert it into value-added products, which approach has received extensive attention in the past decades [13–15]. Therefore, the conversion of CO_2 has been regarded as a promising route for closing the carbon cycle and producing value-added chemicals and fuels.

The conversion of CO_2 can be realized by a variety of technologies such as thermochemical, electrochemical, photochemical, radiochemical and biochemical reactions [16–24]. Among these, the reduction of CO_2 by electrochemical strategies is attractive and exhibits many advantages [25,26]. For instance, the energy required for electrochemical reduction reactions can be provided by renewable energy such as solar, geothermal or wind energy. In addition, the reaction can be performed under ambient pressure and temperature. Moreover, the external voltages as well as electrolyte solutions can be adjusted to produce specific products. However, the physicochemical properties of the CO_2 molecule make electrochemical conversion processes challenging. To convert CO_2 into other products, the dissociation of the C=O bond is essential and must overcome high-energy barriers of about 750 kJ/mol. In addition, electrolyte solutions are generally water-based, which makes the reaction inefficient due to the poor CO_2 dissolution in water. In the past decades, both theoretical and experimental work have disclosed that the electrocatalysts play a vital role in catalytic processes [27–32]. For example, it has been proven that traditional metal electrocatalysts, such as copper, platinum and gold, can activate CO_2 and reduce it into valuable chemical products [33–35]. However, these catalysts suffer drawbacks such as high overpotential, poor stability, low selectivity, complex separation and low efficiency for specific products. In addition, the prices of precious metals hamper the large-scale application of Pt catalysts. Therefore, developing efficient, cost-effective and durable alternatives to the traditional metal catalysts for electrocatalytic CO_2 reduction (ECR) reaction is urgent.

In recent years, two-dimensional (2D) materials with novel geometric, electronic and optical properties greatly accelerated the development of catalysts. Two-dimensional materials, sometimes referred to as single-layer materials, are crystalline materials consisting of a single layer of atoms. These materials have promising applications in fields such as photovoltaics, semiconductors, electrodes and water purification. Two-dimensional materials can be categorized as either 2D allotropes of various elements or as compounds consisting of two or more covalently bonded elements. The elemental 2D materials generally carry the -ene suffix in their names, while the compounds have -ane or -ide suffixes. A wide range of 2D compounds, including metals, chalcogenides, group IV and V elements, oxides, carbides, nitrides, halides, hydroxides, hydrides, phosphates, phosphonates and covalent organic frameworks, have been investigated for various applications. Two-dimensional materials can exhibit semiconductive, insulative or even metallic behavior. Some of them with direct or indirect band gaps have great responses to ultraviolet and visible light. The electronic and optical properties of these 2D materials are tunable by adjusting the number of layers because of quantum confinement. Two-dimensional semiconductive materials display strong enhancements of Coulomb interactions among charge carriers and defects, contributing to longer-lived excitons compared to their bulk structures [36]. The specific surface area of 2D materials is usually quite high and more active atoms can be exposed. The physicochemical properties of 2D materials, especially, can be effectively modulated by different engineering strategies, including heterostructure, doping, chemical functionalization, etc. [37].

When employed as catalysts, 2D materials with nanosheets can show unique properties and excellent performance in catalytic reactions. Compared with conventional bulk materials, they have much higher specific surface areas and high percentages of bare surface atoms that can offer abundant active sites, boosting catalytic reactions. Note that the highly exposed surface atoms can potentially escape and form defect structures, leading to decreased coordination numbers of surface atoms, which are the preferential sites for the adsorption of reactants or intermediates. Similarly, the edge atoms of nanosheets with low coordination numbers can also exhibit novel catalytic properties. Therefore, 2D structures can promote the chemisorption of reactants and improve catalytic performance. A large class of 2D materials, such as noble metals, metal oxides, graphene, graphite carbon nitride (g–C_3N_4), transition metal dichalcogenides (TMDs), metal–organic frameworks (MOFs), etc., has been demonstrated to have great potential to catalyze CO_2 conversion

reactions [38–43]. Particularly, graphene, known as the first invented 2D material, has attracted extensive attention for many applications [44]. Its unique mechanical characteristics, electronic structures and optical properties make it applicable in fields such as solar cells, LED transistors, sensors and catalysts [45–48]. More importantly, the properties of 2D materials can be easily tuned via doping atoms, hybridizing with other nanostructures, surface engineering and defect generation, further improving their electronic properties and catalytic performance.

Numerous studies have been reported for ECR, and a few excellent reviews have been published. For example, Wang et al. reviewed the principles for electrocatalyst design and performance evaluation as well as the factors influencing ECR activity [49]. Nitopi et al. described the various experimental and theoretical approaches used to explore the mechanisms for the formation of ECR products on Cu catalysts. They concluded that nanostructuring and constructing bimetallic electrodes can be effective strategies to enhance activity and selectivity of Cu based catalysts [50]. Jin et al. highlighted the utilization of in situ spectroscopy, including X-ray absorption, X-ray photoelectron, Raman, infrared and mass spectroscopy, which greatly refined the understanding of ECR from intermediates, reaction pathways, active sites and the effects of a reaction environment on product distribution [51]. Zhu et al. summarized controlled synthesis methods for embedding a single atom on different carbon materials as an ECR catalyst. The effects of precursors and preparation environments on the structure of single-atom catalysts (SACs) were discussed. They also compared the intrinsic activity of different metal centers and methods for enhancing ECR efficiency [52]. Zhu et al. reviewed the latest progress on developing 2D materials for ECR from the perspective of theoretical simulation and discussed the reaction mechanisms of various 2D materials for ECR [53]. Zhang et al. reviewed recent advances on materials development for CO_2 conversion by thermocatalysis, photocatalysis and photothermocatalysis, highlighting the reaction pathways and mechanism on C=O bond activation and intermediate formation [54]. Very recently, they also summarized CO_2 conversion by electro- and photoelectrocatalysis, emphasizing the importance of operando characterization theoretical simulations [55]. Li et al. briefly reviewed bimetallic chalcogenides for ECR application in the past five years [56]. They disclosed that hybridization between metal atoms, such as that of intermetallic compounds, heterostructures and metal doping, shows positive effects on ECR selectivity and activity. Wang et al. reviewed recent advances on non-noble-metal-based ECR catalysts, focusing on the synthesis strategies for engineering the electrocatalysts and the ECR mechanism [57]. Therefore, a wide range of topics have been covered for ECR. In this work, we systematically review the recent progress on both theoretical and experimental work on 2D materials applied in ECR according to the materials type. We start with the introduction to 2D materials and CO_2 conversion as well as the fundamentals of ECR. Thereafter, the emerging 2D materials for ECR, including metal, graphene-based materials, TMDs, MOFs, metal oxides and single-atom anchored 2D materials, are discussed in detail, and the effects of structure and modification strategies on catalytic performance for ECR are emphasized. We also summarize GDE and MEA electrolyzers which could solve the problem of limited CO_2 solubility and energy loss of conventional H-type cells for potential industrial ECR applications. Based on these, future perspectives for ECR catalysts design and synthesis are proposed. We aim for this contribution to enlighten future research directions and strategies for exploiting novel 2D materials for ECR and energy conversion in general.

2. Fundamentals of Electrochemical CO_2 Reduction

2.1. CO_2 Properties and the Reduction Products

CO_2 is one of the most stable molecules with a strong O=C=O double bond, and its bond energy is higher than that of C–H and C–C bonds. During electrocatalytic processes, the breaking of the O=C=O bond requires a high activation energy. In addition, since ECR consists of multiple elementary steps, these electrocatalytic processes are more demanding

than, for example, water-splitting reactions. As ECR reactions are normally carried out in aqueous solutions, another critical issue is the low solubility of CO_2 in water, which impedes the diffusion-controlled reactions. There are certain ways to improve CO_2 dissolution, including using nonaqueous electrolytes and increasing CO_2 partial pressure. For instance, some metal catalysts with low activity for ECR under atmospheric pressure, however, can reduce CO_2 to CO and HCOOH efficiently at high pressures [58].

Electrocatalysts can effectively reduce activation energy, accelerate reactions or increase desired product selectivity in ECR. It should also dissociate water in solution to promote proton–electron transfer because the proton-assisted multiple-electron transfer can be beneficial for CO_2 activation. Depending on the different pathways and the number of protons and electrons transferred, a range of products can be formed, including C_1 products, such as carbon monoxide (CO), methanol (CH_3OH), formic acid (HCOOH), methane (CH_4), or C_2 products, such as ethylene (C_2H_4), ethanol (C_2H_5OH) and others [59]. C_2 products with higher energy densities are more valuable, but the synthesis of C_2 products is more difficult than that of C_1 products because of larger numbers of required protons during conversion. Meanwhile, high formation energy of the C–C bonds can decrease the efficiency of the reaction. To achieve specific product selectivity, the design and synthesis of high-performance ECR electrocatalysts is essential.

2.2. Single-Electron vs. Proton-Coupled Electron Reactions

Research on ECR has been conducted ever since the early 19th century. ECR contains two half reactions occurring in the anode and the cathode, where different numbers of proton-coupled electron transfers occur. The standard electrode potentials of different reactions with reference to standard hydrogen electrons (SHEs) for different products in aqueous solutions are summarized in Table 1. For a typical single-electron ECR, CO_2 is reduced to the CO_2 anion radical (CO_2^-) at the cathode and water is oxidized to oxygen at the anode. Since the kinetics of the reactions are quite sluggish, the first step for converting CO_2 into reduced carbon species is difficult. The thermodynamic potential for driving single-electron CO_2 reduction to CO_2^- is about −1.90 V vs. SHE at a PH of 7, indicating that this reaction is highly energetic and unfavorable [60–62]. In addition, this first step is also the rate-limiting step, and the generation of the CO_2^- intermediate plays a significant role in forming $2e^-$ reduction products. Interestingly, a more favorable route that bypasses the formation of CO_2^- by proton-coupled electron transfer processes has been identified. The transfer of proton-coupled electrons benefits ECR within the potential range of −0.20 to −0.60 V vs. SHE, and the final products are determined by the choices of electrocatalysts and electrolytes as well as the numbers of electrons and protons transferred [63,64]. For instance, two-proton-coupled electron transfer in a CO_2 hydrogenation reaction mainly produces HCOOH and CO.

Table 1. Standard electrochemical potentials for reducing CO_2 into different products.

CO_2 Reduction Reactions	Standard Electrode Potentials vs. SHE (V)
$CO_2 + e^- \rightarrow CO_2^-$	−1.900
$CO2 + 2H^+ + 2e^- \rightarrow HCOOH$	−0.610
$CO2 + 2H^+ + 2e^- \rightarrow CO + H_2O$	−0.530
$2CO_2 + 2H^+ + 2e^- \rightarrow H_2C_2O_4$	−0.913
$CO_2 + 4H^+ + 4e^- \rightarrow HCHO + H_2O$	−0.480
$CO_2 + 6H^+ + 6e^- \rightarrow CH_3OH + H_2O$	−0.380
$CO_2 + 8H^+ + 8e^- \rightarrow CH_4 + 2H_2O$	−0.240
$2CO_2 + 12H^+ + 12e^- \rightarrow C_2H_4 + 4H_2O$	−0.349
$2CO_2 + 12H^+ + 12e^- \rightarrow C_2H_5OH + 3H_2O$	−0.329
$2CO_2 + 14H^+ + 14e^- \rightarrow C_2H_6 + 4H_2O$	−0.270
$3CO_2 + 18H^+ + 18e^- \rightarrow C_3H_7OH + 5H_2O$	−0.310

As shown in Figure 1, ECR starts by transferring a proton–electron pair to form carboxyl (*COOH) or formate (*OCHO) intermediate species [53]. These two intermediates

can be further reduced by accepting different numbers of proton–electron pairs. Note that there is much competition between intermediate species. For example, the OHCO* species can be converted to HCOOH, and the biformate (H_2COO*) can also be reduced to HCOOH. Meanwhile, the different products also show similar reduction potentials. Thus, further reactions of these intermediate species are important for the reaction rate and formation of the final products. Moreover, as the equilibrium potential of a hydrogen evolution reaction (HER) (0 V vs. reversible hydrogen electrode (RHE)) is more positive than that of CO_2 reduction to HCOOH (−0.17 V vs. RHE), H_2 will be the by-product, which seriously limits ECR efficiency [65].

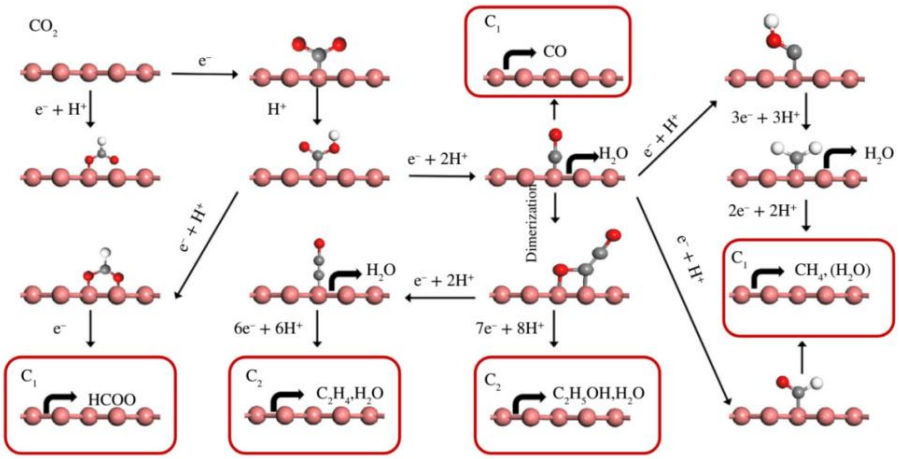

Figure 1. Potential electrochemical CO_2 reduction pathways to form the C_1 products CO, HCOOH and CH_4 and the C_2 products C_2H_4 and C_2H_5OH. Reprinted from [53], Copyright (2019), with permission from Wiley.

2.3. Factors Determining Product Selectivity

Factors such as the type of electrocatalyst (morphology, composition, chemical state and crystallographic structure), type of electrolyte (composition, concentration and pH), temperature, pressure and applied potential all influence ECR. For instance, solid and aqueous electrolytes have been used in ECR, exhibiting remarkable differences in efficiency [66,67]. To date, $NaHCO_3$ and $KHCO_3$ solutions are frequently chosen as electrolytes because they can maintain the pH at the electrode surface. Meanwhile, the pH of the solution can affect the generation of by-products such as H_2.

ECR, with a more positive potential vs. SHE, is thermodynamically more favourable. In this regard, the conversion of CO_2 to alcohol or hydrocarbon products should be thermodynamically more favourable than to other products, including CO, HCOOH and HCHO (Table 1). Nevertheless, ECR not only needs to overcome the thermodynamic barrier but also the kinetic challenge determined by the concentration of available protons in reaction. Namely, the electrocatalysts prefer to transfer electrons from their catalytic sites to adjacent sites which can provide protons. Thus, the formation of hydrogenated C_1 intermediates such as HCOOH can be kinetically more favourable than the formation of C–C bonds, which hinders the selectivity to C_2 and higher hydrocarbon products. To date, only the Faradaic efficiency (FE) of C_1 products CO and HCOOH can reach 100%, while the maximum FE of C_2 product C_2H_4 is 80% and the maximum FE of C_3 product C_3H_7OH is 30% [68,69].

Many theoretical studies proposed that for multielectron transfer reduction of CO_2, the adsorption energies of intermediates follow linear scaling relationships, and breaking such linear scaling relationships can improve catalytic performance. Some strategies have been proposed, including reducing coordination numbers, doping with *p*-block elements, engineering oxyphilic sites and coating the catalyst surface with active ligands. Up to now, the majority of the ECR electrocatalysts have been metal- and carbon-based materials. It has been demonstrated that some heterogeneous electrocatalysts follow the two-electron-transfer mechanisms in CO_2 reduction to HCOOH or CO. For example, Hori et al. investigated a series of metals for ECR reaction and indicated that metallic electrocatalysts, such as Cd, Sn, Hg and Pb, prefer HCOOH formation [70]. However, noble metals, including Pt, Ag and Au, can convert CO_2 into CO. Copper-based electrocatalysts are the only electrocatalysts that have been reported for converting CO_2 into alcohols and hydrocarbons with good activity and selectivity. However, as mentioned above, the interaction between intermediates and electrocatalysts plays a crucial role in forming final products, demonstrating the importance of electrocatalysts.

2.4. Key Parameters for Evaluating ECR Efficiency

In experimental ECR study, there are several key parameters for evaluating electrocatalyst performance, including overpotential, current density, Tafel slope, FE, turnover frequency (TOF) and stability of electrocatalysts. The overpotential can be regarded as the energy needed to drive the reaction. In other words, the higher the overpotential, the higher the energy required for the reaction and the more difficult the reaction to be realized. Current density reflects the rate of electrochemical reaction, and the larger the current density, the faster the electrocatalytic reaction. The Tafel slope can be obtained by fitting the linear region of the Tafel curve. With the increase in overpotential, if the current density increases dramatically, the slope will be small. FE is regarded as the fraction between charges transferred to specific products and the total charges in the electrocatalytic process, accounting for the selectivity and efficiency of the reaction. Larger FE suggests less energy loss, and smaller FE indicates more energy loss. TOF is the catalytic activity of each site under a certain overpotential, indicating the intrinsic activity of catalysts. The stability of electrocatalysts can be evaluated by long-term use under a specific voltage.

In summary, the electrocatalytic reaction is a complicated multistep reaction occurring at the multiphase interface. Small overpotential and high current density can boost ECR, but it is difficult to satisfy them simultaneously. Developing excellent electrocatalysts to overcome these problems is the key.

3. Two-Dimensional Materials as Efficient ECR Electrocatalysts

Compared to bulk materials, 2D materials have a disordered state in their normal direction and a long-range order in the plane, showing a sheet structure. In addition, 2D materials can be exfoliated to single- or multiple-atom thickness, exhibiting interatomic covalent bonds in the plane. The physicochemical properties of 2D materials are different from that of bulk materials. The high atomic exposure rate, large specific surface area and flexible structure make them promising ECR catalysts. Some reported 2D-materials-based electrocatalysts for ECR are summarized in Table 2 and are illustrated in detail in the following sections. Many metals (Ag, Cu, Au, Pt, Pd, etc.), graphene-based materials, Ni/Fe/Zn-doped nitric carbide, metal-doped TMDs and MOFs can produce CO. Particularly, single TM atoms embedded in 2D materials as SACs can exhibit great CO selectivity. Metal oxides and graphene-based materials can produce HCOOH. Interestingly, only Cu-based materials can produce CH_4, C_2H_4 and other C^{2+} products.

Table 2. Typical electrocatalysts in ECR.

Electrocatalyst	Product	FE (%)	Potential	Reference
Pd-Pt/C	HCOOH	88	−0.40 V vs. RHE	[16]
nanoporous silver	CO	92	−0.50 V vs. RHE	[30]
copper foam	CO	80	−1.00 V vs. Ag/AgCl	[66]
Cu-Al	C_2H_4	80	−1.50 V vs. RHE	[68]
GN/ZnO/Cu_2O	C_3H_7OH	30	−0.90 V vs. Ag/AgCl.	[69]
graphene-supported MoS_x	CO	85.1	−0.65 V vs. RHE	[71]
Au NW	CO	94	−0.35 V vs. RHE	[72]
ultrathin Pd nanosheets	CO	94	−0.50 V vs. RHE	[73]
Pd-Au	CO	80	−0.50 V vs. RHE	[74]
nitrogen-doped 3D graphene foam	CO	85	−0.58 V vs. RHE	[75]
ultrathin Bi	HCOOH	86	−1.10 V vs. RHE	[76]
ultrathin porous Cu nanosheets	CO	74.1	−1.00 V vs. RHE	[77]
Cu nanocubes	C_2H_4	60	−0.50 V vs. RHE	[78]
B-doped graphene	HCOOH	66	−1.40 V vs. SCE	[79]
N-doped graphene	HCOOH	73	−0.84 vs. RHE	[38]
N-doped graphene quantum dots	$C_2H_5OH + C_2H_4$	45	−0.75 V vs. RHE	[59]
Au NPs x-embedded graphene nanoribbon	CO	92	−0.66 V vs. RHE	[80]
Ni-N modified graphene	CO	90	−0.70 V vs. RHE	[81]
N-doped graphene monolayer-coated Sn foil	HCOOH	92	−1.00 V vs. RHE	[82]
Sn quantum sheets confined in graphene	HCOOH	86	−1.80 V vs. SCE	[83]
SnS_2 supported on graphene oxide	HCOOH	84.5	−1.40 V vs. Ag/AgCl	[84]
g–C_3N_4/MWCNTs	CO	60	−0.75 V vs. RHE	[85]
Co_3O_4-CDots-C_3N_4	CO	89	−0.60 V vs. RHE	[86]
Nb-doped vertically aligned MoS_2	CO	82	−0.80 V vs. RHE	[87]
MoS_2	CO	98	−0.764 V vs. RHE	[88]
WSe_2 nanoflake	CO	24	−0.164 V vs. RHE	[89]
Cobalt–porphyrin MOF	CO	76	−0.70 V vs. RHE	[90]
Zn MOF	CO	71.9	−0.89 V vs. RHE	[91]
Co-based phthalocyanine	CO	99	−0.80 V vs. RHE	[92]
ultrathin Co_3O_4	HCOOH	64.3	−0.88 V vs. SCE	[93]
oxygen-deficient Co_3O_4	HCOOH	87.6	−0.87 V vs. SCE	[94]
atomic Co_3O_4	HCOOH	90	−0.85 V vs. SCE	[28]
mesoporous SnO_2 nanosheets	HCOOH	87	−1.60 V vs. Ag/AgCl	[95]
Cu-CeO_2	CH_4	58	−1.80 V vs. RHE	[96]
Fe–N_4–C	CO	80	−0.50 V vs. RHE	[97]
Fe–N_4–C	CO	80	−0.57 V vs. RHE	[98]
Fe–N_5–C	CO	97	−0.46 V vs. RHE	[99]
Fe–N_4–C	CO	94.9	−0.5 V vs. RHE	[100]
Fe^{3+}–N–C	CO	90	−0.45 V vs. RHE	[101]
Zn–N–C	CO	95	−0.43 V vs. RHE	[102]
Ni-graphene oxide	CO	96.5	−0.63 V vs. RHE	[103]
Ni(I)–N_4–C	CO	97	−0.61 V vs. RHE	[104]
Ni–N_4–C	CO	90	−0.65 V vs. RHE	[105]
Ni–N_2–C	CO	98	−0.80 V vs. RHE	[106]
STPyP–Co	CO	96	−0.62 V vs. RHE	[107]
Cu–N_2/GN nanosheets	CO	81	−0.50 V vs. RHE	[108]

3.1. Two-Dimensional Metallic Materials

Bulk metal catalysts in ECR have been investigated for decades [109–111]. Metal electrocatalysts can be divided into two groups: noble metal (Au, Ag, Pt, etc.) and other earth-abundant transition metals (Co, Ni, Cu, etc.). Theoretical work has well disclosed that noble metals are better electrocatalysts compared with earth-abundant metals. Nevertheless, some intermediates, such as CO, could poison the active sites, which affects their stability. Large-scale application of precious metals is also not possible due to their high price and scarcity.

It has been revealed that precious metals with 2D nanosheet structures can enhance their electrocatalytic performance effectively and improve the utilization of noble

metals [72]. Huang et al. prepared a hexagonal Pd structure with 2.5 times higher electrocatalytic activity for the oxidation of formic acid compared to commercial Pd black [112]. The high performance could be attributed to nanosheet structure with more active sites, better electronic structure and larger surface area, as well as high atom utilization. Zhu et al. synthesized ultrathin Pd nanosheets for ECR, which exhibited an FE of 94% for CO production at a potential of −0.50 V vs. RHE [73]. Meanwhile, experimental and theoretical work revealed that ultrathin Pd nanosheets with high edge exposure ratios are beneficial for CO_2 adsorption and CO desorption as well as suppressing HER. Nanostructured Au also shows great activity in ECR. Mistry et al. studied the electrocatalytic activity of Au nanoparticles (NPs) in the range of 1–8 nm for CO_2 reduction to CO [113]. The results suggested that the current density increases with the decrease in particle size.

Moreover, multimetal composite nanosheets also exhibit excellent performance in electrocatalytic reactions because of the synergistic effect of different metals compared to single-metal electrocatalysts [114–116]. Wang et al. showed that a 2D Pd–Au bimetallic catalyst has lower activation energy than monometallic Au in ECR via density functional theory (DFT) calculation [74]. Very recently, Au–Cu bimetallic thin films with various ratios were synthesized for ECR [117]. The activity of the Au–Cu alloy was found to be correlated with the variation of electronic structures determined by alloy composition. As shown in Figure 2a, the surface valence bands of the Au–Cu catalysts present different patterns with different alloy compositions. The *d*-band center gradually moves away from the Fermi level with the increase in Au concentration (Figure 2b), which could influence the occupancy of antibonding states. Meanwhile, the interaction strength between substrate and intermediates decreases. The *d*-band center does not shift after ECR, implying great stability. Therefore, the catalytic performance for CO formation is enhanced as Au concentration increases, with the highest current density and FE at −0.80 V vs. RHE (Figure 2c,d).

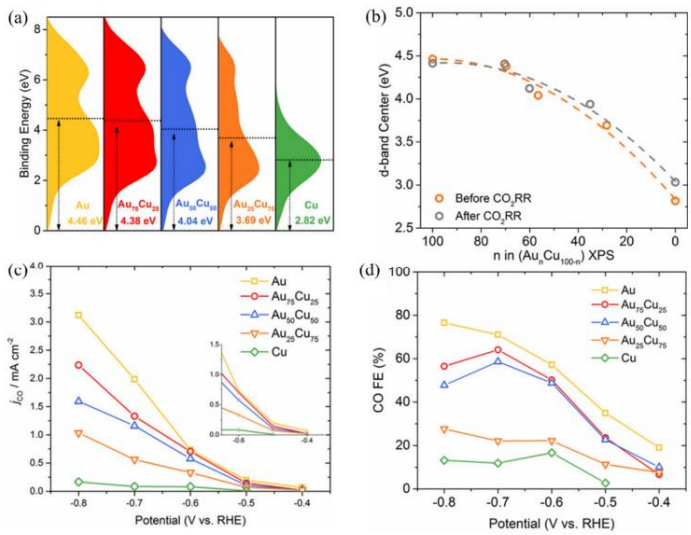

Figure 2. (**a**) Surface valence band X-ray photoemission spectra of the as-prepared Au, Cu and Au–Cu alloys. (**b**) *d*-band center of different samples before and after ECR at −0.7 V vs. RHE for 1 h. The gravity center of the valance band center is shown by the dotted lines compared to 0 eV. The binding energy is the value of $|E - E_{Fermi}|$. (**c**) Faradaic efficiency of and (**d**) partial current densities of CO. Reprinted from [117], Copyright (2018), with permission from American Chemical Society.

Nonprecious metals, including Fe, Co, Ni, etc., have also attracted much attention in electrocatalysis due to low prices, abundant resources and promising electrochemical properties as well as tunable electronic structures [118,119]. Studies have shown that Fe, Ni and Ti produce H_2 as the major product in ECR due to their low HER overpotential and strong CO adsorption capability. Sn, Pb and In have poor binding energy with CO_2^- intermediates and the final products are usually formate or formic acid. Moreover, Cu is the only metal catalyst that can produce C_3 hydrocarbons by a C–C coupling mechanism [120]. Generally, modulating the electronic and surface structures of these metals could effectively enhance their electrocatalytic activity. Kuang et al. synthesized ultrathin Ni nanosheet arrays by an in situ topology reduction technique. In their study, the electrocatalyst showed excellent HER activity compared with Pt/C because ultrathin nanosheet structure could expose more active sites which boost electrocatalytic reactions [121]. In addition, 2D-structured bismuth (Bi) exhibited more active sites and promising selectivity to formate compared to bulk Bi. Zhang et al. prepared ultrathin Bi by a liquid phase stripping technique. The ultrathin Bi displayed excellent electrocatalytic performance for formate generation with an FE of 86% and a current density of 16.5 mA/cm^2 at −1.1 V vs. RHE, which is obviously higher than bulk Bi and acetylene black decorated carbon paper (AB/CP) (Figure 3a,b). As presented in Figure 3c,d, CO_2 conversion to HCOOH underwent lower Gibbs free energy change on edges (003) and (012) [76]. Special surface structure can also improve the catalytic efficiency and selectivity. It has been reported that ultrathin porous Cu nanosheets synthesized by a simple replacement method can achieve an FE of 74.1% and current density of 23.0 mA/cm^2 at −1.0 V vs. RHE for CO_2 conversion to CO, remarkably better than that of traditional bulk Cu [77]. DFT calculations clarified that the porous Cu nanosheet structure can accelerate the formation of CO intermediate, thus promoting ECR efficiency. Similarly, Wang et al. synthesized Cu nanocubes which demonstrated better electrocatalytic activity and selectivity in comparison with Cu nanospheres of the same size. The nanocubes could reach an FE of 60% and a partial current density of 144 mA/cm^2 towards C_2H_4 production [78]. Zhang et al. prepared the pipet-like bismuth (Bi) nanorods semifilled in nitrogen-doped carbon nanotubes (BiNRs@NCNTs) for ECR [122]. The catalyst acted as a nanoscale conveyor which could facilitate mass transport and reactant adsorption on active sites. As a result, the FE for formate generation reached 90.9% at a moderate applied potential of −0.9 V (vs. RHE).

Therefore, metal catalysts are effective for electrocatalysis due to their intrinsic activity and good conductivity. When the metal catalysts are synthesized with 2D nanosheets or other special nanostructures, the atom utilization, activity and selectivity could be improved, thus increasing electrocatalytic efficiency. Precious metals, such as Pd or Au, or multimetals with different ratios show excellent selectivity for CO generation. Nonprecious metals, such as Fe, Co and Ni, show poor ECR performance, while Sn, Pb and In can have good activity for the production of formate or formic acid. Particularly, Cu-based catalysts with different morphologies can exhibit different activities and selectivities for different products. Accordingly, the choice of metal, small nanosheet size and different morphology will have a positive effect on ECR activity and selectivity.

3.2. Graphene and Graphene-Based Materials

Generally, graphene is a single layer of graphite with a zero-band gap. It is a promising electrocatalyst for CO_2 reduction due to its high electron mobility, conductivity, unique electronic structure and large surface area. In addition, the high thermal conductivity can improve heat diffusion during the exothermic process, benefiting electrocatalysis. However, pristine graphene exhibits some drawbacks in ECR. For instance, the delocalized π bonding network of graphene negatively affects the adsorption of intermediates such as *COOH or *OCHO; therefore, graphene cannot effectively activate the CO_2 molecule and presents high-energy barriers for intermediate formation, leading to low ECR activity [123]. Some studies have clarified that the undoped zigzag edge of graphene shows a metastable adsorbed CO_2 state, and the energy barrier is quite high at about 1.3 eV [124]. As the

modification of electronic structures can efficiently tackle these problems, many researchers have focused on tailing its electronic structures. For example, incorporating heteroatoms, such as B or N, can effectively modify graphene structures and decrease the CO_2 adsorption barrier. Studies have disclosed that N-doped graphene can exhibit a low overpotential of around 0.19 V for converting CO_2 into CO [75]. Duan et al. reported that doping boron can stabilize the negatively polarized O atoms of CO_2 and improve CO_2 chemisorption on carbon surfaces [125]. Similarly, Sreekanth et al. reported B-doped graphene as a metal-free electrocatalyst for CO_2 reduction in 0.1 M $KHCO_3$ solutions. They concluded that the presence of boron dopants can introduce spin density distribution and these atoms can be active sites for intermediate adsorption [79]. Some doped systems have been investigated in more detail by DFT calculations. Wu and coworkers systematically studied the effect of N-doped graphene for ECR. Three different N atom sites, including graphitic N, pyrrolic N and pyridinic N, were investigated as active sites for ECR. The authors suggested that the three different N sites can significantly decrease the free energy barrier for intermediate adsorption. The triple-pyridinic N can most effectively reduce the barrier for COOH adsorption, indicating that pyridinic N is a highly active site for converting CO_2 to CO [75]. However, there are different views on the mechanism of N-doped graphene for ECR. Chai et al. reported that the graphitic N-doped edges of graphene sites have low CO_2 activation barriers and are the most active sites for ECR among graphene-based materials [124]. Liu et al. demonstrated that a pyrrolic N site performs the best for CO_2 reduction to HCOOH with a low overpotential [126]. It has also been reported that N-doped graphene quantum dots with predominant pyridinic N at the edges can electrochemically convert CO_2 to C_2 compounds with low overpotentials [59].

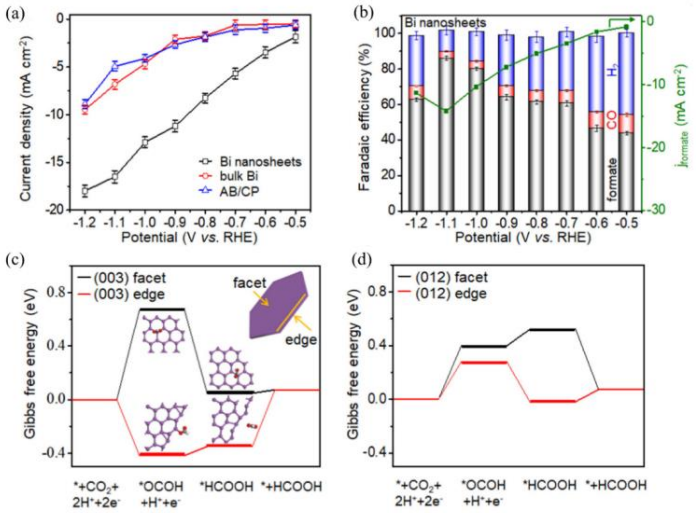

Figure 3. (**a**) Current densities of Bi nanosheets, bulk Bi and acetylene black decorated carbon paper (AB/CP) within a potential window of −0.5 to −1.2 V vs. RHE in CO_2-saturated 0.1 M $KHCO_3$ aqueous solution. (**b**) Faradaic efficiencies (left Y axes) and partial current densities of formate product (right Y axes) of Bi nanosheets. DFT calculated ΔG in the reaction pathways of CO_2 conversion to formate from the facet sites and edge sites of the (**c**) (003) plane and (**d**) (012) plane on Bi. Reprinted from [76], Copyright (2018), with permission from Elsevier.

Compared with nonmetal dopants, introducing single or multiple metal dopants to construct special graphene nanostructures could also exploit materials with excellent catalytic performance. Au nanoparticles embedded in graphene nanoribbon exhibit low overpotential, high FE for CO generation and excellent stability compared to amorphous carbon-supported Au nanoparticles, attributed to the change in electronic properties and the increase in active sites [127]. Liu et al. synthesized Pd and Cu mono- and bimetallic nanoparticle-embedded graphene and suggested that 1 wt.% Pd–2 wt.% Cu/graphene had the highest ECR efficiency [80]. Su et al. prepared nickel–nitrogen comodified graphene (Ni–N–Gr) with more active centers by short-duration heat treatment and found that the Ni–N site was the active center for CO_2 reduction [81]. As shown Figure 4a,c, the Ni–N–Gr and the Ni foil exhibit obvious enhancement of current density in the presence of CO_2. However, there is a remarkable difference in FE of CO. The Ni–N–Gr showed an FE of 90% at −0.7 to −0.9 V vs. RHE for CO production, where Ni foil produced mostly H_2 (Figure 4b,d), demonstrating that the synergistic effect of Ni and N is critical for improving CO selectivity.

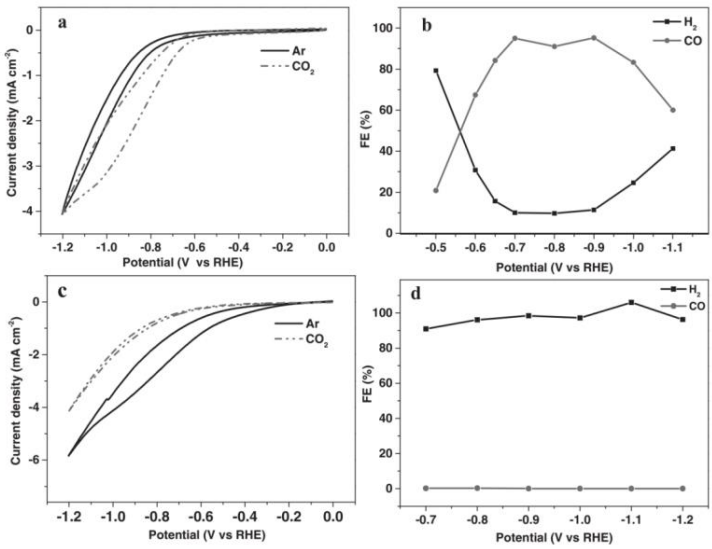

Figure 4. (**a**) Cyclic voltammograms of nickel–nitrogen comodified graphene (Ni–N–Gr) catalyst and (**c**) Ni foil in CO_2-saturated 0.1 M $KHCO_3$ and Ar-saturated 0.1 M KH_2PO_4/K_2HPO_4 (pH = 6.8) at 10 mV s^{-1}. FEs for the reduction products by (**b**) Ni–N–Gr catalyst and (**d**) Ni foil. Reprinted from [81], Copyright (2016), with permission from Wiley.

Graphene-based composite materials also possess excellent conductivities and larger surface areas compared to pristine graphene. Huang et al. synthesized N-doped graphene monolayer-coated Sn foil, showing excellent flexibility with a high FE of 92% for formate at −1.0 V vs. RHE [82]. Lei et al. prepared Sn quantum sheets confined in graphene, offering more active sites for CO_2 adsorption [83]. Li et al. successfully prepared SnS_2 nanosheets supported on reduced graphene oxide for CO_2 conversion to formate, displaying a low overpotential of 0.23 V and a maximum Faradaic efficiency of 84.5%. The spectroscopic and electrochemical characterizations suggested that the improvement of electrocatalytic performance can be attributed to the residual SnS_2 [84].

For graphene-like materials, graphitic carbon nitride (g–C_3N_4) typically exhibits good chemical and thermal stability under ambient conditions. However, poor conductivity and less active sites limit its potential application in ECR. Strategies, including doping metal and constructing composite, have been developed to increase the activity of g–C_3N_4. Metal atoms can effectively modulate the electronic structure of g–C_3N_4, thus improving the catalytic activity. The g–C_3N_4 nanosheet and multiwalled carbon nanotubes composite have been shown to exhibit excellent stability and good electrocatalytic performance for CO_2 reduction to CO [85]. The electrocatalytic activity of the composite arises from the C–N bonds, and the high conductivity allows numerous electrons to transfer rapidly to the C–N sites. Guo et al. synthesized Co_3O_4–CDots–g–C_3N_4 tricomponent electrocatalysts for syngas production [86]. They suggested that different catalytic components have different functionalities. For instance, g–C_3N_4 and Co_3O_4 provide active sites for ECR and HER, respectively, whereas CDots are the sites for proton generation.

It can be concluded that the electronic structure of graphene-based materials can be tuned to effectively improve ECR selectivity. Doping nonmetal or metal atoms is an efficient way for the design and synthesis of high-performance ECR catalysts. To date, nitrogen and metal atom codoping has been widely reported and shown excellent activity for CO production. Constructing highly active interfaces in graphene-based nanocomposite is also a good strategy in ECR catalyst design.

3.3. Two-Dimensional Transition Metal Dichalcogenides

Transition metal dichalcogenides (TMDs), such as MoS_2, $MoSe_2$ and WS_2, have the general formula MX_2, where M is a transition metal atom and X represents a chalcogen atom. The layers of X–M–X are stacked together by the van der Waals interaction. This is another class of 2D materials with exceptional physical and chemical properties to be applied as electrocatalysts [88]. The large surface area of 2D TMDs can provide more active sites for reactions such as CO_2 reduction and water splitting [128,129]. DFT calculations suggested that the excellent catalytic properties for metal-terminated edges of 2D TMDs can be attributed to its metallic character and high *d*-electron density [87]. It has been confirmed that intermediates, such as COOH and CHO, prefer to adsorb on MoS_2 and $MoSe_2$ edges than the bridge S or Se atoms, and CO species adsorb selectively on the metal atoms during ECR [130,131]. Four different TMD materials, MoS_2, $MoSe_2$, WS_2 and WSe_2, have been investigated as ECR catalysts; of which, WSe_2 nanoflakes exhibit the highest activity at an overpotential of 65 mV with an exceptional current density of 330 mA/cm^2 and an FE of 85% for CO generation, surpassing other electrocatalysts [89]. The excellent performance can be attributed to WSe_2 nanoflakes' much lower charge transfer resistance and low work function. DFT calculations showed that the formation of CO is kinetically favorable.

Further efforts have been made to enhance intrinsic activity, suppress the competing HER reaction and improve catalyst stability. It has been reported that doping and alloying different metal atoms with TMDs could enhance electrocatalytic efficiency by tuning the binding strengths of reaction intermediates and the reaction energy barrier. For instance, in one study, 5% niobium (Nb)-doped vertically aligned MoS_2 showed the largest CO_2 reduction current density of ca. 237 mA/cm^2 at the potential of −0.80 V, which was about two to three times higher than that of pristine and Ta-doped MoS_2 (Figure 5a). Nb-doped MoS_2 displayed an order of magnitude higher TOF for CO generation than pure MoS_2 at an overpotential of 20–150 mV and two orders of magnitude higher TOF for CO formation than Ag nanoparticles at the potential range of 0–650 mV (Figure 5b). The Nb atom could facilitate rapid CO release from the TMD edge, which remarkably increased ECR efficiency [87]. Theoretical calculation elucidated that there is a linear scaling relationship between the adsorption energies of the crucial intermediates, including COOH*, *CHO and *CO. It means that the stabilities of these intermediates are closely related, which causes a persistent overpotential for ECR. Theoretically, to improve ECR activity, breaking the linear scaling relationship between the binding energies of intermediates would be a good solution. Norskøv et al. have revealed that if the intermediates bind to different active sites,

the linear scaling relation can be broken at the edge site of MoS_2 and $MoSe_2$, which can increase ECR activity. They further showed that the doped S edge of MoS_2 can meet this requirement with *CO bonding on the doped metal atoms and *COH, *CHO and *COOH binding on the S sites [130]. Therefore, the binding energies of these three intermediates are higher than that of CO*, suggesting the breaking of the linear scaling relationship.

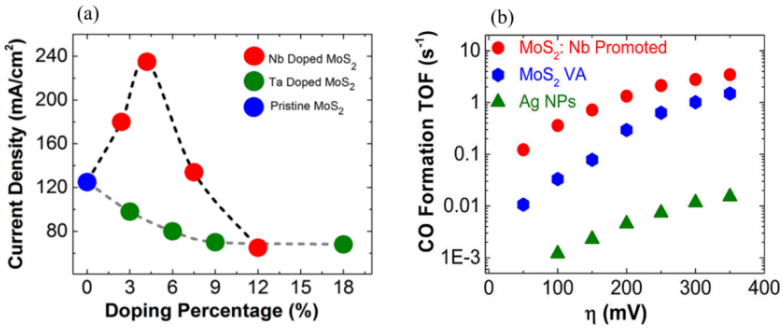

Figure 5. (**a**) Current density as a function of dopant percentage for Nb doped and Ta doped MoS_2 samples. (**b**) Calculated CO formation TOF at different applied overpotentials for 0.5% Nb-doped MoS_2, pristine VA-MoS_2 and Ag nanoparticles. Reprinted from [87], Copyright (2017), with permission from American Chemical Society.

Among four different TMD materials, MoS_2, $MoSe_2$, WS_2 and WSe_2, WSe_2 exhibits good CO selectivity because of its lower work function and charge transfer resistance. Metal doping is also an effective way to improve ECR performance of TMD materials. More importantly, breaking the linear scaling relationship between the binding energies of intermediates will be a good strategy for designing excellent TMD catalysts.

3.4. MOF Materials

MOFs are a new type of porous material with metal ions or clusters coordinated with organic ligands. Due to their high porosity, large specific surface area and flexible structure, MOFs have been applied in electrocatalytic research recently [43,132]. However, some disadvantages, such as poor conductivity and less active centers, hamper their electrocatalytic activity. Studies have shown that low-dimensional MOFs can achieve high electrocatalytic performance because MOF nanosheets can expose more active atoms and exhibit excellent electron transfer. Moreover, the metal atoms, ligand and the connection of metal centers with ligands also play vital roles in the electrocatalytic activity of MOFs. Kornienko et al. synthesized a thin film cobalt–porphyrin MOF on a carbon substrate. The FE of this sample was 76% at −0.70 V vs. RHE for CO_2 conversion to CO. In addition, it possessed a low Tafel slope of 165 mV/decade and the electrocatalytic stability was excellent [90]. A Zn MOF synthesized by ionic exchange of Zn nodes with adsorbed Ni salts achieved an FE of 71.9% for CO at 10.48 mA/cm^2 under the potential of −0.89V vs. RHE [91]. Zhang et al. prepared a series of transition-metal-based MOF electrocatalysts by using phthalocyanine (Pc), which can convert CO_2 to CO efficiently [92]. Under controlled potential electrolysis tests of different samples in CO_2-saturated solution, the Co-based MOF exhibited the lowest onset potential and largest current density (Figure 6a). Remarkably, Co-based MOF also showed the largest CO current density in a wide potential range (Figure 6b). Moreover, Co-based MOF exhibited 99% FE of CO formation under the potential of −0.80 V, as shown in Figure 6c,d, demonstrating that Co-based MOF is the best catalyst for CO_2 conversion to CO among others. DFT calculations suggested that the rate-limiting step for CO_2 conversion to CO had the lowest Gibbs energy change (Figure 6e). As shown in the inset of Figure 6e, the adsorption energy of *COOH on N and C sites was 0.95 and 0.90 eV,

which is much larger than that of −0.1 eV on the Co site, indicating that metal center is the most stable adsorption site. Moreover, two linear relationships disclosed a volcano curve (Figure 6f) in which the location of Co-based MOF is closest to the volcano peak. Therefore, it shows the best intrinsic activity for ECR into CO.

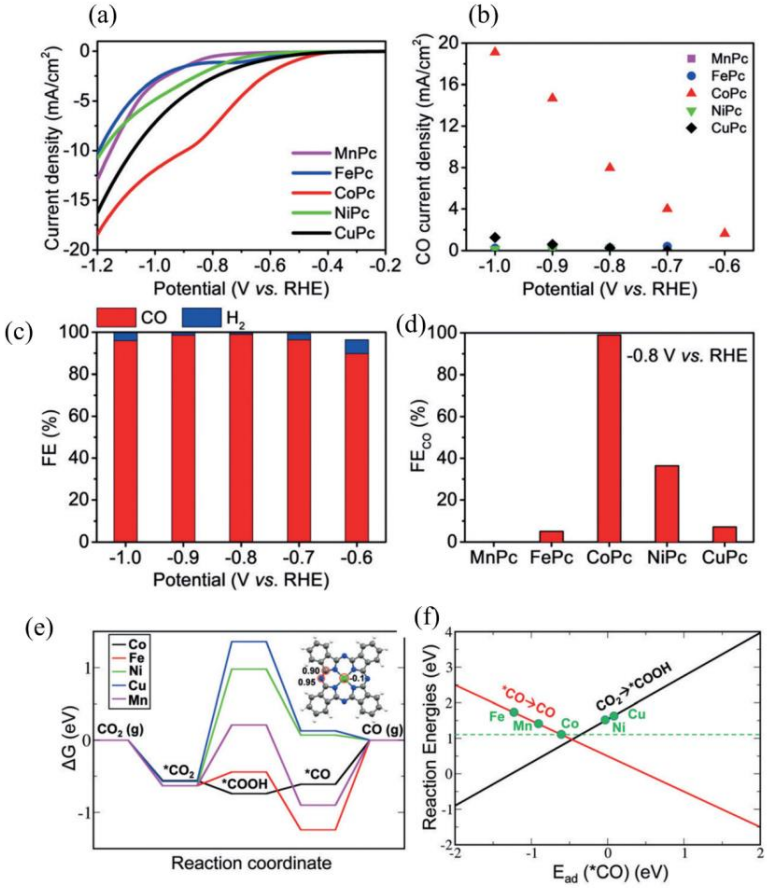

Figure 6. (**a**) Linear-sweep voltametric (LSV) tests in CO_2-saturated electrolyte. (**b**) CO current density of MePcs at various potentials. (**c**) Faradaic efficiency of CO and H_2 formation at different potentials for the CoPc sample. (**d**) Faradaic efficiency of CO formation at −0.8 V versus RHE for the different MePc samples. (**e**) The calculated free-energy diagram for all the MePc electrodes. The inset shows the adsorption energy of *COOH (unit eV) on different sites of CoPc. (**f**) Fitted *CO desorption and *COOH formation trends over the five MePc electrodes. Reprinted from [92], Copyright (2018), with permission from Wiley.

Recently, Perfecto-Irigaray et al. developed Cu-based MOF by doping metals (Zn, Pd and Ru) into HKUST-1 with different ratios [133]. They reported that the Ru-doped sample (10 wt.% Ru) showed an FE of 47.2% for methanol and ethanol generation, while other

metal-doped samples performed worse compared to the pristine HKUST-1. Nevertheless, all doped samples exhibited increased ethanol selectivity. This is ascribed to the formation of C–C bonds on metal sites that boost the formation of C_2 or C_3 intermediates, which are finally converted into alcohol or other high-carbon products. Very recently, 2D copper tetrahydroxyquinone conductive MOF (Cu-THQ) was reported for ECR at a low overpotential. Cu-THQ nanoflakes with an average particle size of 140 nm showed the largest current density of about 173 mA/cm^2 under −0.45 V vs. RHE, an average Faradaic efficiency FE_{CO} of about 91% and a remarkable TOF of 20.82 s^{-1}. Spectroscopic characterization and DFT calculations uncovered the importance of reduced Cu^+ during ECR, which was reversibly oxidized to Cu^{2+} after the reaction [134].

Overall, the metal atoms, ligand and the connection of metal center with ligand of MOF materials can determine electrocatalytic activity. Doping of a different metal to the original MOF materials, on the other hand, could either increase or decrease ECR activity.

3.5. Metal Oxide Nanosheets

Metal/metal oxide composites and oxide-derived metal have also been developed as ECR electrocatalysts with high performance [33,135,136]. Nevertheless, metal oxides still suffer problems such as instability and poor conductivity. It has been demonstrated that low-coordinated surface metal cations can be beneficial for CO_2 adsorption during ECR. First principles calculation revealed that both the density of states (DOS) and the charge density around the conduction band edges can be greatly enhanced [137]. Therefore, faster carrier transport along the 2D ultrathin layer during ECR can be expected. One excellent example is the ultrathin Co_3O_4 layers, with thicknesses of 1.72 nm and 3.51 nm, synthesized by fast-heating treatment [93]. The ultrathin Co_3O_4 layer exhibited higher DOS at the conduction band edges than the bulk structure (Figure 7a,b). Moreover, the charge density of the ultrathin Co_3O_4 layer around the conduction band edge was larger and more delocalized than the bulk Co_3O_4 (Figure 7c,d). These changes can be beneficial for faster carrier transport, thus accelerating ECR. Co_3O_4 layers with 1.72 nm thickness displayed a maximum current density of 0.68 mA/cm^2 and FE of 64.3% for formate production at −0.88 V vs. the saturated calomel electrode (SCE) (Figure 7e,f). Figure 7g indicates that the electrochemically active surface area (ECSA) increased with the decrease in thickness from bulk to 1.72 nm, which clearly evidences the close relationship between structure and activity. The intrinsic activity of Co_3O_4 with 1.72 nm thickness was over 1.5 times higher than the 3.51 nm thick Co_3O_4 layers and 20 times higher than the bulk structure (Figure 7h).

Moreover, the authors elucidated an atomic-level relationship between oxygen vacancies and ECR performance by constructing a model of oxygen vacancies confined in atomic Co_3O_4 single-unit cell layers [94]. DFT calculations uncovered that the main defect was oxygen (II), and X-ray absorption fine structure spectroscopy (XAFS) and X-ray photoelectron spectroscopy (XPS) indicated the distinct oxygen vacancy concentration. CO_2 adsorption isotherms demonstrated that the presence of oxygen (II) vacancy can promote CO_2 adsorption, while DFT calculations verified that oxygen (II) vacancy benefits spontaneous HCOO* desorption and prevents catalyst deactivation. More importantly, oxygen (II) vacancy facilitated the rate-limiting proton transfer step by stabilizing the HCOO* intermediate, which was confirmed by the drop of the activation energy barrier from 0.51 to 0.40 eV. This may also improve ECR kinetics because of the decreases in onset potential from 0.81 to 0.78 V vs. SCE and Tafel slope from 48 to 37mV dec^{-1}. Thus, oxygen (II)-vacancy-rich Co_3O_4 nanosheets (0.84 nm) exhibited a current density of about 2.7 mA/cm^2 with 85% formate selectivity for 40 h, which is promising for an ECR electrocatalyst. The researches further prepared a Co-based nanosheet with a thickness of only four atoms (about 0.84 nm) via solvothermal growth. The partial oxidation of the four-atom-thick Co layer can be formed on its surface by controlling the reaction time [28]. Interestingly, the four-atom-thick Co sheets exhibited great potential in ECR because the thinner 2D structures presented more surface-active sites and higher electrical conductivity. In LSV experiments, the partially oxidized four-atom-thick Co layers displayed a distinct CO_2 reduction peak at −0.85 V

vs. SCE with a current density of 10.59 mA/cm^2. It was a performance enhancement by about 10, 40 and 260 times in comparison with Co four-atom-thick layer without oxidation, oxidized bulk Co and unoxidized bulk Co, respectively. More importantly, the partially oxidized four-atom-thick Co layers showed great stability with a current density of 10 mA/cm^2 over 40 h and a high FE for formate generation of about 90% under a low overpotential of 0.24 V. Such a noticeable improvement can be partly attributed to the increase in ECSA. Another reason is that the partially oxidized four-atom-thick Co layer (atomic Co_3O_4) further increased their intrinsic activity and selectivity compared with pristine four-atom-thick Co layer.

Zhang's group prepared mesoporous SnO_2 nanosheets by a facile combination of hydrothermal reaction and calcination on carbon cloth [95]. As shown in Figure 8a,b, dense SnO_2 nanosheets grew uniformly on carbon cloth, and these nanosheets also contained numerous pores. The study showed a high partial current density of about 50 mA/cm^2 at −1.6 V vs. Ag/AgCl, with a high Faradaic efficiency of about 87% for formate generation, which outperformed most gas diffusion electrodes (Figure 8c,d). After electrolysis for 24 h, the current density and FE of formate were still stable (Figure 8e). Moreover, Figure 8f indicates that the current density also remained unchanged after folding or twisting the electrode 10 times. The excellent performance can be attributed to the following factors: Firstly, the SnO_2 nanosheet could provide intrinsically active sites for ECR; secondly, the highly porous structure could increase the specific surface area, which facilitated charge and mass transfer during ECR; the third reason is that the robustness of the hierarchical structures ensured high stability of the electrocatalyst during long-term use.

Therefore, metal oxide nanosheets mainly produce formate during ECR. The low-coordinated surface metal cations can be active centers for ECR. Ultrathin metal oxides exhibit higher DOS at the conduction band compared to the bulk structure. The charge density is more delocalized, which benefits the carrier transport. In addition, building oxygen vacancy could also increase ECR performance by improving the reaction kinetics.

3.6. Two-Dimensional Materials Incorporated Single-Atom Catalysts

Single-atom catalysts (SACs) have enormous advantages in electrocatalysis in terms of 100% atom utilization and intriguing electronic structures [138,139]. The traditionally supported nanoparticles or clusters exhibit structural irregularities on the nanoparticle surface. The surface reactivity has a close relationship with surface free energy, and the ratio between fully coordinated surface atoms and the number of vacancies distinguishes the reactivity of atoms with identical chemical compositions but different positions [140–142]. Therefore, the conventional clusters with different surface reactivities can result in poor product selectivity. SACs are different from clusters because the surface free energy is homogeneous and the number of vacancies in the nearest neighbors is the same. Thus, SACs can show good stability and special intrinsic activity [143]. Single-atom catalysts exhibit uniform active sites as ideal catalysts; however, one major challenge for SACs is synthesis because SACs are unstable and can agglomerate quickly due to high surface energy. Furthermore, the supported structures in the neighboring environment increase the heterogeneity of SACs' active sites, and thus uniform activity cannot be easily achieved. However, 2D materials can be utilized as supports to improve the uniformity and performance of SACs in electrocatalytic reactions [144,145]. Studies have evidenced that 2D materials, such as MoS_2, graphene and MXene, could stabilize the SACs and maintain their single-atom state [96,146–151]. For instance, Back et al. investigated single transition metal atoms anchored on graphene with single or double vacancies as ECR catalysts by DFT calculations [152]. They suggested that many SACs exhibit high selectivity for ECR over the competitive HER because of favorable adsorption of *COOH or *OCHO over *H on the catalysts (Figure 9). SACs for CH_3OH production, Ni and Pt, showed limiting potentials of −0.41 V and −0.27 V, respectively, while Os and Ru systems had the same limiting potential (−0.52 V) for CH_4 production. The activity improvement of SACs can be partially attributed to the unique electronic structure of the SACs and orbital interaction.

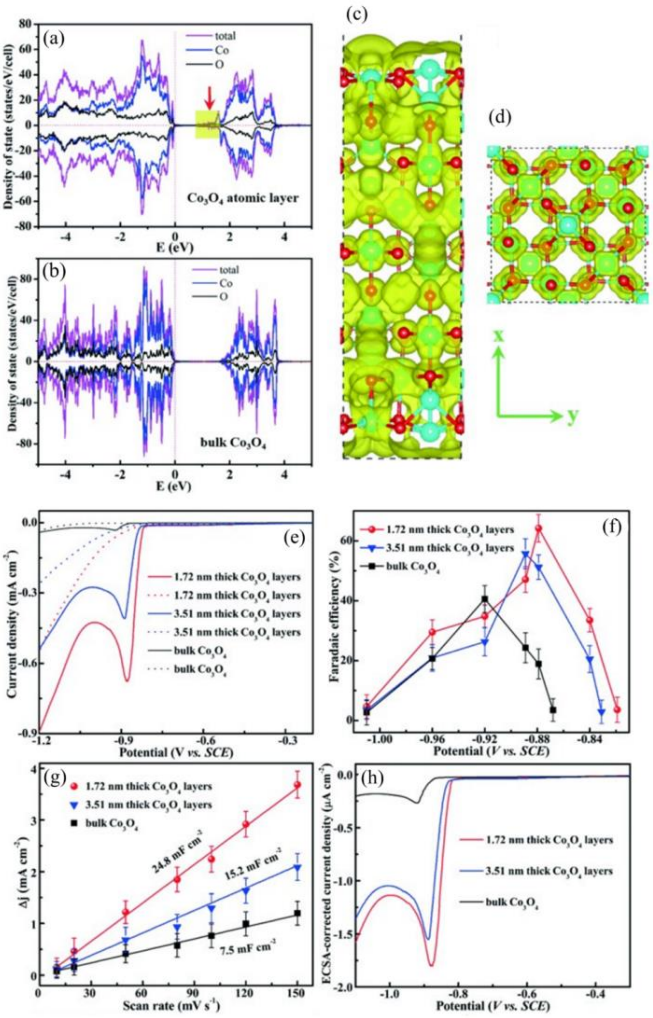

Figure 7. The calculated DOS for (**a**) Co_3O_4 atomic layer slab with a thickness of 1.72 nm and (**b**) bulk Co_3O_4 slab. The yellow shaded parts represent the increased DOS at the conduction band edges of Co_3O_4 atomic layer. The partial charge density around the conduction band minimum of (**c**) Co_3O_4 atomic layer slab and (**d**) bulk Co_3O_4 slab, in which yellow refers to charge density contour with the isovalue of 0.0001 e/bohr^3. Cyan represents Co and red represents O atoms. Electroreduction of CO_2 to formate by Co_3O_4 with different thicknesses: (**e**) LSV curves in the CO_2-saturated (solid line) and N_2-saturated (dashed line) 0.1 M $KHCO_3$ aqueous solutions. (**f**) Faradaic efficiencies for formate at each applied potential for 4 h. (**g**) Charging current density differences plotted against scan rates. (**h**) ECSA—corrected current densities vs. applied potentials. Reprinted from [93], Copyright (2016), with permission from Wiley.

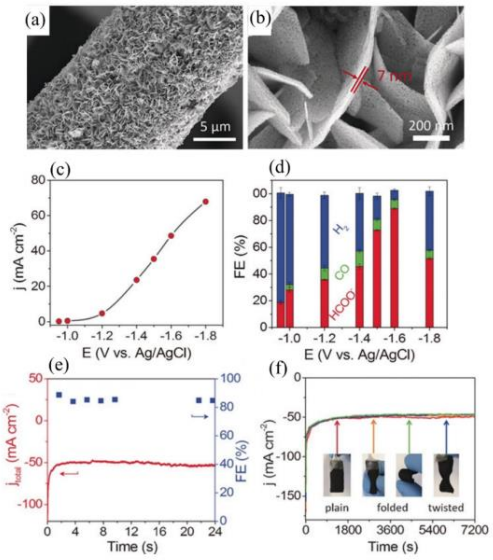

Figure 8. (**a**,**b**) The scanning electron microscope (SEM) images of porous SnO_2 nanosheets on carbon cloth (SnO_2/CC). (**c**) Current density of the SnO_2/CC electrode in CO_2-saturated 0.5 M $NaHCO_3$ solution at different applied potentials. (**d**) Corresponding FE for formate, CO and H_2. (**e**) i–t curve and FE for formate of SnO_2/CC electrode in CO_2-saturated 0.5 M $NaHCO_3$ solution at an applied potential of −1.6 V for 24 h. (**f**) i–t curves of the SnO_2/CC electrode at −1.6 V after folding or twisting 10 times. Reprinted from [95], Copyright (2017), with permission from Wiley.

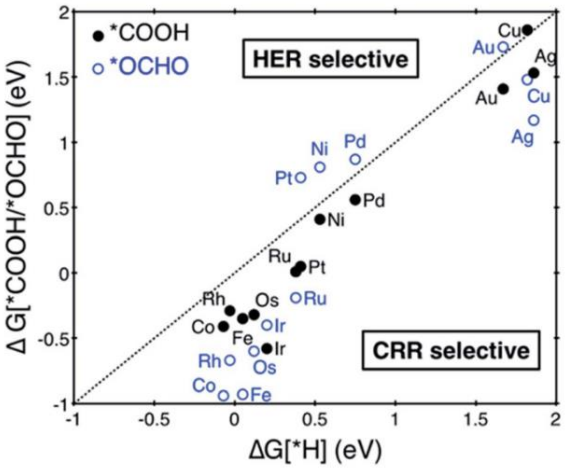

Figure 9. Free energy change in the first protonation step in ECR and HER on different SACs. Catalysts below the dotted parity line are ECR selective. Reprinted from [152], Copyright (2017), with permission from Royal Society of Chemistry.

Constructing a 3*d* transition metal-Nitrogen atom (M–N_x) system based on 2D materials for ECR is prevailing. Huan et al. investigated activity and selectivity of N-doped Fe–N_4 and Fe nanoparticles' moieties. They reported that samples with Fe–N_4 active sites had an FE of 80% for CO generation, but Fe nanoparticles could mostly only produce H_2 [97]. Zhang et al. synthesized Fe single atoms anchored on N-doped graphene and revealed that Fe–N_4 with an Fe^{2+} oxidation state was the active site for ECR [98]. They also recognized that N dopants on the graphene substrate can be beneficial for ECR. However, there are some debates on the active sites and the corresponding ECR mechanisms on Fe SACs. For instance, Zhang et al. synthesized single Fe atoms anchored on N–doped graphene by prolonged thermal pyrolysis [99]. The SAC exhibited a high FE of about 97.0% for CO production under a low overpotential of 0.35 V. The excellent performance resulted from the presence of highly efficient dispersed Fe–N_5 active sites. Theoretical calculations disclosed that a fifth N atom coordinated to Fe^{3+} to form Fe–N_5 moieties, where the additional axial pyrrolic N ligand further depleted the electron density of Fe 3*d* orbitals and reduced the π back-donation of Fe–CO bonding, which resulted in rapid CO desorption and high selectivity for CO formation.

Zhang et al. reported on single Fe atoms confined in carbon foams forming Fe–N_4 active sites [100]. However, they also detected an Fe^{3+} state in their samples because Fe^{2+} can be oxidized to Fe^{3+} when the samples are exposed to air, but the difference was not distinguishable in ECR. Gu et al. investigated single Fe atoms loaded on N-doped carbon with an overpotential as low as 0.08 V for CO production [101]. They confirmed the persistent presence of Fe^{3+} in the whole ECR process by in situ X-ray absorption near edge structure (XANES) measurements. Further studies indicated that Fe^{3+}–N–C showed better performance for CO formation than that of Fe^{2+}–N–C because of weaker CO absorption on the Fe^{3+} sites. Yang et al. prepared a N-anchored Zn single-atom catalyst on carbon [102]. From HAADF-STEM characterization, it can be clearly seen that an individual single Zn atom was supported on carbon (Figure 10a), and extended X-ray absorption fine-structure (EXAFS) spectra demonstrated the existence of a Zn-N_4 moiety (Figure 10b). The catalyst could reduce CO_2 to CO with high selectivity and a high FE of about 95% under the potential of −0.43 V (Figure 10c). It also exhibited remarkable durability over 75 h without any FE_{CO} decay (Figure 10d). Further experimental work and DFT calculations suggested that the remarkable activity can be attributed to the existence of Zn–N_4, which was the main active site for ECR and had a low free energy barrier for the rate-limiting step of *COOH formation. Zhao et al. synthesized a single Ni atom loaded on graphene oxide. The catalyst showed an FE for CO production of 96.5% at a potential of −0.63V, with a TOF of 325.9/h [103].

Yang et al. prepared a single Ni atom catalyst supported on N-doped graphene. The TOF reached 14,800/h, and the FE of CO was 97% at a potential of −0.61 V [104]. The catalyst also displayed great stability with very stable electrocatalytic activity for 100 h. Liu et al. constructed a model SAC with precise structure using two-steps by linking Ni–TAPc to CNTs and by C–C coupling [105]. This model Ni SAC exhibited excellent activity, selectivity and durability in CO_2 conversion to CO. Experimental study suggested that Ni^+ in Ni–TAPc is highly active for CO_2 activation and is the catalytically active site. In addition, the study suggested that $*CO_2^-$ + H^+ to *COOH is the rate-determining step. Gong et al. prepared a series of single-atom Ni catalysts (Ni–SA–N_x–C) with different N coordination numbers by controlling the pyrolysis temperature [106]. Figure 11a,b clearly indicates the existence of isolated Ni atoms from TEM characterizations. The homogeneous distribution of Ni, N and C is demonstrated by energy dispersive spectroscopy (EDS) mapping (Figure 11c). It was found that the sample with Ni–N_2 moiety showed a higher current density than Ni–N_3–C and Ni–N_4 in CO_2-saturated 0.5 M $KHCO_3$, indicating the best activity of NiSA–N_2–C among all three SACs (Figure 11d). In addition, it exhibited a maximum FE_{CO} of 98% at −0.8 V, which is also the highest (Figure 11e). The TOF for CO production on NiSA–N_2–C reached 3467 h^{-1} at the potential of −1.0 V, which is much higher than those of NiSA–N_4–C and NiSA-N_3-C (Figure 11f), elucidating that the coordi-

nation environment plays a crucial role in ECR performance. The current density and FE for CO generation were almost unchanged on the NiSA–N_2–C catalyst after electrolyzation for 10 h at the potential of −0.8 V vs. RHE (Figure 11g), demonstrating excellent stability. DFT calculations suggested that the reaction path is proton-coupled electron transfer (Figure 11h). The low N coordinated single-atom Ni sites in NiSA–N_2–C are beneficial for the formation of *COOH intermediate, thereby enhancing ECR activity (Figure 11i).

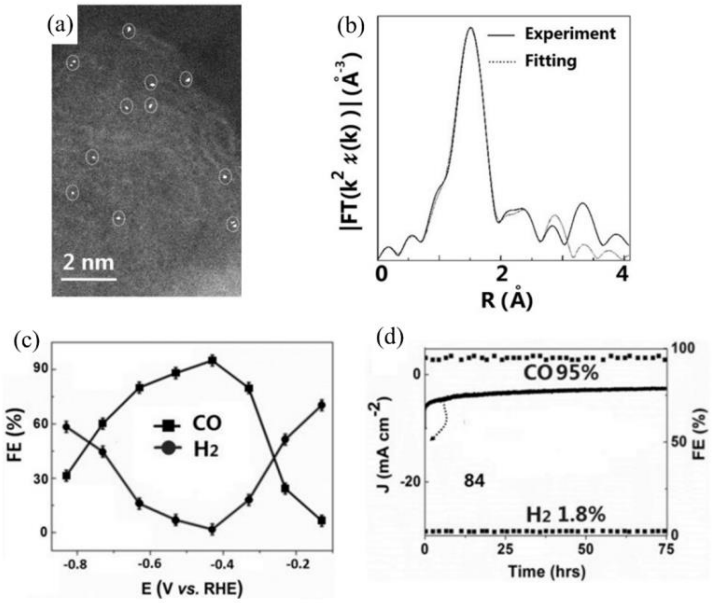

Figure 10. (**a**) Typical high-angle annular dark-field scanning transmission electron microscope (HAADF-STEM) image of the optimal ZnN_x/C catalyst. The circles indicate the individual Zn atoms. (**b**) A typical fitting curve of the EXAFS signal in R-space for the adsorbed ZnN_x/C catalyst. (**c**) FEs of CO and H_2 at various applied potentials on ZnN_x/C catalyst. (**d**) Long-term stability of ZnN_x/C at a potential load of −0.43 V and the corresponding FEs of CO and H_2. Reprinted from [102] Copyright (2018), with permission from Wiley.

Han et al. designed a free-standing ultrathin 2D SAC by self-assembly of a Co–porphyrin complex, which showed a CO production FE of 96% under an overpotential of 0.5 V [107]. They indicated that the improvement of activity was attributed to nitrogen coordination from the bottom layer, which increased the d_z energy level of the Co atoms. Jiang et al. investigated a series of SACs supported on graphene nanosheets with different defect structures [153]. Ni SAC exhibited a CO formation FE of 95% under an overpotential of 0.55 V and excellent stability. Experimental study and theoretical calculations suggested that Ni sites with slightly larger vacancies benefit CO_2 conversion to CO by decreasing CO desorption barrier. Recently, Zheng et al. investigated ECR performance of Cu SACs on a N-doped graphene matrix with a highly exposed and coordinatively unsaturated Cu–N_2 center, as shown in Figure 12a [108]. Experimental work showed an onset potential of −0.33 V and FE for CO production of about 81% under a low potential of −0.50 V vs. RHE, obviously higher than the sample with Cu–N_4 moiety (Figure 12b). DFT calculations manifested that Cu–N_2 centers can facilitate CO_2 activation and accelerate electron transfer from Cu–N_2 sites to *CO_2, which can greatly improve *COOH generation and the overall

ECR activity. Jiao et al. investigated a single Cu atom catalyst anchored on g-C_3N_4 as an electrocatalyst for CO_2 conversion to various hydrocarbons [154]. A slightly negative shift of photon energy demonstrated that N accepts extra charges from the Cu atom (Figure 12c). The authors reckoned that the *d*-orbital of Cu can be efficiently elevated by coordination with the g–C_3N_4 framework, enhancing the adsorption of carbonaceous intermediates. Therefore, Cu–g–C_3N_4 had better ECR activity with lower onset potential and exhibited a higher C_2 product rate than conventional Cu supported on nitrogen-doped graphene (Figure 12d).

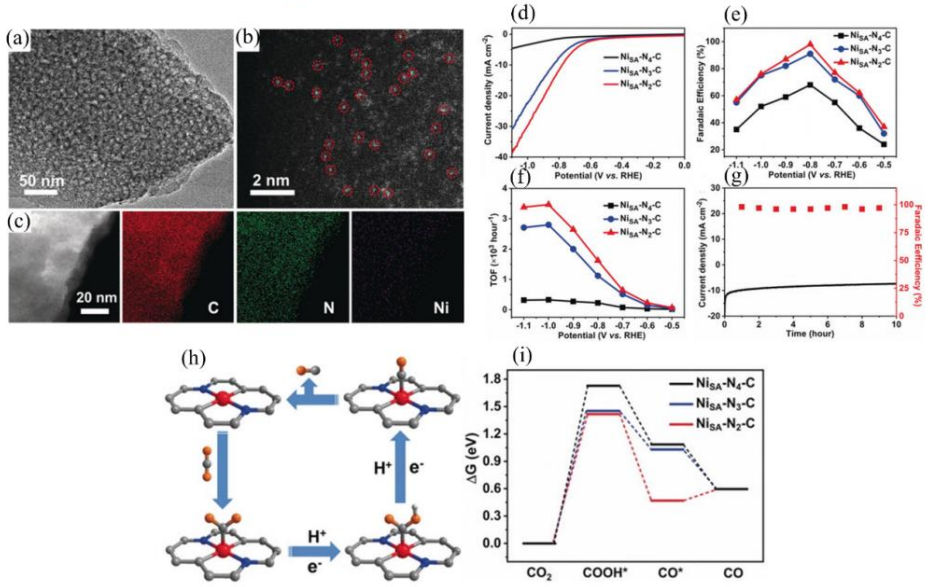

Figure 11. (**a**) Transmission electron microscope (TEM) and (**b**) HAADF-STEM images of NiSA–N_2–C. (**c**) EDS mapping of Ni, N and C elements in NiSA–N_2–C. (**d**) LSV curves in CO_2-saturated 0.5 M $KHCO_3$ electrolyte. (**e**) FEs of CO at different applied potentials. (**f**) The corresponding TOFs of CO production over NiSA–N_x–C. (**g**) Stability of NiSA–N_2–C at −0.8 V during 10 h. (**h**) Proposed reaction paths for ECR with NiSA–N_2–C as an example. (**i**) Free-energy diagram of CO_2 reduction to CO over NiSA–N_x–C catalysts. Reprinted from [106], Copyright (2020), with permission from Wiley.

Single-metal-atom-loaded 2D materials are a class of very promising catalysts for ECR due to their high atom utilization and catalytic activity. Their activity is determined by the type of metal atom and the electronic structures of the metal atom. Furthermore, the coordination number of metal atoms can be tuned by the 2D materials' support, which can further optimize the activity and selectivity of the SACs.

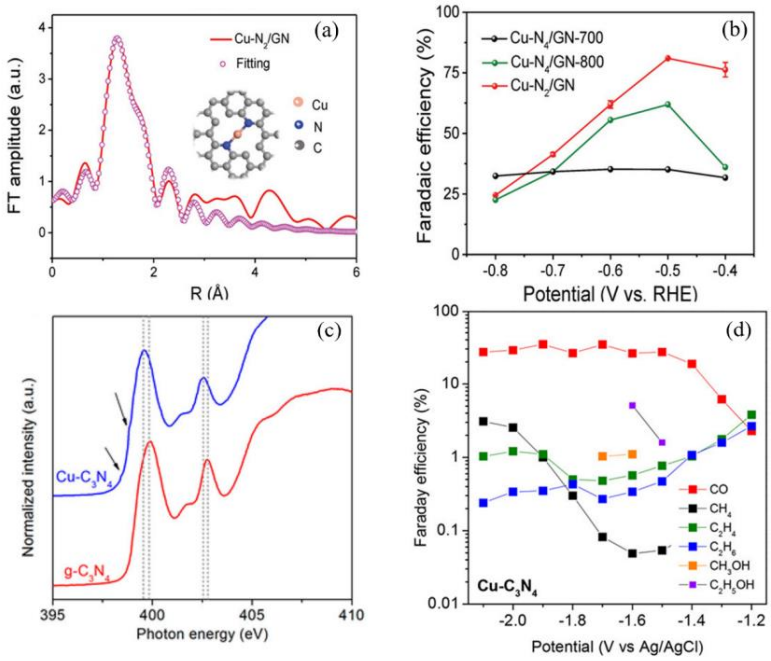

Figure 12. (**a**) Fourier transformed (FT)-EXAFS fitting results of Cu–N_2/GN. (**b**) CO FE of Cu–N_4/GN–700, Cu–N_4/GN–800 and Cu–N_2/GN. Reprinted from [108], Copyright 2020, with permission from Wiley. (**c**) Nitrogen K-edge NEXAFS of Cu–C_3N_4 and pure g–C_3N_4. Arrows show the weak shoulders in the N K-edge assigned to the Cu–N interaction. Dotted lines show the channels of photon energy in the two samples. (**d**) Measured Faradaic efficiencies of various products on Cu–C_3N_4. Reprinted from [154], Copyright (2017), with permission from American Chemical Society.

4. The Design of Electrolyzers

Numerous ECR studies are based on H-cells because they can be used conveniently to evaluate the activity of catalysts due to their easy operation and adaptability to different electrode materials and configurations [155,156]. A typical H-cell electrolyzer contains two chambers that are separated by an ion exchange membrane. The counter electrode is in the anodic chamber, whereas the working electrode and reference electrode are in the cathodic chamber. During the ECR process, CO_2 is first dissolved in the liquid catholyte, such as $KHCO_3$ and $NaHCO_3$, and then transferred to the surface of the working electrode where ECR occurs. However, the thick diffusion layer and low solubility of CO_2 in water limit CO_2 mass transport to the catalyst surface, impeding its practical applications [157].

Commercial ECR application requires continuous operation to realize high production efficiency. A microfluidic reactor for ECR has been designed where the electrolyte can continuously flow through the electrolyzer [158,159]. The cathode and anode are separated by a very thin channel that is filled with flowing electrolytes. CO_2 is supplied from the back of the cathodic gas diffusion electrode (GDE), and ECR occurs when CO_2 reaches the surface of catalysts. The operation parameters, such as the composition and pH of the electrolyte, can be adjusted, which promotes ECR rates. GDEs are high-surface-area and porous electrodes. A typical GDE consists of a catalytic layer, a gas diffusion layer and a gas flow field. The structure and composition of GDE layers play a vital

role in the transport of reactants and products because the transport processes influence the accumulation or depletion of intermediates on the catalysts, which determine ECR performance [160,161]. Lim et al. prepared Sn electrocatalysts with dense tips (SnDT) GDE, showing formate productivity of 65 mg h^{-1}. It was stable for 72 h without changes in FE or current density [162]. A 2D nanosheet Cu-loaded GDE achieved the highest partial current density of 131 mA cm^{-2} for acetate production [163]. Although high current density was realized, the microfluidic reactor still suffered product crossover, where the reduction of oxygen diffused to the cathode and the reoxidation of cathodic products diffused to the anode, decreasing the overall energy efficiency and productivity.

The membrane electrode assembly (MEA) electrolyzers have been exploited to solve problems of the microfluidic reactors. The catalytic layer of cathodic GDEs is in direct contact with the polymer electrolyte membranes. MEAs can decrease ohmic losses and prevent the poison of cathode catalysts by impurities through removing catholyte between the membrane and GDE. As a result, MEAs can exhibit excellent stability and high energy efficiency [164]. Gas and liquid products flow out of the cathode flow plate with little diffusion into catholyte through the membrane, resulting in high concentration liquid product. Cobalt phthalocyanine (Co-Pc) has been widely studied for ECR to CO in both immobilized and homogeneous forms and was also used in an MEA system with FE of CO >90% over 8 h at 50 mA cm^{-2} [165]. Gabardo et al. designed an MEA electrolyzer that achieved an FE of ~80% for higher carbon products such as ethylene, ethanol, acetate and 1-propanol with current densities >100 mA cm^{-2} for 100 h [164].

5. Conclusions and Perspectives

Electrochemical reduction reactions are a promising strategy to convert CO_2 into valuable fuels and chemical products, which can offer potential technological solutions for energy problems and greenhouse effects. An effective electrocatalyst is the key to the potential deployment of commercial ECR processes. In this contribution, we review a series of 2D materials, including metal, graphene-based materials, TMDs, MOFs materials, metal oxide nanosheets and 2D materials incorporated with single atoms as ECR catalysts. Compared to the conventional metal-based electrocatalysts, 2D materials show unique physicochemical properties and electronic structures benefiting ECR activity.

Nevertheless, there are still challenges in the design and synthesis of 2D electrocatalysts for ECR. To date, most ECR catalysts can only produce C_1 products, especially CO, while producing more valuable products, such as C_2 and C_3 products, is desired. In general, the intrinsic activity can be modified in various ways such as doping, constructing special structures and morphologies, etc. Meanwhile, the choices of different classes of 2D materials are important for producing specific products. Strategies, such as constructing composite electrocatalyst materials and surface engineering of electrocatalysts, could be employed. Composite electrocatalyst materials could have different properties and catalytic performance in comparison with individual components due to synergistic effects. They could possess excellent properties for ECR such as better conductivity, high specific surface area, more active sites, better transport property and high durability. Another strategy is surface engineering of electrocatalysts by synthesizing nanotubes, nanosheets, nanospheres, isolated single atoms and defects. These properties are beneficial for effective contact for electrolyte ions and adsorption and desorption of intermediates. It is worth noting that single metal atoms anchored on the surface of 2D materials as SACs have rather high efficiency in ECR. However, the synthesis of SAC loaded on 2D materials is still a challenge, and key aspects, including suitable mononuclear metal complex precursors and stabilization of single metal atoms on the 2D materials, should be considered. Future research opportunities could be to develop new 2D materials such as MXenes and COFs.

Combining theoretical calculation and experimental work is necessary to obtain a fundamental understanding on the design and synthesis of 2D electrocatalysts. Although theoretical calculations are conducted with simplified models under idealized conditions, they could always be beneficial for revealing the reaction mechanism and providing guid-

ance for design principles. For instance, breaking the scaling relationships between adsorption energies of different intermediates is of great significance to improve the activity of catalysts, which can be revealed from theoretical calculations. Similarly, to mitigate catalyst deactivation in ECR, it is necessary to understand the deactivation mechanisms. Theoretical models could be constructed to predict the intermediates which affect the stability of electrocatalysts. Finally, rapid development of characterization techniques, especially in situ spectroscopy, can greatly promote the development of catalysts of ECR. In situ spectroscopy can investigate catalytic reactions under reaction conditions and provide insights into the true active sites and reaction mechanisms. Through in situ techniques, such as infrared spectroscopy, Raman spectroscopy, X-ray absorption spectroscopy, X-ray photoelectron spectroscopy, mass spectrometry, etc., crucial issues in ECR, including identifying reaction intermediates, active sites and reaction pathways, can be resolved.

H-type cells are widely used in ECR. The current density of an H-type cell is limited to tens of milliamps, which is far from industrial application due to limited CO_2 solubility and energy loss. The design of microfluidic flow cells has made great progress recently. For example, the GDE and MEA electrolyzers can effectively tune reaction conditions and local environments in ECR. GDEs utilize a porous catalyst layer along with diffusion media, which can promote reactant transport. Thus, high current density can be realized, and transport losses can be effectively avoided. In the flow cell, higher carbon products are favored at high pH values, which can be hardly realized in an H-type cell. Flow cells and MEA make the separation of products convenient. These advantages could effectively accelerate the large-scale application of ECR at the industrial level.

It has been demonstrated that 2D nanomaterials possess great potential for ECR. Nevertheless, most of the 2D materials discussed in this review are still far from practical application. It is still demanding to synthesize 2D electrocatalysts with excellent performance at a large scale. Therefore, it is important to narrow the gap between laboratory- and commercial-scale production. Currently, some techniques, such as strip and salt–temperature, have been applied in the large-scale synthesis of 2D materials, but scalable routes to prepare ultrathin nanosheets remain to be developed.

Author Contributions: Conceptualization, S.L., F.L. and Z.Y.; investigation, S.L. and Z.Y.; writing—original draft preparation, S.L. and Z.Y.; writing—review and editing, S.L., F.L. and Z.Y.; funding acquisition, Z.Y.; supervision, F.L. and Z.Y. All authors have read and agreed to the published version of the manuscript.

Funding: This work was funded by the Norwegian Ministry of Education and Research.

Data Availability Statement: Not applicable.

Conflicts of Interest: The authors declare no conflict of interest.

References

1. Caldeira, K.; Wickett, M.E. Anthropogenic carbon and ocean pH. *Nature* **2003**, *425*, 365. [CrossRef] [PubMed]
2. Fu, Y.; Sun, D.; Chen, Y.; Huang, R.; Ding, Z.; Fu, X.; Li, Z. An amine-functionalized titanium metal-organic framework photocatalyst with visible-light-induced activity for CO_2 reduction. *Angew. Chem. Int. Ed.* **2012**, *51*, 3364–3367. [CrossRef]
3. Li, J.R.; Ma, Y.; McCarthy, M.C.; Sculley, J.; Yu, J.; Jeong, H.K.; Balbuena, P.B.; Zhou, H.C. Carbon dioxide capture-related gas adsorption and separation in metal-organic frameworks. *Coord. Chem. Rev.* **2011**, *255*, 1791–1823. [CrossRef]
4. Li, X.; Yu, J.; Jaroniec, M.; Chen, X. Cocatalysts for Selective Photoreduction of CO_2 into Solar Fuels. *Chem. Rev.* **2019**, *119*, 3962–4179. [CrossRef] [PubMed]
5. Rubin, E.S.; Davison, J.E.; Herzog, H.J. The cost of CO_2 capture and storage. *Int. J. Greenh. Gas Control* **2015**, *40*, 378–400. [CrossRef]
6. Keith, D.W.; Holmes, G.; St Angelo, D.; Heidel, K. A Process for Capturing CO_2 from the Atmosphere. *Joule* **2018**, *2*, 1573–1594. [CrossRef]
7. Drage, T.C.; Snape, C.E.; Stevens, L.A.; Wood, J.; Wang, J.; Cooper, A.I.; Dawson, R.; Guo, X.; Satterley, C.; Irons, R. Materials challenges for the development of solid sorbents for post-combustion carbon capture. *J. Mater. Chem.* **2012**, *22*, 2815–2823. [CrossRef]
8. Orr, J.F.M. CO_2 capture and storage: Are we ready? *Energy Environ. Sci.* **2009**, *2*, 449–458. [CrossRef]
9. Maginn, E.J. What to Do with CO_2. *J. Phys. Chem. Lett.* **2010**, *1*, 3478–3479. [CrossRef]

10. Ramdin, M.; de Loos, T.W.; Vlugt, T.J.H. State-of-the-Art of CO_2 Capture with Ionic Liquids. *Ind. Eng. Chem. Res.* **2012**, *51*, 8149–8177. [CrossRef]
11. Wang, J.Y.; Huang, L.; Yang, R.Y.; Wu, J.W.; Gao, Y.S.; Wang, Q.; O'Hare, D.; Zhong, Z.Y. Recent advances in solid sorbents for CO_2 capture and new development trends. *Energy Environ. Sci.* **2014**, *7*, 3478–3518. [CrossRef]
12. Yu, C.H.; Huang, C.H.; Tan, C.S. A Review of CO_2 Capture by Absorption and Adsorption. *Aerosol Air Qual. Res.* **2012**, *12*, 745–769. [CrossRef]
13. Inoue, T.; Fujishima, A.; Konishi, S.; Honda, K. Photoelectrocatalytic reduction of carbon dioxide in aqueous suspensions of semiconductor powders. *Nature* **1979**, *277*, 637–638. [CrossRef]
14. Halmann, M. Photoelectrochemical reduction of aqueous carbon dioxide on p-type gallium phosphide in liquid junction solar cells. *Nature* **1978**, *275*, 115–116. [CrossRef]
15. Li, W. Electrocatalytic Reduction of CO_2 to Small Organic Molecule Fuels on Metal Catalysts. In *Advances in CO_2 Conversion and Utilization*; ACS Symposium Series; ACS Publisher: Washington, DC, USA, 2010; Volume 1056, pp. 55–76. [CrossRef]
16. Kortlever, R.; Peters, I.; Koper, S.; Koper, M.T.M. Electrochemical CO_2 Reduction to Formic Acid at Low Overpotential and with High Faradaic Efficiency on Carbon-Supported Bimetallic Pd–Pt Nanoparticles. *ACS Catal.* **2015**, *5*, 3916–3923. [CrossRef]
17. Zafar, Q.; Mattisson, T.; Gevert, B. Integrated Hydrogen and Power Production with CO_2 Capture Using Chemical-Looping ReformingsRedox Reactivity of Particles of CuO, Mn_2O_3, NiO, and Fe_2O_3 Using SiO_2 as a Support. *Ind. Eng. Chem. Res.* **2005**, *44*, 3485–3496. [CrossRef]
18. Chen, X.; Wang, J.; Huang, C.; Zhang, S.; Zhang, H.; Li, Z.; Zou, Z. Barium zirconate: A new photocatalyst for converting CO_2 into hydrocarbons under UV irradiation. *Catal. Sci. Technol.* **2015**, *5*, 1758–1763. [CrossRef]
19. Ding, J.; Bu, Y.; Ou, M.; Yu, Y.; Zhong, Q.; Fan, M. Facile decoration of carbon fibers with Ag nanoparticles for adsorption and photocatalytic reduction of CO_2. *Appl. Catal. B Environ.* **2017**, *202*, 314–325. [CrossRef]
20. Wang, W.; Wang, S.; Ma, X.; Gong, J. Recent advances in catalytic hydrogenation of carbon dioxide. *Chem. Soc. Rev.* **2011**, *40*, 3703–3727. [CrossRef]
21. Shi, J.F.; Jiang, Y.J.; Jiang, Z.Y.; Wang, X.Y.; Wang, X.L.; Zhang, S.H.; Han, P.P.; Yang, C. Enzymatic conversion of carbon dioxide. *Chem. Soc. Rev.* **2015**, *44*, 5981–6000. [CrossRef]
22. Gong, Q.; Ding, P.; Xu, M.; Zhu, X.; Wang, M.; Deng, J.; Ma, Q.; Han, N.; Zhu, Y.; Lu, J.; et al. Structural defects on converted bismuth oxide nanotubes enable highly active electrocatalysis of carbon dioxide reduction. *Nat. Commun.* **2019**, *10*, 2807. [CrossRef] [PubMed]
23. Li, T.T.; Shan, B.; Xu, W.; Meyer, T.J. Electrocatalytic CO_2 Reduction with a Ruthenium Catalyst in Solution and on Nanocrystalline TiO_2. *ChemSusChem* **2019**, *12*, 2402–2408. [CrossRef] [PubMed]
24. Grodkowski, J.; Neta, P. Copper-Catalyzed Radiolytic Reduction of CO_2 to CO in Aqueous Solutions. *J. Phys. Chem. B* **2001**, *105*, 4967–4972. [CrossRef]
25. Agarwal, A.S.; Zhai, Y.; Hill, D.; Sridhar, N. The electrochemical reduction of carbon dioxide to formate/formic acid: Engineering and economic feasibility. *ChemSusChem* **2011**, *4*, 1301–1310. [CrossRef]
26. Pritchard, J.; Filonenko, G.A.; van Putten, R.; Hensen, E.J.; Pidko, E.A. Heterogeneous and homogeneous catalysis for the hydrogenation of carboxylic acid derivatives: History, advances and future directions. *Chem. Soc. Rev.* **2015**, *44*, 3808–3833. [CrossRef]
27. Zhu, Q.; Sun, X.; Yang, D.; Ma, J.; Kang, X.; Zheng, L.; Zhang, J.; Wu, Z.; Han, B. Carbon dioxide electroreduction to C_2 products over copper-cuprous oxide derived from electrosynthesized copper complex. *Nat. Commun.* **2019**, *10*, 3851. [CrossRef]
28. Gao, S.; Lin, Y.; Jiao, X.; Sun, Y.; Luo, Q.; Zhang, W.; Li, D.; Yang, J.; Xie, Y. Partially oxidized atomic cobalt layers for carbon dioxide electroreduction to liquid fuel. *Nature* **2016**, *529*, 68–71. [CrossRef]
29. Kaneco, S.; Katsumata, H.; Suzuki, T.; Ohta, K. Electrochemical reduction of carbon dioxide to ethylene at a copper electrode in methanol using potassium hydroxide and rubidium hydroxide supporting electrolytes. *Electrochim. Acta* **2006**, *51*, 3316–3321. [CrossRef]
30. Lu, Q.; Rosen, J.; Zhou, Y.; Hutchings, G.S.; Kimmel, Y.C.; Chen, J.G.; Jiao, F. A selective and efficient electrocatalyst for carbon dioxide reduction. *Nat. Commun.* **2014**, *5*, 3242. [CrossRef]
31. Durand, W.J.; Peterson, A.A.; Studt, F.; Abild-Pedersen, F.; Nørskov, J.K. Structure effects on the energetics of the electrochemical reduction of CO_2 by copper surfaces. *Surf. Sci.* **2011**, *605*, 1354–1359. [CrossRef]
32. Siahrostami, S.; Jiang, K.; Karamad, M.; Chan, K.; Wang, H.; Nørskov, J. Theoretical Investigations into Defected Graphene for Electrochemical Reduction of CO_2. *ACS Sustain. Chem. Eng.* **2017**, *5*, 11080–11085. [CrossRef]
33. Chen, Y.; Li, C.W.; Kanan, M.W. Aqueous CO_2 reduction at very low overpotential on oxide-derived Au nanoparticles. *J. Am. Chem. Soc.* **2012**, *134*, 19969–19972. [CrossRef]
34. Sui, S.; Wang, X.; Zhou, X.; Su, Y.; Riffat, S.; Liu, C.j. A comprehensive review of Pt electrocatalysts for the oxygen reduction reaction: Nanostructure, activity, mechanism and carbon support in PEM fuel cells. *J. Mater. Chem. A* **2017**, *5*, 1808–1825. [CrossRef]
35. Gattrell, M.; Gupta, N.; Co, A. A review of the aqueous electrochemical reduction of CO_2 to hydrocarbons at copper. *J. Electroanal. Chem.* **2006**, *594*, 1–19. [CrossRef]
36. Chernikov, A.; van der Zande, A.M.; Hill, H.M.; Rigosi, A.F.; Velauthapillai, A.; Hone, J.; Heinz, T.F. Electrical Tuning of Exciton Binding Energies in Monolayer WS_2. *Phys. Rev. Lett.* **2015**, *115*, 126802. [CrossRef] [PubMed]

37. Wang, H.; Yuan, H.; Sae Hong, S.; Li, Y.; Cui, Y. Physical and chemical tuning of two-dimensional transition metal dichalcogenides. *Chem. Soc. Rev.* **2015**, *44*, 2664–2680. [CrossRef]
38. Wang, H.; Chen, Y.; Hou, X.; Ma, C.; Tan, T. Nitrogen-doped graphenes as efficient electrocatalysts for the selective reduction of carbon dioxide to formate in aqueous solution. *Green Chem.* **2016**, *18*, 3250–3256. [CrossRef]
39. Ao, C.; Feng, B.; Qian, S.; Wang, L.; Zhao, W.; Zhai, Y.; Zhang, L. Theoretical study of transition metals supported on g-C_3N_4 as electrochemical catalysts for CO_2 reduction to CH_3OH and CH_4. *J. CO2 Util.* **2020**, *36*, 116–123. [CrossRef]
40. Zhi, X.; Jiao, Y.; Zheng, Y.; Qiao, S.Z. Impact of Interfacial Electron Transfer on Electrochemical CO_2 Reduction on Graphitic Carbon Nitride/Doped Graphene. *Small* **2019**, *15*, e1804224. [CrossRef]
41. Kong, D.; Cha, J.J.; Wang, H.; Lee, H.R.; Cui, Y. First-row transition metal dichalcogenide catalysts for hydrogen evolution reaction. *Energy Environ. Sci.* **2013**, *6*, 3553–3558. [CrossRef]
42. Chhowalla, M.; Shin, H.S.; Eda, G.; Li, L.J.; Loh, K.P.; Zhang, H. The chemistry of two-dimensional layered transition metal dichalcogenide nanosheets. *Nat. Chem.* **2013**, *5*, 263–275. [CrossRef] [PubMed]
43. Wang, Q.; Zhang, Y.; Lin, H.; Zhu, J. Recent Advances in Metal-Organic Frameworks for Photo-/Electrocatalytic CO_2 Reduction. *Chem. Eur. J.* **2019**, *25*, 14026–14035. [CrossRef] [PubMed]
44. Olabi, A.G.; Abdelkareem, M.A.; Wilberforce, T.; Sayed, E.T. Application of Graphene in Energy Storage Device—A Review. *Renew. Sustain. Energy Rev.* **2021**, *135*, 110026. [CrossRef]
45. Yu, Y.; Wang, T.; Chen, X.; Zhang, L.; Wang, Y.; Niu, Y.; Yu, J.; Ma, H.; Li, X.; Liu, F.; et al. Demonstration of epitaxial growth of strain-relaxed GaN films on graphene/SiC substrates for long wavelength light-emitting diodes. *Light Sci. Appl.* **2021**, *117*. [CrossRef] [PubMed]
46. Ishikawa, R.; Yamazaki, S.; Watanabe, S.; Tsuboi, N. Layer dependency of graphene layers in perovskite/graphene solar cells. *Carbon* **2021**, *172*, 597–601. [CrossRef]
47. Nag, A.; Mitra, A.; Mukhopadhyay, S.C. Graphene and its sensor-based applications: A review. *Sens. Actuators A Phys.* **2018**, *270*, 177–194. [CrossRef]
48. Nemiwal, M.; Zhang, T.C.; Kumar, D. Graphene-based electrocatalysts: Hydrogen evolution reactions and overall water splitting. *Int. J. Hydrogen Energy* **2021**, *46*, 21401–21418. [CrossRef]
49. Wang, G.; Chen, J.; Ding, Y.; Cai, P.; Yi, L.; Li, Y.; Tu, C.; Hou, Y.; Wen, Z.; Dai, L. Electrocatalysis for CO_2 conversion: From fundamentals to value-added products. *Chem. Soc. Rev.* **2021**, *50*, 4993–5061. [CrossRef]
50. Nitopi, S.; Bertheussen, E.; Scott, S.B.; Liu, X.; Engstfeld, A.K.; Horch, S.; Seger, B.; Stephens, I.E.L.; Chan, K.; Hahn, C.; et al. Progress and Perspectives of Electrochemical CO2 Reduction on Copper in Aqueous Electrolyte. *Chem. Rev.* **2019**, *119*, 7610–7672. [CrossRef]
51. Jin, L.; Seifitokaldani, A. In Situ Spectroscopic Methods for Electrocatalytic CO_2 Reduction. *Catalysts* **2020**, *10*, 481. [CrossRef]
52. Zhu, Y.; Yang, X.; Peng, C.; Priest, C.; Mei, Y.; Wu, G. Carbon-Supported Single Metal Site Catalysts for Electrochemical CO_2 Reduction to CO and Beyond. *Small* **2021**, *17*, e2005148. [CrossRef] [PubMed]
53. Zhu, X.; Li, Y. Review of two-dimensional materials for electrochemical CO_2 reduction from a theoretical perspective. *Wiley Interdiscip. Rev. Comput. Mol. Sci.* **2019**, *9*, e1416. [CrossRef]
54. Zhang, W.; Ma, D.; Pérez-Ramírez, J.; Chen, Z. Recent Progress in Materials Materials Exploration for Thermocatalytic, Photocatalytic, and Integrated Photothermocatalytic CO_2 to Fuel Conversion. *Adv. Sustain. Syst.* **2021**, *3*, 2100169. [CrossRef]
55. Zhang, W.; Jin, Z.; Chen, Z. Rational-Designed Principles for Electrochemical and Photoelectrochemical Upgrading of CO_2 to Value-Added Chemicals. *Adv. Sci.* **2022**, e2105204. [CrossRef]
56. Li, Q.; Wang, Y.C.; Zeng, J.; Zhao, X.; Chen, C.; Wu, Q.M.; Chen, L.M.; Chen, Z.Y.; Lei, Y.P. Bimetallic chalcogenides for electrocatalytic CO_2 reduction. *Rare Met.* **2021**, *40*, 3442–3453. [CrossRef]
57. Wang, J.J.; Li, X.P.; Cui, B.F.; Zhang, Z.; Hu, X.F.; Ding, J.; Deng, Y.D.; Han, X.P.; Hu, W.B. A review of non-noble metal-based electrocatalysts for CO_2 electroreduction. *Rare Met.* **2021**, *40*, 3019–3037. [CrossRef]
58. Sun, Z.; Ma, T.; Tao, H.; Fan, Q.; Han, B. Fundamentals and Challenges of Electrochemical CO_2 Reduction Using Two-Dimensional Materials. *Chem* **2017**, *3*, 560–587. [CrossRef]
59. Zou, X.; Liu, M.; Wu, J.; Ajayan, P.M.; Li, J.; Liu, B.; Yakobson, B.I. How Nitrogen-Doped Graphene Quantum Dots Catalyze Electroreduction of CO_2 to Hydrocarbons and Oxygenates. *ACS Catal.* **2017**, *7*, 6245–6250. [CrossRef]
60. García Rey, N.; Dlott, D.D. Structural Transition in an Ionic Liquid Controls CO_2 Electrochemical Reduction. *J. Phys. Chem. C* **2015**, *119*, 20892–20899. [CrossRef]
61. Ma, T.; Fan, Q.; Li, X.; Qiu, J.; Wu, T.; Sun, Z. Graphene-based materials for electrochemical CO_2 reduction. *J. CO2 Util.* **2019**, *30*, 168–182. [CrossRef]
62. Benson, E.E.; Kubiak, C.P.; Sathrum, A.J.; Smieja, J.M. Electrocatalytic and homogeneous approaches to conversion of CO_2 to liquid fuels. *Chem. Soc. Rev.* **2009**, *38*, 89–99. [CrossRef] [PubMed]
63. Qiao, J.; Liu, Y.; Hong, F.; Zhang, J. A review of catalysts for the electroreduction of carbon dioxide to produce low-carbon fuels. *Chem. Soc. Rev.* **2014**, *43*, 631–675. [CrossRef] [PubMed]
64. Sun, Z.; Talreja, N.; Tao, H.; Texter, J.; Muhler, M.; Strunk, J.; Chen, J. Catalysis of Carbon Dioxide Photoreduction on Nanosheets: Fundamentals and Challenges. *Angew. Chem. Int. Ed.* **2018**, *57*, 7610–7627. [CrossRef]
65. Zhang, L.; Zhao, Z.J.; Gong, J. Nanostructured Materials for Heterogeneous Electrocatalytic CO_2 Reduction and their Related Reaction Mechanisms. *Angew. Chem. Int. Ed.* **2017**, *56*, 11326–11353. [CrossRef] [PubMed]

66. DeCiccio, D.; Ahn, S.T.; Sen, S.; Schunk, F.; Palmore, G.T.R.; Rose-Petruck, C. Electrochemical reduction of CO_2 with clathrate hydrate electrolytes and copper foam electrodes. *Electrochem. Commun.* **2015**, *52*, 13–16. [CrossRef]
67. Appel, A.M.; Bercaw, J.E.; Bocarsly, A.B.; Dobbek, H.; DuBois, D.L.; Dupuis, M.; Ferry, J.G.; Fujita, E.; Hille, R.; Kenis, P.J.; et al. Frontiers, opportunities, and challenges in biochemical and chemical catalysis of CO_2 fixation. *Chem. Rev.* **2013**, *113*, 6621–6658. [CrossRef]
68. Zhong, M.; Tran, K.; Min, Y.; Wang, C.; Wang, Z.; Dinh, C.T.; De Luna, P.; Yu, Z.; Rasouli, A.S.; Brodersen, P.; et al. Accelerated discovery of CO_2 electrocatalysts using active machine learning. *Nature* **2020**, *581*, 178–183. [CrossRef]
69. Geioushy, R.A.; Khaled, M.M.; Alhooshani, K.; Hakeem, A.S.; Rinaldi, A. Graphene/ZnO/Cu_2O electrocatalyst for selective conversion of CO_2 into n-propanol. *Electrochim. Acta* **2017**, *245*, 456–462. [CrossRef]
70. Hori, Y. Electrochemical CO_2 Reduction on Metal Electrodes. *Mod. Aspect. Electroc.* **2008**, *42*, 89–189. [CrossRef]
71. Li, F.; Zhao, S.F.; Chen, L.; Khan, A.; MacFarlane, D.R.; Zhang, J. Polyethylenimine promoted electrocatalytic reduction of CO_2 to CO in aqueous medium by graphene-supported amorphous molybdenum sulphide. *Energy Environ. Sci.* **2016**, *9*, 216–223. [CrossRef]
72. Zhu, W.; Zhang, Y.J.; Zhang, H.; Lv, H.; Li, Q.; Michalsky, R.; Peterson, A.A.; Sun, S. Active and selective conversion of CO_2 to CO on ultrathin Au nanowires. *J. Am. Chem. Soc.* **2014**, *136*, 16132–16135. [CrossRef] [PubMed]
73. Zhu, W.; Zhang, L.; Yang, P.; Hu, C.; Luo, Z.; Chang, X.; Zhao, Z.J.; Gong, J. Low-Coordinated Edge Sites on Ultrathin Palladium Nanosheets Boost Carbon Dioxide Electroreduction Performance. *Angew. Chem. Int. Ed.* **2018**, *57*, 11544–11548. [CrossRef] [PubMed]
74. Wang, Y.; Cao, L.; Libretto, N.J.; Li, X.; Li, C.; Wan, Y.; He, C.; Lee, J.; Gregg, J.; Zong, H.; et al. Ensemble Effect in Bimetallic Electrocatalysts for CO_2 Reduction. *J. Am. Chem. Soc.* **2019**, *141*, 16635–16642. [CrossRef] [PubMed]
75. Wu, J.; Liu, M.; Sharma, P.P.; Yadav, R.M.; Ma, L.; Yang, Y.; Zou, X.; Zhou, X.D.; Vajtai, R.; Yakobson, B.I.; et al. Incorporation of Nitrogen Defects for Efficient Reduction of CO_2 via Two-Electron Pathway on Three-Dimensional Graphene Foam. *Nano Lett.* **2016**, *16*, 466–470. [CrossRef]
76. Zhang, W.; Hu, Y.; Ma, L.; Zhu, G.; Zhao, P.; Xue, X.; Chen, R.; Yang, S.; Ma, J.; Liu, J.; et al. Liquid-phase exfoliated ultrathin Bi nanosheets: Uncovering the origins of enhanced electrocatalytic CO_2 reduction on two-dimensional metal nanostructure. *Nano Energy* **2018**, *53*, 808–816. [CrossRef]
77. Pan, J.; Sun, Y.; Deng, P.; Yang, F.; Chen, S.; Zhou, Q.; Park, H.S.; Liu, H.; Yu Xia, B. Hierarchical and ultrathin copper nanosheets synthesized via galvanic replacement for selective electrocatalytic carbon dioxide conversion to carbon monoxide. *Appl. Catal. B Environ.* **2019**, *255*, 117736. [CrossRef]
78. Wang, Y.; Shen, H.; Livi, K.J.T.; Raciti, D.; Zong, H.; Gregg, J.; Onadeko, M.; Wan, Y.; Watson, A.; Wang, C. Copper Nanocubes for CO_2 Reduction in Gas Diffusion Electrodes. *Nano Lett.* **2019**, *19*, 8461–8468. [CrossRef]
79. Sreekanth, N.; Nazrulla, M.A.; Vineesh, T.V.; Sailaja, K.; Phani, K.L. Metal-free boron-doped graphene for selective electroreduction of carbon dioxide to formic acid/formate. *Chem. Commun.* **2015**, *51*, 16061. [CrossRef]
80. Liu, X.; Zhu, L.; Wang, H.; He, G.; Bian, Z. Catalysis performance comparison for electrochemical reduction of CO_2 on Pd–Cu/graphene catalyst. *RSC Adv.* **2016**, *6*, 38380–38387. [CrossRef]
81. Su, P.; Iwase, K.; Nakanishi, S.; Hashimoto, K.; Kamiya, K. Nickel-Nitrogen-Modified Graphene: An Efficient Electrocatalyst for the Reduction of Carbon Dioxide to Carbon Monoxide. *Small* **2016**, *12*, 6083–6089. [CrossRef]
82. Huang, J.; Guo, X.; Wei, Y.; Hu, Q.; Yu, X.; Wang, L. A renewable, flexible and robust single layer nitrogen-doped graphene coating Sn foil for boosting formate production from electrocatalytic CO_2 reduction. *J. CO2 Util.* **2019**, *33*, 166–170. [CrossRef]
83. Lei, F.; Liu, W.; Sun, Y.; Xu, J.; Liu, K.; Liang, L.; Yao, T.; Pan, B.; Wei, S.; Xie, Y. Metallic tin quantum sheets confined in graphene toward high-efficiency carbon dioxide electroreduction. *Nat. Commun.* **2016**, *7*, 12697. [CrossRef] [PubMed]
84. Li, F.; Chen, L.; Xue, M.; Williams, T.; Zhang, Y.; MacFarlane, D.R.; Zhang, J. Towards a better Sn: Efficient electrocatalytic reduction of CO_2 to formate by Sn/SnS_2 derived from SnS_2 nanosheets. *Nano Energy* **2017**, *31*, 270–277. [CrossRef]
85. Lu, X.; Tan, T.H.; Ng, Y.H.; Amal, R. Highly Selective and Stable Reduction of CO_2 to CO by a Graphitic Carbon Nitride/Carbon Nanotube Composite Electrocatalyst. *Eur. J. Chem.* **2016**, *22*, 11991–11996. [CrossRef]
86. Guo, S.; Zhao, S.; Wu, X.; Li, H.; Zhou, Y.; Zhu, C.; Yang, N.; Jiang, X.; Gao, J.; Bai, L.; et al. A Co_3O_4-CDots-C_3N_4 three component electrocatalyst design concept for efficient and tunable CO_2 reduction to syngas. *Nat. Commun.* **2017**, *8*, 1828. [CrossRef] [PubMed]
87. Abbasi, P.; Asadi, M.; Liu, C.; Sharifi-Asl, S.; Sayahpour, B.; Behranginia, A.; Zapol, P.; Shahbazian-Yassar, R.; Curtiss, L.A.; Salehi-Khojin, A. Tailoring the Edge Structure of Molybdenum Disulfide toward Electrocatalytic Reduction of Carbon Dioxide. *ACS Nano* **2017**, *11*, 453–460. [CrossRef] [PubMed]
88. Asadi, M.; Kumar, B.; Behranginia, A.; Rosen, B.A.; Baskin, A.; Repnin, N.; Pisasale, D.; Phillips, P.; Zhu, W.; Haasch, R.; et al. Robust carbon dioxide reduction on molybdenum disulphide edges. *Nat. Commun.* **2014**, *5*, 4470. [CrossRef]
89. Asadi, M.; Kim, K.; Liu, C.; Addepalli, A.V.; Abbasi, P.; Yasaei, P.; Phillips, P.; Behranginia, A.; Cerrato, J.M.; Haasch, R.; et al. Nanostructured transition metal dichalcogenide electrocatalysts for CO_2 reduction in ionic liquid. *Science* **2016**, *353*, 467–470. [CrossRef] [PubMed]
90. Kornienko, N.; Zhao, Y.; Kley, C.S.; Zhu, C.; Kim, D.; Lin, S.; Chang, C.J.; Yaghi, O.M.; Yang, P. Metal-organic frameworks for electrocatalytic reduction of carbon dioxide. *J. Am. Chem. Soc.* **2015**, *137*, 14129–14135. [CrossRef]
91. Zhao, C.; Dai, X.; Yao, T.; Chen, W.; Wang, X.; Wang, J.; Yang, J.; Wei, S.; Wu, Y.; Li, Y. Ionic Exchange of Metal-Organic Frameworks to Access Single Nickel Sites for Efficient Electroreduction of CO_2. *J. Am. Chem. Soc.* **2017**, *139*, 8078–8081. [CrossRef]

92. Zhang, Z.; Xiao, J.; Chen, X.J.; Yu, S.; Yu, L.; Si, R.; Wang, Y.; Wang, S.; Meng, X.; Wang, Y.; et al. Reaction Mechanisms of Well-Defined Metal-N_4 Sites in Electrocatalytic CO_2 Reduction. *Angew. Chem. Int. Ed.* **2018**, *57*, 16339–16342. [CrossRef] [PubMed]
93. Gao, S.; Jiao, X.; Sun, Z.; Zhang, W.; Sun, Y.; Wang, C.; Hu, Q.; Zu, X.; Yang, F.; Yang, S.; et al. Ultrathin Co_3O_4 Layers Realizing Optimized CO_2 Electroreduction to Formate. *Angew. Chem. Int. Ed.* **2016**, *55*, 698–702. [CrossRef] [PubMed]
94. Gao, S.; Sun, Z.; Liu, W.; Jiao, X.; Zu, X.; Hu, Q.; Sun, Y.; Yao, T.; Zhang, W.; Wei, S.; et al. Atomic layer confined vacancies for atomic-level insights into carbon dioxide electroreduction. *Nature. Commun.* **2017**, *8*, 14503. [CrossRef] [PubMed]
95. Li, F.; Chen, L.; Knowles, G.P.; MacFarlane, D.R.; Zhang, J. Hierarchical Mesoporous SnO_2 Nanosheets on Carbon Cloth: A Robust and Flexible Electrocatalyst for CO_2 Reduction with High Efficiency and Selectivity. *Angew. Chem. Int. Ed.* **2017**, *56*, 505–509. [CrossRef] [PubMed]
96. Wang, Y.; Chen, Z.; Han, P.; Du, Y.; Gu, Z.; Xu, X.; Zheng, G. Single-Atomic Cu with Multiple Oxygen Vacancies on Ceria for Electrocatalytic CO_2 Reduction to CH_4. *ACS Catal.* **2018**, *8*, 7113–7119. [CrossRef]
97. Huan, T.N.; Ranjbar, N.; Rousse, G.; Sougrati, M.; Zitolo, A.; Mougel, V.; Jaouen, F.; Fontecave, M. Electrochemical Reduction of CO_2 Catalyzed by Fe-N-C Materials: A Structure–Selectivity Study. *ACS Catal.* **2017**, *7*, 1520–1525. [CrossRef]
98. Zhang, C.; Yang, S.; Wu, J.; Liu, M.; Yazdi, S.; Ren, M.; Sha, J.; Zhong, J.; Nie, K.; Jalilov, A.S.; et al. Electrochemical CO_2 Reduction with Atomic Iron-Dispersed on Nitrogen-Doped Graphene. *Adv. Energy Mater.* **2018**, *8*, 1703487. [CrossRef]
99. Zhang, H.; Li, J.; Xi, S.; Du, Y.; Hai, X.; Wang, J.; Xu, H.; Wu, G.; Zhang, J.; Lu, J.; et al. A Graphene-Supported Single-Atom FeN_5 Catalytic Site for Efficient Electrochemical CO_2 Reduction. *Angew. Chem. Int. Ed.* **2019**, *58*, 14871–14876. [CrossRef]
100. Zhang, Z.; Ma, C.; Tu, Y.; Si, R.; Wei, J.; Zhang, S.; Wang, Z.; Li, J.-F.; Wang, Y.; Deng, D. Multiscale carbon foam confining single iron atoms for efficient electrocatalytic CO_2 reduction to CO. *Nano Res.* **2019**, *12*, 2313–2317. [CrossRef]
101. Gu, J.; Hsu, C.S.; Bai, L.; Chen, H.M.; Hu, X. Atomically dispersed Fe^{3+} sites catalyze efficient CO_2 electroreduction to CO. *Science* **2019**, *364*, 1091–1094. [CrossRef]
102. Yang, F.; Song, P.; Liu, X.; Mei, B.; Xing, W.; Jiang, Z.; Gu, L.; Xu, W. Highly Efficient CO_2 Electroreduction on ZnN_4-based Single-Atom Catalyst. *Angew. Chem. Int. Ed.* **2018**, *57*, 12303–12307. [CrossRef] [PubMed]
103. Zhao, S.; Chen, G.; Zhou, G.; Yin, L.C.; Veder, J.P.; Johannessen, B.; Saunders, M.; Yang, S.Z.; De Marco, R.; Liu, C.; et al. A Universal Seeding Strategy to Synthesize Single Atom Catalysts on 2D Materials for Electrocatalytic Applications. *Adv. Funct. Mater.* **2019**, *30*, 1906157. [CrossRef]
104. Yang, H.B.; Hung, S.F.; Liu, S.; Yuan, K.; Miao, S.; Zhang, L.; Huang, X.; Wang, H.Y.; Cai, W.; Chen, R.; et al. Atomically dispersed Ni(i) as the active site for electrochemical CO_2 reduction. *Nat. Energy* **2018**, *3*, 140–147. [CrossRef]
105. Liu, S.; Yang, H.B.; Hung, S.F.; Ding, J.; Cai, W.; Liu, L.; Gao, J.; Li, X.; Ren, X.; Kuang, Z.; et al. Elucidating the Electrocatalytic CO_2 Reduction Reaction over a Model Single-Atom Nickel Catalyst. *Angew. Chem. Int. Ed.* **2020**, *59*, 798–803. [CrossRef]
106. Gong, Y.N.; Jiao, L.; Qian, Y.; Pan, C.Y.; Zheng, L.; Cai, X.; Liu, B.; Yu, S.H.; Jiang, H.L. Regulating the Coordination Environment of MOF-Templated Single-Atom Nickel Electrocatalysts for Boosting CO_2 Reduction. *Angew. Chem. Int. Ed.* **2020**, *59*, 2705–2709. [CrossRef]
107. Han, J.; An, P.; Liu, S.; Zhang, X.; Wang, D.; Yuan, Y.; Guo, J.; Qiu, X.; Hou, K.; Shi, L.; et al. Reordering d Orbital Energies of Single-Site Catalysts for CO_2 Electroreduction. *Angew. Chem. Int. Ed.* **2019**, *58*, 12711–12716. [CrossRef]
108. Zheng, W.; Yang, J.; Chen, H.; Hou, Y.; Wang, Q.; Gu, M.; He, F.; Xia, Y.; Xia, Z.; Li, Z.; et al. Atomically Defined Undercoordinated Active Sites for Highly Efficient CO_2 Electroreduction. *Adv. Func. Mater.* **2019**, *30*, 1907658. [CrossRef]
109. Murata, A.; Hori, Y. Product Selectivity Affected by Cationic Species in Electrochemical Reduction of CO_2 and CO at a Cu Electrode. *Bull. Chem. Soc. Jpn.* **1991**, *64*, 123–127. [CrossRef]
110. Qin, B.; Li, Y.; Fu, H.; Wang, H.; Chen, S.; Liu, Z.; Peng, F. Electrochemical Reduction of CO_2 into Tunable Syngas Production by Regulating the Crystal Facets of Earth-Abundant Zn Catalyst. *ACS Appl. Mater. Interfaces* **2018**, *10*, 20530–20539. [CrossRef]
111. Jiang, K.; Huang, Y.; Zeng, G.; Toma, F.M.; Goddard, W.A.; Bell, A.T. Effects of Surface Roughness on the Electrochemical Reduction of CO_2 over Cu. *ACS Energy Lett.* **2020**, *5*, 1206–1214. [CrossRef]
112. Huang, X.; Tang, S.; Mu, X.; Dai, Y.; Chen, G.; Zhou, Z.; Ruan, F.; Yang, Z.; Zheng, N. Freestanding palladium nanosheets with plasmonic and catalytic properties. *Nat. Nanotechnol.* **2011**, *6*, 28–32. [CrossRef] [PubMed]
113. Mistry, H.; Reske, R.; Zeng, Z.; Zhao, Z.J.; Greeley, J.; Strasser, P.; Cuenya, B.R. Exceptional size-dependent activity enhancement in the electroreduction of CO_2 over Au nanoparticles. *J. Am. Chem. Soc.* **2014**, *136*, 16473–16476. [CrossRef]
114. Yang, Q.; Shi, L.; Yu, B.; Xu, J.; Wei, C.; Wang, Y.; Chen, H. Facile synthesis of ultrathin Pt–Pd nanosheets for enhanced formic acid oxidation and oxygen reduction reaction. *J. Mater. Chem. A* **2019**, *7*, 18846–18851. [CrossRef]
115. Gao, F.; Zhang, Y.; Ren, F.; Shiraishi, Y.; Du, Y. Universal Surfactant-Free Strategy for Self-Standing 3D Tremella-Like Pd–M (M = Ag, Pb, and Au) Nanosheets for Superior Alcohols Electrocatalysis. *Adv. Funct. Mater.* **2020**, *30*, 2000255. [CrossRef]
116. Zhang, S.; Fan, Q.; Xia, R.; Meyer, T.J. CO_2 Reduction: From Homogeneous to Heterogeneous Electrocatalysis. *Acc. Chem. Res.* **2020**, *53*, 255–264. [CrossRef] [PubMed]
117. Liu, K.; Ma, M.; Wu, L.; Valenti, M.; Cardenas-Morcoso, D.; Hofmann, J.P.; Bisquert, J.; Gimenez, S.; Smith, W.A. Electronic Effects Determine the Selectivity of Planar Au–Cu Bimetallic Thin Films for Electrochemical CO_2 Reduction. *ACS Appl. Mater. Interfaces* **2019**, *11*, 16546–16555. [CrossRef] [PubMed]
118. Wu, Z.P.; Lu, X.F.; Zang, S.Q.; Lou, X.W. Non-Noble-Metal-Based Electrocatalysts toward the Oxygen Evolution Reaction. *Adv. Funct. Mater.* **2020**, *30*, 1910274. [CrossRef]

119. Zhu, Y.P.; Guo, C.; Zheng, Y.; Qiao, S.Z. Surface and Interface Engineering of Noble-Metal-Free Electrocatalysts for Efficient Energy Conversion Processes. *Acc. Chem. Res.* **2017**, *50*, 915–923. [CrossRef]
120. Kuhl, K.P.; Cave, E.R.; Abram, D.N.; Jaramillo, T.F. New insights into the electrochemical reduction of carbon dioxide on metallic copper surfaces. *Energy Environ. Sci.* **2012**, *5*, 7050–7059. [CrossRef]
121. Kuang, Y.; Feng, G.; Li, P.; Bi, Y.; Li, Y.; Sun, X. Single-Crystalline Ultrathin Nickel Nanosheets Array from In Situ Topotactic Reduction for Active and Stable Electrocatalysis. *Angew. Chem. Int. Ed.* **2016**, *55*, 693–697. [CrossRef]
122. Zhang, W.; Yang, S.; Jiang, M.; Hu, Y.; Hu, C.; Zhang, X.; Jin, Z. Nanocapillarity and Nanoconfinement Effects of Pipet-like Bismuth@Carbon Nanotubes for Highly Efficient Electrocatalytic CO_2 Reduction. *Nano Lett.* **2021**, *21*, 2650–2657. [CrossRef] [PubMed]
123. Tao, H.; Gao, Y.; Talreja, N.; Guo, F.; Texter, J.; Yan, C.; Sun, Z. Two-dimensional nanosheets for electrocatalysis in energy generation and conversion. *J. Mater. Chem. A* **2017**, *5*, 7257–7284. [CrossRef]
124. Chai, G.L.; Guo, Z.X. Highly effective sites and selectivity of nitrogen-doped graphene/CNT catalysts for CO_2 electrochemical reduction. *Chem. Sci.* **2016**, *7*, 1268–1275. [CrossRef] [PubMed]
125. Duan, X.; Xu, J.; Wei, Z.; Ma, J.; Guo, S.; Wang, S.; Liu, H.; Dou, S. Metal-Free Carbon Materials for CO_2 Electrochemical Reduction. *Adv. Mater.* **2017**, *29*, 201701784. [CrossRef]
126. Liu, Y.; Zhao, J.; Cai, Q. Pyrrolic-nitrogen doped graphene: A metal-free electrocatalyst with high efficiency and selectivity for the reduction of carbon dioxide to formic acid: A computational study. *Phys. Chem. Chem. Phys.* **2016**, *18*, 5491–5498. [CrossRef]
127. Rogers, C.; Perkins, W.S.; Veber, G.; Williams, T.E.; Cloke, R.R.; Fischer, F.R. Synergistic Enhancement of Electrocatalytic CO_2 Reduction with Gold Nanoparticles Embedded in Functional Graphene Nanoribbon Composite Electrodes. *J. Am. Chem. Soc.* **2017**, *139*, 4052–4061. [CrossRef]
128. Zeng, M.; Li, Y. Recent advances in heterogeneous electrocatalysts for the hydrogen evolution reaction. *J. Mater. Chem. A* **2015**, *3*, 14942–14962. [CrossRef]
129. Xie, Y.; Li, X.; Wang, Y.; Li, B.; Yang, L.; Zhao, N.; Liu, M.; Wang, X.; Yu, Y.; Liu, J.M. Reaction mechanisms for reduction of CO_2 to CO on monolayer MoS_2. *Appl. Surf. Sci.* **2020**, *499*, 143964. [CrossRef]
130. Hong, X.; Chan, K.; Tsai, C.; Nørskov, J.K. How Doped MoS_2 Breaks Transition-Metal Scaling Relations for CO_2 Electrochemical Reduction. *ACS Catal.* **2016**, *6*, 4428–4437. [CrossRef]
131. Chan, K.; Tsai, C.; Hansen, H.A.; Nørskov, J.K. Molybdenum Sulfides and Selenides as Possible Electrocatalysts for CO_2 Reduction. *ChemCatChem* **2014**, *6*, 1899–1905. [CrossRef]
132. Shao, P.; Yi, L.; Chen, S.; Zhou, T.; Zhang, J. Metal-organic frameworks for electrochemical reduction of carbon dioxide: The role of metal centers. *J. Energy Chem.* **2020**, *40*, 156–170. [CrossRef]
133. Perfecto-Irigaray, M.; Albo, J.; Beobide, G.; Castillo, O.; Irabien, A.; Pérez-Yáñez, S. Synthesis of heterometallic metal–organic frameworks and their performance as electrocatalyst for CO_2 reduction. *RSC Adv.* **2018**, *8*, 21092–21099. [CrossRef]
134. Majidi, L.; Ahmadiparidari, A.; Shan, N.; Misal, S.N.; Kumar, K.; Huang, Z.; Rastegar, S.; Hemmat, Z.; Zou, X.; Zapol, P.; et al. 2D Copper Tetrahydroxyquinone Conductive Metal-Organic Framework for Selective CO_2 Electrocatalysis at Low Overpotentials. *Adv. Mater.* **2021**, *33*, e2004393. [CrossRef] [PubMed]
135. Chen, Y.; Kanan, M.W. Tin oxide dependence of the CO_2 reduction efficiency on tin electrodes and enhanced activity for tin/tin oxide thin-film catalysts. *J. Am. Chem. Soc.* **2012**, *134*, 1986–1989. [CrossRef] [PubMed]
136. Li, C.W.; Kanan, M.W. CO_2 reduction at low overpotential on Cu electrodes resulting from the reduction of thick Cu_2O films. *J. Am. Chem. Soc.* **2012**, *134*, 7231–7234. [CrossRef]
137. Liu, J.; Guo, C.; Vasileff, A.; Qiao, S. Nanostructured 2D Materials: Prospective Catalysts for Electrochemical CO_2 Reduction. *Small Methods* **2017**, *1*, 1600006. [CrossRef]
138. Yang, X.F.; Wang, A.Q.; Qiao, B.T.; Li, J.; Liu, J.Y.; Zhang, T. Single-Atom Catalysts: A New Frontier in Heterogeneous Catalysis. *Acc. Chem. Res.* **2013**, *46*, 1740–1748. [CrossRef]
139. Wang, A.; Li, J.; Zhang, T. Heterogeneous single-atom catalysis. *Nat. Rev. Chem.* **2018**, *2*, 65–81. [CrossRef]
140. Chorkendorff, I.; Niemantsverdriet, J.W. *Concepts of Modern Catalysis and Kinetics*; Wiley: Weinheim, Germany, 2003. [CrossRef]
141. Jaramillo, T.F.; Jorgensen, K.P.; Bonde, J.; Nielsen, J.H.; Horch, S.; Chorkendorff, I. Identification of Active Edge Sites for Electrochemical H_2 Evolution from MoS_2 Nanocatalysts. *Science* **2007**, *317*, 100–102. [CrossRef]
142. Seh, Z.W.; Kibsgaard, J.; Dickens, C.F.; Chorkendorff, I.; Norskov, J.K.; Jaramillo, T.F. Combining theory and experiment in electrocatalysis: Insights into materials design. *Science* **2017**, *355*, aad4998. [CrossRef]
143. Kyriakou, G.; Boucher, M.W.; Jewell, A.D.; Lewis, E.A.; Lawton, T.J.; Baber, A.E.; Tierney, H.L.; Flytzani-Stephanopoulos, M.; Sykes, E.C. Isolated Metal Atom Geometries as a Strategy for Selective Heterogeneous Hydrogenations. *Science* **2012**, *335*, 1209–1212. [CrossRef] [PubMed]
144. Zhang, N.; Zhou, T.; Chen, M.; Feng, H.; Yuan, R.; Zhong, C.a.; Yan, W.; Tian, Y.; Wu, X.; Chu, W.; et al. High-purity pyrrole-type FeN4 sites as a superior oxygen reduction electrocatalyst. *Energy Environ. Sci.* **2020**, *13*, 111–118. [CrossRef]
145. Yin, X.P.; Wang, H.J.; Tang, S.F.; Lu, X.L.; Shu, M.; Si, R.; Lu, T.B. Engineering the Coordination Environment of Single-Atom Platinum Anchored on Graphdiyne for Optimizing Electrocatalytic Hydrogen Evolution. *Angew. Chem. Int. Ed.* **2018**, *57*, 9382–9386. [CrossRef] [PubMed]

146. Xiao, M.; Gao, L.; Wang, Y.; Wang, X.; Zhu, J.; Jin, Z.; Liu, C.; Chen, H.; Li, G.; Ge, J.; et al. Engineering Energy Level of Metal Center: Ru Single-Atom Site for Efficient and Durable Oxygen Reduction Catalysis. *J. Am. Chem. Soc.* **2019**, *141*, 19800–19806. [CrossRef]
147. Zhang, H.; Yu, L.; Chen, T.; Zhou, W.; Lou, X.W.D. Surface Modulation of Hierarchical MoS_2 Nanosheets by Ni Single Atoms for Enhanced Electrocatalytic Hydrogen Evolution. *Adv. Funct. Mater.* **2018**, *28*, 1807086. [CrossRef]
148. Li, H.; Wang, L.; Dai, Y.; Pu, Z.; Lao, Z.; Chen, Y.; Wang, M.; Zheng, X.; Zhu, J.; Zhang, W.; et al. Synergetic interaction between neighbouring platinum monomers in CO_2 hydrogenation. *Nat. Nanotechnol.* **2018**, *13*, 411–417. [CrossRef]
149. Ye, S.; Luo, F.; Zhang, Q.; Zhang, P.; Xu, T.; Wang, Q.; He, D.; Guo, L.; Zhang, Y.; He, C.; et al. Highly stable single Pt atomic sites anchored on aniline-stacked graphene for hydrogen evolution reaction. *Energy Environ. Sci.* **2019**, *12*, 1000–1007. [CrossRef]
150. Yuan, J.; Zhang, W.; Li, X.; Yang, J. A high-performance catalyst for methane conversion to methanol: Graphene supported single atom Co. *Chem. Commun.* **2018**, *54*, 2284–2287. [CrossRef]
151. Ramalingam, V.; Varadhan, P.; Fu, H.C.; Kim, H.; Zhang, D.; Chen, S.; Song, L.; Ma, D.; Wang, Y.; Alshareef, H.N.; et al. Heteroatom-Mediated Interactions between Ruthenium Single Atoms and an MXene Support for Efficient Hydrogen Evolution. *Adv. Mater.* **2019**, *31*, e1903841. [CrossRef]
152. Back, S.; Lim, J.; Kim, N.Y.; Kim, Y.H.; Jung, Y. Single-atom catalysts for CO_2 electroreduction with significant activity and selectivity improvements. *Chem. Sci.* **2017**, *8*, 1090–1096. [CrossRef]
153. Jiang, K.; Siahrostami, S.; Zheng, T.T.; Hu, Y.F.; Hwang, S.Y.; Stavitski, E.; Peng, Y.D.; Dynes, J.; Gangisetty, M.; Su, D.; et al. Isolated Ni single atoms in graphene nanosheets for high-performance CO_2 reduction. *Energy Environ. Sci.* **2018**, *11*, 893–903. [CrossRef]
154. Jiao, Y.; Zheng, Y.; Chen, P.; Jaroniec, M.; Qiao, S.Z. Molecular Scaffolding Strategy with Synergistic Active Centers to Facilitate Electrocatalytic CO_2 Reduction to Hydrocarbon/Alcohol. *J. Am. Chem. Soc.* **2017**, *139*, 18093–18100. [CrossRef] [PubMed]
155. Choi, C.; Cai, J.; Lee, C.; Lee, H.M.; Xu, M.; Huang, Y. Intimate atomic Cu-Ag interfaces for high CO_2RR selectivity towards CH_4 at low over potential. *Nano Res.* **2021**, *14*, 3497–3501. [CrossRef]
156. Chen, B.; Li, B.; Tian, Z.; Liu, W.; Liu, W.; Sun, W.; Wang, K.; Chen, L.; Jiang, J. Enhancement of Mass Transfer for Facilitating Industrial-Level CO_2 Electroreduction on Atomic Ni-N_4 Sites. *Adv. Energy Mater.* **2021**, *11*, 2102152. [CrossRef]
157. Yang, Y.; Li, F. Reactor design for electrochemical CO_2 conversion toward large-scale applications. *Curr. Opin. Green Sustain. Chem.* **2021**, *27*, 100419. [CrossRef]
158. Jayashree, R.S.; Mitchell, M.; Natarajan, D.; Markoski, L.J.; Kenis, P.J.A. Microfluidic Hydrogen Fuel Cell with a Liquid Electrolyte. *Langmuir* **2007**, *23*, 6871–6874. [CrossRef]
159. Whipple, D.T.; Finke, E.C.; Kenis, P.J.A. Microfluidic Reactor for the Electrochemical Reduction of Carbon Dioxide: The Effect of pH. *Electrochem. Solid-State Lett.* **2010**, *13*, 9. [CrossRef]
160. Higgins, D.; Hahn, C.; Xiang, C.; Jaramillo, T.F.; Weber, A.Z. Gas-Diffusion Electrodes for Carbon Dioxide Reduction: A New Paradigm. *ACS Energy Lett.* **2018**, *4*, 317–324. [CrossRef]
161. Lees, E.W.; Mowbray, B.A.W.; Parlane, F.G.L.; Berlinguette, C.P. Gas diffusion electrodes and membranes for CO_2 reduction electrolysers. *Nat. Rev. Mater.* **2021**, *7*, 55–64. [CrossRef]
162. Lim, J.; Kang, P.W.; Jeon, S.S.; Lee, H. Electrochemically deposited Sn catalysts with dense tips on a gas diffusion electrode for electrochemical CO_2 reduction. *J. Mater. Chem. A* **2020**, *8*, 9032–9038. [CrossRef]
163. Rabiee, H.; Ge, L.; Zhang, X.; Hu, S.; Li, M.; Yuan, Z. Gas diffusion electrodes (GDEs) for electrochemical reduction of carbon dioxide, carbon monoxide, and dinitrogen to value-added products: A review. *Energy Environ. Sci.* **2021**, *14*, 1959–2008. [CrossRef]
164. Gabardo, C.M.; O'Brien, C.P.; Edwards, J.P.; McCallum, C.; Xu, Y.; Dinh, C.T.; Li, J.; Sargent, E.H.; Sinton, D. Continuous Carbon Dioxide Electroreduction to Concentrated Multi-carbon Products Using a Membrane Electrode Assembly. *Joule* **2019**, *3*, 2777–2791. [CrossRef]
165. Ren, S.X.; Joulié, D.; Salvatore, D.; Torbensen, K.; Wang, M.; Robert, M.; Berlinguette, C.P. Molecular electrocatalysts can mediate fast, selective CO_2 reduction in a flow cell. *Science* **2019**, *365*, 367–369. [CrossRef] [PubMed]

Appendix B – Paper II

Efficient Electrochemical Reduction of CO_2 to CO by Ag-Decorated B-Doped g-C_3N_4: A Combined Theoretical and Experimental Study

S. Lu, Y. Zhang, M. F. Mady, W. M. Tucho, F. Lou and Z. Yu

Industrial & Engineering Chemistry Research, 2022, 61, 10400–10408.
DOI: 10.1021/acs.iecr.2c00152

I&EC research
Industrial & Engineering Chemistry Research

pubs.acs.org/IECR Article

Efficient Electrochemical Reduction of CO_2 to CO by Ag-Decorated B-Doped g-C_3N_4: A Combined Theoretical and Experimental Study

Song Lu, Yang Zhang, Mohamed F. Mady, Wakshum Mekonnen Tucho, Fengliu Lou,* and Zhixin Yu*

Cite This: *Ind. Eng. Chem. Res.* 2022, 61, 10400−10408 Read Online

ACCESS | Metrics & More | Article Recommendations | Supporting Information

ABSTRACT: Electrochemical CO_2 reduction (ECR) has received great attention in energy conversion and CO_2 mitigation. In recent years, graphitic carbon nitride (g-C_3N_4) has been regarded as a very promising support for metal nanoparticles (NPs) for many catalytic reactions. In this work, we reported the silver- (Ag) loaded boron-doped g-C_3N_4 nanocomposite (Ag-B-g-C_3N_4) for efficient ECR to CO by a joint first-principles study and experimental work. Theoretical simulation demonstrated that the B dopant and Ag NPs could be easily incorporated into g-C_3N_4. The introduction of Ag NPs and the B atom could greatly decrease the adsorption free energy for the *COOH intermediate generation. Meanwhile, an electron-rich region at the Ag-B-g-C_3N_4 interface was observed, contributing to improved electrical conductivity and electron transport. B-g-C_3N_4 could not exhibit the obvious enhancement of ECR performance, while the Ag-B-g-C_3N_4 catalyst with an average Ag diameter of 4.95 nm exhibited a total current density of 2.08 mA cm^{-2} and a CO Faradaic efficiency (FE_{CO}) of 93.2% under the potential of −0.8 V vs the reversible hydrogen electrode (RHE), indicating that Ag is the only active center. Ag-B-g-C_3N_4 also displayed excellent stability without any deactivation in a 12-h electrocatalysis. This work revealed the mechanism of electrocatalytic CO_2 reduction over metal- (Ag) and nonmetal- (B) modified g-C_3N_4, which paves the way for broader application of the g-C_3N_4 nanocomposite in electrocatalytic reactions.

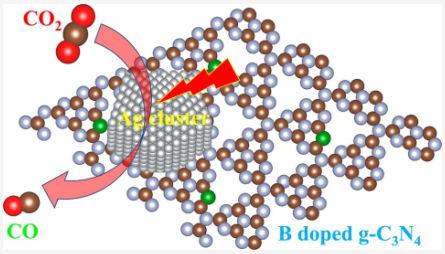

INTRODUCTION

Over the past decades, the huge consumption of fossil energy and the dramatic rise in atmospheric CO_2 concentration have led to various issues such as an energy crisis and global warming. Converting CO_2 to value-added chemicals and fuels has been considered as an effective approach to mitigate the above dilemma.[1,2] Among which, electrochemical CO_2 reduction (ECR) shows several advantages.[3,4] ECR can be proceeded under ambient temperatures and pressures. Besides, the required electricity input can be produced by wind, solar, and tidal energy. More importantly, a diverse range of products can be formed by tuning the external potentials and other reaction parameters.[5] Nevertheless, the activation of the CO_2 molecule is quite difficult because it requires an energy of 803 kJ/mol to break the C═O bond.[6,7] In addition, as the competitive hydrogen evolution reaction (HER) and multi-proton coupled electron transfer commonly take place, ECR suffers low selectivity toward specific products.[8,9] To date, carbon- and metal-based materials have been widely explored and demonstrated as effective electrocatalysts in ECR.[10−13] Shi et al. used the Au/C electrode to investigate the role of wettability in ECR.[14] They suggested that CO_2 concentration of the interfaces could influence ECR efficiency under high current densities. Carbon-supported single-atom catalysts (SACs) have been widely investigated, as they demonstrated outstanding performance in ECR to CO. For instance, a Ni SAC exhibits a 98.9% CO Faradaic efficiency (FE_{CO}) at −1.2 V.[15] It has been reported that Ag can be a good candidate for ECR to CO due to its relatively weak binding energy to the *CO intermediate.[16] Nevertheless, Ag-based catalysts generally show sluggish kinetics in ECR. Meanwhile, the stability and selectivity are not satisfactory. Therefore, the design of high-performance Ag-based electrocatalysts for ECR application is of interest.

Recently, loading metal nanoparticles (NPs) on two-dimensional (2D) materials as catalysts has gained intensive attention.[17−20] It is worth noting that 2D organic semiconductor graphitic carbon nitride (g-C_3N_4) possesses sp^2 hybridization of C and N atoms that form the π-conjugated graphitic plane, exhibiting excellent stability in a variety of catalytic reactions.[21−23] Besides, g-C_3N_4 also possesses other merits such as high surface area, low cost, and easy preparation,

Special Issue: Engineered Methodologies for CO2 Utilization

Received: January 12, 2022
Revised: March 7, 2022
Accepted: March 10, 2022
Published: March 22, 2022

https://doi.org/10.1021/acs.iecr.2c00152
Ind. Eng. Chem. Res. 2022, 61, 10400−10408

which enables it to be an ideal molecular scaffold for engineering metal NPs for excellent performance in multiple electrocatalytic applications.[12,24,25] Especially, the existence of pyridinic nitrogen atoms and high oxophilicity C atoms will boost the interaction between the catalysts and reactants/intermediates such as *COOH and *CO in ECR.[26,27] Zhang et al. reported that g-C_3N_4-supported gold (Au) NPs exhibit better ECR activity than carbon-supported Au NPs, achieving a FE_{CO} above 90% in a wide potential window between −0.45 and −0.85 V vs a reversible hydrogen electrode (vs RHE).[28] Density functional theory (DFT) calculations evidenced that the interaction between Au and g-C_3N_4 induces the generation of negative charges on the Au surface, promoting the generation of key intermediates. Recently, studies demonstrated that doping nonmetal atoms to modify the g-C_3N_4 support has positive effects on the overall ECR activity. For instance, Ag NP-loaded S-decorated g-C_3N_4/CNT exhibits a FE_{CO} of over 90% under −0.77 V (vs RHE) with a high current density of 21.3 mA cm^{-2}. Theoretical calculations revealed that S atoms could increase the electron density of the Ag-loaded g-C_3N_4 interface, promoting CO_2 molecule activation.[29] In other words, effective interfacial electron transfer between support and NPs could improve catalytic activity. Meanwhile, doping nonmetal atoms into the framework can change its electronic structures, while the modified framework could serve as a better support for metal NP deposition and to activate metal NPs.

A previous study had also indicated that boron- (B) modified g-C_3N_4 (B-g-C_3N_4) could effectively alter its electronic structures and improve its performance in various reactions.[30,31] Nevertheless, there is little research on B-g-C_3N_4 as a substrate for NPs used in ECR, while we can envisage that NPs-B-g-C_3N_4 hybrid nanomaterials could exhibit excellent ECR performance. In this work, we chose Ag NPs for the preparation of the Ag-B-g-C_3N_4 composite for ECR. We first investigated the geometric configurations, formation energies, and electronic structures of g-C_3N_4, B-g-C_3N_4, and Ag-B-g-C_3N_4 by first-principles calculation to predict their ECR performance. Our simulation results suggested that the composite electrocatalyst could show excellent stability, electronic conductivity, and low free energy barrier for the generation of the *COOH intermediate. The corresponding ECR to the CO mechanism on these three electrocatalysts was studied by calculating the adsorption free energy of each step, indicating that the generation of *COOH is the potential determining step. Thereafter, we prepared the three electrocatalysts for experimental verification. Only Ag-decorated B-g-C_3N_4 could reduce CO_2 to CO, while the other two catalysts only produced H_2. Meanwhile, no liquid product was detected. The Ag-B-g-C_3N_4 catalyst displayed the maximum FE_{CO} of 93.2% under a potential of −0.8 V (vs RHE) with a total current density of 2.08 mA cm^{-2}. It also exhibited excellent stability, as evidenced by negligible decay after a 12-h ECR activity test.

■ SIMULATION

All calculations in this work were conducted by using plane-wave DFT implemented in the Vienna ab initio simulation package (VASP).[32,33] The electronic exchange-correlation energy was treated by the Perdew−Burke−Ernzerhof (PBE) functional within the generalized gradient approximation (GGA).[34,35] The projector augmented wave (PAW) method with a cutoff energy of 500 eV was used to describe the ionic cores. In the z direction, the thickness of the vacuum was set to 20 Å to avoid periodic interactions. We chose a 4 × 4 × 1 k-point grid for structure optimization, and an 8 × 8 × 1 k-point grid for electronic structure calculations. The convergence criterion of the energy and force were 10^{-5} eV and 10^{-2} eV/Å. To better describe the dispersion interaction from molecules, the vdW correction was included by Grimme's scheme (DFT-D3).[36]

The substituted energy (E_{sub}) of B-g-C_3N_4 can be used to estimate its thermal stability by the following equation

$$E_{sub} = E(\text{doped}) - E(\text{g-}C_3N_4) + \mu(\text{N}) - \mu(\text{B}) \quad (1)$$

where E(doped) and E(g-C_3N_4) are the energy of the B-modified and pristine g-C_3N_4 monolayers, while μ(N) and μ(B) are the energy of N and B atoms from the reference phase.

The adsorption energy of the Ag cluster can be calculated by the equation below

$$E_{ads} = E(\text{Ag-B-g-}C_3N_4) - E(\text{Ag}_4\text{ cluster}) - E(\text{B-g-}C_3N_4) \quad (2)$$

where E(Ag-B-g-C_3N_4), E(Ag_4 cluster), and E(B-g-C_3N_4) denote the energy of the Ag_4 cluster loaded on B-g-C_3N_4, the Ag_4 cluster, and B-g-C_3N_4, respectively.

Based on the computational hydrogen electrode (CHE) model,[37] the chemical potential of H_2 (g) can be equal to $\mu(H^+ + e^-) = 1/2\mu(H_2)$. The Gibbs free energy change for adsorbates can be expressed as $\Delta G = \Delta E + \Delta E_{ZPE} - T\Delta S$, where E is the electronic energy from the DFT calculation, ZPE and TS are the zero-point energy and entropy correction, and T is the temperature which is set to be 298.15 K.

The adsorption and desorption of intermediates for CO generation can be expressed as below

$$* + CO_2 + (H^+ + e^-) \rightarrow *\text{COOH} \quad (3)$$

$$*\text{COOH} + (H^+ + e^-) \rightarrow *\text{CO} + H_2O \quad (4)$$

$$*\text{CO} \rightarrow \text{CO} + * \quad (5)$$

where * denotes the catalytic site.

■ EXPERIMENTAL SECTION

Chemicals. All chemicals are analytical reagents and used as-received without further purification. Deionized water generated by a Milli-Q (18.2 MΩ cm) system was used in all experiments. Silver nitrate ($AgNO_3$), boric acid (H_3BO_3), and sodium borohydride ($NaBH_4$) were ordered from Sigma-Aldrich. Trisodium citrate ($C_6H_5Na_3O_7$), potassium bicarbonate ($KHCO_3$), Nafion D-521 dispersion, Nafion-117 ionic exchange membrane, and urea ($CO(NH_2)_2$) were purchased from Alfa Aesar. Hydrogen peroxide (H_2O_2) and sulfuric acid (H_2SO_4) were bought from VWR. Carbon paper was purchased from Toray.

Pretreatment of the Ionic Exchange Membrane and Carbon Paper. The Nafion-117 membrane was boiled in a 5 wt % H_2O_2 aqueous solution at 80 °C for 1 h to remove organic impurities in the membrane. The membrane was rinsed repeatedly with deionized water, soaked in deionized water at 80 °C, and further boiled for 1 h to completely remove residual H_2O_2. The membrane was then boiled again in a H_2SO_4 (1.0 M) solution at 80 °C for 1 h. Finally, the membrane was rinsed repeatedly with deionized water and immersed in deionized water at 80 °C for 1 h to completely

https://doi.org/10.1021/acs.iecr.2c00152
Ind. Eng. Chem. Res. 2022, 61, 10400−10408

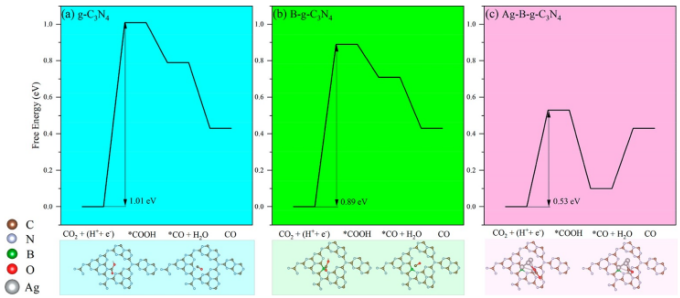

Figure 1. Calculated free energy profiles for ECR to CO on (a) g-C_3N_4, (b) B-g-C_3N_4, and (c) Ag-B-g-C_3N_4. The adsorption structures of key intermediates *COOH and *CO are depicted below.

remove the residual H_2SO_4. The carbon paper was immersed in an ethanol solution, ultrasonicated for 5 min, and then dried vacuum at 60 °C for 12 h before use.

Synthesis of Electrocatalysts. For the synthesis of g-C_3N_4, 20 g of $CO(NH_2)_2$ was put into a covered crucible, heated to 600 °C with a ramp rate of 5 °C min^{-1}, and kept for 2 h in the muffle furnace. After cooling to room temperature, the g-C_3N_4 sample was obtained. The sample was further sonicated in deionized water for 2 h to obtain a thin g-C_3N_4 nanosheet.

For the synthesis of B-doped g-C_3N_4, the mixture of 20 g of $CO(NH_2)_2$ and 0.3 g of H_3BO_3 was ground evenly and placed in a covered crucible. The crucible was heated to 600 °C with a ramp rate of 5 °C min^{-1} and held at 600 °C for 2 h in a muffle furnace. After cooling down, the sample was washed with hot water in order to remove B_2O_3 and then vacuum dried for 24 h at 60 °C. The as-prepared B-g-C_3N_4 sample was sonicated for 2 h to obtain a thin nanosheet.

The loading of Ag NPs on B-g-C_3N_4 was performed according to a procedure from a previous study.[28] Typically, 1.176 g of $Na_3C_6H_5O_7$ and 0.085 g of $AgNO_3$ were dissolved in 300 mL of deionized water under a dark environment. Then, the mixture of 0.081 g of B-g-C_3N_4 and the above solution was sonicated for 1 h. Subsequently, 50 mL of a 0.05 M $NaBH_4$ solution was added dropwise under vigorous stirring for 8 h. The sample was collected by centrifugation, washed with deionized water, and finally vacuum dried at 60 °C overnight. The Ag loading was 13.9 wt % based on inductively coupled plasma optical emission spectroscopy (ICP-OES).

Electrocatalyst Characterization. The structures of the electrocatalysts were investigated by an X-ray diffractometer (Bruker-AXS Microdiffractometer D8 ADVANCE) with a CuKα radiation source (λ = 1.54 Å) at a scan rate of 3° min^{-1}. The morphologies were examined by transmission electron microscopy (TEM) and high-resolution transmission electron microscopy (HRTEM, JEOLJEM-2100F, 200 kV). The surface compositions and element states of the catalysts were tested by X-ray photoelectron spectroscopy (XPS, ESCALAB Xi$^+$) using Al Kα excitation at 1486.6 eV.

Electrochemical Measurement. The electrocatalytic CO_2 reduction was carried out in a three-electrode sealed H-type cell consisting of a working electrode (carbon paper, CP), a reference electrode (saturated Ag/AgCl (3 M KCl)), and a counter electrode (Pt (1 cm^2)). All potentials were controlled by the AUTOLAB PGSTAT302N workstation and converted to RHE by E (vs RHE) = E (vs Ag/AgCl) + 0.197 V + 0.059 × pH. For each experiment, the mixture of 1 mg of the catalyst and 1 mg of carbon black was dispersed in a solution containing 500 μL of ethanol, 440 μL of H_2O, and 60 μL of a 0.5 wt % Nafion-D521 solution by sonication for 90 min. Then, 100 μL of the electrocatalyst ink was dropped uniformly on a piece of CP (1 × 2 cm) as the working electrode, followed by drying under an infrared lamp for 30 min. The area of the electrocatalyst was controlled to 1 cm^2 with a loading of 0.1 mg cm^{-2}. The Nafion-117 membrane was used to separate the anode and cathode chambers. The pH value of the 0.5 M $KHCO_3$ electrolyte is 7.2. High purity CO_2 was bubbled into the cathode chamber at a flow rate of 20 mL min^{-1} for 1 h before and during the test. Meanwhile, the electrolyte in the cathode was stirred at 1200 rmp. The linear sweep voltammetry (LSV) was collected in 0.5 M $KHCO_3$ at a scan rate of 10 mV s^{-1}. Electrochemical impedance spectroscopy (EIS) was measured in 0.5 M $KHCO_3$ at −0.8 V (vsRHE) with an amplitude of 5 mV from 10^{-2} to 10^{-5} Hz.

Gaseous products CO and H_2 were quantified by an online gas chromatograph (GC, Agilent 7890B) with two TCD detectors equipped with a HayeSep Q column and a 5A molecular sieve column. Liquid products were determined by nuclear magnetic resonance (NMR) spectroscopy with a 400 MHz Bruker NMR spectrometer. The FE of gaseous products under different potentials was calculated by the equation below

$$FE = (Z \times P \times F \times V \times \nu)/(R \times T \times I) \quad (6)$$

where Z is the number of transferred electrons for one CO_2 molecule reduction to the gaseous product, which is 2 for CO and H_2; P is the atmospheric pressure of 1.01 × 10^5 Pa; F is the Faraday constant 96485 C mol^{-1}; V is the gas flow rate; ν is the volumetric concentration of the gas product; T is the temperature of 298.15 K; R is the ideal gas constant 8.314 J mol^{-1} K^{-1}; and I is the steady-state current at each applied potential.

■ RESULTS AND DISCUSSION

DFT Results. There are three different N atoms (N1, N2, and N3 sites) and two different C atoms (C1 and C2 sites) in g-C_3N_4, as shown in Figure S1. Previous studies have demonstrated that the N2 atom with a low coordination number is preferable to be substituted by nonmetal atoms.[30,31] Therefore, the B-doped g-C_3N_4 monolayer was built with one B atom substituting for one N2 atom. After geometric

https://doi.org/10.1021/acs.iecr.2c00152
Ind. Eng. Chem. Res. 2022, 61, 10400−10408

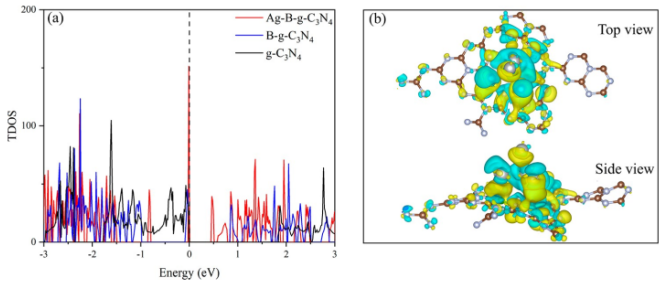

Figure 2. (a) Total density of states (TDOS) of g-C_3N, B- g-C_3N_4, and Ag-B-g-C_3N_4, where Fermi energy locates at 0 eV. (b) Charge density difference between Ag NPs and B-g-C_3N_4 for Ag-B-g-C_3N_4, where yellow and cyan denote electron accumulation and depletion, respectively. The isosurface value is set to be 0.001 e/Bohr^3.

optimization, the B atom bonds with the nearest N2 atom and C1 atom, forming pentagonal and hexagonal rings. The E_{sub} of B-doped g-C_3N_4 is −1.38 eV, indicating the ease of introducing the B atom into the g-C_3N_4 skeleton. The E_{ads} of the Ag cluster on B-g-C_3N_4 is −1.98 eV, demonstrating that the Ag_4 cluster is loaded stably on the B-g-C_3N_4 support, and the resulting composite catalyst could possess good stability.

The calculated Gibbs free energy change (ΔG) of the intermediates on g-C_3N_4, B-g-C_3N_4, and Ag-B-g-C_3N_4 was displayed in Figure 1a−c. The formation of intermediate *COOH is the potential determining step on the three electrocatalysts. The free energy barrier for CO production on pristine g-C_3N_4 is quite large at 1.01 eV, while the free energy barrier decreases by only 0.12 eV after introducing B atoms, indicating the B atom alone cannot effectively improve the ECR performance. However, the combination of B and Ag atoms shows a large drop in the free energy barrier of 0.53 eV, which suggested that the B dopant and Ag NPs could be promising to enhance the ECR performance of g-C_3N_4. We further considered the possible active sites after the doping of B and Ag, including S1 (B atom), S2 (N atom), S3 (C atom), S4 (N atom), S5 (N atom), and S6 (C atom) around the Ag cluster (Figure S2a). It turns outs that the intermediates could not be adsorbed on S1, S2, S3, S4, and S6. Only S5 can be a stable adsorption site for intermediates but with a free energy barrier of 1.16 eV (Figure S2b), larger than that of the Ag site. Thus, B, C, and N atoms will not be the active sites for CO_2 activation, and the Ag cluster is the only active center. The adsorption configurations of *COOH and *CO intermediates on the three electrocatalysts suggest that *COOH could bond with N, B, and Ag atoms with different strengths, leading to uphill Gibbs free energy. In contrast, *CO could not bond well with the N and B atoms, exhibiting an exothermic nature for CO desorption from pristine and B-doped g-C_3N_4. However, it could interact strongly with Ag atoms, resulting in an endothermic reaction for CO desorption.

We further investigated the electronic structures of Ag-B-g-C_3N_4 by calculating the total density of states, Bader charge, and charge density difference. It is worth noting that there are more electron states between the conduction band and valence band and even near the Fermi level in B and Ag-modified g-C_3N_4 (Figure 2a). In other words, the introduction of B atoms and the Ag cluster could induce more impurity levels, which could improve the electrical conductivity and increase the ECR activity. Besides, the detailed charge transfer between B, Ag, and g-C_3N_4 was shown in Figure 2b. The B atom transferred 1.71 e to C and N atoms, while the total charge transfer from the Ag cluster to the B-g-C_3N_4 scaffold is 0.74 e, contributing to an electron-rich region at the interface of Ag and B-g-C_3N_4. It can be proposed that the B dopant could improve electrical conductivity of the g-C_3N_4 support, while Ag NPs could sever as the ECR active center. Therefore, we synthesized the three catalysts (g-C_3N_4, B-g-C_3N_4, and Ag-B-g-C_3N_4) to verify the role of B and Ag NPs as proposed by DFT simulations.

Electrocatalyst Characterization. To evidence the formation of nanocomposites, crystal structures were investigated by XRD characterization (Figure 3). Two characteristic

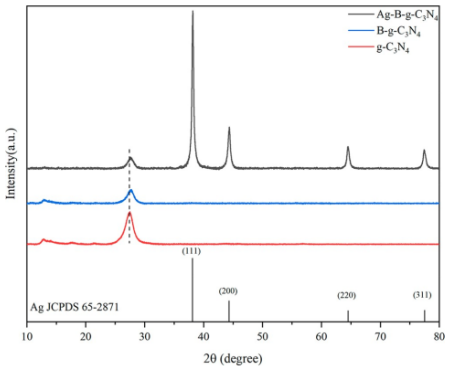

Figure 3. XRD patterns of g-C_3N_4, B-g-C_3N_4, and Ag-B-g-C_3N_4.

peaks located at 13.0° (100) and 27.6° (002) are assigned to the in-plane structure of tri-*s*-triazine motifs and the periodic stacking of layers of conjugated aromatic rings.[38,39] The slight shift of the (002) peak toward the high angle for B-g-C_3N_4 and Ag-B-g-C_3N_4 was probably related to structural variations such as the decreased interlayer distance after introducing B atoms.[40] The gradual decrease of the characteristic peak of g-C_3N_4 could be explained by the less ordered structure and reduced crystallinity after the doping of B and Ag. The XRD result could be supported by the structure deformation after introducing B and Ag NPs from the DFT simulation study

https://doi.org/10.1021/acs.iecr.2c00152
Ind. Eng. Chem. Res. 2022, 61, 10400−10408

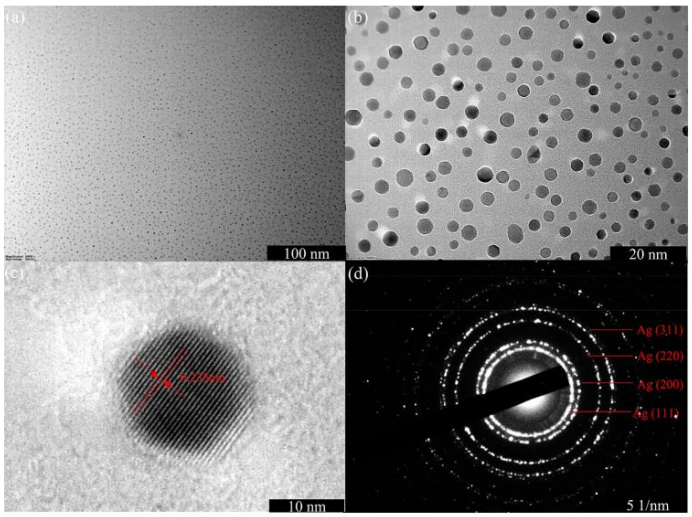

Figure 4. (a) and (b) TEM images of Ag-B-g-C_3N_4 with different magnifications. (c) HRTEM image of Ag-B-g-C_3N_4, which shows an interlayer distance of 0.235 nm for Ag. (d) SAED pattern of Ag NPs.

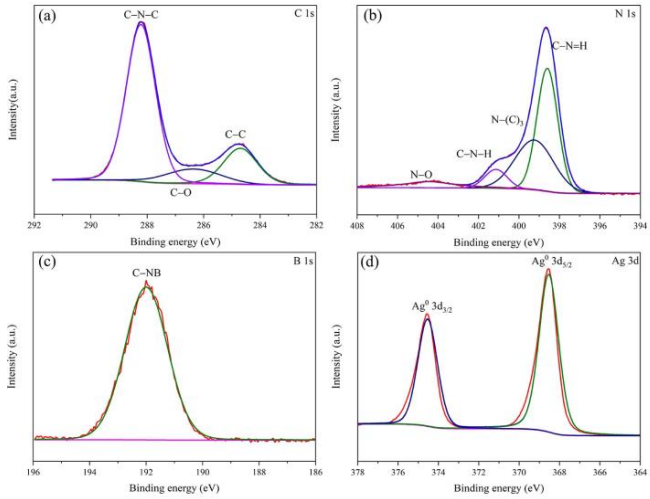

Figure 5. XPS spectra of Ag-B-g-C_3N_4 (a) C 1s, (b) N 1s, (c) B ls, and (d) Ag 3d.

(Figure S1). Diffraction peaks located at 2θ = 38.1°, 44.3°, 64.4°, and 77.4° are the characteristic peaks of (111), (200), (220), and (311) crystal planes of Ag (Joint Committee for Powder Diffraction Standards (JCPDS) No. 65-2871). Meanwhile, the main characteristic peak of the B-g-C_3N_4 support was maintained. In addition, diffraction peaks of B_2O_3 or Ag_2O were not observed. Therefore, metallic Ag NP-loaded B-doped g-C_3N_4 (Ag-B-g-C_3N_4) was successfully prepared.

TEM was employed to study the morphology and size of Ag-B-g-C_3N_4. As exhibited in Figure 4a,b, spherical Ag NPs were evenly deposited on the B-g-C_3N_4. The average diameter of NPs is 4.95 nm, as further exemplified by TEM images in Figure S3, where the particle size distribution was also shown.

https://doi.org/10.1021/acs.iecr.2c00152
Ind. Eng. Chem. Res. 2022, 61, 10400−10408

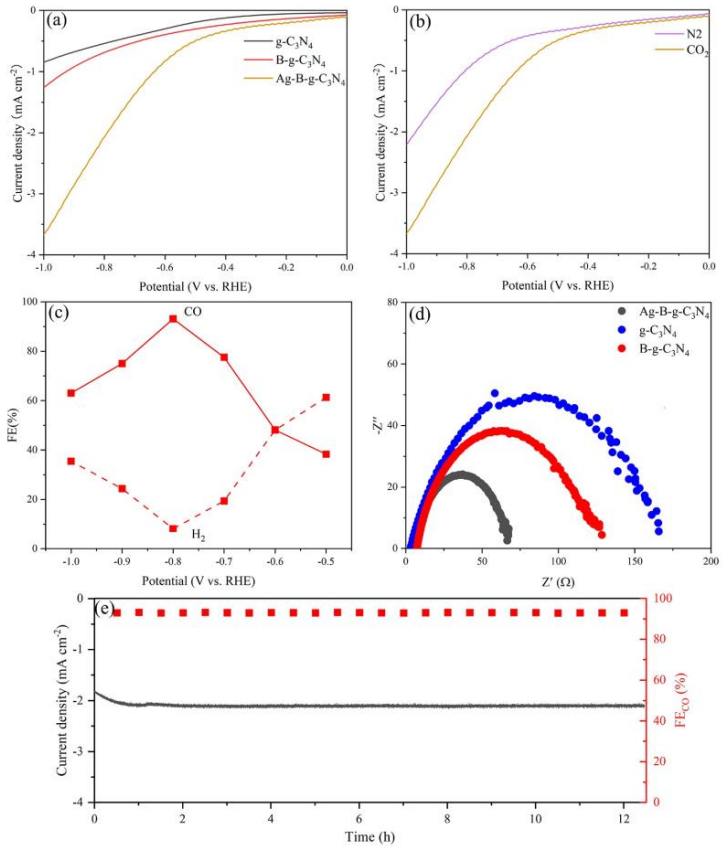

Figure 6. (a) LSV curves of g-C_3N_4, B-g-C_3N_4, and Ag-B-g-C_3N_4 catalysts in a CO_2-saturated 0.5 M $KHCO_3$ solution at a scan rate of 10 mV s^{-1}. (b) LSV curves of the Ag-B-g-C_3N_4 catalyst in N_2- and CO_2-saturated 0.5 M $KHCO_3$ solutions at a scan rate of 10 mV s^{-1}. (c) The Faradaic efficiencies of CO generation and H_2 generation on the Ag-B-g-C_3N_4 catalyst. (d) EIS Nyquist plots for g-C_3N_4, B-g-C_3N_4, and Ag-B-g-C_3N_4 catalysts in 0.5 M $KHCO_3$ under the potential of −0.8 V (vs RHE). (e) Stability test of the Ag-B-g-C_3N_4 catalyst in 0.5 M $KHCO_3$ under −0.8 V (vs RHE) for 12 h.

It can be clearly seen that an interplanar spacing of 0.235 nm was obtained from the lattice fringes for Ag NPs (Figure 4c), attributing to the (111) plane of metallic Ag and close to the theoretical value of 0.236 nm. The selected area electron diffraction pattern (SAED) of Ag-B-g-C_3N_4 was shown in Figure 4d. The diffraction circles corresponding to the (111), (200), (220), and (311) planes of Ag are apparent, consistent with the XRD results.

The high-resolution XPS spectra of C 1s, N 1s, B 1s, and Ag 3d levels for Ag-B-g-C_3N_4 are shown in Figure 5a−d. As the samples have been calcinated in air, O atoms would be inevitably introduced into the skeletons. Therefore, C−O and N−O spectra were detected. For C 1s spectra (Figure 5a), three typical peaks at 288.3, 286.3, and 284.7 eV can be assigned to sp^2-bonded C−N−C of the skeleton, the C−O group, and C−C of carbon contamination, respectively.[41] The N 1s spectrum could be deconvoluted into four peaks with binding energies at 404.3, 401.2, 399.4, and 398.7 eV (Figure 5b), which were attributed to the N−O, C−H−N, N−$(C)_3$, and C−N═C groups, respectively. A broad peak at 192.0 eV could be found in the B 1s level (Figure 5c), which is ascribed to the C-NB group. This is also evidence of the successful doping of B atoms in g-C_3N_4. The spectra of Ag 3d consists of two peaks with binding energies of 374.5 and 368.5 eV (Figure 5d), which are the standardized Ag $3d_{3/2}$ and Ag $3d_{5/2}$ levels of metallic Ag,[12] demonstrating that Ag NPs were successfully loaded on B-doped g-C_3N_4. The XPS spectra of g-C_3N_4 and B-g-C_3N_4 are shown in Figure S4 for comparison. The similar C 1s, N 1s, and B ls spectra for the three catalysts indicate that

https://doi.org/10.1021/acs.iecr.2c00152
Ind. Eng. Chem. Res. 2022, 61, 10400−10408

the structure of the g-C_3N_4 support remains intact after doping with B and Ag.

ECR Activity Test. The ECR catalytic performances were first evaluated by LSV, as exhibited in Figure 6a. In the presence of CO_2 feed gas, the Ag-B-g-C_3N_4 catalyst showed apparently higher reduction current density in comparison with the other two samples, achieving a current density of −2.08 mA cm^{-2} at −0.8 V (vs RHE). The bare carbon paper and carbon black coated carbon paper were also tested as working electrodes but only exhibited a negligible weak current density (Figure S5). In N_2-saturated $KHCO_3$, the Faradaic currents can be attributed to HER, whereas it displayed a much higher current in CO_2-saturated $KHCO_3$ at the same potential (Figure 6b), indicting the catalytic activity of Ag-B-g-C_3N_4 for ECR. These results also suggested that Ag is the active center of the Ag-B-g-C_3N_4 electrocatalyst.

Constant potential electrolysis was performed by choosing the potential ranging from −0.5 V to −1.0 V (vs RHE) to study the ECR selectivity over the Ag-B-g-C_3N_4 catalyst. The resultant gaseous products were analyzed by online GC, while liquid products were analyzed by ^{1}H NMR spectroscopy. CO and H_2 were the only gaseous products with a total FE over 98% (Figure 6c). There is no liquid product found, as evidenced by ^{1}H NMR (Figure S6). The FE_{CO} of Ag-B-g-C_3N_4 increased first and then dropped with the increase of the applied potentials, achieving the maximum FE_{CO} of 93.2% at −0.8 V (vs RHE). It was worth mentioning that both pristine g-C_3N_4 and B-g-C_3N_4 did not produce CO but only H_2 under potentials between −0.5 V and −1.0 V (vs RHE). The bare carbon paper and carbon black coated carbon paper also only generate H_2. These results are consistent with DFT calculations that Ag-B-g-C_3N_4 catalysts show the lowest Gibbs free energy for *COOH generation, while B doping alone could not obviously decrease its Gibbs free energy. Therefore, it can be concluded that Ag NPs are the only active center for ECR to CO.

EIS was carried out at −0.8 V (vs RHE) to disclose the origin of the excellent reactivity of the Ag-B-g-C_3N_4 nanocomposite. The Nyquist plots of g-C_3N_4, B-g-C_3N_4, and Ag-B-g-C_3N_4 were displayed in Figure 6d. Notably, B atoms could effectively improve g-C_3N_4 electron transport due to the generation of the impurity levels. After loading Ag NPs, a much lower charge transfer resistance (R_{CT}) was achieved on Ag-B-g-C_3N_4, validating that the decoration of Ag NPs could enhance electron transportation between the catalyst and CO_2 molecules, thus the ECR capability. These results are in line with the DFT calculations that the electron accumulations at the Ag/B-g-C_3N_4 interface could improve electrical conductivity and promote electron transport.

The long-term stability of the Ag-B-g-C_3N_4 catalyst was examined at −0.8 V (vs RHE) (Figure 6e). Remarkably, the reduction current densities increased during the first hour and then remained stable at −2.08 mA cm^{-2} for 12 h. The corresponding FE_{CO} exhibited no obvious decay during the electrolysis process, indicating excellent stability of the catalyst for selective ECR to CO.

CONCLUSIONS

In this work, Ag NPs loaded on B-decorated g-C_3N_4 was chosen as the nanocomposite electrocatalyst system for ECR study. The ECR performance of the composite catalyst had been investigated through theoretical calculations and experimental work. DFT calculations showed that the Ag-B-g-C_3N_4 catalyst could remarkably decrease the adsorption free energy for *COOH generation. Besides, electron accumulation at the Ag-B-g-C_3N_4 interface could improve electrical conductivity and promote electron transport. The simulation results suggested that the introduction of B atoms and Ag NPs could improve the ECR performance of g-C_3N_4 effectively. Experimentally, we successfully prepared g-C_3N_4, B-g-C_3N_4, and Ag-B-g-C_3N_4 electrocatalysts, which was evidenced by XRD, TEM, and XPS characterizations. Only Ag-B-g-C_3N_4 could produce CO, indicating that Ag is the only active center. Meanwhile, EIS revealed that Ag atoms could promote electron transport. Consequently, the Ag-B-g-C_3N_4 catalyst with an average diameter of 4.95 nm exhibited a FE_{CO} of 93.2% at the potential of −0.8 V (vs RHE) with a total current density of −2.08 mA cm^{-2}. Moreover, the FE_{CO} and current density were maintained without obvious decay for an electrocatalysis of 12 h, demonstrating excellent stability. Therefore, the ECR mechanism on the g-C_3N_4 nanocomposite was understood by combined theoretical and experimental studies, which could offer insight of g-C_3N_4-based catalysts for other electrocatalytic applications.

ASSOCIATED CONTENT

Supporting Information

The Supporting Information is available free of charge at https://pubs.acs.org/doi/10.1021/acs.iecr.2c00152.

Optimized structures of g-C_3N_4, B-g-C_3N_4, and Ag-B-g-C_3N_4; possible active sites and free energy profiles for ECR to CO; TEM images of Ag NPs on B-g-C_3N_4 substrate and particle size distribution of Ag NPs; XPS spectra of C 1s and N 1s of g-C_3N_4 and B ls, C 1s, and N 1s of B-g-C_3N_4; LSV curves of bare carbon paper and carbon paper coated with carbon black; and ^{1}H NMR of possible liquid products (PDF)

AUTHOR INFORMATION

Corresponding Authors

Zhixin Yu − *Department of Energy and Petroleum Engineering, University of Stavanger, 4036 Stavanger, Norway;* orcid.org/0000-0003-2446-6537; Email: zhixin.yu@uis.no

Fengliu Lou − *Beyonder AS, 4033 Stavanger, Norway;* Email: fengliu@beyonder.no

Authors

Song Lu − *Department of Energy and Petroleum Engineering, University of Stavanger, 4036 Stavanger, Norway*

Yang Zhang − *Department of Energy and Petroleum Engineering, University of Stavanger, 4036 Stavanger, Norway; Beyonder AS, 4033 Stavanger, Norway*

Mohamed F. Mady − *Deaprtment of Chemistry, Bioscience and Environmental Engineering, University of Stavanger, 4036 Stavanger, Norway;* orcid.org/0000-0002-4636-0066

Wakshum Mekonnen Tucho − *Department of Mechanical and Structural Engineering and Material Science, University of Stavanger, 4036 Stavanger, Norway*

Complete contact information is available at: https://pubs.acs.org/10.1021/acs.iecr.2c00152

Notes

The authors declare no competing financial interest.

https://doi.org/10.1021/acs.iecr.2c00152
Ind. Eng. Chem. Res. 2022, 61, 10400−10408

■ ACKNOWLEDGMENTS

This work was funded by the Norwegian Ministry of Education and Research. The computations were performed on resources provided by UNINETT Sigma2 - the National Infrastructure for High Performance Computing and Data Storage in Norway.

■ REFERENCES

(1) Chu, S.; Cui, Y.; Liu, N. The path towards sustainable energy. *Nat. Mater.* **2017**, *16*, 16−22.
(2) Quan, Y.; Zhu, J.; Zheng, G. Electrocatalytic reactions for converting CO_2 to value-added products. *Small Science* **2021**, *1*, 2100043.
(3) Agarwal, A. S.; Zhai, Y.; Hill, D.; Sridhar, N. The electrochemical reduction of carbon dioxide to formate/formic Acid: engineering and economic feasibility. *ChemSusChem* **2011**, *4*, 1301−1310.
(4) Pritchard, J.; Filonenko, G. A.; van Putten, R.; Hensen, E. J.; Pidko, E. A. Heterogeneous and homogeneous catalysis for the hydrogenation of carboxylic acid derivatives: history, advances and future directions. *Chem. Soc. Rev.* **2015**, *44*, 3808−3833.
(5) Ling, Y.; Ma, Q.; Yu, Y.; Zhang, B. Optimization strategies for selective CO_2 electroreduction to fuels. *Trans. Tianjin Univ.* **2021**, *27*, 180−200.
(6) Bushuyev, O. S.; De Luna, P.; Dinh, C. T.; Tao, L.; Saur, G.; van de Lagemaat, J.; Kelley, S. O.; Sargent, E. H. What should we make with CO_2 and how can we make it? *Joule* **2018**, *2*, 825−832.
(7) Zhu, D. D.; Liu, J. L.; Qiao, S. Z. Recent advances in inorganic heterogeneous electrocatalysts for reduction of carbon dioxide. *Adv. Mater.* **2016**, *28*, 3423−3452.
(8) Liang, Z.; Wang, H. Y.; Zheng, H.; Zhang, W.; Cao, R. Porphyrin-based frameworks for oxygen electrocatalysis and catalytic reduction of carbon dioxide. *Chem. Soc. Rev.* **2021**, *50*, 2540−2581.
(9) Wang, G.; Chen, J.; Ding, Y.; Cai, P.; Yi, L.; Li, Y.; Tu, C.; Hou, Y.; Wen, Z.; Dai, L. Electrocatalysis for CO_2 conversion: from fundamentals to value-added products. *Chem. Soc. Rev.* **2021**, *50*, 4993−5061.
(10) Li, Y.; Chen, C.; Cao, R.; Pan, Z.; He, H.; Zhou, K. Dual-atom Ag_2/graphene catalyst for efficient electroreduction of CO_2 to CO. *Appl. Catal. B: Environ.* **2020**, *268*, 118747.
(11) Zhang, H.; Li, J.; Xi, S. B.; Du, Y. H.; Hai, X.; Wang, J. Y.; Xu, H. M.; Wu, G.; Zhang, J.; Lu, J.; Wang, J. Z. A graphene-supported single-Atom FeN_5 catalytic site for efficient electrochemical CO_2 reduction. *Angew. Chem., Int. Ed.* **2019**, *58*, 14871−14876.
(12) Zhang, S.; Mo, Z.; Wang, J.; Liu, H.; Liu, P.; Hu, D.; Tan, T.; Wang, C. Ultra-stable oxygen species in Ag nanoparticles anchored on g-C_3N_4 for enhanced electrochemical reduction of CO_2. *Electrochim. Acta* **2021**, *390*, 138831.
(13) Mistry, H.; Reske, R.; Zeng, Z.; Zhao, Z. J.; Greeley, J.; Strasser, P.; Cuenya, B. R. Exceptional size-dependent activity enhancement in the electroreduction of CO_2 over Au nanoparticles. *J. Am. Chem. Soc.* **2014**, *136*, 16473−16476.
(14) Shi, R.; Guo, J.; Zhang, X.; Waterhouse, G. I. N.; Han, Z.; Zhao, Y.; Shang, L.; Zhou, C.; Jiang, L.; Zhang, T. Efficient wettability-controlled electroreduction of CO_2 to CO at Au/C Interfaces. *Nat. Commun.* **2020**, *11*, 3028.
(15) Yang, H.; Shang, L.; Zhang, Q.; Shi, R.; Waterhouse, G. I. N.; Gu, L.; Zhang, T. A universal ligand mediated method for large scale synthesis of transition metal single atom catalysts. *Nat. Commun.* **2019**, *10*, 4585.
(16) Back, S.; Yeom, M. S.; Jung, Y. Active sites of Au and Ag nanoparticle catalysts for CO_2 electroreduction to CO. *ACS Catal.* **2015**, *5*, 5089−5096.
(17) Li, H.; Wu, Y.; Li, C.; Gong, Y.; Niu, L.; Liu, X.; Jiang, Q.; Sun, C.; Xu, S. Design of Pt/T-ZrO_2/g-C_3N_4 efficient photocatalyst for the hydrogen evolution reaction. *Appl. Catal. B: Environ.* **2019**, *251*, 305−312.
(18) Kumar, A.; Xu, Q. Two-dimensional layered materials as catalyst supports. *ChemNanoMat* **2018**, *4*, 28−40.
(19) Cui, B.; Hu, B.; Liu, J.; Wang, M.; Song, Y.; Tian, K.; Zhang, Z.; He, L. Solution-plasma-assisted bimetallic oxide alloy nanoparticles of Pt and Pd embedded within two-dimensional $Ti_3C_2T_X$ nanosheets as highly active electrocatalysts for overall water splitting. *ACS Appl. Mater. Interfaces* **2018**, *10*, 23858−23873.
(20) Kuang, S.; Li, M.; Xia, R.; Xing, L.; Su, Y.; Fan, Q.; Liu, J.; Hensen, E. J. M.; Ma, X.; Zhang, S. Stable surface-anchored Cu nanocubes for CO_2 electroreduction to ethylene. *ACS Appl. Nano Mater.* **2020**, *3*, 8328−8334.
(21) Zheng, Y.; Jiao, Y.; Zhu, Y.; Cai, Q.; Vasileff, A.; Li, L. H.; Han, Y.; Chen, Y.; Qiao, S. Z. Molecule-level g-C_3N_4 coordinated transition metals as a new class of electrocatalysts for oxygen electrode reactions. *J. Am. Chem. Soc.* **2017**, *139*, 3336−3339.
(22) Yan, Q.; Huang, G. F.; Li, D. F.; Zhang, M.; Pan, A. L.; Huang, W. Q. Facile synthesis and superior photocatalytic and electrocatalytic performances of porous B-doped g-C_3N_4 nanosheets. *J. Mater. Sci. Technol.* **2018**, *34*, 2515−2520.
(23) Sun, J.; Bian, J.; Li, J.; Zhang, Z.; Li, Z.; Qu, Y.; Bai, L.; Yang, Z. D.; Jing, L. Efficiently photocatalytic conversion of CO_2 on ultrathin metal phthalocyanine/g-C_3N_4 heterojunctions by promoting charge transfer and CO_2 activation. *Appl. Catal. B: Environ.* **2020**, *277*, 119199.
(24) Guo, S.; Zhao, S. Q.; Wu, X. Q.; Li, H.; Zhou, Y. J.; Zhu, C.; Yang, N. J.; Jiang, X.; Gao, J.; Bai, L.; Liu, Y.; Lifshitz, Y.; Lee, S. T.; Kang, Z. H. A Co_3O_4-Cdots-C_3N_4 three component electrocatalyst design concept for efficient and tunable CO_2 reduction to syngas. *Nat. Commun.* **2017**, *8*, 1828.
(25) Wang, H.; Sun, T.; Chang, L.; Nie, P.; Zhang, X.; Zhao, C.; Xue, X. The g-C_3N_4 nanosheets decorated by plasmonic Au nanoparticles: A heterogeneous electrocatalyst for oxygen evolution reaction enhanced by sunlight illumination. *Electrochim. Acta* **2019**, *303*, 110−117.
(26) Jiao, Y.; Zheng, Y.; Smith, S. C.; Du, A.; Zhu, Z. Electrocatalytically switchable CO_2 capture: first principle computational exploration of carbon nanotubes with pyridinic nitrogen. *ChemSusChem* **2014**, *7*, 435−441.
(27) Zheng, Y.; Jiao, Y.; Chen, J.; Liu, J.; Liang, J.; Du, A. J.; Zhang, W. M.; Zhu, Z. H.; Smith, S. C.; Jaroniec, M.; Lu, G. Q.; Qiao, S. Z. Nanoporous graphitic-C_3N_4@carbon metal-free electrocatalysts for highly efficient oxygen reduction. *J. Am. Chem. Soc.* **2011**, *133*, 20116−20119.
(28) Zhang, L.; Mao, F.; Zheng, L. R.; Wang, H. F.; Yang, X. H.; Yang, H. G. Tuning metal catalyst with metal-C_3N_4 interaction for efficient CoO_2 electroreduction. *ACS Catal.* **2018**, *8*, 11035−11041.
(29) Chen, J.; Wang, Z.; Lee, H.; Mao, J.; Grimes, C. A.; Liu, C.; Zhang, M.; Lu, Z.; Chen, Y.; Feng, S. P. Efficient electroreduction of CO_2 to CO by Ag-decorated S-doped g-C_3N_4/CNT nanocomposites at industrial scale current density. *Mater. Today Phys.* **2020**, *12*, 100176.
(30) Lu, S.; Li, C.; Li, H. H.; Zhao, Y. F.; Gong, Y. Y.; Niu, L. Y.; Liu, X. J.; Wang, T. The effects of nonmetal dopants on the electronic, optical and chemical performances of monolayer g-C_3N_4 by first-principles study. *Appl. Surf. Sci.* **2017**, *392*, 966−974.
(31) Wei, B.; Wang, W.; Sun, J.; Mei, Q.; An, Z.; Cao, H.; Han, D.; Xie, J.; Zhan, J.; He, M. Insight into the effect of boron doping on electronic structure, photocatalytic and adsorption performance of g-C_3N_4 by first-principles study. *Appl. Surf. Sci.* **2020**, *511*, 145549.
(32) Kresse, G.; Furthmüller, J. Efficiency of ab-initio total energy calculations for metals and semiconductors using a plane-wave basis set. *Comput. Mater. Sci.* **1996**, *6*, 15−50.
(33) Kresse, G.; Furthmüller. Efficient iterative schemes for ab initio total-energy calculations using a plane-wave basis set. *Phys. Rev. B* **1996**, *54*, 11169−11186.
(34) Perdew, J. P.; Burke, K.; Ernzerhof, M. Generalized gradient approximation made simple. *Phys. Rev. Lett.* **1996**, *77*, 3865−3868.
(35) Kresse, G.; Joubert, D. From ultrasoft pseudopotentials to the projector augmented-wave method. *Phys. Rev. B* **1999**, *59*, 1758−1775.

https://doi.org/10.1021/acs.iecr.2c00152
Ind. Eng. Chem. Res. 2022, 61, 10400−10408

(36) Grimme, S.; Antony, J.; Ehrlich, S.; Krieg, H. A consistent and accurate ab Initio parametrization of density functional dispersion correction (DFT-D) for the 94 Elements H-Pu. *J. Chem. Phys.* **2010**, *132*, 154104.
(37) Nørskov, J. K.; Rossmeisl, J.; Logadottir, A.; Lindqvist, L.; Kitchin, J. R.; Bligaard, T.; Jónsson, H. Origin of the overpotential for oxygen reduction at a fuel-cell cathode. *J. Phys. Chem. B* **2004**, *108*, 17886−17892.
(38) Thaweesak, S.; Lyu, M.; Peerakiatkhajohn, P.; Butburee, T.; Luo, B.; Chen, H.; Wang, L. Two-dimensional g-C_3N_4/$Ca_2Nb_2TaO_{10}$ nanosheet composites for efficient visible light photocatalytic hydrogen evolution. *Appl. Catal. B: Environ.* **2017**, *202*, 184−190.
(39) Thorat, N.; Yadav, A.; Yadav, M.; Gupta, S.; Varma, R.; Pillai, S.; Fernandes, R.; Patel, M.; Patel, N. Ag loaded B-doped-g-C_3N_4 nanosheet with efficient properties for photocatalysis. *J. Environ. Manage* **2019**, *247*, 57−66.
(40) Hong, J.; Xia, X.; Wang, Y.; Xu, R. Mesoporous carbon nitride with in situ sulfur doping for enhanced photocatalytic hydrogen evolution from water under visible light. *J. Mater. Chem.* **2012**, *22*, 15006−15012.
(41) Caux, M.; Fina, F.; Irvine, J. T. S.; Idriss, H.; Howe, R. Impact of the annealing temperature on Pt/g-C_3N_4 structure, activity and selectivity between photodegradation and water splitting. *Catal. Today* **2017**, *287*, 182−188.

https://doi.org/10.1021/acs.iecr.2c00152
Ind. Eng. Chem. Res. 2022, 61, 10400−10408

Supporting Information

Efficient electrochemical reduction of CO_2 to CO by Ag-decorated B-doped g-C_3N_4: A combined theoretical and experimental study

Song Lu[a], Yang Zhang[ad], Mohamed F. Mady[b], Wakshum Mekonnen Tucho[c], Fengliu Lou[d]*, Zhixin Yu[a]*

[a]Department of Energy and Petroleum Engineering, University of Stavanger, 4036 Stavanger, Norway

[b]Deaprtment of Chemistry, Bioscience and Environmental Engineering, University of Stavanger, 4036 Stavanger, Norway

[c]Department of Mechanical and Structural Engineering and Material Science, University of Stavanger, 4036 Stavanger, Norway

[d]Beyonder AS, Kanalsletta 2, 4033 Stavanger, Norway

***Corresponding author:**

Prof. Zhixin Yu

E-mail address: zhixin.yu@uis.no

Department of Energy and Petroleum Engineering, University of Stavanger, 4036 Stavanger, Norway

Tel: +47 51 83 22 38

Dr. Fengliu Lou

E-mail address: fengliu@beyonder.no

Beyonder AS, Kanalsletta 2, 4033 Stavanger, Norway

Figure S1. The optimized structures of (a) g-C_3N_4, (b) B-g-C_3N_4 and (c) Ag-B-g-C_3N_4.

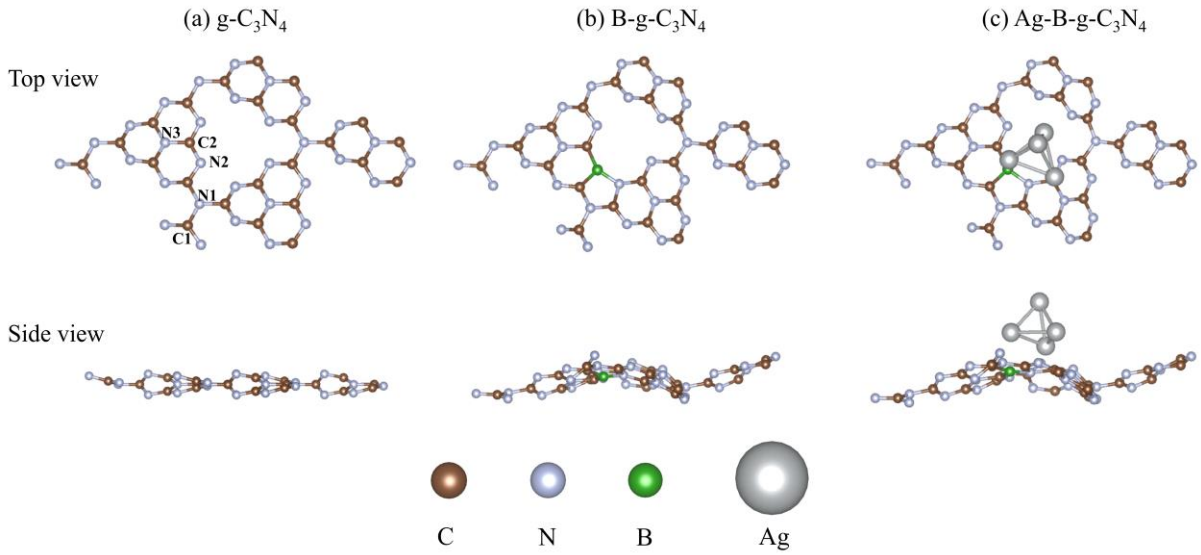

Figure S2. (a) The possible active sites S1(B atom), S2(N atom), S3 (C atom), S4(N atom), S5(N atom) and S6 (C atom) for ECR to CO after Ag cluster loading on B-g-C_3N_4; (b) Calculated free energy profiles for ECR to CO on S5.

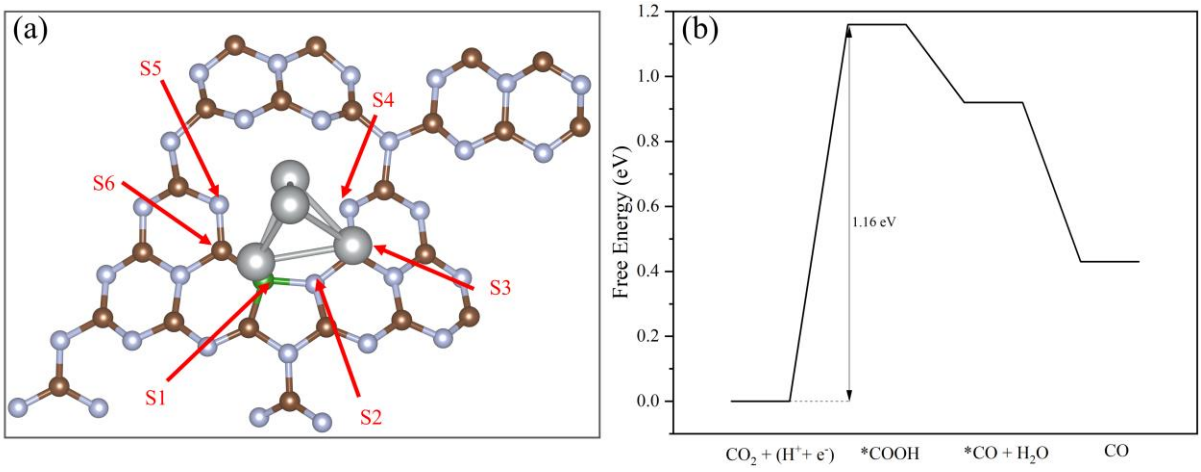

Figure S3. (a) TEM images of Ag NPs on B-g-C_3N_4 substrate; (b) Particle size distribution of Ag NPs with an average size of 4.95 nm.

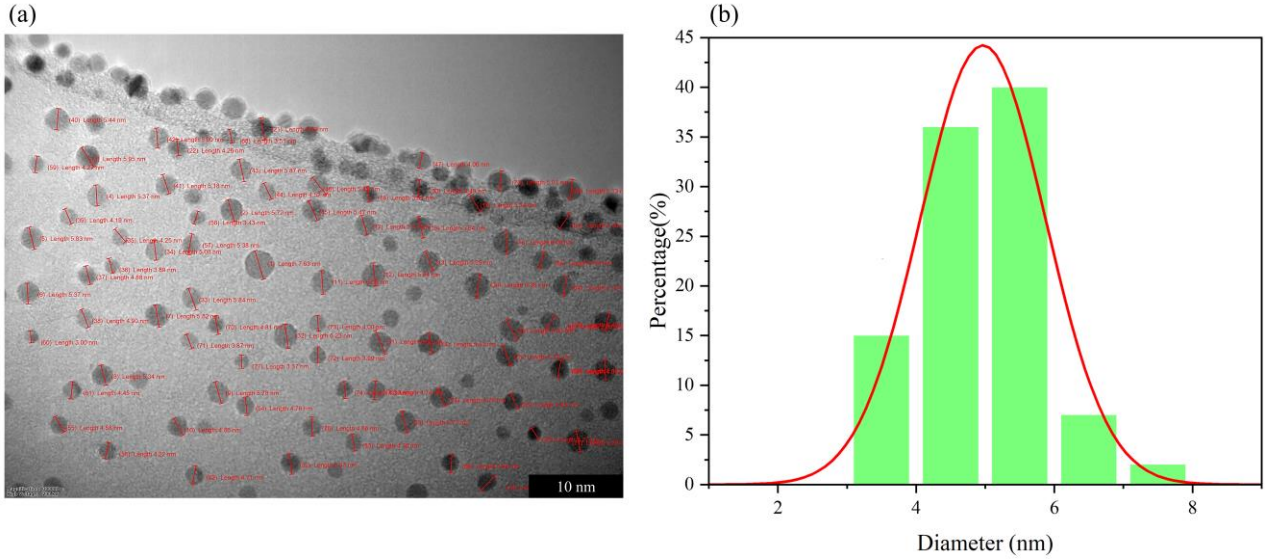

Figure S4. XPS spectra of (a) C1s and N1s of g-C_3N_4 and (b) B ls, C1s and N1s of B-g-C_3N_4.

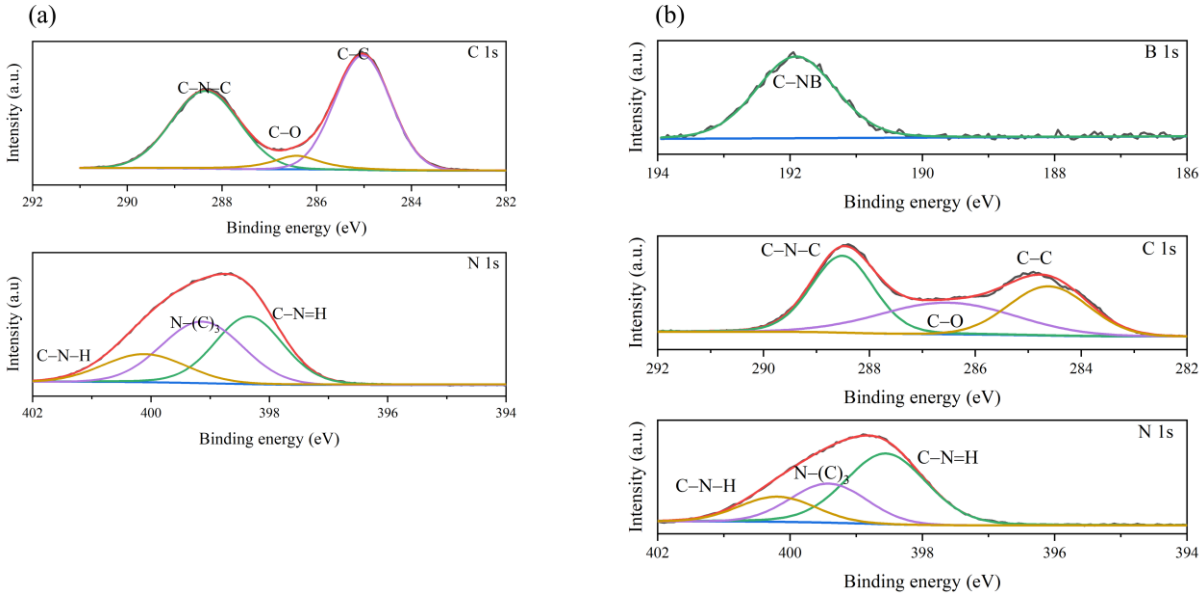

Figure S5. The LSV curves of bare carbon paper and carbon paper coated with carbon black catalysts in the CO_2-saturated 0.5M $KHCO_3$ solution at a scan rate of 10 mV s^{-1}.

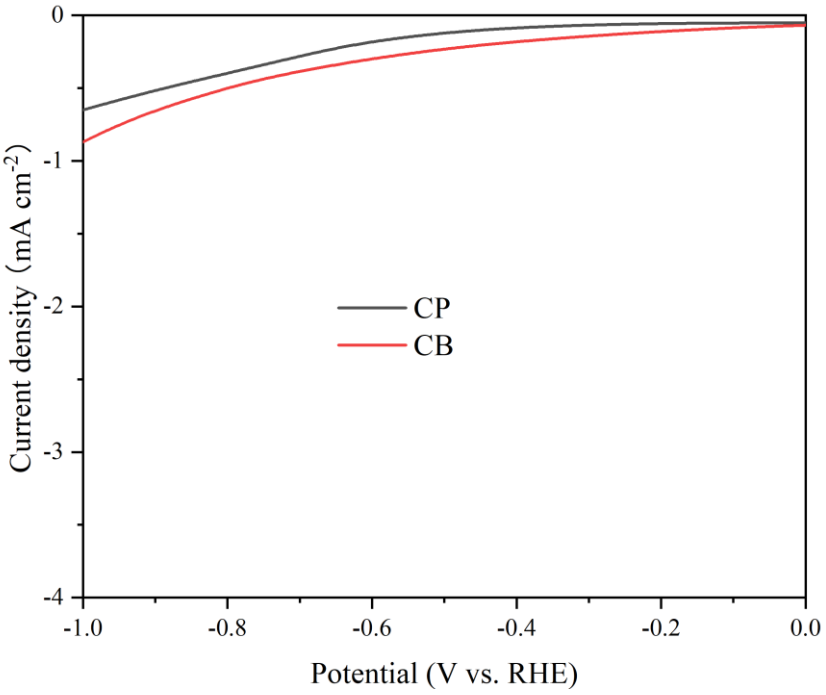

Figure S6. ^1H NMR of the possible liquid products after electrolysis for 1 h over the Ag-B-g-C_3N_4 catalyst at –0.80 V (vs. RHE) in CO_2-saturated 0.5 M $KHCO_3$.

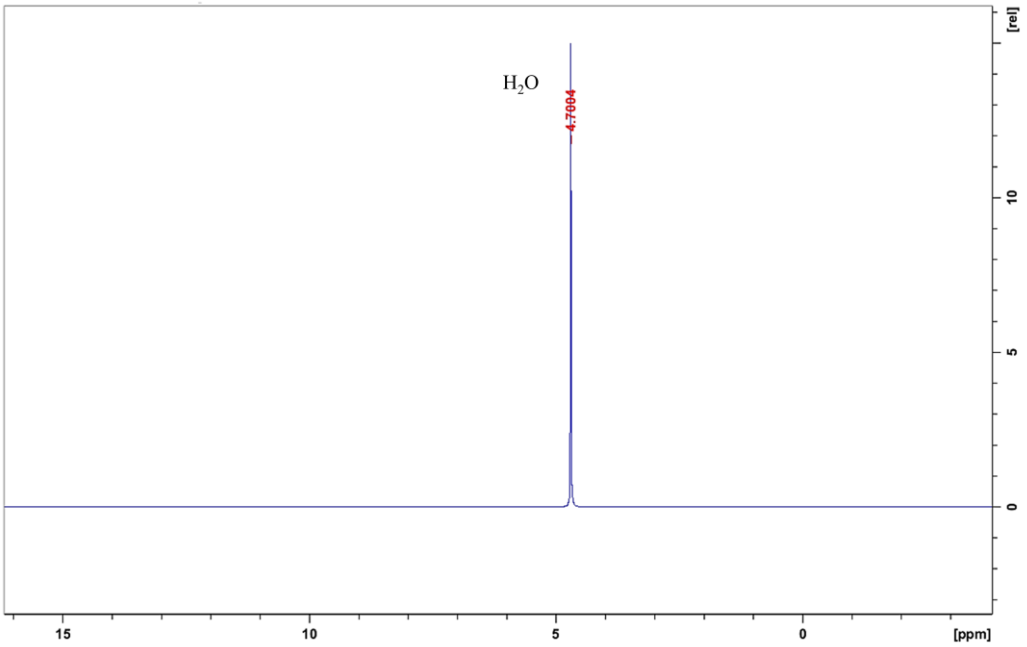

Appendix C – Paper III

Theoretical study of single transition metal atom catalysts supported on two-dimensional Nb_2NO_2 for efficient electrochemical CO_2 reduction to CH_4

S. Lu, Y. Zhang, F. Lou and Z. Yu

Journal of CO_2 Utilization, 2022, 62, 102069

DOI: 10.1016/j.jcou.2022.102069

Journal of CO2 Utilization 62 (2022) 102069

Contents lists available at ScienceDirect

Journal of CO2 Utilization

journal homepage: www.elsevier.com/locate/jcou

Theoretical study of single transition metal atom catalysts supported on two-dimensional Nb_2NO_2 for efficient electrochemical CO_2 reduction to CH_4

Song Lu [a], Yang Zhang [a], Fengliu Lou [b,*], Zhixin Yu [a,*]

[a] Department of Energy and Petroleum Engineering, University of Stavanger, 4036 Stavanger, Norway
[b] Beyonder AS, Kanalsletta 2, 4033 Stavanger, Norway

ARTICLE INFO

Keywords:
Nb_2NO_2 MXene
CO_2 electrocatalytic reduction
Single-atom catalysts
First-principles calculation

ABSTRACT

The design of highly efficient catalysts for electrochemical reduction CO_2 (ECR) to value-add chemicals and fuels is important for CO_2 conversion technologies. In this work, earth abundant transition metal (TM = V, Cr, Mn, Fe, Co and Ni) atoms embedded into two-dimensional (2D) Nb_2NO_2 (TM@Nb_2NO_2) as single-atom catalysts (SACs) for ECR was investigated by first-principles study. We demonstrated that Nb_2NO_2 can be an excellent substrate for anchoring single TM atom due to its excellent stability and electronic conductivity. Besides, V, Cr and Ni@Nb_2NO_2 could effectively promote CO_2 adsorption and reduction. All TM@Nb_2NO_2 exhibit high selectivity towards CH_4, and V, Cr and Ni@Nb_2NO_2 show low limiting potentials. The activity origin was revealed by analysing adsorption energy, *d* band centre, bonding/antibonding population and the change of valence state of TM atoms.

1. Introduction

With the rapid development of the global economy, energy crisis and environment issues have become increasingly prominent. Carbon dioxide (CO_2) is a primary greenhouse gas, while it could also be a valuable carbon source. In recent years, electrochemical CO_2 reduction reaction (ECR) has received considerable attention among various CO_2 conversion technologies due to numerous advantages [1,2]. For instance, ECR can be driven under ambient temperature and pressure using renewable energy source such as wind and solar power [3,4]. The external voltages as well as electrolytes solutions can be adjusted for the generation of specific products. Furthermore, ECR technology could not only mitigate CO2 emission, but also effectively convert CO_2 to value-added chemicals and fuels, which has been regarded as an appealing technology path for closing the carbon circle [5–7]. Nevertheless, physicochemical properties of the CO_2 molecule make electrochemical conversion of CO_2 challenging [8,9]. In the past decades, metals or related oxides, carbon-based materials and nanocomposites have been widely investigated as electrocatalysts for ECR. Despite that great progress has been made to exploit electrocatalysts for ECR, the process is still impeded by the sluggish kinetics, poor product selectivity, catalyst stability, and high overpotential [10–13]. Taking copper as an example, it can electrochemically convert CO_2 to CH_4 with a high overpotential around 0.9 V, but the selectivity to specific products is low [14,15]. Therefore, it is highly desirable to develop electrocatalysts with high activity and selectivity for ECR.

It has been well established that the catalytic activity can be improved by reducing the size of catalysts. Specifically, single atoms catalysts (SACs) with single atom as active centre have aroused huge interest due to maximum atom utilization and excellent performance in various catalytic reactions such as water splitting, CO_2 reduction, N_2 reduction, etc. [16–20]. It is worth noting that the preparation of SACs is a challenge because single atoms with high surface energy are easy to aggregate into clusters, leading to catalyst deactivation. Thus, a suitable support which could offer anchoring sites and possesses good stability will greatly improve the activity of SACs. Two-dimensional (2D) materials are appealing substrates for anchoring single transition metal atom due to their unique structures and electronic properties [21–23]. Moreover, it has been disclosed that the interaction between *p*-orbital of substrates and *d*-orbitals of single transition metal atom are beneficial for highly effective electrocatalysts [24,25]. For example, single transition metal atoms embedded into graphene, graphitic carbon nitride (g-C_3N_4), graphyne, boron nitride (BN), phthalocyanine (PC), etc. have been widely studied as promising SACs for CO_2 reduction [26–29].

* Corresponding author.
E-mail addresses: fengliu@beyonder.no (F. Lou), zhixin.yu@uis.no (Z. Yu).

https://doi.org/10.1016/j.jcou.2022.102069
Received 23 March 2022; Received in revised form 10 May 2022; Accepted 20 May 2022
Available online 26 May 2022

Recently, a family of 2D transition metal carbides, nitrides and carbonitrides, known as MXenes, were reported and synthesized from the layered $M_{n+1}AX_n$ phase [30]. In $M_{n+1}AX_n$, M stands for early transition metals, A denotes the group 13 or 14 elements, X denotes C or N, and n is between 1 and 3 [31]. There are a variety of MXenes that have been predicted and synthesized experimentally, which are explored for applications in many fields [32]. For instance, Li et al. reported that MXenes from the group IV to VI series are active for CO_2 capture, while Cr_3C_2 and Mo_3C_2 are promising catalysts for CO_2 conversion to CH_4 [33]. Both simulation study and experimental work have shown that MXenes have large surface areas, excellent electronic conductivity, tunable surface composition and great stability [32,34]. Thanks to these merits, MXenes have also been demonstrated to be promising substrates for anchoring single transition metal atoms in catalytic reactions [35]. Generally, $M_{n+1}N_n$ is more difficult to synthesize compared to $M_{n+1}C_n$. Interestingly, it has been demonstrated that nitride MXenes exhibit better conductivity in comparison with carbide MXenes [36]. During synthesis, the basal plane of MXenes could be functionalized by various atoms or groups including O, OH and F, which affect their inherent properties [30]. Recent investigations have demonstrated that under high temperature treatment the F group can be eliminated and OH group can be converted to O groups [37,38]. Studies have confirmed that these different functional groups could tune the work function and electronic properties of MXenes [39].

Nb-based MXenes have gained great attention in energy storage and conversion [40,41]. Pt-doped Nb-based MXene has been reported to be an excellent bifunctional OER/ORR catalyst [42], while nitride Nb_2N for ECR has not been studied. In this work, for the first time, we investigated the single transition metal atoms (V, Cr, Mn, Fe, Co, Ni) embedded O group terminated Nb_2N monolayer (Nb_2NO_2) as ECR catalysts by first-principles calculation. It is found that Nb_2NO_2 can be an ideal support for anchoring sing TM atoms because of excellent stability and conductivity. TM@Nb_2NO_2 show excellent CO_2 adsorption capacity, which benefits CO_2 activation and reduction. Among six SACs catalysts, V, Cr and Ni@ Nb_2NO_2 are identified as efficient electrocatalysts for ECR to CH_4, with smaller limiting potential of − 0.45, − 0.47 and − 0.28 V, respectively. Meanwhile, the origin of the ECR activity was revealed by several key descriptors.

2. Computational method

All calculations were carried out by spin-polarized density functional theory (DFT) in the Vienna Ab initio Simulation Package (VASP) with projector augmented wave (PAW) [43,44]. The generalized gradient approximation (GGA) implemented Perdew-Burke-Ernzerhof (PBE) was used to calculate the exchange-correlation energy [45,46]. The empirical correction (DFT-D3) was employed to describe the van der Waals (vdW) interactions [47]. The parameter for dipole correction along z-direction are considered in our calculations. DFT+U calculations are also considered for single TM atoms. The values of U−J were set to be 2.72, 2.79, 3.06, 3.29, 3.42 and 3.4 eV for V, Cr, Mn, Fe, Co, and Ni, respectively [18]. A 3 × 3 × 1 TM@Nb_2NO_2 containing 45 atoms was constructed by anchoring one TM atom in site1 (N site) and site 2 (Nb site) (Fig. 1a). The 18 Å thickness vacuum region in the z-direction was added to eliminate the spurious interactions from periodic boundary. The cutoff energy was set to 500 eV. The K-points for geometry optimization and electronic calculations were set to be 6 × 6 × 1 and 10 × 10 × 1, respectively. The convergence of energy and force was set to be 1.0×10^{-5} eV and 1.0×10^{-2} eV/Å, respectively. Solvent effect was included in our calculations by using implicit solvent model based on VASPsol, and the dielectric constant of water was 78.4 [48]. Moreover, to explore structure stability, the ab initio molecular dynamics (AIMD) simulation was performed in NVT ensemble and phonon spectra was calculated based on the density functional perturbation theory (DFPT)

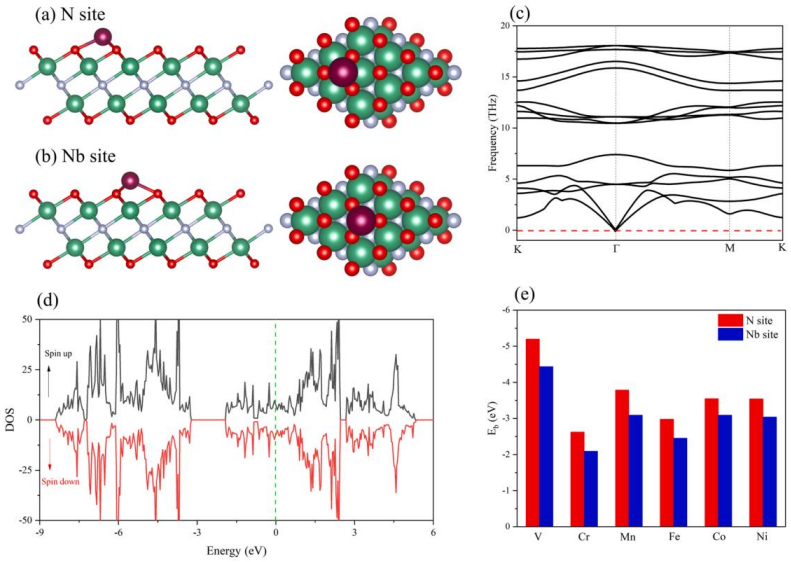

Fig. 1. The two possible adsorption sites for TM atoms (a)N site and (b) Nb site, where the whitesmoke, red, turquoise and purple ball denote the N, O, Nb and TM atoms; (c) The phonon curves of Nb_2NO_2; (d) The total density of state of Nb_2NO_2, where the green dash line is Fermi energy level; (e) The binding energies of TM atoms on N site and Nb site.

[49,50]. The TM atom transition energy barrier on Nb_2NO_2 monolayer was calculated by the climbing image nudged elastic band method (CINEB) [51], transition states were confirmed by vibration frequency analysis. The Bader charge analysis was used to analyze electron transfer [52].

The binding energy (E_b) of TM atoms on Nb_2NO_2 monolayer was calculated by Eq. 1:

$$E_b = E(TM@Nb_2NO_2) - E(TM) - E(Nb_2NO_2) \quad (1)$$

where E(TM), $E(Nb_2NO_2)$ and $E(TM@Nb_2NO_2)$ denote the total energies of single TM atom, Nb_2NO_2, and $TM@Nb_2NO_2$, respectively. With such definition, a more negative value indicates a stronger binding of TM atoms to the Nb_2NO_2 substrate.

The gas adsorption energy (E_{ads}) was calculated by Eq. 2:

$$E_{ads} = E(gas@Nb_2NO_2) - E(gas) - E(Nb_2NO_2) \quad (2)$$

where E(gas), $E(Nb_2NO_2)$ and $E(gas@Nb_2NO_2)$ are the total energies of gas, Nb_2NO_2 and gas adsorbed Nb_2NO_2.

The Gibbs free energy of ECR were calculated by the computational hydrogen electrode (CHE) method [53]. After intermediate was adsorbed on the surface of catalyst, the translation and rotation freedom could be ignored and only vibration freedom is contributed to the entropy. The free energy of H^+/e^- pair is equivalent to the chemical potential of H_2 at standard conditions. The Gibbs free energy change (ΔG) can be obtained by Eq. 3:

$$\Delta G = \Delta E + \Delta E(ZPE) - T\Delta S + \Delta G(pH) + \Delta G(U) \quad (3)$$

in which ΔE was the energy difference between reactants and products directly obtained from DFT calculations, $\Delta E(ZPE)$ and ΔS are zero-point energy correction and entropy change at temperature T of 298.15 K. $\Delta G(pH)$ is the free energy correction due to the effect of H concentration, and was calculated by the formula $\Delta G(pH) = k_BTln10 \times pH$. In this work, the pH value was set to be zero under acidic condition. $\Delta G(U)$ is the contribution of the applied electrode potentials. The limiting potential (U_L) from potential-determining step (PDS) can be obtained by Eq. 4:

$$U_L = -\Delta G_{max}/e \quad (4)$$

where ΔG_{max} is the maximum free energy change in the ECR process along the most favourable pathway.

3. Result and discussion

3.1. Structure and stability of Nb_2NO_2

After geometry optimization, the obtained lattice parameter *a* of clean Nb_2N monolayer is 3.11 Å, consistent with previous study [54]. Nb_2N monolayer shows a hexagonal symmetry with P63/mmc space group. O was then added on the centre of three Nb atoms, similar to the O functionalized Ti_2C MXene (Fig. 1a and b) [55]. The binding energy (E_b) of O on Nb_2N monolayer was calculated by the equation: $E_b = (E(Nb_2NO_2) - E(O_2) - E(Nb_2N))/2$, where $E(Nb_2NO_2)$, $E(O_2)$, $E(Nb_2N)$ are the total energy of Nb_2NO_2, O_2 and Nb_2N [56]. A negative value of E_b = –5.34 eV demonstrates that Nb_2N monolayer can be easily covered by O atoms. It is possible for O group transforming to OH during ECR process. Therefore, we calculated the Gibbs free energy for H adsorption on O atoms, with ΔG^*H of −0.16 eV. A moderate ΔG^*H indicates that the proton can easily adsorb on and desorb from the surficial O atom, which may promote protonation of the ECR intermediates. The phonon curves and AIMD simulation were performed to check its stability, as shown in Fig. 1c and Fig. S1. There are no imaginary bands in phonon spectra. The fluctuation of the total energy of Nb_2NO_2 is quite small and around the equilibrium. Meanwhile, the structure does not show any obvious changes, confirming that Nb_2NO_2 monolayer possesses excellent stability. On the other hand, the calculated density of state of Nb_2NO_2 exhibits metallic behaviour, indicting good capability for electron transfer (Fig. 1d). This endows Nb_2NO_2 monolayer excellent electrical conductivity, a prerequisite for an ideal substrate for SACs used in ECR.

3.2. Structure and stability of $TM@Nb_2NO_2$

The stability of TM anchored Nb_2NO_2 will be the key for the synthesis and application of MXene based SACs. As presented in Fig. 1a and b, there are two possible anchoring sites for single TM atoms: (1) the centre site between three neighbouring N atoms and the top of Nb atom (Nb site), (2) the centre site between three neighbouring Nb atoms and the top of N atom (N site). After structure relaxation, the anchored TM atoms have slight effects on lattice parameters *a*. The thermodynamic stabilities of $TM@Nb_2N$ were investigated by calculating E_b (Fig. 1e and Table S1). Notably, a more negative value of E_b on N site indicates that TM atoms prefer to bind on N site. Moreover, the transition energy barriers (E_T) of single TM atoms from N to Nb site were calculated to evaluate its kinetic stability. The E_T were calculated by $E_T = E_{TS} - E_{IS}$, in which E_{TS} is the total energy of transition state (TS) from N to Nb site, while E_{IS} is the total energy of TM embedded in N site. As shown in Table S1, the E_T of TM atoms are quite large in the range of 0.87–2.58 eV, implying that it is difficult for TM atoms to diffuse and aggregate into clusters. These results suggest that single TM atom can firmly anchor on N site. We therefore will only consider this site as active site for further study. In addition, Bader charge analysis show that the charge transfer from TM atoms to substrate decreases with the atomic number. Consequently, V and Cr atom present higher oxidation state (+1.08 and +1.02), while Ni atom shows lower oxidation value (+0.50).

3.3. CO_2 adsorption and activation on $TM@Nb_2NO_2$

CO_2 adsorption on the surface of electrocatalysts is important for CO_2 activation and transformation into intermediates such as *COOH and *OCHO [57]. The optimized CO_2 adsorption configurations on $TM@Nb_2NO_2$ were shown in Fig. 2. Obviously, the carbon or oxygen atom of CO_2 molecule is absorbed on TM atoms. Meanwhile, it can be observed that CO_2 molecule is not absorbed on $TM@Nb_2NO_2$ in linear state, but with a certain degree of bending. The corresponding adsorption energies, bond lengths of C−TM and O−TM, bond angels of CO_2 molecule, and charge transfer between TM and CO_2 molecule are summarized in Table 1. It is clear that the bond angle of CO_2 molecule on $TM@Nb_2NO_2$ increases with the atomic number, ranging from 138.39° to 154.34°. Specially, $V@Nb_2NO_2$ greatly deviated from the linear state, which indicates higher CO_2 adsorption capacity. The bond lengths of C−TM and O−TM are quite close to 2.00 Å, demonstrating strong adsorption between substrate and CO_2 molecule, consistent with previous studies [26,58]. The CO_2 adsorption energies on $TM@Nb_2NO_2$ range from − 0.77 and − 0.30 eV. The negative values indicate that CO_2 adsorption on the SACs is thermodynamically favourable. V, Cr and $Ni@Nb_2NO_2$ exhibit relatively strong interaction with CO_2. Bader charge analysis confirm that there is a significant net charge transfer from V, Cr and Ni atoms to CO_2, with a value of − 0.60e, − 0.53e, − 0.31e, respectively. Thus, CO_2 molecules can be effectively activated by V, Cr and $Ni@Nb_2NO_2$, and these three SACs potentially exhibit high performance for producing specific ECR products.

3.4. Competition between HER and ECR during first protonation

The ECR process starts with the hydrogenation of CO_2 molecule to form *COOH ($* + CO_2 + (H^+ + e^-) \rightarrow$ *COOH) or *OCHO ($* + CO_2 + (H^+ + e^-) \rightarrow$ *OCHO) on active centres by H atom binding O or C atom. However, the side-reaction HER ($* + H^+ + e^- \rightarrow$ *H) may occur due to the direct interaction between proton and TM atoms, resulting in low ECR selectivity. It has been widely accepted that the Gibbs free energy change (ΔG) for *COOH/*OCHO and *H formation can be used to

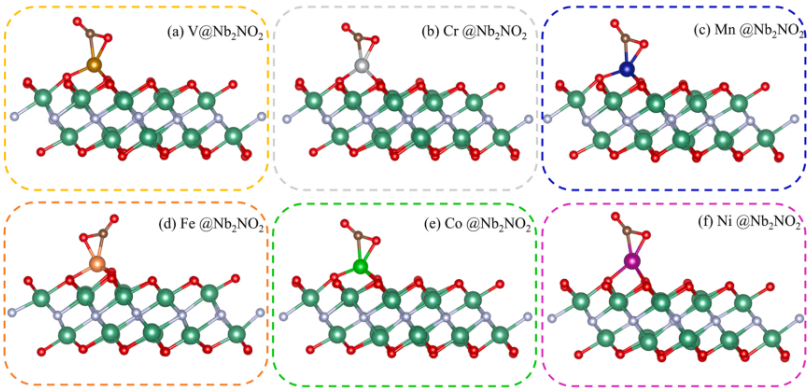

Fig. 2. The most stable CO_2 adsorption configurations on (a) $V@Nb_2NO_2$, (b) $Cr@Nb_2NO_2$, (c) $Mn@Nb_2NO_2$, (d) Fe $Ni@Nb_2NO_2$, (e) $Co@Nb_2NO_2$ and (f) $Ni@Nb_2NO_2$.

Table 1
CO_2 adsorption on $TM@Nb_2NO_2$: adsorption energy (E_{ads}) with unit eV, the angel of O−C−O with unit °, the bond length of TM−O and TM−C with unit Å, net charge accepted by CO_2 molecule with unit e.

Catalysts	E_{ads} (CO_2)	O−C−O angle	d_{TM-C}	d_{TM-O}	Q
$V@Nb_2NO_2$	− 0.77	138.39	2.00	1.93	− 0.60
$Cr@Nb_2NO_2$	− 0.51	142.59	2.00	1.97	− 0.53
$Mn@Nb_2NO_2$	− 0.34	141.62	2.00	1.93	− 0.58
$Fe@Nb_2NO_2$	− 0.46	150.77	2.04	2.00	− 0.25
$Co@Nb_2NO_2$	− 0.30	154.34	2.05	1.99	− 0.26
$Ni@Nb_2NO_2$	− 0.54	151.74	1.96	1.92	− 0.31

evaluate the ECR selectivity versus HER selectivity [59]. Therefore, $\Delta G_{*COOH/*OCHO}$ were calculated and compared with ΔG_{*H}. As plotted in Fig. 3, all $TM@Nb_2NO_2$ electrocatalysts prefer ECR (below the diagonal) to HER (above the diagonal). Notably, V, Cr and $Fe@Nb_2NO_2$ are ECR selective with two favourable initial protonation processes (*COOH and *OCHO), while Ni, Co and $Mn@Nb_2NO_2$ exhibit ECR selectivity only with one favourable initial protonation step (*COOH or *OCHO). Meanwhile, ΔG_{*OCHO} is smaller than ΔG_{*COOH} for V, Cr and Fe@Nb_2NO_2, demonstrating that the formation of *OCHO is more energetically favourable. Therefore, the *COOH reduction path and the corresponding CO product will not be considered on these three SACs in the further protonation process.

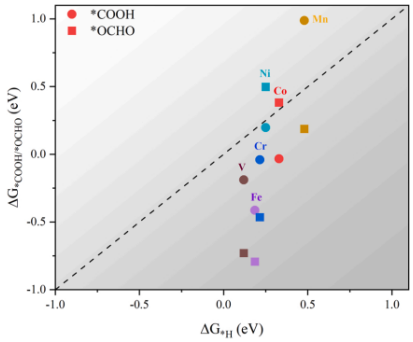

Fig. 3. The Gibbs free energy changes (ΔG (eV)) for the first protonation step in ECR and HER on $TM@Nb_2NO_2$.

3.5. ECR to C1 products on $TM@Nb_2NO_2$

The reduction products from CO_2 could involve C_1, C_2 and C_3 due to complex protonation and C−C coupling. However, the formation of high carbon products (C_{2+}) is impossible because C−C coupling will not occur on SACs. Therefore, only C_1 products by accepting 2e to 8e electrons, including CO, HCOOH, HCHO, CH_3OH, CH_4, were investigated in this work. These different products are formed by different number of protons binding C or O atoms. A possible pathway was plotted in Fig. 4 by taking the optimized configuration of intermediates on $Fe@Nb_2NO_2$ as an example. It is obvious that only TM atom binds with the C or O atoms during the whole ECR process, demonstrating TM atom as active site.

After *COOH or *OCHO formation via accepting first proton-electron pair, further hydrogenation by obtaining a second proton-electron pair will produce *OCHOH or *CO intermediates. Therefore, the binding strength between these two intermediates and active centre will decide HCOOH or CO generation. We calculated the E_{ads} of HCOOH and CO on $TM@Nb_2NO_2$ (Table 2). For HCOOH formation from *OCHO, V, Cr, Mn and $Fe@Nb_2NO_2$ show a large E_{ads} with − 1.07, − 1.25, − 0.87 and − 1.51 eV, respectively. For CO formation from *COOH, the E_{ads} of CO on Co and $Ni@Nb_2NO_2$ are − 1.95 and − 1.73 eV, respectively. It means that both HCOOH and CO could be further protonated on these SACs instead of desorbing from the SACs as final products. In addition, the generation of *OCHOH or *CO on Fe, Co, Cr, Ni and $V@Nb_2NO_2$ are overall exothermic. The generation of *OCHOH is only slightly endothermic on $Mn@Nb_2NO_2$, benefiting the further reduction of intermediates.

For further hydrogenation of *OCHOH or *CO, three possible intermediate including *CHO, *COH and *OCH could be generated. Notably, *COH from *CO (*CO + (H^+ + e^-) →*COH) on Co and $Ni@Nb_2NO_2$ underwent a larger energy uphill in comparison with the formation of *CHO (*CO + (H^+ + e^-) →*CHO). Similarly, For V, Cr, Mn and $Fe@Nb_2NO_2$, the formation of *OCH from*OCHOH (*OCHOH + (H^+ + e^-) →*OCH + H_2O) are more energy consuming than the production of *CHO. Thus, it can be concluded that *CHO will be the key intermediates for the third hydrogenation process.

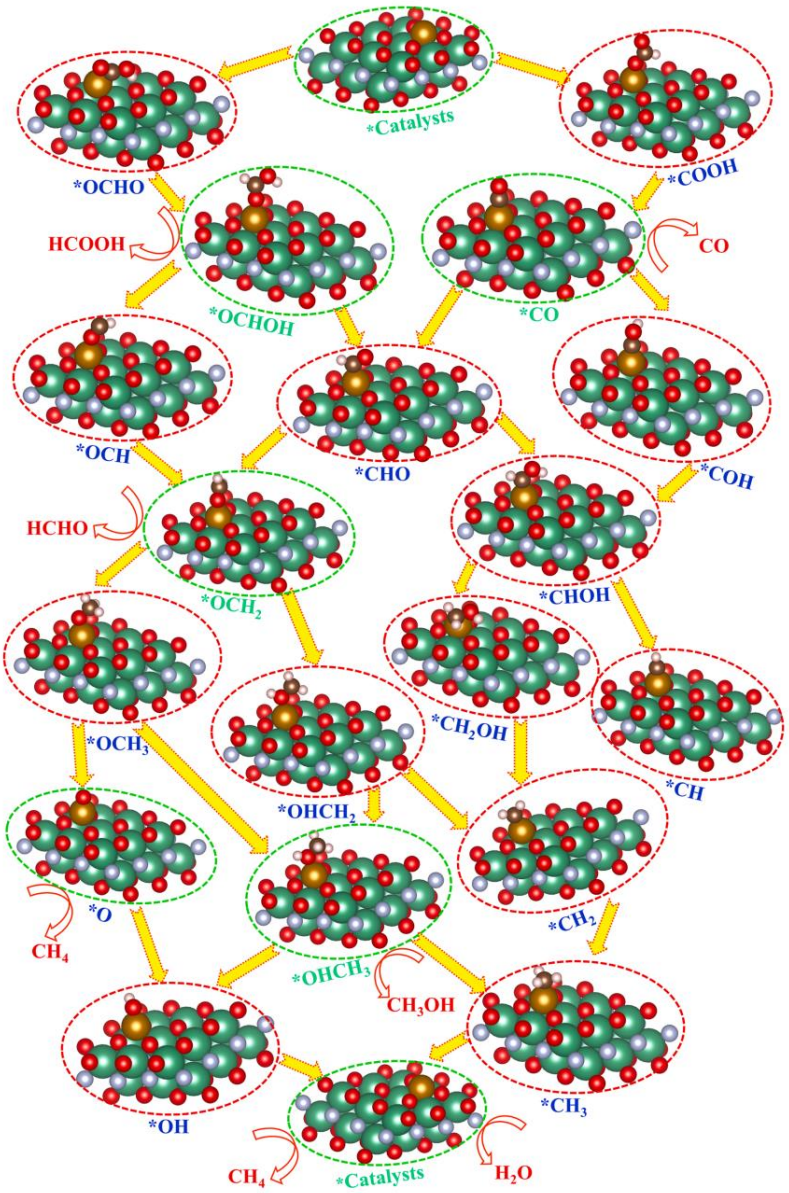

Fig. 4. The optimized configuration of intermediates adsorbed on $Fe@Nb_2NO_2$ during the whole ECR process from one-electron to eight-electron products.

Table 2
The adsorption energy of different products CO, HCOOH, HCHO, CH_3OH and CH_4 with unit eV, and the limiting potential for generating final product CH_4 with unit V.

Catalysts	E_{ads} (CO)	E_{ads} (HCOOH)	E_{ads} (HCHO)	E_{ads} (CH_3OH)	E_{ads} (CH_4)	U_L (CH_4)
V@Nb_2NO_2	–	− 1.07	− 1.59	− 1.15	− 0.35	−0.45
Cr@Nb_2NO_2	–	− 1.25	− 1.48	− 1.17	− 0.47	−0.47
Mn@Nb_2NO_2	–	− 1.20	− 0.96	− 0.88	− 0.23	−0.62
Fe@Nb_2NO_2	–	− 1.51	− 1.06	− 0.75	− 0.41	−0.89
Co@Nb_2NO_2	− 1.95	–	− 1.08	− 1.07	− 0.38	−0.57
Ni@Nb_2NO_2	− 1.73	–	− 1.20	− 1.03	− 0.36	−0.28

$*OCH_2$ and *CHOH intermediates can be produced after *CHO accepting the fourth proton-electron pair. It is evident from Fig. 5 that the ΔG of *CHOH on these six SACs show energy uphill, while the ΔG for the formation of $*OCH_2$ on these SACs show energy downhill. Therefore, these TM atoms exhibit strong oxophilicity to form TM−O bonds. The four-electron product HCHO will be desorbed from the electrocatalyst if the interaction between $*OCH_2$ and TM atom is too weak. The calculated E_{ads} of HCHO on these SACs are in the range of − 1.59 to − 0.96 eV, suggesting that it is difficult for HCHO to desorb and thus can be further reduced.

*CHOH then accepted the fifth proton-electron pair to produce *CH and $*CH_2OH$ intermediates, while the hydrogenation products of $*OCH_2$ are $*OCH_3$ and $*OHCH_2$. However, ΔG of *CH and $*OHCH_2$ are energetically unfavourable and will not form. In contrast, $*CH_2OH$ and $*OCH_3$ will be the key intermediates and participate in later hydrogenation. CH_3OH is the six-electron product via $*OCH_3 + (H^+ + e^-) \rightarrow *OHCH_3 \rightarrow * + CH_3OH$. Nevertheless, the formation of $*OHCH_3$ only show energy downhill on Fe and Mn@Nb_2NO_2. The E_{ads} on V, Cr, Mn, Fe, Co, Ni@ Nb_2NO_2 is − 1.15, − 1.17, − 0.88, − 0.75, − 1.07 and − 1.03 eV, respectively. Thus, CH_3OH can still be stably bonded with

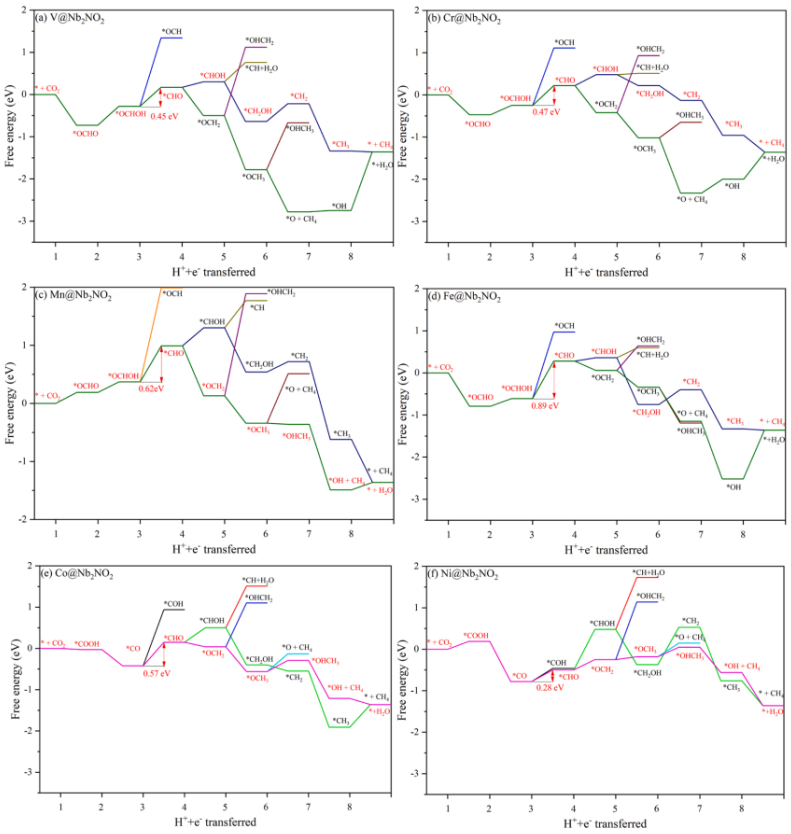

Fig. 5. The Gibbs free energy diagram for ECR on TM@Nb_2NO_2 to produce the final product CH_4 under U = 0 V; the red pathway denotes the optimal pathway.

SACs and further reduced. The eight-electron product CH_4 can be generated from diverse paths such as $*CH_3 + (H^+ + e^-) \rightarrow * + CH_4$, $*OCH_3 + (H^+ + e^-) \rightarrow CH_4 + *O$ and $*OHCH_3 + (H^+ + e^-) \rightarrow CH_4 + *OH$. Remarkably, the E_{ads} of CH_4 on $TM@Nb_2NO_2$ are significantly smaller than the other C_1 products, ranging from − 0.47 to − 0.23 eV, indicating that CH_4 can easily desorb from the SACs and become the final product. According to principle of minimum free energy increase at each step, the optimized paths for ECR to CH_4 on $TM@Nb_2NO_2$ were concluded as below (Fig. 5):

(I) V,Cr and $Fe@Nb_2NO2$:$*+CO_2 \rightarrow *OCHO \rightarrow *OCHOH \rightarrow *CHO \rightarrow *CHOH \rightarrow *CH_2OH \rightarrow *CH_2 \rightarrow *CH_3 \rightarrow * + CH_4$

(II) $Mn@Nb_2NO_2$:$*+CO_2 \rightarrow *OCHO \rightarrow *OCHOH \rightarrow *CHO \rightarrow *OCH_2 \rightarrow *OCH_3 \rightarrow *OHCH_3 \rightarrow *OH + CH_4 \rightarrow * + H_2O$

(III) Co and Ni $@Nb_2NO_2$: $* + CO_2 \rightarrow *COOH \rightarrow *CO \rightarrow *CHO \rightarrow *OCH_2 \rightarrow *OCH_3 \rightarrow *OHCH_3 \rightarrow *OH + CH_4 \rightarrow * + H_2O$

Thus, $TM@Nb_2NO_2$ can be promising candidates in electrochemically converting CO_2 to CH_4.

To evaluate the ECR performance of $TM@Nb_2NO_2$, the PDSs and the corresponding U_L were summarized in Table 2. Generally, the lower the value of U_L, the higher the activity of SACs. In path I and II, $*OCHOH \rightarrow *CHO$ was identified as PDS for V, Cr, Mn and $Fe@Nb_2NO_2$. The U_L for CH_4 generation on these four SACs are − 0.45, − 0.47, − 0.62 and − 0.89 V. The PDS of Co and $Ni@Nb_2NO_2$ in path III is $*CO \rightarrow *CHO$, and the corresponding U_L are − 0.57 and − 0.28 V. Intriguingly, U_L for the ECR to CH_4 on V, Cr, Co and $Ni@Nb_2NO_2$ are lower than that the state-of-the-art catalyst Cu (211) (−0.74 V) [60], demonstrating potentially excellent performance of $TM@Nb_2NO_2$ for ECR to CH_4. Particularly, the U_L of $Ni@Nb_2NO_2$ is among the best reported in literature. Finally, we investigated the stability of $Ni@Nb_2NO_2$ by AIMD simulations with a time step of 3 fs at the temperature of 300 K for 18 ps (Fig. S2). It can be found that Ni atom can still stay at the vacancy, which evidenced that diffusion will not occur.

3.6. Electronic structure of intermediates adsorbed $TM@Nb_2NO_2$

The excellent activity of $TM@Nb_2NO_2$ for CH_4 generations is mainly related to the interaction between active TM atom and substrate. As shown in Table S1, the Nb_2NO_2 monolayer is negatively charged by TM atoms. The different amount of charge transfer indicates the different interaction strength. Consequently, the single TM atom with different

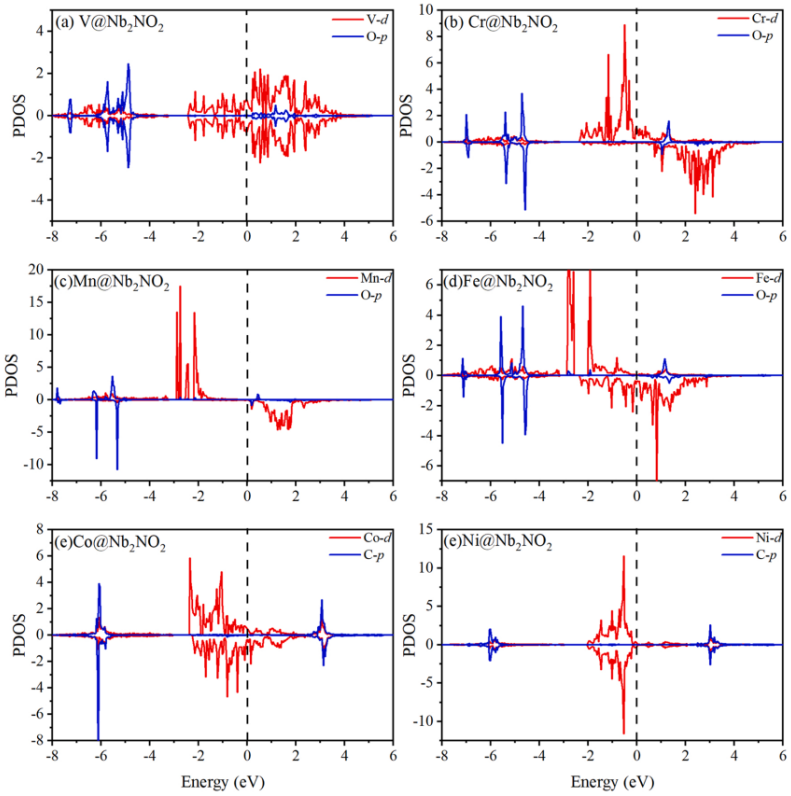

Fig. 6. The PDOS of *OCHOH adsorbed on (a) V, (b) Cr, (c) Mn and (d) $Fe@Nb_2NO_2$; and *CO adsorbed on (e) $Co@Nb_2NO_2$ and (f) $Ni@Nb_2NO_2$; the dashed line represents the Fermi energy level.

positive charge will contribute to different catalytic activity. After intermediate adsorption on the single TM atom, the binding strength between them will directly determine U_L. According to the Sabatier principle, too strong or too weak binding strength will result in low catalytic activity [61]. As shown in Fig. 6, the PDOS of key intermediates from PDSs of TM@Nb_2NO_2 exhibit deferent interaction between TM and C or O atoms. For instance, the Mn-*3d* orbitals and the O-*2p* orbitals of *OCHOH in Mn@Nb_2NO_2 have slight overlap, contributing to weak binding strength. Fe-*3d* orbitals interacts greatly with O-*2p*, exhibiting strong interaction. The corresponding adsorption energy of OCHOH on these two SACs is − 0.95 and − 1.51 eV, suggesting that too strong or weak interaction could increase the free energy of PDSs.

3.7. Activity origin of ECR to CH_4 on TM@Nb_2NO_2

We further investigated the activity origin on TM@Nb_2NO_2 by using descriptors. The PDSs of TM@Nb_2NO_2 can be assigned to *OCHOH and *CO, therefore we distinguish them by two different areas (palegreen and slateblue in Fig. 7). Since the *d*-band centre of TM atoms has often been used to correlate the catalytic properties, the locations of *d* band centres (ε) were calculated and plotted against U_L, as shown in Fig. S3 and Fig. 7a. With the increase of the TM-*d* electron number, ε shifts to a more negative energy level, resulting in the increase of U_L. When the key intermediate is *OCHOH, there is a good linear relationship between ε and U_L ($U_L = 0.35\varepsilon - 0.40$, $R^2 = 0.97$). For *CO as key intermediate, only Co and Ni@Nb_2NO_2 are distinguished. Generally, the more negative the value of ε, the weaker the adsorption between intermediates and catalysts. For example, it can be found that Mn@Nb_2NO_2 shows a lower ε, while the E_{ads} for *OCHOH is smaller, indicating weak adsorption and a large U_L. However, ε is not associated with E_{ads} for a specific TM atom in a small range, because of the neglect of the *d*-band shape and the effect of the TM-*s* and *p* orbitals. Thus, the linear relationship is not apparent (Fig. 7b). For *CO intermediate, the higher ε of Co atoms contributed a strong E_{ads} of *CO and high U_L.

The crystal orbital Hamilton populations (COHP) were employed to analyse the bonding and antibonding states of the TM and key intermediates *OCHOH and *CO [13]. Meanwhile, the integrated COHP (ICOHP) was calculated to give a more quantitative explanation (Fig. S4). For O atom bonding with V, Cr, Mn and Fe@Nb_2NO_2, it shows obvious antibonding states below Fermi level, demonstrating weak adsorption. The corresponding ICOHP values are − 1.32, − 1.44/− 1.57, − 1.47/− 1.75, − 1.28/− 1.61 eV, respectively. V and Cr@Nb_2NO_2 have similar antibonding states in spin up state, resulting in similar U_L. For C atom bonding with Co and Ni@Nb_2NO_2, there is no antibonding state below Fermi level with value of − 2.56/− 2.66 and − 2.40 eV, respectively, indicating strong adsorption. The more negative the ICOHP, the more stable of bonding, thus Fe@Nb_2NO_2 shows a large U_L. A good linear relationship between ICOHP and U_L was obtained for V, Cr, Mn and Fe@Nb_2NO_2 ($U_L = 1.58\Phi + 1.70$, $R^2 = 0.86$), disclosing the role of different metal centres in the bonding/antibonding orbital populations.

Recently, charge transfers of active atoms have been reported as descriptor to explain the performance of catalysts [62]. Herein, we calculated the valence state (δ) of TM atoms after adsorbing intermediates. The δ of different atoms for different binding atoms vary in a range from + 0.55 to + 1.32, indicating an increase of charge transfer from TM atoms after intermediates adsorption and different interaction strength between them. Fe atom had the largest Δδ increase of 0.37 after intermediates adsorption, implying a possible strong interaction between Fe and *OCHOH and a large U_L. Meanwhile, an approximate linear relationship ($U_L = -3.02\Delta\delta - 0.31$, $R^2 = 0.86$) was obtained, demonstrating that binding strength between catalysts and intermediates can be represented by Δδ. Therefore, ε, Φ and Δδ can be used as descriptors to describe the activity origin well. Meanwhile, the E_{ads} can be a nominal descriptor for the ECR activity to CH_4 due to the close connection between energy and electronic structure, while ε, Φ and Δδ can quantitively describe the intrinsic activity of ECR to CH_4 on TM@ Nb_2NO_2. Overall, the results show that Ni@Nb_2NO_2 is the best

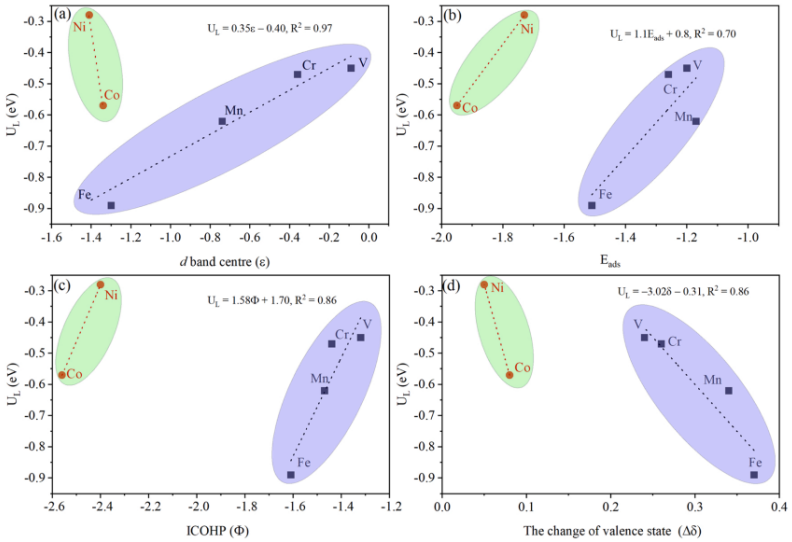

Fig. 7. The limiting potential for the generation of CH_4 on TM@Nb_2NO_2 as a function of (a) *d* band centre (ε), (b) adsorption energy (E_{ads}), (c) ICOHP (Φ), and (d) the change of TM atom.

ECR catalyst for CH_4 generation, while Fe@Nb_2NO_2 is not an ideal catalyst.

4. Conclusion

Single TM atoms (V, Cr, Mn, Fe, Co and Ni) anchored Nb_2NO_2 monolayer as potential SACs for electrochemical CO_2 reduction were studied by first-principles calculation. Results demonstrate that TM atoms can be stably embedded into N site and will not aggregate into clusters. CO_2 molecules can be effectively activated by V, Cr and Ni@Nb_2NO_2 due to charge transfer and large adsorption energy. All TM@Nb_2NO_2 electrocatalysts exhibit high selectivity for ECR in comparison with HER. The E_{ads} of C_1 products (CO, HCOOH, HCHO, CH_3OH) is too large for them to desorb from the surface of catalysts, while CH_4 can easily desorb due to the small E_{ads}. The PDS on these SACs for ECR to CH_4 can be divided into two categories: *OCHOH to *CHO for V, Cr, Mn and Fe, and *COOH to *CHO for Co and Ni. The U_L for CH_4 generation on V, Cr and Ni@Nb_2NO_2 SACs are − 0.45, − 0.47 and − 0.28 V, exhibiting high performance for ECR to CH_4 and is even better than the Cu (211) electrocatalyst. Furthermore, the adsorption energy of the key intermediates (E_{ads}) can serve as a nominal descriptor to indicate ECR activity, while *d* band center (ε), ICOHP (Φ), the change of valence state (Δδ) can quantitatively describe the ECR activity. This work demonstrated that MXene based earth abundant metal SACs are promising for electrocatalytic CO_2 reduction.

CRediT authorship contribution statement

Song Lu: Methodology, Formal analysis, Investigation, Writing – original draft, Writing – review & editing, Visualization. **Yang Zhang:** Investigation, Formal analysis, Writing – review & editing. **Fengliu Lou:** Investigation, Formal analysis, Writing – review & editing. **Zhixin Yu:** Conceptualization, Formal analysis, Validation, Resources, Supervision, Writing – review & editing

Declaration of Competing Interest

The authors declare that they have no known competing financial interests or personal relationships that could have appeared to influence the work reported in this paper.

Acknowledgements

This work is supported by the Norwegian Ministry of Education and Research. The computations were performed on resources provided by UNINETT Sigma2 - the National Infrastructure for High Performance Computing and Data Storage in Norway.

Appendix A. Supporting information

Supplementary data associated with this article can be found in the online version at doi:10.1016/j.jcou.2022.102069.

References

[1] W.J. Zhang, Y. Hu, L.B. Ma, G.Y. Zhu, Y.R. Wang, X.L. Xue, R.P. Chen, S.Y. Yang, Z. Jin, Progress and perspective of electrocatalytic CO_2 reduction for renewable carbonaceous fuels and chemicals, Adv. Sci. 5 (2018) 1700275.
[2] J. Resasco, A.T. Bell, Electrocatalytic CO_2 reduction to fuels: progress and opportunities, Trends Chem. 2 (2020) 825–836.
[3] J. Qiao, Y. Liu, F. Hong, J. Zhang, A review of catalysts for the electroreduction of carbon dioxide to produce low-carbon fuels, Chem. Soc. Rev. 43 (2014) 631–675.
[4] H. Jin, C. Guo, X. Liu, J. Liu, A. Vasileff, Y. Jiao, Y. Zheng, S.Z. Qiao, Emerging two-dimensional nanomaterials for electrocatalysis, Chem. Rev. 118 (2018) 6337–6408.
[5] T. Inoue, A. Fujishima, S. Konishi, K. Honda, Photoelectrocatalytic reduction of carbon dioxide in aqueous suspensions of semiconductor powders, Nature 277 (1979) 637–638.
[6] M. Halmann, Photoelectrochemical reduction of aqueous carbon dioxide on p-type gallium phosphide in liquid junction solar cells, Nature 275 (1978) 115–116.
[7] W. Li, Electrocatalytic reduction of CO_2 to small organic molecule fuels on metal catalysts, ACS Symp. Ser. 5 (2010) 55–76.
[8] T. He, L. Zhang, G. Kour, Electrochemical reduction of carbon dioxide on precise number of Fe atoms anchored graphdiyne, J. CO2 Util. 37 (2020) 272–277.
[9] D. Gao, R.M. Arán-Ais, H.S. Jeon, B.R. Cuenya, Rational catalyst and electrolyte design for CO_2 electroreduction towards multicarbon products, Nat. Catal. 2 (2019) 198–210.
[10] Z. Wang, J. Zhao, Q. Cai, CO_2 electroreduction performance of a single transition metal atom supported on porphyrin-like graphene: a computational study, Phys. Chem. Chem. Phys. 19 (2017) 23113–23121.
[11] J. Xie, X. Zhao, M. Wu, Q. Li, Y. Wang, J. Yao, Metal-free fluorine-doped carbon electrocatalyst for CO_2 reduction outcompeting hydrogen evolution, Angew. Chem. Int. Ed. 57 (2018) 9640–9644.
[12] T. Ma, Q. Fan, X. Li, J. Qiu, T. Wu, Z. Sun, Graphene-based materials for electrochemical CO_2 reduction, J. CO_2 Util. 30 (2019) 168–182.
[13] J. Zhang, T.S. Xu, D. Yuan, J.L. Tian, D.W. Ma, CO_2 electroreduction by transition metal embedded two-dimensional C_3N: A theoretical study, J. CO2 Util. 43 (2021), 101367.
[14] T. Cheng, H. Xiao, W.A. Goddard III, Reaction mechanisms for the electrochemical reduction of CO_2 to CO and formate on the Cu (100) surface at 298 K from quantum mechanics free energy calculations with explicit water, J. Am. Chem. Soc. 138 (2016) 13802–13805.
[15] K.P. Kuhl, E.R. Cave, D.N. Abram, T.F. Jaramillo, New insights into the electrochemical reduction of carbon dioxide on metallic copper surfaces, Energy Environ. Sci. 5 (2012) 7050–7059.
[16] B. Qiao, A. Wang, X. Yang, L.F. Allard, Z. Jiang, Y. Cui, J. Liu, J. Li, T. Zhang, Single-atom catalysis of CO oxidation using Pt_1/FeO_x, Nat. Chem. 3 (2011) 634–641.
[17] A.Q. Wang, J. Li, T. Zhang, Heterogeneous single-atom catalysis, Nat. Rev. Chem. 2 (2018) 65–81.
[18] T. Jin, D.M. Liang, M.S. Deng, S.H. Cai, X.S. Qi, Density functional theory studies of heteroatom-doped graphene-like GaN monolayers as electrocatalysts for oxygen evolution and reduction, ACS Appl. Nano Mater. 4 (2021) 7125–7133.
[19] S. Liu, H.B. Yang, S.F. Hung, J. Ding, W. Cai, L. Liu, J. Gao, X. Li, X. Ren, Z. Kuang, Y. Huang, T. Zhang, B. Liu, Elucidating the electrocatalytic CO_2 reduction reaction over a model single-atom nickel catalyst, Angew. Chem. Int. Ed. 59 (2020) 798–803.
[20] C. Ren, Q. Jiang, W. Lin, Y. Zhang, S. Huang, K. Ding, Density functional theory study of single-atom V, Nb, and Ta catalysts on graphene and carbon nitride for selective nitrogen reduction, ACS Appl. Nano Mater. 3 (2020) 5149–5159.
[21] X. Zhang, A. Chen, L. Chen, Z. Zhou, 2D materials bridging experiments and computations for electro/photocatalysis, Adv. Energy Mater. 12 (2021) 2003841.
[22] L.X. Chen, Z.W. Chen, M. Jiang, Z.L. Lu, C. Gao, G.M. Cai, C.V. Singh, Insights on the dual role of two-dimensional materials as catalysts and supports for energy and environmental catalysis, J. Mater. Chem. A 9 (2021), 2018-204223.
[23] X.Y. Chia, M. Pumera, Characteristics and performance of two-dimensional materials for electrocatalysis, Nat. Catal. 1 (2018) 909–921.
[24] S. Back, Y. Jung, TiC- and TiN-supported single-atom catalysts for dramatic improvements in CO_2 electrochemical reduction to CH_4, ACS Energy Lett. 2 (2017) 969–975.
[25] G. Xu, R. Wang, Y. Ding, Z. Lu, D. Ma, Z. Yang, First-principles study on the single Ir atom embedded graphdiyne: an efficient catalyst for CO oxidation, J. Phys. Chem. C 122 (2018) 23481–23492.
[26] C. Ao, B. Feng, S. Qian, L. Wang, W. Zhao, Y. Zhai, L. Zhang, Theoretical study of transition metals supported on g-C_3N_4 as electrochemical catalysts for CO_2 reduction to CH_3OH and CH_4, J. CO_2 Util. 36 (2020) 116–123.
[27] L. Fu, R. Wang, C.X. Zhao, J.R. Huo, C.Z. He, K.H. Kim, W. Zhang, Construction of Cr-embedded graphyne electrocatalyst for highly selective reduction of CO_2 to CH_4: A DFT study, Chem. Eng. J. 414 (2021), 128857.
[28] W.J. Wang, D. Li, T. Cui, Carbon and oxygen coordinating atoms adjust transition metal single-atom catalysts based on boron nitride monolayers for highly efficient CO_2 electroreduction, ACS Appl. Mater. Interfaces 13 (2021) 18934–18943.
[29] X. Wan, Z. Zhang, H. Niu, Y.H. Yin, C.G. Kuai, J. Wang, C. Shao, Y.Z. Guo, Machine-learning-accelerated catalytic activity predictions of transition metal phthalocyanine dual-metal-site catalysts for CO_2 reduction, J. Phys. Chem. Lett. 12 (2021) 6111–6118.
[30] M. Naguib, M. Kurtoglu, V. Presser, J. Lu, J. Niu, M. Heon, L. Hultman, Y. Gogotsi, M.W. Barsoum, Two-dimensional nanocrystals produced by exfoliation of Ti_3AlC_2, Adv. Mater. 23 (2011) 4248–4253.
[31] V. Kamysbayev, A.S. Filatov, H.C. Hu, X. Rui, F. Lagunas, D. Wang, R.F. Klie, D. V. Talapin, Covalent surface modifications and superconductivity of two-dimensional metal carbide MXenes, Science 369 (2020) 979–983.
[32] Y. Gogotsi, B. Anasori, The rise of mXenes, ACS Nano 13 (2019) 8491–8494.
[33] N. Li, X. Chen, W.J. Ong, D.R. MacFarlane, X. Zhao, A.K. Cheetham, C.H. Sun, Understanding of electrochemical mechanisms for CO_2 capture and conversion into hydrocarbon fuels in transition-metal carbides (MXenes), ACS Nano 11 (2017) 10825–10833.
[34] B.M. Jun, S. Kim, J. Heo, C.M. Park, N. Her, M. Jang, Y. Huang, J. Han, Y. Yoon, Review of MXenes as new nanomaterials for energy storage/delivery and selected environmental applications, Nano Res 12 (2018) 471–487.
[35] D. Zhao, Z. Chen, W. Yang, S. Liu, X. Zhang, Y. Yu, W.C. Cheong, L.R. Zheng, F. Q. Ren, G.B. Ying, X. Cao, D.S. Wang, Q. Peng, G.X. Wang, C. Chen, MXene (Ti_3C_2) Vacancy-confined single-atom catalyst for efficient functionalization of CO_2, J. Am. Chem. Soc. 141 (2019) 4086–4093.

[36] P. Urbankowski, B. Anasori, T. Makaryan, D. Er, S. Kota, P.L. Walsh, M. Zhao, V. B. Shenoy, M.W. Barsoum, Y. Gogotsi, Synthesis of two-dimensional titanium nitride Ti_4N_3 (MXene), Nanoscale 8 (2016) 11385–11391.

[37] X.H. Zha, K. Luo, Q. Li, Q. Huang, J. He, X. Wen, S. Du, Role of the surface effect on the structural, electronic and mechanical properties of the carbide MXenes, EPL 111 (2015) 26007.

[38] Y. Xie, M. Naguib, V.N. Mochalin, M.W. Barsoum, Y. Gogotsi, X. Yu, K.W. Nam, X. Q. Yang, A.I. Kolesnikov, P.R. Kent, Role of surface structure on Li-ion energy storage capacity of two-dimensional transition-metal carbide, J. Am. Chem. Soc. 136 (2014) 6385–6394.

[39] T. Schultz, N.C. Frey, K. Hantanasirisakul, S. Park, S.J. May, V.B. Shenoy, Y. Gogotsi, N. Koch, Surface termination dependent work function and electronic properties of $Ti_3C_2T_x$ MXene, Chem. Mater. 31 (2019) 6590–6597.

[40] O. Mashtalir, M.R. Lukatskaya, M.Q. Zhao, M.W. Barsoum, Y. Gogotsi, Amine-assisted delamination of Nb_2C MXene for Li-ion energy storage devices, Adv. Mater. 27 (2015) 3501–3506.

[41] T. Su, R. Peng, Z.D. Hood, M. Naguib, I.N. Ivanov, J.K. Keum, Z. Qin, Z. Guo, Z. Wu, One-step synthesis of Nb_2O_5/C/Nb_2C (MXene) composites and their use as photocatalysts for hydrogen evolution, ChemSusChem 11 (2018) 688–699.

[42] D. Kan, D. Wang, X. Zhang, R. Lian, J. Xu, G. Chen, Y. Wei, Rational design of bifunctional ORR/OER catalysts based on Pt/Pd-doped Nb_2CT_2 MXene by first-principles calculations, J. Mater. Chem. A 8 (2020) 3097–3108.

[43] G. Kresse, D. Joubert, From ultrasoft pseudopotentials to the projector augmented-wave method, Phys. Rev. B 59 (1999) 1758.

[44] G. Kresse, J. Furthmüller, Efficiency of ab-initio total energy calculations for metals and semiconductors using a plane-wave basis set, Comput. Mater. Sci. 6 (1996) 15–50.

[45] J.P. Perdew, K. Burke, M. Ernzerhof, Generalized gradient approximation made simple, Phys. Rev. Lett. 77 (1996) 3865–3868.

[46] J.P. Perdew, M. Ernzerhof, K. Burke, Rationale for mixing exact exchange with density functional approximations, J. Chem. Phys. 105 (1996) 9982–9985.

[47] S. Grimme, J. Antony, S. Ehrlich, H. Krieg, A consistent and accurate ab initio parametrization of density functional dispersion correction (DFT-D) for the 94 elements H-Pu, J. Chem. Phys. 132 (2010) 154104–154123.

[48] K. Mathew, R. Sundararaman, K.L. Weaver, T.A. Arias, R.G. Hennig, Implicit solvation model for density-functional study of nanocrystal surfaces and reaction pathways, J. Chem. Phys. 140 (2014) 084106–084114.

[49] G. Kresse, J. Hafner, Ab initio molecular dynamics for liquid metals, Phys. Rev. B 47 (1993) 558.

[50] S. Baroni, S. de Gironcoli, A. dal Corso, P. Giannozzi, Phonons and related crystal properties from density-functional perturbation theory, Rev. Mod. Phys. 73 (2001) 515.

[51] D. Sheppard, R. Terrell, G. Henkelman, Optimization methods for finding minimum energy paths, J. Chem. Phys. 128 (2008), 134106.

[52] G. Henkelman, A. Arnaldsson, H. Jónsson, A fast and robust algorithm for Bader decomposition of charge density, Comp. Mater. Sci. 36 (3) (2006) 354–360.

[53] J.K. Nørskov, J. Rossmeisl, A. Logadottir, L. Lindqvist, J.R. Kitchin, T. Bligaard, H. Jonsson, Origin of the overpotential for oxygen reduction at a fuel-cell cathode, J. Phys. Chem. B 108 (2004) 17886–17892.

[54] Y. Wang, W. Tian, H. Zhang, Y. Wang, Nb2N monolayer as a promising anode material for Li/Na/K/Ca-ion batteries: a DFT calculation, Phys. Chem. Chem. Phys. 23 (2021) 12288–12295.

[55] S.S. Zheng, C.J. Zuo, X.H. Liang, S.N. Li, F. Pan, Valence state of transition metal center as an activity descriptor for CO_2 reduction on single atom catalysts, J. Energy Chem. 56 (2021) 444–448.

[56] F.F. Li, H.Q. Ai, C.M. Shi, K.H. Lo, H. Pan, Single transition metal atom catalysts on Ti_2CN_2 for efficient CO_2 reduction reaction, Int. J. Hydrog. Energy 46 (2021) 12886–12896.

[57] Y. Hori, H. Wakebe, T. Tsukamoto, O. Koga, Electrocatalytic process of CO selectivity in electrochemical reduction of CO_2 at metal electrodes in aqueous media, Electrochim. Acta 39 (1994) 1833–1839.

[58] C. Guo, T. Zhang, X. Deng, X. Liang, W. Guo, X. Lu, C.M.L. Wu, Electrochemical CO_2 reduction to C1 products on single nickel/cobalt/iron-doped graphitic carbon nitride: a DFT study, ChemSusChem 12 (2019) 5126–5132.

[59] S. Lu, H.L. Huynh, F.L. Lou, M. Guo, Z.X. Yu, Electrochemical reduction of CO_2 to CH_4 over transition metal atom embedded antimonene: first-principles study, J. CO_2 Util. 51 (2021), 101645.

[60] G. Kour, X. Mao, A.J. Du, Computational screening of transition metal–phthalocyanines for the electrochemical reduction of carbon dioxide, J. Phys. Chem. C 124 (2020) 7708–7715.

[61] J.K. Nørskov, T. Bligaard, A. Logadottir, J.R. Kitchin, J.G. Chen, S. Pandelov, U. Stimming, Trends in the exchange current for hydrogen evolution, J. Electrochem. Soc. 152 (2005) J23–J26.

[62] L. Li, X. Wang, H. Guo, G. Yao, L. Chen, Theoretical screening of single transition metal atoms embedded in MXene defects as superior electrocatalyst of nitrogen reduction reaction, Small Methods 3 (2019) 1900337.

Supporting Information

Theoretical study of single transition metal atom catalysts supported on two-dimensional Nb_2NO_2 for efficient electrochemical CO_2 reduction to CH_4

Song Lu[a], Yang Zhang[ab], Fengliu Lou[b]*, Zhixin Yu[a]*

[a]Department of Energy and Petroleum Engineering, University of Stavanger, 4036 Stavanger, Norway

[b]Beyonder AS, Kanalsletta 2, 4033 Stavanger, Norway

***Corresponding author:**

Prof. Zhixin Yu

E-mail address: zhixin.yu@uis.no

Department of Energy and Petroleum Engineering, University of Stavanger, 4036 Stavanger, Norway

Tel: +47 51 83 22 38

Dr. Fengliu Lou

Beyonder AS, Kanalsletta 2, 4033 Stavanger, Norway

E-mail address: fengliu@beyonder.no

Table S1. The binding energy (E_b) of TM atom on N site and Nb site with unit eV, the translation energy barrier (E_T) from N site to Nb site with unit eV, the lattice parameter of TM@Nb_2NO_2 with unit Å, the lost charge of TM atom before (Q_1) and after (Q_2) adsorbing key intermediates with unit e.

Catalysts	E_b (N site)	E_b (Nb site)	E_T	*a*	Q_1	Q_2
V@Nb_2NO_2	-5.19	-4.43	1.89	3.11	−1.08	−1.32
Cr@Nb_2NO_2	-2.62	-2.09	2.12	3.09	−1.02	−1.28
Mn@Nb_2NO_2	-3.78	-3.10	2.58	3.08	−1.00	−1.34
Fe@Nb_2NO_2	-2.97	-2.45	1.43	3.08	−0.61	−0.98
Co@Nb_2NO_2	-3.54	-3.09	1.04	3.07	−0.51	−0.59
Ni@Nb_2NO_2	-3.54	-3.04	0.87	3.07	−0.50	−0.55

Fig. S1 The total energy variations of Nb_2NO_2 monolayer at 400 K under AIMD simulation for 18 ps with a time step of 3 fs.

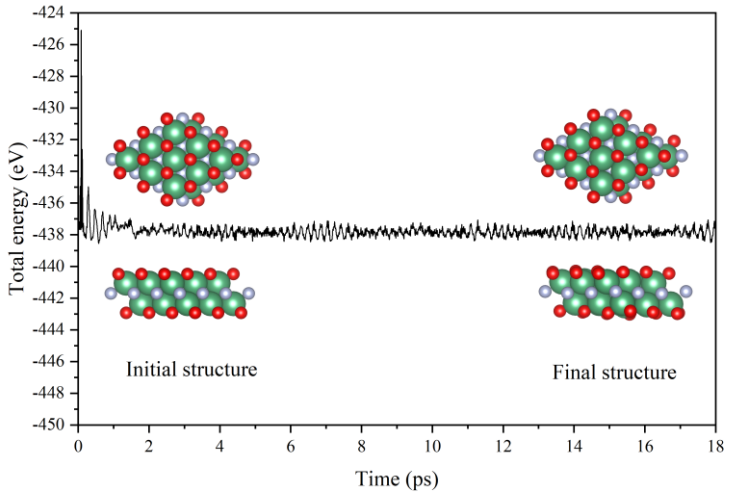

Fig. S2 The total energy variations of Ni@Nb_2NO_2 monolayer at 300 K under AIMD simulation for 18 ps with a time step of 3 fs.

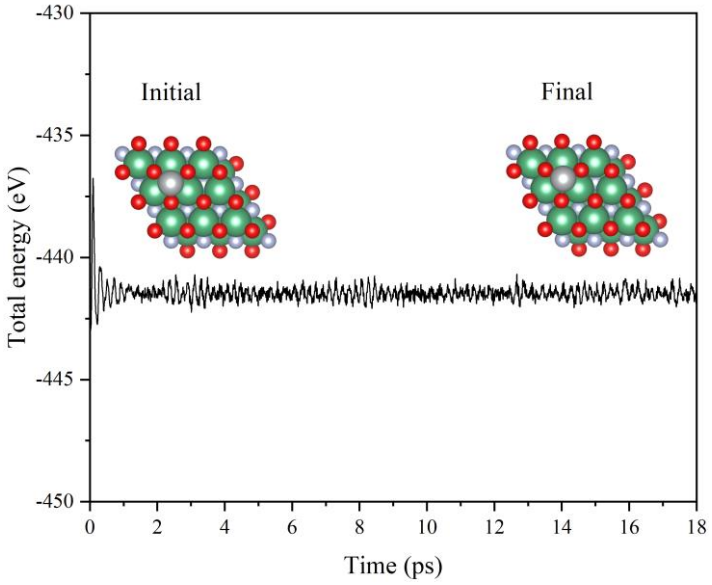

Fig. S3 The *d* band centre of TM atoms.

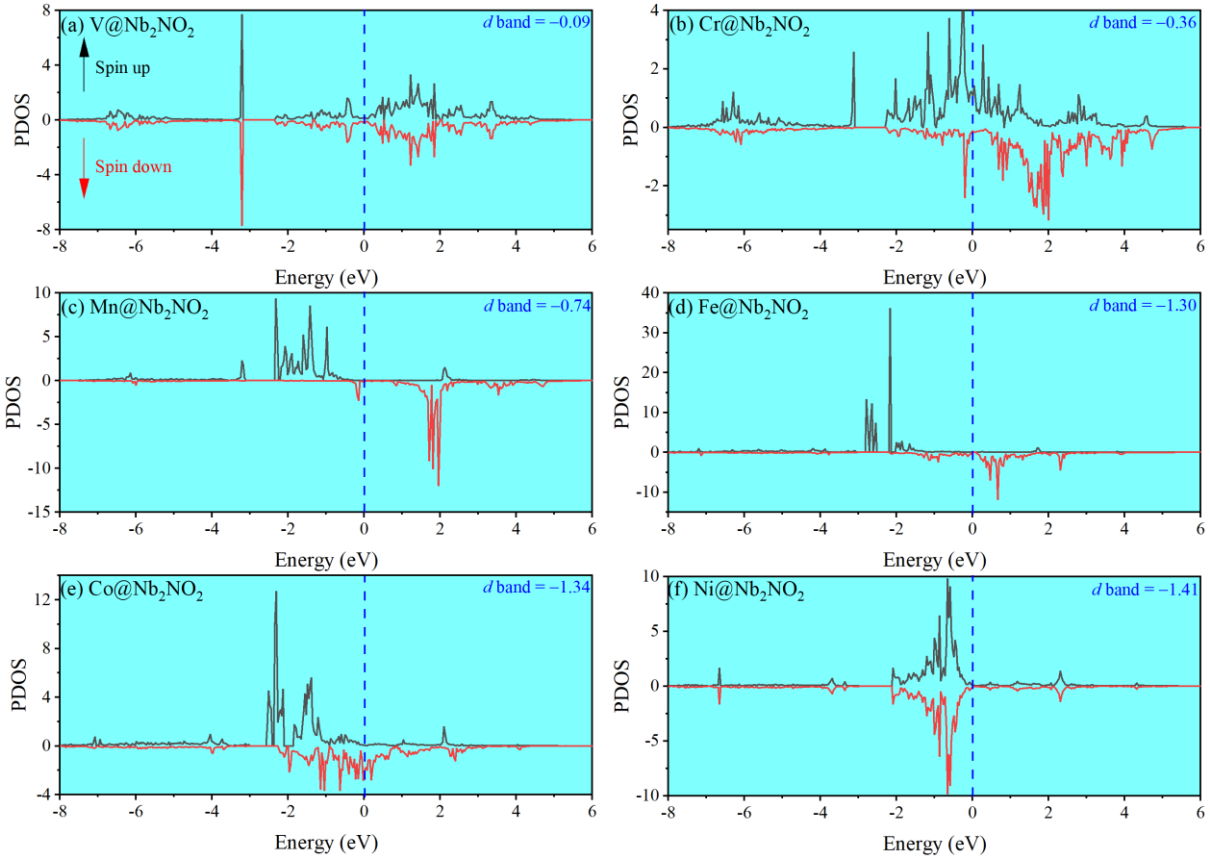

Fig. S4 The calculated crystal orbital Hamilton populations (COHPs) between *OCHOH and (a) V, (b) Cr, (c) Mn and (d) Fe atom; between *CO and (e) Co, (f) Ni atom. The horizontal dashed line is the Fermi energy level. The corresponding integrated COHP (ICOHP) are shown with black and red for spin up and spin down state, whereas V and Co only have spin up state.

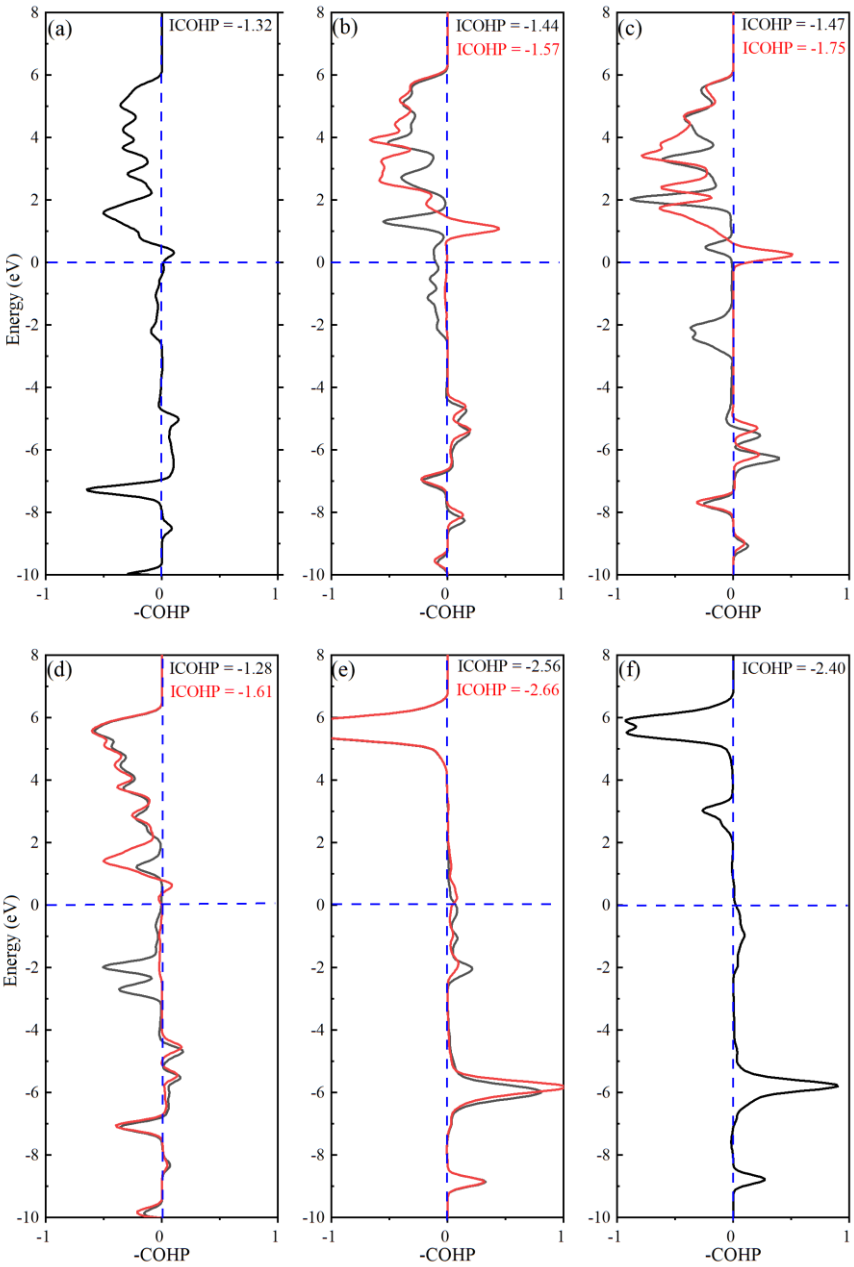

Appendix D – Paper IV

Electrochemical reduction of CO_2 to CH_4 over transition metal atom embedded antimonene: First-principles study

S. Lu, H. L. Huynh, F. Lou, M. Guo and Z. Yu

Journal of CO_2 Utilization, 2021, 51, 101645

DOI: 10.1016/j.jcou.2021.101645

Journal of CO2 Utilization 51 (2021) 101645

Contents lists available at ScienceDirect

Journal of CO2 Utilization

journal homepage: www.elsevier.com/locate/jcou

Electrochemical reduction of CO_2 to CH_4 over transition metal atom embedded antimonene: First-principles study

Song Lu [a], Huong Lan Huynh [a], Fengliu Lou [b], Min Guo [c,*], Zhixin Yu [a,*]

[a] Department of Energy and Petroleum Engineering, University of Stavanger, 4036 Stavanger, Norway
[b] Beyonder AS, Kanalsletta 2, 4033 Stavanger, Norway
[c] Institute of New Energy, School of Chemistry and Chemical Engineering, Shaoxing University, Shaoxing 312000, China

ARTICLE INFO

Keywords:
Antimonene
Electrochemical CO_2 reduction reaction
Transition metal atoms
Single-atom catalysts

ABSTRACT

Electrocatalytic CO_2 reduction (ECR) represents a promising way for the utilization of renewable energy such as wind and solar to produce value-added fuels or chemicals. The process mainly suffers from the sluggish CO_2 reaction kinetics and the lack of efficient electrocatalysts. Herein, we investigated a wide range of transition metal (TM = Sc, Ti, V, Cr, Mn, Fe, Co, Ni, Cu, Zn, Mo, Ru, Rh, Pd, Ag, Cd, Ir, Pt and Au) atoms anchored into monovacancy of antimonene (Sb monolayer) as single-atom catalysts (SACs) for ECR by first- principles calculation. Interestingly, non-precious TM atoms from the 3*d* group (TM = Sc, V, Cr, Mn, Fe, Co, Zn) supported on Sb monolayer show higher ECR selectivity than hydrogen evolution reaction selectivity. Moreover, the primary ECR product of these non-precious metal-based SACs is CH_4, except for Zn which produces HCOOH. Co@Sb monolayer exhibits the lowest overpotential 0.50 V, which is comparable to reported excellent electrocatalysts. The interaction between TM atom and Sb monolayer greatly affects the intrinsic activity of SACs. Meanwhile, the interaction between TM atoms and intermediates of the potential determining steps (PDS) will determine the overpotential and final products of ECR. This work opens a new family of stable and selective SACs based on antimonene monolayer and provides new insights for screening SACs by charge transfer of bonding atoms.

1. Introduction

With the expansion of global economy and the continuous improvement of human living standard, the massive consumption of fossil fuels has caused energy crisis and severe environmental issues [1–4]. Therefore, finding a strategy to alleviate these problems effectively will be of paramount importance for sustainable development. In this regard, the electrochemical reduction of CO_2 into value-added fuels and chemicals driven by renewable energy such as wind and solar is attracting growing attention [5–10]. The common C_1 products include CO, HCOOH, CH_3OH, CH_4, etc., and C_2 products such as C_2H_4, C_2H_5OH, CH_3COOH, etc. with high energy density, good economic value, and infrastructure compatibility are mostly desirable [11–15]. However, given the fact that the CO_2 molecule is chemically inert, the electrocatalytic CO_2 reduction (ECR) is difficult because it requires high dissociation energy of 750 kJ/mol for the breakage of C═O bond. The multiple proton-electron pairs involved in the reaction also result in complications as CO_2 reduction will generate different products when accept different numbers of proton-electron pairs [16,17]. Noteworthily, these products show similar reduction potentials, which limits the selectivity to specific products. Moreover, as the ECR reactions generally take place under aqueous solution, the hydrogen evolution reaction (HER) is the main competitive reaction [18–21]. As a result, strong HER activity will inhibit the efficiency of ECR. Thus, developing efficient catalysts with excellent ECR activity and selectivity to targeted chemicals is highly desirable.

To date, there are various electrocatalysts such as noble metals, Cu-based materials, carbon-based materials, etc. that have been investigated for ECR reactions [22–25]. Nevertheless, these electrocatalysts generally suffer some drawbacks, including high overpotential, poor selectivity, low electron mobility, etc [26]. Inspiringly, the development of two-dimensional (2D) materials has brought new light for outstanding ECR catalysts [8,27–29]. Compared to their bulk structure, the atomically thin 2D materials significantly increase the density of state near Fermi level, benefiting electron transfer and accelerating the activation of CO_2 molecule, as the CO_2 molecule is regarded as an electron acceptor [7,30]. Besides, ultrathin 2D materials have high specific surface area and a high percentage of surface atoms that can offer abundant active

* Corresponding authors.
E-mail addresses: gm@usx.edu.cn (M. Guo), zhixin.yu@uis.no (Z. Yu).

https://doi.org/10.1016/j.jcou.2021.101645
Received 29 April 2021; Received in revised form 29 June 2021; Accepted 4 July 2021
Available online 12 July 2021

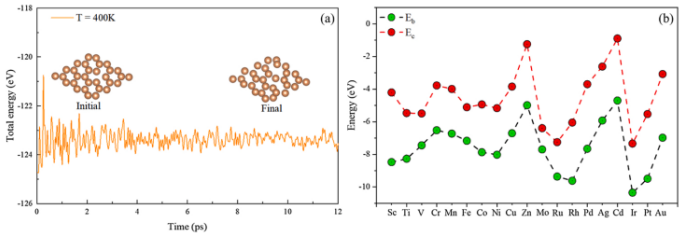

Fig. 1. (a) The total energy variations of defective Sb monolayer under a target temperature of 400 K for AIMD simulation for 12 ps with a time step of 3 fs; (b) The binding energy E_b of TM embedded into Sb monolayers, the cohesive energy E_c of bulk metal.

sites for ECR. Moreover, 2D materials can be easily modified, such as doping heterogeneous atoms, hybridizing with other nanostructures, surface engineering, and defect generation, all significantly influence their electronic properties and catalytic performance [31–36]. For instance, doping extra atoms in graphene can not only improve the stability of electrocatalysts but also increase their catalytic activity. Similarly, the hybridization of graphene with other materials could generate synergistic effect that boosts ECR. Other 2D materials, including transition metal dichalcogenides (TMD), metal-organic frameworks (MOFs) and MXenes, also exhibit specific ECR activity [37–39]. Recently, new 2D materials arsenene and antimonene in VA group have been reported to be promising candidate in energy devices, electrocatalysts and gas sensors, because of their excellent thermodynamic stability, electron mobility and suitable bandgap [40–43].

The continuous exploration of novel structures promotes the rational design and synthesis of highly active catalysts. In recent years, the single-atom catalysts (SACs) have become increasingly popular in electrocatalysis as they surpass conventional catalysts in terms of high atom utilization and unique electronic structure, which significantly affect the catalytic performance [44]. It is worth noting that the single transition metal (TM) atoms anchored 2D materials even attract more attention in catalysis and can be a promising candidate for ECR. For instance, Zhao et al. synthesized 2D materials-based SACs with high ECR activity and CO selectivity by seeding strategy. Density of function (DFT) calculation demonstrated that Ni atom could be stabilized by surrounding carbon and nitride atoms, preventing Ni atoms from aggregation [45]. TM atoms supported on graphitic carbon nitride as SACs for ECR revealed that the catalytic activities are highly correlated with the strength of interaction between TM atoms and intermediates (OH and OCH) [46]. Single transition metal embedded on 2D InSe for ECR has been investigated by density of function (DFT). It was disclosed that excellent ECR selectivity and overpotential can be attributed to the hybridization between InSe and d-/s-bands of metal atoms [47]. 2D material arsenene from the VA group has recently been reported as a promising electrocatalyst for N_2 reduction to NH_3 by first-principles calculation [48]. The outstanding electrochemical properties of antimonene have also been verified experimentally [43], while there is little study on antimonene applied as electrocatalysts. Furthermore, to the best of our knowledge, there is no study on single TM atom anchored antimonene for ECR.

In this work, we built SACs by embedding TM atoms (Sc, Ti, V, Cr, Mn, Fe, Co, Ni, Cu, Zn, Mo, Ru, Rh, Pd, Ag, Cd, Ir, Pt and Au) into Sb vacancy of antimonene monolayer (TM@Sb) and investigated their ECR performance by first-principles study. We disclosed that non-precious atom anchored on Sb monolayer possess remarkable ECR selectivity. Meanwhile, the primary ECR product on TM@Sb monolayer is CH_4. Co@Sb monolayer shows the smallest overpotential of 0.50 V for CH_4. The interactions between TM atom and intermediate hold the key to the catalytic activity.

2. Computational methods

All spin-polarized calculations based on DFT were carried out via the Vienna ab initio Simulation Package (VASP) code [49,50]. A 4 × 4 ×1 TM@Sb monolayer supercell containing a Sb vacancy with TM atom embedded in this vacancy was built (Fig. S1). A large vacuum of 20 Å along the z-direction was used to avoid the spurious interactions between adjacent units. The projector augmented wave (PAW) method was adopted to describe the interactions between ions and electrons, the generalized gradient approximation (GGA) in the form of Perdew-Burke-Ernzerh (PBE) function was chosen to describe the electron exchange-correlation interaction [51–53]. In order to accurately explain the long-range van der Waals (vdW) interactions, the empirical correction (DFT-D3) was included [54]. The kinetic energy cutoff was set as 500 eV for the plane-wave basis set, and a k-point sampling of 5 × 5×1 in the first Brillouin zone for structure relaxation, while a 9 × 9×1 sampling was chosen for the electronic structure calculations. The convergence criterion of energy and force was set to 1.0×10^{-5} eV and 1.0×10^{-2} eV/Å, respectively. Moreover, to explore defective structure stability, the ab initio molecular dynamics (AIMD) simulation was performed in NVT ensemble [55,56]. The TM atom diffusion barrier was calculated by the climbing image nudged elastic band method (CINEB) [57]. The Bader charge analysis was employed to calculate the charge transfer [58]. An implicit solvation model performed in VASPsol and the relative permittivity of the solvent was set to 78.4 [59]. The free energy diagrams of ECR were calculated by the computational hydrogen electrode (CHE) method [60]. The adsorption energies (E_{ads}) of intermediates in ECR reactions can be determined by Eq. (1):

$$E_{ads} = E_{TM@Sb\text{-}X} - E_{TM@Sb} - E_X \quad (1)$$

where $E_{TM@Sb\text{-}X}$, $E_{TM@Sb}$ and E_X denote the total energies of intermediates adsorbed on the TM@Sb monolayer surface, TM@Sb monolayer and isolated intermediates, respectively.

The Gibbs free energy of each step can be expressed as Eq. (2):

$$\Delta G = \Delta E + \Delta E_{ZPE} - T\Delta S + \Delta G_{pH} + \Delta G_U \quad (2)$$

where ΔE, ΔE_{ZPE} and ΔS are the total energy changes obtained from DFT calculations, zero-point energy, and entropy between the reactants and the products, respectively. T is the temperature which is set to 298.15 K in our calculations. ΔG_{pH} was calculated by the formula $\Delta G_{pH} = 2.303 k_B T pH$, and it will be zero as we assume a pH of zero under acidic conditions. ΔG_U represents the free energy correction due to the difference of the electrode potential. The limiting potential (U_L) can be calculated by $U_L = -\Delta G_{max}/ne$, where ΔG_{max} is the free energy change of the rate-determining step in ECR reactions. Then the overpotential can be calculated by the equation $\eta = U_{equ} - U_L$, where U_{equ} is the equilibrium potentials.

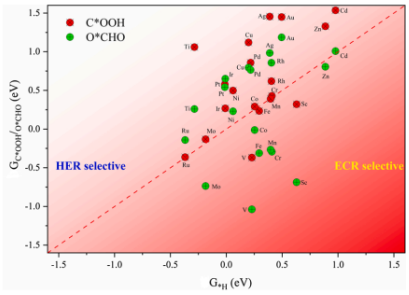

Fig. 2. The Gibbs free energy changes for the first protonation steps in ECR and HER on TM @Sb monolayers.

3. Results and discussion

3.1. Structure and stability

After structure optimization, the lattice parameter *a* (4.11 Å) of pristine Sb monolayer and bond length d_{Sb-Sb} (2.89 Å) agree well with previous reports [61,62]. The lattice parameter a of Sb monolayer with monovacancy decrease to 4.05 Å. The embedded TM atoms slightly affect the lattice parameter *a*. However, the d_{Sb-TM} of newly formed bond Sb–TM shows obvious decrease. The average d_{Sb-TM} (TM bonding three Sb atoms) ranges from 2.45 (Co) to 2.88 Å (Sc), resulting from the different atomic radius of TM and the relative positions of host and TM atoms. These results are similar to arsenene based SACs [48].

The vacancy formation energy E_f of Sb single vacancy was estimated to be 1.77 eV, which is smaller than previous studies on defective formation energies of other 2D materials [63–66]. Meanwhile, the total energy and structure exhibit slight change through AIMD simulation under 400 K. These results verify excellent stability of defective Sb monolayer (Fig. 1a).

To evaluate the stability of the SACs, the binding energies (E_b) of TM atoms in the Sb monolayer were calculated (Fig. 1b). All TM@Sb monolayers show a negative E_b, demonstrating that Sb monolayer can stably anchor single TM atoms. The cohesive energies of bulk metal (E_c) were also investigated. All Ec are larger than their corresponding E_b of TM@Sb monolayer. Remarkably, the E_b and E_c of Mo@Sb monolayer are quite close, implying weakly intrinsic activity of Mo@Sb monolayer. To better explore the ECR activity of different TM atoms, only TM atoms will be considered as the active site in this work.

3.2. Competition between ECR and HER for the first hydrogeneration step

As ECR reactions accept a proton-electron pair in each step, the first protonation will form different intermediates. The first hydrogenation step can be expressed as below [67]

$$* + CO_2 + (H^+ + e^-) \rightarrow C^*OOH \quad (3)$$

$$* + CO_2 + (H^+ + e^-) \rightarrow O^*CHO \quad (4)$$

$$* + (H^+ + e^-) \rightarrow *H \quad (5)$$

Thus, there are three possible intermediates after the first step. The proton binding sites will determine the intermediates. If proton binds with carbon (C) or oxygen (O) atom, then the intermediate C*OOH or O*CHO is formed. However, if proton directly adsorbs on the surface of catalysts, then *H intermediate is generated, resulting in HER. These two reactions are competitive due to the similar reduction potentials, and ECR is inhibited by HER. ΔG_{C^*OOH} and ΔG_{O^*CHO} are plotted against ΔG_{*H} in Fig. 2, and the respective values are summarized in Table S1. If

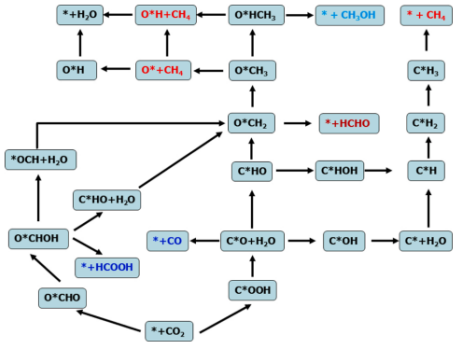

Fig. 3. The possible reaction pathways for ECR and C_1 products on TM @Sb monolayer.

ΔG_{*H} is larger than ΔG_{C^*OOH} or ΔG_{O^*CHO}, then the formation of C*OOH or O*CHO is preferred to H_2 evolution. This can be attributed to little active sites for proton adsorption after the occupation by COOH or OCHO radicals, giving rise to inferior HER activity. In our work, eight SACs (Sc@, V@, Cr@, Mn@, Fe@, Co@, Zn@ and Mo@Sb monolayer) are calculated to be more ECR selective than HER, which are located below the dashed line in Fig. 2. In contrast, the SACs located above the dashed line will be dominated by HER. Therefore, these SACs will not be considered for further ECR reaction calculations. It is worth noting that Cr@, Co@, Zn@ and Mo@Sb monolayers can only catalyse the formation of O*CHO, because ΔG_{C^*OOH} is larger than ΔG_{*H}. Therefore, for these four SACs, only O*CHO intermediate will be considered in the first hydrogenation step. Meanwhile, it can be highlighted that these SACs are nonprecious TM atoms exhibiting great ECR selectivity, which is obviously more valuable than noble TM based ECR catalysts reported previously.

3.3. Reaction pathways of ECR

In general, various C_1 and C_2 products can be produced from ECR. For C_2 products formation, an essential requirement is the coupling of C_1 to form C—C bond based on Langmuir-Hinshelwood mechanism. However, for SACs the adjacent two metal atoms will be intrinsically distant. Consequently, the formation of C_2 carbon products is less plausible. Therefore, only C_1 products were investigated. For the addition of proton-electron pair in each reaction step, the proton can bind C or O atom to produce various intermediates. To fully describe ECR on antimonene based SACs, the possible reaction pathways for C_1 products are summarized in Fig. 3. There are $2e^-$ reduction product (HCOOH and CO), $4e^-$ reduction product (HCHO), $6e^-$ reduction product (CH_3OH) and $8e^-$ reduction product (CH_4). The optimized configurations of key intermediates during ECR were shown in Fig. 4. The final products and optimal reaction pathways of eight SACs in ECR will be discussed by introducing several crucial parameters, including adsorption energy (E_{ads}), Gibbs free energy change (ΔG) of each step and overpotential (η).

As shown in Fig. 5, due to different carbophilicity and oxophilicity of active atoms, TMs could bind C or O atom in the initial step of protonation, resulting in O*CHO and C*OOH for Sc@, V@, Mn@ and Fe@Sb monolayers, while only O*CHO for the other monolayers. The two intermediates can be further reduced by proton-electron pairs. The hydrogenation of O*CHO and C*OOH will produce O*CHOH and (C*O + H_2O), respectively. The formation of C_1 products including CO and HCOOH will be determined by E_{ads}. If the E_{ads} of CO or HCOOH is large enough, CO or HCOOH will participate in further ECR reactions as

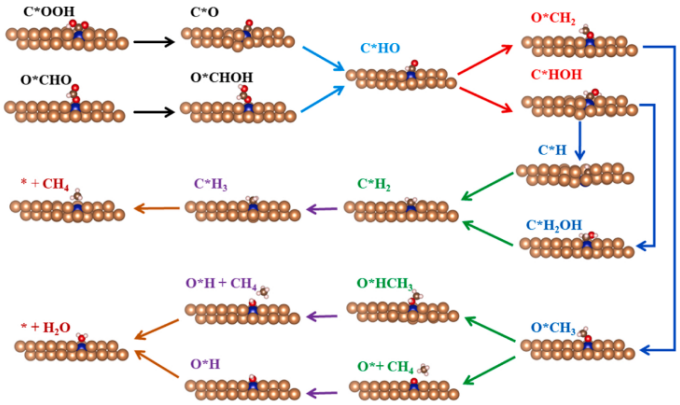

Fig. 4. The optimized configuration of key intermediates during ECR, where blue, black, white and red balls denote the TM, C, H and O atom, respectively.

intermediates. In contrast, if their E_{ads} are too small, CO or HCOOH will detach from the active site and be released as the final products. The calculated E_{ads} of CO and HCOOH for these SACs were listed in Table 1. Obviously, only Zn@Sb monolayer shows physisorption property for HCOOH with E_{ads} of −0.32 eV, resulting in HCOOH desorption from the surface of catalysts. We also assumed that HCOOH could be reduced further, but a big uphill of ΔG for O*CH and C*HO will not favor its hydrogenation (Fig. 5g). The optimal pathway for HCOOH generation is $* + CO_2 \rightarrow O*CHO \rightarrow O*CHOH \rightarrow * + HCOOH$.

The E_{ads} of CO and HCOOH of the remaining seven SACs range from −0.99 to −1.77 eV and −0.62 to −1.80 eV, suggesting strong chemisorption of both on the SACs. This suggests that CO and HCOOH will be further reduced on these seven SACs. Among which, V@ and Fe@Sb monolayers exhibit stronger adsorption of CO and HCOOH, implying that these two catalysts possess the best capability in further ECR. Three different intermediates C*HO, C*OH and O*CH will be generated from CO and HCOOH hydrogenation. As shown in Fig. 5, ΔG_{C*HO} is lower than ΔG_{C*OH} and ΔG_{O*CH}, demonstrating that C*HO is the crucial intermediate in the third hydrogenation process. These two processes can be expressed by $C*O + (H^+ + e^-) \rightarrow C*HO$ and $O*CHOH + (H^+ + e^-) \rightarrow C*HO + H_2O$. C*HO could further accept the fourth proton-electron pair to produce $O*CH_2$ and C*HOH. It is evident from Fig. 5 that the formation of C*HOH on these seven SACs underwent an uphill in energy. On the contrary, the formation of $O*CH_2$ on Sc@, V@, Cr@ and Mn@Sb monolayer is energetically favorable, suggesting these TM atoms have strong oxophilicity to form TM—O configurations. This also indicates that the protonation of C*HO ($C*HO + (H^+ + e^-) \rightarrow C*HOH$ or $O*CH_2$) is most likely the PDS for further ECR products. The E_{ads} of 4e- reduction product HCHO was estimated and summarized in Table 1. The E_{ads} of HCHO for these seven SACs is still quite negative from −0.86 to −1.39 eV, meaning that HCHO is difficult to desorb from the surface. Two intermediates $O*CH_3$ and $O*HCH_2$ could be generated in the next protonation step. However, ΔG_{O*HCH2} for all the seven SACs is big uphill. Then $O*CH_3$ will be the only intermediate for later reactions. When C*HOH intermediate accepting one proton-electron pair, the formation of $*CH_2OH$ is thermodynamically favorable with a large energy downhill.

With the addition of one more proton-electron pair, $6e^-$ reduction product CH_3OH appears. The step can be expressed as: $O*CH_3 + (H^+ + e^-) \rightarrow O*HCH_3 \rightarrow * + CH_3OH$. Nevertheless, ΔG_{O*HCH3} also shows a large uphill, meaning that the step is thermodynamically unfavorable. Meanwhile, the E_{ads} of CH_3OH on these seven TM@Sb monolayers is large between −0.90 and −1.55 eV, showing strong adsorption capability. As a result, CH_3OH will continue in ECR reactions as an intermediate. Interestingly, the E_{ads} of 8e- reduction product CH_4 are quite small, ranging from -0.19 to -0.48 eV. Thus, CH_4 can easily desorb from the surface of these SACs and become the final product in ECR. In Fig. 5 the optimized pathways for CH_4 production from ECR are proposed for different TM@Sb electrocatalysts based on minimum free energy increase in each protonation step. Sc@, V@, Cr@ and Mo@Sb monolayer possibly follow path (I) for CH_4 formation:

$$C*HO \rightarrow C*HOH \rightarrow C*H_2OH \rightarrow C*H_2 + H_2O \rightarrow C*H_3 \rightarrow * + CH_4 \quad (I)$$

While Mn@, Fe@ and Co@Sb monolayers may follow pathway (II):

$$C*HO \rightarrow O*CH_2 \rightarrow O*CH_3 \rightarrow O* + CH_4 \rightarrow O*H \rightarrow * + H_2O \quad (II)$$

As a result, we can conclude that antimonene based SACs can electrocatalytically convert CO_2 into CH_4.

To evaluate the performance of these SACs for CO_2 conversion to CH_4, it is essential to calculate the overpotential. The smaller the overpotential, the better the electrocatalytic efficiency. In our work, we calculated the free energy change ΔG of each step, and the maximum change in free energy will be the potential determining steps (PDS) that determine U_L. η was then estimated according to the equation $\eta = U_{equ} - U_L$. The PDS, U_L and η for these SACs are summarized in Table 1. The PDS of these electrocatalysts are different, e.g., the PDS of V@Sb monolayer for CH_4 formation is C*HO → C*HOH, whereas the PDS of Cr@Sb monolayer is O*CHOH → C*HO. This demonstrates that different TM atoms exhibit different interactions with the intermediates. It is worth noting that the reaction $O* \rightarrow O*H \rightarrow H_2O + *$ is included in pathway (II), which is part of an ORR process. According to the Sabatier principle, too strong or too weak interaction between catalysts and the intermediates is not beneficial for catalytic activity [68]. Too strong interaction will poison the electrode, whereas too weak interaction will not activate the reactants or intermediates to drive the further reactions. For Sc@, V@, Cr@ and Mo@Sb monolayers, ΔG for the formation of H_2O show big uphill, indicating strong interaction between O*H and TM, which is not an optimal pathway and leads to high overpotential. Thus, path (I) is more favourable. In contrast, the proper interaction between Mn, Fe and Co atom and O*H brings about a small overpotential, making path (II) ideal for CO_2 converting into CH_4. Zn@Sb monolayer exbibit an overpotential of 0.45 V for the HCOOH product. For CH_4, the remaining seven SACs have overpotentials less than 0.90 V. Especially, Co@Sb monolayer shows an overpotential of only 0.50 V,

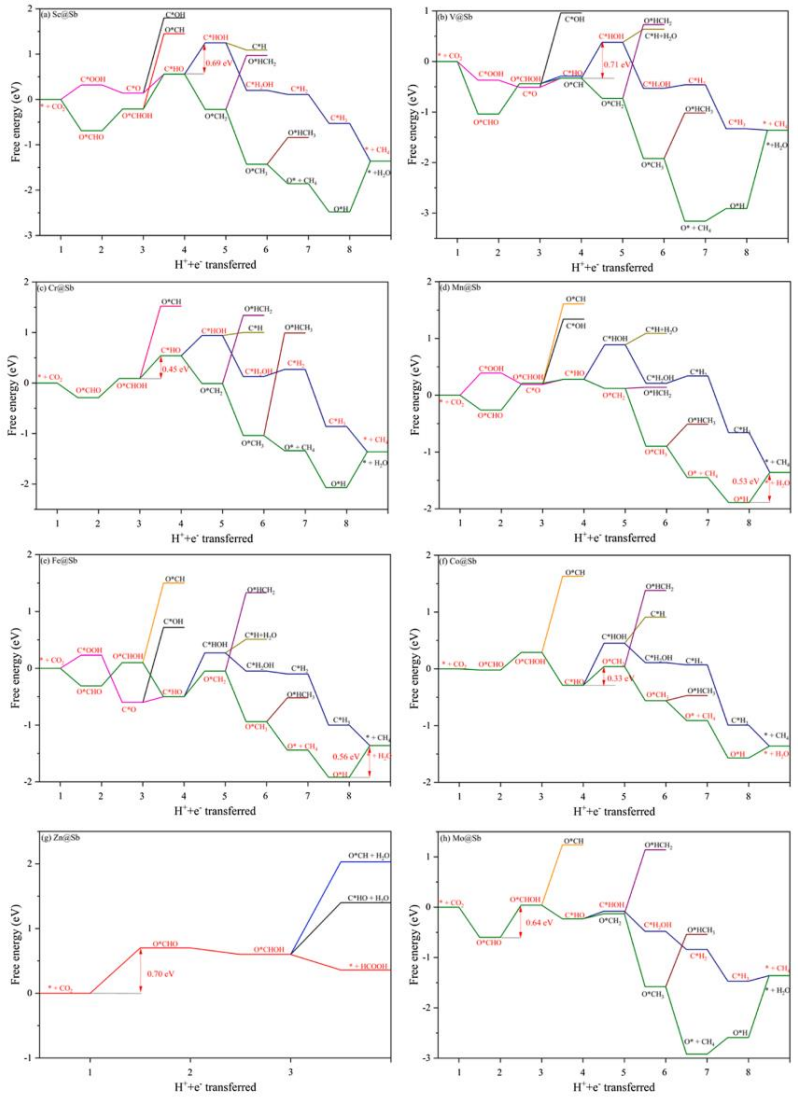

Fig. 5. The Gibbs free energy diagram for ECR to the final C_1 product on TM@Sb monolayer under U = 0 V.

which is comparable to or even smaller than the state-of-the-art catalysts Cu (211). Therefore, TM atoms and particularly non-precious TM atoms anchored on antimonene can effectively convert CO_2 into CH_4 in ECR.

3.4. Electronic properties

Electrical conductivity is a crucial parameter to evaluate the electron transfer efficiency. The band structure of pristine and defective Sb monolayer was calculated and displayed in Fig. S2a and b. The electron state of spin up and down are completely symmetric, demonstrating its nonmagnetic property. The pristine Sb monolayer shows an indirect bandgap of 1.28 eV, which is well consistent with previous studies [69, 70]. New energy levels crossing the Fermi level are beneficial for electron transfer. In the projected density of states (PDOS) of the TM@Sb

Table 1
Adsorption energy (E_{ads}) of different reduction products CO, HCOOH, HCHO, CH_3OH and CH_4 (unit eV); The potential determining steps (PDS) for CH_4 or HCOOH formation on TM@Sb monolayer; The limiting potential U_L, the equilibrium potential U_{eq} under pH = 0 of different products, and the overpotential η (all units in V).

System	E_{CO}	E_{HCOOH}	E_{HCHO}	E_{CH3OH}	E_{CH4}	PDS	U_L	U_{eq}	η
Sc	−0.99	−1.12	−1.33	−1.30	−0.42	C*HO→C*HOH	0.69	0.17(CH_4)	0.86
V	−1.64	−1.39	−1.82	−1.55	−0.48	C*HO→C*HOH	0.71	0.17(CH_4)	0.88
Cr	–	−0.81	−1.08	−1.04	−0.23	O*CHOH→C*HO	0.45	0.17(CH_4)	0.62
Mn	−0.99	−0.72	−0.86	−0.98	−0.25	O*H→* + H_2O	0.53	0.17(CH_4)	0.70
Fe	−1.77	−1.80	−1.17	−1.01	−0.26	O*H→* +H_2O	0.56	0.17(CH_4)	0.73
Co	–	−0.62	−1.04	−0.90	−0.23	C*HO→O*CH_2	0.33	0.17(CH_4)	0.50
Zn	–	−0.32	–	–	–	*+CO_2→O*CHO	0.70	−0.25(HCOOH)	0.45
Mo	–	−0.80	−1.39	−0.95	−0.19	O*CHO→O*CHOH	0.64	0.17(CH_4)	0.81

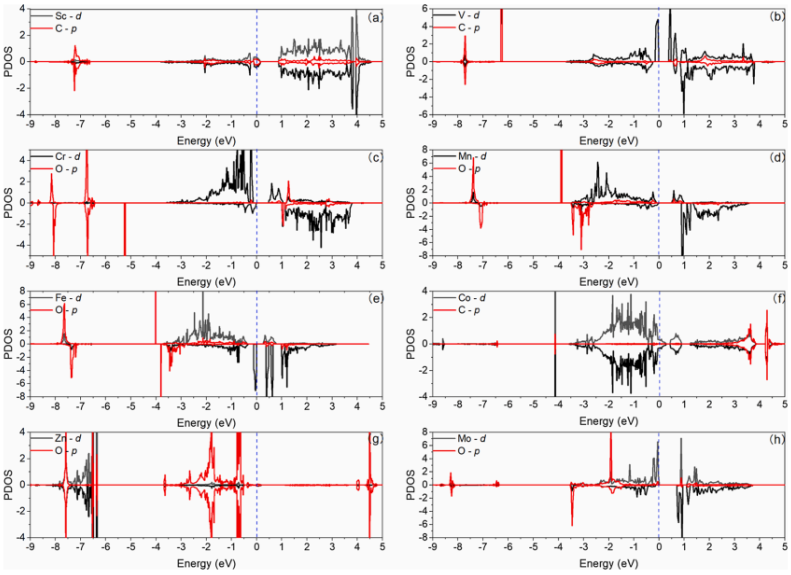

Fig. 6. The PDOS of C*HO adsorbed on (a) Sc, (b) V and (f) Co@Sb monolayer, O*CHOH adsorbed on (c) Cr@Sb monolayer, O*H adsorbed on (d) Mn and (e) Fe@Sb monolayer, and O*CHO adsorbed on (g) Zn and (h) Mo@Sb monolayer. The dashed line represents the Fermi level.

monolayer (Fig. S3), for instance, Sc@, Co@ and Zn@Sb monolayaer present nonmagnetic property, while others such as V@, Cr@, Mn@, Fe@ and Mo@Sb exhibit magnetic nature. Almost all samples exhibit the electron states crossing the Fermi level, and the main contribution is from TM atoms. Thus, the conductivity of these SACs is improved.

The interaction between TM atoms and Sb monolayer will greatly affect the ECR performance. It can be seen from Fig. S3 that the *p* orbitals of the Sb atom have a different degree of overlap with *d* orbitals of TM atoms among the conduct band and valence band for these eight SACs. Particularly, the *d* orbitals of Co overlap better with *p* orbitals of the Sb atom from −4.0 to 4.0 eV, indicating that the interaction between Co atom and Sb monolayer is stronger than others. Indeed, Table 1 shows that Co@Sb monolayer has the smallest overpotential for CH_4 generation. In contrast, Zn@Sb monolayer is preferred for HCOOH production with a smaller overpotential, but the value is still larger than those reported in other studies [71–74]. This is manifested by the fact that the PDOS of Zn@Sb monolayer exhibits weak interaction, which suggests a low intrinsic activity for ECR. Therefore, the stronger the interaction between TM atoms and Sb monolayer, the higher the catalytic activity

Table 2
The charge transfer of TM (Q_{TM-1}) on clean TM@Sb monlayer, the charge transfer of TM (Q_{TM-2}) after adsorption of intermediates of PDS, and the charge transfer of C (Q_C), H (Q_C) and O(Q_O) after adsorption of intermediates of PDS on TM@Sb monlayer (all units in e); the positive or negative value denotes electron-acceptor and electron-donor, respectively; The bond length $d_{TM-C/O}$ between TM atoms and intermediates of PDS (unit Å).

System	Q_{TM-1}	Q_{TM-2}	Q_C	Q_H	Q_O	$d_{TM-C/O}$
Sc	−0.50	−0.86	−2.49	0.23	0.99	2.12
V	−0.26	−0.27	−2.83	0.27	0.96	1.92
Cr	0.04	−0.42	−3.27	−0.59, 0.22	1.02, 0.81	1.99
Mn	0.04	−0.16	–	−0.35	0.98	1.80
Fe	0.35	−0.14	–	−0.33	0.95	1.76
Co	0.49	0.14	−2.43	0.42	0.80	1.88
Zn	0.16	−0.13	−3.05	0.26	0.87, 0.82	1.93
Mo	0.33	−0.52	−3.11	0.17	0.93, 0.70	1.92

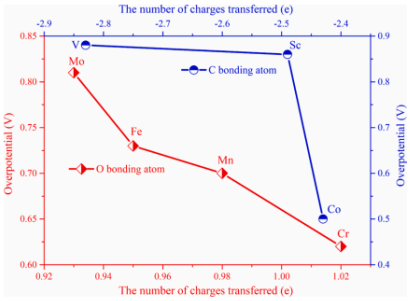

Fig. 7. (a) Relationship between overpotential and bonding C or O atom from C*HO, O*H, O*CHO and O*CHOH.

for CH_4 formation. The strength of the interaction between the catalysts and intermediates also holds the key to the ECR efficiency as manifested by the Sabatier principle. Too strong interaction will make the Gibbs free energy of the protonation process increase, and the energy barrier of PDS will increase. The PDOS of intermediates in the PDS of TM@Sb monolayer for ECR is displayed in Fig. 6. The Sc@, V@, Fe@ and Mo@Sb monolayer show stronger interaction between TM and C or O atoms both in the conduct band and valence band compared with the other samples, suggesting that these monolayers could interact strongly with the intermediates of PDS. Thus, these four SACs exhibit a relatively high overpotential for the final products in ECR. Meanwhile, the Bader charge analysis (Q_{TM-1}) in Table 2 shows that Sc and V atoms act as an electron donor on clean TM@Sb monolayer, while others are electron acceptor. Mn and Fe exhibit only $0.14e^-$ transfer, demonstrating a weak interaction and poor intrinsic ECR activity. After the key intermediates adsorbed on the TM@Sb monolayer, the roles of TM atom were changed. The negative value of Q_{TM-2} indicate that all TM atoms act as electron donor except Co atom. The total charge transfer of C, H and O atom in respective intermediates suggests that OH in Mn@ and Fe@Sb monolayers is electron-accepting group, while CHO, OCHO, OCHOH in other TM@Sb monolayers work as electron-donating groups. Thus, Co as electron acceptor and CHO as electron-donating group will contribute to an appropriate interaction between them, resulting in a small overpotential. This is also verified by the optimal d_{Co-C} (1.88 Å), which is well consistent with the sum of atomic covalent radii of Co and C (1.86 Å) [75]. We also compared the charge transfer between TM atoms and intermediates before and after adsorption. The total charge transfer from C*HO to Co@Sb is $1.21e^-$ (Table 2) on C*HO adsorbed Co@Sb. Meanwhile, Co only accepts $0.14e^-$, implying $1.07\ e^-$ is shared by three Sb atoms bonded with Co. Thus, it manifests a strong interaction between Co and Sb atom, which is consistent with the PDOS analysis. Thus, the excellent CH_4 selectivity on Co@Sb during ECR could also be attributed to the synergistic effect between Co and Sb atom.

Interestingly, we identified a strong relationship between the overpotential for CH_4 generation and the amount of charge transfer of TM bonding C or O atom of intermediates of PDS. As shown in Fig. 7, for O*H, O*CHO and O*CHOH, the more charge the bonding O atom accept, the smaller the overpotential for CH_4 formation. Whereas the more charge the bonding C atom lose, the larger overpotential for CH_4 formation from C*HO.

As Co@Sb monolayer shows excellent performance in ECR to CH_4, we further assess its stability by AIMD under a target temperature of 400 K (Fig. 8a). The final structure of Co@Sb monolayer remains almost the same as the initial structure, while the total energy exhibits slight oscillation, demonstrating excellent stability of the Co@Sb monolayer. Besides, the diffusion barrier of Co atom is calculated, as displayed in Fig. 8b. There is a large energy barrier of 3.02 eV to overcome for Co atom to diffuse from the anchored defective site to the neighboring hollow site, verifying that the embedded Co atom can hardly diffuse to form cluster. Thus, Co@Sb monolayer could be a highly efficient and stable SACs for CH_4 production from ECR.

4. Conclusions

TM atoms anchored Sb monolayer as SACs were investigated systemically for electrochemical reduction of CO_2 via first-principles calculation. TM atoms from 3*d* group (Sc, V, Cr, Mn, Fe, Co) are preferable for ECR, whereas precious TM atoms from 4*d* and 5*d* prefer HER. Only Zn@Sb monolayer could reduce CO_2 into HCOOH with an overpotential of 0.45 V. These SACs with high ECR selectivity could convert CO_2 into CH_4 with small overpotential. Two optimal pathways for the reduction of CO_2 into CH_4 are proposed. Particularly, Co@Sb monolayer shows the smallest overpotential of 0.50 V for CH_4, which is better than previously reported ECR electrocatalysts. Meanwhile, the high intrinsic activity can be attributed to the interaction between TM atoms and Sb monolayer, and the interaction between TM atoms and intermediates play a key role in determining the overpotential. More importantly, there is a certain relation between the amount of charge transfer of TM bonding atoms of intermediates of PDS and overpotential of ECR to CH_4 on different TM@Sb monolayers. This work suggests that TM embedded on Sb monolayer can actively and selectively catalyze CO_2 into CH_4, and provides useful guidelines for the design and synthesis of antimonene based SACs for ECR applications.

Author statement

Song. Lu: Conceptualization, Methodology, Investigation, Writing - Original Draft, Writing - Review & Editing, Visualization.

Huong Lan Huynh: Investigation, Writing - Review & Editing.

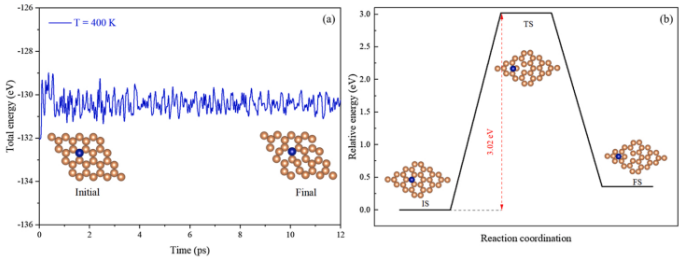

Fig. 8. (a) The total energy variations of Co@Sb monolayer under a target temperature 400 of K for AIMD simulation for 12 ps with a time step of 3 fs; (b) The minimum energy pathway of adsorbed Co atom to diffuse from the vacancy site to neighboring site.

Fengliu Lou: Investigation.
Min. Guo: Supervision, Writing - Review & Editing.
Zhixin. Yu: Conceptualization, Supervision, Writing - Review & Editing.

Declaration of Competing Interest

The authors report no declarations of interest.

Acknowledgements

This work is supported by the Norwegian Ministry of Education and Research. The computations were performed on resources provided by UNINETT Sigma2 - the National Infrastructure for High Performance Computing and Data Storage in Norway.

Appendix A. Supplementary data

Supplementary material related to this article can be found, in the online version, at doi:https://doi.org/10.1016/j.jcou.2021.101645.

References

[1] S. Chu, Y. Cui, N. Liu, Nat. Mater. 16 (2017) 16–22.
[2] B. Obama, Science 355 (2017) 126–129.
[3] D.D. Zhu, J.L. Liu, S.Z. Qiao, Adv. Mater. 28 (18) (2016) 3423–3452.
[4] S.C. Roy, O.K. Varghese, M. Paulose, C.A. Grimes, ACS Nano 4 (2010) 1259–1278.
[5] W.J. Zhang, Y. Hu, L.B. Ma, G.Y. Zhu, Y.R. Wang, X.L. Xue, R.P. Chen, S.Y. Yang, Z. Jin, Adv. Sci. 5 (2017), 1700275.
[6] P.R. Yaashikaa, P.S. Kumar, S.J. Varjani, A. Saravanan, J. CO2 Util. 33 (2019) 131–147.
[7] S. Gao, X.C. Jiao, Z.T. Sun, W.H. Zhang, Y.F. Sun, C.M. Wang, Q.T. Hu, X.L. Zu, F. Yang, S.Y. Yang, L. Liang, J. Wu, Y. Xie, Angew. Chem. Int. Ed. 54 (2015) 698–702.
[8] Y. Zhang, L.B. Li, S.X. Guo, X.L. Zhang, F.W. Li, A.M. Bond, J. Zhang, ChemSusChem 13 (2020) 59–77.
[9] L.M. Wang, W.H. Chen, D.D. Zhang, Y.P. Du, R. Amal, S.Z. Qiao, J.B. Wu, Z.Y. Yin, Chem. Soc. Rev. 48 (2019) 5310–5349.
[10] X. Tan, C. Yu, Y.W. Ren, S. Cui, W.B. Li, J.S. Qiu, Energy Environ. Sci. 14 (2021) 765–780.
[11] W. Luc, X.B. Fu, J.J. Shi, J.J. Lv, M. Jouny, B.H. Ko, Y.B. Xu, Q. Tu, X.B. Hu, J. S. Wu, Q. Yue, Y.Y. Liu, F. Jiao, Y.J. Kang, Nat. Catal. 2 (2019) 423–430.
[12] Z.X. Gu, N. Yang, P. Han, M. Kuang, B.B. Mei, Z. Jiang, J. Zhong, L. Li, G.F. Zheng, Small Methods 3 (2019), 1800550.
[13] D.F. Gao, R.M. Arán-Ais, H.S. Jeon, B.R. Cuenya, Nat. Catal. 2 (2019) 198–210.
[14] Q. Lu, F. Jiao, Nano Energy 29 (2016) 439–456.
[15] R. Kortlever, J. Shen, K.J.P. Schouten, F. Calle-Vallejo, M.T. Koper, J. Phys. Chem. Lett. 6 (2015) 4073–4082.
[16] A. Corma, H. Garcia, J. Catal. 308 (2013) 168–175.
[17] J.L. Qiao, Y.Y. Liu, F. Hong, J.J. Zhang, Chem. Soc. Rev. 43 (2014) 631–675.
[18] M. Ross, P. Luna, Y. Li, C.T. Dinh, D. Kim, P. Yang, E. Sargent, Nat. Catal. 2 (2019) 648–658.
[19] S. Gao, Y. Lin, X. Jiao, Y. Sun, Q. Luo, W. Zhang, D. Li, J. Yang, Y. Xie, Nature 529 (2016) 68–71.
[20] X. Zheng, Y. Ji, J. Tang, J. Wang, B. Liu, H.-G. Steinrück, K. Lim, Y. Li, M. Toney, K. Chan, Y. Cui, Nat. Catal. 2 (2019) 55–61.
[21] C.S. Diercks, Y. Liu, K.E. Cordova, O.M. Yaghi, Nat. Mater. 17 (2018) 301–307.
[22] K.P. Kuhl, E.R. Cave, D.N. Abram, T.F. Jaramillo, Energy Environ. Sci. 5 (2012) 7050–7059.
[23] R. Kortlever, I. Peters, S. Koper, M.T.M. Koper, ACS Catal. 5 (2015) 3916–3923.
[24] G.L. Chai, Z.X. Guo, Chem. Sci. 7 (2016) 1268–1275.
[25] H. Mistry, R. Reske, Z.H. Zeng, Z.J. Zhao, J. Greeley, P. Strasser, B.R. Cuenya, J. Am. Chem. Soc. 136 (2014) 16473–16476.
[26] Z.W. Seh, J. Kibsgaard, C.F. Dickens, I. Chorkendorff, J.K. Nørskov, T.F. Jaramillo, Science 355 (2017), eaad4998.
[27] X.Y. Chia, M. Pumera, Nat. Catal. 1 (2018) 909–921.
[28] X. Li, S. Wang, L. Li, X. Zu, Y. Sun, Y. Xie, Acc. Chem. Res. 53 (2020) 2964–2974.
[29] L.X. Chen, Z.W. Chen, M. Jiang, Z.L. Lu, C. Gao, G.M. Cai, C.V. Singh, J. Mater. Chem. A 9 (2021) 2018–2042.
[30] G. Ménard, D.W. Stephan, Angew. Chem. Int. Ed. 50 (2011) 8396–8399.
[31] P. Luo, F.W. Zhuge, Q.F. Zhang, Y.Q. Chen, L. Lv, Y. Huang, H.Q. Li, T.Y. Zhai, Nanosc. Horiz. 4 (2019) 26–51.
[32] Y. Wu, C. Li, W. Liu, H.H. Li, Y.Y. Gong, L.Y. Niu, X.J. Liu, C.Q. Sun, Nanoscale 11 (2019) 5064–5071.
[33] Q.M. Yu, Y.T. Luo, A. Mahmood, B. Liu, H.M. Cheng, Electrochem. Energy Rev. 2 (2019) 373–394.
[34] J. Zhao, J.X. Zhao, F.Y. Li, Z.F. Chen, J. Phys. Chem. C 122 (2018) 19712–19721.
[35] H.W. Zhang, R.T. Lv, J. Materiomics 4 (2018) 95–107.
[36] J. Choi, J. Kim, P. Wagner, S. Gambhir, R. Jalili, S. Byun, S. Sayyar, Y.M. Lee, D. R. MacFarlane, G.G. Wallace, D.L. Officer, Energy Environ. Sci. 12 (2019) 747–755.
[37] X. Hong, K. Chan, C. Tsai, J.K. Nørskov, ACS Catal. 6 (2016) 4428–4437.
[38] N. Kornienko, Y.B. Zhao, C.S. Kley, C.H. Zhu, D. Kim, S. Lin, C.J. Chang, O. M. Yaghi, P.D. Yang, J. Am. Chem. Soc. 137 (2015) 14129–14135.
[39] N.H. Attanayake, H.R. Banjade, A.C. Thenuwara, B.B. Anasori, Q.M. Yan, D. R. Strongin, Chem. Commun. 57 (2021) 1675–1678.
[40] S.L. Zhang, Z. Yang, Y.F. Li, Z.F. Chen, H.B. Zeng, Angew. Chem. 127 (2015) 3155–3158.
[41] H.S. Tsai, S.W. Wang, C.H. Hsiao, C.W. Chen, H. Ouyang, Y.L. Chueh, H.C. Kuo, J. H. Liang, Chem. Mater. 28 (2016) 425–429.
[42] J.P. Ji, X.F. Song, J.Z. Liu, Z. Yan, C.X. Huo, S.L. Zhang, M. Su, L. Liao, W.H. Wang, Z.H. Ni, Y.F. Hao, H.B. Zeng, Nat. Commun. 7 (2016) 13352.
[43] R.G. Mao, Z. sofer, D. Bousa, M. Pumera, Angew. Chem. 129 (2017) 14609–14614.
[44] B. Qiao, A. Wang, X. Yang, L.F. Allard, Z. Jiang, Y. Cui, J. Liu, J. Li, T. Zhang, Nat. Chem. 3 (2011) 634–641.
[45] S. Zhao, G. Chen, G. Zhou, L.C. Yin, J.P. Veder, B. Johannessen, M. Saunders, S. Z. Yang, R. De Marco, C. Liu, S.P. Jiang, Adv. Funct. Mater. 30 (2019), 1906157.
[46] H. Yuan, Z.Y. Li, X.C. Zeng, J.L. Yang, J. Phys. Chem. Lett. 11 (2020) 3481–3487.
[47] C.X. Zhao, G.X. Zhang, W. Gao, Q. Jiang, J. Mater. Chem. A 7 (2019) 8210–8217.
[48] Z.W. Xu, R.F. Song, M.Y. Wang, X.Z. Zhang, G.W. Liu, G.J. Qiao, Phys. Chem. Chem. Phys. 22 (2020) 26223–26230.
[49] G. Kresse, D. Joubert, Phys. Rev. B 59 (1999) 1758.
[50] G. Kresse, J. Furthmüller, Comput. Mater. Sci. 6 (1996) 15–50.
[51] P.E. Blöchl, Phys. Rev. B: Condens. Matter Mater. Phys. 50 (1994) 17953–17979.
[52] J.P. Perdew, K. Burke, M. Ernzerhof, Phys. Rev. Lett. 77 (1996) 3865–3868.
[53] J.P. Perdew, M. Ernzerhof, K. Burke, J. Chem. Phys. 105 (1996) 9982–9985.
[54] S. Grimme, J. Antony, S. Ehrlich, H. Krieg, J. Chem. Phys. 132 (2010) 154104–154123.
[55] G. Kresse, J. Hafner, Phys. Rev. B 47 (1993) 558.
[56] C. Su, H. Jiang, J. Feng, Phys. Rev. B 87 (2013), 075453.
[57] G. Henkelman, A. Arnaldsson, H. Jonsson, Comput. Mater. Sci. 36 (2006) 354–360.
[58] R. Bader, Atoms in Molecules: A Quantum Theory, Oxford University Press: New York (1990).
[59] K. Mathew, R. Sundararaman, K.L. Weaver, T.A. Arias, R.G. Hennig, J. Chem. Phys. 140 (2014), 084106.
[60] J.K. Nørskov, J. Rossmeisl, A. Logadottir, L. Lindqvist, J.R. Kitchin, T. Bligaard, H. Jonsson, J. Phys. Chem. B 108 (2004) 17886–17892.
[61] P. Aghdasi, R. Ansari, Solid State Commun. 311 (2020), 113849.
[62] P. Aghdsi, S. Yousefi, R. Ansari, J. Mol. Model. 15 (2021) 27.
[63] A.A. El-Barbary, R.H. Telling, C.P. Ewels, M.I. Heggie, P.R. Briddon, Phys. Rev. B 68 (2003), 144107.
[64] L. Oakes, R. Carter, C.L. Pint, Nanoscale 8 (2016) 19368–19375.
[65] Q.X. Zhou, W.W. Ju, Y.L. Yong, X.H. Li, J. Magn. Magn. Mater. 491 (2019), 165613.
[66] C. Freysoldt, B. Grabowski, T. Hickel, J. Neugebauer, G. Kresse, A. Janotti, C.G.V. D. Walle, Rev. Mod. Phys. 86 (2014) 253–305.
[67] J.H. Liu, L.M. Yang, E. Ganz, ACS Sustain. Chem. Eng. 6 (2018) 15494–15502.
[68] J.K. Nørskov, T. Bligaard, A. Logadottir, J.R. Kitchin, J.G. Chen, S. Pandelov, U. Stimming, J. Electrochem. Soc. 152 (2005) J23–J26.
[69] D. Singh, S.K. Gupta, Y. Sonvane, I. Lukacevic, J. Mater. Chem. C 4 (2016) 6386–6390.
[70] O. Üzengi Aktürk, V. Ongun Özçelik, S. Ciraci, Phys. Rev. B: Condens. Matter Mater. Phys 91 (2015), 235446.
[71] X.D. Cui, W. An, X.Y. Liu, H. Wang, Y. Men, J.G. Wang, Nanoscale 10 (2018) 15262–15272.
[72] S.K. Kim, Y.J. Zhang, H. Bergstrom, R. Michalsky, A. Pretrson, ACS Catal. 6 (2016) 2003–2013.
[73] H.L. Dong, Y.Y. Li, D.D. Jiang, J. Phys. Chem. C 122 (2018) 11392–11398.
[74] J.H. Liu, L.M. Yang, E. Ganz, RSC Adv. 9 (2019) 27710–27719.
[75] P. Pyykkö, M. Atsumi, Chem. Eur. J. 15 (2009) 186–197.

Supporting Information

Electrochemical Reduction of CO_2 to CH_4 over Transition Metal Atom Embedded Antimonene: First-Principles Study

Song Lu[a], Huong Lan Huynh[a], Fengliu Lou[b], Min Guo[c]*, Zhixin Yu[a]*

[a]Department of Energy and Petroleum Engineering, University of Stavanger, 4036 Stavanger, Norway

[b]Beyonder AS, Kanalsletta 2, 4033 Stavanger, Norway

[c]Institute of New Energy, School of Chemical Engineering, Chemistry and Shaoxing University, Shaoxing 312000, China

Computational methods

The formation energy (E_f) of vacancy was estimated by formula S1[1]:

$$E_f = E_{V-Sb} - n \times E_{Sb} \quad \text{(S1)}$$

where E_{V-Sb}, n and E_{Sb} are the total energy of defective Sb monolayer, the number of Sb atoms and energy of each Sb atom in a pristine Sb monolayer, respectively.

The binding energy (E_b) of TM atoms embedded in the defected Sb monolayer was calculated based on equation S2:

$$E_b = E_{TM-Sb} - E_{Sb} - E_{TM} \quad \text{(S2)}$$

where E_{TM-Sb}, E_{Sb} and E_{TM} denote the total energies of TM embedded Sb monolayer, defective Sb monolayer and TM atoms, respectively. With such a definition, a more negative value of E_b indicates better thermodynamic stability.

The cohesive energies of bulk metal materials (E_c) can be obtained by equation S3:

$$E_c = (E_{bulk} - n \times E_{TM})/n \quad \text{(S3)}$$

Where the E_{bulk} is the energies of bulk metal, E_{TM} is the energies of single metal atoms, and n is the number of metal atom in its bulk structure.

Reference

1. Q. X. Zhou, W. W. Ju, Y. L. Yong and X. H. Li, *J. Magn. Magn. Mater*., 2019, **491**, 165613.

Table S1. The calculated free energies change of ΔG_{*H}, ΔG_{*COOH} and ΔG_{*OCHO} (eV).

TM@Sb	ΔG_{*H}	ΔG_{*COOH}	ΔG_{*OCHO}
Sc	0.63	0.32	-0.69
Ti	-0.28	1.06	0.26
V	0.23	-0.37	-1.04
Cr	0.41	0.43	-0.29
Mn	0.39	0.39	-0.27
Fe	0.29	0.23	-0.31
Co	0.25	0.29	-0.01
Ni	0.06	0.50	0.23
Cu	0.20	1.12	0.79
Zn	0.89	1.33	0.81
Mo	-0.19	-0.13	-0.77
Ru	-0.37	-0.36	-0.14
Rh	0.40	0.62	0.86
Pd	0.22	0.86	0.77
Ag	0.39	1.46	0.98
Cd	0.98	1.54	1.01
Ir	-0.01	0.27	0.65
Pt	-0.01	0.58	0.54
Au	0.49	1.45	1.17

Fig. S1. Top view (a) and side view (b) of schematic structure of 4×4 monolayer Sb with one TM atom embedded into Sb vacancy, where medium-orchid ball and red ball represent the Sb and TM atoms respectively.

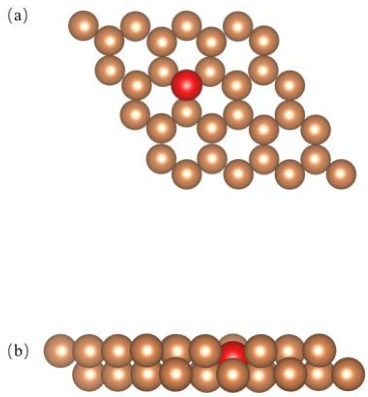

Fig. S2. The band structure of pristine Sb monolayer (a), and defective Sb monolayer (b); Fermi level was set to zero (horizontal dashed line).

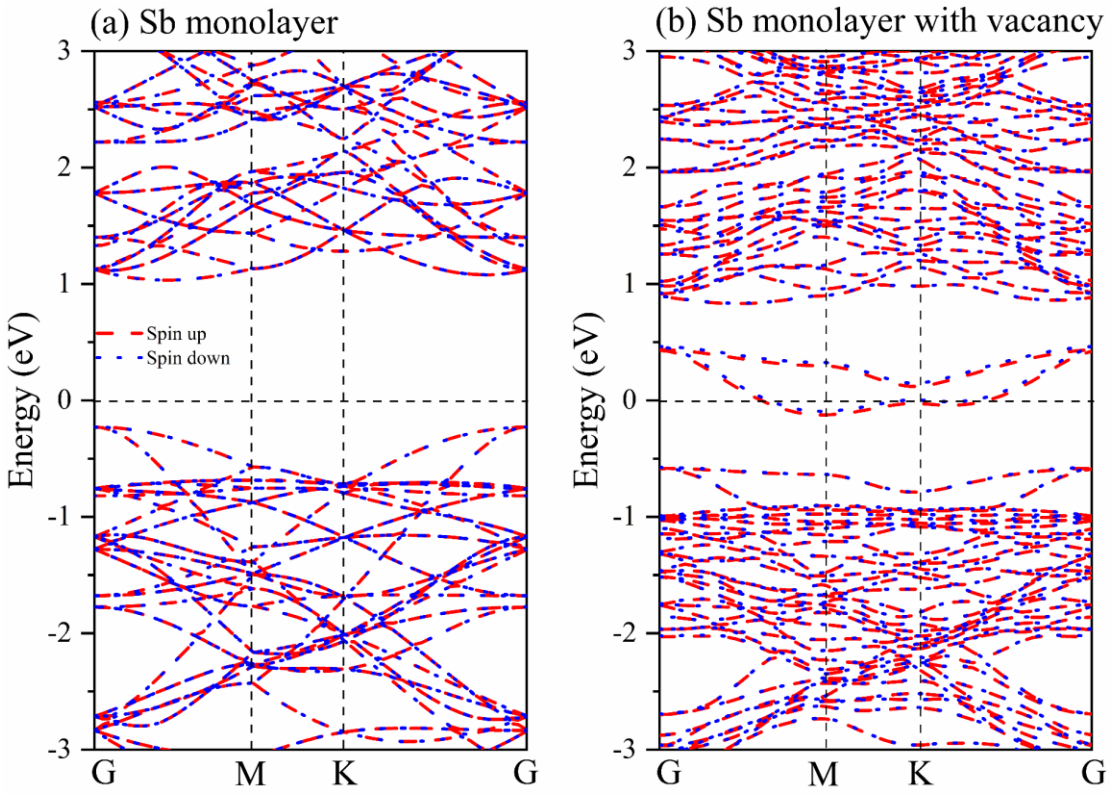

Fig. S3. The projected density of states of TM@Sb monolayers; Fermi level was set to zero (dashed line).

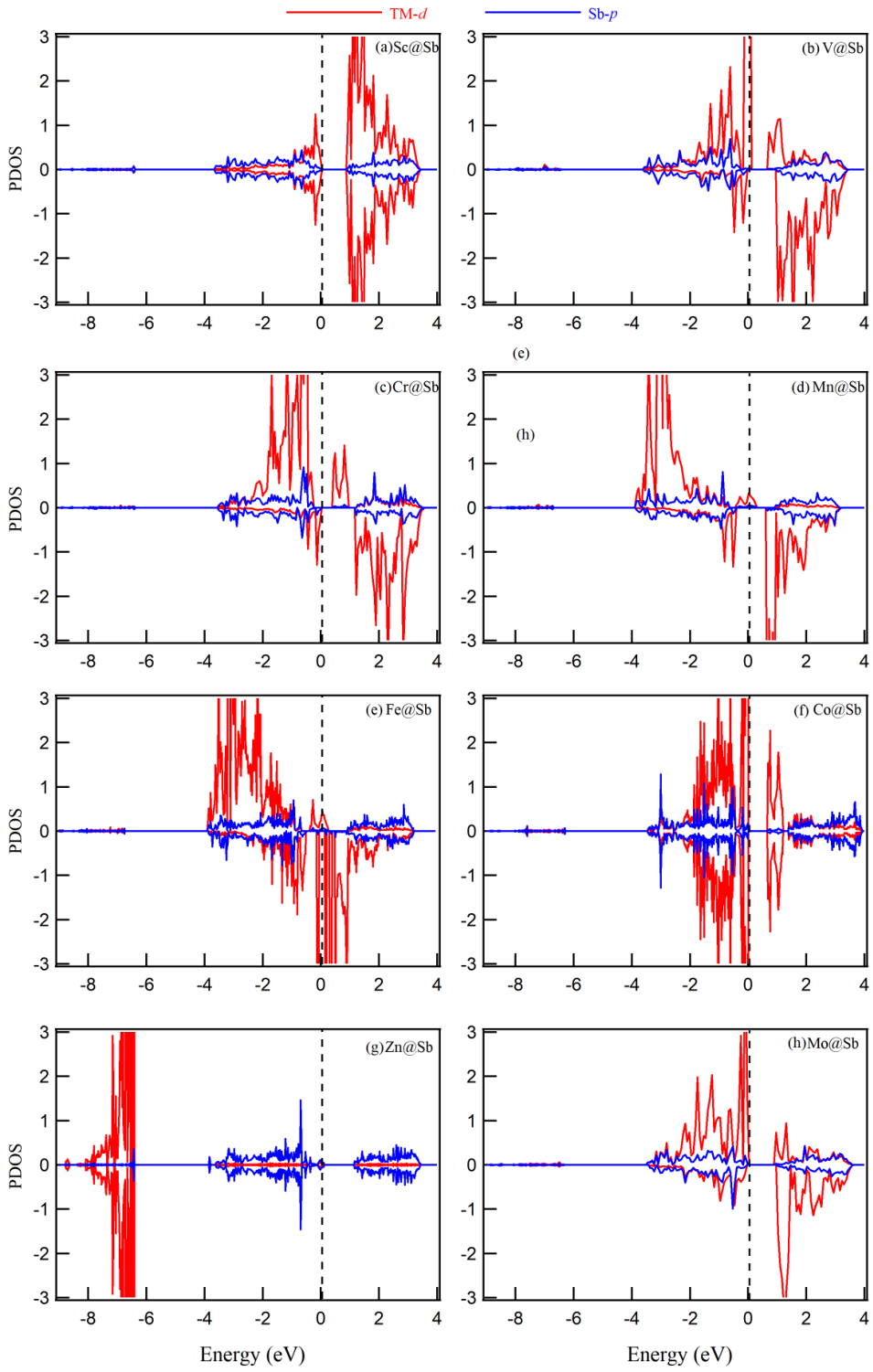

Appendix E – Paper V

Sulfur-Decorated Ni−N−C Catalyst for Electrocatalytic CO_2 Reduction with Near 100 % CO Selectivity

S. Lu, Y. Zhang, M. F. Mady, O. E. Eleri, W. M. Tucho, M. Mazur, A. Li, F. Lou, M. Gu and Z. Yu

ChemSusChem, 2022, 15, e202200870

DOI: 10.1002/cssc.202200870

Check for updates

ChemSusChem

Research Article
doi.org/10.1002/cssc.202200870

Chemistry Europe
European Chemical Societies Publishing

www.chemsuschem.org

Sulfur-Decorated Ni–N–C Catalyst for Electrocatalytic CO_2 Reduction with Near 100% CO Selectivity

Song Lu,[a] Yang Zhang,[a, b] Mohamed F. Mady,[c] Obinna Egwu Eleri,[a, b] Wakshum Mekonnen Tucho,[d] Michal Mazur,[e] Ang Li,[e] Fengliu Lou,[b] Minfen Gu,*[f] and Zhixin Yu*[a]

Developing highly efficient electrocatalysts for electrochemical CO_2 reduction (ECR) to value-added products is important for CO_2 conversion and utilization technologies. In this work, a sulfur-doped Ni–N–C catalyst is fabricated through a facile ion-adsorption and pyrolysis treatment. The resulting Ni–NS–C catalyst exhibits higher activity in ECR to CO than S-free Ni–N–C, yielding a current density of 20.5 mA cm^{-2} under −0.80 V versus a reversible hydrogen electrode (vs. RHE) and a maximum CO faradaic efficiency of nearly 100%. It also displays excellent stability with negligible activity decay after electrocatalysis for 19 h. A combination of experimental investigations and DFT calculations demonstrates that the high activity and selectivity of ECR to CO is due to a synergistic effect of the S and Ni–N_x moieties. This work provides insights for the design and synthesis of nonmetal atom-decorated M–N–C-based ECR electrocatalysts.

Introduction

About 500 gigatons of carbon dioxide will be generated from the combustion of fossil fuels in the next half century.[1] Excessive CO_2 emissions have aroused environmental issues such as global warming and erratic weather.[2,3] To alleviate these adverse effects, developing efficient carbon capture, utilization and storage (CCUS) technologies is of paramount importance. In recent years, electrochemical CO_2 reduction (ECR), potentially powered by renewable electricity sources, has received extensive attention. ECR can convert CO_2 to value-added products such as C_1 (e.g., CO, HCOOH, CH_4), C_2 (e.g., C_2H_4, C_2H_5OH), and C_3 (e.g., C_3H_7OH) under ambient temperature and pressure.[4–7] In particular, it has been shown that ECR to CO by a two-electron reduction process is the most promising for commercialization, owing to high selectivity and low energy requirement.[8,9] Moreover, CO as an important chemical feedstock plays a vital role in various industries.[10] Even though much progress has been made in ECR to CO, it is still far from commercial application for reasons such as unsatisfactory activity, poor stability, and high cost. In addition, the competing hydrogen evolution reaction (HER) severely suppresses the CO selectivity in aqueous solutions.[11] Therefore, it is desirable to exploit CO_2-to-CO electrocatalysts with excellent activity and high selectivity.

Among CO_2-to-CO electrocatalysts explored, nitrogen-doped carbon-based material-supported transition metal atoms (M–N–C) exhibit great potential for CO generation.[12–17] Carbon-based materials are utilized, owing to good electrical conductivity, which benefits electron transportation. Among these materials, carbon black (CB) not only exhibits merits such as large surface area and confinement of metal atoms, but also facilitates CO_2 diffusion across the gas diffusion barrier and accelerate the reaction rate.[18–20] Therefore, CB serves as substrate that could cost-effectively improve the atomic dispersion of M and the activity of ECR to CO. The M–N_x moieties in these catalysts are usually regarded as active center where *X* denotes the coordination number of metal atoms. In addition, the M–N_x moiety with a planar coordination structure has been confirmed to stabilize the metal atoms effectively.[21] More interestingly, nonprecious metals, such as Fe, Co, Ni, or Mn, in M–N_x system could achieve identical and even better performance than noble metal-based electrocatalysts. For instance, isolated Fe–N_4 structure on carbon materials could lower the energy barrier for the formation of *COOH intermediate during ECR to CO, thus enhancing the CO selectivity with a faradaic efficiency [FE(CO)] up to 93%.[22] Co atom dispersed on N-doped porous carbon sphere was found to have >90% FE(CO) under potentials between −0.57 and −0.88 V versus the reversible hydrogen electrode (vs. RHE). Spectroscopic studies

[a] S. Lu, Y. Zhang, O. Egwu Eleri, Prof. Z. Yu
Department of Energy and Petroleum Engineering
University of Stavanger, 4036 Stavanger (Norway)
E-mail: zhixin.yu@uis.no
[b] Y. Zhang, O. Egwu Eleri, Dr. F. Lou
Beyonder AS
Kanalsletta 2, 4033 Stavanger (Norway)
[c] Dr. M. F. Mady
Department of Chemistry, Bioscience and Environmental Technology
University of Stavanger, 4036 Stavanger (Norway)
[d] Dr. W. Mekonnen Tucho
Department of Mechanical and Structural Engineering and Material Science
University of Stavanger, 4036 Stavanger (Norway)
[e] Dr. M. Mazur, A. Li
Department of Physical and Macromolecular Chemistry, Faculty of Science
Charles University, Hlavova 8, 12843 Prague 2 (Czech Republic)
[f] Prof. M. Gu
Center for Analysis and Testing
Nanjing Normal University, 210023 Nanjing (P. R. China)
E-mail: guminfen@njnu.edu.cn

Supporting information for this article is available on the WWW under https://doi.org/10.1002/cssc.202200870

ChemSusChem
Research Article
doi.org/10.1002/cssc.202200870
Chemistry Europe
European Chemical Societies Publishing

and density functional theory (DFT) calculations revealed that Co–N_5 site serves as the active center for boosting CO_2 activation and facilitating the formation of *COOH as well as CO desorption.[23] Ni–N_4 moiety confined in Ni porphyrin-based framework displayed maximum FE(CO) of 97% at −0.90 V (vs. RHE) and good stability. Theoretical simulation demonstrated that Ni–N_4 center could decrease the energy barrier for *COOH intermediate generation.[24] Mn–N_3 embedded into graphitic carbon nitride shown 98.8% of FE(CO) under a low overpotential of 0.44 V, and the outstanding activity was attributed to Mn–N_3 moiety promoting the formation of the key intermediate *COOH.[25] Therefore, it can be concluded that the superior CO_2-to-CO performance on these non-precious metal-based M–N–C electrocatalysts can be mainly attributed to the proper interaction between M–N_X center and intermediates.

Recently, studies disclosed that the intrinsic activity of M–N–C could be further enhanced by introducing other heteroatoms. For instance, Zhang et al. reported that extra chlorine atoms (Cl) coordinated Mn–N_4–C could change the electron transfer of Mn atom, boosting *COOH adsorption and CO desorption.[26] As a result, the electrocatalyst exhibited a FE(CO) of 97% and a high current density of about 10 mA cm^{-2} under a low overpotential of 0.49 V. Pan et al. reported that S atoms could lift the Fermi energy of Fe3d state and increase the charge density of Fe atoms.[27] The inherent electrocatalytic activity and selectivity for CO_2-to-CO were modulated by S atoms, resulting in improved interaction strength between Fe atom and intermediates. This unique structure and electronic properties endowed the Fe–NS–C electrocatalyst with a FE(CO) of 98% under an overpotential of 0.49 V. Indeed, the local electronic structures of host atoms could be altered by doping heteroatoms, further influencing catalytic properties.[28–30] Thus, it can be anticipated that the incorporation of proper heteroatoms into carbon sites close to the M–N_X center could tune the electronic structure of metal atoms, which would effectively promote the activation of CO_2 and modify the binding strength of intermediates during the ECR process. Specifically, incorporating S atom into host materials has been regarded as an effective strategy to improve the activity of various catalytic reactions.[31–33]

Ni–N–C electrocatalyst have been reported to exhibit good CO_2-to-CO activity. However, there is limited study on S modified Ni–N–C system to regulate the ECR activity for CO_2-to-CO. In this study, we synthesized N,S-codoped CB incorporating Ni atoms by facile ion-adsorption and subsequent pyrolysis treatment. The Ni–NS–C catalyst exhibited a very high conversion efficiency of 99.7% to CO with a high total current density of 20.5 mA cm^{-2} under −0.80 V (vs. RHE), outperforming S-free Ni–N–C electrocatalyst and other ECR catalysts reported in literature. It also displayed excellent stability without activity decay after electrocatalysis for 19 h. First-principles computation was carried out to investigate the effect of the S atom decoration on the electronic structures of Ni atoms, catalytic mechanisms, and activity toward ECR as well as HER.

Results and Discussion

Electrocatalysts characterization

The structures of N–C, NS–C, Ni–N–C, and Ni–NS–C catalysts were firstly characterized by X-ray diffraction (XRD). As shown in Figure 1a, the catalysts exhibit similar XRD patterns with two broad diffraction peaks at around 25.1° and 43.2°, corresponding to the (002) and (100) planes of carbon. It is worth noting that both peaks of NS–C and Ni–NS–C catalysts show low crystallinity and slight right-shift compared with the N–C and Ni–N–C catalysts, which can be explained by lattice contraction and the formation of C vacancy after the introduction of S atoms with larger radius.[34,35] Furthermore, no peaks assignable to metallic Ni or its compounds were observable.

Raman spectra of the four catalysts exhibit two vibrational bands located around 1343 cm^{-1} (D band) and 1594 cm^{-1} (G band; Figure 1b), which are ascribed to the defect and graphitic sp^2 carbon.[36] The intensity ratios of D and G band (I_D/I_G) of N–C, NS–C, Ni–N–C, and Ni–NS–C catalysts were also calculated as marked in Figure 1b. It can be observed that the introduction of S atom into the N–C catalysts induces more defects, consistent with XRD study. However, incorporating Ni atoms decreases the I_D/I_G value, indicating that Ni atoms are embedded into C vacancies. Compared with the Ni–N–C catalyst, the position of

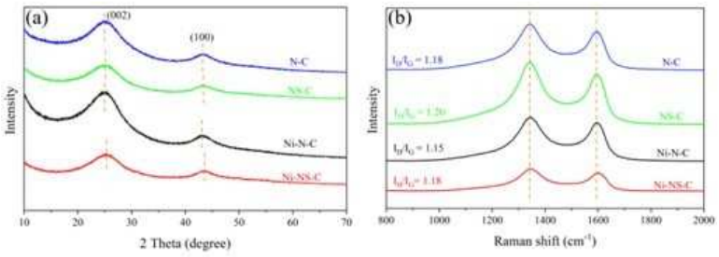

Figure 1. (a) XRD patterns and (b) Raman spectra of N–C, NS–C, Ni–N–C, and Ni–NS–C catalysts.

ChemSusChem
Research Article
doi.org/10.1002/cssc.202200870
Chemistry Europe
European Chemical Societies Publishing

the G band of Ni–NS–C catalysts shows a slight upshift owing to doping of nonmetal S atoms into carbon-based materials.[37–39]

Transmission electron microscopy (TEM) was used to investigate the microscopic morphology of the Ni–NS–C catalyst. Carbon nanospheres with a diameter of 50 nm were observed (Figure 2a). The high resolution transmission electron microscopy (HRTEM) images displays distorted short-range graphic stripes with winkle and interlaces (Figure 2b), indicating defective carbon structure. No distinct nanoparticles or clusters were observed, implying that the Ni atoms are likely to present in the form of single atoms. Moreover, energy-dispersive X-ray spectroscopy (EDX) elemental mapping images clearly demonstrate that Ni, N, S and C species distribute uniformly over the Ni–NS–C catalyst (Figure 2c). Furthermore, the aberration-corrected high-angle annular dark-field scanning transmission electron microscopy (HAADF-STEM) shows the well-dispersed single Ni atoms as bright spots for the Ni–N–C and Ni–NS–C catalysts, which are highlighted by red circles in Figure 2d and e.

The surface area and pore structure of the catalysts were determined by N_2 adsorption-desorption measurements. As depicted in Figure 3a, the isotherms of the four electrocatalysts displayed sharp adsorption under relative pressures greater than 0.40 accompanied by an obvious hysteresis loop, which is indicative of dominant mesopores and is further corroborated by the pore size distributions (Figure 3b). The specific surface area and pore volume are summarized in Table S1 (see the Supporting Information). It can be found that the total pore volume increased from 1.26 to 1.39 $m^3 g^{-1}$ after doping S to the N–C structure, and increased further after introducing Ni atoms. The catalysts show quite close but very high surface areas in the range of 1073 to 1275 $m^2 g^{-1}$, which also increase with the doping of S and Ni atoms. The high surface area and pore

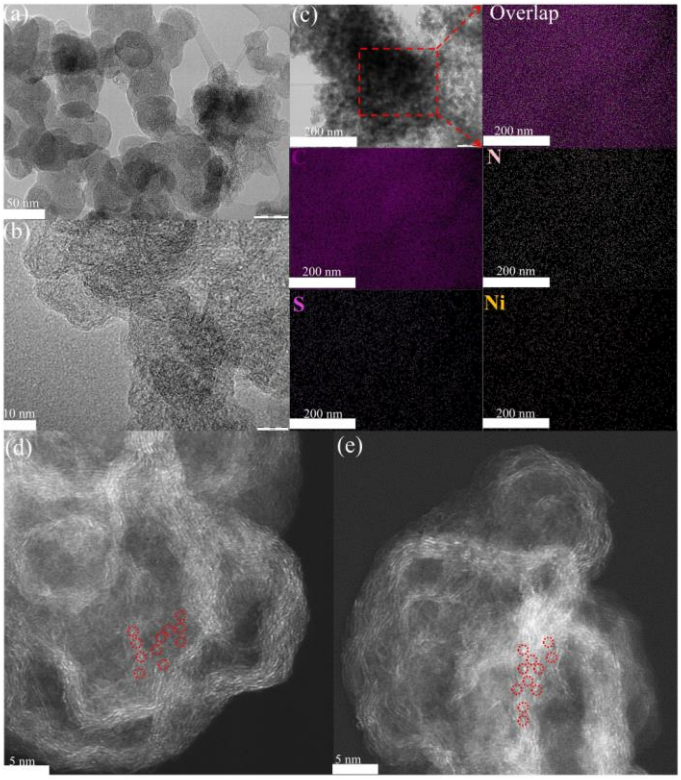

Figure 2. (a) TEM, (b) HRTEM, and (c) C, N, S, and Ni EDX mapping images of Ni–NS–C catalyst; (d, e) HAADF-STEM images for Ni–N–C and Ni–NS–C catalysts, where single Ni atoms are highlighted in red circles.

ChemSusChem
Research Article
doi.org/10.1002/cssc.202200870
Chemistry Europe
European Chemical Societies Publishing

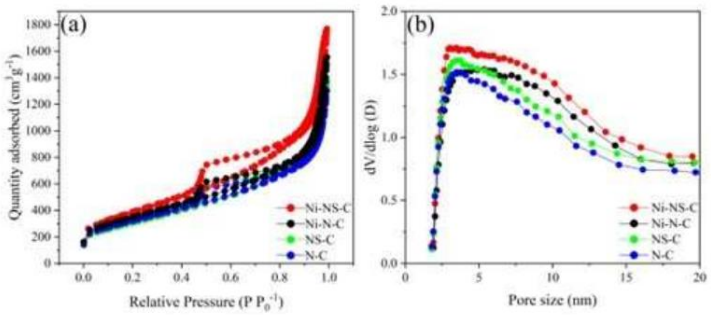

Figure 3. (a) N_2 adsorption–desorption isotherms and (b) pore size distributions of N–C, NS–C, Ni–N–C, and Ni–NS–C catalysts.

volume are beneficial for the dispersion of Ni atoms and the access of reactants to the active centers. As expected, the pore size distribution curve also shows more larger pores with the introduction of S and Ni atoms (Figure 3b).

X-ray photoelectron spectroscopy (XPS) was employed to characterize the chemical state and surface concentration of the elements. The high-resolution N1s spectra of the Ni–NS–C catalyst can be fitted into four peaks cantered at 397.9, 399.7, 400.5 and 403.1 eV (Figure 4a), which can be assigned to pyridinic N (Pyri-N), pyrrolic (Pyrr-N), graphitic N (Grap-N) and oxidized N (Oxid-N), respectively.[40–43] The existence of these types of N could promote the electrocatalytic activity.[44] In addition, N atom concentrations are 4.43, 4.19, 4.11 and 4.18 at.% for N–C, NS–C, Ni–N–C, and Ni–NS–C (Table S1). High-resolution S2p spectra of Ni–NS–C catalyst (Figure 4b) at lower binding energy can be ascribed as C–S–C ($2p_{3/2}$ at 164.1 and $2p_{1/2}$ at 165.3 eV) and C–SO_x–C (167.6 and 168.8 eV).[34,45] The S content was estimated to be 0.37 and 0.42 at.% for the NS–C and Ni–NS–C catalyst, respectively. It was also observed that the percentages of N in these two catalysts remain almost unchanged, implying that introducing S atoms had little effects on the bonding patterns of N atoms. In the high-resolution Ni2p spectrum (Figure 4c), the $Ni2p_{3/2}$ binding energies for Ni–NS–C and Ni–N–C catalyst are 855.90 and 855.66 eV, higher than that of Ni^0 (852.5–853.0 eV) but lower than that of Ni^{2+} (856 eV),[46,47] indicating that Ni species are likely to keep as ionic $Ni^{\delta+}$ ($0<\delta<2$). Therefore, these results further demonstrated the existence of single Ni atoms on the surface of Ni–NS–C and Ni–N–C catalysts.[48] Moreover, the peak of $Ni2p_{3/2}$ shifted slightly towards higher binging energy after incorporating S atoms, indicating that S could influence the electronic structure of Ni. The Ni contents in Ni–N–C and Ni–NS–C catalysts are 0.50

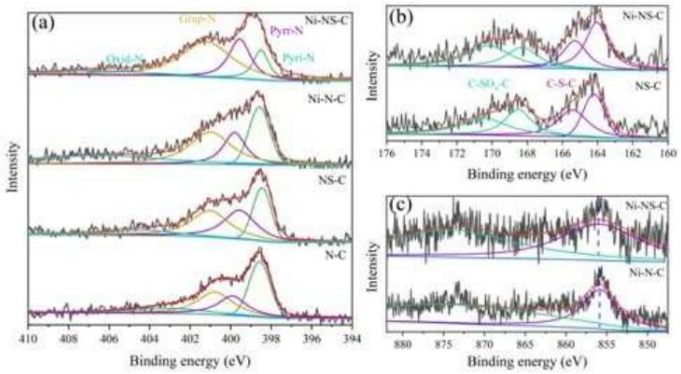

Figure 4. High-resolution XPS spectra: (a) N1s for N–C, NS–C, Ni–N–C, and Ni–NS–C catalysts; (b) S2p for NS–C and Ni–NS–C catalysts; (c) Ni2p for Ni–N–C and Ni–NS–C catalysts.

ChemSusChem
Research Article
doi.org/10.1002/cssc.202200870
Chemistry Europe
European Chemical Societies Publishing

and 0.48 at.%, demonstrating that S atom doping has little effect on surface Ni atom distribution.

Electrocatalytic activity test

The ECR performances of catalysts were evaluated in a membrane-separated two chambers H-type cell with a standard three-electrode system immersed in 0.5 M $KHCO_3$ electrolyte. Under CO_2-saturated electrolyte, the Linear sweep voltammetry (LSV) of N–C and NS–C catalysts show small current density (Figure 5a), exhibiting low electrocatalytic activity. Conversely, the Ni–NS–C and Ni–N–C catalyst display large current density thus high electrocatalytic activity. In addition, the doping of S atoms could boost the current density for both N–C and Ni–N–C, confirming the role of S atom in the activity enhancement. In the presence of CO_2, the current density of Ni–NS–C increases faster in comparison with the reaction under N_2 atmosphere (Figure 5b), suggesting the enhanced current density from ECR. The results demonstrated that introducing Ni–N_x moiety into carbon-based materials could indeed improve its electrocatalytic performance. Meanwhile, the highest current density observed for the Ni–NS–C catalyst could be fairly attributed to the synergistic effect of Ni–N_x moiety and S doping.

To quantify the product selectivity, the ECR test was conducted in constant potentiostatic electrocatalysis under different potentials. H_2 and CO were detected as the only reduction products under the potential window of −0.20 V to −1.20 V (vs. RHE). No other gaseous products were detected by GC, because CO, as a two-electron product, is more easily generated than other four-, six-, or eight-electron products such as CH_3OH and CH_4, consistent with previous studies.[49,50] Moreover, no liquid products were produced, as evidenced by ^1H

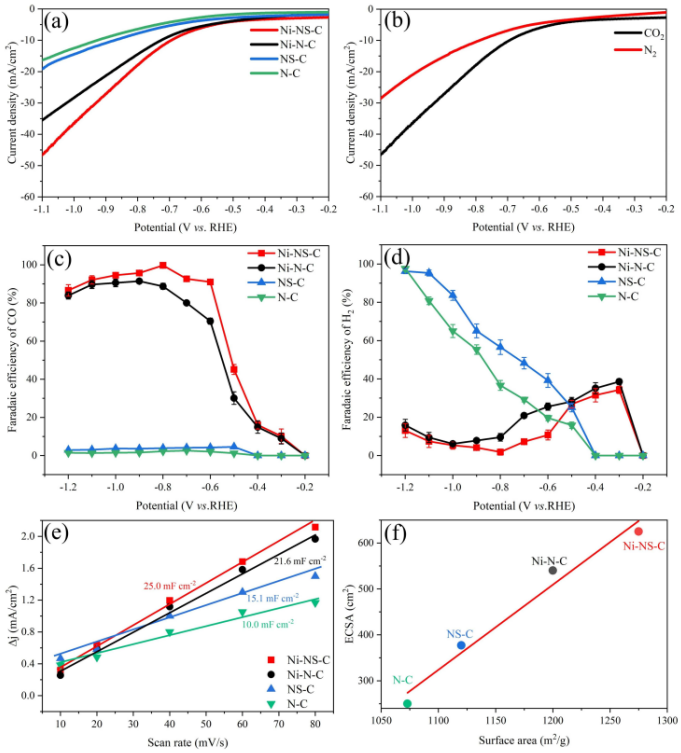

Figure 5. (a) LSV curves of N–C, NS–C, Ni–N–C, and Ni–NS–C catalysts under CO_2-saturated 0.5 M $KHCO_3$ solution at a scan rate of 10 mV s^{-1}; (b) LSV curves of Ni–NS–C catalyst under N_2- and CO_2-saturated 0.5 M $KHCO_3$ solution at a scan rate of 10 mV s^{-1}; (c) faradaic efficiencies of CO generation and (d) faradaic efficiencies of H_2 generation on N–C, NS–C, Ni–N–C, and Ni–NS–C catalysts; (e) Charging current density differences against scan rates over N–C, NS–C, Ni–N–C, and Ni–NS–C catalysts; (f) relationship between double layer capacity and BET surface area of the N–C, NS–C, Ni–N–C, and Ni–NS–C catalysts.

ChemSusChem
Research Article
doi.org/10.1002/cssc.202200870
Chemistry Europe
European Chemical Societies Publishing

NMR analysis (see the Supporting Information, Figure S1). As shown in Figure 5c, the FE(CO) over the four catalysts showed first increase then decrease with the decrease of applied potential. However, the FE(CO) of Ni–N–C and Ni–NS–C catalysts are always higher than the N–C and NS–C catalysts under the same applied potential, indicating that Ni–N_x are the true active centers. Meanwhile, the Ni–NS–C catalyst exhibits larger FE(CO) than Ni–N–C over the entire potential range, demonstrating that S atom could effectively enhance the ECR performance of the Ni–N_x moiety. The competing HER performance for the four catalysts were also compared, as displayed in Figure 5d. The FE(H_2) of Ni–NS–C catalyst is always lower than that of Ni–N–C catalyst, indicating that the HER performance of the Ni–N–C catalyst was suppressed after the doping of S atoms. In contrast, the FE(H_2) of N–C is lower than that of NS–C, suggesting that S atom could promote HER ability of N–C in the absence of Ni. Therefore, it can be deduced that more protons are involved in ECR compared to HER after the introduction of Ni and S atoms, and there is a synergistic effect between Ni and S. As a result, the Ni–NS–C catalyst exhibits high FE(CO) over 90% in a broad potential range of −0.60 to −1.10 V (vs. RHE), and the maximum FE(CO) is as high as 99.7% at a potential of −0.80 V (vs. RHE) with a total current density of 20.5 mA cm^{-2}.

The increase of electrochemical active surface areas (ECSA) also contributes to the excellent activity towards ECR. ECSA can be directly estimated by measuring double layer (D–L) capacitance (Figure 5e and Figure S2). The Ni–NS–C and Ni–N–C catalysts exhibit 25.0 mF cm^{-2} and 21.6 mF cm^{-2}, which are larger than that of the NS–C (15.1 mF cm^{-2}) and N–C catalysts (10.0 mF cm^{-2}). Consequently, the corresponding ECSA for Ni–NS–C, Ni–N–C, NS–C and N–C catalysts were 625, 540, 377 and 250 cm^2_{ECSA}, demonstrating that Ni and S atoms could effectively increase the ESCA (Table S1). It can also be found that there is a positive correlation between ECSA and BET surface area (Figure 5f), validating that larger surface area could expose more active sites.

CO_2 adsorption on catalyst surface plays an important role in ECR. Therefore, we conducted temperature-programmed CO_2 desorption (CO_2-TPD) to investigate the effect of S dopant on their CO_2 adsorption ability. It turns out that Ni–NS–C shows slightly stronger CO_2 adsorption than that of Ni–N–C, which could boost the ECR performance (Figure S3). To further elucidate the effect of S atom on the reaction kinetics, the Tafel slope and electrochemical impedance spectroscopy (EIS) were conducted.

As shown in Figure 6a, the Ni–NS–C catalyst exhibits a lower Tafel slope of 182 mV dec^{-1} than Ni–N–C of 193 mV dec^{-1}, suggesting that the introduction of S atom could improve the reaction kinetics. The Tafel slopes of these two samples are close to the theoretical value, revealing that CO_2-to-CO on these two catalysts proceed via the same mechanism that CO_2 accepting proton-electron pairs to form *COOH intermediate is the potential determining step (PDS).[51] The EIS test was further conducted at −0.80 V (vs. RHE) and the corresponding complex-plane plot of Ni–N–C and Ni–NS–C catalysts is shown in Figure 6b. The Ni–NS–C catalyst exhibited a smaller charge transfer resistance (R_{ct}), demonstrating that incorporating S atom could accelerateelectron exchange between the catalysts

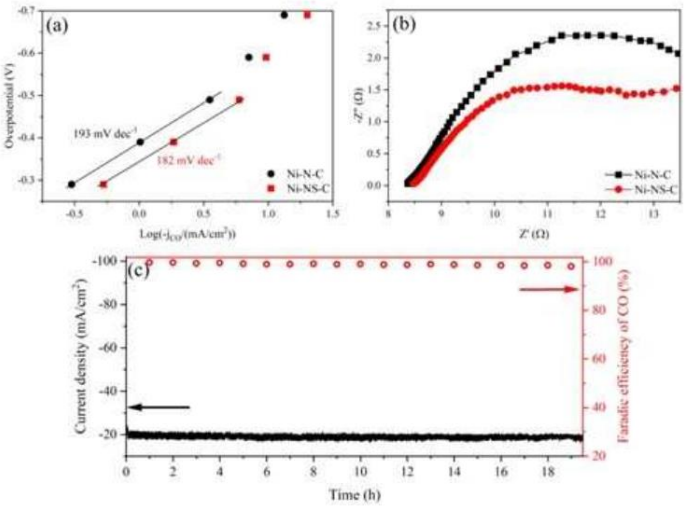

Figure 6. (a) Tafel plots for CO generation on Ni–N–C and Ni–NS–C catalysts; (b) EIS complex-plane plot for Ni–NS–C and Ni–N–C catalysts in 0.5 M $KHCO_3$ at potential of −0.8 V (vs. RHE); (c) Long-term electrocatalysis on Ni–NS–C catalyst in 0.5 M $KHCO_3$ at −0.8 V (vs. RHE).

ChemSusChem
Research Article
doi.org/10.1002/cssc.202200870
Chemistry Europe
European Chemical Societies Publishing

and reactants. In addition, the electrochemical stability of Ni–NS–C was evaluated by chronoamperometric electrolysis under the potential of −0.80 V (vs. RHE) with the largest FE(CO). As shown in Figure 6c, there is a fast drop in current density during the initial 20 min, which can be attributed to unbalanced CO_2 adsorption on the catalyst. After that, the current density and FE (CO) is highly stable with negligible decay. The current density is still around 20.5 mA cm^{-2} and the FE (CO) is about 98% after electrocatalysis reaction for >19 h. We also studied the structure and element information of the spent Ni–NS–C catalyst by TEM, EDX mapping and XPS (Figures S4 and S5; summarized in Table S1). It can be found that there is no obvious change in morphology and element content after ECR reaction, demonstrating excellent stability of the Ni–NS–C catalyst. Very recent reports on nonmetal-decorated M–N–C catalysts are summarized in Table S2. Remarkably, the Ni–NS–C catalyst in this study outperformed most of the catalysts in terms of applied potential, FE(CO) and stability.

DFT simulations

DFT calculations were performed to gain insight into the electrocatalytic reaction mechanisms of ECR and HER on Ni–N–C and Ni–NS–C catalysts based on the CHE model. As Ni atoms are more likely to form stable Ni–N_4 moiety in carbon-based materials, the Ni–N_4 structure was created in carbon matrix as active center in Ni–N_4–C catalyst.[13,52–54] It is worth noting that similar method for synthesizing Fe–N_4–C catalyst has been reported recently.[55] The good ECR activity of Ni-decorated nitrogen-doped carbon catalysts was previously attributed to single Ni atoms instead of Ni nanoparticles.[48] XRD indicated that the introduction of S atoms possibly induced the formation of C atom vacancies because the radius of S atom is larger than that of C atom (Figure 1a). To exclude the possibility of S directly substituting C atom without breaking TM–N_4, we also built a configuration as shown in Figure S6, where S directly substituted C atom but TM–N_4 was maintained. Compared to the pristine S free structure, the CO desorption ability will be quite weak in this structure because of high free energy change of 1.46 eV, whereas the HER ability was strengthened owing to low free energy of −0.53 eV. These results are not consistent with the experimental data. Therefore, S atom embedded into C vacancy close to Ni site (Ni–NS–C) as model was proposed to investigate the effect of S atoms on the ECR performance of the Ni–N_4–C catalyst (Figure 7a). The adsorption energy of CO_2 on the Ni–N–C and Ni–NS–C catalysts were calculated to be −0.28 and −0.39 eV, further demonstrat-

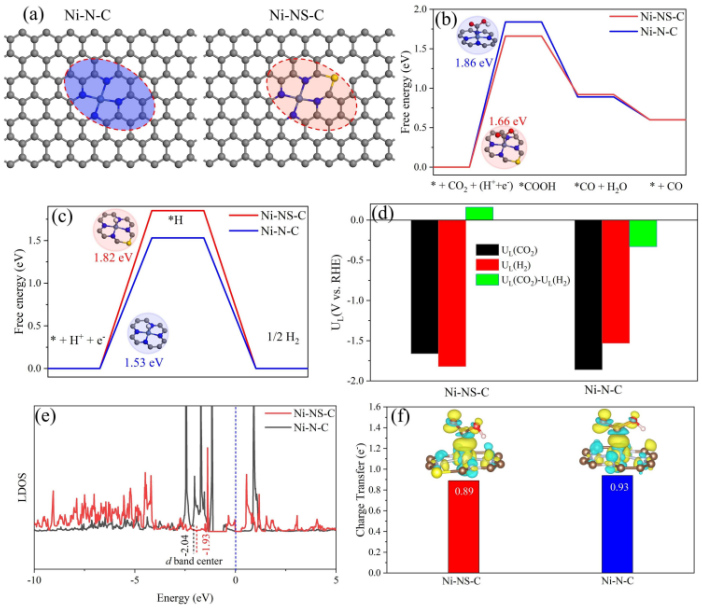

Figure 7. (a) Atomic structure of proposed Ni–N–C and Ni–NS–C catalysts; (b) free energy diagrams for ECR to CO; (c) free energy diagrams for HER; (d) difference between the limiting potentials for ECR and HER; (e) location of d band center; (f) charge density difference after *COOH adsorption on Ni–N–C and Ni–NS–C catalysts, the isosurface value is set to be 0.003 e Bohr^{-3}.

ChemSusChem
Research Article
doi.org/10.1002/cssc.202200870
Chemistry Europe
European Chemical Societies Publishing

ing that S dopant could promote CO_2 adsorption, consistent with the CO_2-TPD results. The adsorbed *COOH, *CO and *H intermediates were considered in ECR and HER. As shown in Figure 7b, the Gibbs free energy change (ΔG) diagram of CO_2-to-CO over these two catalysts suggests that the first proton-electron pair to generate *COOH is the PDS, consistent with the experimental results. The Ni–N–C catalyst shows ΔG_{*COOH} of 1.86 eV, which is higher than that of the Ni–NS–C catalyst at 1.66 eV, confirming that S atom could effectively decrease the CO_2 activation barrier. This is also consistent with the experimental result that introducing S atoms could enhance FE(CO) under all applied potentials. The calculated adsorption energy of CO over the Ni–N–C catalyst was reduced by 0.06 eV after the incorporation of S atom, demonstrating the increase of CO desorption ability. The HER activities over the two catalysts were compared by calculating the Gibbs free energy of *H (ΔG_{*H}; Figure 7c). Notably, the ΔG_{*H} of Ni–NS–C catalyst increases from 1.53 to 1.82 eV, showing that S atom could effectively suppress HER when Ni is present, which again agrees with the experimental observation that FE(H_2) of the Ni–N–C catalyst decreased after doping S (Figure 5d).

It has been well established that the difference between the limiting potentials of ECR and HER [$U_L(CO_2)-U_L(H_2)$] could be a reasonable descriptor for ECR selectivity. A more positive $U_L(CO_2)-U_L(H_2)$ indicates a higher selectivity towards ECR. As displayed in Figure 7d, the Ni–NS–C catalyst shows a positive value of $U_L(CO_2)-U_L(H_2)$, which is negative for the Ni–N–C catalyst, demonstrating increased ECR selectivity after incorporating S atoms. Furthermore, the electronic structure of Ni–NS–C and Ni–N–C catalysts were compared. The d band center of Ni–N–C catalyst moved towards the Fermi level after introducing the S atom, and the Ni3d state of Ni–NS–C catalyst crossed the Fermi level (Figure 7e), thereby improving the intrinsic activity of 3d electrons. When the *COOH intermediate was adsorbed on the catalysts, Ni atom (Ni–NS–C) lost smaller charge (0.89e^-; Figure 7f), accounting for moderate interaction. The results demonstrated that the synergistic effect of the Ni and S atom boosts the ECR performance where the Ni atoms sever as the active center and S atom plays a role in the modification of electronic properties.

Conclusion

We have developed a facile method for the synthesis of a S- and Ni-doped N–C system as an electrocatalyst for CO_2 reduction to CO. The Ni–NS–C catalyst can selectively reduce CO_2 to CO with high a FE(CO) of over 90% in a broad potential range of −0.60 to −1.10 V (vs. RHE). The maximum FE(CO) reaches 99.7% at −0.80 V (vs. RHE) with a total current density of 20.5 mA cm^{-2}. It also exhibits excellent stability for 19 h electrocatalysis without apparent activity decay. Experimental results demonstrated that Ni atoms served as active sites for ECR to CO, whereas S atoms could increase its activity further. Moreover, theoretical calculations disclosed that doping S atoms could decrease and increase the free energy barrier for the formation of *COOH and *H, respectively. Meanwhile, S atoms could lift the d band center of Ni atoms and induce the Ni3d state crossing the Fermi energy level. As a result, the performance of ECR to CO on Ni–NS–C was improved, whereas the hydrogen evolution reaction (HER) was suppressed, contributing to overall higher ECR selectivity. Therefore, the excellent ECR performance of the Ni–NS–C catalyst can be attributed to the synergistic effect of the Ni–N_X moiety and S dopant.

Experimental Section

Chemicals

All chemicals were analytical grade and used without further purification. Ketjenblack EC-600 JD (CB) was purchased from AkzoNobel. Nickel hexahydrate nitrate ($Ni(NO_3)_2\cdot 6H_2O$, 98%) was obtained from Sigma-Aldrich. Urea (CH_4N_2O, 99%), thiourea (CH_4N_2S, 99%) and nitric acid (HNO_3, 65 wt%) were from VMR chemicals. Potassium bicarbonate ($KHCO_3$, 98%), Nafion D-521 dispersion (5% w/w in water and 1-propanol) and Nafion-117 ionic exchange membrane were purchased from Alfa Aesar. Deionized (DI) water was produced by a Milli-Q (18.2 MΩ cm) system.

Electrocatalyst preparation

The CB was firstly activated by concentrated HNO_3 solution to increase surface defects and oxygen-containing groups. Typically, 4 g CB was dispersed in 100 ml of HNO_3 solution followed by refluxing at 100 °C for 8 h with vigorously stirring. Subsequently, the suspension was washed with DI water several times until neutral pH and separated by vacuum filtration. Activated CB was obtained after drying at 120 °C in a vacuum oven for 24 h.

In a typical synthesis of Ni^{2+} adsorbed on CB (Ni^{2+}-CB), 1 g activated CB was dispersed in 400 mL DI water under sonication for 2 h. The Ni^{2+} solution (3 mg mL^{-1}) was prepared by dissolving 240 mg Ni $(NO_3)_2\cdot 6H_2O$ in 80 mL DI water. Thereafter, 40 mL Ni^{2+} solution was added dropwise into the CB solution and kept under vigorous stirring for 12 h. The products were collected by vacuum filtration. After drying at 120 °C in a vacuum oven for 24 h, Ni-CB was obtained.

The Ni–NS–C catalyst was synthesized according to a modified method by Zheng et al.[18] Typically, 0.5 g Ni-CB and with 6.0 g thiourea was mixed and grinded to obtain fine powders. The powder was then transferred into a covered crucible and heated to 800 °C at a heating rate of 3 °C min^{-1} under 10 mL min^{-1} Ar flow and kept at 800 °C for 1 h. For comparison, the Ni–N–C catalyst was synthesized by replacing thiourea with urea. Metal free N–C and NS–C catalysts were also prepared by replacing Ni-CB with CB.

Electrocatalysts characterization

The crystalline structures of the prepared samples were analyzed by XRD (Bruker-AXS Micro-diffractometer D8 ADVANCE) equipped with a $Cu_{K\alpha}$ radiation source ($\lambda = 1.54$ Å) with a scan rate of 3° min^{-1}. The crystallinity was further examined by Raman spectroscopy (Renishaw, with a 532 nm excitation laser). The samples were focused with a ×50LWD objective lens and exposed to emission line for 10 s.

TEM, HRTEM and EDX were conducted by JEM-2100 Plus (JEOL) electron microscope operating at 200 kV. The HAADF-STEM was conducted on JEOL NEOARM 200 F with 200 kV of accelerating voltage.

ChemSusChem
Research Article
doi.org/10.1002/cssc.202200870
Chemistry Europe
European Chemical Societies Publishing

Nitrogen adsorption-desorption isotherms were measured on Micromeritics Tristar II 3020 instrument at −196 °C. The specific surface area was estimated by the Brunauer–Emmett–Teller (BET) method, and the pore size distribution was obtained from the Barrett–Joyner–Halenda (BJH) desorption isotherm. The CO_2-TPD profile was measured on Micromeritics Autochem II ASAP 2920.

XPS was conducted on a 1486.6 eV X-ray photoelectron spectrometer (ESCALAB Xi-type) using $Al_{K\alpha}$ source.

Electrochemical measurements

All electrocatalytic tests were conducted by a standard three-electrode system in an H-type cell with two compartments at room temperature (25 °C). Platinum plate, catalysts coated carbon paper (Toray, TGP-H060) and Ag/AgCl (3 M KCl) served as the counter electrode, working electrode and reference electrode, respectively. All potentials were controlled by AUTOLAB PGSTAT302N workstation and converted to the reversible hydrogen electrode (RHE) by E (vs. RHE) = E (vs. Ag/AgCl) + 0.197 V + 0.059 × pH. The pH of 0.5 M $KHCO_3$ saturated with CO_2 is 7.2. Each chamber contained 40 ml 0.5 M $KHCO_3$. The catalysts ink was prepared by sonicating a mixture of 3.0 mg catalysts, 145 μL ethanol, 90 μL DI water and 65 μL 0.5 wt.% Nafion-D521 solution for 1 h. The working electrode was prepared by loading 60 μL catalysts ink onto a carbon paper (1 cm^2) with a mass loading of 0.6 mg cm^{-2}, followed by drying under an infrared lamp for 30 min. A piece of Nafion-117 ionic exchange membrane was used to separate the anode chamber (counter electrode) and cathode (reference and working electrodes). High purity CO_2 was pumped into the cathode chamber at a flow rate of 20 mL min^{-1} for 1 h before and during the electrolysis test. The 0.5 M $KHCO_3$ electrolyte in the cathode was stirred at 800 rmp during the test. LSV was firstly performed under N_2 and CO_2-saturated 0.5 M $KHCO_3$ electrolyte at a scan rate of 10 mV s^{-1}. The electrochemical double-layer capacitance (C_{dl}) was evaluated by the cyclic voltammetry (CV) method to estimate ECSA of the catalysts. The CV tests were conducted in 0.5 M $KHCO_3$ electrolyte with a potential from 0 to −0.20 V (vs. Ag/AgCl) and various scan rates (10, 20, 40, 60 and 80 mV s^{-1}) to avoid the faradaic process. C_{dl} can be obtained by plotting the anodic and cathodic current difference at −0.10 V against the scan rate. The ECSA can be determined by Equation (1)[56] below:

$$\mathrm{ECSA} = \frac{C_{dl}}{C_s} \tag{1}$$

where C_{dl} is the slope of the double-layer charging current against the scan rate, and the value of C_s was chosen to be 40 μF cm^{-2} $cm^{-2}{}_{ECSA}$.

The gaseous products were analyzed by on-line gas chromatography (Agilent GC-7890B) equipped with a HayeSep Q column and a 5 A molecular sieve column. The possible liquid products were determined by nuclear magnetic resonance (NMR) spectroscopy. The NMR spectra were recorded on a 400 MHz Bruker NMR spectrometer in deuterium oxide (D_2O) with one drop of dimethyl sulfoxide. ^{1}H NMR chemical shifts were recorded in D_2O. The FE of gaseous products (H_2 and CO) under different potentials were calculated according to Equation (2):[23]

$$\mathrm{FE} = \frac{2 \times 96485\ (\mathrm{c\ mol^{-1}}) \times V\ (\mathrm{mL\ min^{-1}}) \times 10^{-6}\ (\mathrm{m^3\ mL^{-1}}) \times v \times 1.013 \times 10^5\ (\mathrm{N\ m^2})}{8.314\ (\mathrm{N{\cdot}m\ /\ mol{\cdot}K}) \times 298.15\ \mathrm{K} \times I\ (\mathrm{C\ s^{-1}}) \times 60\ (\mathrm{s\ min^{-1}})} \tag{2}$$

where V, v and I represent the gas flow rate, volumetric concentration of CO or H_2, and steady-state cell current at different potentials, respectively.

Computational methods

All spin-polarized calculations, including structure relaxation, electronic structure and energy, were performed by Vienna ab initio simulation package (VASP) using the plane-wave basis.[57,58] The generalized gradient approximation (GGA) in the parametrization of Perdew–Burke–Ernzerhof (PBE) were employed to describe the electronic exchange and correction.[59,60] Projector augmented wave (PAW) pseudopotential was used to treat the interaction of core and valence electron.[61] The long-range van der Waals (vdW) interactions was considered by incorporating empirical correction method (DFT-D3).[62] The kinetic cut-off energy was set to 500 eV. k-point sampling of 8×8×1 (structure relaxation) and 10×10×1 (electronic structure calculations) for all systems were tested to achieve convergence. The convergence criterion for energy and force was set to 1.0×10^{-5} eV and 1.0×10^{-2} eV Å^{-1}, respectively.

The Gibbs free energy change ($\triangle G$) of intermediates in each step for ECR and HER were calculated by the computational hydrogen electrode (CHE) model:[63]

$$\Delta G = \Delta E + \Delta E_{ZPE} - T\Delta S \tag{3}$$

where ΔE, ΔE_{ZPE} and ΔS are the differences in total energy obtained from DFT calculations, zero-point energy, and entropy between reactants and products, respectively. T is temperature (298.15 K).

Two gaseous products (CO and H_2) were considered in our calculations. The adsorption and desorption of intermediates are described by Equations (4)–(7):

$$^* + CO_2 + (H^+ + e^-) \rightarrow {}^*COOH \tag{4}$$

$$^*COOH + (H^+ + e^-) \rightarrow {}^*CO + H_2O \tag{5}$$

$$^*CO \rightarrow CO + ^* \tag{6}$$

$$^* + (H^+ + e^-) \rightarrow {}^*H \tag{7}$$

where * indicates an adsorption site.

Acknowledgements

This work was supported by the Norwegian Ministry of Education and Research. The computations were performed on resources provided by UNINETT Sigma2 – the National Infrastructure for High Performance Computing and Data Storage in Norway. M. M. would like to thank the OP VVV "Excellent Research Teams", project no. CZ.02.1.01/0.0/0.0/15_003/0000417 – CUCAM.

Conflict of Interest

The authors declare no conflict of interest.

Data Availability Statement

The data that support the findings of this study are available from the corresponding author upon reasonable request.

ChemSusChem
Research Article
doi.org/10.1002/cssc.202200870
Chemistry Europe
European Chemical Societies Publishing

Keywords: CO_2 reduction · density functional theory · doping · electrocatalysis · nickel

[1] S. J. Davis, K. Caldeira, H. D. Matthews, *Science* **2010**, *329*, 1330–1333.
[2] S. Chu, Y. Cui, N. Liu, *Nat. Mater.* **2016**, *16*, 16–22.
[3] B. Lin, J. Zhu, *Sci. Total Environ.* **2019**, *659*, 505–1512.
[4] L. Wang, W. Chen, D. Zhang, Y. Du, R. Amal, S. Qiao, J. Wu, Z. Yin, *Chem. Soc. Rev.* **2019**, *48*, 5310–5349.
[5] G. Wang, J. Chen, Y. Ding, P. Cai, L. Yi, Y. Li, C. Tu, Y. Hou, Z. Wen, L. Dai, *Chem. Soc. Rev.* **2021**, *50*, 4993–5061.
[6] B. Yang, K. Liu, H. Li, C. Liu, J. Fu, H. Li, J. E. Huang, P. Ou, T. Alkayyali, C. Cai, Y. Duan, H. Liu, P. An, N. Zhang, W. Li, X. Qiu, C. Jia, J. Hu, L. Chai, Z. Lin, Y. Gao, M. Miyauchi, E. Cortés, S. A. Maier, M. Liu, *J. Am. Chem. Soc.* **2022**, *144*, 3039–3049.
[7] S. Zhang, Q. Fan, R. Xia, T. J. Meyer, *Acc. Chem. Res.* **2020**, *53*, 255–264.
[8] O. S. Bushuyev, P. De Luna, C. T. Dinh, L. Tao, G. Saur, J. Van de Lagemaat, S. O. Kelley, E. H. Sargent, *Joule* **2018**, *2*, 825–832.
[9] S. Jin, Z. Hao, K. Zhang, Z. Yan, J. Chen, *Angew. Chem. Int. Ed.* **2021**, *60*, 20627–20648.
[10] W. Zhou, K. Cheng, J. Kang, C. Zhou, V. Subramanian, Q. Zhang, Y. Wang, *Chem. Soc. Rev.* **2019**, *48*, 3193–3228.
[11] S. Lu, H. L. Huynh, F. Lou, M. Guo, Z. Yu, *J. CO_2 Util.* **2021**, *51*, 101645.
[12] C. Xu, A. Vasileff, Y. Zheng, S. Z. Qiao, *Adv. Mater. Interfaces* **2020**, *8*, 2001904.
[13] W. Xiong, H. Li, H. Wang, J. Yi, H. You, S. Zhang, Y. Hou, M. Cao, T. Zhang, R. Cao, *Small* **2020**, *16*, e2003943.
[14] C. Zhang, Z. Fu, Q. Zhao, Z. Du, R. Zhang, S. Li, *Electrochem. Commun.* **2020**, *116*, 106758.
[15] L. Huang, W. Li, M. Zeng, G. He, P. R. Shearing, I. P. Parkin, D. L. Brett, *Compos. B. Eng.* **2021**, *220*, 108986.
[16] C. Ding, C. Feng, Y. Mei, F. Liu, H. Wang, M. Dupuis, C. Li, *Appl. Catal. B* **2020**, *268*, 118391.
[17] H. Zhang, J. Li, S. Xi, Y. Du, X. Hai, J. Wang, H. Xu, G. Wu, J. Zhang, J. Lu, J. Wang, *Angew. Chem. Int. Ed.* **2019**, *58*, 14871–14876; *Angew. Chem.* **2019**, *131*, 15013–15018.
[18] T. Zheng, K. Jiang, N. Ta, Y. Hu, J. Zeng, J. Liu, H. Wang, *Joule* **2019**, 3, 265–278.
[19] K. Guo, M. Gu, Z. Yu, *Energy Technol.* **2017**, *5*, 1228–1234.
[20] F. Yang, P. Song, X. Liu, B. Mei, W. Xing, Z. Jiang, L. Gu, W. Xu, *Angew. Chem. Int. Ed.* **2018**, *57*, 12303–12307; *Angew. Chem.* **2018**, *130*, 12483–12487.
[21] S. G. Han, D. D. Ma, S. H. Zhou, K. Zhang, W. B. Wei, Y. Du, X. T. Wu, Q. Xu, R. Zou, Q. L. Zhu, *Appl. Catal. B* **2021**, *283*, 119591.
[22] X. Li, S. Xi, L. Sun, S. Dou, Z. Huang, T. Su, X. Wang, *Adv. Sci.* **2020**, *7*, 2001545.
[23] Y. Pan, R. Lin, Y. Chen, S. Liu, W. Zhu, X. Cao, W. Chen, K. Wu, W. C. Cheong, Y. Wang, L. Zheng, J. Luo, Y. Lin, Y. Liu, C. Liu, J. Li, Q. Lu, X. Chen, D. Wang, Q. Peng, C. Chen, Y. Li, *J. Am. Chem. Soc.* **2018**, *140*, 4218–4221.
[24] C. Lu, J. Yang, S. Wei, S. Bi, Y. Xia, M. Chen, Y. Hou, M. Qiu, C. Yuan, Y. Su, F. Zhang, H. Liang, X. Zhuang, *Adv. Funct. Mater.* **2019**, *29*, 1806884.
[25] J. Feng, H. Gao, L. Zheng, Z. Chen, S. Zeng, C. Jiang, H. Dong, L. Liu, S. Zhang, X. Zhang, *Nat. Commun.* **2020**, *11*, 4341.
[26] B. Zhang, J. Zhang, J. Shi, D. Tan, L. Liu, F. Zhang, C. Lu, Z. Su, X. Tan, X. Cheng, B. Han, L. Zheng, J. Zhang, *Nat. Commun.* **2019**, *10*, 2980.
[27] F. Pan, B. Li, E. Sarnello, S. Hwang, Y. Gang, X. Feng, X. Xiang, N. M. Adli, T. Li, D. Su, G. Wu, G. Wang, Y. Li, *Nano Energy* **2020**, *68*, 104384.
[28] A. Zhang, Y. Liang, H. Zhang, Z. Geng, J. Zeng, *Chem. Soc. Rev.* **2021**, *50*, 9817–9844.
[29] S. Li, M. Ceccato, X. Lu, S. Frank, N. Lock, A. Roldan, X. M. Hu, T. Skrydstrup, K. Daasbjerg, *J. Mater. Chem. A* **2021**, *9*, 1583–1592.
[30] J. Chen, Z. Wang, H. Lee, J. Mao, C. A. Grimes, C. Liu, M. Zhang, Z. Lu, Y. Chen, S. P. Feng, *Mater. Today Phys.* **2020**, *12*, 100176.
[31] J. Lu, Z. Tang, L. Luo, S. Yin, P. K. Shen, P. Tsiakaras, *Appl. Catal. B* **2019**, *255*, 117737.
[32] L. Xia, X. Wu, Y. Wang, Z. Niu, Q. Liu, T. Li, X. Shi, A. M. Asiri, X. Sun, *Small Methods* **2018**, *3*, 1800251.
[33] Y. Chen, L. Ma, C. Chen, W. Hu, L. Zou, Z. Zou, H. Yang, *J. CO_2 Util.* **2020**, *42*, 101316.
[34] Y. Ito, W. Cong, T. Fujita, Z. Tang, M. Chen, *Angew. Chem. Int. Ed.* **2015**, *54*, 2131–2136; *Angew. Chem.* **2015**, *127*, 2159–2164.
[35] Y. Zheng, Y. Jiao, L. H. Li, T. Xing, Y. Chen, M. Jaroniec, S. Z. Qiao, *ACS Nano* **2014**, *8*, 5290–5296.
[36] A. C. Ferrari, D. M. Basko, *Nat. Nanotechnol.* **2013**, *8*, 235–246.
[37] M. Endo, C. Kim, T. Karaki, T. Tamaki, Y. Nishimura, M. J. Matthews, S. D. M. Brown, M. S. Dresselhaus, *Phys. Rev. B* **1998**, *58*, 8991.
[38] H. Gao, Z. Liu, L. Song, W. Guo, W. Gao, L. Ci, A. Rao, W. Quan, R. Vajtai, P. M. Ajayan, *Nanotechnology* **2012**, *23*, 275605.
[39] Y. A. Kim, K. Fujisawa, H. Muramatsu, T. Hayashi, M. Endo, T. Fujimori, K. Kaneko, M. Terrones, J. Behrends, A. Eckmann, C. Casiraghi, K. S. Novoselov, R. Saito, M. S. Dresselhaus, *ACS Nano* **2012**, *6*, 6293–6300.
[40] K. Qu, Y. Zheng, X. Zhang, K. Davey, S. Dai, S. Z. Qiao, *ACS Nano* **2017**, *11*, 7293–7300.
[41] F. Pan, B. Li, X. Xiang, G. Wang, Y. Li, *ACS Catal.* **2019**, *9*, 2124–2133.
[42] K. Mamtani, D. Jain, D. Dogu, V. Gustin, S. Gunduz, A. C. Co, U. S. Ozkan, *Appl. Catal. B* **2018**, *220*, 88–97.
[43] F. Pan, W. Deng, C. Justiniano, Y. Li, *Appl. Catal. B* **2018**, *226* 463–472.
[44] F. Pan, B. Li, W. Deng, Z. Du, Y. Gang, G. Wang, Y. Li, *Appl. Catal. B* **2019**, *252*, 240–249.
[45] Z. Yang, Z. Yao, G. Li, G. Fang, H. Nie, Z. Liu, X. M. Zhou, X. A. Chen, S. M. Huang, *ACS Nano* **2012**, *6*, 205–211.
[46] J. Yang, Z. Qiu, C. Zhao, W. Wei, W. Chen, Z. Li, Y. Qu, J. Dong, J. Luo, Z. Li, Y. Wu, *Angew. Chem. Int. Ed.* **2018**, *57*, 14095–14100; *Angew. Chem.* **2018**, *130*, 14291–14296.
[47] P. Lu, Y. Yang, J. Yao, M. Wang, S. Dipazir, M. Yuan, J. Zhang, X. Wang, Z. Xie, G. Zhang, *Appl. Catal. B* **2019**, *241*, 113–119.
[48] S. Liang, Q. Jiang, Q. Wang, Y. Liu, *Adv. Energy Mater.* **2021**, *11*, 2101477.
[49] K. Chen, M. Cao, Y. Lin, J. Fu, H. Liao, Y. Zhou, H. Li, X. Qiu, J. Hu, X. Zheng, M. Shakouri, Q. Xiao, Y. Hu, J. Li, J. Liu, E. Cortés, M. Liu, *Adv. Funct. Mater.* **2022**, *32*, 2111322.
[50] K. Chen, M. Cao, G. Ni, S. Chen, H. Liao, L. Zhu, H. Li, J. Fu, J. Hu, E. Cortés, *Appl. Catal. B* **2022**, *306*, 121093.
[51] M. Ma, B. J. Trzesniewski, J. Xie, W. A. Smith, *Angew. Chem. Int. Ed.* **2016**, *55*, 9748–9752; *Angew. Chem.* **2016**, *128*, 9900–9904.
[52] J. Chen, H. Li, C. Fan, Q. Meng, Y. Tang, X. Qiu, G. Fu, T. Ma, *Adv. Mater.* **2020**, *32*, e2003134.
[53] P. Li, G. Zhao, P. Cui, N. Cheng, M. Lao, X. Xu, S. X. Dou, W. Sun, *Nano Energy* **2021**, *83*, 105850.
[54] W. Bi, X. Li, R. You, M. Chen, R. Yuan, W. Huang, X. Wu, W. Chu, C. Wu, Y. Xie, *Adv. Mater.* **2018**, *30*, e1706617.
[55] K. Li, S. B. Zhang, X. L. Zhang, S. Liu, H. X. Jiang, T. L. Jiang, C. Y. Shen, Y. Yu, W. Chen, *Nano Lett.* **2022**, *22*, 1557–1565.
[56] L. X. Liu, Y. Zhou, Y. C. Chang, J. R. Zhang, L. P. Jiang, W. Zhu, Y. Lin, *Nano Energy* **2020**, *77*, 105296.
[57] G. Kresse, D. Joubert, *Phys. Rev. B* **1999**, *59*, 1758.
[58] G. Kresse, J. Furthmüller, *Comput. Mater. Sci.* **1996**, 6,15–50.
[59] J. P. Perdew, K. Burke, M. Ernzerhof, *Phys. Rev. Lett.* **1996**, *77*, 3865–3868.
[60] J. P. Perdew, M. Ernzerhof, K. Burke, *J. Chem. Phys.* **1996**, *105*, 9982–9985.
[61] P. E. Blochl, *Phys. Rev. B* **1994**, *50*, 17953–17979.
[62] S. Grimme, J. Antony, S. Ehrlich, H. Krieg, *J. Chem. Phys.* **2010**, *132*, 154104.
[63] J. K. Norskov, J. Rossmeisl, A. Logadottir, L. Lindqvist, J. R. Kitchin, T. Bligaard, H. Jonsson, *J. Phys. Chem. B* **2004**, *108*, 17886–17892.

Manuscript received: May 4, 2022
Revised manuscript received: August 4, 2022
Accepted manuscript online: August 4, 2022
Version of record online: September 1, 2022

Supporting Information

Sulfur decorated Ni−N−C catalyst for electrocatalytic CO_2 reduction with near 100% CO selectivity

Song Lu[a], Yang Zhang[a,b], Mohamed F. Mady[c], Obinna Egwu Eleri[a,b], Wakshum Mekonnen Tucho[d], Michal Mazur[e], Ang Li[e], Fengliu Lou[b], Minfen Gu*[f], Zhixin Yu*[a]

[a] S. Lu, Y. Zhang, O. E. Eleri, Prof. Z. X. Yu
Department of Energy and Petroleum Engineering
University of Stavanger
4036 Stavanger, Norway
E-mail: zhixin.yu@uis.no

[b] Y. Zhang, O. E. Eleri, Dr. F. L. Lou
Beyonder AS
Kanalsletta 2, 4033 Stavanger, Norway

[c] Dr. M. F. Mady
Department of Chemistry, Bioscience and Environmental Technology
University of Stavanger
4036 Stavanger, Norway

[d] Dr. W. M. Tucho
Department of Mechanical and Structural Engineering and Material Science
University of Stavanger
4036 Stavanger, Norway

[e] Dr. M. Mazur, A. Li
Department of Physical and Macromolecular Chemistry, Faculty of Science
Charles University
Hlavova 8, 12843 Prague 2, Czech Republic

[f] Prof. M. F. Gu
Center for Analysis and Testing
Nanjing Normal University
Nanjing 210023, China
E-mail: guminfen@njnu.edu.cn

***Corresponding author:**

Prof. Zhixin Yu

E-mail address: zhixin.yu@uis.no

Department of Energy and Petroleum Engineering, University of Stavanger, 4036 Stavanger, Norway

Tel: +47 51832238

Prof. Minfen Gu

E-mail address: guminfen@njnu.edu.cn

Center for Analysis and Testing, Nanjing Normal University, Nanjing 210023, China

Figure S1. ^{1}H NMR of the possible liquid products after electrolysis for 1 h over Ni−NS−C catalyst at −0.80 V (vs. RHE) in CO_2-saturated 0.5 M $KHCO_3$.

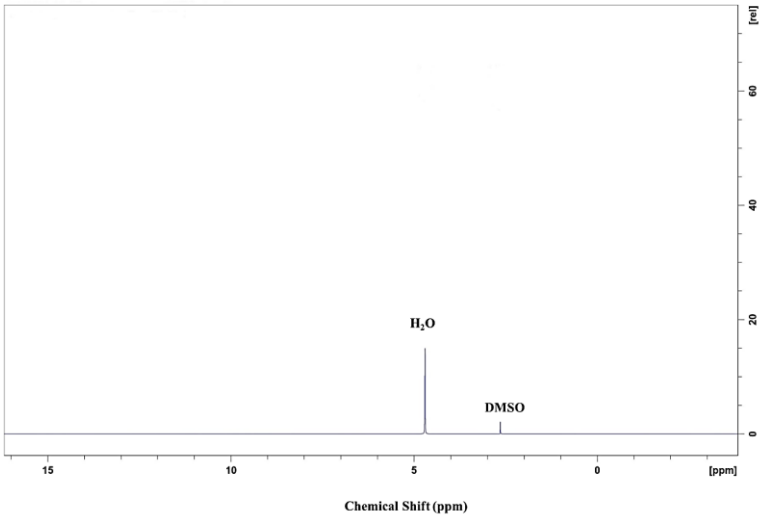

Figure S2. Cyclic voltammetry of (a) Ni−NS−C, (b) Ni−N−C, (c) NS−C, (d) N−C catalysts in CO_2-saturated 0.5 M $KHCO_3$ at various scan rates of 10, 20, 40, 60 and 80 mV/s; Cycle voltammetry was carried out between 0 and −0.2 V vs. Ag/AgCl.

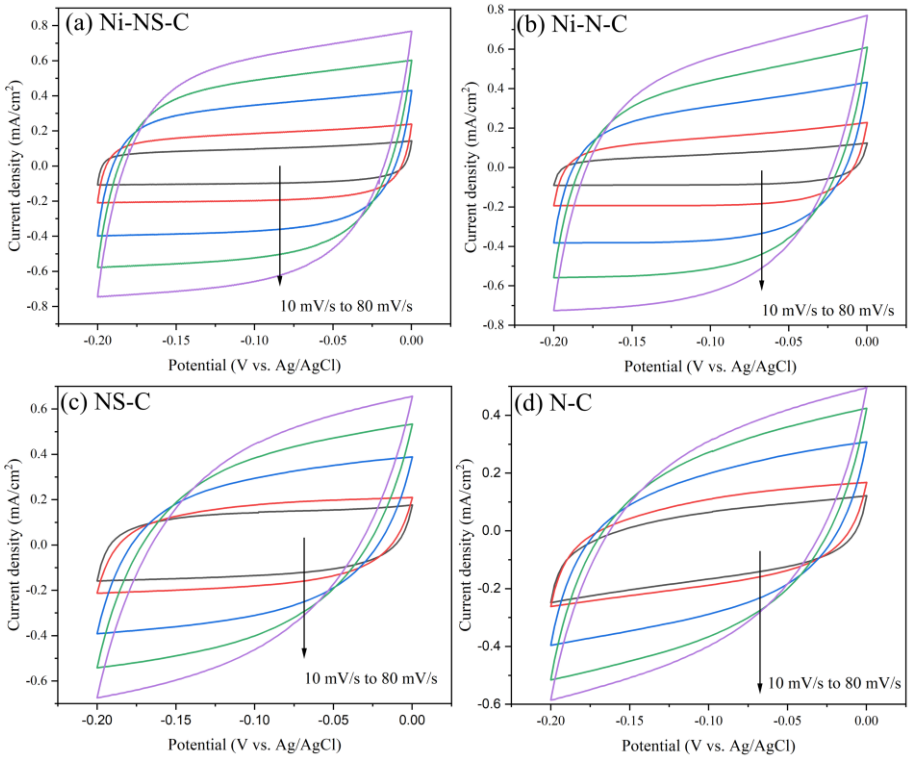

Figure S3. CO_2-TPD profiles of (a) Ni−NS−C and (b) Ni−N−C catalysts.

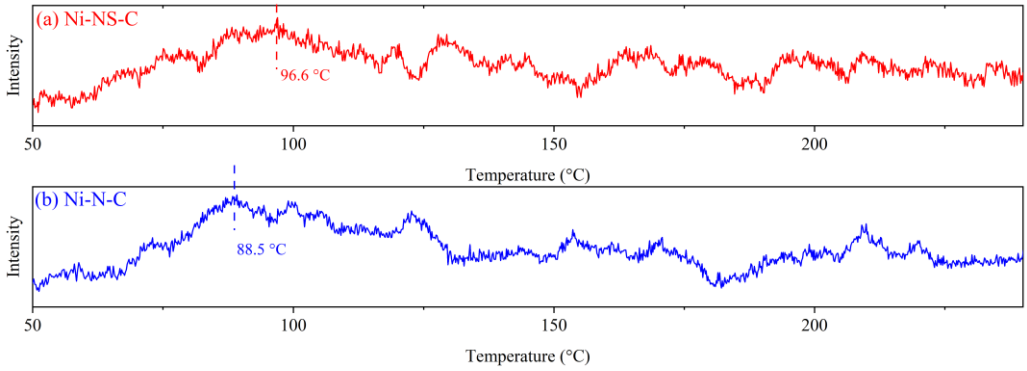

Figure S4. (a)-(c) TEM images and (d)-(g) EDX mapping of the spent Ni−NS−C catalyst.

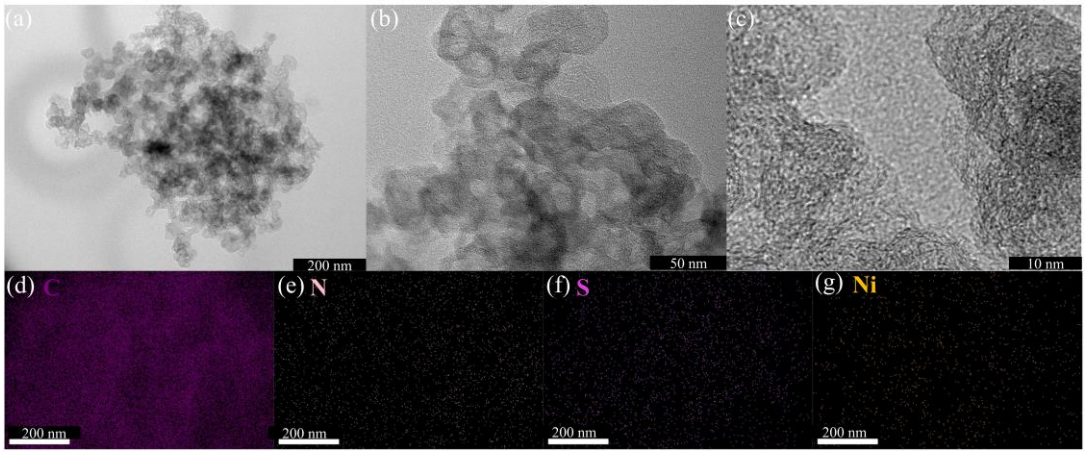

Figure S5. High-resolution XPS spectra (a) Ni 2p and (b) S 2p of the spent Ni−NS−C catalyst.

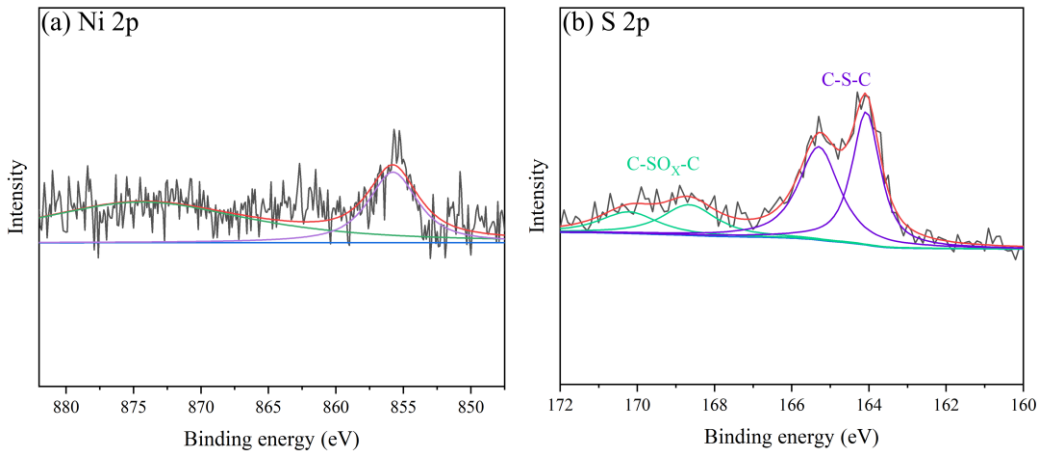

Figure S6. (a) A hypothetical structure, of which S substituted C atom without breaking TM−N_4; (b) free energy change of ECR to CO, and (c) free energy change of HER on the proposed structure.

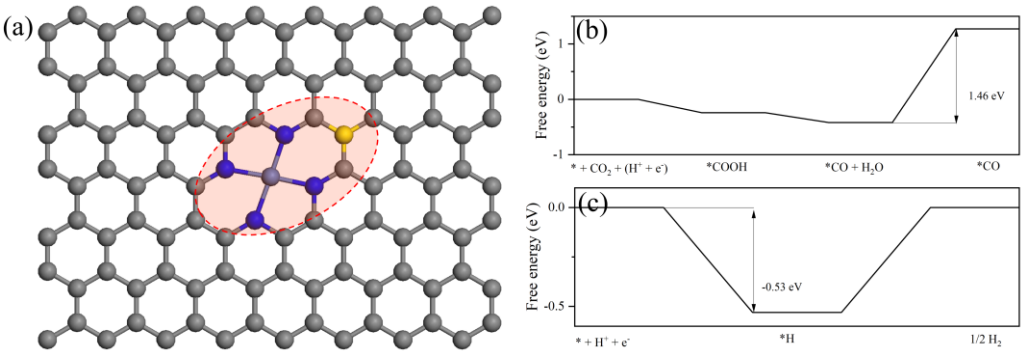

Table S1. Surface area and pore volume from N_2 adsorption-desorption study; Surface element contents from XPS measurement; ECSA from measuring double layer (D−L) capacitance.

Parameters	N−C	NS−C	Ni−N−C	Ni−NS−C	Ni−NS−C(spent)
Surface area (m^2/g)	1073	1120	1200	1275	−
Pore volume (m^3/g)	1.26	1.39	1.58	1.64	−
S (at. %)	−	0.37	−	0.42	0.40
N (at. %)	4.43	4.19	4.11	4.18	4.20
Ni (at. %)	−	−	0.50	0.48	0.45
ECSA (cm^2)	250	377	540	625	−

Table S2. Comparison of ECR performance for CO production on our Ni-NS-C catalyst and catalysts reported in literature.

Catalysts	FE (CO)	Potential vs. RHE	Stability	Reference
Ni−NS−C	99.7%	−0.80	19 h	This work
Ni/Fe−N−C	98%	−0.70	30 h	*Angew. Chem. Int. Ed*. 2019, 58, 6972
Ni_{SA}−N−C	71.9%	−0.90	60 h	*J. Am. Chem. Soc*. 2017, 139, 24, 8078
NiSA/GO	95%	−0.80	20 h	*Energy Environ. Sci*. 2018, 11, 893
Ni^{2+}@NG	92%	−0.68	20 h	*Adv. Mater*. 30 (2018) 1706617
C−Zn_1Ni_4	98%	−0.83	12 h	*Energy Environ. Sci*. 2018, 11, 1204
Ni−NCB	99%	−0.68	20 h	*Joule* 2019, 3, 265-278
Ni−N−C	94.8%	−0.86	29 h	*Chem. Eng. J* 2021, 131965
NiPc/NC	98%	−0.50	7 h	*ACS Sustainable Chem. Eng.* 2020, 8, 28, 10536
Ni−N_4	93%	−0.90	10 h	*Small* 2020, 16, 2003943
S−N−Ni/ACP	91%	−0.77	14 h	*J. Mater. Chem. A*, 2021,9, 1583
SA−Ni@NC	86.2%	−0.60	10 h	*Electrochem. commun* 2020, 116, 106758
Ni−SAs@FNC	95%	−0.77	10 h	*Appl. Catal. B: Environ* 2021, 283, 119591
Fe−NS−C	98%	−0.58	30 h	*Nano Energy* 2020, 68, 104384
FeSA−S/N−C	96.3	−0.49	24 h	*J CO_2 UTIL* 2020, 42 101316
(Cl, N)−Mn/G	97%	−0.60	12 h	*Nat Commun* 2019, 10, 2980

Appendix F – Paper VI

Regulating the Coordination Environment of Single-Atom Catalysts for Electrocatalytic CO_2 Reduction

S. Lu, F. Lou, Y. Zhao and Z. Yu

Journal of Colloid and Interface Science, 2023, 646, 301-310

DOI: 10.1016/j.jcis.2023.05.064

Journal of Colloid and Interface Science 646 (2023) 301–310

Contents lists available at ScienceDirect

Journal of Colloid And Interface Science

journal homepage: www.elsevier.com/locate/jcis

Regulating the coordination environment of single-atom catalysts for electrocatalytic CO_2 reduction

Song Lu [a], Fengliu Lou [b], Yafei Zhao [c,*], Zhixin Yu [a,d,*]

[a] Department of Energy and Petroleum Engineering, University of Stavanger, 4036 Stavanger, Norway
[b] Beyonder AS, 4033 Stavanger, Norway
[c] School of Physics and Engineering, Henan University of Science and Technology, Luoyang 471023, China
[d] Institute of New Energy, School of Chemistry and Chemical Engineering, Shaoxing University, Shaoxing 312000, China

GRAPHICAL ABSTRACT

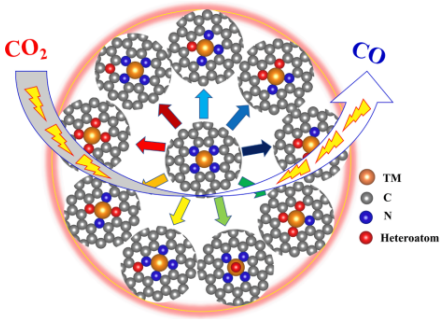

ARTICLE INFO

Keywords:
Electrochemical CO_2 reduction
Single-atom catalysts
Heteroatom doping
DFT calculations

ABSTRACT

Electrochemical CO_2 reduction (ECR) through single-atom catalysts (SACs) consisting of transition metals (TMs) anchored on nitrogenated carbon (TM–N–C) has shown promise for carbon neutralization. However, high overpotentials and low selectivity are still issues. Regulating the coordination environment of anchored TM atom is important to address these problems. In this study, we evaluated nonmetal atom (NM = B, O, F, Si, P, S, Cl, As and Se) modified TM (TM = Fe, Co, Ni, Cu and Zn)@N_4–C catalysts for their ECR to CO performance using density functional theory (DFT) calculations. NM dopants can induce active center distortion and tune electron structure, promoting intermediate formation. Doping heteroatoms can improve ECR to CO activity on Ni and Cu@N_4 but worsen it on Co@N_4 catalysts. Fe@N_4–F_1(I), Ni@N_3–B_1, Cu@N_4–O_1(III), and Zn@N_4–Cl_1(II) have excellent activity for ECR to CO, with overpotentials of 0.75, 0.49, 0.43, and 0.15 V, respectively, and improved selectivity. The catalytic performance is related to the intermediate binding strength, as evidenced by d band center, charge density difference, crystal orbital Hamilton population (COHP), and integrated COHP (ICOHP). It

* Corresponding authors at: Department of Energy and Petroleum Engineering, University of Stavanger, 4036 Stavanger, Norway (Z. Yu).
E-mail addresses: zhaoyafei@haust.edu.cn (Y. Zhao), zhixin.yu@uis.no (Z. Yu).

https://doi.org/10.1016/j.jcis.2023.05.064
Received 13 March 2023; Received in revised form 14 April 2023; Accepted 10 May 2023
Available online 13 May 2023

is expected that our work can be used as the design principle to guide the synthesis of the high-performance heteroatoms modified SACs for ECR to CO.

1. Introduction

The ever-increasing CO_2 emissions due to the combustion of fossil fuels has caused global concerns on climate change [1,2]. Electrochemical CO_2 reduction (ECR) has been considered as a sustainable way to alleviate CO_2 related energy and environmental issues because it can convert CO_2 into value-added fuels and chemicals utilizing green electricity from renewable energy such as solar and wind [3–5]. Nonetheless, the industrial implementation of ECR technology is limited by its sluggish kinetics, low activity and selectivity of electrocatalysts, and competing hydrogen evolution reaction (HER) in the aqueous electrolyte [6–8]. Among different ECR pathways and products, the reduction of CO_2 to CO via a two-electron transfer process is one of the most practical pathways because of less required energy and high CO selectivity. Moreover, CO is an important feedstock for gas-to-liquid technologies that produces gasoline, diesel or kerosene [9,10]. In this regard, it is essential to develop robust and efficient electrocatalysts for ECR to CO.

Over the past decades, numerous efforts have been devoted to exploring high-performance electrocatalysts for ECR to CO including noble metals Ag and Au, molecular complexes and carbon-based catalysts [11–14]. Ag- and Au-based catalysts have demonstrated excellent activity and selectivity with over 90% Faradaic efficiency (FE) for CO with small over potentials. However, the high cost of these precious metals hinders their commercial application. Molecular catalysts such as metalloporphyrin and metallo-phthalocyanine exhibit low current density and poor durability [15,16]. Metal free carbon-based materials show high selectivity for CO, but is limited by low current density [17]. Recently, single-atom catalysts (SACs) with atomically dispersed metal active sites have attracted extensive attention as efficient ECR electrocatalysts due to their maximum atomic utilization, superior activity and high selectivity for CO production [18–21]. 3d transition metal atoms coordinated with N species (TM–N_X, especially TM–N_4) supported on carbon (TM–N_X–C) exhibited excellent conductivity and satisfactory performance for CO production. For example, Zn SAC with Zn–N_4 moiety supported on carbon black exhibited 95% FE for CO at −0.43 V (vs. RHE) [22]. Density functional theory (DFT) calculations revealed that free energy barrier for the formation of *COOH on Zn–N_4/C was much lower than that of *N*-free ZnC_4 and Zn-free N_4/C. Co atoms with four-coordinated N on *N*-doped porous carbon displayed high selectivity for CO with a FE of 82% at a potential of −0.80 V(vs. RHE) [23]. In TM–N_X–C based SACs, TM–N_X moieties have been demonstrated to be the active centers, while carbon severs as the support to stabilize TM–N_X moieties and transfer electrons. However, it is revealed that Fe and Co centers show large free energy barrier for *CO desorption because of strong affinity [24]. Meanwhile, Ni and Cu sites generally exhibit high energy barrier for the formation of *COOH [25]. Notably, as the metal centers are regarded as active sites for ECR, the coordination environment of the metal center such as coordination number and coordinated atoms hold the key for catalytic performance [26–28]. In other words, it greatly influences the geometric and electronic structures of the metal centers in SACs, which further affects the binding strength between metal atoms and the intermediates in the ECR process.

Introducing heteroatom to tune the coordination environment has been considered as a powerful strategy to improve the ECR performance for SACs [29–31]. For example, axial Cl atom coordinated Fe with four N atoms exhibited FE of 90.5% for CO and partial current of 9.78 mA/cm^2 under −0.6 V potential, outperforming Cl free Fe–N_4 SAC [32]. DFT calculations demonstrated that Cl atom could cause a negative shift of the d-band center, weakening the binding strength between Fe atom and the intermediates. In addition, CO adsorption energy decreased after introducing axial Cl atom. Ma et al. investigated the effects of axial ligands such as F, Cl, OH and NH_2 on ECR performances of M–N_4 through DFT calculations [33]. They demonstrated that the axial ligands could change the electronic and magnetic properties of the metal center, resulting in the change of activity and selectivity for ECR to CO. In another study, P ligand was incorporated to N site, and the resulting Fe–PN_3–C shows FE of 98% at a low overpotential of 0.34 V for ECR to CO [34]. Theoretical calculations showed that the introduction of P atom could lower free energy barrier for *COOH formation and *CO desorption. Apparently, incorporating nonmetal (NM) atoms to substitute N or directly coordinate with metal center could effectively tune the electronic and geometric structures of the active moieties, which dictates the performance of ECR to CO. However, most studies could only reveal inadequate structural details of metal centers and NM ligands, due to the limitations of experimental techniques. Meanwhile, structures with subtle differences are treated similarly, resulting in ambiguous reaction mechanisms on active centers. Therefore, it is desirable to develop design principles for advanced NM doped TM–N_X–C SACs for CO generation and investigate their ECR performance and mechanism for different TM atoms in various coordination environments.

In this work, a series of NM (B, O, F, Si, P, S, Cl, As, Se and Br) heteroatom dopants modified TM (Fe, CO, Ni, Cu and Zn)@N_4 configurations embedded on graphene sheet are proposed. We performed a computational screening of the ECR to CO activity and stability of the NM decorated TM@N_4. We found that heteroatom dopants could not effectively activate CO_2 but could induce the distortion of the active center, promoting the formation of intermediates. NM atoms could effectively improve the ECR activity to CO on Ni and Cu@N_4 but deteriorate the ECR activity on Co@N_4. NM dopants could not break linear relationship between key intermediates for the catalysts. Based on the analysis of COHP and ICOHP, NM atoms could tune the binding strength between TM atom and intermediates, thus improving the ECR activity to CO on TM@N_4.

2. Computational methods

Spin-polarized calculations were performed with the Vienna ab initio simulation package (VASP) by density functional theory methods [35,36]. Projector-augmented wave (PAW) pseudopotentials were used to describe the interaction between electrons and ions [37]. The exchange correlation of electrons was described by the Perdew-Burke-Ernzerhof (PBE) functional within the generalized gradient approximation (GGA) [38,39]. Grimme's DFT-D3 method was used to treat the van der Waals (vdW) interaction [40]. The cutoff energy for the plane-wave basis set was taken as 500 eV. The convergence criteria for energy and force were 1.0×10^{-5} eV and 0.02 eV/Å, respectively. A Gamma center k-point mesh of $4 \times 4 \times 1$ was used for structure relaxation, while more accurate k-point of $8 \times 8 \times 1$ was employed for electronic structures calculations. A $5 \times 5 \times 1$ graphene supercell consisting of 50 carbon atoms was built as support for embedding N and dopant heteroatoms (NM = B O, F, Si, P, S, Cl, As and Se) coordinated transition metal atoms (TM = Fe, Co, Ni, Cu and Zn), in which ten different coordination environments were considered. A vacuum layer of 20 Å along the z direction was imposed to avoid periodic images. Implicit model was used for treating H_2O solvation effect, which was implemented in VASPsol. As shown in Fig. 1, the configurations can be classified into three groups: (1) pristine TM@N_4; (2) first shell doping: axial TM@N_4–NM_1(I), TM@N_3–NM_1, TM@N_2–NM_2(I), TM@N_2–NM_2(II), TM@N_2–NM_2(III), TM@N_1–NM_3 and TM@NM_4; (3) Second shell doping: TM@N_4–NM_1(III); (4) high shell doping: TM@N_4–NM_1(II). The stability of NM decorated TM@N_4 catalysts were evalulated by

calculating the formation energy (E_f) through Eq. (1)–(3):

$$Nsubstitution: \quad E_f = E(TM@N_x - NM_y) - 45\mu_C - (4-x)\mu_N - x\mu_{NM} - E(TM) \tag{1}$$

$$Csubstitution: \quad E_f = E(TM@N_x - NM_y) - (45-x)\mu_C - 4\mu_N - x\mu_{NM} - E(TM) \tag{2}$$

$$Axialatombinding: \quad E_f = E(TM@N_4 - NM_1(I)) - 45\mu_C - 4\mu_N - \mu_{NM} \tag{3}$$

where E(TM@N_x–NM_y) is the total energy of dopant heteroatom decorated TM@N_4; E(TM@N_4–NM_1(I)) denotes the total energy of NM atoms binding on axial sites. μ_C, μ_N, and μ_{NM} are the chemical potentials of carbon, host N atom and dopant heteroatom, respectively; E(TM) is the energy of one atom in its most stable bulk metal. x and y represent the coordination numbers of N and dopant heteroatom.

The binding energies of TM atoms for dopant heteroatom incorporating into graphene framework are calculated by Eq. (4):

$$E_b = E(TM@N_x - NM_y) - E(N_x - NM_y) - E(TM) \tag{4}$$

where E(N_x–NM_y) is metal free heteroatom and N co-doped graphene. With such a definition, a more negative value of E_b indicates higher thermodynamic stability.

For CO_2 molecule adsorption and axial atom binding on TM site, the adsorption energy (E_a) can be calculated by Eq. (5) and (6):

$$CO_2\ adsorption: \quad E_a = E(CO_2 - TM - N_x - NM_y) - E(TM - N_x - NM_y) - E(CO_2) \tag{5}$$

$$Axialatombinding: \quad E_a = E(TM@N_4 - NM_1(I)) - E(TM - N_4) - \mu_{NM} \tag{6}$$

where E(CO_2–TM@N_x–NM_y) is the total energy of heteroatom doped TM@N_4 with adsorbed CO_2; E(TM@N_4–NM_1(I)) and E(TM@N_4) indicate the total energies of heteroatom binding on the axial site of TM atoms and pristine TM@N_4, respectively.

The reaction steps of ECR to CO and competing hydrogen evolution reaction (HER) can be described by Eq. (7)–(10) [41]:

$$* + CO_2 + (H^+ + e^-) \rightarrow *COOH \tag{7}$$

$$*COOH + (H^+ + e^-) \rightarrow *CO + H_2O \tag{8}$$

$$*CO \rightarrow CO + * \tag{9}$$

$$* + (H^+ + e^-) \rightarrow *H \tag{10}$$

where * indicates active site. To calculate the Gibbs free energy change (△G) of formation of each intermediate, the computational hydrogen electrode (CHE) model proposed by Nørskov et al. was employed [42]. The △G of each elementary step can be calculated by Eq. (11):

$$\Delta G = \Delta E + \Delta E_{ZPE} - T\Delta S + \Delta G_U + \Delta G_{pH} \tag{11}$$

where △E is the reaction energy from DFT calculations. $\triangle E_{ZPE}$ and △S are the zero-point correction and entropy change of the reaction, respectively. T is standard temperature of 298.15 K. $\triangle G_U$ is the free energy contribution from applied electrode potential and is calculated by $\triangle G_U = neU$, where n is the number of transferred electrons, and U is the applied potential. $\triangle G_{pH}$ is the free energy contributed by H concentration, which is defined as $\triangle G_{pH} = k_BT \times \ln 10 \times pH$. However, the pH value is independent of theoretical overpotential, and is therefore not considered in this work. The limiting potential (U_L) is determined by potential determining step (PDS) that indicates the maximum energy consumption, which can be calculated by $U_L = -\triangle G_{max}/e$. The overpotential can be calculated by the equation $\eta = U_{equ} - U_L$, where U_{equ} is the equilibrium potentials (−0.11 V) for CO production.

3. Results and discussion

3.1. Structures and stabilities of nonmetal modified TM–N

Ten SACs configurations were built, which can be divided into pristine TM@N_4, first shell doping, second shell doing and high shell doping (Fig. 1). After structure relaxation, the host N and TM atoms of the TM@N_4 configuration are on the same plane with all carbon atoms. To introduce axial ligands on TM sites, TM atoms of TM@N_4–NM_1(I) are above the graphene plane. Besides, the bond length of the newly formed bond such as F–Co, O–Fe and Cl–Fe are close to the sum of the respective atomic covalent radius, implying strong interaction between TM atom and axial ligand. For doping heteroatoms into the second and high

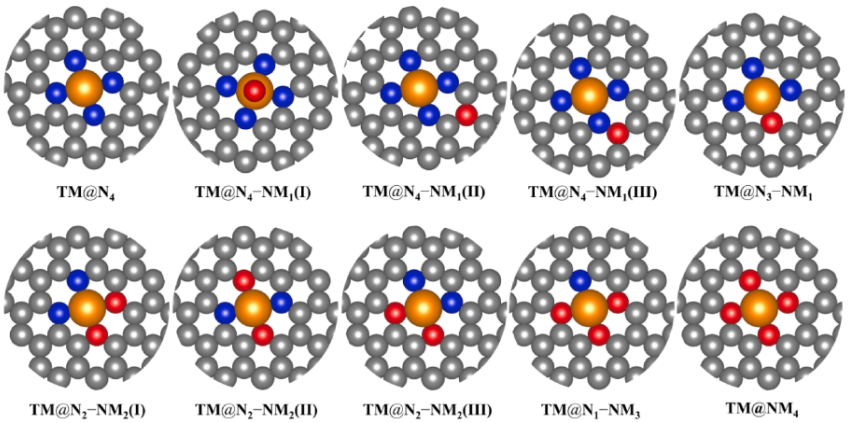

Fig. 1. NM atoms doping sites on TM@N_4-graphene monolayer configurations. Gray, red, blue and orange balls represent C, NM dopants, N and TM atoms. (For interpretation of the references to colour in this figure legend, the reader is referred to the web version of this article.)

shells, all atoms still stay in the graphene plane after structure relaxation. However, the compositions of resulting five- and six-membered rings are various, which can be attributed to the different atomic radius and electronegativity of the introduced heteroatoms. After first shell doping, almost no structures of TM@N_3–NM_1 had obvious changes. Nonetheless, with the increase of the number of dopant heteroatoms, e.g., Fe@N_2–Se_2(II), Co@N_1–F_3, Co@F_4, Co@N_1–As_3, Co@As_4, Co@Se_4, Co@N_2–Se_2(II), Ni@As_4, Ni@Se_4, Ni@N_2–Se_2(II), Cu@As_4, and Zn@N_2–Se_2(II) systems exhibited surface reconstruction, because the large difference in atomic radius in comparison with the host N or C atoms caused local strain and disruption of graphene plane. Therefore, these configurations are unstable and will be difficult to synthesize them experimentally. In Figure S1, a negative value of E_f indicates that heteroatoms doped TM@N_4 structure is thermodynamically stable. One heteroatom substituting N or C atom or binding axially on TM site exhibits great stability with negative E_f, such as Fe@N_3–B_1, Fe@N_3–P_1, Fe@N_4–Cl(I), which have been validated experimentally [32,43]. Besides, it can be found that the value of E_f becomes increasingly larger with the increase of coordination number, implying that introducing more heteroatoms could destabilize the host structure.

To further investigate the stability of anchored single TM atoms with different coordination environment based on formation energy, the binding energies (E_b) of TM atoms were calculated (Fig. 2). In the pristine TM@N_4 systems, the E_b of single Fe, Co, Ni, Cu and Zn atoms are −2.47, −2.94, −2.81, −1.58, and −2.46 eV, respectively. The negative values of E_b indicate that the TM@N_4 configurations are very stable on graphene, in good agreement with experimentally synthesized TM@N_4 on carbon skeletons. For NM heteroatoms decorated Fe@N_4 systems (Fig. 2a), O, F, S, Cl and Se as axial ligands exhibit negative adsorption energy, indicating that these NM atoms could be anchored stably on Fe sites. When incorporated into carbon framework, Fe@N_4–NM(II) and Fe@N_4–NM(III) (second shell) configurations are energetically favorable, whereas only Fe@N_3–B_1, Fe@N_3–O_1 and Fe@N_3–P_1 present negative E_b when one heteroatom substitutes one host N atom. When the dopant heteroatoms increase from two to four, the structures become unstable as confirmed by positive binding energies. For heteroatom doped Co@N_4, Ni@N_4, Cu@N_4 and Zn@N_4, the structures with more than more heteroatoms are more stable with negative E_b values, such as Co@N_2–P_2(I), Co@N_3–S_1, Ni@N_2–P_2(I), Ni@N_3–As_1 and Zn@N_2–O_2(I). Overall, for systems with single heteroatom, it can be concluded that halogen elements can be ideal axial ligand for TM@N_4 moiety. B, O and Si atoms prefer to form TM@N_4–NM_1(III) (second shell), while P, S, As and Se are more likely to form TM@N_4–NM_1(II) (high shell). For dopant heteroatoms substituting one or more host N atoms, B and P could be potential candidates. Therefore, heteroatom decorated TM@N_4 configurations with both negative values of E_f and E_b will be identified as stable structure. Consequently, there are 126 stable structures which are subsequently investigated for their ECR to CO performance.

3.2. CO_2 adsorption on nonmetal modified TM–N

CO_2 adsorption is the key to the subsequent protonation to form *COOH in ECR to CO. However, the activation of CO_2 is difficult due to the inherent chemical inertness and stability. The pristine TM@N_4 structures exhibit CO_2 adsorption energies of −0.12, −0.16, −0.15, −0.14 and −0.12 eV for Fe, Co, Ni, Cu and Zn, respectively (Fig. 3, blackdash line). Despite that the CO_2 adsorption energy on TM@N_4 moieties are negative, it is considered as physisorption because of small adsorption energy and large distance between TM atom and CO_2 molecule (d_{TM-C} larger than 3 Å). After introducing NM dopants, the CO_2 adsorption energy on some configurations can be effectively enhanced except for axial coordination, as demonstrated by the more negative adsorption energy. Noteworthily, CO_2 adsorption energy on some structures increased remarkably, which can be attributed to structure deformation by breaking one NM–C or NM–N bond. Particularly, TM@N_4 moieties modified by introducing halogen, As and Se elements such as Fe@N_4–F_1(III), Co@N_4–Cl_1(II), Ni@N_4–F_1(II), Cu@N_4–As_1(III) and Zn@N_4–Se_1(III) display remarkable structure deformation after CO_2 adsorption (Fig. S2a-e), which is probably due to metastability of the support. In contrast, some configurations such as Fe@N_4–P_1(II), Co@N_4–S_1(II), Ni@N_4–S_1(II), Cu@N_4–P_1(II), and Zn@N_4–S_1(II) show notable enhancement of CO_2 adsorption energy without breaking NM–C or NM–N bonds but slight distortion due to stable substrates (Fig. S2f-j). Nevertheless, the d_{TM-C} of these configurations are still larger than 3 Å,

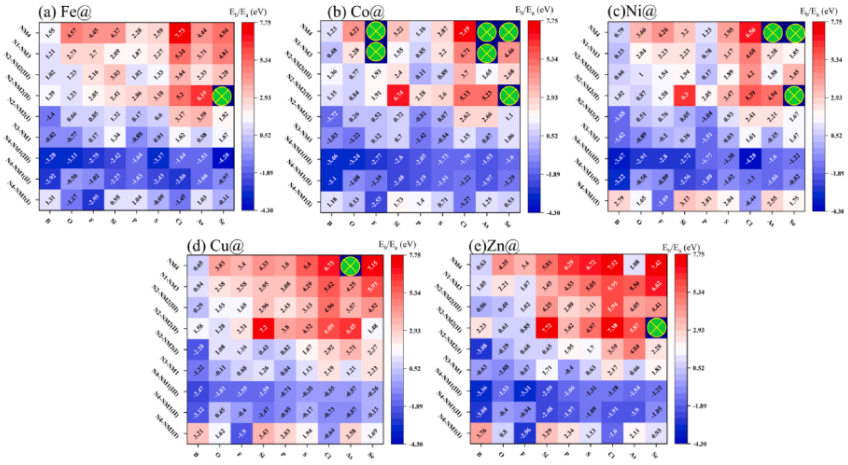

Fig. 2. The binding energy (E_b) of TM atoms on NM doped (a)Fe@N_4, (b) Co@N_4, (c) Ni@N_4, (d) Cu@N_4 and (e) Zn@N_4 configurations, of which F and Cl atom are adsorbed on TM site with adsorption energy E_a. The green circle indicates surface reconstruction. (For interpretation of the references to colour in this figure legend, the reader is referred to the web version of this article.)

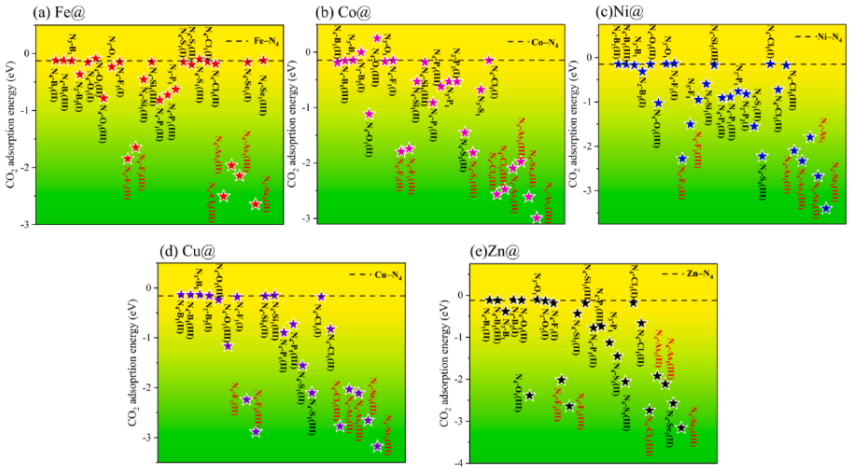

Fig. 3. The adsorption energy of CO_2 on NM decorated (a)Fe@N_4, (b) Co@N_4, (c) Ni@N_4, (d) Cu@N_4 and (e) Zn@N_4 structures, where the black-dashed line is the adsorption energy of CO_2 on pristine TM@N_4 structures. The red and black font indicate that surface experienced serious and slight deformation after CO_2 adsorption, respectively. (For interpretation of the references to colour in this figure legend, the reader is referred to the web version of this article.)

indicating physisorption behaviour. Overall, NM dopants could not effectively enhance CO_2 adsorption on TM site. The large changes in adsorption energy are mainly caused by distortion of TM@N_4 moiety after CO_2 adsorption, while minor structure changes could not affect adsorption energy. Therefore, it can be deduced that CO_2 adsorption on nonmetal doped TM@N_4 moiety could induce transient structures that potentially promote the formation of intermediates. Meanwhile, the structures without deformation after CO_2 adsorption can act as stable support for ECR to CO.

3.3. ECR to CO performance

Fe, Co, Ni, Cu and Zn of TM–N_X–C SACs exhibit good potential in ECR to CO. Meanwhile, it has been demonstrated both theoretically and experimentally that introducing NM dopants can further improve their ECR activity. However, earlier studies of some configurations are oversimplified, which may have ignored other possible structures that affect the catalytic performance for CO generation. As stated previously, only catalysts with negative formation energy and binding energy will be considered. Therefore, we calculated Gibbs free energy changes during ECR to CO for these NM decorated SACs. The ECR to CO process contains three elementary steps, for which $\triangle G_1$ (the formation of *COOH), $\triangle G_2$ (the formation of *CO) and $\triangle G_3$ (the desorption of *CO) are important descriptors for ECR to CO activity. For pristine TM@N_4, the $\triangle G_1$ values are 0.51, 0.29, 1.73, 1.75 and 1.09 eV for Fe, Co, Ni, Cu and Zn, respectively. It can be found that the formation of *COOH on Fe, Co, Ni, Cu and Zn@N_4 structures are endothermic with large free energy barriers, especially for Ni, Cu and Zn@N_4. The values of $\triangle G_2$ are −1.04, −0.08, −0.78, −0.80 and −0.17 eV for Fe, Co, Ni, Cu and Zn@N_4, suggesting that it is easy to form *CO. The values of $\triangle G_3$ are 1.11, 0.37, −0.37, −0.37, −0.34 eV for Fe, Co, Ni, Cu and Zn, respectively. CO selectivity is strongly dependent on the interaction strength between CO and TM sites, *i.e.*, the more negative the value of $\triangle G_3$, the easier the CO desorption from TM sites. CO desorption on Fe and Co@N_4 moieties show energy uphill thus difficult desorption, while CO desorption on Ni, Cu and Zn@N_4 structures are spontaneous. The PDS of ECR to CO on Fe and Co are *CO desorption, while the formation of *COOH is the PDS for Ni, Cu and Zn@N_4 catalysts, consistent with experimental studies. Consequently, the corresponding overpotentials for ECR to CO are 1.00, 0.26, 1.62, 1.64 and 0.98 V for Fe, Co, Ni, Cu and Zn@N_4.

After incorporating heteroatoms into TM@N_4, the $\triangle G_1$, $\triangle G_2$ and $\triangle G_3$ are varying (Table S1-S5), thus the PDS is changed. Interestingly, F and Cl could effectively adjust the PDS for ECR to CO on TM@N_4. Particularly, axial F and Cl atoms could enhance the ECR activity on Fe and Ni@N_4, but inhibit ECR to CO on Co, Cu and Zn@N_4. This is also consistent with previous report that Cl as axial ligands could effectively improve ECR to CO performance on Fe@N_4 catalyst [32]. In addition, the formation of *CO on most NM doped TM@N_4 are energy downhill, revealing that NM dopants cannot affect *CO formation. Furthermore, it can be found that heteroatoms could effectively improve the ECR activity on Ni and Cu@N_4 but decrease the activity on Co@N_4. As shown in Fig. 4, the PDS of Fe@N_4–F_1(I), Ni@N_3–B_1, Cu@N_4–O_1(III) and Zn@N_4–Cl_1(II) exhibit the lowest free energy barrier of 0.86, 0.60, 0.54 and 0.26 eV on NM decorated Fe, Ni, Cu and Zn@N_4, respectively. It is also noteworthy that the decrease of free energy barrier for the formation of *COOH will increase the free energy barrier of *CO desorption and vice versa on these four catalysts with the lowest overpotentials. For example, for the Ni@N_3–B_1 catalyst, the free energy barrier for *COOH formation is greatly reduced, however, the desorption of *CO becomes PDS and changes from exothermic to endothermic reaction. These results indicate a negative relationship between $\triangle G_1$ and $\triangle G_3$. $\triangle G_1$ and $\triangle G_3$ were chosen as descriptors to identify their relationship. As illustrated in Fig. 5, there is a linear relationship between $\triangle G_1$ and $\triangle G_3$, which are $\triangle G_3 = -0.93\triangle G_1 + 1.45$ ($R^2 = 0.79$), $\triangle G_3 = -0.94\triangle G_1 + 1.02$ ($R^2 = 0.91$), $\triangle G_3 = -1.01\triangle G_1 + 1.15$ ($R^2 = 0.96$), $\triangle G_3 = -0.86\triangle G_1 + 1.15$ ($R^2 = 0.79$), $\triangle G_3 = -0.80\triangle G_1 + 0.74$ ($R^2 = 0.74$) for NM doped Fe, Co, Ni, Cu and Zn@N_4 catalysts, respectively. Therefore, NM atoms doped TM@N_4 catalysts are still limited by linear relationship between key intermediates.

The overpotentials of heteroatoms doped TM@N_4 catalysts were further illustrated by two-dimensional contour maps (Fig. 6). The ECR performance increases when it migrates from the blue to red area in this visualized cloud plot. Therefore, the lower overpotential can be found in the red area. Only NM dopants that have positive effect on

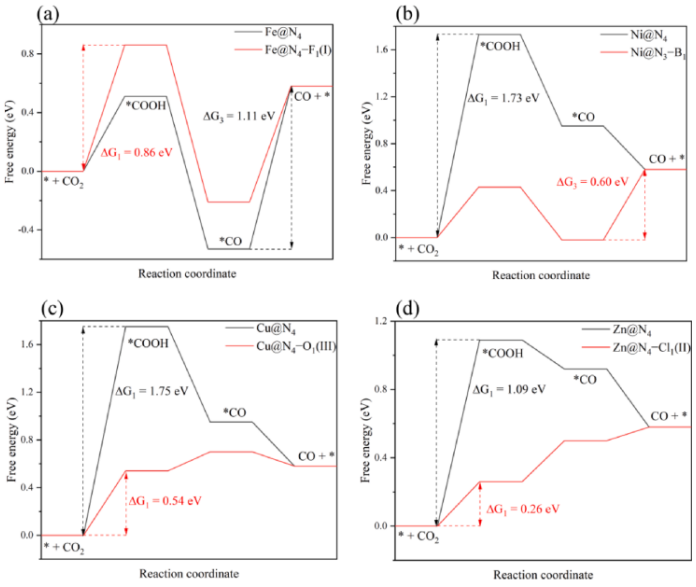

Fig. 4. The Gibbs free energy change for ECR to CO on NM decorated (a)Fe@N_4, (b) Ni@N_4, (c) Cu@N_4 and (d) Zn@N_4 catalysts.

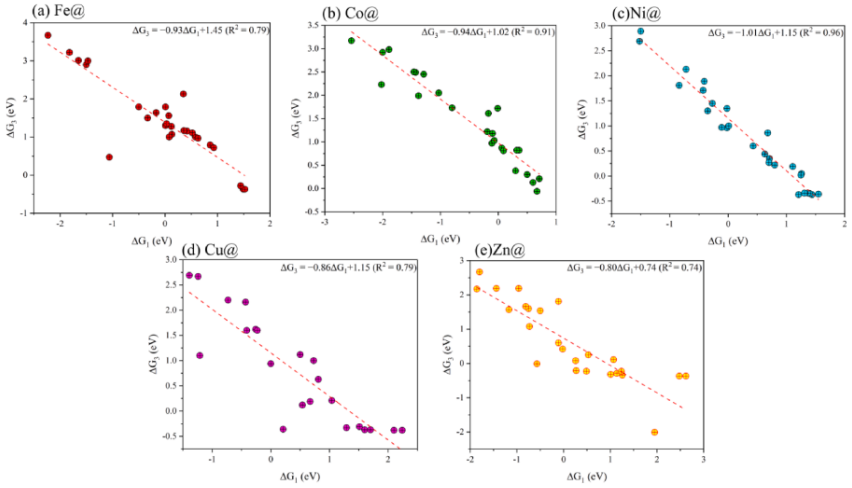

Fig. 5. Scaling relationship between △G_1 and △G_3 on NM decorated (a)Fe@N_4, (b) Co@N_4, (c) Ni@N_4, (d) Cu@N_4 and (e) Zn@N_4 structures.

overpotentials are marked by blue arrows. It can be found that the lowest overpotentials of ECR to CO on NM doped TM@N_4 are 0.75, 0.49, 0.43 and 0.15 V for Fe@N_4–F_1(I), Ni@N_3–B_1, Cu@N_4–O_1(III) and Zn@N_4–Cl_1(II), respectively, indicting remarkable decrease from their pristine TM@N_4 counterpart (Table S6). Remarkably, the overpotentials of Fe@N_4–F_1(I), Ni@N_3–B_1 and Cu@N_4–O_1(III) are lower than that of experimentally synthesized NM doped TM@N_4 catalysts such as axial Cl coordinated Fe with N_4 (0.93 V)[32], Ni@N_4 modified by S atom in C vacancy (1.55 V) [44], and Cu coordinated with three N and one O atoms (1.22 V) [28]. Furthermore, the stability of Fe@N_4–F_1(I),

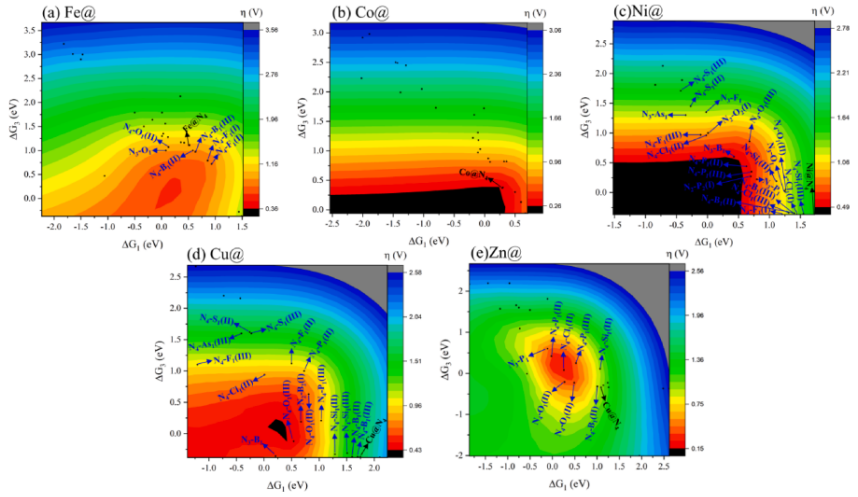

Fig. 6. The contour maps of overpotential (η) for ECR to CO as a function of △G_1 and △G_3 on NM decorated (a)Fe@N_4, (b) Co@N_4, (c) Ni@N_4, (d) Cu@N_4 and (e) Zn@N_4 catalysts, in which blue arrows indicate that the overpotential is lower than pristine TM@N_4. (For interpretation of the references to colour in this figure legend, the reader is referred to the web version of this article.)

Ni@N_3–B_1, Cu@N_4–O_1(III) and Zn@N_4–Cl_1(II) is evaluated by the *ab initio* molecular dynamics (AIMD) simulation under T = 300 K. As shown in Fig. S3a-d, the structures are maintained well, suggesting excellent thermodynamic stability.

3.4. Activity origin

The optimized configurations of *COOH and CO* adsorption on Fe@N_4–F_1(I), Ni@N_3–B_1, Cu@N_4–O_1(III) and Zn@N_4–Cl_1(II) catalysts are shown in Fig. S4a-d. CO_2 adsorption energy on Fe@N_4–F_1(I), Ni@N_3–B_1 and Zn@N_4–Cl_1(II) exhibits slight decrease in comparison with that of pristine Fe, Ni and Zn@N_4, indicting little reinforcement for CO_2 activation. Meanwhile, the substrates are also maintained well without bond breaking. For CO_2 adsorption on Cu@N_4–O_1(III), the adsorption energy is more negative with accompanying bond breakage. However, this configuration did not change after the adsorption of *COOH and CO. In contrast, Co@N_4–Cl_1(II) also exhibits lower adsorption energy for CO_2, but the coordination Cl ligand is altered after the adsorption of different intermediates (Fig. S4e), which apparently changes the configuration of Co@N_4 center. Consequently, the performance of ECR to CO on Co@N_4–Cl_1(II) was reduced. Therefore, it can be deduced that after reactants adsorption on NM doped TM@N_4 SACs, the induced structural changes can promote the ECR to CO performance, which is related to the interaction between the active TM atom and substrate.

d band center (ε_d) is an effective descriptor to reveal the binding strength between intermediates and active sites [45]. The ε_d of Fe, Ni, Cu and Zn@N_4 are −1.20, −2.24, −3.41 and −6.23 eV, respectively. As shown in Table S6, incorporating NM dopants could effectively tune ε_d. The ε_d of Fe@N_4–F_1(I), Ni@N_3–B_1, Cu@N_4–O_1(III) and Zn@N_4–Cl_1(II) are −1.48, −0.86, −3.88 and −6.94 eV, respectively. For Fe@N_4–F_1(I), a negative shift of ε_d contributed to weaker CO binding strength on Fe site, which changed the PDS from *CO desorption to *COOH formation. B dopants induced a positive shift of ε_d, enhancing the interaction strength between *CO and Ni site. As a result, the PDS changed from *COOH formation to *CO desorption. The ε_d of Cu@N_4–O_1(III) and Zn@N_4–Cl_1(II) shifted towards lower energy, which effectively promoted *COOH formation and accelerated the ECR process.

As the changes of structure may influence electronic structures, the charge density difference and charge transfer between the intermediates and TM atoms were calculated and illustrated in Fig. 7 and Figure S5. For *COOH–TM@N_4 moiety, Bader charge analysis reveals that the Fe, Ni, Cu and Zn atom donated 1.09e, 0.91e, 0.88e and 1.08e, respectively. For *CO–TM@N_4 system, the Fe, Ni, Cu and Zn atom lost 0.97e, 0.86e, 0.95e and 1.16e. After introducing NM atoms, for example, Fe atom in *COOH/*CO–Fe@N_4–F_1(I) donated more electrons (1.20e) because of larger electronegativity of F. However, this transfer did not affect the adsorbate, indicating that higher oxidized stated of Fe is not beneficial for *COOH activation as evidenced by the higher free energy for *COOH formation on Fe site. In addition, the yellow area between Fe atom and C atom of *CO was reduced, which weakened the binding strength between Fe and C and promoted CO desorption, in accordance with previous report that Fe with high valence could promote CO desorption [46]. For *COOH/*CO–Ni@N_4–B_1, one N atom was substituted by B atom with lower electronegativity, leading to lower oxidized state of Ni compared with Ni in Ni@N_4. Meanwhile, C atom of *CO lost less electrons (0.94e) than C atom of pristine *CO–Ni@N_4 (1.03e). However, a large yellow area between C and Ni atoms demonstrated a covalent bonding, indicating strong CO adsorption. As a result, CO desorption from Ni site is energy uphill. The valence states of Cu and Zn did not exhibit much change with slight accumulation of electrons between metal and C atom, implying some enhancement of *COOH adsorption. For *CO adsorption on metal site, there is little electron transfer between them, indicating weak interaction of *CO with metal atom. These results are consistent with free energy change for *COOH formation and *CO desorption.

To reveal the relationship between binding strength and activity, projected crystal orbital Hamilton population (COHP) was employed to analysis the interaction between C and metal atoms [47]. Fig. 8 displays the bonding and antibonding contributions on the right and left panel. There are no antibonding states below fermi energy level for COOH–Fe@N_4, however, it appeared at around −3.5 eV after

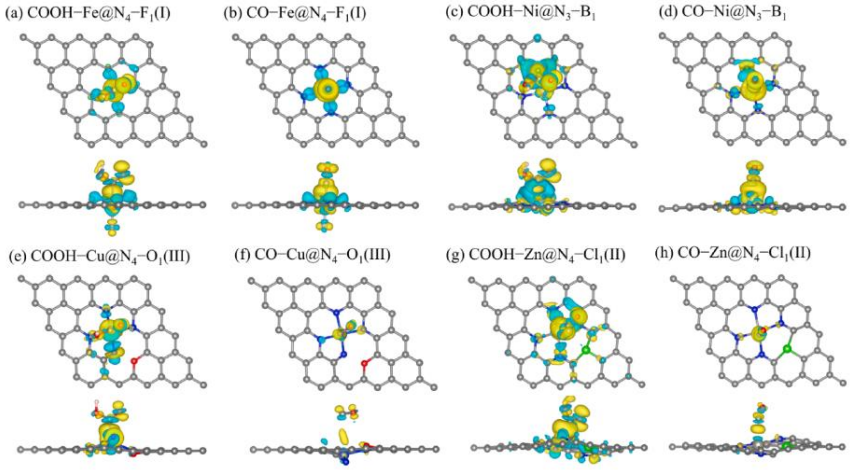

Fig. 7. Charge density difference of *COOH and *CO adsorption on (a)-(b) Fe@N_4–F_1(I), (c)-(d) Ni@N_3–B_1, (e)-(f) Cu@N_4–O_1(III) and (g)-(h) Zn@N_4–Cl_1(II), where the isosurface value is set to be 0.001 e/Bohr^3.

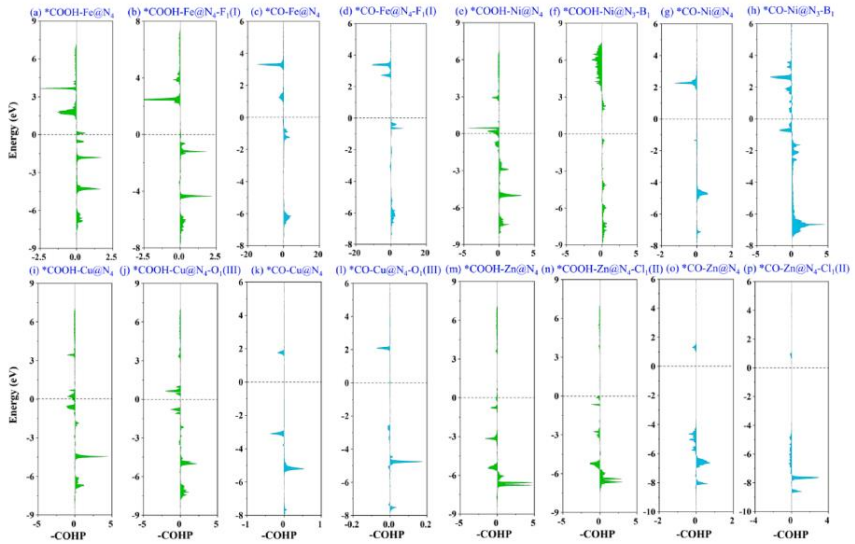

Fig. 8. The COHP between C atom of *COOH and TM atom of catalysts (green), C atom of *CO and TM atom of catalysts (cyan). (a)-(d) Fe@N_4 and Fe@N_4–F_1(I), (e)-(h) Ni@N_4 and Ni@N_3–B_1, (i)-(l) Cu@N_4 and Cu@N_4–O_1(III), and (m)-(p) Zn@N_4 and Zn@N_4–Cl_1(II). The dashed line denotes Fermi level. (For interpretation of the references to colour in this figure legend, the reader is referred to the web version of this article.)

introducing F ligand. Therefore, the binding strength was weakened as evidenced by higher free energy barrier for *COOH formation. Meanwhile, there are antibonding orbital populations appearing between −2 and −4 eV on CO–Fe@N_4–F_1(I), indicating unstable adsorption of CO. Thus, the CO deposition energy barrier decreased. To give a quantitative comparison of the interaction strength, the integrated COHP (ICOHP) was calculated (Table S6). The ICOHP for COOH–Fe@N_4–F_1(I) is −0.76 eV, which is less negative than that of COOH–Fe@N_4 (−0.95 eV), demonstrating that F dopant could weaken *COOH binding strength. The ICOHP of CO–Fe@N_4 after introducing F atom increases from −3.32

to −3.00 eV, suggesting that CO binding strength decreases. B decorated Ni@N_4 also exhibits remarkable difference in bonding and antibonding states. As shown in Fig. 8e-h, the antibonding orbital populations of *COOH adsorption on Ni@N_4 disappear after incorporating B atom, which contributes to the enhanced *COOH interaction with Ni. Meanwhile, there are antibonding states emerging between 0 and −1 eV for CO–Ni@N_3–B_1, indicating reduced CO adsorption strength on Ni. The calculated ICOHP for COOH–Ni@N_4 and COOH–Ni@N_3–B_1 are −1.14 and −0.19 eV or −3.52 eV (B site), while the ICOHP for *CO adsorption on Ni@N_4 and COOH–Ni@N_3–B_1 are −0.21 and −1.97 eV, respectively. Heteroatom doped Cu and Zn@N_4 did not show much difference in the distribution of antibonding and bonding states, however, the binding strength can be distinguished by ICOHP. Table S6 shows that O doped Cu@N_4 exhibits a decrease of ICOHP from −0.66 to −0.84 eV and a slight increase from −0.01 to −0.04 eV for *COOH and *CO adsorption, respectively. For Cl decorated Zn@N_4, the ICOHP for both *COOH and *CO absorption shows a decrease from −0.21 to −0.32 eV and −0.03 to −0.08 eV, respectively. Consequently, O and Cl dopants could improve the binding strengths of *COOH and *CO with TM atom.

3.5. Selectivity of ECR to CO vs. HER

The hydrogen evolution reaction (HER) is a major competing reaction in ECR, which greatly decrease Faradic efficiency of CO product. Especially, under high potentials and low pH, the competitive HER is dominant. As exhibited in Fig. 9a, free energy barriers for HER on Fe@N_4–F_1(I) and Cu@N_4–O_1(III) are 0.51 and 2.00 eV, which are larger than that of pristine Fe@N_4 and Cu@N_4. Therefore, HER is suppressed on Fe@N_4–F_1(I) and Cu@N_4–O_1(III) catalysts. It is worth mentioning that H atom prefers to adsorb on N site not Cu site after geometric relaxation, which caused a large free energy barrier for HER and promoted ECR intermediate adsorption on Cu site. However, the free energy barriers of Ni@N_3–B_1 and Zn@N_4–Cl_1(II) for HER decrease to 0.40 and 0.21 eV, implying increased HER activity. It has been widely accepted that the difference between limiting potentials of ECR and HER (U_L(CO)–U_L(H_2)) can be used to describe ECR selectivity [48]. As shown in Fig. 9b, a more positive value of U_L(CO)–U_L(H_2) indicates a higher selectivity towards CO. Remarkably, four catalysts exhibit increased CO selectivity compared with the pristine TM@N_4. Despite that heteroatom could deteriorate the ECR performance on Co@N_4, Co@N_4–Si_1(III) shows similar overpotential (0.27 V) as pristine Co@N_4 (0.26 V). Interestingly, The HER free energy barrier on Co@N_4–Si_1(III) is 0.18 eV, higher than that of Co@N_4 (0.09 eV). Thus, a larger value of (U_L(CO)–U_L(H_2)) for Co@N_4–Si_1(III) indicates that Si dopant could increase CO selectivity. It is worth noting that the free energy change for HER is not the single descriptor for HER activity, other parameters such as pH of electrolyte can effectively suppress the HER process. For example, the free energy barrier of HER can be tuned according to the relationship $\triangle G_{pH} = k_B T \times \ln 10 \times pH$ [49,50]. Consequently, it will increase 0.42 eV when the pH increased from 0 to 7. Therefore, the Faradic efficiency of ECR to CO on these catalysts can be improved by changing reaction conditions.

4. Conclusion

We developed a computational screening method for NM atoms decorated TM@N_4–C catalysts for ECR to CO. The coordination environments of Fe, Co, Ni, Cu and Zn single atom were tuned by NM dopants (B, O, F, Si, P, S, Cl, As and Se), which results in nine different configurations for each TM atom. Structural stability was investigated by calculating the formation energy and single TM atom binding energy on heteroatom-doped graphene. NM dopants could induce the distortion of active center, thus promoting the formation of intermediates. NM atoms could effectively improve the ECR activity to CO on Ni and Cu@N_4 but deteriorate the activity on Co@N_4 catalyst. However, NM dopants could not break the linear relationship between key intermediates. Compared with pristine TM@N_4, Fe@N_4–F_1(I), Ni@N_3–B_1, Cu@N_4–O_1(III) and Zn@N_4–Cl_1(II) exhibit the lowest overpotentials of 0.75, 0.49, 0.43 and 0.15 V for ECR to CO, respectively. Meanwhile, the selectivity for ECR to CO on the four catalysts are increased. The activity of NM atoms doped TM@N_4 is correlated with the binding strength of the key intermediates on TM site, which was further evidenced by COHP and ICOHP based on antibonding and bonding population. Therefore, NM dopants could effectively tune the interaction strength between TM atom and intermediates, contributing to high activity for ECR to CO. Our work can be used as the design principle to guide the synthesis of high-performance heteroatoms modified SACs for ECR to CO.

CRediT authorship contribution statement

Song Lu: Methodology, Investigation, Writing – original draft, Writing – review & editing, Visualization. **Fengliu Lou:** Investigation, Writing – review & editing. **Yafei Zhao:** Investigation, Formal analysis, Writing – review & editing. **Zhixin Yu:** Conceptualization, Methodology, Validation, Resources, Supervision, Writing – review & editing.

Declaration of Competing Interest

The authors declare that they have no known competing financial interests or personal relationships that could have appeared to influence the work reported in this paper.

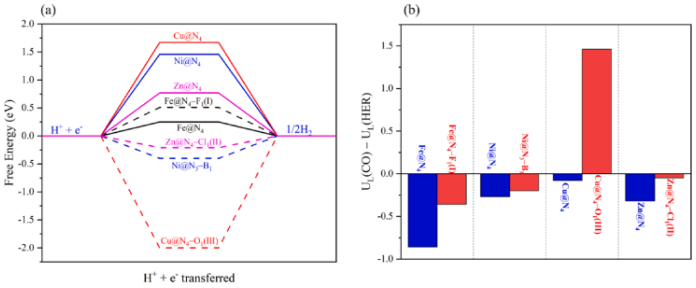

Fig. 9. (a) The Gibbs free energy change for HER, and (b) The difference between the limiting potentials for ECR to CO and HER on pristine TM@N_4 and NM doped TM@N_4.

Data availability

Data will be made available on request.

Acknowledgements

This work is supported by the Norwegian Ministry of Education and Research. The computations were performed on resources provided by UNINETT Sigma2 - the National Infrastructure for High Performance Computing and Data Storage in Norway.

Appendix A. Supplementary data

Supplementary data to this article can be found online at https://doi.org/10.1016/j.jcis.2023.05.064.

References

[1] S. Chu, Y. Cui, N. Liu, The path towards sustainable energy, Nat. Mater. 16 (2016) 16–22.
[2] E.S. Sanz-Perez, C.R. Murdock, S.A. Didas, C.W. Jones, Direct capture of CO_2 from ambient air, Chem. Rev. 116 (2016) 11840–11876.
[3] H. Gu, J. Wu, L. Zhang, Recent advances in the rational design of single-atom catalysts for electrochemical CO_2 reduction, Nano Res. 15 (2022) 9747–9763.
[4] S. Huo, J. Lu, X. Wang, Recent progress in electrochemical reduction of carbon dioxide on metal single-atom catalysts, Energy Sci. Eng. 10 (2021) 1584–1600.
[5] M.B. Ross, P. De Luna, Y. Li, C.T. Dinh, D. Kim, P. Yang, et al., Designing materials for electrochemical carbon dioxide recycling, Nat. Catal. 2 (2019) 648–658.
[6] H. Zhang, J. Li, S. Xi, Y. Du, X. Hai, J. Wang, et al., A graphene-supported single-atom FeN_5 catalytic site for efficient electrochemical CO_2 reduction, Angew. Chem. Int. Ed. 58 (2019) 14871–14876.
[7] F. Franco, C. Rettenmaier, H.S. Jeon, B.R. Cuenya, Transition metal-based catalysts for the electrochemical CO_2 reduction: from atoms and molecules to nanostructured materials, Chem. Soc. Rev. 49 (2020) 6884–6946.
[8] C. Jia, S. Li, Y. Zhao, R.K. Hocking, W. Ren, X. Chen, et al., Nitrogen vacancy induced coordinative reconstruction of single-atom Ni catalyst for efficient electrochemical CO_2 reduction, Adv. Funct. Mater. 31 (2021) 2107072.
[9] S. Ren, D. Joulié, D. Salvatore, K. Torbensen, M. Wang, M. Robert, et al., Molecular electrocatalysts can mediate fast, selective CO_2 reduction in a flow cell, Science 365 (2019) 367–369.
[10] A. Cherevotan, J. Raj, L. Dheer, S. Roy, S. Sarkar, R. Das, et al., Operando generated ordered heterogeneous catalyst for the selective conversion of CO_2 to methanol, ACS Energy Lett. 6 (2021) 509–516.
[11] S.Q. Liu, S.W. Wu, M.R. Gao, M.S. Li, X.Z. Fu, J.L. Luo, Hollow porous Ag spherical catalysts for highly efficient and selective electrocatalytic reduction of CO_2 to CO, ACS Sustain. Chem. Eng. 7 (2019) 14443–14450.
[12] L. Zhang, F. Mao, L.R. Zheng, H.F. Wang, X.H. Yang, H.G. Yang, Tuning metal catalyst with metal–C_3N_4 interaction for efficient CO_2 electroreduction, ACS Catal. 8 (2018) 11035–11041.
[13] C. Costentin, G. Passard, M. Robert, J.M. Saveant, Ultraefficient homogeneous catalyst for the CO_2-to-CO electrochemical conversion, Proc. Natl. Acad. Sci. 111 (2014) 14990–14994.
[14] S. Liu, H. Yang, X. Huang, L. Liu, W. Cai, J. Gao, et al., Identifying active sites of nitrogen-doped carbon materials for the CO_2 reduction reaction, Adv. Funct. Mater. 28 (2018) 1800499.
[15] M.D. Zhang, D.H. Si, J.D. Yi, Q. Yin, Y.B. Huang, R. Cao, Conductive phthalocyanine-based metal-organic framework as a highly efficient electrocatalyst for carbon dioxide reduction reaction, Sci. China Chem. 64 (2021) 1332–1339.
[16] S. Wei, H. Zou, W. Rong, F. Zhang, Y. Ji, L. Duan, Conjugated nickel phthalocyanine polymer selectively catalyzes CO_2-to-CO conversion in a wide operating potential window, Appl. Catal. B: Environ. 284 (2021), 119739.
[17] F. Pan, B. Li, W. Deng, Z. Du, Y. Gang, G. Wang, et al., Promoting electrocatalytic CO_2 reduction on nitrogen-doped carbon with sulfur addition, Appl. Catal. B: Environ. 252 (2019) 240–249.
[18] F. Pan, W. Deng, C. Justiniano, Y. Li, Identification of champion transition metals centers in metal and nitrogen-codoped carbon catalysts for CO_2 reduction, Appl. Catal. B: Environ. 226 (2018) 463–472.
[19] J. Feng, H. Gao, L. Zheng, Z. Chen, S. Zeng, C. Jiang, et al., A Mn-N_3 single-atom catalyst embedded in graphitic carbon nitride for efficient CO_2 electroreduction, Nat. Commun. 11 (2020) 4341.
[20] T. Zheng, K. Jiang, N. Ta, Y. Hu, J. Zeng, J. Liu, et al., Large-scale and highly selective CO_2 electrocatalytic reduction on nickel single-atom catalyst, Joule 3 (2019) 265–278.
[21] Y. Pan, R. Lin, Y. Chen, S. Liu, W. Zhu, X. Cao, et al., Design of single-atom Co-N_5 catalytic site: a robust electrocatalyst for CO_2 reduction with nearly 100% CO selectivity and remarkable stability, J. Am. Chem. Soc. 140 (2018) 4218–4221.
[22] F. Yang, P. Song, X. Liu, B. Mei, W. Xing, Z. Jiang, et al., Highly efficient CO_2 electroreduction on ZnN_4-based single-atom catalyst, Angew. Chem. Int. Ed. 57 (2018) 12303–12307.
[23] Z. Geng, Y. Cao, W. Chen, X. Kong, Y. Liu, T. Yao, et al., Regulating the coordination environment of Co single atoms for achieving efficient electrocatalytic activity in CO_2 reduction, Appl. Catal. B: Environ. 240 (2019) 234–240.
[24] W. Ren, X. Tan, W. Yang, C. Jia, S. Xu, K. Wang, et al., Isolated diatomic Ni-Fe metal-nitrogen sites for synergistic electroreduction of CO_2, Angew. Chem. Int. Ed. 58 (2019) 6972–6976.
[25] H. Han, J. Im, M. Lee, D. Choo, N-bridged Ni and Mn single-atom pair sites: A highly efficient electrocatalyst for CO_2 conversion to CO, Appl. Catal. B: Environ. 320 (2023), 121953.
[26] Y.N. Gong, L. Jiao, Y. Qian, C.Y. Pan, L. Zheng, X. Cai, et al., Regulating the coordination environment of MOF-templated single-Atom nickel electrocatalysts for boosting CO_2 reduction, Angew. Chem. Int. Ed. 59 (2020) 2705–2709.
[27] H. Chen, X. Guo, X. Kong, Y. Xing, Y. Liu, B. Yu, et al., Tuning the coordination number of Fe single atoms for the efficient reduction of CO_2, Green Chem. 22 (2020) 7529–7536.
[28] J. Leverett, T. Tran-Phu, J.A. Yuwono, P. Kumar, C. Kim, Q. Zhai, et al., Tuning the coordination structure of Cu-N-C single atom catalysts for simultaneous electrochemical reduction of CO_2 and NO_3^- to Urea, Adv. Energy Mater. 12 (2022) 2201500.
[29] M. Ma, F. Li, Q. Tang, Coordination environment engineering on nickel single-atom catalysts for CO2 electroreduction, Nanoscale 13 (2021) 19133–19143.
[30] W. Dong, N. Zhang, S. Li, S. Min, J. Peng, W. Liu, et al., A Mn single atom catalyst with Mn–N_2O_2 sites integrated into carbon nanosheets for efficient electrocatalytic CO_2 reduction, J. Mater. Chem. A 10 (2022) 10892–10901.
[31] S.G. Han, D.D. Ma, S.H. Zhou, K. Zhang, W.B. Wei, Y. Du, et al., Fluorine-tuned single-atom catalysts with dense surface Ni-N_4 sites on ultrathin carbon nanosheets for efficient CO_2 electroreduction, Appl. Catal. B: Environ. 283 (2021), 119591.
[32] Z. Li, R. Wu, S. Xiao, Y. Yang, L. Lai, J.S. Chen, et al., Axial chlorine coordinated iron-nitrogen-carbon single-atom catalysts for efficient electrochemical CO_2 reduction, Chem. Eng. J. 430 (2022), 132882.
[33] M. Ma, Q. Tang, Axial coordination modification of M-N_4 single-atom catalysts to regulate the electrocatalytic CO_2 reduction reaction, J. Mater. Chem. C 10 (2022) 15948–15956.
[34] K. Li, S. Zhang, X. Zhang, S. Liu, H. Jiang, T. Jiang, et al., Atomic Tuning of single-atom Fe-N-C catalysts with phosphorus for robust electrochemical CO_2 reduction, Nano Lett. 22 (2022) 1557–1565.
[35] G. Kresse, J. Furthmüller, Efficiency of ab-initio total energy calculations for metals and semiconductors using a plane-wave basis set, Comput. Mater. Sci. 6 (1996) 15–50.
[36] G. Kresse, J. Furthmüller, Efficient iterative schemes forab initiototal- energy calculations using a plane-wave basis set, Phys. Rev. B 54 (1996) 11169–11186.
[37] G. Kresse, D. Joubert, From ultrasoft pseudopotentials to the projector augmented-wave method, Phys. Rev. B 59 (1999) 1758.
[38] P.E. Blochl, Projector augmented-wave method, Phys. Rev. B: Condens. Matter. 50 (1994) 17953–17979.
[39] J.P. Perdew, K. Burke, M. Ernzerhof, Generalized gradient approximation made simple, Phys. Rev. Lett. 77 (1996) 3865–3868.
[40] S. Grimme, J. Antony, S. Ehrlich, H. Krieg, A consistent and accurate ab initio parametrization of density functional dispersion correction (DFT-D) for the 94 elements H-Pu, J. Chem. Phys. 132 (2010), 154104.
[41] W. Liu, J. Liu, Y. Yang, B. Xiong, H. Bai, Tunable trimetallic TM-NiFe catalysts for enhancing the products selectivity of CO_2 electroreduction, Fuel 335 (2023), 127026.
[42] J.K. Nørskov, J. Rossmeisl, A. Logadottir, L. Lindqvist, J.R. Kitchin, T. Bligaard, H. Jonsson, Origin of the overpotential for oxygen reduction at a fuel-cell cathode, J. Phys. Chem. B 108 (2004) 17886–17892.
[43] S. Liu, M. Jin, J. Sun, Y. Qin, S. Gao, Y. Chen, et al., Coordination environment engineering to boost electrocatalytic CO_2 reduction performance by introducing boron into single-Fe-atomic catalyst, Chem. Eng. J. 437 (2022), 135294.
[44] S. Lu, Y. Zhang, M.F. Mady, O. Egwu Eleri, W. Mekonnen Tucho, M. Mazur, et al., Sulfur-decorated Ni-N-C catalyst for electrocatalytic CO_2 reduction with near 100 % CO selectivity, ChemSusChem 15 (2022) e202200870.
[45] S. Lu, H.L. Huynh, F. Lou, K. Guo, Z. Yu, Single transition metal atom embedded antimonene monolayers as efficient trifunctional electrocatalysts for the HER, OER and ORR: a density functional theory study, Nanoscale 13 (2021) 12885–12895.
[46] J. Gu, C.S. Hsu, L. Bai, H.M. Chen, X. Hu, Atomically dispersed Fe^{3+} sites catalyze efficient CO_2 electroreduction to CO, Science 364 (2019) 1091–1094.
[47] X. Liu, Y. Jiao, Y. Zheng, M. Jaroniec, S.Z. Qiao, Building up a picture of the electrocatalytic nitrogen reduction activity of transition metal single-atom catalysts, J. Am. Chem. Soc. 141 (2019) 9664–9672.
[48] W. Bi, X. Li, R. You, M. Chen, R. Yuan, W. Huang, et al., Surface immobilization of transition metal ions on nitrogen-doped graphene realizing high-efficient and selective CO_2 reduction, Adv. Mater. 30 (2018) e1706617.
[49] G. Xing, L. Cheng, K. Li, Y. Gao, H. Tang, Y. Wang, et al., Efficient electroreduction of CO_2 by single-atom catalysts two-dimensional metal hexahydroxybenzene frameworks: A theoretical study, Appl. Surf. Sci. 550 (2021), 149389.
[50] C. Ao, B. Feng, S. Qian, L. Wang, W. Zhao, Y. Zhai, et al., Theoretical study of transition metals supported on g-C_3N_4 as electrochemical catalysts for CO_2 reduction to CH_3OH and CH_4, J. CO_2 Util. 36 (2020) 116–123.

Supporting information

Regulating the Coordination Environment of Single-Atom Catalysts for Electrocatalytic CO_2 Reduction

Song Lu[a], Fengliu Lou[b], Yafei Zhao[c*], Zhixin Yu[a,d*]

[a]Department of Energy and Petroleum Engineering, University of Stavanger, 4036 Stavanger, Norway

[b]Beyonder AS, 4033 Stavanger, Norway

[c]School of Physics and Engineering, Henan University of Science and Technology, Luoyang, 471023, China

[d]Institute of New Energy, School of Chemistry and Chemical Engineering, Shaoxing University, Shaoxing 312000, China

***Corresponding author:**

Dr. Yafei Zhao

E-mail address: zhaoyafei@haust.edu.cn

School of Physics and Engineering, Henan University of Science and Technology, Luoyang, 471023, China

Prof. Zhixin Yu

E-mail address: zhixin.yu@uis.no

Department of Energy and Petroleum Engineering, University of Stavanger, 4036 Stavanger, Norway

Institute of New Energy, School of Chemistry and Chemical Engineering, Shaoxing University, Shaoxing 312000, China

Tel: +47 51832238

Table S1. Gibbs free energy change ΔG_1, ΔG_2 and ΔG_3 on NM doped Fe@N_4 with unit eV.

Fe	TM@N_4-NM_1(I)			TM@N_4-NM_1(II)			TM@N_4-NM_1(III)			TM@N_3-NM_1			TM@N_2-NM_2(I)		
ΔG	ΔG_1	ΔG_2	ΔG_3	ΔG_1	ΔG_2	ΔG_3	ΔG_1	ΔG_2	ΔG_3	ΔG_1	ΔG_2	ΔG_3	ΔG_1	ΔG_2	ΔG_3
B	-	-	-	0.58	-1.00	1.00	0.63	-1.02	0.97	0.07	-1.05	1.56	0.03	-0.80	1.35
O	1.49	-0.54	-0.37	0.13	-0.62	1.07	0.01	-0.73	1.30	0.08	-0.50	1.00	-	-	-
F	0.86	-1.07	0.79	-1.50	-0.82	2.90	-1.06	1.17	0.47	-	-	-	-	-	-
Si	-	-	-	-0.33	-0.59	1.50	0.52	-1.05	1.11	-	-	-	-	-	-
P	-	-	-	-0.50	-0.71	1.79	-0.17	-0.89	1.64	0.01	-1.22	1.79	-	-	-
S	1.52	-0.57	-0.37	0.12	-0.82	1.28	0.42	-1.00	1.16	-	-	-	-	-	-
Cl	0.93	-1.07	0.72	0.35	-1.90	2.13	-1.82	-0.82	3.22	-	-	-	-	-	-
As	-	-	-	-1.65	-0.78	3.01	-1.47	-0.95	3.00	-	-	-	-	-	-
Se	1.44	-0.58	-0.28	-2.23	-0.86	3.67	0.36	-0.95	1.17	-	-	-	-	-	-
Fe@N_4: ΔG_1= 0.51, ΔG_2= -1.04, ΔG_3= 1.11															

Table S2. Gibbs free energy change ΔG_1, ΔG_2 and ΔG_3 on NM doped Co@N_4 with unit eV.

Co	TM@N_4-NM_1(I)			TM@N_4-NM_1(II)			TM@N_4-NM_1(III)			TM@N_3-NM_1			TM@N_2-NM_2(I)		
ΔG	ΔG_1	ΔG_2	ΔG_3	ΔG_1	ΔG_2	ΔG_3	ΔG_1	ΔG_2	ΔG_3	ΔG_1	ΔG_2	ΔG_3	ΔG_1	ΔG_2	ΔG_3
B	-	-	-	0.36	-0.60	0.82	0.32	-0.56	0.82	-0.17	-0.86	1.61	-0.01	-1.13	1.72
O	-	-	-	0.71	-0.34	0.21	0.06	-0.35	0.87	0.60	-0.15	0.13	-	-	-
F	0.50	-0.22	0.30	-1.29	-0.58	2.45	-1.03	-0.44	2.05	-	-	-	-	-	-
Si	-	-	-	-0.11	-0.28	0.97	0.30	-0.10	0.38	-	-	-	-	-	-
P	-	-	-	-0.19	-0.45	1.22	-0.07	-0.38	1.03	-0.10	-0.50	1.18	-0.11	-0.62	1.31
S	-	-	-	-0.80	-0.35	1.73	-1.38	-0.03	1.99	0.09	-0.32	0.81	-	-	-
Cl	0.67	-0.03	-0.06	-2.02	0.35	2.23	-1.89	-0.51	2.98	-	-	-	-	-	-
As	-	-	-	-1.43	-0.48	2.49	-1.46	-0.46	2.50	-	-	-	-	-	-
Se	-	-	-	-2.00	-0.34	2.92	-2.54	-0.05	3.17	-	-	-	-	-	-
Co@N_4: ΔG_1= 0.29, ΔG_2= -0.08, ΔG_3= 0.37															

Table S3. Gibbs free energy change ΔG_1, ΔG_2 and ΔG_3 on NM doped Ni@N_4 with unit eV.

Ni	TM@N_4-NM_1(I)			TM@N_4-NM_1(II)			TM@N_4-NM_1(III)			TM@N_3-NM_1			TM@N_2-NM_2(I)		
ΔG	ΔG_1	ΔG_2	ΔG_3	ΔG_1	ΔG_2	ΔG_3	ΔG_1	ΔG_2	ΔG_3	ΔG_1	ΔG_2	ΔG_3	ΔG_1	ΔG_2	ΔG_3
B	-	-	-	1.40	-0.47	-0.35	1.37	-0.45	-0.34	0.43	-0.45	0.60	0.01	-0.43	1.00
O	-	-	-	1.26	-0.73	0.05	0.68	-0.96	0.86	1.25	-0.69	0.02	-	-	-
F	1.21	-0.26	-0.37	-0.41	-0.90	1.89	-0.11	-0.28	0.97	-0.02	-0.75	1.35	-	-	-
Si	-	-	-	1.11	-0.72	0.19	1.55	-0.61	-0.36	-	-	-	-	-	-
P	-	-	-	0.63	-0.49	0.44	0.71	-0.48	0.35	0.80	-0.44	0.22	0.70	-0.39	0.27
S	-	-	-	-0.27	-0.60	1.45	-0.43	-0.7	1.71	-	-	-	-	-	-
Cl	1.44	-0.49	-0.37	-0.02	-0.36	0.96	1.31	-0.39	-0.34	-	-	-	-	-	-
As	-	-	-	-0.72	-0.83	2.13	-0.84	-0.39	1.81	-0.35	-0.37	1.30	-	-	-
Se	-	-	-	-1.52	-0.59	2.69	-1.50	-0.81	2.89	-	-	-	-	-	-
Ni@N_4: ΔG_1= 1.73, ΔG_2= -0.78, ΔG_3= -0.37															

Table S4. Gibbs free energy change ΔG_1, ΔG_2 and ΔG_3 on NM doped Cu@N_4 with unit eV.

Cu	TM@N_4-NM_1(I)			TM@N_4-NM_1(II)			TM@N_4-NM_1(III)			TM@N_3-NM_1			TM@N_2-NM_2(I)		
ΔG	ΔG_1	ΔG_2	ΔG_3	ΔG_1	ΔG_2	ΔG_3	ΔG_1	ΔG_2	ΔG_3	ΔG_1	ΔG_2	ΔG_3	ΔG_1	ΔG_2	ΔG_3
B	-	-	-	1.60	-0.65	-0.37	1.70	-0.75	-0.37	0.21	0.73	-0.36	0.67	-0.28	0.19
O	-	-	-	0.81	-0.86	0.63,	0.54	0.16	-0.12	-	-	-	-	-	-
F	2.10	-1.14	-0.38	0.50	-1.04	1.12	-1.21	0.69	1.10	-	-	-	-	-	-
Si	-	-	-	1.29	-0.38	-0.33	1.51	-0.62	-0.31	-	-	-	-	-	-
P	-	-	-	0.73	-1.15	1.00	1.04	-0.67	0.21	0.80	-0.44	0.22	0.70	-0.39	0.27
S	-	-	-	-0.26	-0.78	1.62	-0.23	-0.79	1.60	-	-	-	-	-	-
Cl	2.24	-1.28	-0.38	0.01	-0.37	0.94	-0.73	-0.89	2.20	-	-	-	-	-	-
As	-	-	-	-0.43	-1.15	2.16	-0.41	-0.61	1.60	-	-	-	-	-	-
Se	-	-	-	-1.39	-0.72	2.69	-1.24	-0.85	2.67	-	-	-	-	-	-
Cu@N_4: ΔG_1= 1.75, ΔG_2= -0.80, ΔG_3= -0.37															

Table S5. Gibbs free energy change ΔG_1, ΔG_2 and ΔG_3 on NM doped Zn@N_4 with unit eV.

Zn	TM@N_4-NM_1(I)			TM@N_4-NM_1(II)			TM@N_4-NM_1(III)			TM@N_3-NM_1			TM@N_2-NM_2(I)		
ΔG	ΔG_1	ΔG_2	ΔG_3	ΔG_1	ΔG_2	ΔG_3	ΔG_1	ΔG_2	ΔG_3	ΔG_1	ΔG_2	ΔG_3	ΔG_1	ΔG_2	ΔG_3
B	-	-	-	1.01	-0.11	-0.32	1.26	-0.34	-0.34	-0.57	1.16	-0.01	1.24	-0.44	-0.23
O	-	-	-	0.27	0.52	-0.21	-0.11	-1.12	1.81	0.49	0.32	-0.23	1.95	0.64	-2.01
F	2.62	-1.67	-0.37	-0.50	-0.46	1.54	-1.44	-0.17	2.19	-	-	-	-	-	-
Si	-	-	-	1.07	-0.60	0.11	1.14	-0.27	-0.29	-	-	-	-	-	-
P	-	-	-	-0.02	0.18	0.42	0.53	-0.20	0.25	-0.11	0.09	0.60	-	-	-
S	-	-	-	-0.73	0.22	1.09	-0.75	-0.27	1.60	-	-	-	-	-	-
Cl	2.48	-1.53	-0.37	0.26	0.24	0.08	-0.96	-0.65	2.19	-	-	-	-	-	-
As	-	-	-	-1.17	0.18	1.57	-0.81	-0.27	1.66	-	-	-	-	-	-
Se	-	-	-	-1.86	0.27	2.17	-1.80	-0.29	2.67	-	-	-	-	-	-
Zn@N_4: ΔG_1= 1.09, ΔG_2= -0.17, ΔG_3= -0.34															

Table S6. The overpotentials for ECR to CO on perfect TM@N_4 and NM doped TM@N_4; the change transfer after *COOH and *CO adsorption on perfect TM@N_4 and NM doped TM@N_4; The ICOHP of *COOH and *CO adsorption on perfect TM@N_4 and NM doped TM@N_4.

Catalyst	Overpotential (V)	ε_d (eV)	Charge transfer (e)				ICOHP (eV)	
			*COOH		*CO		*COOH	*CO
Fe@N_4	1.00	-1.20	Fe	C	Fe	C	−0.95	-3.32
			-1.09	-1.28	-0.97	-0.86		
			*COOH		*CO		*COOH	*CO
Fe@N_4−F_1(I)	0.75	-1.48	Fe	C	Fe	C	-0.76	-3.00
			-1.20	-1.30	-1.09	-0.87		
			*COOH		*CO		*COOH	*CO
Ni@N_4	1.62	-2.24	Ni	C	Ni	C	-1.14	-0.21
			-0.91	-1.37	-0.86	-1.03		
			*COOH		*CO		*COOH	*CO
Ni@N_3−B_1	0.49	-0.86	Ni	C	Ni	C	-0.19/-3.52	-1.97
			-0.66	-0.94	-0.54	-0.94		
			*COOH		*CO		*COOH	*CO
Cu@N_4	1.64	-3.14	Cu	C	Cu	C	-0.66	-0.01
			-0.88	-1.28	-0.95	-1.07		
			*COOH		*CO		*COOH	*CO
Cu@N_4−O_1(III)	0.43	-3.88	Cu	C	Cu	C	-0.84	-0.04
			-0.90	-1.44	-0.91	-1.08		
			*COOH		*CO		*COOH	*CO
Zn@N_4	0.98	-6.23	Zn	C	Zn	C	-0.21	-0.03
			-1.08	-1.20	-1.16	-1.06		
			*COOH		*CO		*COOH	*CO
Zn@N_4−Cl_1(II)	0.15	-6.94	Zn	C	Zn	C	-0.32	-0.08
			-1.06	-1.18	-1.13	-1.08		

Figure S1. The formation energy (E_f) of NM atom doped (a)Fe@N_4, (b) Co@N_4, (c) Ni@N_4, (d) Cu@N_4 and (e) Zn@N_4 configurations. The green circle indicates surface reconstruction.

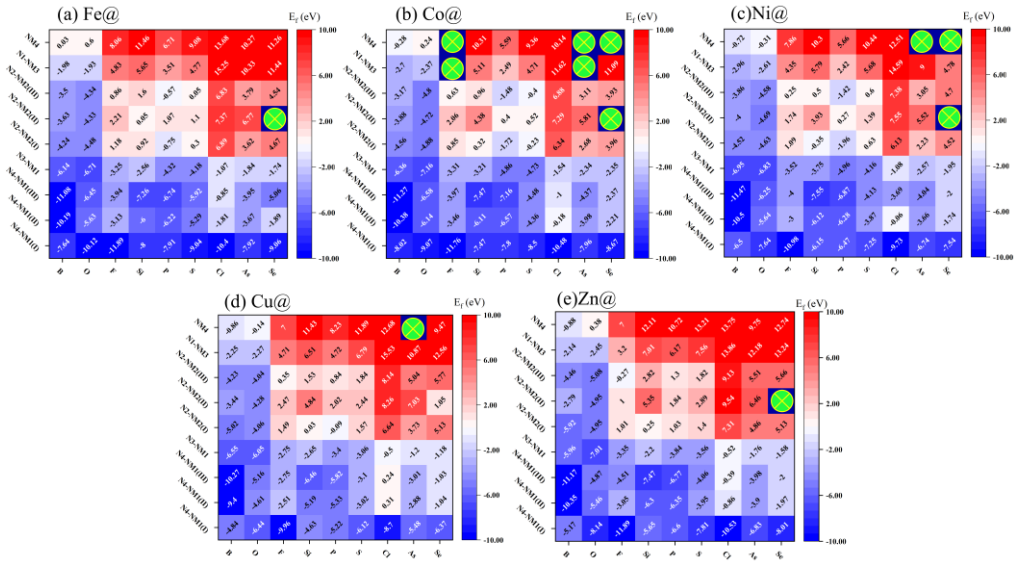

Figure S2. The configurations of CO_2 adsorption on NM docorated TM@N_4.

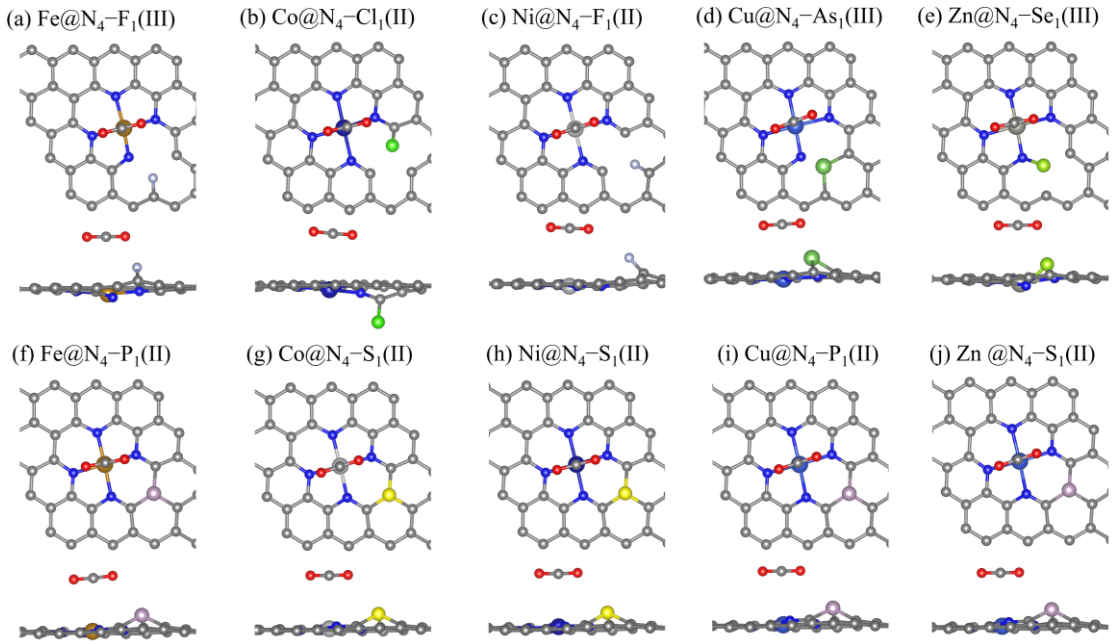

Figure S3. The total energy and structure variations of (a) Fe@N_4−F_1(I), (b)Ni@N_3−B_1, (c) Cu@N_4−O_1(III) and (d) Zn@N_4−Cl_1(II) K at 300K under AIMD simulation.

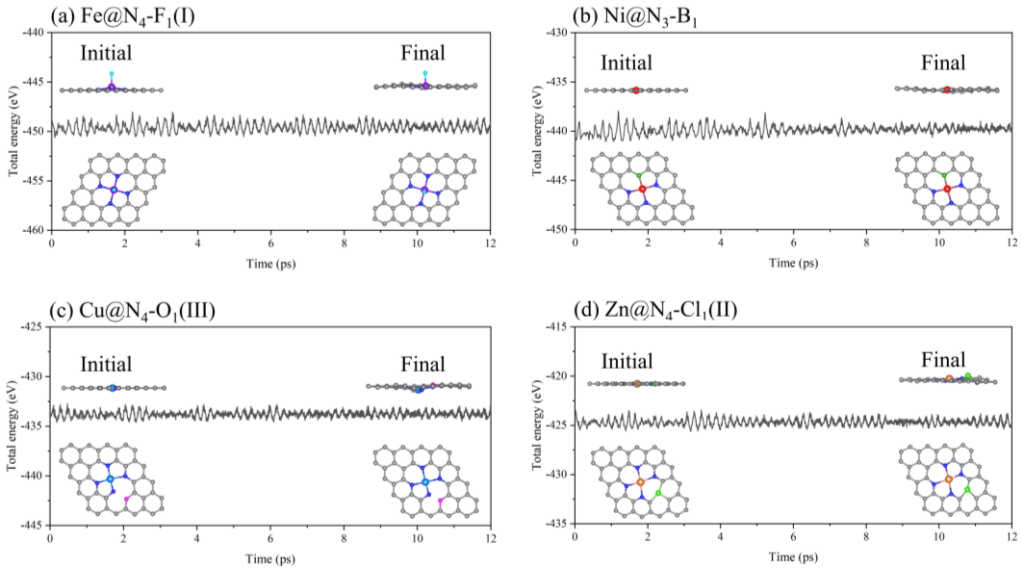

Figure S4. The configurations of intermediates adsorption on NM docorated TM@N_4.

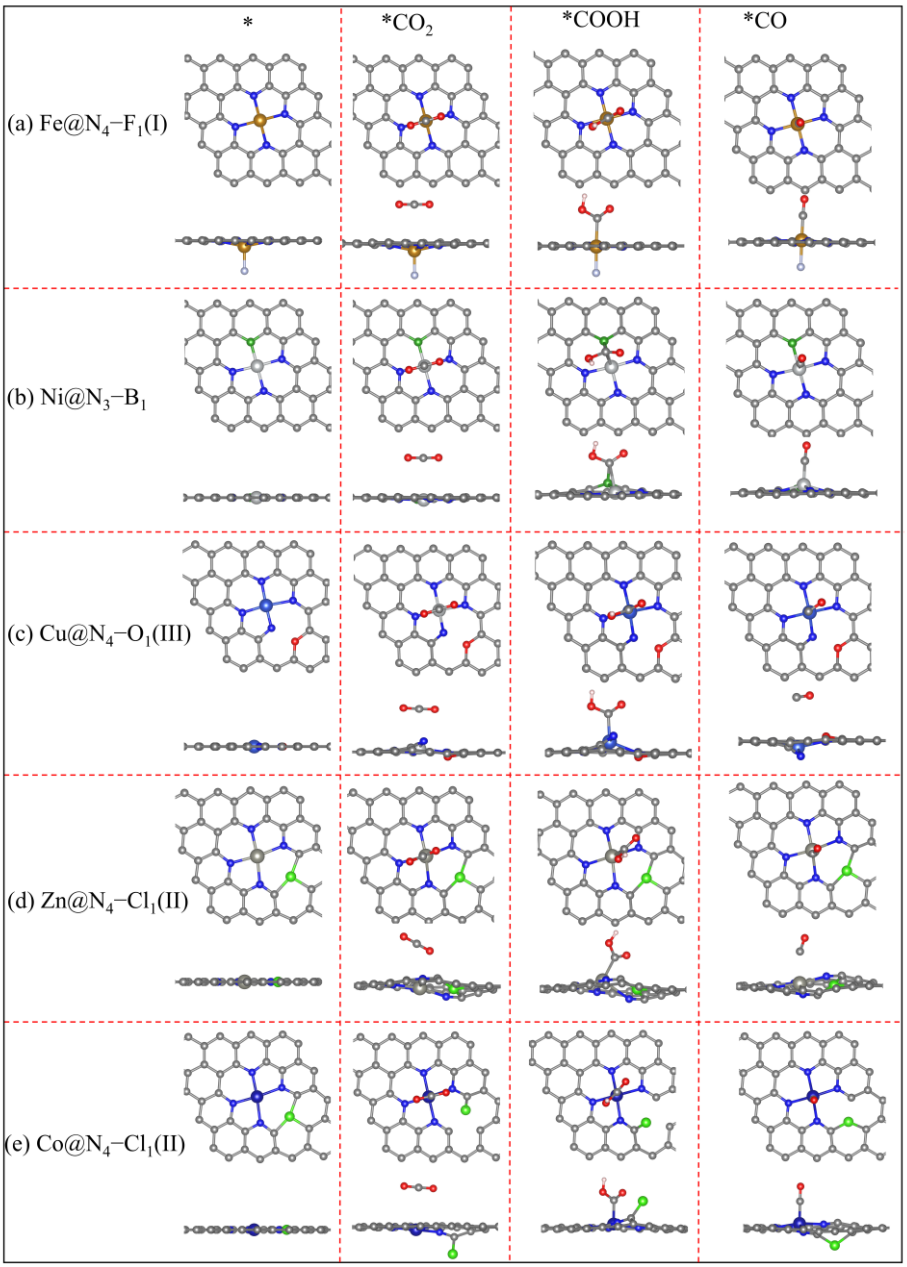

Figure S5. Charge density difference of *COOH and *CO adsorption on pristine TM@N_4, where the isosurface value is set to be 0.001 e/Bohr^3.

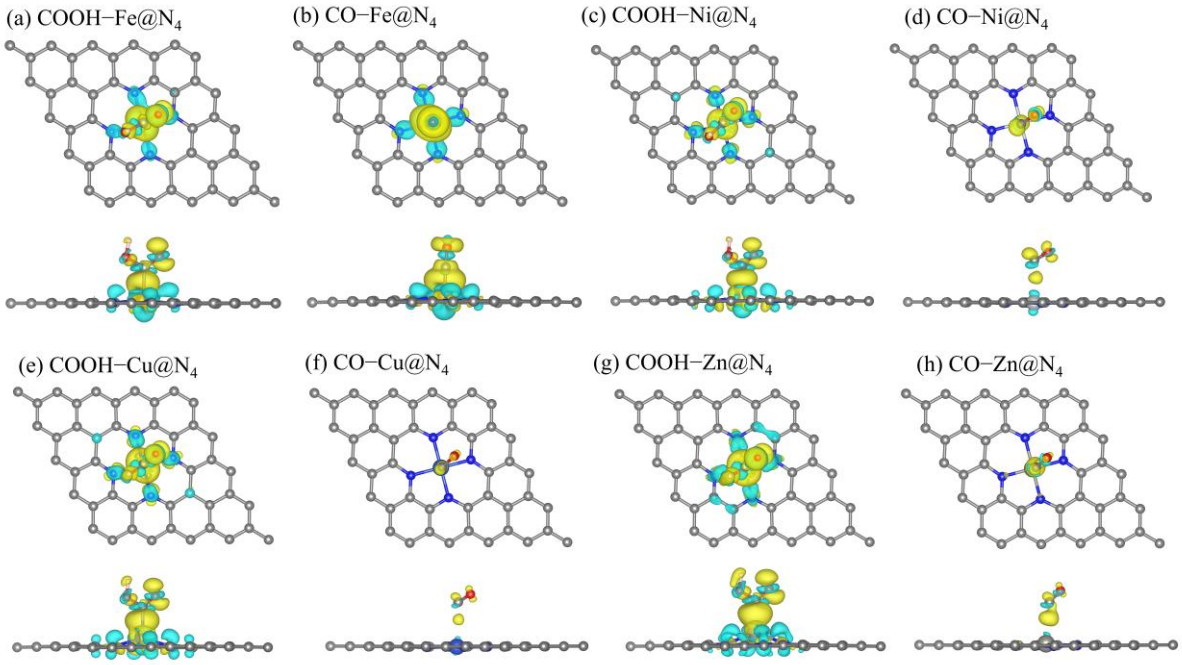

Appendix G – Paper VII

Breaking scaling relations for highly efficient electroreduction of CO_2 to CO on atomically dispersed heteronuclear dual-atom catalyst

S. Lu, M. Mazur, K. Guo, D. C. Stoian, M. Gu, W. M. Wakshum and Z. Yu

(submitted)

Breaking scaling relations for highly efficient electroreduction of CO_2 to CO on atomically dispersed heteronuclear dual-atom catalyst

Song Lu[a], Michal Mazur[b]*, Kun Guo[c], Dragos Constantin Stoian[d], Minfen Gu[e], Wakshum Mekonnen Tucho[f], Zhixin Yu[a]*

[a]Department of Energy and Petroleum Engineering, University of Stavanger, 4036 Stavanger, Norway

[b]Department of Physical and Macromolecular Chemistry, Faculty of Science, Charles University, 12843 Prague 2, Czech Republic

[c]School of Materials Science and Engineering, Huazhong University of Science and Technology, 430074 Wuhan, China

[d]Swiss-Norwegian Beamlines, European Synchrotron Radiation Facility, 38043 Grenoble Cedex 9, France

[e]Center for Analysis and Testing, Nanjing Normal University, Nanjing 210023, China

[f]Department of Mechanical and Structural Engineering and Material Science, University of Stavanger, 4036 Stavanger, Norway

*Corresponding author:

Dr. Michal Mazur

E-mail address: michal.mazur@natur.cuni.cz

Department of Physical and Macromolecular Chemistry, Faculty of Science, Charles University, 12843 Prague 2, Czech Republic

Prof. Zhixin Yu

E-mail address: zhixin.yu@uis.no

Department of Energy and Petroleum Engineering, University of Stavanger, 4036 Stavanger, Norway

Tel: +47 51832238

Abstract: Conversion of CO_2 into value-added products by electrocatalysis provides a promising way to mitigate energy and environment problems. However, it is greatly limited by the scaling relationship between the adsorption strength of intermediates. Herein, Mn and Ni single-atom catalysts (SACs), homonuclear dual-atom catalysts (DACs), and heteronuclear DAC were synthesized. Aberration-corrected annular dark-field scanning transmission electron microscopy (ADF-STEM) and X-ray absorption spectroscopy (XAS) characterization uncovered the existence of Mn-Ni pair in Mn-Ni DAC. X-ray photoelectron spectroscopy (XPS) and X-ray absorption near-edge spectroscopy (XANES) revealed that Mn donated electrons to Ni atom in Mn-Ni DAC. Consequently, Mn-Ni DAC displayed the highest CO Faradaic efficiency of 98.7% at -0.7 V versus reversible hydrogen electrode (vs. RHE) with CO partial current density of 16.8 mA cm^{-2}. Density functional theory (DFT) calculations disclosed that the scaling relationship between binding strength of intermediates was broken, resulting in superior performance for ECR to CO over Mn-Ni-NC catalyst.

Keywords: Electrocatalytic CO_2 reduction, dual-atom catalysts, DFT calculations, electron interaction, breaking scaling relationship

1. Introduction

Electrochemical CO_2 reduction reaction (ECR) driven by green electricity is one of the most promising ways to achieve carbon neutrality and sustainable development. [1-3] Among possible reaction pathways, ECR to CO through two proton-electron pairs transfer is one of the most practical targets due to high selectivity and mild reaction condition. [4,5] Moreover, CO is a key feedstock for a number of industrial processes to produce various fuels and chemicals. [6,7] Despite substantial efforts, this process is still limited by high energy barrier for CO_2 activation, sluggish reaction kinetics and inevitable competitive hydrogen evolution reaction (HER). [8-10]

In the past decade, there has been widespread research on single-atom catalysts (SACs) for electrocatalysis, owing to their high atom-utilization efficiency, unique electronic properties, and well-defined active sites. [11-16] Especially, atomically dispersed transition metal embedded on nitrogen doped carbon (TM-N-C) have demonstrated good activity for ECR to CO. [17-19] However, the single active center makes it difficult to break the constraint of scaling relationship between the adsorption energies of intermediates due to the complicated multiple proton-coupled electron transfer. The overall reaction process for CO generation includes (I) $CO_2 + (H^+ + e^-) \rightarrow$ *COOH, (II) *COOH + $(H^+ + e^-) \rightarrow$ *CO + H_2O and (III) CO* $\rightarrow$ CO + *. [20,21] It has been reported that Ni and Cu SACs generally exhibit excellent CO desorption property and suppress HER, but suffer from the slow *COOH formation step. [22,23] In contrast, Fe and Co SACs to have low energy barrier for the first proton coupled electron transfer step, but *CO desorption can be difficult due to the strong affinity of

CO to Fe and Co. [24,25] Therefore, the performance of ECR to CO on these SACs is restricted by the binding of *COOH and *CO that are either too weak or too strong. It is well known that the geometric and electronic structures of the active sites are closely correlated with the catalytic performance. [26-29] Thus, regulating structural and electronic properties of SAC active center is a potential strategy to tune the binding strength between the reaction intermediates and metal active center to achieve high ECR to CO activity.

Constructing heteronuclear dimer sites to form dual-atom catalysts (DACs) is an efficient way to modify the coordination environment and the electronic properties of the SAC active centers. For instance, heteronuclear DACs such as Fe-Ni, Ni-Cu, Zn-Ni and Co-Cu DACs anchored on nitrogenated carbon exhibited superior activity for ECR to CO due to the lower energy barrier for the formation of *COOH and desorption of *CO. [30-33] In another study, Mn-Ni dual-atoms have been reported to modify the electronic structure of Ni active center, which could tune the binding strength of intermediates and facilitate oxygen evolution reaction (OER). [34] Very recently, ECR to CO were attempted on homonuclear DACs, including Ni-Ni and Mn-Mn, Pd-Pd and Zn-Zn, among which Ni-Ni exhibited Faradaic efficiency for CO generation (FE_{CO}) of 99%. [35] *In situ* characterization combined with theoretical calculation revealed that Ni dual-atom sites could promote *OH adsorption, which trigged electron accumulation at the active centers. As a result, the kinetic barriers of *COOH and *CO desorption were reduced.

Among 3d transition metal-based SACs, Mn SACs displayed weak *CO desorption capability, resulting in low activity for ECR to CO. [36] Meanwhile, the Mn-Ni DAC has been demonstrated great performance in OER because of Mn tuning the electron structure of Ni atom. [34] Therefore, it is intriguing to explore the structural transformation from SAC to DAC during ECR, and the function of the dual atom pairs. This could be achieved by performing a systematic study on SACs, homonuclear DACs and heteronuclear DACs for a specific catalysts system, and the transition of the active sites.

In this work, Ni SAC (Ni-NC), Mn SAC (Mn-NC), Ni-Ni DAC (Ni-Ni-NC), Mn-Mn DAC (Mn-Mn-NC) and Mn-Ni DAC (Mn-Ni-NC) were synthesized by a facile method. The catalyst with Mn-Ni atom pair exhibiting outstanding catalytic activity and selectivity, achieving a maximum FE_{CO} of 98.7% at the potential of -0.7 V (vs. RHE) with a CO partial current density of 16.8 mA cm^{-2}, outperforming the homonuclear Ni-Ni DACs and Ni SACs. It also shows excellent stability in the long-time durability test. Aberration-corrected annular dark-field scanning transmission electron microscopy (ADF-STEM) demonstrated the presence of dual-atom pairs in the DACs. Extended X-ray absorption fine structure (EXAFS) characterization uncovered that non-bridged (metal-metal)N_6 is the most possible coordination in DACs. X-ray photoelectron spectroscopy (XPS) and X-ray absorption near-edge spectroscopy (XANES) confirmed electron transfer from Mn to Ni atom in Mn-Ni DAC. Density functional theory (DFT) calculations uncovered the structural evolution of active sites for different intermediates, in which Mn atom could selectively bond with intermediates during the ECR to CO.

Mn and Ni atoms work synergistically for *COOH formation, which is not possible for the SACs. Then Ni atom works as sole adsorption site for *CO adsorption, which is not observed for the Mn-Mn and Ni-Ni homonuclear DACs. Therefore, for the first time, we disclosed that the highly efficient ECR to CO on heteronuclear DACs is attributed to the electron interaction of Mn-Ni atom pair, which could break the scaling relationship of adsorption energies of intermediates.

2. Results and discussion

2.1 Electrocatalysts characterization

Mn-NC, Ni-NC, Mn-Mn-NC, Ni-Ni-NC, and Mn-Ni-NC catalysts were prepared by facile ion-adsorption and pyrolysis treatment. Homonuclear DACs were synthesized through co-pyrolysis of metal salts and chelating agent complexes adsorbed on carbon carrier mixed with N sources under 800 °C. Mn^{2+} and Ni^{2+} were selected as metal precursors. Carbon black was employed as carbon substrate due to the low cost and excellent conductivity. Citric acid and dicyandiamide acted as chelating agent and N source. Heteronuclear DACs and SACs were fabricated through a similar procedure but with addition of ammonia solution in the first step. The formation mechanism of homonuclear DACs has been reported recently, in which Ni atoms were captured by the double vacancies of the carbon framework during pyrolysis. [35]

The crystal structures of the five catalysts were verified by powder X-ray diffraction (XRD) and Raman spectroscopy analyses. As shown in Figure S1a in the Supporting Information (SI), the five catalysts all present the same diffraction patterns. Two characteristic peaks located around 24.9° and 43.3° can be assigned to the (002) and

(001) planes of graphite with low crystallinity. Besides, no peaks attributable to metal or metallic compounds are identifiable, indicating that the metal atoms are possibly dispersed atomically in the carbon matrix.

Figure S1b presents the Raman spectroscopy of the five electrocatalysts, which exhibits two vibrational bands of graphite at around 1343 cm^{-1} (D band) and 1594 cm^{-1} (G band), corresponding to the defect and graphitic sp^2-hybridized carbon. [37,38] The ratios between D and G bands of the catalysts range from 1.03 to 1.09, suggesting similar graphitization degree and the presence of defects such as vacancies, edge and non-hexagonal rings. [39,40]

The textural properties of the electrocatalysts were investigated by N_2 physisorption analyses. As illustrated in Figure S2, the isotherms of the five catalysts exhibited sharp adsorption under relative pressures higher than 0.40 accompanied with obvious hysteresis loop, which can be attributed to the dominant mesopores and is further confirmed by the pore size distributions. The Brunauer-Emmett-Teller (BET) surface area of Mn-NC, Ni-NC, Mn-Mn-NC, Ni-Ni-NC, and Mn-Ni-NC catalysts are 890, 987, 854, 964, and 935 $m^2 g^{-1}$, respectively (Table S1). The average pore diameters are also very close at around 4.9 nm, while the pore volumes vary very narrowly from 1.02 to 1.11 cm^3g^{-1}. Therefore, all catalysts exhibit large BET surface area and abundant mesopores, which are beneficial for mass transfer and accessible active sites. It is worth emphasizing that the differences on structure properties of the five catalysts are insignificant, implying that the performance of ECR to CO over the five electrocatalysts can be exclusively ascribed to the intrinsic activities of the catalysts.

TEM characterization shows that the catalysts in general exhibit carbon pellets with a diameter of approximately 50 nm (Figure 1a). The high-resolution TEM reveals distorted short-range graphitic stripes with wrinkles and interlaces, suggesting the presence of structural defects in the carbon material (Figure 1b and S4a-S7a). Besides, no aggregates of metallic nanoparticles could be observed. We further employed ADF-STEM to verify the atomically dispersed metal atoms. As exhibited in Figure 1c, Figure S3a and S4b-7b, evenly distributed bright spots could be observed on the carbon framework in the dark field for the Mn-Ni-NC catalyst. These dense bright dots with different brightness could be assigned to metallic Mn and Ni atoms because of the atomic number dependent contrast difference in the dark field. [41] Besides, the binding energy of Mn-Ni, Mn-Mn and Ni-Ni are -11.89, -9.21 and -11.40 eV, respectively. The formation energy of Mn-Ni, Mn-Mn and Ni-Ni are -10.28, -9.38 and -10.02 eV, respectively. These results demonstrate that the formation of Mn-Ni pair is preferable. Moreover, numerous neighboring spots marked with red rectangle were observed, indicating that Mn and Ni atoms present in the form of atom-pairs. Statistical analysis was performed for the Mn-Mn-NC, Ni-Ni-NC and Mn-Ni-NC DAC catalysts. In each sample, 100 dots were fixed and the distance from its the closest bright dots were measured. For the Mn-Ni-NC catalyst, 58% dual-atom Mn-Ni pairs were counted, while 42% Mn and Ni atoms were counted as isolated atoms. The distances of the adjacent spots are estimated to be around 0.24±0.01nm (Figure 1d). Similarly, 39% Mn-Mn atom pairs were found in Mn-Mn-NC, and 46% Ni-Ni atom pairs were observed for the Ni-Ni-NC catalyst. The distances between the adjacent Mn-Mn and Ni-Ni atoms

are both centered at around 0.23±0.01 nm (Figure S6c-S7c). Considering the great challenge to identify each atom by ADF-STEM, this statistic analysis can effectively figure out the distance of neighboring atoms. [41] In contrast, for the Mn-NC and Ni-NC SAC catalysts, isolated Mn and Ni atom can be easily observed, even though some Mn-Mn and Ni-Ni atom pairs are also present. Furthermore, energy-dispersive X-ray spectroscopy (EDS) shows that the in the Mn-Ni-NC catalyst, C, N, Mn and Ni elements are homogeneously distributed (Figure 1e-i), which is also apparent for all other electrocatalysts (Figure S4c-f, S5c-f, S6d-g and S7d-g). Therefore, it is fair to conclude that Mn-NC and Ni-NC are SACs, while Mn-Mn-NC, Ni-Ni-NC and Mn-Ni-NC are DACs.

X-ray photoelectron spectroscopy (XPS) was carried out to investigate the chemical species and element states of Mn, Ni, N and C in the electrocatalysts. As displayed in Figure 2a, the high-resolution N 1s spectra can be deconvoluted into five species: pyridinic (Pyri-N), metallic (Metal-N), pyrrolic (Pyrr-N), graphitic (Grap-N) and oxidized (Oxid-N), with corresponding binding energy of 398.3, 400.3, 401.4 and 404.5 eV, respectively. [42-45] Notably, the peak at 399.1 eV can be assigned to porphyrin-like metal-N coordination structure, which demonstrates that metal atoms are coordinated with N atoms in the carbon framework. [46,47] In particular, the existence of Pyri-N in carbon substrates plays a significant role in anchoring and stabilizing single metal atoms as well as promoting the electrocatalytic activity. [48] The Pyri-N concentration is the lowest for the Mn-Ni-NC catalyst, while its metal-N concentration is the highest among the five electrocatalysts. On the other hand, the concentrations of

Pyrr-N, Grap-N and Oxid-N did not show obvious differences (Table S2). The results indicate that most Mn and Ni atoms prefer to bond with Pyri-N. Moreover, the binding energy of Pyri-N in DACs shows slight downshift in comparison with that in SACs, while the binding energies of metal-N of DACs are similar. Therefore, the electronic structures of SACs and DACs are different. High resolution Mn-2p spectra in Figure 2b shows that the Mn-$2p_{3/2}$ peaks of Mn-NC (640.6 eV), Mn-Mn-NC (640.3 eV) and Mn-Ni-NC (640.5 eV) are located between Mn^0 (638.7 eV) and Mn^{2+} (641.4 eV). [49] The Ni-$2p_{3/2}$ peaks of Ni-NC (855.7 eV), Ni-Ni-NC (855.6 eV) and Mn-Ni-NC (855.5 eV) are located between Ni0 (852.5 eV) and Ni^{2+} (856.0 eV) (Figure 2c). [50,51] Therefore, Mn and Ni species probably both have an oxidation state between 0 and +2. It is worth noting that the binding energies of Mn-$2p_{3/2}$ in Mn-Mn-NC and Mn-Ni-NC exhibit negative shift in comparison to the Mn-NC catalyst. Similarly, the binding energies of Ni-$2p_{3/2}$ in Ni-Ni-NC and Mn-Ni-NC also show a negative shift compared with Ni-NC. Consequently, the oxidation states of Mn and Ni atoms decreased when atom pairs are formed in DACs. Obviously, when the concentration of Metal-N decreases, less electron is donated from metal to coordinated N atoms. In particular, the binding energies of Mn-$2p_{3/2}$ and Ni-$2p_{3/2}$ in Mn-Ni-NC catalyst are more positive and negative than that of Mn-$2p_{3/2}$ in Mn-Mn-NC, and Ni-$2p_{3/2}$ in Ni-Ni-NC, respectively. Consequently, there are apparent electron transfers between Mn and Ni in Mn-Ni-NC, in which Ni atom with higher electronegativity attracted electrons from the paired Mn atom. Therefore, XPS characterization evidenced that when atom pairs are formed,

there are valence changes in the homonuclear DACs and electron transfer in the heteronuclear DAC.

X-ray adsorption spectroscopy (XAS) was conducted to reveal the detailed electronic structure and coordination environment of the metal active centers. Figure 3a and b depicted XANES of Mn and Ni atoms of different catalysts, reference Mn and Ni metal foils, and metal phthalocyanine (Mn-Pc and Ni-Pc). In the Mn K-edge XANES spectra, the near-edge absorption

energies of Mn-NC, Mn-Mn-NC and Mn-Ni-NC are located between those of Mn foil and Mn-Pc, confirming that the oxidation states of Mn are between 0 and +2. Besides, the near-edge absorption energies of Mn atom in Mn-Ni-NC catalyst shows slightly positive shift compared with that of Mn-Mn-NC, indicating that the valence state of Mn atom increased. Similarly, Ni K-edge XANES spectra of Ni-NC, Ni-Ni-NC and Mn-Ni-NC are located between those of Ni foil and Ni-Pc, confirming that the valence states of Ni are also between 0 and +2. In comparison with Ni-Ni-NC, the near-edge absorption energies of Ni in Mn-Ni-NC catalyst show slight negative shift, demonstrating the decrease of the valence state of Ni. Consequently, Mn donated electrons to Ni in the heteronuclear Mn-Ni-NC DAC, in agreement with XPS analysis.

Figure 3c and d display the Fourier transform (FT) of k^3-weighted EXAFS of Mn and Ni K-edge in the R-space. The Mn K-edge spectra shows a major peak at around 1.5 Å, assigned to the Mn-N coordination in the Mn-NC, Mn-Mn-NC and Mn-Ni-NC catalysts. A dominant peak at around 1.3 Å for the Ni K-edge spectra of Ni-NC, Ni-Ni-NC and Mn-Ni-NC catalysts is associated with the Ni-N bonding. The Mn-Mn (2.3 Å)

and Ni-Ni (2.1 Å) bonds are characteristic of Mn and Ni foils. However, the metal-metal bonds are absent in the Mn-NC and Ni-NC catalysts, which confirms atomically dispersed Ni and Mn atoms. Remarkably, peaks at 2.3 and 2.5 Å in the Mn K-edge spectra can be identified for the Mn-Mn-NC and Mn-Ni-NC catalysts, which can be assigned to Mn-Mn and Mn-Ni coordination, respectively. Similarly, peaks at 2.2 Å and 2.5 Å in the Ni K-edge spectra of Ni-Ni-NC and Mn-Ni-NC catalysts are attributed to Ni-Ni and Mn-Ni coordination. Therefore, the FT-EXAFS analysis demonstrated the formation of atom pairs for all three DACs.

Wavelet transform (WT) EXAFS (WT-EXAFS) oscillations was also conducted to discriminate the backscattering atoms and obtain high resolutions in both K and R spaces. As displayed in Figure S8, the WT-EXAFS contour plot of Mn foil shows a strong signal with maximum intensity at around 5.1 $Å^{-1}$ of the Mn-Mn contributions. However, this signal is absent for the Mn-NC and Mn-Ni-NC catalysts but is slightly visible at around 7.5 $Å^{-1}$ for the Mn-Mn-NC catalyst. Similarly, WT-EXAFS of Ni foil shows a prominent feature centered around 7.0 $Å^{-1}$, which is not found for the Ni-NC and Mn-Ni-NC catalysts but visible at 6.8 $Å^{-1}$ for the Ni-Ni-NC catalyst. Similar to the WT-EXAFS contour plots of Mn-Pc, the spectra of Mn-NC, Mn-Mn-NC, Mn-Ni-NC also show strong features at 4.8 $Å^{-1}$, which can be attributed to the Mn-N coordination. Meanwhile, a weak signal at 6.0 $Å^{-1}$ can be observed for the Mn-Ni-NC catalyst, indicating the Mn-Ni coordination. For the Ni WT-EXAFS contour plots of Ni-NC, Ni-Ni-NC and Mn-Ni-NC electrocatalysts, a maximum intensity at 4.0 $Å^{-1}$ due to the Ni-N contribution can be observed (Figure 3e). A weak feature at 6.1 $Å^{-1}$ is also attributed

to the Mn-Ni bonding. It is worth noting that the different models of atomic vibration could cause the difference of signal intensity. [32] The WT-EXAFS analysis demonstrated that Mn and Ni atoms dispersed atomically on the N doped carbon substrate, and the existence of Mn-Mn, Ni-Ni and Mn-Ni bonding for the DACs.

To elaborate the structures of the catalysts, theoretically optimized metal-N configurations based on DFT calculations and fitted-EXAFS curves were constructed. As show in Figure 3f-i and S9ab, the fitted results in R-space and K-space match well with the experimental spectra. The detailed fitting parameters, e.g., metal-N coordination numbers, metal-N path length are summarized in Table S3. The average metal-N coordination numbers are 4, 4, 3.5, 3.5 and 3.5 for Mn-NC, Ni-NC, Mn-Mn-NC and Ni-Ni-NC and Mn-Ni-NC catalysts, suggesting that Mn and Ni SACs have the usual metal-N_4 center, while the DACs exhibit metal-N_3 configurations. The fitting parameters for Ni-Ni, Mn-Mn and Mn-Ni interaction paths indicate that the average coordination number of metal-metal is one in the DACs (Figure S9c-e). More importantly, the average bond lengths of Mn-Mn, Ni-Ni and Mn-Ni are 2.40, 2.35 and 2.40 Å, consistent with ADF-STEM results. Therefore, non-bridged (Mn-Mn)N_6, (Ni-Ni)N_6 and (Mn-Ni)N_6 embedded carbon framework were successfully synthesized for DACs, as evidenced by the combination of EXAFS spectra, fitted curves and DFT calculations.

2.2 Electrocatalytic activity test

The ECR performance of the samples was evaluated in a custom-made H-cell with three electrodes system and CO_2-saturated 0.5 M $KHCO_3$ electrolyte by linear sweep

voltammetry (LSV) method. As illustrated in Figure 4a, the Mn-Ni-NC electrocatalyst exhibits the largest current density at all applied potentials. It also exhibits an enhanced current response and a lower onset potential under CO_2 atmosphere than under Ar (Figure 4b), indicating the occurrence of ECR. The potentiostatic electrolysis was conducted under different potentials from -0.3 to -1.0 V versus reversible hydrogen electrode (vs. RHE). The gaseous and liquid products were detected by online gas chromatography (GC) and ^{1}H nuclear magnetic resonance (NMR). As displayed in Figure 4c, ECR to CO on Mn-Ni-NC, Ni-Ni-NC, Ni-NC catalysts occurred under -0.4 V (vs. RHE), showing the lower onset potential for ECR to CO. With the increase of the applied potential, the Mn-Ni-NC catalyst reaches the maximum FE_{CO} of 98.7% at the potential of -0.7 V (vs. RHE). Besides, FE_{CO} is higher than 90% between -0.5 and -0.9 V (vs. RHE), exhibiting wide potential windows. The Ni-Ni-NC and Ni-NC catalysts present the highest FE_{CO} of 91.6% and 87.8% at the potential of -0.8 V (vs. RHE).

The Ni-Ni-NC shows slower decay of FE_{CO} than the Ni-NC catalyst with the increase of potential, also implying a wide potential window for highly efficient ECR to CO. It has been reported that the formation of *COOH on Ni site is difficult due to a large energy barrier. [52,53] Therefore, the enhanced ECR performance on Ni-Ni-NC could be attributed to the decrease of energy barrier for the formation of *COOH on Ni-Ni dual sites. The Mn-Mn-NC and Mn-NC catalysts exhibit low FE_{CO} at all applied potentials. Even though forming Mn-Mn atom pairs also improved the ECR performance of Mn-NC, the FE_{CO} of Mn-Mn-NC is still less than 40%. This can be

explained by the strong adsorption of *CO on Mn site. The improvement of ECR performance on Mn-Mn-NC demonstrates that Mn-Mn site may moderate *CO adsorption to some certain extent. Nevertheless, the competing hydrogen evolution reaction on Mn and Mn-Mn-NC catalyst is dominating, as shown in Figure 4d. Remarkably, the ECR performance to CO on Mn-Ni DAC is greatly improved compared to the Mn and Ni SACs, implying that forming heteronuclear atom pairs could facilitate either *COOH formation or *CO desorption. This could be further ascribed to the moderate binding energies for intermediates due to the electron interaction between the heteronuclear atoms. For the Mn-Ni-NC catalysts, only CO and H_2 products were identified as the products at all applied potentials, with a total FE_{CO} of around 100%. No liquid products were detected, as evidenced by ^1H NMR (Figure S10).

The CO partial current densities on the five catalysts were also calculated (Figure. 4e). For the Mn-Ni-NC catalyst, it increased with the applied potential, reaching 16.8 mA cm^{-2} at -0.7 V (vs. RHE), which is 1.31, 1.62, 21.3 and 42.2 times higher than that of Ni-Ni-NC, Ni-NC, Mn-Mn-NC and Mn-NC catalysts. The turnover frequency (TOF) of the five catalysts was calculated to uncover the intrinsic activity of the active site [33]. As illustrated in Figure 4f, the TOF on the Mn-Ni-NC catalyst is the highest at 2859 h^{-1} at -0.7 V (vs. RHE), indicating its high intrinsic activity.

Electrochemical active surface areas (ECSA) play a significant role in ECR activity, which is calculated by measuring double layer (D-L) capacitance (Figure 4g and Figure S11). The Mn-Ni-NC catalyst has a capacitance of 53.3 mF cm^{-2}, slightly higher than

the other catalysts. As a result, the ECSA for Mn-Ni-NC, Ni-Ni-NC, Ni-NC, Mn-Mn-NC and Mn-NC catalysts were 1332, 1195, 1120 and 980, 927 cm^2_{ECSA}, demonstrating that the Mn-Ni atoms pair could increase the ESCA. Furthermore, the Tafel slopes on the five samples were compared to disclose the kinetics for CO generation (Figure 4h). An improved Tafel slope of 168 mV dec^{-1} for CO generation on the Mn-Ni-NC catalyst is obtained, attributed to the synergistic effect of Mn-Ni pair. Additionally, the small Tafel slope also indicates that the rate-limiting step of ECR to CO on the Mn-Ni-NC catalyst is the first protonation of CO_2. [54, 55] Overall, the DAC catalysts show lower Tafel slope than their SAC counterparts. Dual atom pairs especially with heteronuclear atoms, could effectively reduce the Tafel slope, which contributes to a more kinetically favorable ECR to CO. Electrochemical impedance spectroscopy (EIS) indicated that Mn-Ni-NC catalyst has the smallest charge-transfer resistance among the five catalysts (Figure S12), implying fastest charge transfer. Therefore, the heteroatomic pairs could act synergistically, which outperforms homoatomic pairs and SACs in ECR to CO. The Mn-Ni-NC catalyst in this study outperformed most of the recently reported SACs and DACs applied for ECR to CO (Figure 4i and Table S4). Finally, continuous potentionstatic activity test for 24 h demonstrated that the Mn-Ni-NC catalyst exhibited stable current density and FE_{CO} with negligible decay under the potential of -0.7 V (vs. RHE) (Figure 4j).

2.3 DFT simulation

To uncover the activity origin, DFT calculations were employed based on the EXAFS fitting results. The distribution of electron density on N and coordinated metal atoms of

catalysts are correlated with intrinsic activity and ECR selectivity. [30] After forming Mn-Mn, Ni-Ni and Mn-Ni atom pairs, the electron density around the N, Mn and Ni atom exhibit apparent changes (Figure S13). For instance, more electrons accumulated around the metal atoms of homonuclear atom pair. Charge transfer between Mn and Ni atoms can also be observed, indicating electron interactions after forming atom pairs. Moreover, Bader charge analysis demonstrated that the Mn and Ni atoms always act as electron-donor in the single atom center, homonuclear atom pair and heteronuclear atom pair. The amount of the lost electrons for Mn atom decreased first and then increased, while it always decreased for Ni atom (Figure 5a). This opposite trend for Mn and Ni atom in the change from homonuclear to heteronuclear pair discloses electron transfer from Mn to Ni atom, which vividly show the electron interaction between Mn and Ni atom. Therefore, the valence state of Mn and Ni atoms show increase and decrease, consistent with XPS and XANES analysis. Consequently, building dual-atom pair can regulate electron density of the active sites in different ways, which directly affects the binding strength of intermediates with active sites.

ECR to CO consists of three steps, i.e., the formation of *COOH, *CO generation, and the desorption of CO. The Gibbs free energy diagrams of each step at U = 0 V (vs. RHE) were calculated in Figure 5b. As expected, Mn and Ni SACs exhibits high energy barrier for *COOH production (1.83 eV) or *CO desorption (0.75 eV), resulting from the binding strength between intermediate and metal site. After forming homonuclear atom pair, the energy barrier for *COOH generation on the Ni-Ni-NC catalyst decreased greatly to 0.70 eV. For the Mn-Mn-NC DAC, although the free energy barrier

for the formation of *COOH decreased, the desorption of *CO deteriorated remarkably with an energy barrier of 1.88 eV. These changes can be explained by the coordination effect of the dual metal atoms. For the SACs, only one C-metal bond will form for *COOH generation. However, when the dual atom pairs are formed, the C atom of intermediates could bond with two metal atoms with two C-metal bonds. Consequently, the binding strength of intermediates to active sites increased. Notably, as the *COOH formation on Mn-Mn site is energy favorable, the rate-limiting step will become *CO desorption from Mn-Mn site, which is controlled by the thermodynamic process. Thus, Mn-Mn sites are potentially passivated by strongly adsorbed *CO, in agreement with other studies. [21,33] An additional active site could be possible for CO_2 activation on CO-adsorbed Mn-Mn site (CO*Mn-Mn-NC). The free energy barrier of CO desorption on the site decreased remarkably (0.54 eV), which promotes *CO desorption from the Mn site. The results proved that the ECR performance is improved after incorporating the second homonuclear atom into SACs, in line with experimental observations. For the Mn-Ni-NC catalyst, the energy barrier for *COOH formation on Ni and Mn sites are 0.40 and 0.51 eV, lower than of Mn, Ni, CO*Mn-Mn, and Ni-Ni catalysts. However, the free energy barrier for *CO desorption from Ni site is only 0.39 eV, much lower than that of Mn site (0.85 eV). Although DACs may offer potential active sites for C-C coupling, it is not considered in this study because of difficult kinetics.

As depicted in Figure 5c, the free energy change for *COOH formation and *CO desorption was built to reveal the scaling relationship of intermediates. Unexpectedly, the scaling relationship of binding strength of intermediates on Mn-Ni DAC was broken.

This can be explained by that C atom of *CO prefer to bond with Ni atom on Ni site, while the C atom of *CO will bond with both Mn and Ni atom on Mn site. In other word, during ECR to CO, the Mn atom can bind the intermediates selectively. For the CO_2 protonation, Mn and Ni atoms act together to accelerate the *COOH formation, which is not possible in Mn and Ni SACs. For the *CO desorption, Mn atom will not bond with *CO, which promotes the CO generation (Figure 5d). However, this cannot be observed in Mn and Ni homonuclear DACs (Figure S14). Therefore, Mn-Ni-NC catalysts with the lowest energy barriers for both *COOH formation and *CO desorption, due to the synergistic effect of Mn and Ni atoms, which can selectively interact with intermediates. As a result, the restriction of scaling relationship on binding strength of intermediates was broken on the Mn-Ni-NC catalyst, resulting in the superior performance of ECR to CO.

As HER is the main competing reaction, the free energy changes of HER on the five catalysts were also calculated. As illustrated in Figure S15a, Ni-NC shows the largest energy barrier of 1.40 eV for *H generation, while both Ni-Ni-NC and Mn-Ni-NC shows an energy barrier of around 0.12 eV. Therefore, an excellent *H generation performance possibly boosts proton transfer, accelerating the ECR to CO process. The selectivity of ECR to CO against HER is evaluated by calculating the difference of limiting potentials between ECR and HER ($U_L(CO_2)$-$U_L(H_2)$), where a more positive value of $U_L(CO_2)$-$U_L(H_2)$ indicates higher ECR selectivity to CO. As depicted in Figure S15b, Mn-Mn-NC and Ni-Ni-NC show more positive values of $U_L(CO_2)$-$U_L(H_2)$ than their SACs counterparts, confirming that DACs have higher ECR selectivity.

Heteronuclear Mn-Ni-NC presents the most positive $U_L(CO_2)$-$U_L(H_2)$ of -0.29 eV, demonstrating its superior ECR selectivity to CO by suppressing HER reaction.

To disclose the effects of electron structure on adsorption performance of intermediates, the crystal orbital Hamilton population (COHP) and integrated COHP (ICOHP) are employed to further study the interaction strength between active site and intermediates, in which a positive -COHP indicates bonding state, while a negative -COHP represents the anti-bonding state below Fermi energy. As shown in Figure 5e and f, more noticeable anti-bonding state appears in CO passivated Mn-Mn-NC catalyst (CO*Mn-Mn-NC) in comparison with Mn-NC, demonstrating weak CO adsorption on the CO*Mn-Mn-NC catalyst. This is also confirmed by the larger ICOHP (-0.48 eV) of CO passivated Mn-Mn-NC catalyst. *COOH cannot adsorb stably on single Ni sites due to the existence of anti-bonding states (Figure 5g). After introducing the second Ni atom, the anti-bonding states almost disappear, implying an improvement of binding strength between Ni and *COOH (Figure 5h). Despite that the ICOHP of C-Ni over Ni-NC is larger that of C-Ni over Ni-Ni-NC, C will bond with two Ni atoms, which increase the binding strength compared with single Ni atom. Finally, we compared the adsorption strength of C and O atoms of *COOH to Ni and Mn atom of the Mn-Ni-NC catalyst (Figure 5i and j). Remarkedly, both C and O atoms could bind with Ni and Mn atom strongly, as demonstrated by the absence of anti-bonding states. Therefore, *COOH generation was enhanced greatly, which endows Mn-Ni-NC with excellent ECR activity. Overall, it can be concluded that Mn atom donated more electron in Mn-Ni than the Mn-Mn atom pairs, causing higher valence state of Mn and stronger *CO

binding strength. However, the valence state of Ni atom decreased in Mn-Ni compared with the Ni-Ni center, resulting in superior *COOH binding strength. Consequently, electron interaction between Mn and Ni atom in Mn-Ni-NC catalyst result in moderate and low valence state for Mn and Ni atom respectively, which directly influenced the binding strength of intermediate. Meanwhile, the selective adsorption of intermediates on active center contribute to breaking the scaling relationship, which greatly improve the performance of ECR to CO.

3. Conclusion

A series of SACs and DACs including Mn-NC, Mn-Mn-NC, Ni-NC, Ni-Ni-NC and Mn-Ni-NC electrocatalysts were systematically studied for ECR to CO to reveal the evolution of the activity. ADF-STEM and EXAFS characterizations demonstrated the presence of atom pairs in DACs, displaying non-bridged (metal-metal)N_6 coordination. Electron transfer from Mn to Ni atom as evidenced for the heteronuclear Mn-Ni-NC catalyst through XPS and XANES. The Mn-Ni-NC catalyst displayed the highest FE_{CO} of 98.7% at the potential of -0.7 V (vs. RHE) with CO partial current density of 16.8 mA cm^{-2}, achieving a TOF of 2859 h^{-1}. DFT calculations disclosed that Mn atoms with high oxidation state resulted in strong CO binding strength, while the low valence state of Ni atom contributed to superior *COOH binding strength, which promotes ECR to CO. More importantly, the *COOH or *CO intermediates could change their binding sites during ECR to CO. The C and O atom of *COOH prefer to bind with Ni and Mn atoms, respectively, promoting CO_2 protonation. Only Ni atom will bind with C atom of *CO, thus accelerating CO generation. However, the change in binding sites is only

observed for heteronuclear DAC, because the heteronuclear metal atom pair could break the scaling relationship of adsorption strength of intermediates.

Acknowledgments

The computations were performed on resources provided by UNINETT Sigma2 - the National Infrastructure for High Performance Computing and Data Storage in Norway. M.M. would like to acknowledge the Czech Science Foundation for the ExPro project (19–27551X) and OP VVV "Excellent Research Teams", project No. CZ.02.1.01/0.0/0.0/15_003/0000417– CUCAM.

References

[1] M.B. Ross, P. De Luna, Y. Li, C.T. Dinh, D. Kim, P. Yang, E.H. Sargent, Designing Materials for Electrochemical Carbon Dioxide Recycling, Nat. Catal. 2 (2019) 648-658.

[2] C. Xu, X. Zhi, A. Vasileff, D. Wang, B. Jin, Y. Jiao, Y. Zheng, S.Z. Qiao, Highly Selective Two-Electron Electrocatalytic CO_2 Reduction on Single-Atom Cu Catalysts, Small Structures 2 (2022) 2000058.

[3] Y. Zhu, X. Yang, C. Peng, C. Priest, Y. Mei, G. Wu, Carbon-Supported Single Metal Site Catalysts for Electrochemical CO_2 Reduction to CO and Beyond, Small 17 (2021) e2005148.

[4] S. Wei, Y. Wang, W. Chen, Z. Li, W. C. Cheong, Q. Zhang, Y. Gong, L. Gu, C. Chen, D. Wang, Q. Peng, Y. Li, Atomically Dispersed Fe Atoms Anchored on COF-Derived N-Doped Carbon Nanospheres as Efficient Multi-Functional Catalysts, Chem. Sci. 11 (2019) 786-790.

[5] M.G. Kibria, J.P. Edwards, C.M. Gabardo, C.T. Dinh, A. Seifitokaldani, D. Sinton, E.H. Sargent, Electrochemical CO_2 Reduction into Chemical Feedstocks: From Mechanistic Electrocatalysis Models to System Design, Adv. Mater. 31 (2019) e1807166.

[6] W. Zhou, K. Cheng, J. Kang, C. Zhou, V. Subramanian, Q. Zhang, Y. Wang, New Horizon in C_1 Chemistry: Breaking the Selectivity Limitation in Transformation of Syngas and Hydrogenation of CO_2 into Hydrocarbon Chemicals and Fuels, Chem. Soc. Rev. 48 (2019) 3193-3228.

[7] M.D. Porosoff, J.G. Chen, Trends in the Catalytic Reduction of CO_2 by Hydrogen Over Supported Monometallic and Bimetallic Catalysts, J. Catal. 301 (2013) 30-37.

[8] Q. Sun, C. Jia, Y. Zhao, C. Zhao, Single Atom-Based Catalysts for Electrochemical CO_2 Reduction, Chinese J. Catal. 43 (2022) 1547-1597.

[9] C. Chen, J.F. Khosrowabadi Kotyk, S.W. Sheehan, Progress toward Commercial Application of Electrochemical Carbon Dioxide Reduction, Chem-Us 4 (2018) 2571-2586.

[10] X. Tan, X. Sun, B. Han, Ionic Liquid-Based Electrolytes for CO_2 Electroreduction and CO_2 Electroorganic Transformation, Natl. Sci. Rev. 9 (2022) nwab022.

[11] S. Ji, Y. Chen, X. Wang, Z. Zhang, D. Wang, Y. Li, Chemical Synthesis of Single Atomic Site Catalysts, Chem. Rev. 120 (2020) 11900-11955.

[12] Y. Zhao, Z. Pei, X. Lu, D. Luan, X. Wang, X.W. Lou, Rationally Designed Nitrogen-Doped Carbon Macroporous Fibers with Loading of Single Cobalt Sites for Efficient Aqueous Zn-CO_2, Chem Catalysis 2 (2022) 1480-1493.

[13] Y. Pan, R. Lin, Y. Chen, S. Liu, W. Zhu, X. Cao, W. Chen, K. Wu, W. C. Cheong, Y. Wang, L. Zheng, J. Luo, Y. Lin, Y. Liu, C. Liu, J. Li, Q. Lu, X. Chen, D. Wang, Q. Peng, C. Chen, Y. Li, Design of Single-Atom Co-N_5 Catalytic Site: A Robust Electrocatalyst for CO_2 Reduction with Nearly 100% CO Selectivity and Remarkable Stability, J. Am. Chem. Soc. 140 (2018) 4218-4221.

[14] K. Jiang, S. Siahrostami, T. Zheng, Y. Hu, S. Hwang, E. Stavitski, Y. Peng, J. Dynes, M. Gangisetty, D. Su, K. Attenkofer, H. Wang, Isolated Ni Single Atoms in Graphene Nanosheets for High-performance CO_2 Reduction, Energ. Environ. Sci. 11 (2018) 893-903.

[15] W. Guo, X. Tan, J. Bi, L. Xu, D. Yang, C. Chen, Q. Zhu, J. Ma, A. Tayal, J. Ma, Y. Huang, X. Sun, S. Liu, B. Han, Atomic Indium Catalysts for Switching CO_2 Electroreduction Products from Formate to CO, J. Am. Chem. Soc. 143 (2021) 6877-6885.

[16] B. Qiao, A. Wang, X. Yang, L. F. Allard, Z. Jiang, Y. Cui, J. Liu, J. Li, T. Zhang, Single-Atom Catalysis of CO Oxidation Using Pt_1/FeO_x, Nat. Chem. 3 (2011) 634-641.

[17] W. Ju, A. Bagger, G. P. Hao, A. S. Varela, I. Sinev, V. Bon, B. Roldan Cuenya, S. Kaskel, J. Rossmeisl, P. Strasser, Understanding Activity and Selectivity of Metal-Nitrogen-Doped Carbon Catalysts for Electrochemical Reduction of CO_2, Nat. Commun. 8 (2017) 944.

[18] F. Yang, P. Song, X.Z. Liu, B.B. Mei, W. Xing, Z. Jiang, L. Gu, W.L. Xu, Highly Efficient CO_2 Electroreduction on ZnN_4-based Single-Atom Catalyst, Angew. Chem. Int. Ed. 2018, 130, 12483-12487.

[19] T. Zheng, K. Jiang, N. Ta, Y. Hu, J. Zeng, J. Liu, H. Wang, Large-Scale and Highly Selective CO_2 Electrocatalytic Reduction on Nickel Single-Atom Catalyst, Joule 3 (2019) 265-278.

[20] X. Wang, Z. Chen, X. Zhao, T. Yao, W. Chen, R. You, C. Zhao, G. Wu, J. Wang, W. Huang, J. Yang, X. Hong, S. Wei, Y. Wu, Y. Li, Regulation of Coordination Number over Single Co Sites: Triggering the Efficient Electroreduction of CO_2, Angew. Chem. Int. Ed. 57 (2018) 1944-1948.

[21] W. Ren, X. Tan, W. Yang, C. Jia, S. Xu, K. Wang, S.C. Smith, C. Zhao, Isolated Diatomic Ni-Fe Metal-Nitrogen Sites for Synergistic Electroreduction of CO_2, Angew. Chem. Int. Ed. 58 (2019) 6972-6976.

[22] W. Xie, H. Li, G. Cui, J. Li, Y. Song, S. Li, X. Zhang, J.Y. Lee, M. Shao, M. Wei, NiSn Atomic Pair on an Integrated Electrode for Synergistic Electrocatalytic CO_2 Reduction, Angew. Chem. Int. Ed. 60 (2021) 7382-7388.

[23] S.G. Han, D.D. Ma, S.H. Zhou, K. Zhang, W.B. Wei, Y. Du, X.T. Wu, Q. Xu, R. Zou, Q.L. Zhu, Fluorine-Tuned Single-Atom Catalysts with Dense Surface Ni-N_4 Sites on Ultrathin Carbon Nanosheets for Efficient CO_2 Electroreduction, Appl. Catal. B: Environ. 283 (2021) 119591.

[24] H. Zhang, J. Li, S. Xi, Y. Du, X. Hai, J. Wang, H. Xu, G. Wu, J. Zhang, J. Lu, J. Wang, A Graphene-Supported Single-Atom FeN_5 Catalytic Site for Efficient Electrochemical CO_2 Reduction, Angew. Chem. Int. Ed. 58 (2019) 14871-14876.

[25] A.S. Varela, N. Ranjbar Sahraie, J. Steinberg, W. Ju, H.S. Oh, P. Strasser, Metal-Doped Nitrogenated Carbon as an Efficient Catalyst for Direct CO_2 Electroreduction to CO and Hydrocarbons, Angew. Chem. Int. Ed. 54 (2015) 10758-10762.

[26] K. Li, S. Zhang, X. Zhang, S. Liu, H. Jiang, T. Jiang, C. Shen, Y. Yu, W. Chen, Atomic Tuning of Single-Atom Fe-N-C Catalysts with Phosphorus for Robust Electrochemical CO_2 Reduction, Nano Lett. 22 (2022) 1557-1565.

[27] F. Pan, B. Li, E. Sarnello, Y. Fei, X. Feng, Y. Gang, X. Xiang, L. Fang, T. Li, Y.H. Hu, G. Wang, Y. Li, Pore-Edge Tailoring of Single-Atom Iron-Nitrogen Sites on Graphene for Enhanced CO_2 Reduction, ACS Catal. 10 (2020) 10803-10811.

[28] S. Chen, X. Li, C. W. Kao, T. Luo, K. Chen, J. Fu, C. Ma, H. Li, M. Li, T. S. Chan, M. Liu, Unveiling the Proton-Feeding Effect in Sulfur-Doped Fe-N-C Single-Atom Catalyst for Enhanced CO_2 Electroreduction, Angew. Chem. Int. Ed. 61 (2022)

e202206233.

[29] W. Zhu, L. Zhang, S. Liu, A. Li, X. Yuan, C. Hu, G. Zhang, W. Deng, K. Zang, J. Luo, Y. Zhu, M. Gu, Z. J. Zhao, J. Gong, Enhanced CO_2 Electroreduction on Neighboring Zn/Co Monomers by Electronic Effect, Angew. Chem. Int. Ed. 59 (2020) 12664-12668.

[30] J.D. Yi, X. Gao, H. Zhou, W. Chen, Y. Wu, Design of Co-Cu Diatomic Site Catalysts for High-efficiency Synergistic CO_2 Electroreduction at Industrial-level Current Density, Angew. Chem. Int. Ed. 61 (2022) e202212329.

[31] H. Cheng, X. Wu, M. Feng, X. Li, G. Lei, Z. Fan, D. Pan, F. Cui, G. He, Atomically Dispersed Ni/Cu Dual Sites for Boosting the CO_2 Reduction Reaction, ACS Catal. 11 (2021) 12673-12681.

[32] Y. Li, B. Wei, M. Zhu, J. Chen, Q. Jiang, B. Yang, Y. Hou, L. Lei, Z. Li, R. Zhang, Y. Lu, Synergistic Effect of Atomically Dispersed Ni-Zn Pair Sites for Enhanced CO_2 Electroreduction, Adv. Mater. 33 (2021) e2102212.

[33] Y. Li, W. Shan, M.J. Zachman, M. Wang, S. Hwang, H. Tabassum, J. Yang, X. Yang, S. Karakalos, Z. Feng, G. Wang, G. Wu, Atomically Dispersed Dual-Metal Site Catalysts for Enhanced CO_2 Reduction: Mechanistic Insight into Active Site Structures, Angew. Chem. Int. Ed. 61 (2022) e202205632.

[34] W. Cheng, X.F. Lu, D. Luan, X.W. Lou, NiMn-Based Bimetal-Organic Framework Nanosheets Supported on Multi-Channel Carbon Fibers for Efficient Oxygen Electrocatalysis, Angew. Chem. Int. Ed. 59 (2020) 18234-18239.

[35] Q. Hao, H. X. Zhong, J. Z. Wang, K. H. Liu, J. M. Yan, Z. H. Ren, N. Zhou, X. Zhao, H. Zhang, D. X. Liu, X. Liu, L. W. Chen, J. Luo, X. B. Zhang, Nickel Dual-Atom Sites for Electrochemical Carbon Dioxide Reduction, Nat. Synth. 1 (2022) 719-728.

[36] B. Zhang, J. Zhang, J. Shi, D. Tan, L. Liu, F. Zhang, C. Lu, Z. Su, X. Tan, X. Cheng, B. Han, L. Zheng, J. Zhang, Manganese Acting as a High-Performance Heterogeneous Electrocatalyst in Carbon Dioxide Reduction, Nat. Commun. 10 (2019) 2980.

[37] S. Lu, Y. Zhang, M.F. Mady, O. Egwu Eleri, W. Mekonnen Tucho, M. Mazur, A. Li, F. Lou, M. Gu, Z. Yu, Sulfur-Decorated Ni-N-C Catalyst for Electrocatalytic CO_2 Reduction with Near 100 % CO Selectivity, ChemSusChem 15 (2022) e202200870.

[38] J. Leverett, T. Tran-Phu, J.A. Yuwono, P. Kumar, C. Kim, Q. Zhai, C. Han, J. Qu, J. Cairney, A.N. Simonov, R.K. Hocking, L. Dai, R. Daiyan, R. Amal, Tuning the Coordination Structure of Cu-N-C Single Atom Catalysts for Simultaneous Electrochemical Reduction of CO_2 and NO_3^- to Urea, Adv. Energy Mater. 12 (2022) 12, 2201500.

[39] Y. Zheng, Y. Jiao, L. Ge, M. Jaroniec, S.Z. Qiao, Two-Step Boron and Nitrogen Doping in Graphene for Enhanced Synergistic Catalysis, Angew. Chem. Int. Ed. 52 (2013) 3110-3116.

[40] W. Dong, N. Zhang, S. Li, S. Min, J. Peng, W. Liu, D. Zhan, H. Bai, A Mn Single Atom Catalyst with Mn-N_2O_2 Sites Integrated into Carbon Nanosheets for Efficient Electrocatalytic CO_2 reduction, J. Mater. Chem. A 10 (2022) 10892-10901.

[41] D. Yao, C. Tang, X. Zhi, B. Johannessen, A. Slattery, S. Chern, S.Z. Qiao, Inter-Metal Interaction with a Threshold Effect in NiCu Dual-Atom Catalysts for CO_2 Electroreduction, Adv. Mater. 35 (2023) e2209386.

[42] Z. Lu, J. Wang, S. Huang, Y. Hou, Y. Li, Y. Zhao, S. Mu, J. Zhang, Y. Zhao, N, B-co-doped Defect-Rich Graphitic Carbon Nanocages as High Performance Multifunctional Electrocatalysts, Nano Energy 42 (2017) 334-340.

[43] X. Li, X. Huang, S. Xi, S. Miao, J. Ding, W. Cai, S. Liu, X. Yang, H. Yang, J. Gao, J. Wang, Y. Huang, T. Zhang, B. Liu, Single Cobalt Atoms Anchored on Porous N-Doped Graphene with Dual Reaction Sites for Efficient Fenton-like Catalysis, J. Am. Chem. Soc. 140 (2018) 12469-12475.

[44] H. Cheng, X. Wu, X. Li, Y. Zhang, M. Feng, Z. Fan, G. He, Zeolitic Imidazole Framework-Derived FeN_5-Doped Carbon as Superior CO_2 Electrocatalysts, J. Catal. 395 (2021) 63-69.

[45] H. Chen, X. Guo, X. Kong, Y. Xing, Y. Liu, B. Yu, Q. X. Li, Z. Geng, R. Si, J. Zeng, Tuning the Coordination Number of Fe Single Atoms for the Efficient Reduction of CO_2, Green Chem. 22 (2020) 7529-7536.

[46] H. Yang, P. Zhang, X. Yi, C. Yan, D. Pang, L. Chen, S. Wang, C. Wang, B. Liu, G. Zhang, Z. Zhou, X. Li, Constructing Highly Utilizable Fe-N_4 Single-Atom Sites by

One-Step Gradient Pyrolysis for Electroreduction of O_2 and CO_2, Chem. Eng. J. 440 (2022) 135749.

[47] Z. Li, R. Wu, S. Xiao, Y. Yang, L. Lai, J.S. Chen, Y, Axial Chlorine Coordinated Iron-Nitrogen-Carbon Single-Atom Catalysts for Efficient Electrochemical CO_2 Reduction, Chem. Eng. J. 430 (2022) 132882.

[48] F. Pan, B. Li, W. Deng, Z. Du, Y. Gang, G. Wang, Y. Li, Promoting Electrocatalytic CO_2 Reduction on Nitrogen-Doped Carbon with Sulfur Addition, Appl. Catal. B: Environ. 252 (2019) 240-249.

[49] J. Feng, H. Gao, L. Zheng, Z. Chen, S. Zeng, C. Jiang, H. Dong, L. Liu, S. Zhang, X. Zhang, A Mn-N_3 Single-Atom Catalyst Embedded in Graphitic Carbon Nitride for Efficient CO_2 Electroreduction, Nat. Commun. 11 (2020) 4341.

[50] J. Yang, Z. Qiu, C. Zhao, W. Wei, W. Chen, Z. Li, Y. Qu, J. Dong, J. Luo, Z. Li, Y. Wu, In Situ Thermal Atomization to Convert Supported Nickel Nanoparticles into Surface-Bound Nickel Single-Atom Catalysts, Angew. Chem. Int. Ed. 57 (2018) 14095-14100.

[51] Y.N. Gong, L. Jiao, Y. Qian, C.Y. Pan, L. Zheng, X. Cai, B. Liu, S.H. Yu, H.L. Jiang, Regulating the Coordination Environment of MOF-Templated Single-Atom Nickel Electrocatalysts for Boosting CO_2 Reduction, Angew. Chem. Int. Ed. 59 (2020) 2705-2709.

[52] R. Yun, F. Zhan, X. Wang, B. Zhang, T. Sheng, Z. Xin, J. Mao, S. Liu, B. Zheng, Design of Binary Cu-Fe Sites Coordinated with Nitrogen Dispersed in the Porous Carbon for Synergistic CO_2 Electroreduction, Small 17 (2021) e2006951.

[53] H. Yang, Q. Lin, C. Zhang, X. Yu, Z. Cheng, G. Li, Q. Hu, X. Ren, Q. Zhang, J. Liu, C. He, Carbon Dioxide Electroreduction on Single-Atom Nickel Decorated Carbon Membranes with Industry Compatible Current Densities, Nat. Commun. 11 (2020) 593.

[54] M. Ma, B.J. Trzesniewski, J. Xie, W.A. Smith, Selective and Efficient Reduction of Carbon Dioxide to Carbon Monoxide on Oxide-Derived Nanostructured Silver Electrocatalysts, Angew. Chem. Int. Ed. 55 (2016) 9748-9752.

[55] N. Zhang, X. Zhang, L. Tao, P. Jiang, C. Ye, R. Lin, Z. Huang, A. Li, D. Pang, H. Yan, Y. Wang, P. Xu, S. An, Q. Zhang, L. Liu, S. Du, X. Han, D. Wang, Y. Li, Silver Single-Atom Catalyst for Efficient Electrochemical CO_2 Reduction Synthesized from Thermal Transformation and Surface Reconstruction, Angew. Chem. Int. Ed. 60 (2021) 6170-6176.

Figure Captions:

Figure 1. (a) TEM, (b) HRTEM, and (c) ADF-STEM of Mn-Ni-NC, where Mn-Ni atom pair are highlighted in red rectangles, and the histogram shows the proportion of different distances; (d) The intensity profile of distance between Mn and Ni atoms; (e)-(i) C, N, Mn, and Ni EDX mapping images of Mn-Ni-NC catalyst.

Figure 2. (a) High-resolution N 1s XPS spectra of Mn-NC, Ni-NC, Mn-Mn-NC, Ni-Ni-NC and Mn-Ni-NC catalysts; (b) High-resolution Mn 2p XPS spectra of Mn-Nc, Mn-Mn-NC and Mn-Ni-NC catalysts; (c) High-resolution Ni 2p XPS spectra of Ni-NC, Ni-Ni-NC and Mn-Ni-NC catalysts.

Figure 3. (a) Mn K-edge and (b) Ni K-edge XANES spectra of the catalysts; (c) Mn K-edge and (d) Ni K-edge Fourier transform (FT) k^3-weighted EXAFS (FT-EXAFS) spectra of the samples at R space; (e) Ni K-edge Wavelet transformed k^2-weighted EXAFS plots of Ni foil, Ni-Pc, Ni-NC, Ni-Ni-NC and Mn-Ni-NC; (f) Ni–N, (g) Ni-N, (h) Ni-N and (i) Mn-N fittings of the FT-EXAFS spectra for Ni-NC, Ni-Ni-NC, Mn-Ni-NC and Mn-Ni-NC catalysts. The gray, blue, red and green balls refer to C, N, Ni and Mn atoms, respectively.

Figure 4. ECR to CO activity of different catalysts. (a) LSV curves of the catalysts obtained in CO_2-saturated 0.5 M $KHCO_3$ electrolyte at the scan rate of 10 mV s^{-1}; (b) LSV curves of the Mn-Ni-NC catalyst in Ar- and CO_2-saturated electrolyte; (c) Faradaic efficiency for CO; (d) Faradaic efficiency for H_2; (e) Partial current densities of CO and (f) TOF for different catalysts at different applied potentials; (g) Charge current density difference against scan rates of Mn-NC, Ni-NC, Mn-Mn-NC, Ni-Ni-NC and Mn-Ni-NC catalysts; (h) Tafel plots for the CO partial current density; (i) Comparison of Faradaic efficiency and current density on reported SACs and DACs in H-cell; (j) Stability test for Mn-Ni-NC at -0.7 V (vs. RHE) with 24 hours continuous electrocatalytic reaction.

Figure 5. (a) Electron transfer between Mn and Ni atoms on different catalysts; (b) Gibbs free energy change diagram for ECR to CO on different catalysts; (c) Scaling relationship between *COOH and *CO; (d) The activity mechanism of ECR to CO on Mn-Ni-NC; The COHP distribution of (e) CO*Mn-NC, (f) the second CO adsorbed on CO passivated Mn-Mn-N, (g) COOH*Ni-NC, (h) COOH*Ni-Ni-NC, (i) COOH*Mn-Ni-NC (O bonded Mn); (j) COOH*Mn-Ni-NC (C bonded Ni), where Fermi level is set to zero.

Figure 1

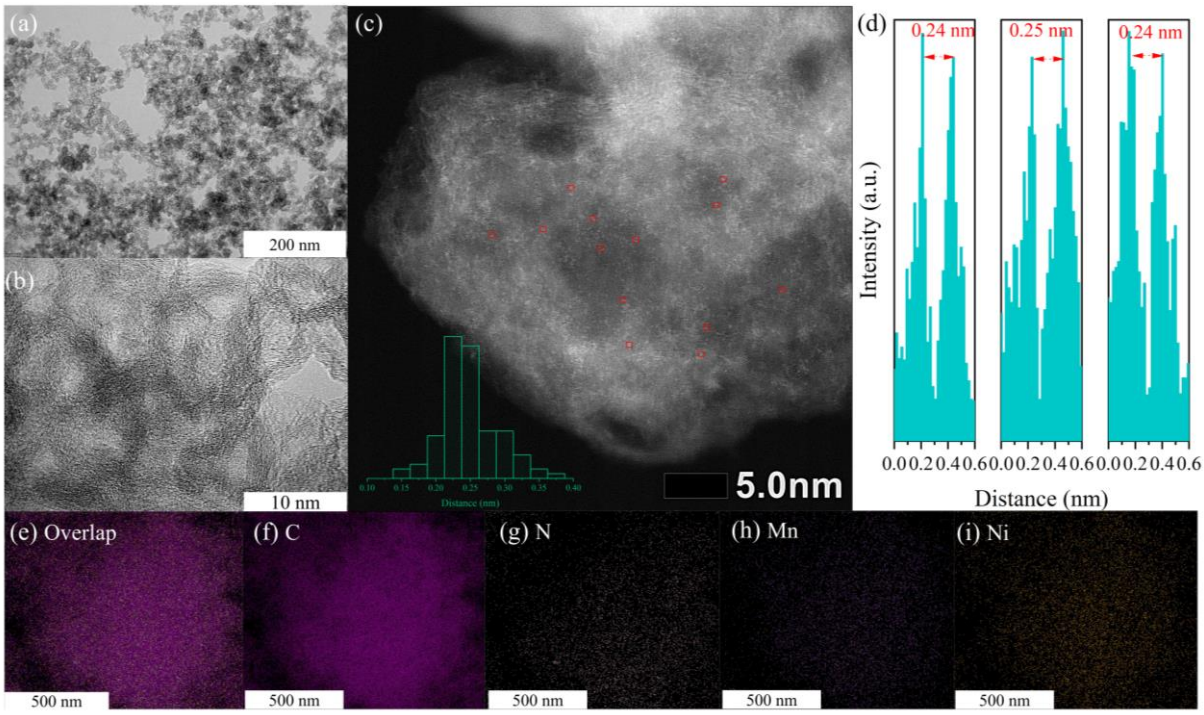
(a)
200 nm
(b)
10 nm
(c)
5.0nm
(d)
0.24 nm
0.25 nm
0.24 nm
Intensity (a.u.)
0.0 0.2 0.4 0.6 0.0 0.2 0.4 0.6 0.0 0.2 0.4 0.6
Distance (nm)
(e) Overlap
(f) C
(g) N
(h) Mn
(i) Ni
500 nm
500 nm
500 nm
500 nm
500 nm

Figure 2

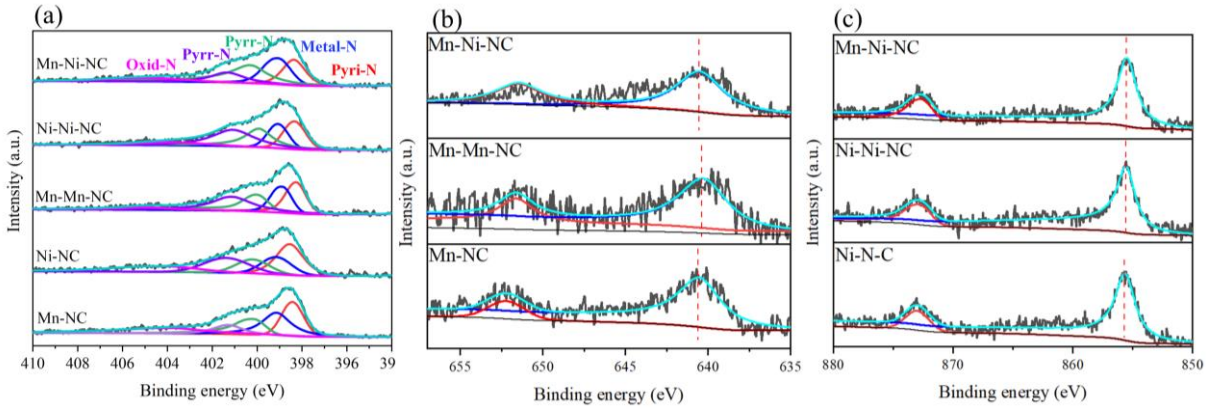
(a)
Mn-Ni-NC
Oxid-N
Pyrr-N
Pyrr-N
Metal-N
Pyri-N
Ni-Ni-NC
Mn-Mn-NC
Ni-NC
Mn-NC
Intensity (a.u.)
410 408 406 404 402 400 398 396 39
Binding energy (eV)
(b)
Mn-Ni-NC
Mn-Mn-NC
Mn-NC
Intensity (a.u.)
655 650 645 640 635
Binding energy (eV)
(c)
Mn-Ni-NC
Ni-Ni-NC
Ni-N-C
Intensity (a.u.)
880 870 860 850
Binding energy (eV)

Figure 3

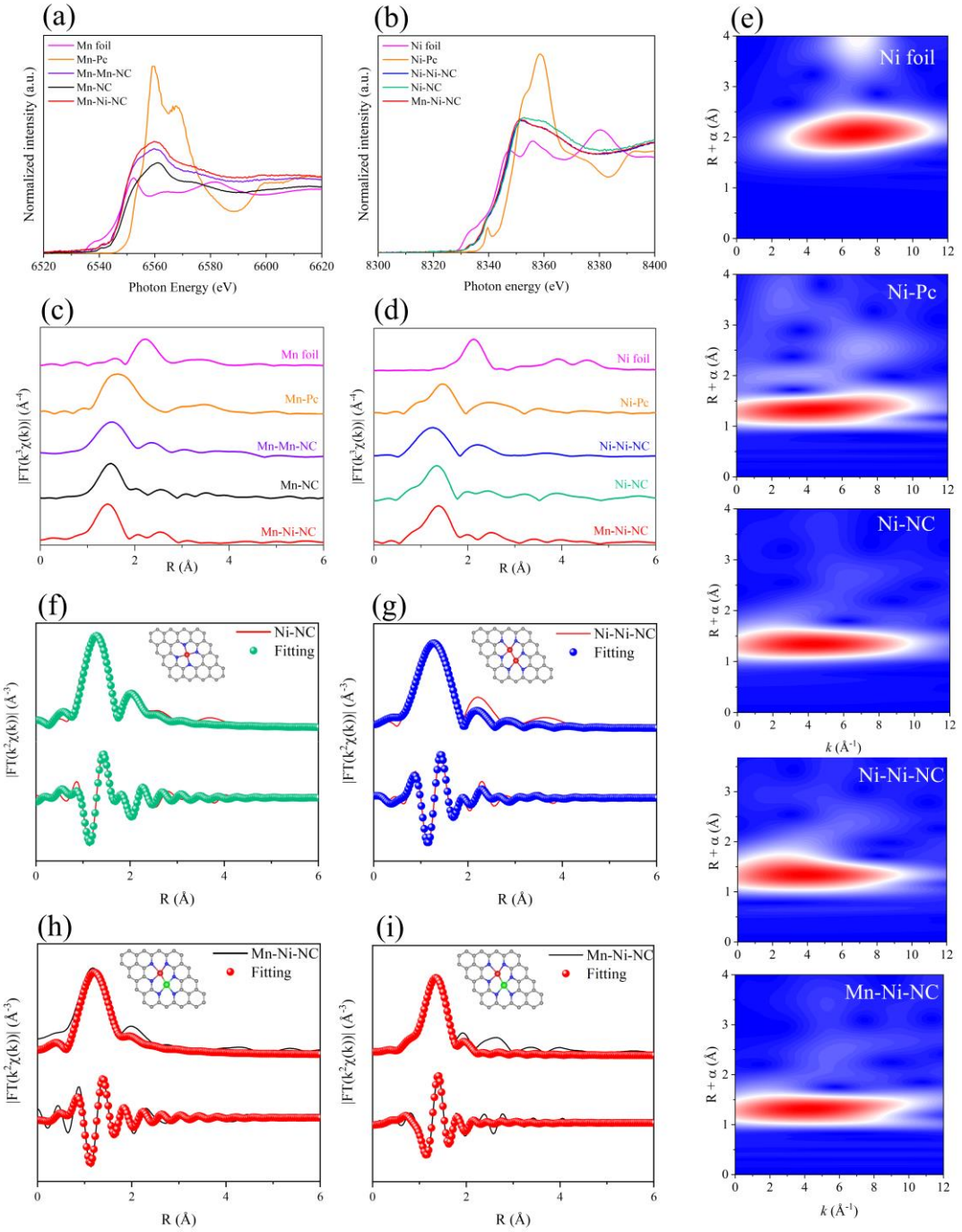
(a)
Mn foil
Mn-Pc
Mn-Mn-NC
Mn-NC
Mn-Ni-NC
Normalized intensity (a.u.)
Photon Energy (eV)
(b)
Ni foil
Ni-Pc
Ni-Ni-NC
Ni-NC
Mn-Ni-NC
Normalized intensity (a.u.)
Photon energy (eV)
(c)
Mn foil
Mn-Pc
Mn-Mn-NC
Mn-NC
Mn-Ni-NC
R (Å)
(d)
Ni foil
Ni-Pc
Ni-Ni-NC
Ni-NC
Mn-Ni-NC
R (Å)
(e)
Ni foil
Ni-Pc
Ni-NC
Ni-Ni-NC
Mn-Ni-NC
R + α (Å)
k (Å-1)
(f)
Ni-NC
Fitting
R (Å)
(g)
Ni-Ni-NC
Fitting
R (Å)
(h)
Mn-Ni-NC
Fitting
R (Å)
(i)
Mn-Ni-NC
Fitting
R (Å)

Figure 4

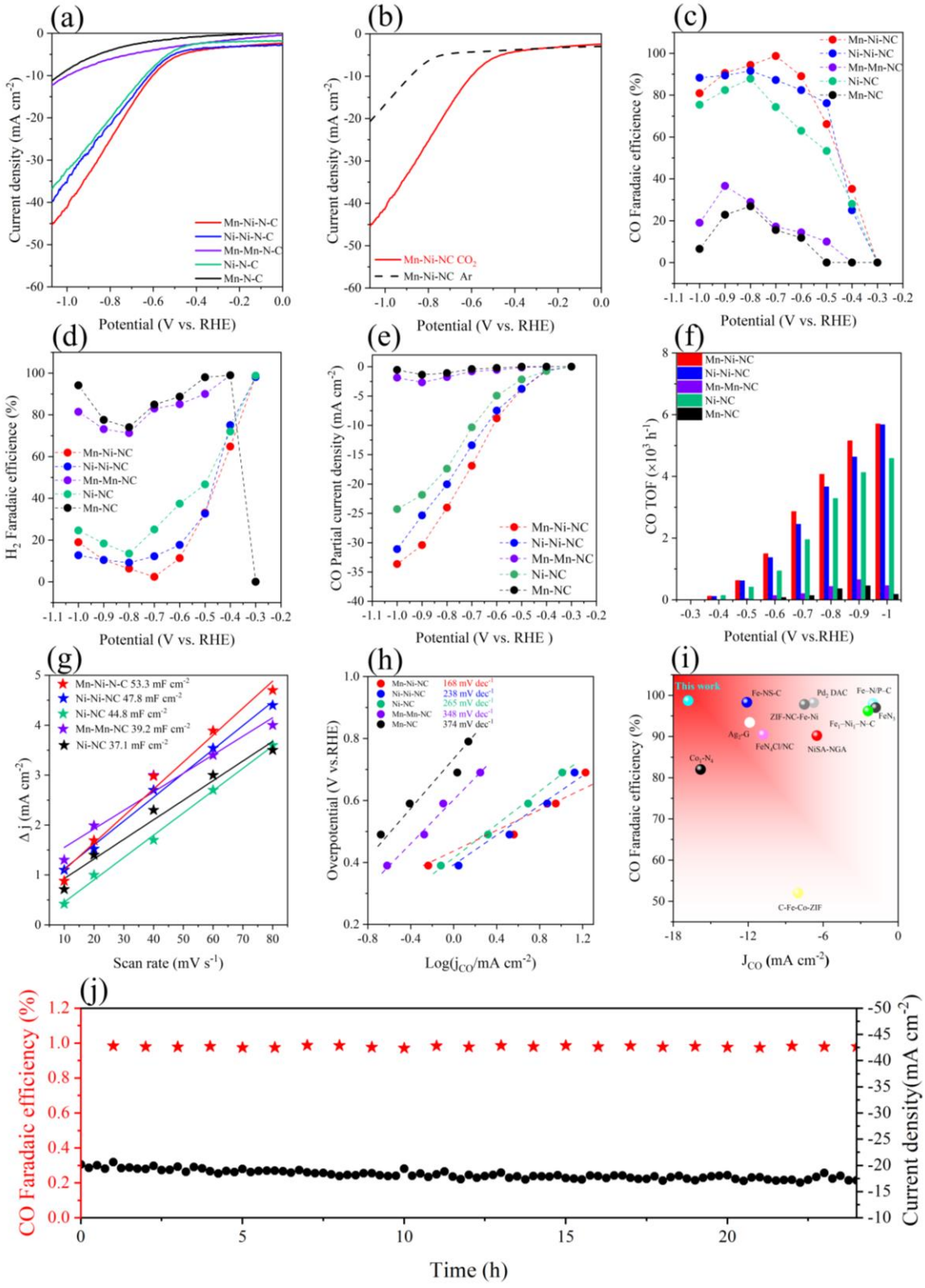
(a)
Current density (mA cm-2)
Potential (V vs. RHE)
Mn-Ni-N-C
Ni-Ni-N-C
Mn-Mn-N-C
Ni-N-C
Mn-N-C
(b)
Current density (mA cm-2)
Potential (V vs. RHE)
Mn-Ni-NC CO2
Mn-Ni-NC Ar
(c)
CO Faradaic efficience (%)
Potential (V vs. RHE)
Mn-Ni-NC
Ni-Ni-NC
Mn-Mn-NC
Ni-NC
Mn-NC
(d)
H2 Faradaic efficience (%)
Potential (V vs. RHE)
Mn-Ni-NC
Ni-Ni-NC
Mn-Mn-NC
Ni-NC
Mn-NC
(e)
CO Partial current density (mA cm-2)
Potential (V vs. RHE)
Mn-Ni-NC
Ni-Ni-NC
Mn-Mn-NC
Ni-NC
Mn-NC
(f)
CO TOF (×10³ h-1)
Potential (V vs.RHE)
Mn-Ni-NC
Ni-Ni-NC
Mn-Mn-NC
Ni-NC
Mn-NC
(g)
Δ j (mA cm-2)
Scan rate (mV s-1)
Mn-Ni-N-C 53.3 mF cm-2
Ni-Ni-NC 47.8 mF cm-2
Ni-NC 44.8 mF cm-2
Mn-Mn-NC 39.2 mF cm-2
Ni-NC 37.1 mF cm-2
(h)
Overpotential (V vs.RHE)
Log(jCO/mA cm-2)
Mn-Ni-NC 168 mV dec-1
Ni-Ni-NC 238 mV dec-1
Ni-NC 265 mV dec-1
Mn-Mn-NC 348 mV dec-1
Mn-NC 374 mV dec-1
(i)
CO Faradaic efficiency (%)
JCO (mA cm-2)
This work
Fe-NS-C
Pd2 DAC
Fe-N/P-C
FeN5
ZIF-NC-Fe-Ni
Fe1-Ni1-N-C
Ag2-G
FeN4Cl/NC
NiSA-NGA
Co1-N4
C-Fe-Co-ZIF
(j)
CO Faradaic efficiency (%)
Current density(mA cm-2)
Time (h)

Figure 5

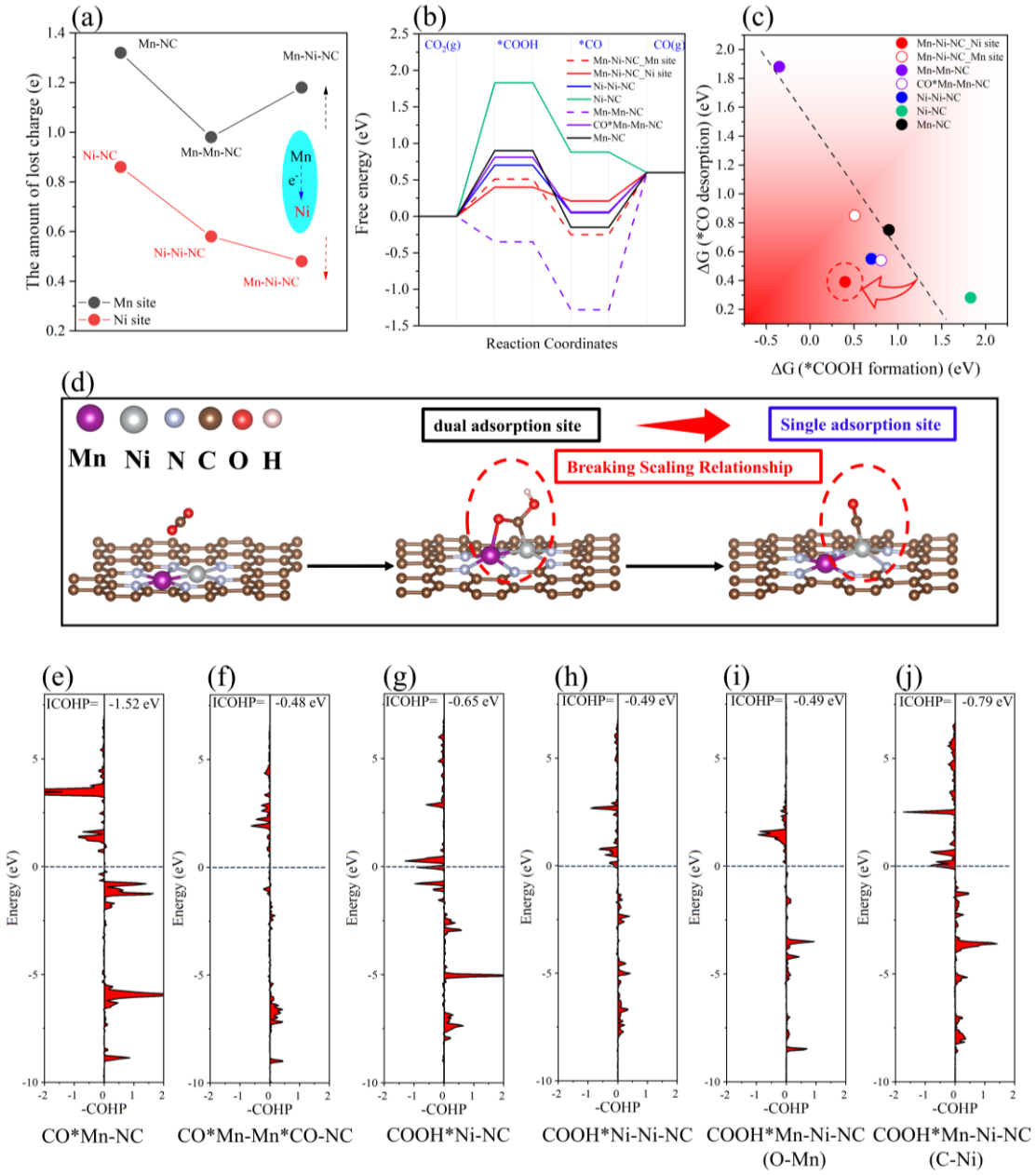
(a)
Mn-NC
Mn-Ni-NC
Mn-Mn-NC
Ni-NC
Ni-Ni-NC
Mn-Ni-NC
Mn
e⁻
Ni
Mn site
Ni site
The amount of lost charge (e)
(b)
CO2(g)
*COOH
*CO
CO(g)
Mn-Ni-NC_Mn site
Mn-Ni-NC_Ni site
Ni-Ni-NC
Ni-NC
Mn-Mn-NC
CO*Mn-Mn-NC
Mn-NC
Free energy (eV)
Reaction Coordinates
(c)
Mn-Ni-NC_Ni site
Mn-Ni-NC_Mn site
Mn-Mn-NC
CO*Mn-Mn-NC
Ni-Ni-NC
Ni-NC
Mn-NC
ΔG (*CO desorption) (eV)
ΔG (*COOH formation) (eV)
(d)
Mn Ni N C O H
dual adsorption site
Single adsorption site
Breaking Scaling Relationship
(e)
ICOHP= -1.52 eV
CO*Mn-NC
(f)
ICOHP= -0.48 eV
CO*Mn-Mn*CO-NC
(g)
ICOHP= -0.65 eV
COOH*Ni-NC
(h)
ICOHP= -0.49 eV
COOH*Ni-Ni-NC
(i)
ICOHP= -0.49 eV
COOH*Mn-Ni-NC (O-Mn)
(j)
ICOHP= -0.79 eV
COOH*Mn-Ni-NC (C-Ni)
Energy (eV)
-COHP

Supporting Information

Breaking scaling relations for highly efficient electroreduction of CO_2 to CO on atomically dispersed heteronuclear dual-atom catalyst

Song Lu, Michal Mazur*, Kun Guo, Dragos Constantin Stoian, Minfen Gu, Wakshum Mekonnen Tucho, Zhixin Yu*

1. Chemicals and materials

All chemicals were analytical grade and were used as purchased without further purification. Nickel(II) chloride hexahydrate ($NiCl_2 \cdot 6H_2O$, 98%), manganese(II) chloride tetrahydrate ($MnCl_2 \cdot 4H_2O$, 98%), citric acid monohydrate ($C_6H_8O_7 \cdot H_2O$, 99%), ammonium hydroxide solution ($NH_3 \cdot H_2O$, 28% NH_3 in H_2O), dicyandiamide ($C_2H_4N_4$, 99%), manganese(II) phthalocyanine ($C_{32}H_{16}MnN_8$, MnPc), Nickel(II) phthalocyanine ($C_{32}H_{16}NiN_8$, NiPc) were purchased from Sigma-Aldrich. Potassium bicarbonate ($KHCO_3$, 98 %), Nafion D-521 dispersion (5 % w/w in water and 1-propanol), Nafion-117 ionic exchange membrane and carbon paper were purchased from Alfa Aesar. Carbon dioxide (CO_2, > 99.999%) and Argon (Ar, >99.999%) were purchased form Nippon gases. Ultrapure water with 18.2 MΩ cm is produced by Milli-Q from VWR. Absolute ethanol was purchased from Arcus.

2. Electrocatalyst preparation

2.1. Preparation of carbon substrate

Ketjen black EC-600 JD (carbon black, AkzoNobel) was pre-treated before use. Typically, 2g carbon black was dispersed in 50 ml of HNO_3 solution (65 wt%) and refluxed at 100 °C for 8 h with vigorously stirring. After cooling down, the suspension was washed by ultrapure water until neutral pH and separated by vacuum filtration. After that, the activated carbon black was dried at 120 °C in a vacuum oven for 24 h.

2.2. Preparation of electrocatalysts

For the preparation of Mn-Ni-NC catalyst, 9.89 mg $MnCl_2 \cdot 4H_2O$, 11.88 mg $NiCl_2 \cdot 6H_2O$ and 64.4 mg $C_6H_8O_7 \cdot H_2O$ were dissolved in 2 ml ethanol and the solution was sonicated for 30 minutes. Meanwhile, 100 mg activated carbon black was dissolved in 3 ml ethanol and the solution was sonicated for 30 minutes. The two solutions were then mixed and stirred continuously under room temperature for 12 hours. The obtained suspension became black solid after drying at 75 ℃ for 12 h. The black solid was mixed with 1 g dicyandiamide and grinded for 10 minutes. Finally, the black mixture was transfer to a covered crucible and calcinated under Argon atmosphere (100 sccm) at 800 °C for 2 hours. The collected samples were washed by 3 M HCl several times, then

were marked it as Mn-Ni-NC catalyst.

2.3. Preparation of Mn-Mn-NC and Ni-Ni-NC catalysts

The preparation of Mn-Mn-NC and Ni-Ni-NC catalysts follows same procedure, except for adding single metal resource and 32.2 mg $C_6H_8O_7 \cdot H_2O$.

2.4 Preparation of Mn-NC and Ni-NC catalysts

The preparation of Mn-NC and Ni-NC catalysts use similar procedure, except that 50 μL $NH_3 \cdot H_2O$ solution was added in the first step.

3. Characterization

X-ray diffraction (XRD) diffractograms were collected on Bruker-AXS Micro-diffractometer D8 ADVANCE equipped with a CuKα radiation source (λ=1.54 Å) with a scan rate of 3° min^{-1} in the range of 10-80°.

Raman spectroscopy was recorded by Renishaw inVia instrument with a 532 nm excitation laser, and the sample was focused with a ×50LWD objective lens and exposed to the emission line for 10 s.

Transmission electron microscopy (TEM), high-resolution TEM (HR-TEM) and energy-dispersive X-ray spectroscopy (EDS) mapping were conducted on JEM-2100 Plus (JEOL) electron microscope at 200 kV. Aberration-corrected annular dark-filed scanning transmission electron microscopy (ADF-STEM) was performed on JEOL NEOARM 200 F with an accelerating voltage of 200 KV.

Physisorption measurements were performed using Tristar II 3020 instrument at liquid nitrogen temperature of −196 °C.

X-ray photoelectron spectrometer was conducted on ESCALAB Xi using AlKα source.

X-ray absorption fine structure (XAFS) spectra at the Mn and Ni K-edge was collected at Station Bending Magnet 31 (BM31) in European Synchrotron Radiation Facility (ESRF), Grenoble, France. The Mn and Ni K-edge X-ray absorption near edge structure (XANES)data were recorded in a fluorescence mode. Mn foil, Ni-Pc, Mn foil, and Mn-Pc were used as references.

4. Electrocatalysts characterization

The electrochemical performance was tested in a gas-tight H-cell with two-compartments separated by a cation exchange membrane, where each chamber contains 40 ml electrolyte (0.5 M $KHCO_3$). All measurements were controlled by AUTOLAB PGSTAT302N workstation. Platinum plate, carbon paper coated with catalysts and Ag/AgCl (saturated KCl solution) worked as counter electrode, working electrode and reference electrode, respectively. The working electrode was prepared by coating catalyst ink on carbon paper. The ink was a mixture of 4 mg catalyst, 50 μL water, 300 μL ethanol and 50 μL nafion solution, ultrasonically dispersed for 1 hour. A 100 μl of the catalyst ink was dropped onto a carbon paper (1 cm × 2 cm) and dried under an infrared heat lamp, giving a catalyst loading of 1.0 mg cm^{-2}. Prior to the electrochemical measurements, the electrolyte solution was purged with CO_2 at a flow of 20 mL min^{-1} for 1 hours to obtain CO_2-saturated solution. Meanwhile, CO_2 flow was kept at 20 mL min^{-1} during the activity test. The pH is 7.2 for CO_2-saturated 0.5 M $KHCO_3$ electrolyte. The potentials were converted to reversible hydrogen electrode (RHE) by using the formula E (vs. RHE) = E (vs. Ag/AgCl) + 0.196 V +0.059 × pH at 25 °C. Linear sweep voltammetry (LSV) curves were conducted at a scan rate of 10 mV/s. The electrochemical double-layer capacitance (C_{dl}) was estimated by the cyclic voltammetry (CV) method. To avoid the faradaic process, the CV scans were performed under 0.5 M $KHCO_3$ electrolyte between 0−0.20 V (vs. Ag/AgCl) with scan rates of 10, 20, 40, 60 and 80 mV s^{-1}. The C_{dl} of was calculated by plotting the anodic and cathodic current difference against the scan rate. The electrochemical surface areas (ECSA) of the catalysts were determined by the formula ECSA = C_{dl}/C_s, where C_s was chosen to be 40 μF cm^{-2} per cm^2_{ECSA} [1]. Electrochemical impedance spectroscopy (EIS) was performed in a frequency range from 105 Hz to 0.01 Hz. The gaseous products were quantified by an on-line gas chromatography (Agilent GC-7890B) equipped with two separated TCD detectors for H_2 and CO detection. The liquid products were detected by a 400 MHz Bruker nuclear magnetic resonance (NMR) spectrometer. In a typical test, 0.5 ml electrolyte was uniformly mixed with 0.1 ml deuterated water (D_2O) as well

as 0.05 μl dimethyl sulfoxide (DMSO) as the internal standard.

The FE of gaseous products (H_2 and CO) under different potentials were calculated by Equation 1 [2]:

$$FE = (N \times P \times F \times v \times \nu_i)/(R \times T \times I) \quad (1)$$

where N is the number of electrons transferred per mole CO_2 to gas product, which is 2 for CO and H_2 products. P is atmospheric pressure and F is Faraday's constant. ν is the gas flow rate. ν_i is the volume concentration of gas product determined by online GC. T is the reaction temperature, and R is the idea gas constant. I is the steady-state cell current at each potential.

The partial current densities of CO and H_2 are calculated by Equation 2:

$$J_{CO(H2)} = J_{total} \times FE_{CO(H2)} \quad (2)$$

The turnover frequency (TOF, h^{-1}) was calculated through the Equation 3 [3]:

$$TOF = (3600 \times I_{product} \times M)/(N \times F \times \omega \times m_{cat}) \quad (3)$$

where $I_{product}$ is partial current for CO or H_2 products. M is atomic mass of the metal. ω is the mass percentage of metal loading determined by XPS. m_{cat} is the mass of the catalyst coated on the carbon paper.

5. Density functional theory (DFT) calculations

Spin-polarized DFT calculations were performed by employing the Vienna ab initio simulation package (VASP) code with projector augmented wave (PAW) [4]. The generalized gradient approximation (GGA) implemented Perdew-Burke-Ernzerhof (PBE) was chosen to calculate exchange-correlation energy [5,6]. The van der Waals (vdW) interactions was corrected by using the empirical correction (DFT-D3) [7]. A cubic graphene monolayer (12.30 × 12.78 Å) with 60 carbon atoms was used as carbon substrate. A vacuum region of 15 Å was applied in z direction to avoid the spurious interactions. The energy cutoff is set to 600 eV. A Gamma centre k-point sampling of 2 × 2 × 1 and 4 × 4 × 1 were chosen for structure relaxation and electronic structure calculations, respectively. The convergence criterion for energy and force was 1.0×10^{-5} eV and 1.0×10^{-2} eV/Å, respectively.

The binding energy (E_b) of TM atom on substrate can be calculated by Equation 4:

$$E_b = E(\text{support with TM atom}) - E(\text{support}) - E(\text{TM}) \quad (4)$$

Where E(support with TM atom), E(support) and Tm indicate the total energy of TM anchored N doped carbon framework, N doped carbon framework and TM atom.

The formation energy (E_f) of DACs can be calculated by Equation 5:

$$E_f = E(\text{support with TM atom}) - 50\mu(C) - 6\mu(N) - n\mu(TM) \quad (5)$$

Where μ(C), (N), (TM) indicate the chemical potential of C, N, TM, which are obtained from their stable phase.

The adsorption energies (E_{ads}) of intermediate is estimated by Equation 6:

$$E_{ads} = E_{*sub} - E_{sub} - E_{Inter} \quad (6)$$

where E_{*sub}, E_{sub}, E_{Inter} are the total energies of intermediates adsorbed substrate, bare substrate and intermediates, respectively.

The formation path of gaseous products (CO and H_2) are described by Equations 7-10:

$$* + CO_2 + H^+ + e^- \rightarrow *COOH \quad (7)$$

$$*COOH + H^+ + e^- \rightarrow *CO + H_2O \quad (8)$$

$$*CO \rightarrow CO + * \quad (9)$$

$$H^+ + e^- \rightarrow 1/2H_2 \quad (10)$$

where * indicates an adsorption site.

The Gibbs free energy change (ΔG) of each step is calculated by the computational hydrogen electrode (CHE) model [8]:

$$\Delta G = \Delta E + \Delta ZPE - T\Delta S \quad (11)$$

where ΔE, ΔZPE and ΔS are the differences in total energy from DFT calculations, zero-point energy, and entropy between reactants and products, respectively. T is temperature (298.15 K).

Figure S1. (a) XRD diffractograms and (b) Raman spectra of Mn-NC, Ni-NC, Mn-Mn-NC, Ni-Ni-NC and Mn-Ni-NC catalysts.

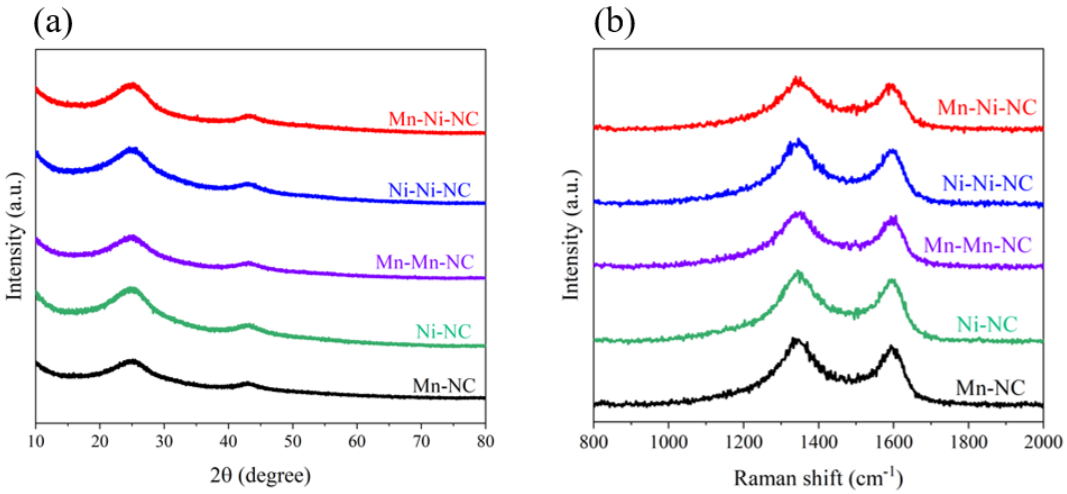

Figure S2. N_2 adsorption–desorption isotherms of Mn-NC, Ni-NC, Mn-Mn-NC, Ni-Ni-NC and Mn-Ni-NC catalysts

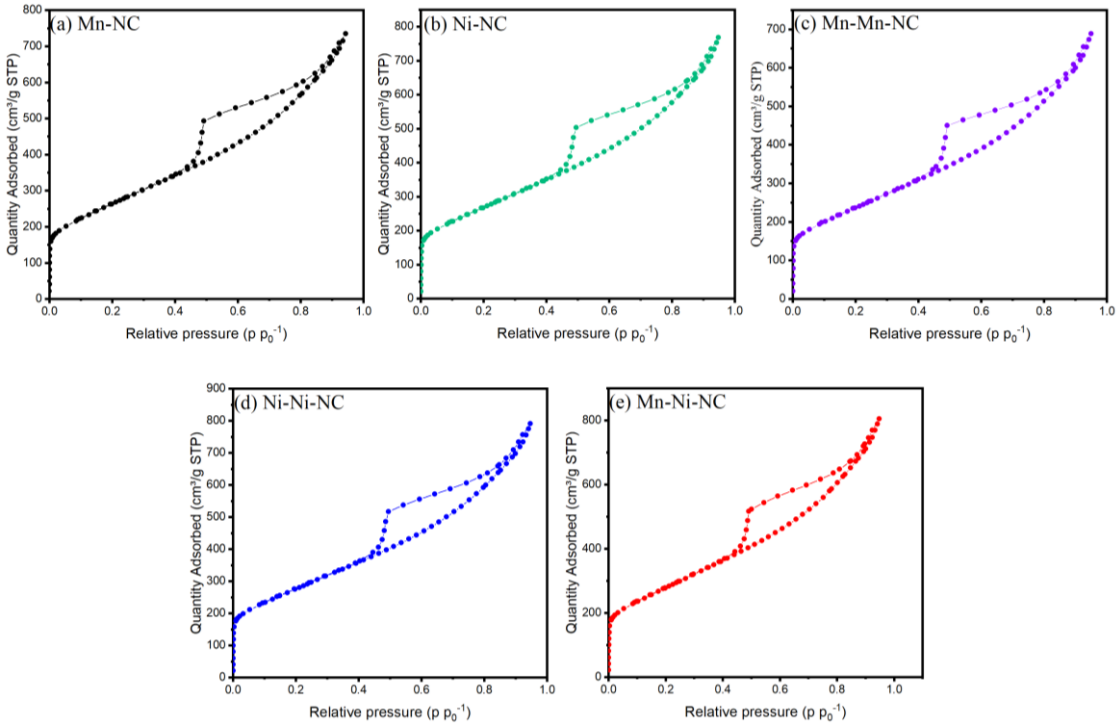

Figure S3. The zoomed-in view of Mn-Ni atom pair over Mn-Ni-NC sample.

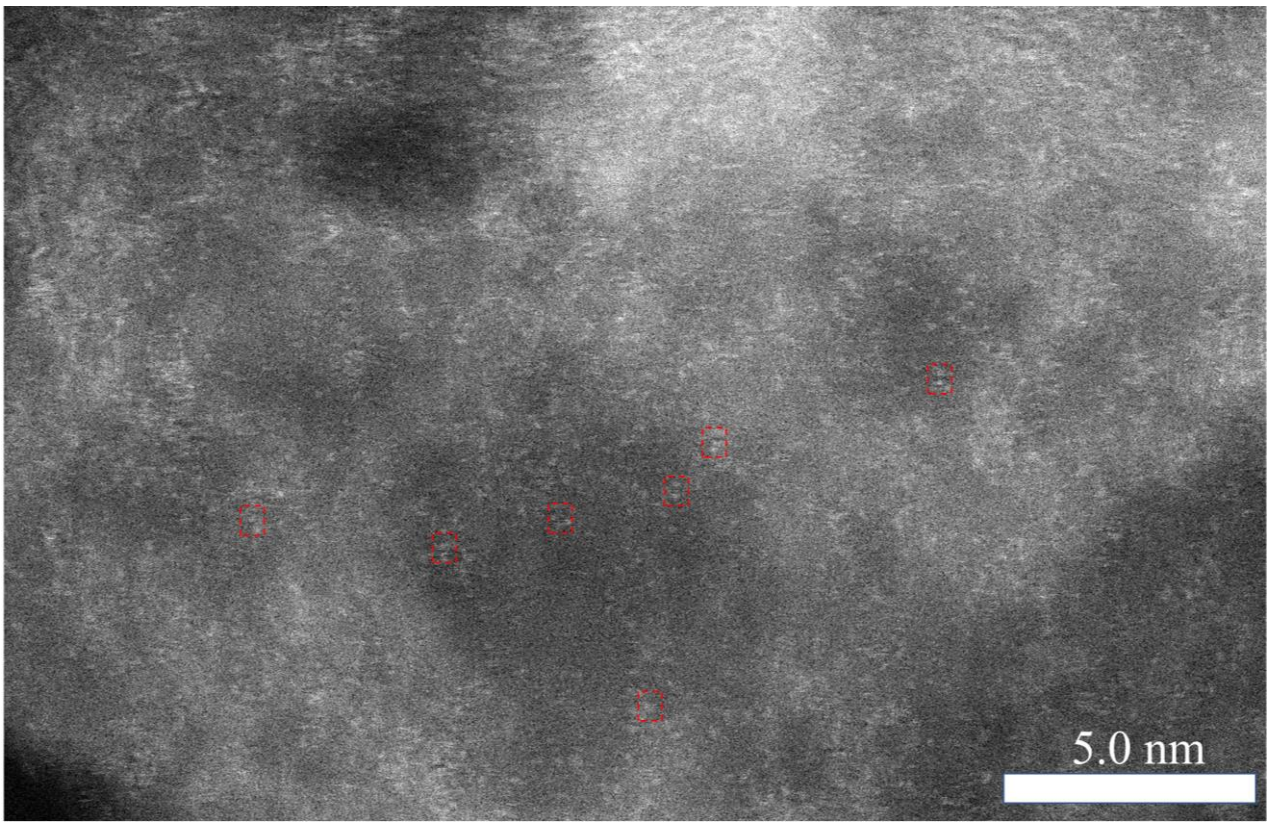

Figure S4 (a) HRTEM, (b) ADF-STEM of Ni-N-NC, where Ni single atoms are highlighted in red circles; (c)-(f) C, N, and Ni EDX mapping images of Ni-NC catalyst.

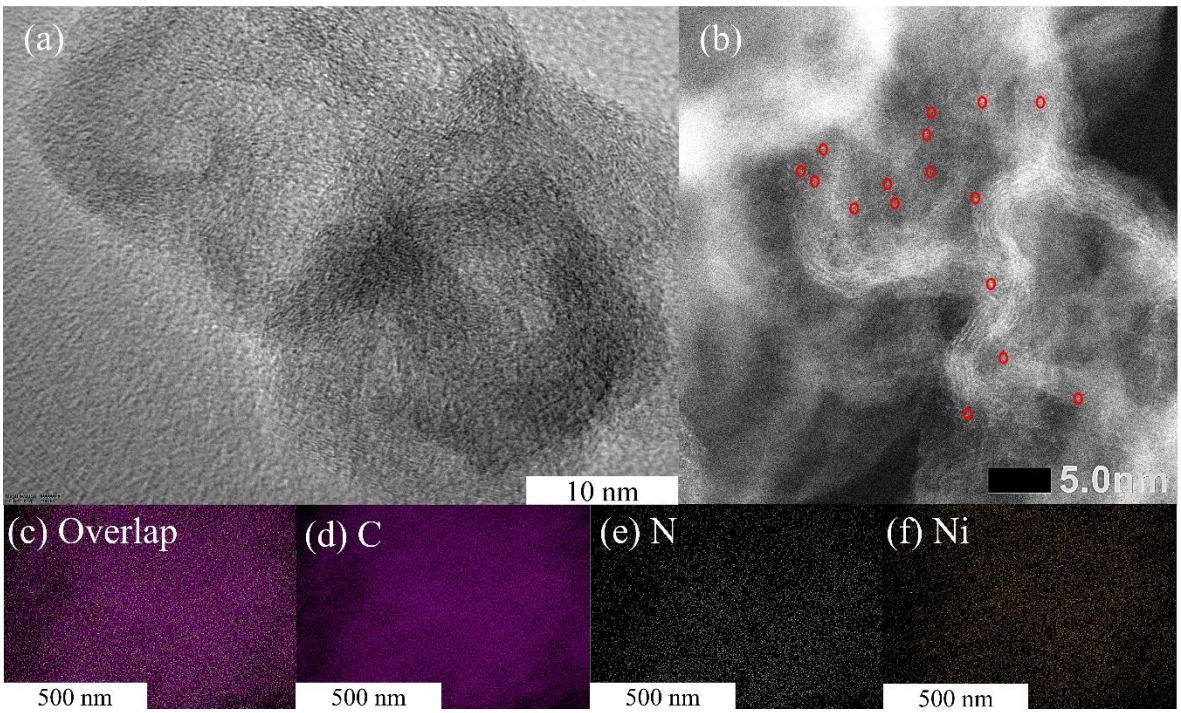

Figure S5. (a) HRTEM, (b) ADF-STEM of Mn-N-NC, where Mn single atoms are highlighted in red circles; (c)-(f) C, N, and Mn EDX mapping images of Mn -NC catalyst.

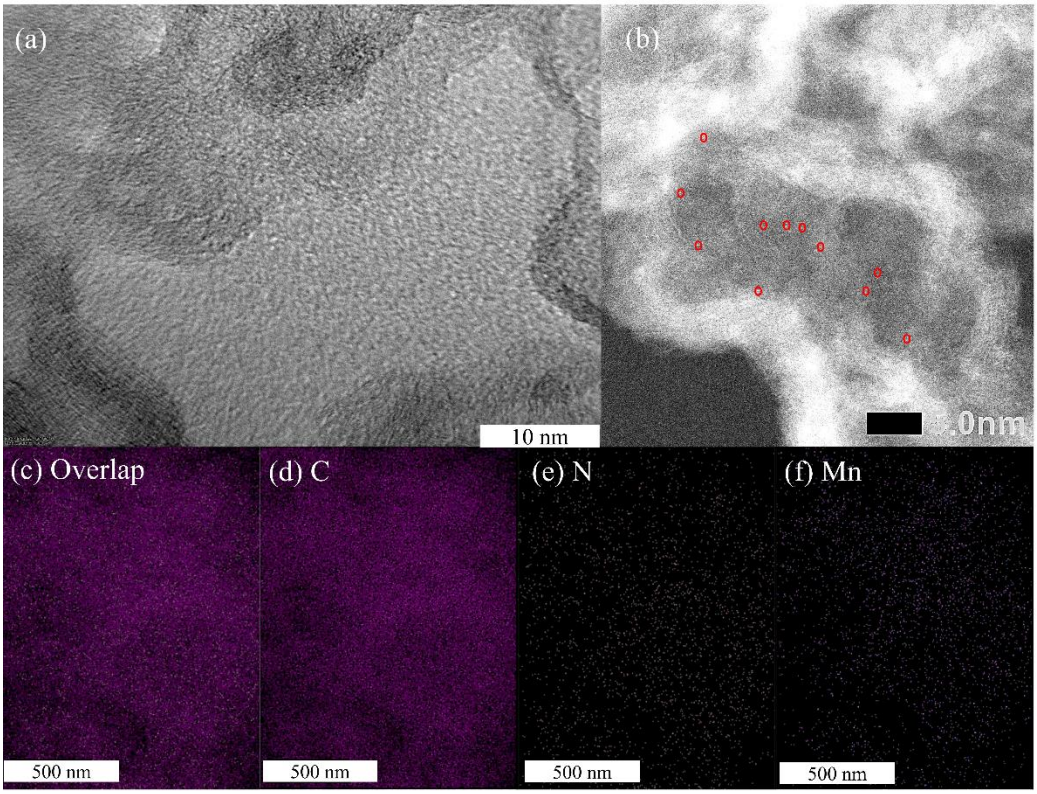

Figure S6. (a) HRTEM, (b) ADF-STEM of Mn-Mn-NC, where Mn-Mn atom pairs are highlighted in red rectangles, and the histogram shows the proportion of different distances; (c) The intensity profile of distance between Mn and Mn atom; (d)-(g) C, N, and Mn EDX mapping images of Mn-Mn-NC catalyst.

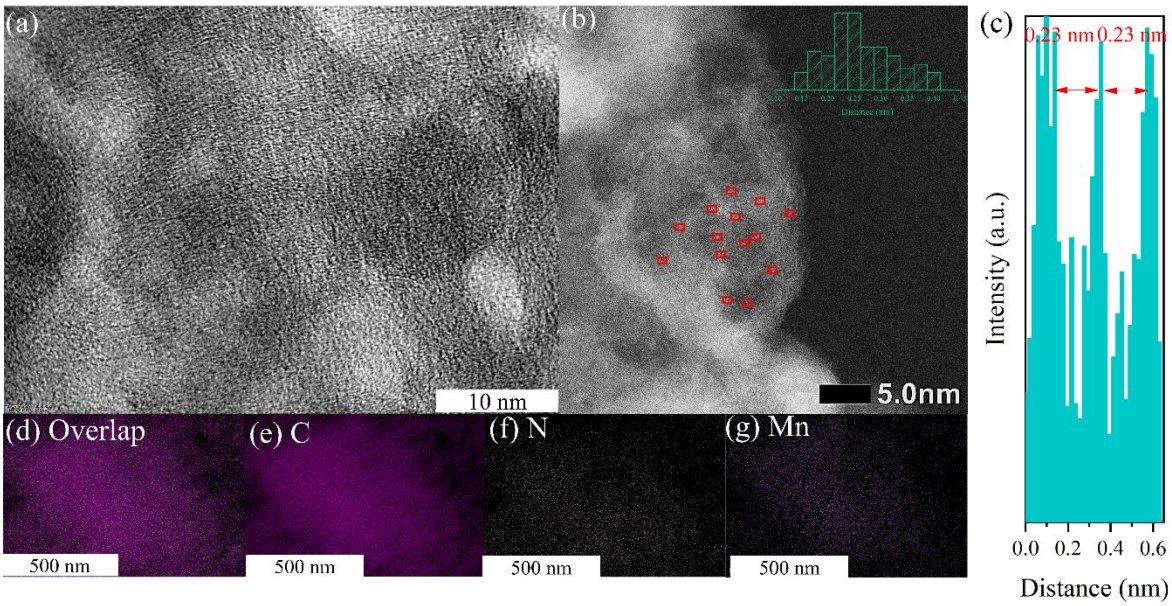

Figure S7. (a) HRTEM, and (b) ADF-STEM of Ni-Ni-NC catalyst, where Ni-Ni atom pairs are highlighted in red rectangles, and the histogram shows the proportion of different distances; (c) The intensity profile of distance between Ni and Ni atom; (d)-(g) C, N, and Ni EDX mapping images of Ni-Ni-NC catalyst.

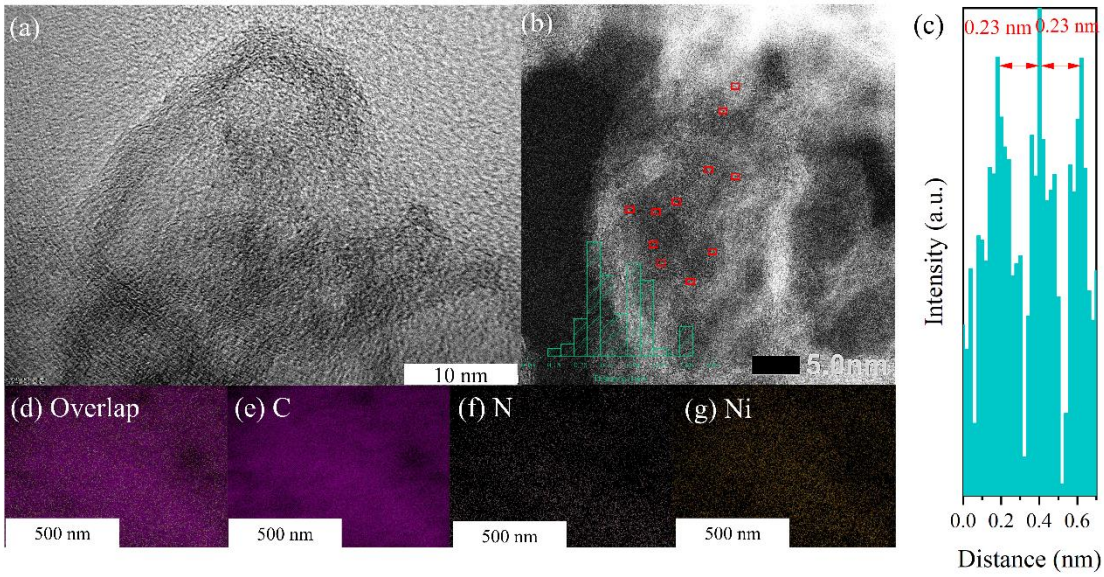

Figure S8. Mn K-edge Wavelet transformed k^2-weighted EXAFS (WT-EXAFS) plots of Mn foil, Mn-Pc, Mn-NC, Mn-Mn-NC and Mn-Ni-NC catalysts.

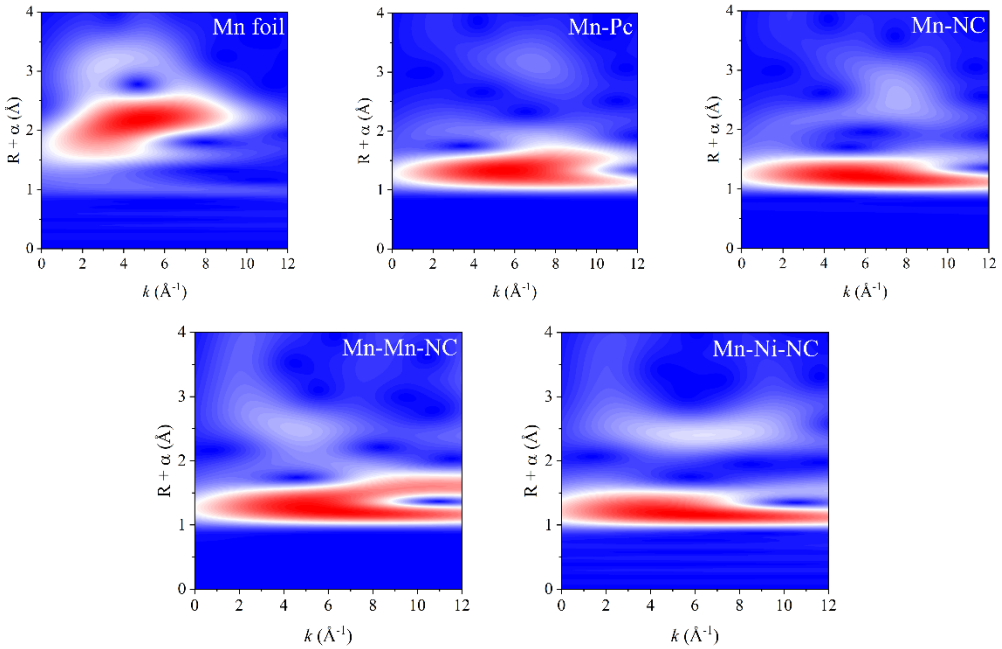

Figure S9. The first shells: (a) Mn–N, (b) Mn-N fittings of the FT–EXAFS spectra of Mn-NC and Mn-Mn-NC catalysts; (c) Mn-Mn, (d) Ni-Ni and (e) Mn-Ni fittings of the FT–EXAFS spectra of Mn-Mn-NC, Ni-Ni-NC and Mn-Ni-NC catalysts.

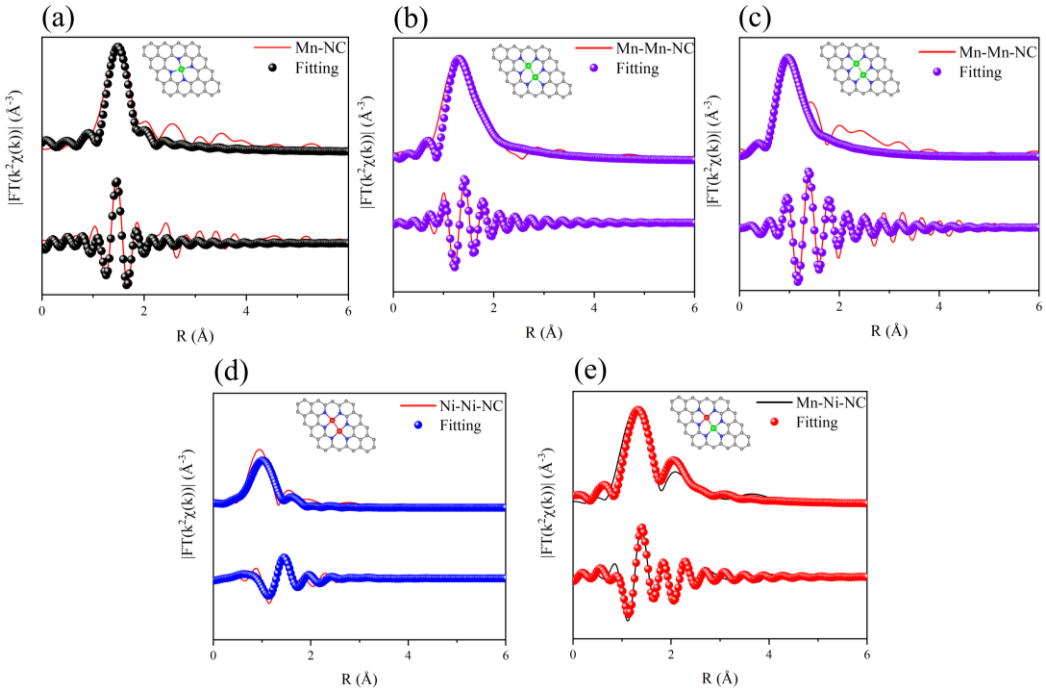

Figure S10. The ^{1}H NMR test for liquid product of Mn-Ni-NC catalyst at -0.7 V (vs. RHE).

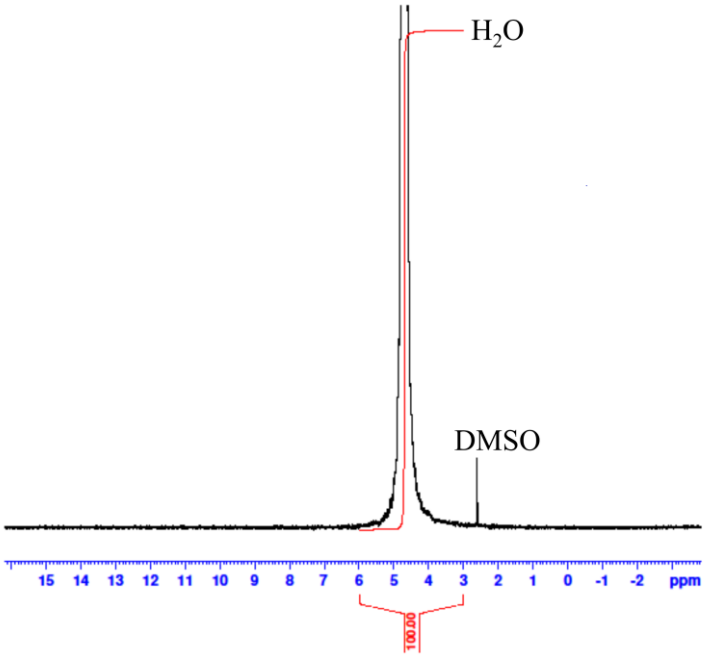

Figure S11. Cyclic voltammetry of (a) Mn-NC, (b) Ni−NC, (c)Mn-Mn-NC, (d) Ni-Ni-NC and (e) Mn-Ni-NC catalysts in CO_2-saturated 0.5 M $KHCO_3$ at various scan rates of 10, 20, 40, 60 and 80 mV/s; Cycle voltammetry was carried out between 0 and −0.2 V vs. Ag/AgCl.

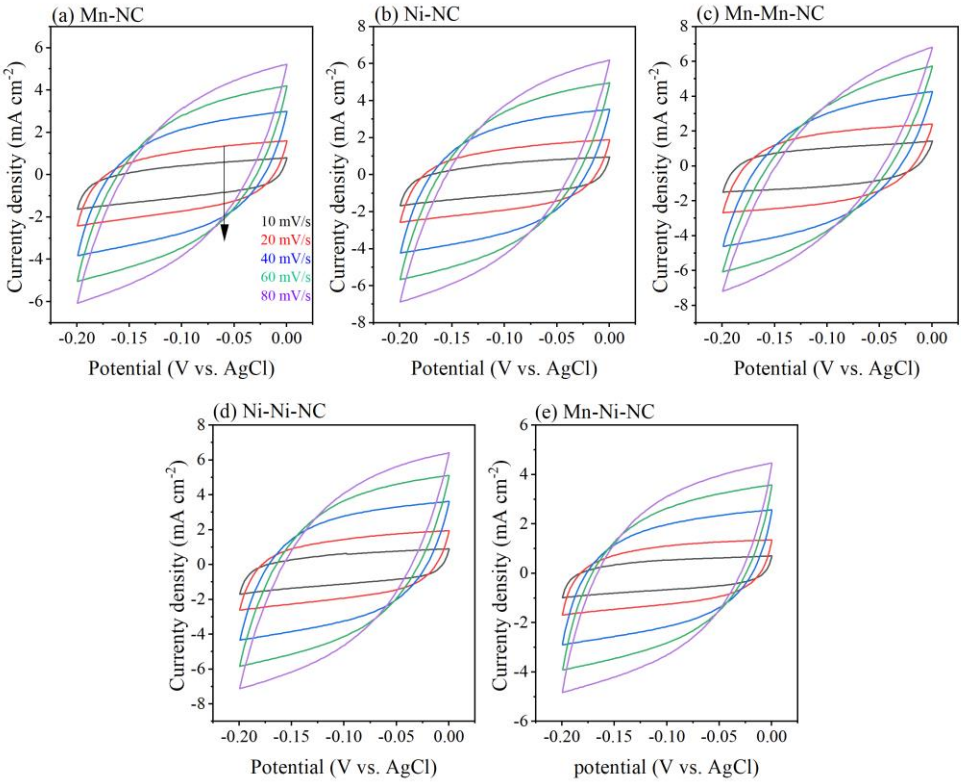

Figure S12. Nyquist plots of Mn-NC, Ni-NC, Mn-Mn-NC, Ni-Ni-NC and Mn-Ni-NC catalysts.

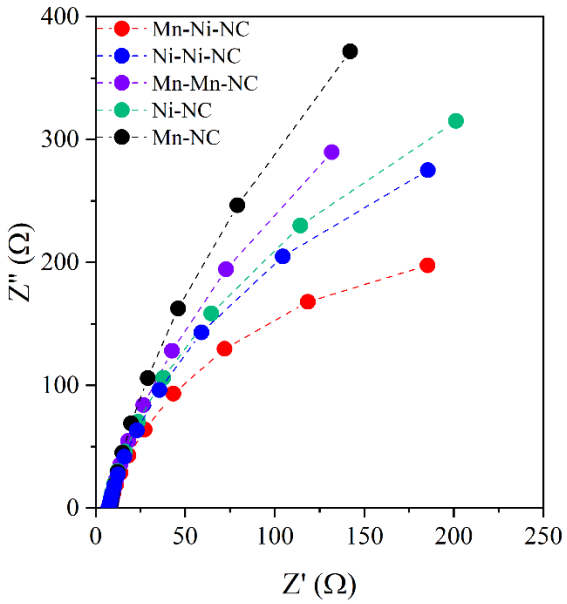

Figure S13. Charge density difference of Mn-NC, Ni-NC, Mn-Mn-NC, Ni-Ni-NC and Mn-Ni-NC catalysts, where the yellow and cyan area indicate the charge accumulation and depletion, respectively. The isosurface value is 0.0024 e/Bohr^3.

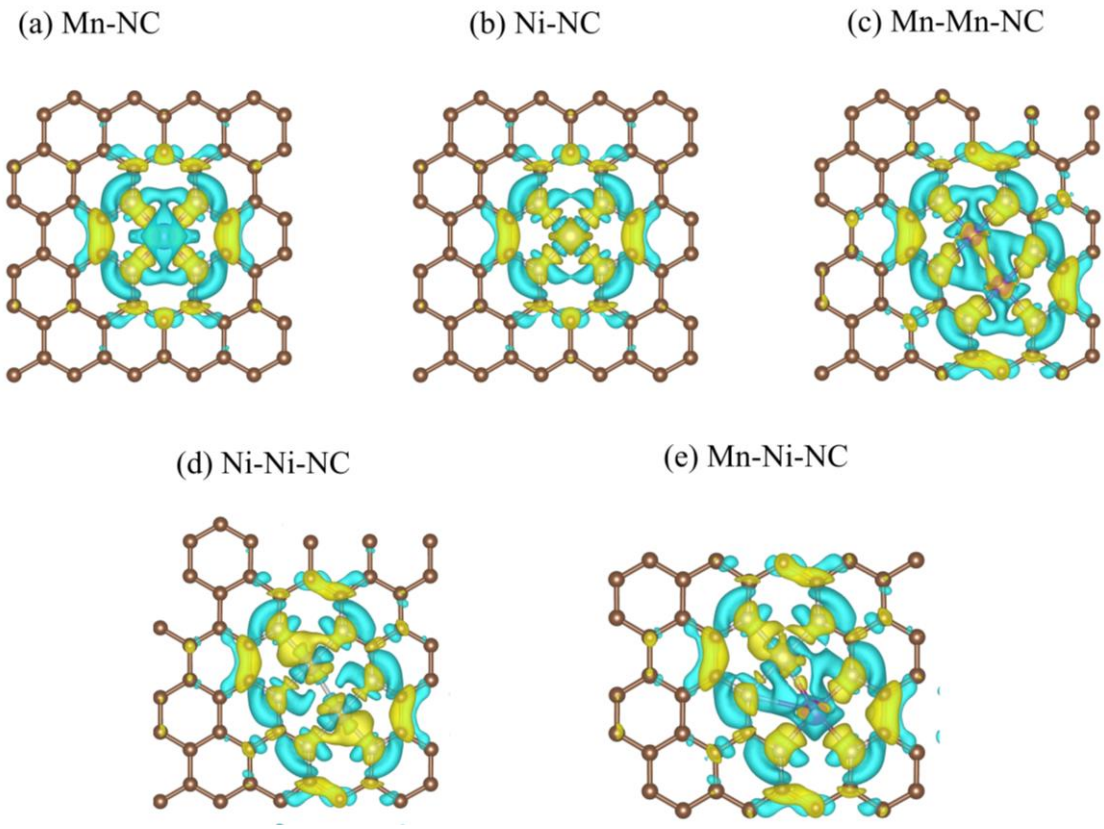

S14. Adsorption configuration of CO_2, COOH and CO on the Mn-Mn-NC and Ni-Ni-NC catalysts.

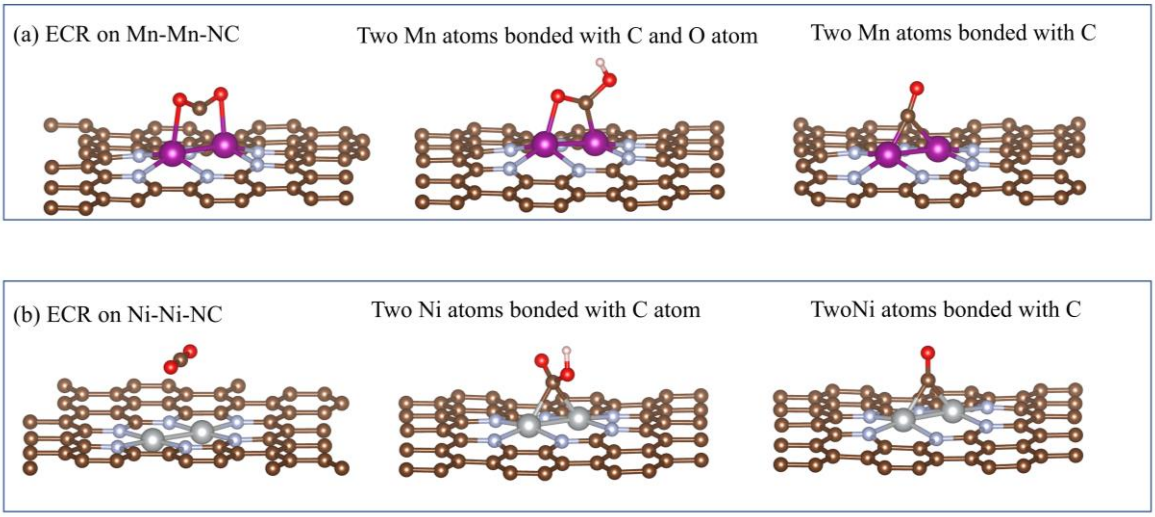

Figure S15. (a) HER free energy diagram and (b) difference in limiting potentials for ECR to CO on different catalysts.

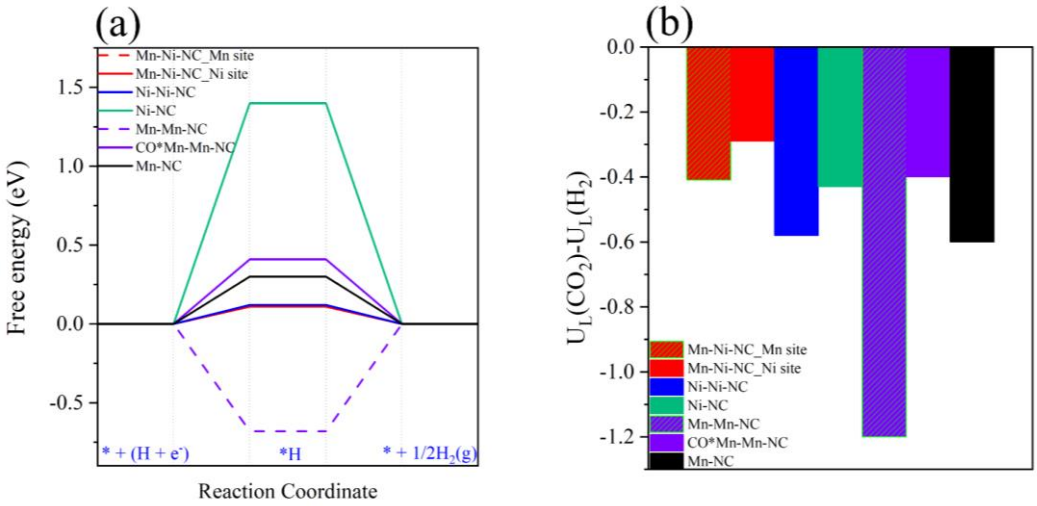

Table S1. Textural properties of different catalysts.

Electrocatalysts	BET surface area ($m^2 g^{-1}$)	Average pore diameter (nm)	Pore volume ($cm^3 g^{-1}$)
Mn-NC	890	4.92	1.02
Ni-NC	987	4.89	1.05
Mn-Mn-NC	854	4.96	1.11
Ni-Ni-NC	964	4.93	1.08
Mn-Ni-NC	935	4.88	1.02

Table S2. Concentration of Mn, Ni and N in different catalysts from XPS analysis, and the proportion of different type of N in total N concentration.

Electrocatalysts	Mn (at%)	Ni (at%)	N (at%)	Pyri-N (%)	Metal-N (%)	Pyrr-N (%)	Grap-N (%)	Oxid-N (%)
Mn-NC	0.31	0	6.06	25	19	23	23	10
Ni-NC		0.58	6.40	27	17	16	22	18
Mn-Mn-NC	0.32	0	6.23	27	21	19	14	19
Ni-Ni-NC	0	0.60	6.29	21	20	23	25	11
Mn-Ni-NC	0.25	0.38	6.85	19	30	25	13	13

Table S3. EXAFS fitting results of Mn K-edge and Ni K-edge for Mn-NC, Ni-NC, Mn-Mn-NC, Ni-Ni-NC and Mn-Ni-NC catalysts.

Samples	Shell	CN[a]	R (Å)[b]	$\triangle E_0$ (eV)[c]	σ^2 (10^{-3} Å^2)[d]	R-factor	K range	R range
Ni-NC	Ni-N	4±0.76	1.87±0.01	-8.65±1.47	8.82±2.92	0.019	1.7-10 Å^{-1}	1-3 Å
Mn-NC	Mn-N	4±0.64	1.90±0.07	-11.71±3.01	7.31±2.75	0.026	1.5-10.4 Å^{-1}	1-2 Å
Mn-Mn-NC	Mn-N	3.5±0.75	1.96±0.06	-13.29±6.01	4.75±3.33	0.024	1.7-10 Å^{-1}	1-2 Å
Ni-Ni-NC	Ni-N	3.5±0.85	1.85±0.01	-12.55±7.39	12.61±7.1	0.031	3-10 Å^{-1}	1-3 Å
Mn-Ni-NC	Mn-N	3.5±0.92	1.95±0.08	-16.56±9.56	3.24±8.51	0.021	1.6-10 Å^{-1}	1-2 Å
Mn-Ni-NC	Ni-N	3.5±0.74	1.93±0.04	-8.00±2.73	8.85±3.69	0.010	1.8-10 Å^{-1}	1-3 Å
Ni-Ni-NC	Ni-Ni	1±0.95	2.35±0.07	-6.34±5.33	19.22±9.55	0.105	1.7-9 Å^{-1}	1-2 Å
Mn-Mn-NC	Mn-Mn	1±0.97	2.40±0.25	-19.88±15.43	15.91±6.39	0.131	2.3-9 Å^{-1}	1-3 Å
Mn-Ni-NC	Mn-Ni	1±0.65	2.40±0.02	-1.99±8.56	17.73±8.80	0.016	1.7-9 Å^{-1}	1-2 Å

[a] Average coordination number for the metal atoms.
[b] Distance of N and metal atoms.
[c] Edge energy shift.
[d] Debye-Waller factor.

Table S4. Comparison of ECR performance for CO production on the Mn-Ni-NC catalyst in this work and catalysts reported in literature.

Catalysts	FE_{CO}	j_{CO} (mA cm^{-2})	Reference
Mn-Ni-NC	98.7	-16.8	This work
Co_1-N_4	82	-15.8	[9]
Ag_2-G	93.4	-11.9	[2]
Fe-NS-C	98.3	-12.1	[10]
FeN_4Cl/NC	90.5	-10.8	[11]
ZIF-NC-Fe-Ni	97.8	-7.5	[3]
Pd_2 DAC	98.2	-6.76	[12]
NiSA-NGA	90.2	-6.5	[13]
C-Fe-Co-ZIF	-8	52	[14]
Fe_1–Ni_1–N–C	-2.4	96.2	[15]
FeN5	-1.8	97	[16]
Fe–N/P–C	-2	98	[17]

Reference

1. Liu, L.X.; Zhou, Y.; Chang, Y.C.; Zhang, J.R.; Jiang, L.P.; Zhu, W.; Lin, Y. Tuning Sn_3O_4 for CO_2 reduction to formate with ultra-high current density. *Nano Energy* **2020**, *77*, 105296.

2. Li, Y.; Chen, C.; Cao, R.; Pan, Z.; He, H.; Zhou, K. Dual-atom Ag_2/graphene catalyst for efficient electroreduction of CO_2 to CO. *Appl. Catal. B: Environ.* **2020**, *268*, 118747.

3. Li, Y.; Shan, W.; Zachman, M.J.; Wang, M.; Hwang, S.; Tabassum, H.; Yang, J.; Yang, X.; Karakalos, S.; Feng, Z.; et al. Atomically Dispersed Dual-Metal Site Catalysts for Enhanced CO_2 Reduction: Mechanistic Insight into Active Site Structures. *Angew. Chem. Int. Ed.* **2022**, *61*, e202205632.

4. Blochl, P.E. Projector augmented-wave method. *Phys. Rev. B Condens. Matter.* **1994**, *50*, 17953-17979.

5. Perdew, J.P.; Burke, K.; Ernzerhof, M. Generalized Gradient Approximation Made Simple. *Phys. Rev. Lett.* **1996**, *77*, 3865.

6. Perdew, J.P.; Ernzerhof, M.; Burke, K. Rationale for mixing exact exchange with density functional approximations. *J. Chem. Phys.* **1996**, *105*, 9982-9985.

7. Grimme, S.; Antony, J.; Ehrlich, S.; Krieg, H. A consistent and accurate ab initio parametrization of density functional dispersion correction (DFT-D) for the 94 elements H-Pu. *J. Chem. Phys.* **2010**, *132*, 154104.

8. Nørskov, J. K.; Rossmeisl, J.; Logadottir, A.; Lindqvist, L.; Kitchin, J. R.; Bligaard, T.; Jónsson, H. Origin of the Overpotential for Oxygen Reduction at a Fuel-Cell Cathode. *J. Phys. Chem. B* **2004**, *108*, 17886–17892.

9. Geng, Z.; Cao, Y.; Chen, W.; Kong, X.; Liu, Y.; Yao, T.; Lin, Y. Regulating the coordination environment of Co single atoms for achieving efficient electrocatalytic activity in CO_2 reduction. *Appl. Catal. B: Environ.* **2019**, *240*, 234-240,

10. Pan, F.; Li, B.; Sarnello, E.; Hwang, S.; Gang, Y.; Feng, X.; Xiang, X.; Adli, N.M.; Li, T.; Su, D.; et al. Boosting CO_2 reduction on Fe-N-C with sulfur incorporation: Synergistic electronic and structural engineering. *Nano Energy* **2020**, *68*, 104384.

11. Li, Z.; Wu, R.; Xiao, S.; Yang, Y.; Lai, L.; Chen, J.S.; Chen, Y. Axial chlorine coordinated iron-nitrogen-carbon single-atom catalysts for efficient electrochemical CO_2 reduction. *Chem. Eng. J.* **2022**, *430*, 132882.

12. Zhang, N.; Zhang, X.; Kang, Y.; Ye, C.; Jin, R.; Yan, H.; Lin, R.; Yang, J.; Xu, Q.; Wang, Y.; et al. A Supported Pd_2 Dual-Atom Site Catalyst for Efficient Electrochemical CO_2 Reduction. *Angew. Chem. Int. Ed.* **2021**, *60*, 13388-13393.

13. Zhu, Y.P.; Guo, C.; Zheng, Y.; Qiao, S.Z. Surface and Interface Engineering of Noble-Metal-Free Electrocatalysts for Efficient Energy Conversion Processes. *Acc. Chem. Res.* **2017**, *50*, 915-923.

14. Chen, Z.; Zhang, G.; Wen, Y.; Chen, N.; Chen, W.; Regier, T.; Dynes, J.; Zheng, Y.; Sun, S. Atomically Dispersed Fe-Co Bimetallic Catalysts for the Promoted Electroreduction of Carbon Dioxide. *Nanomicro. Lett.* **2021**, *14*, 25.

15. Jiao, L.; Zhu, J.; Zhang, Y.; Yang, W.; Zhou, S.; Li, A.; Xie, C.; Zheng, X.; Zhou, W.; Yu, S.H.; et al. Non-Bonding Interaction of Neighboring Fe and Ni Single-Atom Pairs on MOF-Derived N-Doped Carbon for Enhanced CO_2 Electroreduction. *J. Am. Chem. Soc.* **2021**, *143*, 19417-19424..

16. Zhang, H.; Li, J.; Xi, S.; Du, Y.; Hai, X.; Wang, J.; Xu, H.; Wu, G.; Zhang, J.; Lu, J.; et al. A Graphene-Supported Single-Atom FeN_5 Catalytic Site for Efficient Electrochemical CO_2 Reduction. *Angew. Chem. Int. Ed.* **2019**, *58*, 14871-14876.

17. Li, K.; Zhang, S.; Zhang, X.; Liu, S.; Jiang, H.; Jiang, T.; Shen, C.; Yu, Y.; Chen, W. Atomic Tuning of Single-Atom Fe-N-C Catalysts with Phosphorus for Robust Electrochemical CO_2 Reduction. *Nano Lett.* **2022**, *22*, 1557-1565,